

IMPACT FACTOR  
**10.057**

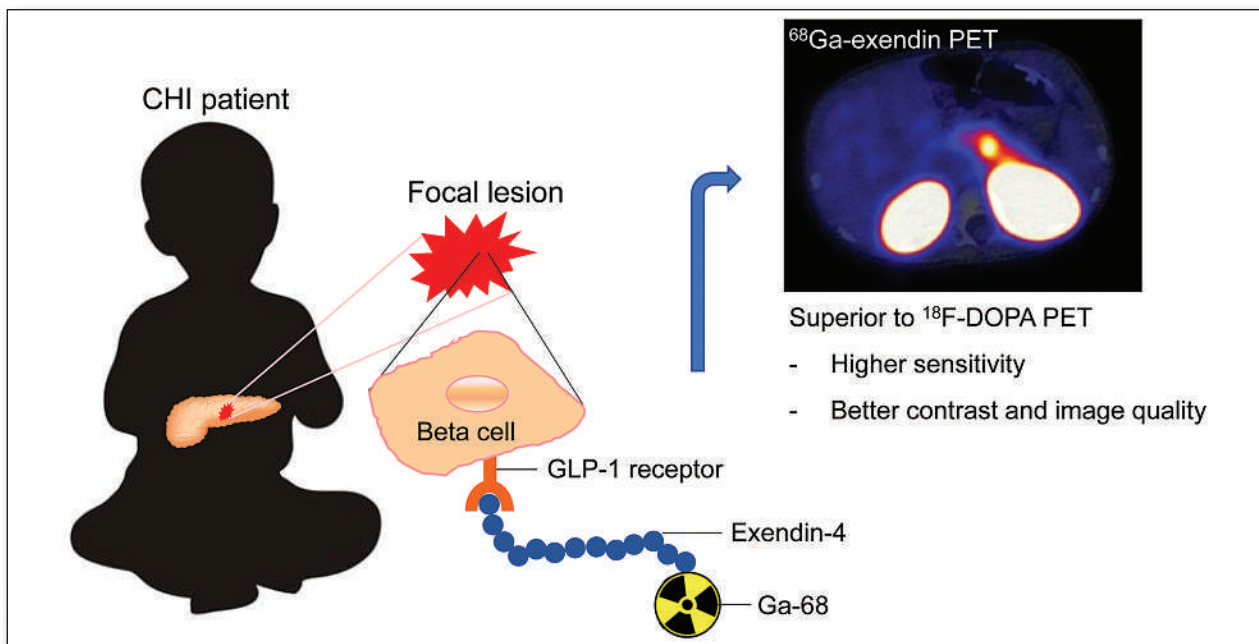
#1 NUCLEAR MEDICINE,  
MOLECULAR IMAGING AND  
MOLECULAR RADIOTHERAPY  
JOURNAL

# JNM

The Journal of Nuclear Medicine

## FEATURED ARTICLE

<sup>68</sup>Ga-NODAGA-Exendin-4 PET/CT Improves the Detection of Focal Congenital Hyperinsulinism. Marti Boss et al. See page 310.



Improved  $\alpha$ -particle emitter for prostate cancer: <sup>211</sup>At-labeled PSMA targeting with a promising clinical profile. Ronnie Mease et al. See page 259.

# SPECT

## ISN'T IT TIME TO EVOLVE YOUR CARDIAC IMAGING PROGRAM INTO A STATE-OF-THE-ART PRACTICE?

**Cardiac PET offers advanced imaging with stronger prognostic power<sup>1</sup> and shorter acquisition time.**

While SPECT maintains its relevance, *“the non-invasive gold standard for the assessment of myocardial blood flow, and coronary microvascular disease, is positron emission tomography (PET) MPI.”*<sup>2</sup> –*Journal of Nuclear Cardiology*

**RUBY™** can partner with you to help establish your cardiac PET program today – and well into the future. Our RUBY-FILL® (Rubidium Rb 82 generator) and RUBY Rubidium Elution System™ is supported by comprehensive value-added services, including reimbursement, education, and training, to ensure your department runs smoothly and efficiently.

Learn more at the **Jubilant Radiopharma booth**

### INDICATION FOR USE:

RUBY-FILL is a closed system used to produce rubidium Rb 82 chloride injection for intravenous use. Rubidium Rb 82 chloride injection is a radioactive diagnostic for Positron Emission Tomography (PET) imaging of the myocardium under rest or pharmacologic stress conditions to evaluate regional myocardial perfusion in adult patients with suspected or existing coronary artery disease. (1)

### IMPORTANT SAFETY INFORMATION:

**WARNING: HIGH LEVEL RADIATION EXPOSURE WITH USE OF INCORRECT ELUENT AND FAILURE TO FOLLOW QUALITY CONTROL TESTING PROCEDURE**

Please see full prescribing information for complete boxed warning

**High Level Radiation Exposure with Use of Incorrect Eluent**

Using the incorrect eluent can cause high Strontium (Sr 82) and (Sr 85) breakthrough levels (5.1)

- Use only additive-free 0.9% Sodium Chloride Injection USP to elute the generator (2.5)
- Immediately stop the patient infusion and discontinue the use of the affected RUBY-FILL generator if the incorrect solution is used to elute the generator (4)
- Evaluate the patient's radiation absorbed dose and monitor for the effects of radiation to critical organs such as bone marrow (2.9)

**Excess Radiation Exposure with Failure to Follow the Quality Control Testing Procedure**

Excess radiation exposure occurs when the levels of Sr 82 or Sr 85 in the Rubidium Rb 82 Chloride injection exceed specified limits (5.2)

- Strictly adhere to the generator quality control testing procedure (2.6)
- Stop using the generator if it reaches any of its Expiration Limit (2.7)

The risk information provided here is not comprehensive. Please visit [RUBY-FILL.com](http://RUBY-FILL.com) for full Prescribing Information including the **BOXED WARNING**. You are encouraged to report negative side effects of prescription drugs to the FDA. Visit [www.fda.gov/Safety/MedWatch](http://www.fda.gov/Safety/MedWatch) or call 1-800-FDA-1088.

**References:** 1. Dorbala, S, DiCarli, M, Cardiac PET perfusion: prognosis, risk stratification, and clinical management. *Semin Nucl Med.* 2014;44(5):344-357. 2. Hage FG. Is SPECT myocardial perfusion imaging on its dying bed? *J Nucl Cardiol.* 2021; in press.

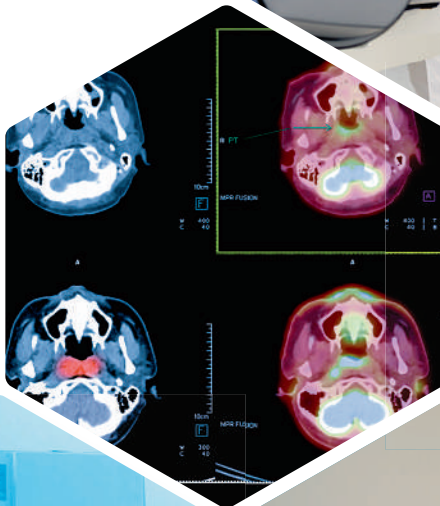


**MIRION**  
TECHNOLOGIES

# RADIATION SAFETY, EXPERTISE AND INNOVATION

Powered by an unstoppable drive for discovery. Backed by 60+ years of radiation measurement, innovation, and science expertise. Mirion's trusted family of brands and industry-leading products and services are helping to advance human health around the world.

- *Nuclear Medicine Devices*
- *Radiation Shielding and Accessories*



*Driving Innovation, Together:*



**CAPINTEC, INC.**  
Part of Mirion Technologies



**BIODESEX**  
Part of Mirion Technologies

Visit [capintec.com](http://capintec.com) to learn how we can support your unique requirements.

Mirion, the Mirion logo, and other trade names of Mirion products listed herein are registered trademarks or trademarks of Mirion Technologies, Inc. or its affiliates in the United States and other countries.



**BLUE EARTH**

D I A G N O S T I C S

A Bracco Company

# EMPOWERING THE EVOLUTION OF CARE FOR PATIENTS WITH CANCER

**Innovative solutions that transform  
clinical management and patient care**

Learn more about Blue Earth Diagnostics' innovative approach at

**[www.BlueEarthDiagnostics.com](http://www.BlueEarthDiagnostics.com)**

Blue Earth Diagnostics, a subsidiary of Bracco Imaging S.p.A., is a growing international molecular imaging company focused on developing and delivering **innovative molecular imaging technologies that inform diagnosis and treatment decisions for optimized patient outcomes.**

Formed in 2014, the company's success is driven by its management expertise and supported by a demonstrated track record of rapid development and commercialization of positron emission tomography (PET) radiopharmaceuticals. Blue Earth Diagnostics' expanding oncology portfolio encompasses a variety of disease states, including prostate cancer and neuro-oncology.

## SNMMI NEWSLINE

- 23N** Joint NIBIB/NCI/SNMMI Workshop on Directly Imaging Targeted Radionuclide Therapy Isotopes  
I. George Zubal and Jacek Capala
- 26N** DOE and HHS Certify Sufficient <sup>99</sup>Mo Supplies
- 26N** FDA Approves New <sup>68</sup>Ga Kit for Prostate Cancer PET
- 27N** SNMMI Leadership Update: SNMMI to Host Summits on Artificial Intelligence and Patient Access  
Richard L. Wahl
- 28N** Newsbriefs
- 30N** From the Literature

## DISCUSSIONS WITH LEADERS

- 169** A European Oncology Leader Looks at PSMA: A Conversation Between Silke Gillissen, Johannes Czernin, and Ken Herrmann  
Silke Gillissen, Johannes Czernin, and Ken Herrmann

## THE STATE OF THE ART

- 172** A Guide to ComBat Harmonization of Imaging Biomarkers in Multicenter Studies  
Fanny Orlhac, Jakoba J. Eertink, Anne-Ségolène Cottureau, José M. Zijlstra, Catherine Thieblemont, Michel Meignan, Ronald Boellaard, and Irène Buvat

## HOT TOPICS

- 180** Is It Too Soon to Know When It's LATE?  
Angela C. Rieger and Daniel H.S. Silverman

## FOCUS ON MOLECULAR IMAGING

- 183** Visualizing T-Cell Responses: The T-Cell PET Imaging Toolbox  
Chao Li, Chaozhe Han, Shao Duan, Ping Li, Israt S. Alam, and Zunyu Xiao

## STANDARD OF CARE

- 189** Management of Differentiated Thyroid Cancer: The Standard of Care  
Anca M. Avram, Katherine Zukotynski, Helen Ruth Nadel, and Luca Giovannella

## EDITORIAL

- 196** Managing a High-Specific-Activity Iobenguane Therapy Clinic: From Operations to Reimbursement  
Sophia R. O'Brien and Daniel A. Pryma

## ONCOLOGY

### Clinical

- 199** <sup>18</sup>F-FDG PET/CT Imaging Biomarkers for Early and Late Evaluation of Response to First-Line Chemotherapy in Patients with Pancreatic Ductal Adenocarcinoma  
Matthias R. Benz, Wesley R. Armstrong, Francesco Ceci, Giulia Polverari, Timothy R. Donahue, Zev A. Wainberg, Andrew Quon, Martin Auerbach, Mark D. Girgis, Ken Herrmann, et al.
- 205** <sup>131</sup>I-GD2-ch14.18 Scintigraphy to Evaluate Option for Radioimmunotherapy in Patients with Advanced Tumors  
Ying Zhang, Juergen Kupferschlaeger, Peter Lang, Gerald Reischl, Rupert J. Handgretinger, Christian la Fougère, and Helmut Dittmann

## THERANOSTICS

### Clinical

- 212** Detecting Fibroblast Activation Proteins in Lymphoma Using <sup>68</sup>Ga-FAPI PET/CT  
Xiao Jin, Maomao Wei, Shuailiang Wang, Guochang Wang, Yumei Lai, Yunfei Shi, Yan Zhang, Zhi Yang, and Xuejuan Wang
- 218** Efficacy and Safety of <sup>177</sup>Lu-DOTATATE in Lung Neuroendocrine Tumors: A Bicenter study  
Lamiaa Zidan, Amir Iravani, Kira Oleinikov, Simona Ben-Haim, David J. Gross, Amichay Meirovitz, Ophra Maimon, Tim Akhurst, Michael Michael, Rodney J. Hicks, et al.
- 226** Tumor Sink Effect in <sup>68</sup>Ga-PSMA-11 PET: Myth or Reality?  
Andrei Gafita, Hui Wang, Andrew Robertson, Wesley R. Armstrong, Raphael Zaum, Manuel Weber, Farid Yagubbayli, Clemens Kratochwil, Tristan R. Grogan, Kathleen Nguyen, et al.
- 233** aPROMISE: A Novel Automated PROMISE Platform to Standardize Evaluation of Tumor Burden in <sup>18</sup>F-DCFPyL Images of Veterans with Prostate Cancer  
Nicholas Nickols, Aseem Anand, Kerstin Johnsson, Johan Brynolfsson, Pablo Borrelli, Neil Parikh, Jesus Juarez, Lida Jafari, Mattias Eiber, and Matthew Rettig
- 240** Diagnostic Performance and Clinical Impact of <sup>68</sup>Ga-PSMA-11 PET/CT Imaging in Early Relapsed Prostate Cancer After Radical Therapy: A Prospective Multicenter Study (IAEA-PSMA Study)  
Juliano J. Cerci, Stefano Fanti, Enrique E. Lobato, Jolanta Kunikowska, Omar Alonso, Sebastian Medina, Fuad Novruzov, Thabo Lengana, Carlos Granados, Rakesh Kumar, et al.
- 248** ■ **BRIEF COMMUNICATION.** The European Association of Urology Biochemical Recurrence Risk Groups Predict Findings on PSMA PET in Patients with Biochemically Recurrent Prostate Cancer After Radical Prostatectomy  
Liang Dong, Yun Su, Yinjie Zhu, Mark C. Markowski, Mei Xin, Michael A. Gorin, Baijun Dong, Jiahua Pan, Martin G. Pomper, Jianjun Liu, et al.

**253** **Kidney Doses in <sup>177</sup>Lu-Based Radioligand Therapy in Prostate Cancer: Is Dose Estimation Based on Reduced Dosimetry Measurements Feasible?**

Michael Mix, Tobias Renaud, Felix Kind, Ursula Nemer, Elham Yousetzadeh-Nowsha, Tumelo C.G. Moalosi, Aymen M. Ormrane, Philipp T. Meyer, and Juri Ruf

**Basic**

- 259** ■ **FEATURED BASIC SCIENCE ARTICLE. An Improved <sup>211</sup>At-Labeled Agent for PSMA-Targeted  $\alpha$ -Therapy**  
Ronnie C. Mease, Choong Mo Kang, Vivek Kumar, Sangeeta Ray Banerjee, Il Minn, Mary Brummet, Kathleen L. Gabrielson, Yutian Feng, Andrew Park, Ana P. Kiess, et al.

**INFECTIOUS DISEASE**

**Clinical**

- 268** ■ **INVITED PERSPECTIVE. Imaging in Post-COVID Lung Disease: Does <sup>18</sup>F-FDG PET/CT Have the Key?**  
Olivier Gheysens, Leïla Belkhir, and François Jamar
- 270** ■ **BRIEF COMMUNICATION. Evolution of <sup>18</sup>F-FDG PET/CT Findings in Patients After COVID-19: An Initial Investigation**  
Andrew Thornton, Francesco Fraioli, Simon Wan, Helen S. Garthwaite, Balaji Ganeshan, Robert I. Shortman, Raymond Endozo, Stefan Vöö, Irfan Kayani, Deena Neriman, et al.
- 274** **Incidental Findings Suggestive of COVID-19 Pneumonia in Oncologic Patients Undergoing <sup>18</sup>F-FDG PET/CT Studies: Association Between Metabolic and Structural Lung Changes**  
Cristina Gamila Wakfie-Corieh, Federico Ferrando-Castagnetto, Alba María Blanes García, Marta García García-Esquinas, Aída Ortega Candil, Cristina Rodríguez Rey, María Nieves Cabrera-Martín, Ana Delgado Cano, and José Luis Carreras Delgado

**CARDIOVASCULAR**

**Clinical**

- 280** **Comparing Semiquantitative and Qualitative Methods of Vascular <sup>18</sup>F-FDG PET Activity Measurement in Large-Vessel Vasculitis**  
Himanshu R. Dashora, Joel S. Rosenblum, Kaitlin A. Quinn, Hugh Alessi, Elaine Novakovich, Babak Saboury, Mark A. Ahlman, and Peter C. Grayson

**NEUROLOGY**

**Clinical**

- 287** **Dynamic Amyloid PET: Relationships to <sup>18</sup>F-Flortaucipir Tau PET Measures**  
Fabio Raman, Yu-Hua Dean Fang, Sameera Grandhi, Charles F. Murchison, Richard E. Kennedy, John C. Morris, Parinaz Massoumzadeh, Tammie Benzinger, Erik D. Roberson, and Jonathan McConathy

**Basic**

- 294** **Relative Strengths of Three Linearizations of Receptor Availability: Saturation, Inhibition, and Occupancy Plots**  
Javad Khodaii, Mostafa Araj-Khodaie, Manouchehr S. Vafae, Dean F. Wong, and Albert Gjedde
- 302** **<sup>11</sup>C-PiB and <sup>124</sup>I-Antibody PET Provide Differing Estimates of Brain Amyloid- $\beta$  After Therapeutic Intervention**  
Silvio R. Meier, Dag Sehlin, Sahar Roshanbin, Victoria Lim Falk, Takashi Saito, Takaomi C. Saido, Ulf Neumann, Johanna Rokka, Jonas Eriksson, and Stina Syvänen

**ENDOCRINOLOGY**

**Clinical**

- 310** ■ **FEATURED ARTICLE OF THE MONTH. <sup>68</sup>Ga-NODAGA-Exendin-4 PET/CT Improves the Detection of Focal Congenital Hyperinsulinism**  
Marti Boss, Christof Rottenburger, Winfried Brenner, Oliver Blankenstein, Vikas Prasad, Sonal Prasad, Paolo de Coppi, Peter Kühnen, Mijke Buitinga, Pirjo Nuutila, et al.

**SPECIAL CONTRIBUTION**

- 316** **RADAR Guide: Standard Methods for Calculating Radiation Doses for Radiopharmaceuticals, Part 1—Collection of Data for Radiopharmaceutical Dosimetry**  
Michael G. Stabin, Richard E. Wendt, and Glenn D. Flux

**LETTERS TO THE EDITOR**

- 323** **Commercially Competitive Vendor-Agnostic Image Reconstruction Could Be a Leap Forward for PET Harmonization**  
Adam L. Kesner
- 324** **A VISION of ALSYMPCA**  
Paulo Schiavom Duarte
- 324** **Reply: A VISION of ALSYMPCA**  
Oliver Sartor
- 325** **On Semiquantitative Methods for Assessing Vascular <sup>18</sup>F-FDG PET Activity in Large-Vessel Vasculitis**  
Eric Laffon and Roger Marthan
- 326** **Reply: On Semiquantitative Methods for Assessing Vascular <sup>18</sup>F-FDG PET Activity in Large-Vessel Vasculitis**  
Mark A. Ahlman, Roberto Maass-Moreno, and Peter C. Grayson

**DEPARTMENTS**

- 10A** **This Month in JNM**
- 19A** **Recruitment**
- 252** **Erratum**

The Official Publication of **SNMMI**

## Publications Committee

TODD E. PETERSON, PhD, FSNMMI  
*Chair*

CAROLYN ANDERSON, PhD, FSNMMI  
PAIGE B. BENNETT, MD  
JOYITA DUTTA, PhD  
MICHAEL M. GRAHAM, PhD, MD, FSNMMI  
HOSSEIN JADVAR, MD, PhD, FACNM,  
FSNMMI  
STEVEN M. LARSON, MD, FACNM  
HEINRICH R. SCHELBERT, MD, PhD, FSNMMI  
HEIKO SCHÖDER, MD, MBA  
DAVID M. SCHUSTER, MD  
JESSICA WILLIAMS, CNMT, RT(N),  
FSNMMI-TS  
HARVEY A. ZIESSMAN, MD, FSNMMI

## *Ex officio*

JOHANNES CZERNIN, MD  
KATHY S. THOMAS, MHA, CNMT,  
PET, FSNMMI-TS  
HENRY F. VANBROCKLIN, PhD, FSNMMI  
RICHARD L. WAHL, MD, FACNM

## Associate Director of Communications

SUSAN ALEXANDER

## Senior Copyeditor

SUSAN NATH

## Senior Publications & Marketing Service Manager

STEVEN KLEIN

## Editorial Production Manager

PAULETTE MCGEE

## Editorial Project Manager

MARK SUMIMOTO

## Director of Communications

REBECCA MAXEY

## CEO

VIRGINIA PAPPAS

**MISSION STATEMENT:** *The Journal of Nuclear Medicine* advances the knowledge and practice of molecular imaging and therapy and nuclear medicine to improve patient care through publication of original basic science and clinical research.

*JNM* (ISSN 0161-5505 [print]; ISSN 2159-662X [online]) is published monthly by SNMMI, 1850 Samuel Morse Drive, Reston, VA 20190-5316. Periodicals postage is paid at Herndon, VA, and additional mailing offices. Postmaster, send address changes to *The Journal of Nuclear Medicine*, 1850 Samuel Morse Drive, Reston, VA 20190-5316. The costs of publication of all nonsolicited articles in *JNM* were defrayed in part by the payment of page charges. Therefore, and solely to indicate this fact, these articles are hereby designated "advertisements" in accordance with 18 USC section 1734.

**DISCLOSURE OF COMMERCIAL INTEREST:** Johannes Czernin, MD, editor-in-chief of *The Journal of Nuclear Medicine*, has indicated that he is a founder of Sofie Biosciences and holds equity in the company and in intellectual property invented by him, patented by the University of California, and licensed to Sofie Biosciences. He is also a founder and board member of Trethera Therapeutics and holds equity in the company and in intellectual property invented by him, patented by the University of California, and licensed to Triangle. He also serves on the medical advisory board of Actinium Pharmaceuticals and on the scientific advisory boards of POINT Biopharma, RayzeBio, and Jubilant Pharma and is a consultant for Amgen. No other potential conflicts of interest were reported. Manuscripts submitted to *JNM* with potential conflicts are handled by a guest editor.

**EDITORIAL COMMUNICATIONS** should be sent to: Editor-in-Chief, Johannes Czernin, MD, *JNM* Office, SNMMI, 1850 Samuel Morse Drive, Reston, VA 20190-5316. Phone: (703) 326-1185; Fax: (703) 708-9018. To submit a manuscript, go to <https://submit-jnm.snmjournals.org>.

**BUSINESS COMMUNICATIONS** concerning permission requests should be sent to the publisher, SNMMI, 1850 Samuel Morse Drive, Reston, VA 20190-5316; (703) 708-9000; home page address: [jnm.snmjournals.org](http://jnm.snmjournals.org). Subscription requests and address changes should be sent to Membership Department, SNMMI at the address above. Notify the Society of change of address and telephone number at least 30 days before date of issue by sending both the old and new addresses. Claims for copies lost in the mail are allowed within 90 days of the date of issue. Claims are not allowed for issues lost as a result of insufficient notice of change of address. For information on advertising, contact Team SNMMI (Kevin Dunn, Rich Devanna, and Charlie Meitner; (201) 767-4170; fax: (201) 767-8065; [TeamSNMMI@cunnasso.com](mailto:TeamSNMMI@cunnasso.com)). Advertisements are subject to editorial approval and are restricted to products or services pertinent to nuclear medicine. Closing date is the first of the month preceding the date of issue.

**INDIVIDUAL SUBSCRIPTION RATES** for the 2022 calendar year are \$603 within the United States and Canada; \$648 elsewhere. Make checks payable to the SNMMI. CPC IPM Sales Agreement No. 1415158. Sales of individual back copies from 1999 through the current issue are available for \$60 at <http://www.snmgi.org/subscribe> ([subscriptions@snmgi.org](mailto:subscriptions@snmgi.org); fax: (703) 667-5134). Individual articles are available for sale online at <http://jnm.snmjournals.org>.

COPYRIGHT © 2022 by the Society of Nuclear Medicine and Molecular Imaging. All rights reserved. No part of this work may be reproduced or translated without permission from the copyright owner. Individuals with inquiries regarding permission requests, please visit <http://jnm.snmjournals.org/site/misc/permission.xhtml>. Because the copyright on articles published in *The Journal of Nuclear Medicine* is held by the Society, each author of accepted manuscripts must sign a statement transferring copyright (available for downloading at <http://jnm.snmjournals.org/site/misc/ifora.xhtml>). See Information for Authors for further explanation (available for downloading at <http://www.snmjournals.org/site/misc/ifora.xhtml>).

The ideas and opinions expressed in *JNM* do not necessarily reflect those of the SNMMI or the Editors of *JNM* unless so stated. Publication of an advertisement or other product mentioned in *JNM* should not be construed as an endorsement of the product or the manufacturer's claims. Readers are encouraged to contact the manufacturer with any questions about the features or limitations of the products mentioned. The SNMMI does not assume any responsibility for any injury or damage to persons or property arising from or related to any use of the material contained in this journal. The reader is advised to check the appropriate medical literature and the product information currently provided by the manufacturer of each drug to be administered to verify the dosage, the method and duration of administration, and contraindications.

## EDITOR-IN-CHIEF

**Johannes Czernin, MD**  
University of California at Los Angeles  
Los Angeles, California

## IMMEDIATE PAST EDITOR

**Dominique Delbeke, MD, PhD**  
Vanderbilt University Medical Center  
Nashville, Tennessee

## NEWSLINE EDITOR

**Harvey A. Ziessman, MD**  
Takoma Park, Maryland

## ASSOCIATE EDITORS, CONTINUING EDUCATION

**Heiko Schöder, MD**  
Memorial Sloan Kettering Cancer Center  
New York, New York

**H. William Strauss, MD**  
Memorial Sloan Kettering Cancer Center  
New York, New York

## ASSOCIATE EDITORS

**Ramsey Derek Badawi, PhD**  
UC Davis Medical Center  
Sacramento, California

**Henryk Barthel, MD, PhD**  
Leipzig University  
Leipzig, Germany

**Frank M. Bengel, MD**  
Hannover Medical School  
Hannover, Germany

**Lisa Bodei, MD, PhD**  
Memorial Sloan Kettering Cancer Center  
New York, New York

**Irene Buvat, PhD**  
Université Paris Sud  
Orsay, France

**Jérémie Calais, MD**  
University of California at Los Angeles  
Los Angeles, California

**Marcelo F. Di Carli, MD**  
Brigham and Women's Hospital  
Boston, Massachusetts

**Alexander E. Drzezga**  
University Hospital of Cologne  
Cologne, Germany

**Jan Grimm, MD, PhD**  
Memorial Sloan Kettering Cancer Center  
New York, New York

**Ken Herrmann, MD, MBA**  
Universitätsklinikum Essen  
Essen, Germany

**Lale Kostakoglu, MD, MPH**  
University of Virginia Health System  
Charlottesville, Virginia

**Jason S. Lewis, PhD**  
Memorial Sloan Kettering Cancer Center  
New York, New York

**David A. Mankoff, MD, PhD**  
University of Pennsylvania  
Philadelphia, Pennsylvania

**Wolfgang Weber, MD**  
Technical University of Munich  
München, Germany

## SERIES EDITOR, FOCUS ON MI

**Carolyn J. Anderson, PhD**  
University of Missouri  
Columbia, Missouri

## SERIES EDITOR, HOT TOPICS

**Heinrich R. Schelbert, MD, PhD**  
University of California at Los Angeles  
Los Angeles, California

## CONSULTING EDITORS

**Nancy Knight, PhD**  
University of Maryland School of Medicine  
Baltimore, Maryland

**Barry A. Siegel, MD**  
Mallinckrodt Institute of Radiology  
St. Louis, Missouri

**Arnold M. Strashun, MD**  
SUNY Downstate Medical Center  
Scarsdale, New York

## ASSOCIATE EDITORS (INTERNATIONAL)

**Gerald Antoch, MD**  
Dusseldorf, Germany

**Richard P. Baum, MD, PhD**

Bad Berka, Germany  
**Ambros J. Beer, MD**  
Ulm, Germany

**Francois Benard, MD**  
Vancouver, Canada

**Thomas Beyer, PhD**  
Vienna, Austria

**Andreas K. Buck, MD**  
Würzburg, Germany

**Ignasi Carrió, MD**  
Barcelona, Spain

**June-Key Chung, MD**  
Seoul, Korea

**Stefano Fanti, MD**  
Bologna, Italy

**Markus Hacker, MD**  
Wien, Austria

**Rodney J. Hicks, MD**  
Melbourne, Australia

**Michael S. Hofman, MBBS**  
Melbourne, Australia

**Ora Israel, MD**  
Haifa, Israel

**Andreas Kjaer, MD, PhD, DMSc**  
Copenhagen, Denmark

**Adriaan A. Lammertsma, PhD**  
Amsterdam, The Netherlands

**Michael Lassman, PhD**  
Würzburg, Germany

**Helmut R. Mäcke, PhD**  
Freiburg, Germany

**Wim J.G. Oyen, MD, PhD**  
Milan, Italy

**John O. Prior, MD, PhD**  
Lausanne, Switzerland

**Osman Ratib, MD, PhD**  
Geneva, Switzerland

**Mike Sathekge, MChB, MMed, PhD**  
Pretoria, South Africa

**Markus Schwaiger, MD**  
München, Germany

**Andrew M. Scott, MD**  
Heidelberg, Australia

**Nagara Tamaki, MD, PhD**  
Kyoto, Japan

**Jia-He Tian, PhD**  
Beijing, China

**Mei Tian, MD, PhD**  
Hangzhou, China

**EDITORIAL CONSULTANTS**

**Martin S. Allen-Auerbach, MD**  
Los Angeles, California

**Magnus Dahlbom, PhD**  
Los Angeles, California

**Andrew Quon, MD**  
Los Angeles, California

**Christiaan Schiepers, MD, PhD**  
Los Angeles, California

**Daniel H. Silverman, MD, PhD**  
Los Angeles, California

**Roger Slavik, PhD**  
Winterthur, Switzerland

## EDITORIAL BOARD

**Diane S. Abou, PhD**  
St. Louis, Missouri

**Valentina Ambrosini, MD, PhD**  
Bologna, Italy

**Norbert Avril, MD**  
Cleveland, Ohio

**Shadfar Bahri**  
Los Angeles, California

**Jacques Barbet, PhD**  
Saint-Herbalin, France

**Bradley Jay Beattie, PhD**  
New York, New York

**Matthias Richard Benz, MD**  
Los Angeles, California

**Pradeep Bhambhvani, MD**  
Birmingham, Alabama

**Angelika Bischof-Delaloye, MD**  
Lausanne, Switzerland

**Christina Bluemel, MD**  
Würzburg, Germany

**Ronald Boellaard, PhD**

Groningen, The Netherlands

**Nicolaas Bohnen, MD**  
Ann Arbor, Michigan

**Wesley E. Bolch, PhD**  
Gainesville, Florida

**Elias H. Botvinick, MD**  
San Francisco, California

**Winfried Brenner, MD, PhD**  
Berlin, Germany

**Richard C. Brunken, MD**  
Cleveland, Ohio

**Ralph Buchert, PhD**  
Hamburg, Germany

**Alfred Buck, MD**  
Menzingen, Switzerland

**Denis B. Buxton, PhD**  
Bethesda, Maryland

**Weibo Cai, PhD**  
Madison, Wisconsin

**Federico Caobelli, MD**  
Basel, Switzerland

**Giuseppe Carlucci, PhD**  
Los Angeles, California

**Richard E. Carson, PhD**  
New Haven, Connecticut

**Paolo Castellucci, MD**  
Bologna, Italy

**Francesco Ceci, MD, PhD**  
Turin, Italy

**Juliano J. Cerci**  
Curitiba, Brazil

**Delphine Chen, MD**  
Seattle, Washington

**Xiaoyuan Chen, PhD**  
Singapore

**Simon R. Cherry**  
Davis, California

**Arturo Chiti, MD**  
Rozzano, Italy

**Peter M. Clark, PhD**  
Los Angeles, California

**Christian Cohade, MD**  
Montreal, Canada

**Ekaterina (Kate) Dadachova, PhD**  
Saskatoon, Canada

**Issa J. Dahabreh, MD**  
Boston, Massachusetts

**Heike Elisabeth Daldrop-Link, MD, PhD**  
Stanford, California

**Farrokh Dehdashti, MD**  
St. Louis, Missouri

**Robert C. Delgado-Bolton, MD, PhD**  
Logroño, Spain

**Thorsten Derlin, MD**  
Hannover, Germany

**Elisabeth G.E. de Vries, PhD**  
Groningen, The Netherlands

**David W. Dick, PhD**  
Iowa City, Iowa

**Vasken Dilisizian, MD**  
Baltimore, Maryland

**Sharmila Dorbala, MBBS**  
Lexington, Massachusetts

**Jacob Dubroff, MD, PhD**  
Philadelphia, Pennsylvania

**Janet F. Eary, MD**  
Bethesda, Maryland

**W. Barry Edwards, PhD**  
Columbia, Missouri

**Matthias Eiber, MD**  
Munich, Germany

**David Eidelberg, MD**  
Manhasset, New York

**Georges El Fakhri, PhD**  
Boston, Massachusetts

**Peter J. Ell, MD**  
London, United Kingdom

**Keigo Endo, MD**  
Nantan, Japan

**Einat Even-Sapir, MD, PhD**  
Tel Aviv, Israel

**Frederic H. Fahey, DSc**  
Boston, Massachusetts



# Your Success is our Success



The individuals who appear are for illustrative purposes. All persons depicted are models and not real patients or healthcare professionals.

## We are **Cardiac PET**™

Since 1989, Bracco has been committed to cardiac PET and patient care through our unparalleled support.

- An extensive team of **accessible, locally-based** experts stand ready to support you and your staff.
- Exclusive, **customized business case tools** help ensure you meet your financial goals.
- Drive clinical and operational excellence in your organization with Bracco's **peer-to-peer support** program.
- Ongoing, **complimentary clinical training** at your facility keeps your staff at its best.
- Bracco supports the business side of your practice with **personalized reimbursement training** and updates.
- **Bracco Mobile Isotope Service** makes starting your cardiac PET imaging program easier with flexible, customized delivery options.

**Tap into the expertise that more than 30 years in nuclear cardiology brings.**

Learn more at [www.wearecardiacpet.com](http://www.wearecardiacpet.com) or talk with your Bracco representative at **1-877-BRACCO-9 (1-877-272-2269)**

Bracco Diagnostics Inc.  
259 Prospect Plains Road, Building H  
Monroe Township, NJ 08831 USA  
Phone: 609-514-2200  
Toll Free: 1-877-272-2269 (U.S. only)  
Fax: 609-514-2446

©2021 Bracco Diagnostics Inc. All Rights Reserved.

Committed to Science,  
Committed to You™



**EDITORIAL BOARD, continued**

**Melpomeni Fani, PhD, MSc**  
Basel, Switzerland

**Wolfgang Peter Fendler, MD**  
Essen, Germany

**James W. Fletcher, MD**  
Indianapolis, Indiana

**Amy M. Fowler, MD, PhD**  
Madison, Wisconsin

**Kirk A. Frey, MD, PhD**  
Ann Arbor, Michigan

**Andrei Gafita**  
Los Angeles, California

**Victor H. Gerbaudo, PhD, MSHCA**  
Boston, Massachusetts

**Frederik L. Giesel, MD, PhD, MBA**  
Düsseldorf, Germany

**Serge Goldman, MD, PhD**  
Brussels, Belgium

**Stanley J. Goldsmith, MD**  
New York, New York

**Martin Gotthardt, MD, PhD**  
Nijmegen, The Netherlands

**Michael Graham, MD, PhD**  
Iowa City, Iowa

**David Groheux, MD, PhD**  
Paris, France

**Uwe A. Haberkorn, MD**  
Heidelberg, Germany

**Mathieu Hatt, PhD, HDR**  
Brest, France

**Wolf-Dieter Heiss, MD**  
Cologne, Germany

**Karl Herholz, MD**  
Manchester, United Kingdom

**Thomas F. Heston, MD**  
Las Vegas, Nevada

**John M. Hoffman, MD**  
Salt Lake City, Utah

**Carl K. Hoh, MD**  
San Diego, California

**Jason P. Holland, DPhil**  
Zurich, Switzerland

**Thomas A. Hope, MD**  
San Francisco, California

**Roland Hustinx, MD, PhD**  
Liege, Belgium

**Andrei H. Iagaru, MD**  
Stanford, California

**Masanori Ichise, MD**  
Chiba, Japan

**Heather A. Jacene, MD**  
Boston, Massachusetts

**Hossein Jadvar, MD, PhD, MPH, MBA**  
Los Angeles, California

**Francois Jamar, MD, PhD**  
Brussels, Belgium

**Jae Min Jeong, PhD**  
Seoul, Korea

**John A. Katzenellenbogen, PhD**  
Urbana, Illinois

**Kimberly A. Kelly, PhD**  
Charlottesville, Virginia

**Laura M. Kenny, MD, PhD**  
London, United Kingdom

**Fabian Kiessling, MD**  
Aachen, Germany

**E. Edmund Kim, MD, MS**  
Orange, California

**Francoise Kraeber-Bodéré, MD, PhD**  
Nantes, France

**Clemens Kratochwil, MD**  
Heidelberg, Germany

**Kenneth A. Krohn, PhD**  
Portland, Oregon

**Brenda F. Kurland, PhD**  
Pittsburgh, Pennsylvania

**Constantin Lapa, MD**  
Augsburg, Germany

**Suzanne E. Lapi, PhD**  
Birmingham, Alabama

**Steven M. Larson, MD**  
New York, New York

**Dong Soo Lee, MD, PhD**  
Seoul, Korea

**Jeffrey Leyton, PhD**  
Sherbrooke, Canada

**Hannah M. Linden, MD**  
Seattle, Washington

**Martin A. Lodge, PhD**  
Baltimore, Maryland

**Egesta Lopci, MD, PhD**  
Milan, Italy

**Katharina Lückeroth, PhD**  
Los Angeles, California

**Susanne Lütje, MD, PhD**  
Bonn, Germany

**Umar Mahmood, MD, PhD**  
Boston, Massachusetts

**H. Charles Manning, PhD**  
Nashville, Tennessee

**Giuliano Mariani, MD**  
Pisa, Italy

**Chester A. Mathis, PhD**  
Pittsburgh, Pennsylvania

**Alan H. Maurer, MD**  
Philadelphia, Pennsylvania

**Jonathan McConathy, MD, PhD**  
Birmingham, Alabama

**Alexander J.B. McEwan, MD**  
Edmonton, Canada

**Yusuf Menda, MD**  
Iowa City, Iowa

**Philipp T. Meyer, MD, PhD**  
Freiburg, Germany

**Matthias Miederer, MD**  
Mainz, Germany

**Erik Mittra, MD, PhD**  
Portland, Oregon

**Christine E. Mona, PhD**  
Los Angeles, California

**Dae Hyuk Moon, MD**  
Seoul, Korea

**Jennifer Murphy, PhD**  
Los Angeles, California

**Helen Nadel, MD, FRCPC**  
Stanford, California

**Matthias Nahrendorf, MD, PhD**  
Boston, Massachusetts

**Yuji Nakamoto, MD, PhD**  
Kyoto, Japan

**David A. Nathanson, PhD**  
Los Angeles, California

**Sridhar Nimmagadda, PhD**  
Baltimore, Maryland

**Egbert U. Nitzsche, MD**  
Aarau, Switzerland

**Medhat M. Osman, MD, PhD**  
Saint Louis, Missouri

**Christopher J. Palestro, MD**  
New Hyde Park, New York

**Miguel Hernandez Pampaloni, MD, PhD**  
San Francisco, California

**Neeta Pandit-Taskar, MD**  
New York, New York

**Michael E. Phelps, PhD**  
Los Angeles, California

**Gerold Porenta, MD, PhD**  
Vienna, Austria

**Sophie Poty, PhD**  
Montpellier, France

**Edwin (Chuck) Pratt, PhD, MS Eng**  
New York, New York

**Daniel A. Pryma, MD**  
Philadelphia, Pennsylvania

**Valery Radchenko, PhD**  
Vancouver, Canada

**Caius G. Radu, MD**  
Los Angeles, California

**Isabel Rauscher, MD**  
Munich, Germany

**Nick S. Reed, MBBS**  
Glasgow, United Kingdom

**Mark Rijpkema, PhD**  
Nijmegen, The Netherlands

**Steven P. Rowe, MD, PhD**  
Baltimore, Maryland

**Mehran Sadeghi, MD**  
West Haven, Connecticut

**Orazio Schillaci, MD**  
Rome, Italy

**Charles Ross Schmidlein, PhD**  
New York, New York

**David M. Schuster, MD**  
Atlanta, Georgia

**Travis Shaffer, PhD**  
Stanford, California

**Sai Kiran Sharma, PhD**  
New York, New York

**Anthony F. Shields, MD, PhD**  
Detroit, Michigan

**Barry L. Shulkin, MD, MBA**  
Memphis, Tennessee

**Yu Shyr, PhD**  
Nashville, Tennessee

**Albert J. Sinusas, MD**  
New Haven, Connecticut

**Riemer H.J.A. Slart, MD, PhD**  
Groningen, The Netherlands

**Piotr Slomka, PhD, FACC**  
Los Angeles, California

**Ida Sonni, MD**  
Los Angeles, California

**Michael G. Stabin, PhD**  
Richland, Washington

**Lisa J. States, MD**  
Philadelphia, Pennsylvania

**Sven-Erik Strand, PhD**  
Lund, Sweden

**Rathan M. Subramaniam, MD, PhD, MPH**  
Dunedin, New Zealand

**John Sunderland, PhD**  
Iowa City, Iowa

**Suleman Surti, PhD**  
Philadelphia, Pennsylvania

**Julie Sutcliffe, PhD**  
Sacramento, California

**Laura H. Tang, MD, PhD**  
New York, New York

**Ukihide Tateishi, MD, PhD**  
Tokyo, Japan

**James T. Thackeray, PhD**  
Hannover, Germany

**Mathew L. Thakur, PhD**  
Philadelphia, Pennsylvania

**Alexander Thiel, MD**  
Montreal, Canada

**Daniel L.J. Thorek, PhD**  
St. Louis, Missouri

**David W. Townsend, PhD**  
Singapore

**Timothy Turkington, PhD**  
Durham, North Carolina

**Gary A. Ulaner, MD, PhD**  
Irvine, California

**David Ulmert, MD, PhD**  
Los Angeles, California

**Christopher H. van Dyck, MD**  
New Haven, Connecticut

**Douglas Van Nostrand, MD**  
Washington, District of Columbia

**Patrick Veit-Haibach, MD**  
Toronto, Canada

**Nerissa Viola-Villegas, PhD**  
Detroit, Michigan

**John R. Votaw, PhD**  
Atlanta, Georgia

**Richard L. Wahl, MD**  
St. Louis, Missouri

**Anne Marie Wallace, MD**  
La Jolla, California

**Martin A. Walter, MD**  
Geneva, Switzerland

**Rudolf A. Werner, MD**  
Wuerzburg, Germany

**Andreas G. Wibmer, MD**  
New York, New York

**Anna M. Wu, PhD**  
Duarte, California

**Randy Yeh, MD**  
New York, New York

**Hyewon (Helen) Youn, PhD**  
Seoul, Korea

**Pat B. Zanzonico, PhD**  
New York, New York

**Brian M. Zeglis, PhD**  
New York, New York

**Robert Zeiser, MD**  
Freiburg, Germany

**Hong Zhang, MD, PhD**  
Hangzhou, China

**Hongming Zhuang, MD, PhD**  
Philadelphia, Pennsylvania

**Sibylle I. Ziegler, PhD**  
Munich, Germany

**ASSISTANT TO THE EDITOR**  
**Joshua N. Wachtel**  
Los Angeles, California



Achieve the True Mark of  
**Quality & Safety**  
for Your Facility with IAC

A leader in accreditation for 30 years and counting, **IAC accreditation clearly indicates a 'seal of approval'** to current and prospective patients — proof that the facility has undergone a rigorous evaluation, by clinical experts, of all aspects of the operations deemed relevant to providing quality patient care.

IAC's quality solutions and resources provide facilities with a foundation to create and achieve realistic patient care goals:



The **IAC Quality Improvement (QI) Tool** allows facilities to assess their case studies and final reports, receive a quantitative report targeting opportunities for continuous improvement and satisfy a component of the MIPS Improvement Activity score.



Free access to the IAC **Online Accreditation** application including the capability to upload cases to a HIPAA-compliant, secure medical image sharing service. Trained, clinical staff are dedicated to guiding you through the process via phone, live chat or e-mail.



The IAC website offers **helpful resources** including a robust calendar of CE courses and free access to live special topic webinars, accreditation webinars and webcasts offering CE credit. Plus sample and guidance documents, accreditation checklist and more!

What can **IAC accreditation** do for *your* facility?

VASCULAR TESTING  
ECHOCARDIOGRAPHY  
NUCLEAR/PET  
MRI . CT . DENTAL CT



CAROTID STENTING  
VEIN CENTER  
CARDIAC ELECTROPHYSIOLOGY  
CARDIOVASCULAR CATHETERIZATION

**Discussions with leaders:** *JNM* editor-in-chief Johannes Czernin, with Ken Herrmann, continues a series of interviews with leaders in nuclear and molecular imaging and therapy with a conversation with Silke Gillissen, an internationally recognized European oncologist. . . . . **Page 169**

**ComBat harmonization guide:** Orhac and colleagues explain and illustrate with practical examples the use of the ComBat method for harmonization and reduction of imaging “scanner effects” on biomarker values in multicenter studies. . . . . **Page 172**

**Evaluating LATE:** Reiger and Silverman offer commentary on the challenges of differential diagnoses of dementia-related proteinopathy disorders, particularly those associated with frontotemporal lobar degeneration, amyotrophic lateral sclerosis, and limbic-predominant age-related TDP-43 encephalopathy (LATE). . . . . **Page 180**

**T-cell PET imaging toolbox:** Li and colleagues provide a state-of-the-art overview of the applications of T-cell PET imaging and its potential to improve clinical management of cancer immunotherapy and T-cell-driven diseases. . . . . **Page 183**

**Thyroid cancer standard of care:** Avram and colleagues summarize the essential information needed for multidisciplinary management of differentiated thyroid cancer, emphasizing individualization of  $^{131}\text{I}$  therapy based on risk of tumor recurrence. . . . . **Page 189**

**Managing a  $^{131}\text{I}$ -MIBG therapy clinic:** O’Brien and Pryma discuss the operational aspects of clinical implementation and use of high-specific-activity  $^{131}\text{I}$ -MIBG in patients with advanced pheochromocytoma/paraganglioma, including observations from a decade of personal experience. . . . . **Page 196**

**Imaging biomarkers in PDAC:** Benz and colleagues assess  $^{18}\text{F}$ -FDG PET/CT as an early and late interim imaging biomarker in patients with pancreatic ductal adenocarcinoma who undergo first-line systemic therapy. **Page 199**

**$^{131}\text{I}$ -GD2 scintigraphy before RIT:** Zhang and colleagues assess tumor targeting and biodistribution of a  $^{131}\text{I}$ -labeled chimeric GD2-antibody clone 14/18 in patients with late-stage neuroblastoma, sarcoma, pheochromocytoma, or neuroendocrine tumors to identify eligibility for radioimmunotherapy. **Page 205**

**$^{68}\text{Ga}$ -FAPI PET/CT in lymphoma:** Jin and colleagues profile fibroblast activation proteins in different subtypes of lymphomas and explore the potential utility of  $^{68}\text{Ga}$ -FAPI PET/CT in characterizing lesions and extent of disease. . . . . **Page 212**

**$^{177}\text{Lu}$ -DOTATATE in lung NETs:** Zidan and colleagues report on the efficacy and safety of  $^{177}\text{Lu}$ -DOTATATE in patients with somatostatin receptor-positive lung neuroendocrine tumors. . . . . **Page 218**

**Tumor sink effect in PSMA PET:** Gafita and colleagues determine in an international, multicenter study the impact of tumor burden on  $^{68}\text{Ga}$ -PSMA-11 PET biodistribution using quantitative measurements. . . . . **Page 226**

**aPROMISE standardized PSMA analysis:** Nickols and colleagues introduce an automated platform to extend the Prostate Cancer Molecular Imaging Standardized Evaluation criteria in  $^{18}\text{F}$ -DCFPyL PET/CT imaging in patients with prostate cancer. . . . . **Page 233**

**PSMA PET/CT IAEA study:** Cerci and an international consortium of researchers report on a prospective multicenter study evaluating the diagnostic performance and clinical impact of PSMA-based PET/CT in biochemical recurrence of prostate cancer. . . . . **Page 240**

**EAU BCR risk groups and PSMA PET:** Dong and colleagues identify associations between PSMA-targeted PET/CT findings and European Association of Urology-defined risk stratification for biochemical recurrence in prostate cancer. . . . . **Page 248**

**Dose estimation in RLT:** Mix and colleagues investigate the value of pretherapeutic kidney function and post-first-cycle dosimetry in predicting cumulative dose at the end of PSMA-based radioligand therapy in prostate cancer. . . . . **Page 253**

**$^{211}\text{At}$ -labeled therapy for prostate cancer:** Mease and colleagues detail synthesis of and initial preclinical investigations with a new  $^{211}\text{At}$ -labeled radiotracer targeting PSMA in prostate cancer. . . . . **Page 259**

**Post-COVID PET/CT in lung disease:** Gheysens and colleagues look at current experience and limited data on the value of  $^{18}\text{F}$ -FDG PET/CT in COVID-19 lung disease sequelae and preview related articles in this issue of *JNM*. . . . . **Page 268**

**PET/CT findings after COVID-19:** Thornton and colleagues describe experience with the temporal evolution of pulmonary  $^{18}\text{F}$ -FDG uptake in patients with COVID-19 and post-COVID-19 lung disease. . . . . **Page 270**

**COVID-19 PET and CT lung changes:** Wakfie-Corieh and colleagues explore the potential added diagnostic value of  $^{18}\text{F}$ -FDG PET/CT in asymptomatic cancer patients with suspected COVID-19 pneumonia by investigating associations between metabolic and structural changes in lung parenchyma. . . . . **Page 274**

**$^{18}\text{F}$ -FDG PET in vasculitis:** Dashora and colleagues evaluate the performance of qualitative and semiquantitative scoring methods for  $^{18}\text{F}$ -FDG PET assessment in images from patients with large-vessel vasculitis. . . . . **Page 280**

**Hippocampal eFAP and tau PET:** Raman and colleagues investigate whether early-frame amyloid PET correlates with the presence of tau pathology in a study group of amyloid-positive and -negative patients. . . . . **Page 287**

**Linearization of receptor availability:** Khodaii and colleagues determine the accuracy and precision of 3 widely used linearizations of receptor availability (saturation, inhibition, and occupancy plots) in molecular imaging with PET. . . . . **Page 294**

**$^{11}\text{C}$ -PiB versus  $^{124}\text{I}$ -antibody PET:** Meier and colleagues compare an antibody-based PET ligand targeting nonfibrillar amyloid- $\beta$  with  $^{11}\text{C}$ -PiB after  $\beta$ -secretase inhibition in Alzheimer disease mouse models of advanced-stage amyloid- $\beta$  pathology. . . . . **Page 302**

**$^{68}\text{Ga}$ -NODAGA-exendin-4 PET/CT in focal CHI:** Boss and colleagues compare the performance of this new radiolabeled exendin-4 tracer with that of  $^{18}\text{F}$ -DOPA PET/CT in preoperative detection of focal congenital hyperinsulinism. . . . . **Page 310**

**Standard methods for dose calculations:** Stabin and colleagues present standardized methods for collecting data to be used in radiopharmaceutical dose calculations, with steps that can be used as a template for calculating radiation dose estimates from animal or human data. . . . . **Page 316**

Visit our  
new website  
[northstarm.com](http://northstarm.com)

# RadioGenix<sup>®</sup> SYSTEM

(technetium Tc 99m generator)



**3 Years of  
Reliable,  
On-time,  
Domestic  
Mo-99 Supply**

## Indication

The RadioGenix<sup>®</sup> System is a technetium Tc-99m generator used to produce Sodium Pertechnetate Tc 99m Injection, USP. Sodium Pertechnetate Tc 99m Injection is a radioactive diagnostic agent and can be used in the preparation of FDA-approved diagnostic radiopharmaceuticals.

Sodium Pertechnetate Tc 99m Injection is also indicated in

- Adults for Salivary Gland Imaging and Nasolacrimal Drainage System Imaging (dacryoscintigraphy).
- Adults and pediatric patients for Thyroid Imaging and Vesicoureteral Imaging (direct isotopic cystography) for detection of vesicoureteral reflux.

## Important Risk Information

- Allergic reactions (skin rash, hives, or itching) including anaphylaxis have been reported following the administration of Sodium Pertechnetate Tc 99m Injection. Monitor all patients for hypersensitivity reactions.
- Sodium Pertechnetate Tc 99m Injection contributes to a patient's long-term cumulative radiation exposure. Ensure safe handling to protect patients and health care workers from unintentional radiation exposure. Use the lowest dose of Sodium Pertechnetate Tc 99m Injection necessary for imaging and ensure safe handling and preparation to protect the patient and health care worker from unintentional radiation exposure. Encourage patients to drink fluids and void as frequently as possible after intravenous or intravesicular administration. Advise patients to blow their nose and wash their eyes with water after ophthalmic administration.
- Radiation risks associated with the use of Sodium Pertechnetate Tc 99m Injection are greater in children than in adults and, in general, the younger the child, the greater the risk owing to greater absorbed radiation doses and longer life expectancy. These greater risks should be taken firmly into account in all benefit-risk assessments involving children. Long-term cumulative radiation exposure may be associated with an increased risk of cancer.
- Temporarily discontinue breastfeeding. A lactating woman should pump and discard breastmilk for 12 to 24 hours after Sodium Pertechnetate Tc 99m Injection administration.
- Sodium Pertechnetate Tc 99m Injection should be given to pregnant women only if the expected benefits to be gained clearly outweigh the potential hazards.
- Only use potassium molybdate Mo-99, processing reagents, saline and other supplies, including kit/packs, provided by NorthStar Medical Radioisotopes. Do not administer Sodium Pertechnetate Tc 99m Injection after the 0.15 microCi of Mo-99/mCi of Tc-99m limit has been reached or when the 24 hour expiration time from elution is reached, whichever occurs earlier. Follow step-by-step instructions for use provided in the Operator's Guide, RadioGenix System 1.2.

**To report SUSPECTED ADVERSE REACTIONS, contact NorthStar Medical Radioisotopes, LLC at 1-844-438-6659; or FDA at 1-800-332-1088 or [www.fda.gov/medwatch](http://www.fda.gov/medwatch).**

**Please visit [RadioGenixSystem.com](http://RadioGenixSystem.com) for Full Prescribing Information**



Providing Patients Global Access  
to Game-Changing Radiopharmaceuticals

[www.northstarm.com](http://www.northstarm.com) | 1-844-GET-MOLY (438-6659)





**NOW  
APPROVED**

Consider Illuccix® when evaluating patients with suspected prostate cancer metastasis, who are candidates for initial definitive therapy, or suspected recurrence based on elevated serum prostate-specific antigen (PSA) level.<sup>1</sup>

# GUIDED BY ILLUMINATION

<sup>68</sup>Ga-PSMA-11 (also known as gallium Ga 68 gozetotide) is a widely accessible radioisotope for PSMA PET imaging with:

- Nationwide distribution network of generators and cyclotrons, including those within major academic centers and community health systems<sup>2</sup>
- Capability for either high-volume production or on-site, on-demand production<sup>2,3</sup>
- Flexibility to image patients throughout the day, even on short notice<sup>3</sup>

**Illuccix® for the preparation of <sup>68</sup>Ga-PSMA-11 is poised to expand the potential of PSMA PET imaging and help guide more informed management decisions in prostate cancer.<sup>1-4</sup>**



References: 1. Illuccix (kit for the preparation of gallium Ga 68 gozetotide injection) prescribing information. 2. Massat MB. Nuclear medicine prepares for greater <sup>68</sup>Ga demand. *Appl Radiol*. 2021;50(2):30-31. <https://appliedradiology.com/articles/nuclear-medicine-prepares-for-greater-ga-68-demand>. Accessed July 13, 2021. 3. Velikyan I. <sup>68</sup>Ga-based radiopharmaceuticals: production and application relationship. *Molecules*. 2015;20(7):12913-12943. 4. ARTMS and Telix Pharmaceuticals announce successful production of PSMA-11 with cyclotron produced <sup>68</sup>Ga from a solid target [news release]. Telix Pharmaceuticals; January 12, 2021. <https://telixpharma.com/news-media/artms-and-telix-pharmaceuticals-announce-successful-production-of-68ga-psma-11-with-cyclotron-produced-68ga-from-a-solid-target/>.



Illuccix® is a trademark of Telix Pharmaceuticals (US) Inc.  
© 2021 Telix Pharmaceuticals (US) Inc.  
All rights reserved.  
US-2100010 12/2021

## Introducing Illuccix® in your practice

Speak with a live representative to get all your questions answered and prep work completed ahead of time so you receive reimbursement upon delivery of your first dose of Illuccix®. Schedule your one-on-one onboarding appointment by:

- Calling 1-(844) 45-TELIX (1-844-455-8638)
- Going to <https://illuccixhcp.com/booking>

This service is available Monday through Friday 8:00 AM to 8:00 PM ET.

### INDICATIONS AND USAGE

Illuccix®, after radiolabeling with Ga 68, is a radioactive diagnostic agent indicated for positron emission tomography (PET) of prostate-specific membrane antigen (PSMA) positive lesions in men with prostate cancer:

- with suspected metastasis who are candidates for initial definitive therapy
- with suspected recurrence based on elevated serum prostate-specific antigen (PSA) level

### Important Safety Information

#### CONTRAINDICATIONS

None

#### WARNINGS AND PRECAUTIONS

**Risk for Misdiagnosis:** Image interpretation errors can occur with gallium Ga 68 gozetotide PET. A negative image does not rule out the presence of prostate cancer and a positive image does not confirm the presence of prostate cancer. The performance of gallium Ga 68 gozetotide for imaging of biochemically recurrent prostate cancer seems to be affected by serum PSA levels and by site of disease. The performance of gallium Ga 68 gozetotide for imaging of metastatic pelvic lymph nodes prior to initial definitive therapy seems to be affected by Gleason score. Gallium Ga 68 gozetotide uptake is not specific for prostate cancer and may occur with other types of cancer as well as non-malignant processes such as Paget's disease, fibrous dysplasia, and osteophytosis. Clinical correlation, which may include histopathological evaluation of the suspected prostate cancer site, is recommended.

**Radiation Risks:** Gallium Ga 68 gozetotide contributes to a patient's overall long-term cumulative radiation exposure. Long-term cumulative radiation exposure is associated with an increased risk for cancer. Ensure safe handling to minimize radiation exposure to the patient and health care workers. Advise patients to hydrate before and after administration and to void frequently after administration.

**Adverse Reactions:** The most commonly reported adverse reactions were nausea, diarrhea, and dizziness, occurring at a rate of < 1%.

**Drug Interactions:** Androgen deprivation therapy (ADT) and other therapies targeting the androgen pathway, such as androgen receptor antagonists, can result in changes in uptake of gallium Ga 68 gozetotide in prostate cancer. The effect of these therapies on performance of gallium Ga 68 gozetotide PET has not been established.

#### OVERDOSAGE

In the event of an overdose of gallium Ga 68 gozetotide, reduce the radiation absorbed dose to the patient where possible by increasing the elimination of the drug from the body using hydration and frequent bladder voiding. A diuretic might also be considered. If possible, an estimate of the radiation effective dose given to the patient should be made.

**Adequate Hydration:** Instruct patients to drink a sufficient amount of water to ensure adequate hydration before their PET study and urge them to drink and urinate as often as possible during the first hours following the administration of Gallium Ga 68 Gozetotide Injection, in order to reduce radiation exposure.

You are encouraged to report negative side effects of prescription drugs to the FDA. Visit MedWatch at [www.fda.gov/medwatch](http://www.fda.gov/medwatch) or call 1-800-FDA-1088. You may also report adverse reactions to Telix by calling 1-844-455-8638 or emailing [pharmacovigilance@telixpharma.com](mailto:pharmacovigilance@telixpharma.com).

**For important risk and use information about ILLUCCIX® Injection, please see full Prescribing Information.**

REGISTRATION IS NOW AVAILABLE!

June 11-14  
2022

# SNMMI ANNUAL MEETING

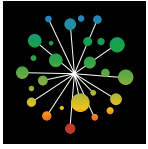
Vancouver, British Columbia Canada



Register Today

[WWW.SNMMI.ORG/AM2022](http://WWW.SNMMI.ORG/AM2022)





# SOFIE

From start to clinic



## It's here...

Our brand new Theranostics Center of Excellence in Totowa, New Jersey.

Advancing the worldwide development of next generation theranostic agents.

**20,000** square feet

**5** clean rooms

Class **5** to Class **7** classifications



For more information, visit [www.sofie.com](http://www.sofie.com)



## The 2022 ACNM/SNMMI **HOT TOPICS** Webinar Series

This monthly webinar series—complimentary for ACNM and SNMMI members—will focus on newly FDA-approved radiotracers, next generation technology, and mastering focused topics with expert presenters.

All webinars will take place at 12:00 pm ET

▶ **PSMA PET: FDA Approved and Coming to a Hospital Near You**

On-Demand | Speaker: Steven Rowe, MD, PhD

▶ **Pediatric PET: High Yield Uses and Opportunities**

February 22 | Speaker: Helen Nadel, MD, FRCPC, FSNMMI

▶ **Fluciclovine (Axumin) PET/CT for Prostate Cancer**

March 15 | Speaker: Jonathan McConathy, MD, PhD

▶ **ER Targeted PET with <sup>18</sup>F-Fluoroestradiol (Cerianna): Applications and Interpretation**

April 19 | Speaker: Gary Ulaner, MD, PhD, FACNM

▶ **PET/MR: Where Can My Patients Benefit?**

May 17 | Speaker: Patrick Veit-Haibach, MD

▶ **Cardiac Amyloid and Sarcoid: Tips for Reading like an Expert**

July 19 | Speaker: Sharmila Dorbala, MD

▶ **Lung Nodules on PET/CT: Mastering the Proper Work-Up**

August 16 | Speaker: David M. Naeger, MD

▶ **Neuroendocrine Tumor (NET) Theranostics: Only the Beginning**

September 20 | Speaker: Lisa Bodej, MD, PhD

▶ **Dementia imaging: Rapidly Growing Youth in Nuclear Medicine**

October 18 | Speaker: Phillip Kuo, MD, PhD

▶ **Head & Neck: Critical Anatomy for PET/CT**

November 15 | Speaker: Twyla B. Bartel, DO, FACNM, FSNMMI

▶ **Sodium Fluoride PET: Mastering Normal and Abnormal**

December 20 | Speaker: Ora Israel, Sr., MD, FSNMMI





**TEMA**  
SINERGIE  
High tech, high care

# KARL100

Automatic Syringe Dispensing System



## PET Evolution

**MORE THAN 170  
UNITS INSTALLED  
AROUND THE WORLD**

**2000+  
PATIENTS  
TREATED DAILY**

**EASY & SAFE  
WORKFLOW  
FIVE SIMPLE STEPS**

[temasinergie.com](http://temasinergie.com)

[karl100.com](http://karl100.com)

# Enhance Your Membership

## JOIN AN SNMMI COUNCIL OR CENTER OF EXCELLENCE

Add an SNMMI Council or Center of Excellence affiliation to your membership and receive additional networking and educational opportunities tied to a specialty area of SNMMI.

### Councils

- Academic Council
- Advanced Associate Council
- Brain Imaging Council
- Cardiovascular Council
- Correlative Imaging Council
- General Clinical Nuclear Medicine Council
- Pediatric Imaging Council
- Physics, Instrumentation and Data Sciences Council
- Radiopharmaceutical Sciences Council

Learn about the benefits of each council at [www.snmmi.org/councils](http://www.snmmi.org/councils)

### Centers of Excellence

- Therapy Center of Excellence
- Center for Molecular Imaging Innovation and Translation
- PET Center of Excellence

Learn more about the work of all three Centers of Excellence. [www.snmmi.org/COE](http://www.snmmi.org/COE)

Joining one (more more!) of these groups is a great way to develop a professional network within a specific interest area of the Society. Add them to your membership today!

Learn more  
about becoming  
a Value Initiative  
Industry Alliance  
Member Company:



[valueinitiative.snmmi.org](http://valueinitiative.snmmi.org)

The Nuclear Medicine clinic of the Department of Molecular and Medical Pharmacology, David Geffen School of Medicine at UCLA, is currently recruiting residents and fellows for its clinical programs.

The clinic features a busy outpatient theranostics program targeting PSMA and SSRs and extensive experience in 68Ga-PSMA and DOTATATE imaging. We are also involved in broad translational research activities utilizing state of the art preclinical imaging and basic biology facilities, multiple state of the art PET/CT and SPECT/CT systems, and a leading brain imaging research program.

We are accepting applications for:

Three-year program for Nuclear Medicine ABNM eligibility/certification. Completion of prior one-year clinical internship is required before the start of the program.

One-year program for those who are ABR board eligible/board certified after completion of Radiology residency training.

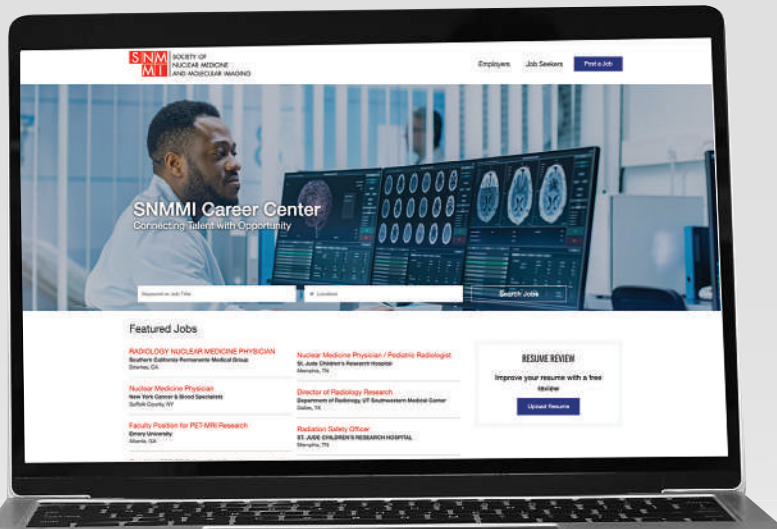
Two-year program for ABNM eligibility for ABIM eligible/board certified candidates who have completed Internal Medicine residency.

Applicants should submit a CV and three letters of reference to Pawan Gupta, MD, [pawangupta@mednet.ucla.edu](mailto:pawangupta@mednet.ucla.edu) or to Soosan Roodbari, [sroodbari@mednet.ucla.edu](mailto:sroodbari@mednet.ucla.edu). For more information about our programs, visit our website: <https://www.uclahealth.org/nuc/residency>

The University of California is an Equal Opportunity/Affirmative Action Employer. All qualified applicants will receive consideration for employment without regard to race, color, religion, sex, sexual orientation, gender identity, national origin, disability, age or protected veteran status. For the complete University of California nondiscrimination and affirmative action policy, see: [UC Nondiscrimination & Affirmative Action Policy](#).

## Explore SNMMI's Online Career Center!

Explore the benefits of SNMMI's online career center by logging in or creating a new account today.

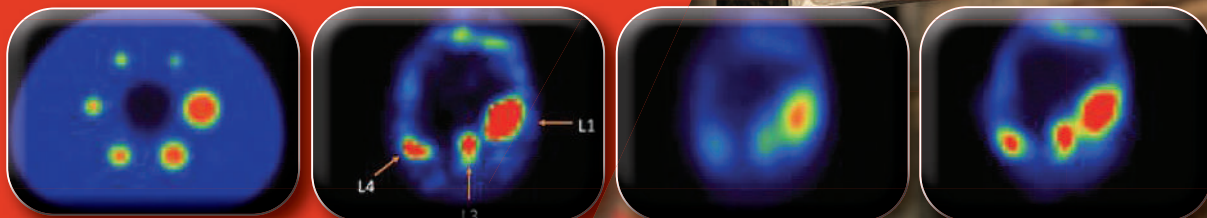


[careercenter.snmmi.org](http://careercenter.snmmi.org)

\*Note: Single sign-on has been enabled for this platform and you can use your member login credentials to access the Career Center. If you are unsure of your password, to go to the SNMMI password reset link to create a new password.

# SNMMI Therapeutics Conference

MARCH 10-12, 2022 • NEW ORLEANS, LA



Rue Bourbon  
**Bourbon**

## Explore the Latest Innovations and Clinical Applications in Radiopharmaceutical Therapy

Register now to attend the **SNMMI 2022 Therapeutics Conference**, taking place **March 10-12** in **New Orleans, LA**.

As an attendee, you'll have the opportunity to connect directly with an esteemed group of experts and learn more about the latest innovations and clinical applications in radiopharmaceutical therapy.

### Topics include:

- Operational Issues
- Radiation Safety and Research
- MIBG
- Dosimetry
- Lymphoma/Leukemia
- Neuroendocrine Cancer
- Prostate Cancer
- Thyroid
- Future Strategies for Radiopharmaceutical Therapy

Join us in New Orleans, reconnect with colleagues, and be part of the discussion on the future of personalized medicine.



Learn more and register today!  
[www.snmmi.org/TC2022](http://www.snmmi.org/TC2022)

# See NET imaging in a different light

The high **accuracy** and **accessibility** of Detectnet enable timely neuroendocrine tumor (NET) detection, diagnosis, and treatment planning<sup>1</sup>

## INCLUDED IN NCCN CLINICAL PRACTICE GUIDELINES IN ONCOLOGY (NCCN GUIDELINES®)

Effective 4/14/2021, included in the NCCN Guidelines® version 1.2021 for the evaluation of NETs.<sup>2</sup>

### ACCURACY

- In a phase 3 study, Detectnet had over 98% accuracy, 100% sensitivity, and 96.8% specificity to confirm or exclude presence of disease<sup>1\*</sup>

### ACCESS

- 12.7-hour half-life of Cu 64 facilitates an **unrestricted number of doses** and allows **flexible scheduling** for you and your patients<sup>1,3,4</sup>

Visit [Detectnet.com](http://Detectnet.com) to learn more.

### INDICATIONS

Detectnet is indicated for use with positron emission tomography (PET) for localization of somatostatin receptor positive neuroendocrine tumors (NETs) in adult patients.

### IMPORTANT RISK INFORMATION

#### WARNINGS AND PRECAUTIONS

**Risk for Image Misinterpretation:** The uptake of copper Cu 64 dotatate reflects the level of somatostatin receptor density in NETs, however, uptake can also be seen in a variety of other tumors that also express somatostatin receptors. Increased uptake might also be seen in other non-cancerous pathologic conditions that express somatostatin receptors including thyroid disease or in subacute inflammation, or might occur as a normal physiologic variant (e.g. uncinat process of the pancreas).

A negative scan after the administration of Detectnet in patients who do not have a history of NET disease does not rule out disease.

Please see Brief Summary of Prescribing Information on the following page.

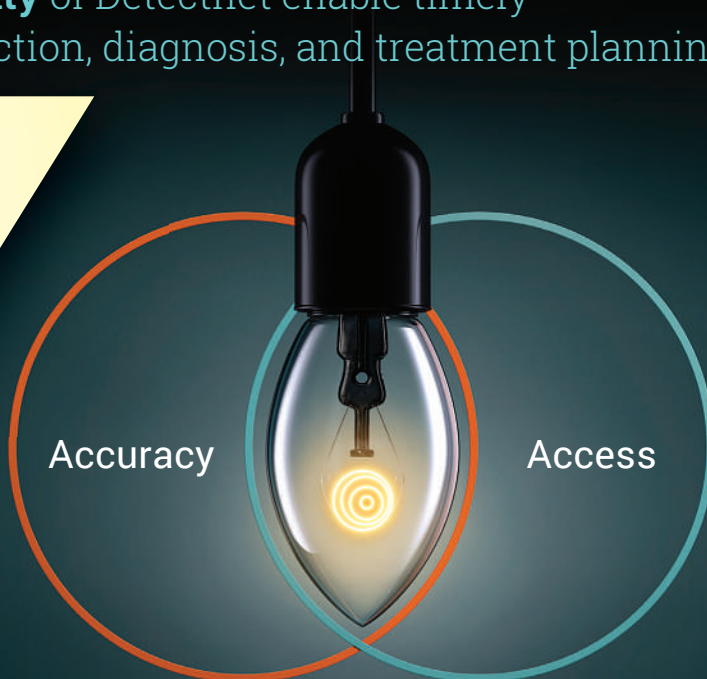
**\*Study design<sup>1</sup>:** An open-label, single-dose, single-arm, single-center prospective study to evaluate the sensitivity and specificity of Detectnet PET/computed tomography (CT) imaging in 63 subjects (42 with known or suspected NETs and 21 healthy volunteers) against an independent reader's standard of truth (SOT) for each subject. PET/CT scans were taken ~60 minutes after a single IV dose of 148 MBq ± 10% of Detectnet.

A limitation was 3 mistaken SOT determinations, but these were revised. The SOT reads for 3 subjects were incorrectly recorded as NET-positive instead of NET-negative. Because the objective of the study was to assess the performance of the PET/CT scan and not the SOT, the corrected values are shown.

**References:** 1. Delpassand ES, Ranganathan D, Wagh N, et al. *J Nucl Med.* 2020. doi:10.2967/jnumed.119.236091. 2. Referenced with permission from the NCCN Clinical Practice Guidelines in Oncology (NCCN Guidelines®) for Neuroendocrine and Adrenal Tumors V.1.2021. © National Comprehensive Cancer Network, Inc. 2021. All rights reserved. Accessed April 15, 2021. To view the most recent and complete version of the guideline, go online to NCCN.org. 3. Pfeifer A, Knigge U, Mortensen J, et al. *J Nucl Med.* 2012;53(8):1207-1215. 4. Detectnet. Package insert. Curium US LLC; September 2020.

CURIUM™

© 2021 Curium US LLC. Detectnet™ and Curium™ are trademarks of a Curium company.  
CD0103 0721



Detectnet™  
(copper Cu 64 dotatate injection)

Scan to learn more  
about Detectnet  
and place an order.



## **Detectnet™ (copper Cu 64 dotatate injection), for intravenous use**

### **BRIEF SUMMARY OF FULL PRESCRIBING INFORMATION**

(For complete details, please see full Prescribing Information available at [www.curiumpharma.com](http://www.curiumpharma.com))

### **INDICATIONS AND USAGE**

Detectnet is a radioactive diagnostic agent indicated for use with positron emission tomography (PET) for localization of somatostatin receptor positive neuroendocrine tumors (NETs) in adult patients.

### **CONTRAINDICATIONS**

None.

### **WARNINGS AND PRECAUTIONS**

**Radiation Risk:** Diagnostic radiopharmaceuticals, including Detectnet, contribute to a patient's overall long-term cumulative radiation exposure. Long-term cumulative radiation exposure is associated with an increased risk of cancer. Ensure safe handling and preparation procedures to protect patients and health care workers from unintentional radiation exposure. Advise patients to hydrate before and after administration and to void frequently after administration [see *Dosage and Administration (2.1, 2.3) in the full Prescribing Information*].

**Risk for Image Misinterpretation:** The uptake of copper Cu 64 dotatate reflects the level of somatostatin receptor density in NETs, however, uptake can also be seen in a variety of other tumors that also express somatostatin receptors. Increased uptake might also be seen in other non-cancerous pathologic conditions that express somatostatin receptors including thyroid disease or in subacute inflammation, or might occur as a normal physiologic variant (e.g. uncinate process of the pancreas) [see *Dosage and Administration (2.5) in the full Prescribing Information*].

A negative scan after the administration of Detectnet in patients who do not have a history of NET disease does not rule out disease [see *Clinical Studies (14) in the full Prescribing Information*].

### **ADVERSE REACTIONS**

**Clinical Trials Experience:** Because clinical trials are conducted under widely varying conditions, adverse reaction rates observed in the clinical trials of a drug cannot be directly compared to rates in the clinical trials of another drug and may not reflect the rates observed in practice.

In safety and efficacy trials, 71 subjects received a single dose of Detectnet. Of these 71 subjects, 21 were healthy volunteers and the remainder were patients with known or suspected NET.

The following adverse reactions occurred at a rate of < 2%:

- *Gastrointestinal Disorders:* nausea, vomiting
- *Vascular Disorders:* flushing

In published clinical experience, 126 patients with known history of NET received a single dose of copper Cu 64 dotatate injection. Four patients were reported to have experienced nausea immediately after injection.

### **DRUG INTERACTIONS**

**Somatostatin Analogs:** Non-radioactive somatostatin analogs and copper Cu 64 dotatate competitively bind to somatostatin receptors (SSTR2). Image patients just prior to dosing with somatostatin analogs. For patients on long-acting somatostatin analogs,

a wash-out period of 28 days is recommended prior to imaging. For patients on short-acting somatostatin analogs, a washout period of 2 days is recommended prior to imaging [see *Dosage and Administration (2.3) in the full Prescribing Information*].

### **USE IN SPECIFIC POPULATIONS**

#### **Pregnancy**

##### Risk Summary

All radiopharmaceuticals, including Detectnet, have the potential to cause fetal harm depending on the fetal stage of development and the magnitude of the radiation dose. Advise a pregnant woman of the potential risks of fetal exposure to radiation from administration of Detectnet.

There are no data on Detectnet use in pregnant women to evaluate for a drug-associated risk of major birth defects, miscarriage, or adverse maternal or fetal outcomes. No animal reproduction studies have been conducted with copper Cu 64 dotatate injection.

The estimated background risk of major birth defects and miscarriage for the indicated population is unknown. All pregnancies have a background risk of birth defects, loss, or other adverse outcomes. In the U.S. general population, the estimated background risk of major birth defects and miscarriage in clinically recognized pregnancies is 2% to 4% and 15% to 20%, respectively.

#### **Lactation**

##### Risk Summary

There are no data on the presence of copper Cu 64 dotatate in human milk, the effect on the breastfed infant, or the effect on milk production. Lactation studies have not been conducted in animals.

Advise a lactating woman to interrupt breastfeeding for 12 hours after Detectnet administration in order to minimize radiation exposure to a breastfed infant.

**Pediatric use:** The safety and effectiveness of Detectnet have not been established in pediatric patients.

**Geriatric use:** Clinical studies of Detectnet did not include sufficient numbers of subjects aged 65 and over to determine whether they respond differently from younger subjects. Other reported clinical experience has not identified differences in responses between the elderly and younger patients. In general, dose selection for an elderly patient should be cautious, usually starting at the low end of the dosing range, reflecting the greater frequency of decreased hepatic, renal, or cardiac function, and of concomitant disease or other drug therapy.

### **OVERDOSAGE**

In the event of a radiation overdose, the absorbed dose to the patient should be reduced where possible by increasing the elimination of the radionuclide from the body by reinforced hydration and frequent bladder voiding. A diuretic might also be considered. If possible, estimation of the radioactive dose given to the patient should be performed.

This Brief Summary is based on Detectnet Full Prescribing Information Revised: 9/2020

Manufactured, Packed and Distributed by: Curium US LLC, 2703 Wagner Place, Maryland Heights, MO 63043

© 2020 Curium US LLC. Detectnet™ and Curium™ are trademarks of a Curium company.

CD0041 0920a

# Joint NIBIB/NCI/SNMMI Workshop on Directly Imaging Targeted Radionuclide Therapy Isotopes

*I. George Zubal, PhD, National Institute of Biomedical Imaging and Bioengineering, Bethesda, MD, and Jacek Capala, PhD, DSc, National Cancer Institute, Bethesda, MD*

The National Institute of Biomedical Imaging and Bioengineering (NIBIB), the National Cancer Institute (NCI), and SNMMI organized a virtual workshop titled “Engineering New Instrumentation for Imaging Unsealed Source Radiotherapy Agents” on August 16 and 17, 2021. The impetus for this workshop was introduced by an earlier Newsline article, “Time for a next-generation nuclear medicine  $\gamma$  camera?” (2020;61[7]:16N), asking whether we need to reconsider instrumentation used for theranostic methods with electron- and  $\alpha$ -emitting unsealed sources for recently emerging cancer therapies.

The workshop convened physicians and scientists from relevant fields to investigate the clinical challenges of treating cancer and to discuss possible technical developments in imaging instrumentation for improving outcomes. Panel sessions focused on the clinical applications of radiopharmaceutical therapy (RPT), as well as isotope production and dosimetry’s roles in delivering safe and effective therapies. The workshop was moderated by George Zubal, PhD, Program Director for Nuclear Medicine (NIBIB), and Jacek Capala, PhD, DSc, Program Director, Radiation Research Program, Division of Cancer Treatment and Diagnosis (NCI).

Kris Kandarpa, MD, PhD, Director of NIBIB’s Research Sciences and Strategic Directions, opened the workshop with a welcome message outlining NIBIB’s mission to develop imaging methods that lead to personalized precision medicine. He encouraged participants to evaluate recent achievements in PET and consider how similar future improvements could be achieved with  $\alpha$ -emitter imaging.

## Session 1: Overview of Diagnostic/Therapy Practice

The first workshop session started with a talk by Steven Larson, MD (Memorial Sloan Kettering Cancer Center; New York, NY), describing the therapeutic advantages of  $\alpha$ -emitting isotopes. Alpha particles are characterized by double-strand break triggering, high linear energy transfer, relatively short range, greater relative biological effectiveness, and a low oxygen enhancement ratio. Dr. Larson and his team have demonstrated 3 separate therapy protocols that work quite well, with good therapeutic indices associated with cures. Reporting from the same institution, John Humm, PhD, covered specific classes of  $\alpha$ -emitting radionuclides, which can be simple (those that decay to stable or non- $\alpha$ -emitting progeny) or complex (those with radioactive  $\alpha$ -emitting progeny). He pointed to  $^{211}\text{At}$  as possibly the best  $\alpha$  emitter that does not exhibit problematic progeny. This has great potential if concerns about its challenging radiochemistry can be resolved. He emphasized dosimetry problems with imaging  $\alpha$ -emitting radionuclides,

related to the limited resolution of current SPECT cameras, where images of  $\alpha$  sources cannot provide accurate information at the relevant cellular target level for microdosimetry.

Daniel Pryma, MD (University of Pennsylvania; Philadelphia) explained current RPT practices using  $^{131}\text{I}$ -MIBG, which was developed in 1980 and received therapeutic FDA approval in 2018. Several dosimetric challenges are associated with these studies, including the fact that dosimetry image acquisition requires several visits to the imaging department. Work is being done to use population inputs and information about typical patient kinetics to simplify this process. Michael King, PhD (University of Massachusetts Medical School; Worcester), reviewed manufacturers who have developed dedicated cardiac SPECT systems. These have smaller heads to get closer to patients or 2 heads oriented at  $90^\circ$  for efficient acquisition over  $180^\circ$ . Other advancements (new radiopharmaceutical developments, imaging system design optimization, software advances, and guidelines/standards) facilitated by medical societies have played a role in establishing and enhancing the clinical utility of cardiac SPECT. The hope is that SPECT will also play a role in similar developments for unsealed source radiotherapy agents. The last speaker in this session, Robert Mach, PhD (University of Pennsylvania; Philadelphia), detailed his research findings indicating that SPECT is comparable to PET in studies with high target density or in studies with lower target density in a control group. He further noted that SPECT can be used to separate the photopeaks between  $^{123}\text{I}$  and  $^{99\text{m}}\text{Tc}$  to quantify uptake of the 2 isotopes and measure both terminal density and cerebral blood flow. This could be applied to imaging parent and progeny isotopes in RTP, which is not possible with PET because of the 511-keV emissions of all PET isotopes.

*Panel Discussion:* Sarah Cheal, PhD (Memorial Sloan Kettering; New York, NY), Robert Miyaoka, PhD (University of Washington School of Medicine; Seattle), Emilie Roncali, PhD (University of California Davis), and Vikram Bhadrasain, MD (NCI) participated in a discussion and Q&A with session presenters. Several interesting topics were raised, including  $^{213}\text{Bi}$  dosimetry, comparison to external-beam doses, and development of cameras for specific tasks. Other topics included antibodies in theranostics and sensitivity of SPECT for dosimetry imaging. This led to a discussion of possible new  $\gamma$  detectors and collimator-less cameras. Concluding comments addressed the SNMMI Dosimetry Challenge and ways in which customizing doses to specific patients could improve outcomes.

## Session 2: Overview of Imaging

The next workshop session began with an overview from Ben Tsui, PhD (Johns Hopkins University School of Medicine;

Baltimore, MD), who summarized SPECT development over the past decades. He noted that 2 major breakthroughs have made quantitative SPECT more practical: maximum-likelihood expectation maximization and ordered-subset expectation maximization algorithms. In addition, quantitative SPECT has several important implementation requirements, including good quality of SPECT images, good quality of CT images, and accurate alignment of SPECT and CT images to reduce misregistration of image artifacts and to apply attenuation corrections. Also from Johns Hopkins, Eric Frey, PhD, reminded attendees that, when conducting targeted radionuclide therapy, the main objectives are to avoid significant toxicity in normal tissues and to deliver a lethal dose to tumors; hence, it is necessary to image both large and small organs to obtain accurate voxels for 3D dosimetry. He explained issues that must be addressed to achieve these improvements: new detector materials with improved energy resolution and better intrinsic spatial resolution, novel collimation geometries, improved intrinsic resolution, and more detector areas with larger axial fields of view.

The third speaker in the session, Ling-Jian Meng, PhD (University of Illinois at Urbana-Champaign), reviewed a proposed camera design applying the concept of hyperspectral SPECT imaging, which could allow multiisotopic, multifunctional molecular imaging using various combinations of radiotracers. Based on his innovative sensor work, his team has been developing preclinical and clinical imaging systems that show promise for routine imaging in humans. He concluded that, given improvements in sensor spatial resolution and sensitivity, it may be time to revisit Compton cameras as a possibility to improve SPECT imaging. Todd Peterson, PhD (Vanderbilt University; Nashville, TN), presented his unique camera design integrating a high-purity germanium detector camera with a MicroCAT II CT scanner. Using this system, he was able to demonstrate multiisotope capabilities and compared his camera to other systems, demonstrating that germanium could set very narrow photopeak energy windows. His team is also working on mechanical cooling to reduce power consumption. Lars Furenlid, PhD (University of Arizona; Tucson), oversees a lab that develops technologies to image  $\gamma$  rays, principally for SPECT, which are either semiconductor- or scintillator-based. His current designs include a third-generation cross-strip cadmium telluride detector, a hybrid photomultiplier tube/silicon photomultiplier (SiPM) scintillation camera, and a third-generation large-area ionizing radiation quantum imaging detector camera. He summarized the many opportunities for fundamental advancements in SPECT imaging of  $\alpha$  emitters, noting that development is needed in the theory of mathematics as well as new mathematical observers, estimation methods, and spectrum-aware reconstruction methods. Also needed are larger area high-Z semiconductors; high-Z, high-light-output scintillators; large-area gaseous or solid-state electron multipliers; and advances in SiPMs.

*Panel Discussion:* The panel discussion for this session focused on topics concerning germanium detectors for

scatter rejection, higher sensitivity imaging systems, and associated reconstruction methods. Additional discussions covered microdosimetry and high-energy photon imaging with camera geometries positioned close to the patient.

### Session 3: Overview of Isotopes: Dosimetry and Future Directions

Session 3 opened with an overview from Jehanne Gillo, PhD (U.S. Department of Energy [DOE]; Germantown, MD), of the DOE Isotope Program (DOE-IP), which has a mission to produce and distribute radioisotopes that are not commercially available. She described a dramatic increase in the numbers of reactor- and accelerator-based isotope production facilities at DOE National Laboratories and their academic partners, providing diagnostic and therapeutic radioisotopes, including  $\alpha$  emitters ( $^{223}\text{Ra}$ ,  $^{221}\text{At}$ , and  $^{225}\text{Ac}$ , as well as  $^{227}\text{Ac}$  used by Bayer to obtain  $^{223}\text{Ra}$  for production of Xofigo). In addition to production and distribution of currently used isotopes, the DOE-IP also operates a discovery arm focused on identifying new radioisotopes that might be of interest to the RPT community. A funding opportunity announcement to support research on new isotopes entering preclinical and clinical trials was recently issued (<https://www.isotopes.gov/FOA-Advancing-Novel-Medical-Isotopes-for-Clinical-Trials>). DOE has also started an isotope traineeship to apply advanced manufacturing techniques to isotope production.

Douglas Van Nostrand, MD (Georgetown University Medical Center; Washington, DC), provided a comprehensive overview of radioiodine as a paradigm of theranostics. He pointed out its diagnostic ( $^{123}\text{I}$  and  $^{124}\text{I}$ ) and therapeutic ( $^{131}\text{I}$ ) utility, facilitating: (1) definition of maximal safe administered therapeutic activity to minimize unacceptable side effects; (2) determination of minimal administered activity to achieve desired therapeutic outcomes; and (3) assessment and mitigation of altered genomic cancer molecular biology (redifferentiation). These permit  $^{131}\text{I}$  therapy in patients with negative scans and enhance therapeutic results in patients with positive scans. Because MEK-inhibitors increase iodine accumulation in tumor cells (which can be monitored by PET) the  $^{124}\text{I}/^{131}\text{I}$  theranostic pair allows successful treatment of non-iodine-avid tumors.

In contrast to external-beam radiotherapy, where the absorbed dose can be precisely inferred from measurements, tissue absorbed dose in nuclear medicine must be approximated using different models. Wesley Bolch, PhD (University of Florida; Gainesville), presented 3 principal methods to compute tissue absorbed dose: (1) direct Monte Carlo (MC) radiation transport simulation; (2) dose-point kernel (DPK) convolution; and (3) the Medical Internal Radiation Dose (MIRD) S-value formalism. Because of the high degree of accuracy, MC simulations are the reference standard for tissue dosimetry and the most reliable tool for computing radionuclide S-values. DPK convolution is commonly used at the voxel level, between the application regimes of S-value and direct MC methods. S-values, the most practical

method because of the link to the MIRDS schema, are applicable at any scale, although the underlying approximations of the method mostly limit their use to the organ and suborgan levels.

Yuni Dewaraja, PhD (University of Michigan; Ann Arbor), presented advances in SPECT and PET imaging for patient-specific dosimetry, focusing on imaging methods used for  $^{90}\text{Y}$  and  $^{177}\text{Lu}$ .  $^{90}\text{Y}$  can be imaged by both SPECT and PET. SPECT detects bremsstrahlung that has continuous energy spectra. MC reconstruction, model-based scatter estimation, and deep learning-based scatter estimation are used to enable quantification of the bremsstrahlung. The main challenges in PET imaging of  $^{90}\text{Y}$  are low positron yield and coincidences with bremsstrahlung photons. These challenges can be addressed by dedicated reconstruction algorithms and new instrumentation, such as time-of-flight, digital, and whole-body PET. A relatively low intensity of  $\gamma$  rays is a challenge for SPECT imaging of  $^{177}\text{Lu}$ , which requires efficient counting methods, application of deep learning, and joint dual-photopeak reconstruction or the option of combining SPECT with data from  $^{68}\text{Ga}$  PET.

**Panel Discussion:** The panelists addressed the limitations of current dosimetry methods and the latest progress in development. Uncertainty in dose estimates was deemed the major problem. Contributing factors, particularly for bone marrow and small structures (metastases), include definition of the region of interest, low signal, and reliability of data obtained using standard partial-volume correction methods. Several methods to improve the reliability of dose estimates and the need to define standards for the whole dosimetry workflow were mentioned. Barriers to wider adoption of radioiodine treatment and challenges and opportunities in combining RPT with conventional radiation therapy were also discussed.

### Keynote Overview: Peering into the Black Box of Cancer Therapy

In the keynote lecture, George Sgouros, PhD (Johns Hopkins University School of Medicine; Baltimore, MD) addressed RPT efforts in the context of conventional systemic cancer therapies. He described the latter using a black box analogy, in which inputs are mechanism, target validation, preclinical model toxicity, patient selection, genomics, and theranostics. Treatment is the black box itself, and outputs are tumor response, time to progression, overall survival, quality of life, and clinical toxicity. In this scenario, researchers can understand mechanisms by changing inputs and looking at responses; this is the long-standing process for agents that cannot be imaged. This approach, unfortunately, is not effective. In a paper published in 2018, Wong

et al. examined the success rate of oncologic drugs and found that 97% of cancer drugs evaluated in humans fail (*Biostatistics*. 2018;20:273–286). Many of these agents are targeted therapies blocking signaling pathways that control cancer cell growth, division, and spread. In many cases, targeted therapies miss their target; a 2019 paper by Lin et al. found that many cancer drugs work as a result of off-target effects (*Sci Transl Med*. 2019;11[509]:eaaw8412). Consequently, over the past decade the cost of cancer drugs has gone up, but the clinical benefits of those drugs have not increased proportionately, adding to financial concerns.

RPTs present a promising alternative. They are administered systemically and regionally and can target metastatic cancer, leading to radiation-induced DNA damage and killing cells rather than controlling cell behavior. Their efficacy depends on differential delivery of radiation, which can be assessed by imaging. Dr. Sgouros presented several examples of such approaches in clinical trials using  $^{131}\text{I}$ ,  $^{90}\text{Y}$ ,  $^{213}\text{Bi}$ ,  $^{223}\text{Ra}$ ,  $^{227}\text{Th}$ ,  $^{212}\text{Pb}$ , and  $^{225}\text{Ac}$ . In 1 example, implementation of personalized dosimetry in hepatic artery infusion of  $^{90}\text{Y}$  microspheres for hepatocellular carcinoma doubled patient survival time, without changing the agent or the patient population. These examples showed that imaging and individualized dosimetry-based treatment planning can further improve RPT outcomes.

**Keynote Overview Q&A:** The panel discussion focused on obstacles to implementing dosimetry for RPT, including: a need for more examples (preferably randomized clinical trials) showing that dosimetry has a huge impact; a need for consistent, well-validated, and standardized dosimetry methodologies; lack of knowledge of radiation and radionuclide therapy; reimbursement challenges; and the need for multiple scans. Panelists noted that some of these problems can be addressed by simplifying dosimetry procedures and enhancing education of both patients and physicians.

### Conclusion

This workshop represented a first step in evaluating and combining physicians' needs for cancer treatment and imaging scientists' knowledge of instrumentation and dosimetry calculations to improve cancer treatment outcomes. We invite the community to view the recorded sessions of this workshop under "Engineering New Instrumentation for Imaging Unsealed Source Radiotherapy Agents" at the NIBIB events page (<https://www.nibib.nih.gov/NIBIB-Webinars-and-Conferences>). NIBIB looks forward to continuing this workshop in early 2023 with additional discussions and a review of progress made based on insights and discussions from the workshop reported here.

## DOE and HHS Certify Sufficient $^{99}\text{Mo}$ Supplies

On December 20, U.S. Secretary of Energy Jennifer M. Granholm and U.S. Secretary of Health and Human Services (HHS) Xavier Becerra jointly certified the achievement of a sufficient supply of  $^{99}\text{Mo}$  made without using highly enriched uranium (HEU) to meet the needs of patients in the United States. According to a press release from the agencies, this certification “paves the way for a nuclear nonproliferation milestone and supports U.S. companies by triggering a congressionally mandated ban on exports of HEU for foreign medical isotope production.” HEU is a sensitive and critical product in terms of nuclear proliferation, and the Department of Energy (DOE) National Nuclear Security Administration (NNSA) works to minimize the global civilian use and availability of HEU.

“Doctors and patients across the globe can be confident that the critical medical isotope  $^{99}\text{Mo}$  will be there when they need it, and we can provide that assurance without making any further exports of HEU,” said Granholm. “Today’s certification is another example of DOE’s world-leading expertise creating win–win outcomes that make the world safer while advancing jobs, improving health care, and increasing the quality of life here at home.”

$^{99}\text{Mo}$  is used in more than 40,000 medical diagnostic procedures in the United States each day. For decades, the United States had no capability for domestic production of the isotope. To ensure a stable supply, HEU was exported to foreign medical isotope producers that used the material to produce  $^{99}\text{Mo}$  for the U.S. and global markets.

Achieving a sufficient supply of  $^{99}\text{Mo}$  produced without the use of HEU is the result of significant accomplishments by DOE, HHS, and the commercial  $^{99}\text{Mo}$  industry. The DOE NNSA has provided financial and technical assistance to help global  $^{99}\text{Mo}$  producers convert from HEU to low-enriched uranium (LEU). DOE/NNSA has also supported development of a domestic production capability for non-HEU  $^{99}\text{Mo}$  by awarding more than \$200 million in cost-shared cooperative agreements with commercial entities, providing technical support from the U.S. National Laboratories, and establishing a Uranium Lease and Take-Back Program for industry.

HHS’s role in achieving this milestone included approvals for use of  $^{99}\text{Mo}$  produced by global suppliers using LEU and the 2018 FDA approval of the New Drug Application for the  $^{99}\text{Mo}$  production system of NorthStar Medical Radioisotopes, one of NNSA’s commercial partners. Both the DOE and HHS noted that they will continue to work together and with commercial entities to further bolster the U.S. supply of non-HEU  $^{99}\text{Mo}$ .

“With more than 80% of diagnostic imaging in the U.S. relying on nuclear medicine isotopes like  $^{99}\text{Mo}$ , the FDA has a key role to play to ensure a sufficient supply is available for critical daily medical procedures,” said Acting FDA Commissioner Janet Woodcock, MD. “We’re pleased to partner with DOE and other federal partners to contribute to this important achievement.”

*U.S. Department of Energy*

*U.S. Department of Health and Human Services*

## FDA Approves New $^{68}\text{Ga}$ Kit for Prostate Cancer PET

Telix Pharmaceuticals (Melbourne, Australia; Indianapolis, IN) announced on December 20 that the U.S. Food and Drug Administration (FDA) had approved Illucix (TLX591-CDx), the company’s kit for preparation of  $^{68}\text{Ga}$ -gozetotide ( $^{68}\text{Ga}$ -prostate-specific membrane antigen [PSMA]-11). The product is approved for PET imaging in patients with prostate cancer with suspected metastasis who are candidates for initial definitive therapy or in whom recurrence is suspected based on elevated serum prostate-specific antigen levels.

The FDA first approved  $^{68}\text{Ga}$ -PSMA-11 PET for prostate cancer imaging in December 2020, but access was available only through the University of California Los Angeles and the University of California San Francisco. “The approval of Illucix will give patients considerably improved access to PSMA PET imaging, an advanced diagnostic tool that was recently included in the National Comprehensive Cancer Network Clinical Practice Guidelines in Oncology for Prostate Cancer,” said A. Oliver Sartor, MD, Medical Director of the Tulane Cancer Center (New Orleans, LA). “With patient doses able to be

prepared onsite or via commercial radiopharmacy networks, either via generator or cyclotron, Illucix delivers flexible patient scheduling and on-demand access throughout the day.”

According to a Telix press release issued on December 20, Illucix can be prepared with  $^{68}\text{Ga}$  via either GE’s FASTlab cyclotrons or in nuclear pharmacies and health care centers using the Eckert and Ziegler GalliaPharm generator or the IRE ELiT Galli Eo generator. Along with a 4-hour shelf life after radiolabeling, these generation options will allow expansion of PSMA PET in prostate cancer. “This product offers a level of flexibility and accessibility to health care professionals we really haven’t seen before in this class of products and may help us provide better patient experiences as a result,” said Dr. Sartor. With a distribution network encompassing more than 140 nuclear pharmacies through an agreement with Cardinal Health and PharmaLogic, Telix noted that Illucix will be available to more than 85% of eligible PET imaging sites in the United States.

*Telix Pharmaceuticals*

## SNMMI to Host Summits on Artificial Intelligence and Patient Access

Richard L. Wahl, MD, SNMMI President

**A**dvances in medical technology are improving patient care as never before. At the same time, great health disparities exist, and not all patients have access to these advances; urban and rural populations can be underserved. SNMMI recognizes that in order to provide high-quality patient care, we need to support the growth of the field as well as fight for access for all.

Next month SNMMI will host back-to-back summits on 2 hot topics in nuclear medicine, molecular imaging, and radiopharmaceutical therapy: artificial intelligence and patient access to and health disparities in nuclear medicine procedures. Held at the end of March in Bethesda, MD, the summits will provide opportunities for in-depth discussions on these highly relevant topics.

The Artificial Intelligence Summit, organized by the SNMMI Artificial Intelligence Task Force, will be held March 21 and 22. Attendees will include stakeholders in academia, medical device manufacturing and pharmaceutical companies, start-up companies, hospital administrators, and end users of artificial intelligence technology. Representatives from the Food and Drug Administration (FDA), Centers for Medicare & Medicaid Services, and National Institutes of Health will also attend.

This summit will kick off with a plenary session on the role of ethics in artificial intelligence, presented by Melissa McCradden, PhD, bioethicist with the department of bioethics at the Hospital for Sick Children (Toronto, Canada). Irène Buvat, PhD, head of the Laboratory of Translational Imaging in Oncology Research at the Institut Curie Research Center (Orsay, France), will then discuss the state of the art in artificial intelligence.

Four panel discussions will follow on standardization initiatives; current challenges; the landscape of artificial intelligence regulations, coverage, and funding; and what end users (physicians, technologists, hospital administrators, etc.) want from artificial intelligence. The speakers from the panel discussions will give updates on current status as well as what is needed from other stakeholders to advance their respective artificial intelligence agendas. The summit will conclude with a session on next steps and a call to action.

The SNMMI Summit on Patient Access to and Health Disparities in Nuclear Medicine Procedures will take place on March 22 and 23, immediately following the Artificial Intelligence Summit. The goal of the summit is to gather representatives from major stakeholders in the nuclear medicine and health equity spaces to identify and address barriers, including health disparities, that prevent patients from accessing high-quality nuclear medicine scans and therapies.

The invitation-only summit will include approximately 120 attendees from nuclear medicine and molecular imaging industry, regulators, legislators, and payers. Although SNMMI has elected to keep this meeting small, we recognize the widespread interest

in this topic in the wider oncology and imaging/radiopharmaceutical therapy communities. The meeting will be available online via a webinar for those who would like to listen to the talks and associated discussions.

Andrew Scott, MD, director of the department of molecular imaging and therapy at Austin Health (Victoria, Australia), will begin the meeting with lessons from *The Lancet Oncology* in regard to global access to nuclear medicine and radiology. Eliseo Pérez-Stable,

MD, director of the National Institute on Minority Health and Health Disparities, will follow with a keynote speech on social determinants of health. Richard L. Wahl, MD, Elizabeth Malinckrodt professor and chair of radiology and director of the Malinckrodt Institute of Radiology at Washington University School of Medicine (St. Louis, MO), will then speak on the changing landscape in nuclear medicine, with a special focus on areas where patient access limitations are apparent—including both inner urban and rural care delivery spaces.

The summit will also include 6 panels covering a range of topics related to patient access to and health disparities in nuclear medicine procedures. Two panels will be held on the first day of the summit. The first will discuss health disparities in imaging and focus on lessons learned in mammography and prostate imaging, as well as clinical trial participation. A panel on federal regulatory efforts to ensure access to nuclear medicine will conclude the day.

The remaining 4 panels, on the following day, will begin with radiopharmaceutical production and distribution challenges, with a focus on rural America. Next, attendees will learn about the foundational infrastructure of nuclear medicine, followed by appropriate utilization and reimbursement for products. The final panel will be a “Payer Panel,” in which insurance companies will discuss what steps are being taken to address social disparities in health care access. The meeting will end with a working session to review solutions and next steps.

SNMMI recognizes that the field of nuclear medicine and molecular imaging is rapidly evolving, and nuclear medicine procedures are fundamental components of many patient care pathways. Through summits like these, our goal is to provide strategic vision and a roadmap to address these changes, demonstrate the true value of the field, and elevate nuclear medicine and molecular imaging. By doing so we can improve access for patients and provide increased value to the medical community, regulators, payers, patients, and the public.



Richard L. Wahl, MD

## Call to Action for Federal Research Funding

SNMMI and the Academy of Radiology and Biomedical Imaging Research announced on December 14 a partnership to urge the U.S. Congress to pass an FY22 appropriations package with support for the National Institutes of Health (NIH) and biomedical imaging and to curtail the use of harmful continuing resolutions. In early December, Congress passed its second continuing resolution for the 2022 fiscal year, which should have begun on October 1, 2021. That continuing resolution will keep the government funded until February 18, which means there will be no increases in government funding until well after the first third of the 2022 fiscal year. NIH, for example, does not know its final funding level for the year already in progress. NIH and other research agencies cannot issue new funding awards until formal appropriations are determined. In addition, researchers working on existing awards may receive notification of funding cuts to maintain conservative spending levels mandated by the continuing resolution. Early career researchers and those with new proposals are especially adversely affected as they wait for federal support for research plans already determined to be meritorious. In their December 14 statement, SNMMI and the Academy of Radiology and Biomedical Imaging Research said “This extended delay will only hold back research. Already, research has suffered greatly due to the negative scientific and economic effects of the COVID-19 pandemic. We must remain committed to assisting Congress in the nation’s recovery from the pandemic and support the continuous funding of scientific and medical research to ensure improved patient outcomes and U.S. competitiveness.” Members of the nuclear medicine and molecular imaging and therapy communities were urged to contact their members of Congress to emphasize the importance of biomedical research and

the deleterious effects of chronic continuing resolutions. Additional information is available at: <https://www.acadrad.org/take-action/#/5>.

SNMMI

## CMS Grants Pass-Through Payment Status for $^{18}\text{F}$ -Piflufolastat

On November 22, the Centers for Medicare & Medicaid Services (CMS) granted transitional pass-through payment status for  $^{18}\text{F}$ -piflufolastat (Pylarify;  $^{18}\text{F}$ -DCFPyL), increasing patient access to prostate-specific membrane antigen (PSMA)-based imaging in prostate cancer. The decision was effective as of January 1. The Medicare Transitional Pass-Through Payment program is designed to facilitate patient access to cutting-edge treatments by allowing adequate payment for new agents while permanent reimbursement rates are being established.

$^{18}\text{F}$ -piflufolastat is the first fluorinated PSMA agent approved for reimbursement by CMS. The agent, manufactured by Lantheus Holdings (North Billerica, MA), was approved in May 2021 by the U.S. Food and Drug Administration for PET imaging of PSMA-positive lesions in men with prostate cancer with suspected metastasis who are candidates for initial definitive therapy or with suspected disease recurrence based on elevated serum prostate-specific antigen levels.

“We have been thrilled with the response to Pylarify in the prostate cancer community,” said Mary Anne Heino, president and chief executive officer of Lantheus. “Pylarify is a transformative diagnostic tool that identifies disease earlier and more accurately than conventional imaging, providing more information to guide treatment decisions. The granting of transitional pass-through payment status for Pylarify further facilitates patient access to our game-changing PSMA-

targeted imaging agent for prostate cancer.”

Centers for Medicare & Medicaid Services  
Lantheus Holdings

## 2022 Hal O’Brien Rising Star Award

Yale University School of Medicine (New Haven, CT) announced in December that Attila Feher, MD, a clinical fellow in cardiovascular medicine at the Yale



Attila Feher, MD

Translational Research Imaging Center, would receive the Hal O’Brien Rising Star Award at the High Country Nuclear Medicine Conference (HCNMC) to be held in Sun Valley, ID, March 5–8. The award honors junior faculty, postdoctoral trainees, and fellows performing exemplary work in the radiopharmaceutical sciences, clinical applications, or research in oncology, cardiology, and neurology. A \$1,000 travel grant included in the award is intended to enable travel to the meeting and presentation of research as part of HCNMC proceedings.

Dr. Feher is being recognized for his work in development of imaging tools to evaluate microcirculation in heart transplant recipients. Albert Sinusas, MD, director of the Yale Translational Research Imaging Center, said, “Attila is one of the best fellows that I have had the pleasure of training over my 30-year career on faculty at Yale. He has received multiple awards, including a recent award for the best manuscript in the *Journal of the American College of Cardiology: CardioOncology*. He is an outstanding clinician scientist who excels both in clinical care and translational and clinical research. He is also a humble and caring person.”

The Rising Star Award was created to celebrate the leadership legacy of the High Country meeting and to recognize the vision of Hal O'Brien, MD, in creating a unique and productive format for bringing together leaders from across the spectrum of nuclear medicine and molecular imaging. The conference includes experts from academia and industry, with leaders in medical specialties, the regulatory agencies, and health care researchers in an informal setting to facilitate exchanges of ideas. The Education and Research Foundation for Nuclear Medicine and Molecular Imaging manages the program as an endowed fund to support the award in perpetuity. Each year in July the HCNMC Award Subcommittee initiates a call for nominations directed to the SNMMI Councils and Centers of Excellence and to the American Society of Nuclear Cardiology. The subcommittee reviews nominations and selects the awardee.

A preliminary program for the 2022 meeting, including streaming

sessions, is available at: <https://www.hcnmc.org/>.

### **FDA Approves Near-Infrared Imaging Agent for Ovarian Cancer**

The U.S. Food and Drug Administration (FDA) on November 29 approved Cytalux (pafolacianine), an optical imaging agent indicated in patients with ovarian cancer as a near-infrared adjunct to intraoperative identification of malignant lesions. The drug is manufactured by On Target Laboratories (West Lafayette, IN) and was previously granted Orphan Drug, Priority, and Fast Track designations.

“The FDA’s approval of Cytalux can help enhance the ability of surgeons to identify deadly ovarian tumors that may otherwise go undetected,” said Alex Gorovets, MD, deputy director of the Office of Specialty Medicine in the FDA Center for Drug Evaluation and Research. “By supplementing current methods of detecting ovarian cancer during surgery, Cytalux offers health care professionals an

additional imaging approach for patients with ovarian cancer.”

The drug is administered intravenously 1–9 h before surgery and binds to and fluoresces folate receptors. Cytalux is used with a near-infrared fluorescence imaging system cleared by the FDA for specific use with pafolacianine.

The safety and effectiveness of Cytalux was evaluated in 3 trials, including a randomized, multicenter, open-label study of women diagnosed with ovarian cancer or with high clinical suspicion of ovarian cancer who were scheduled to undergo surgery. The study included 134 women (ages, 33–81 y) who received a single dose of Cytalux and were evaluated under both normal and fluorescent light during surgery. More than a fourth of participants (26.9%) had at least 1 cancerous lesion detected under fluorescence imaging not observed by stand-ard visual or tactile inspection.

*U.S. Food and Drug Administration  
On Target Laboratories*

Each month the editor of *Newsline* selects articles on diagnostic, therapeutic, research, and practice issues from a range of international publications. Most selections come from outside the standard canon of nuclear medicine and radiology journals. These briefs are offered as a monthly window on the broad arena of medical and scientific endeavor in which nuclear medicine now plays an essential role. The lines between diagnosis and therapy are sometimes blurred, as radiolabels are increasingly used as adjuncts to therapy and/or as active agents in therapeutic regimens, and these shifting lines are reflected in the briefs presented here. We have also added a small section on noteworthy reviews of the literature.

### PSMA PET/CT Risk-Stratification Tool

Xiang, from the University of California at Los Angeles, and a multiinstitutional cohort of investigators reported in the December 1 issue of *JAMA Network Open* (2021;4[12]:e2138550) on the prognostic significance of a nomogram developed to model an individual's risk of nonlocalized upstaging of high-risk prostate cancer on prostate-specific membrane antigen (PSMA)-based PET/CT. The researchers also compared the nomogram's performance with that of existing risk-stratification tools. The 15-center, multinational study included 5,275 patients diagnosed with high- or very high-risk prostate cancer (prostate-specific antigen [PSA] >20 ng/mL, Gleason score of 8–10, and/or clinical stage of T3–T4, with no evidence of nodal or metastatic disease on conventional workup). Data calculated in the nomogram for PSMA upstaging included the biopsy Gleason score, percentage positive systematic biopsy cores, clinical T category, and PSA levels. Over a median follow-up of 5.1 y, 1,895 (36%) participants had biochemical recurrence, 851 (16%) developed distant metastases, and 242 (5%) died of

prostate cancer. The PSMA upstage probability was significantly prognostic for all clinical endpoints, with 8-y concordance indices of 0.63 for biochemical recurrence, 0.69 for distant metastases, 0.71 for prostate cancer-specific mortality, and 0.60 for overall survival. The PSMA nomogram outperformed existing risk-stratification tools, except for performance similar to that of the Staging Collaboration for Cancer of the Prostate for prostate cancer-specific mortality. Results were validated against secondary cohorts from a national database. The authors concluded that these findings suggest that PSMA upstage probability is associated with long-term, clinically meaningful endpoints, with superior risk discrimination compared with existing tools. They added that “formerly occult, PSMA PET/CT-detectable nonlocalized disease may be the main driver of outcomes in high-risk patients.”

*JAMA Network Open*

### SPECT/CT in Complex Foot and Ankle Diagnosis

In an article published on December 7 ahead of print in *Foot & Ankle Specialist*, Ghani et al. from the Royal National Orthopaedic Hospital (Stanmore, UK) reported on an assessment of the value of SPECT/CT in patients with complex but nonarthritic and nonneoplastic foot and ankle pathology with unclear diagnoses after conventional imaging. The retrospective research, which began with a dataset of 297 SPECT/CT foot and ankle studies, found only 18 (age range, 16–56 y) performed for nonarthritic/nonneoplastic diagnoses. The resulting SPECT/CT findings differed from provisional diagnoses in 10 (56%) of the 18 patients, leading to changes in treatment planning and significant improvements in 8 of these 10 patients. In the remaining 8 patients, SPECT/CT was useful in confirming provisional diagnoses, which had been uncertain on conventional imaging. A total of 15 of the 18 patients (83%) showed improvements in symptoms after

management affected by SPECT/CT diagnoses. The authors concluded that these results highlight “the added value of SPECT/CT in patients presenting with nonarthritic and nonneoplastic foot and ankle conditions in which there is diagnostic uncertainty after conventional imaging” and noted that in their practice they have found SPECT/CT to be a useful investigative modality in assessing these cases.

*Foot & Ankle Specialist*

### Dual-Tracer PET/CT in Renal Cell Carcinoma

Tariq et al. from the Royal Brisbane and Women's Hospital (Brisbane), the University of Queensland (Brisbane), Redcliffe Hospital, Wesley Urology Clinic/The Wesley Hospital (Brisbane), and the Princess Alexandra Hospital (Brisbane; all in Australia) reported on December 8 online ahead of print in *Urologic Oncology* on dual-tracer  $^{18}\text{F}$ -FDG and prostate-specific membrane antigen (PSMA)-based PET/CT compared with standard-of-care imaging for the characterization, staging, and restaging of renal cell carcinoma. The retrospective, multicenter study included 11 patients (mean age, 65.5 y; 7 men, 4 women) who underwent dual-tracer PET/CT after conventional imaging. Indications for referral to dual-tracer PET were staging (36%) and restaging after radical/partial nephrectomy (64%). Mixed patterns of uptake in primary tumor assessment were concordant in 40% and discordant in 60% (20% favoring PSMA and 40% favoring  $^{18}\text{F}$ -FDG). Tracer uptake in metastatic disease was concordant in 6 patients (55%), in agreement as negative in 3 (27%), and discordant in 2 (favoring PSMA). PET was superior to standard-of-care imaging for assessment of metastatic disease in 5 patients (45%) and equivalent for the remainder, with resulting management changes in 3 (27%). The authors noted that PSMA tracers and  $^{18}\text{F}$ -FDG offer complimentary advantages in PET/CT assessment of primary and metastatic

renal cell carcinoma and that the intensity of avidity of the tracers may assist in prognostication.

*Urologic Oncology*

### US-Based Respiratory Motion Detection in PET/CT

In an article published on December 10 ahead of print in *Physics in Medicine and Biology*, Madore et al. from the Harvard Medical School/Brigham and Women's Hospital (Boston, MA), the University of Oxford (UK), National Sun Yat-Sen University (Kaohsiung, Taiwan), Amazon Robotics (Westborough, MA), Eindhoven University of Technology (The Netherlands), and the University of Pennsylvania Perelman School of Medicine (Philadelphia) reported on development and testing of small ultrasound-based sensors, referred to as organ-configuration motion (OCM) sensors, that attach to the skin and provide motion-sensitive information to allow respiratory gating during PET imaging. In the study, both a motion phantom with an  $^{18}\text{F}$ -FDG solution and imaging in 2 cancer patients were used to test the sensors. In the phantom and in patients, the OCM signals were used to help reconstruct data into time series of motion-resolved images accurately capturing underlying motion. In 1 patient, a single large lesion was seen to be mostly stationary through the breathing cycle. In the second patient, several small lesions were mobile during breathing, and the sensors captured breathing-related displacements. The authors noted that this relatively inexpensive and simple hardware solution, which attaches to the skin rather than walls or ceilings, is advantageous because it can accompany patients from 1 procedure to another, with the potential for gathering more consistent and useful data on breathing motion-related changes.

*Physics in Medicine and Biology*

### Brain Metabolism Patterns and Epilepsy Death Risk

Whatley, from the University College of London/Queen Square Institute of Neurology (UK), and a consortium of researchers from the UK, Canada, and

the United States reported on November 23 ahead of print in *Frontiers in Neurology* on a study using  $^{18}\text{F}$ -FDG PET to characterize regional brain metabolic differences in patients with epilepsy at high risk of sudden unexpected death. The study included patients with refractory focal epilepsy at high ( $n = 56$ ) and low ( $n = 69$ ) risk of sudden unexpected death who underwent interictal  $^{18}\text{F}$ -FDG PET as part of presurgical assessment. Whole-brain analyses were used to explore regional differences in interictal metabolic patterns and were contrasted with regional brain metabolism more directly related to frequency of focal-to-bilateral tonic-clonic seizures. Imaging found that regions associated with cardiorespiratory and somatomotor regulation differed in interictal metabolism. Tracer uptake was increased in the basal ganglia, ventral diencephalon, midbrain, pons, and deep cerebellar nuclei in patients in the high-risk of sudden death group, and uptake was decreased in the left planum temporale. These patterns differed from those associated with focal-to-bilateral tonic-clonic seizure frequency (decreased uptake in bilateral medial superior frontal gyri, extending into the left dorsal anterior cingulate cortex). PET-identified changes in interictal metabolic activity in regions critical to cardiorespiratory and somatomotor regulation in patients considered to be at relatively high risk of sudden death from epilepsy have the potential to elucidate processes that may predispose such patients to sudden death and to identify such patients and affect management.

*Frontiers in Neurology*

### Benzodiazepine and AD: $^{18}\text{F}$ -Florbetapir PET and MRI

In an article published on December 10 ahead of print in *Neuropsychopharmacology*, Gallet, from University Hospital (Angers, France), and French re-searchers in the MEMENTO study looked at data from that cohort correlating benzodiazepine (BZD) use and neuroimaging markers of Alzheimer disease (AD) in nondemented older individuals with isolated memory complaints or light cognitive impairment at baseline. The study's goals were to replicate/assess findings on

BZD use and brain amyloid load with  $^{18}\text{F}$ -florbetapir PET and to investigate associations between BZD use and hippocampal volume with MRI. Chronic BZD user and nonuser data on multiple-variable clinical, symptomatic, and genetic data were compared. The authors found that BZD users were more likely to manifest symptoms of depression, anxiety, and apathy. Total SUV ratios and hippocampal volumes were significantly lower and larger, respectively, in BZD users than in nonusers. Short-acting BZDs and Z-drugs (Zopiclone/Zolpidem) were more significantly associated with larger hippocampal volumes, with no significant effects associated with dose and duration of BZD use. The authors concluded that these results "support the involvement of the GABAergic system as a potential target for blocking AD-related pathophysiology, possibly via reduction in neuronal activity and neuroinflammation" and noted that additional longitudinal studies may confirm the causal effect of BZDs in blocking amyloid accumulation and hippocampal atrophy.

*Neuropsychopharmacology*

### DCE CT vs PET in Solitary Pulmonary Nodules

Gilbert, from the University of Cambridge (UK), and a large group of UK researchers reported on December 9 ahead of print in *Thorax* on a study comparing the accuracy and cost effectiveness of dynamic contrast-enhanced CT (DCE CT) and PET/CT in diagnosis of malignancy in solitary pulmonary nodules. The prospective multicenter trial included individuals with a solitary pulmonary nodule (range, 8–30 mm) and no recent history of malignancy. The protocol included both types of imaging and either biopsy with histologic diagnosis or completed CT follow-up. A total of 312 participants (53% men, 47% women; ages,  $68.1 \pm 9.0$  y) completed the study, with a 61% rate of malignancy at 2-y follow-up. The sensitivity, specificity, and positive- and negative-predictive values for DCE-CT were 95.3%, 29.8%, 68.2%, and 80.0%, respectively. For PET/CT the respective percentages were 79.1%, 81.8%, 87.3%, and 71.2%. The areas under the receiver

operator characteristic curves for DCE-CT and PET/CT were 0.62 and 0.80, respectively. Combining results from the 2 imaging modalities significantly increased diagnostic accuracy over PET/CT alone. In a cost analysis, DCE-CT was preferred when the “willingness to pay” per incremental cost per correctly treated malignancy was below £9,000. Above £15,500 a combined approach was preferred. The authors concluded that “PET/CT has a superior diagnostic accuracy to DCE-CT for the diagnosis of solitary pulmonary nodules” and that “combining both techniques improves the diagnostic accuracy over either test alone and could be cost effective.”

*Thorax*

### **PET/CT Textural Features in Follicular Lymphoma**

In an article published in the December 10 issue of *Scientific Reports* (2021;11[1]:23812), Faudemer et al. from Caen University Hospital, Normandy University (Caen), and the Comprehensive Cancer Centre François Baclesse (Caen; all in France) reported on a study assessing the value of baseline <sup>18</sup>F-FDG PET/CT radiomics (skeletal textural features) in the diagnosis of bone marrow involvement in patients with follicular lymphoma. The retrospective study included 66 patients newly diagnosed with follicular lymphoma. For visual assessment, patients with obvious bone focal uptake were considered positive. For textural analysis, skeletal volumes of interest were automatically extracted from segmented CT images. Bone marrow biopsy and visual assessment were used as a gold standard in categorizing participants as bone-negative (negative bone marrow biopsy/negative PET) or bone-positive (positive bone marrow biopsy/negative PET, negative bone marrow biopsy/positive PET, or positive bone marrow biopsy/positive PET). Thirty-six patients (54.5%) were classified as bone-negative and 30 (45.5%) as bone-positive. Software analysis identified a cut-off of -0.190 as optimal for diagnosis of bone marrow involvement using a PET predictive score. The corresponding sensitivity, specificity, and positive- and negative-predictive values for PET were

70.0%, 83.3%, 77.8%, and 76.9%, respectively. A significant difference was found between bone marrow biopsy results and visual PET assessments, whereas bone marrow biopsy results and the PET radiomics predictive score were concordant. The authors concluded that “skeleton texture analysis is worth exploring to improve the performance of <sup>18</sup>F-FDG PET/CT for the diagnosis of bone marrow involvement at baseline in follicular lymphoma patients.”

*Scientific Reports*

### **PET/CT Prediction of Urinary Retention After Hysterectomy**

Davidson et al. from Chaim Sheba Medical Center (Tel Hashomer), Tel Aviv University (Ramat Aviv), and Hebrew University of Jerusalem (all in Israel) reported on December 14 ahead of print in *Minerva Obstetrics and Gynecology* on a study using <sup>18</sup>F-FDG PET/CT to measure residual urinary volume both before and after radical hysterectomy to determine whether scanned abnormal residual bladder volume is predictive of future urinary symptoms. The study included 64 women. Postvoid bladder volumes were  $\geq 150 \text{ cm}^3$  on postoperative PET/CT in 24 (38%) patients, with 9 (37.5%) of these experiencing some degree of voiding difficulty. In 3 of the 24 patients, the high bladder volume on PET/CT was seen 2–4 mo before complaints of voiding difficulty. Of the 40 (62%) remaining patients whose postoperative bladder volumes were  $< 150 \text{ cm}^3$ , only 1 (2.5%) had urinary retention. Symptomatic voiding difficulties were higher in the postvoid volume  $\geq 150 \text{ cm}^3$  group than in the  $< 150 \text{ cm}^3$  group (13 and 6, respectively). The authors concluded that “measuring bladder volume on postoperative <sup>18</sup>F-FDG PET/CT may facilitate early identification of urinary retention, possibly enabling early treatment and possibly preventing complications.”

*Minerva Obstetrics and Gynecology*

### **Machine Learning and SPECT MPI Polar Maps**

In an article published on November 11 in *Frontiers in Cardiovascular*

*Medicine* (2021;8:741667), Marques de Souza Filho et al. from the Universidade Federal Fluminense (Rio de Janeiro, Brazil), Universidade Federal Rural do Rio de Janeiro (Rio de Janeiro, Brazil), the University of Ottawa Heart Institute (Canada), and the Hospital Pró-Cardíaco/Americas Serviços Médicos (Rio de Janeiro, Brazil) reported on a study using machine learning algorithms to differentiate normal from abnormal gated SPECT myocardial perfusion polar map images. The authors analyzed 1,007 polar maps from a database of patients referred for clinically indicated myocardial perfusion imaging. Studies were first visually assessed and reported by experts as a comparative standard. Image features were then extracted using polar map segmentation based on horizontal and vertical slices. Cross-validation divided the dataset into training and testing subsets. All machine learning models (except for 1) had accuracy  $> 90\%$  and area under the receiver operating characteristics curves  $> 0.80$ . Overall machine learning precision and sensitivity were  $> 96\%$  and  $92\%$ , respectively. The authors concluded that machine learning algorithms performed well in image classification and were remarkably capable of distinguishing normal from abnormal polar maps.

*Frontiers in Cardiovascular Medicine*

### **Nanoparticle Radioenhancer Plus RIT**

Hu et al. from the University of Texas MD Anderson Cancer Center (Houston, TX), Nanobiotix (Paris, France), the Shandong Cancer Hospital and Institute/Shandong First Medical University/Shandong Academy of Medical Sciences (Jinan, China), and the Koc University School of Medicine (Istanbul, Turkey) reported on December 11 in the *Journal of Nanobiotechnology* (2021;19[1]:416) on results from a study of multicomination therapy in which NBTXR3, a clinically approved nanoparticle radioenhancer, was combined with high-dose radiation to a primary tumor plus low-dose radiation to a secondary tumor along with

immune checkpoint inhibitor blockade in a mouse model of anti-PD1-resistant metastatic lung cancer. In the complex protocol, mice were injected with a metastatic mouse lung cancer cell line in the right leg on d 0 for the primary tumor and the left leg on d 3 for the secondary tumor. Immune checkpoint inhibitors (anti-PD1 and anti-CTLA4) were administered intraperitoneally. Primary tumors were injected with NBTXR3 on d 6 and irradiated with 12 Gy on d 7, 8, and 9. Secondary tumors were irradiated with 1 Gy on d 12 and 13. Surviving mice at d 178 were rechallenged with the original lung cancer cell lines, and tumors were monitored. The researchers found that the combination of therapies resulted in significant antitumor effects against both primary and secondary tumors, improving the survival rate from 0 to 50%. Immune profiling in secondary tumors showed that the nanoparticle enhancer plus low- and high-dose radiation increased CD8 T-cell infiltration and decreased the number of regulatory T cells. None of the rechallenged mice developed tumors. These rechallenged mice were found to have higher percentages of CD4 memory T cells and CD4 and CD8 T cells in both blood and spleen than untreated mice. The authors concluded that the NBTXR3 nanoparticle “in combination with radioimmunotherapy significantly improves anti-PD1-resistant lung tumor control via promoting antitumor immune response.”

*Journal of Nanobiotechnology*

### Coffee Consumption and Cognitive Decline

Gardener, from Edith Cowan University (Joondalup, Australia), and a consortium of researchers from the Australian Imaging, Biomarkers, and Lifestyle (AIBL) study reported on November 19 in *Frontiers in Aging Neuroscience* (2021;13:744872) on the results of an investigation of the relationship between self-reported habitual coffee intake and cognitive decline. The report included AIBL data with comprehensive neuropsychological battery assessments from 227 cognitively normal older adults over more than 10 y. The researchers also investigated the relationship between habitual coffee intake and

cerebral amyloid- $\beta$  accumulation in 60 of the individuals and brain volumes in 51. The researchers found that higher baseline coffee consumption was associated with slower cognitive decline in executive function, attention, and performance on the AIBL Preclinical Alzheimer Disease Cognitive Composite assessment and with lower likelihood of transitioning to mild cognitive impairment or AD status over the duration of the study. Higher baseline coffee consumption was also associated with slower amyloid- $\beta$  accumulation and lower risk of progressing to moderate, high, or very high categories of amyloid- $\beta$  burden. No associations were noted between coffee intake and atrophy in total gray matter, white matter, or hippocampal volumes. The authors concluded that these results “support the hypothesis that coffee intake may be a protective factor against Alzheimer disease, with increased coffee consumption potentially reducing cognitive decline by slowing cerebral A $\beta$ -amyloid accumulation, and thus attenuating the associated neurotoxicity from A $\beta$ -amyloid-mediated oxidative stress and inflammatory processes.”

*Frontiers in Aging Neuroscience*

### Delayed PET and Glioblastoma Conspicuity

In an article in the November 16 issue of *Frontiers in Neurology* (2021; 12:740280), Johnson et al. from the University of Texas MD Anderson Cancer Center and Baylor College of Medicine (both in Houston, TX) reported on a study designed to determine the ideal timepoint for  $^{18}\text{F}$ -FDG PET imaging of suspected glioblastoma. The study was intended as part of preparation for future trials involving noninvasive differentiation of true progression from pseudoprogression in glioblastoma. This initial investigation included 16 adults (9 men, 7 women) with suspected glioblastoma who underwent PET imaging at 1, 5, and 8 h after  $^{18}\text{F}$ -FDG injection within 3 d before scheduled surgery. Maximum SUVs were quantified for the central enhancing component of the lesion and contralateral normal brain. Results showed statistically significant improvements in maximum SUVs and subjective reader

conspicuity of glioblastomas at later time points when compared to the conventional 1-h time point. Tumor-to-background ratios at 1, 5, and 8 h after tracer injection were  $1.4 \pm 0.4$ ,  $1.8 \pm 0.5$ , and  $2.1 \pm 0.6$ , respectively. The authors concluded that these findings “demonstrate that delayed imaging time point provides superior conspicuity of glioblastoma compared to conventional imaging.”

*Frontiers in Neurology*

### Characterizing BRAF-Mutant Papillary Thyroid Cancer Subtypes

Boucai et al. from the Memorial Sloan Kettering Cancer Center (New York, NY), MD Anderson Cancer Center (Houston, TX), and the Cleveland Clinic (OH) reported on November 23 online ahead of print in the *Journal of Clinical Endocrinology and Metabolism* on a study looking at the feasibility of characterizing the molecular and clinical features of 2 subtypes of BRAF-mutant papillary thyroid cancer by their degree of expression of iodine metabolism genes. The study included data from 227 BRAF-mutant papillary thyroid cancer tumors in the Cancer Genome Atlas (Thyroid Cancer), divided into 2 subgroups based on their thyroid differentiation score (TDS; categorized as high or low). A range of data points were compared between the 2 groups. Seventeen percent of tumors were categorized as high BRAF-TDS and 83% as low. High BRAF-TDS tumors were more common in black and Hispanic patients. High BRAF-TDS tumors were also larger, associated with more tumor-involved lymph nodes, and had a higher frequency of distant metastases. Gene set enrichment analyses showed positive enrichment for RAS signatures in the high BRAF-TDS cohort, with corresponding but less pronounced changes in the low group. Several microRNAs (miR-204, miR-205, and miR-144) were overexpressed in the high group. In a subset of data on clinical patient follow-up, those with high BRAF-TDS tumors had higher complete responses to therapy than those in the low BRAF-TDS tumor group

(94% and 57%, respectively). The authors concluded that “enrichment for RAS signatures, key genes involved in cell polarity, and specific miRs targeting the transforming growth factor  $\beta$ -SMAD pathway define 2 subtypes of BRAF-mutant papillary thyroid cancer subtypes with distinct clinical characteristics and prognosis.”

*Journal of Clinical Endocrinology and Metabolism*

### SLN Visualization in Upper Urinary Tract Urothelial Cancer

In an article published on November 23 in the *Journal of Clinical Medicine* (2021;10[23]:5465), Polom et al. from the Medical University of Gdansk (Poland) reported on a radioisotope-based technique for detection of sentinel lymph nodes (SLNs) and analysis of lymphatic outflow in patients with suspected upper-tract urothelial carcinoma (UTUC). The study included 19 such patients (7 men, 12 women; mean age, 73.4 y) who were scheduled for ureterorenoscopy. Staging included  $^{99m}\text{Tc}$ -nanocolloid radioactive tracer injection and tumor biopsy (pathology: 8 patients, T0 [42%]; 7 patients, Ta [36%]; and 4 patients, T1 [21%]). 3D reconstruction and image fusion were performed for better localization of lymph nodes, and SPECT/CT lymphangiography was used for detection of SLNs and analysis of radiotracer outflow. SLNs were detected in 2 patients (10%): 1 in whom a single SLN was visualized and another in

whom multiple radioactive lymph nodes were visualized. SPECT/CT detected no lymphatic outflow in 17 (89.5%) patients. In 5 of these patients (26.3%), however, gravitational leakage of injected radiotracer to the retroperitoneal space was noted. The authors concluded that these results reinforce the challenging nature of detecting SLNs in the upper urinary tract, with associated difficulties in radiotracer injection during ureterorenoscopy. However, “SPECT/CT lymphangiography in cases of UTUC may provide valuable information about a patient's individual anatomy of the lymphatic system and the position of the first lymph nodes draining lymph with potential metastatic cells from the tumor.”

*Journal of Clinical Medicine*

### Reviews

Review articles provide an important way to stay up to date on the latest topics and approaches through valuable summaries of pertinent literature. The Newsline editor recommends several general reviews accessioned into the PubMed database in November and December. Rowe and Pomper, from the Johns Hopkins University School of Medicine (Baltimore, MD), provided an overview of “Molecular imaging in oncology: Current impact and future directions” on December 13 ahead of print in *CA: A Cancer Journal for Clinicians*. In an article in the November 30 issue of *Cancers (Basel)* (2021;13:6026), Guglielmo

et al. from the Veneto Institute of Oncology IOV-IRCCS and the University of Padova (both in Italy) surveyed the “Additional value of PET radiomic features for the initial staging of prostate cancer: A systematic review from the literature.” The role of “Tau biomarkers in dementia: Positron emission tomography radiopharmaceuticals in tauopathy assessment and future perspective” was outlined by Ricci et al. from the University of Rome Tor Vergata and IRCCS Neuromed (Pozzilli; both in Italy) in the November 30 issue of the *International Journal of Molecular Sciences* (2021; 22[23]:13002). Beuthien-Baumann et al. from the Deutsches Krebsforschungszentrum Heidelberg and the Universitätsklinikum Heidelberg (both in Germany) reviewed “Adapting imaging protocols for PET-CT and PET-MRI for immunotherapy monitoring” in the November 30 issue of *Cancers (Basel)* (2021; 13[23]:6019). In the November 24 issue of *Molecules* (2021;26[23]:7111) Prigent and Vigne from Normandie Université (Caen, France) outlined “Advances in radiopharmaceutical sciences for vascular inflammation imaging: Focus on clinical applications.” Rondon et al. from the Université Catholique de Louvain (Brussels, Belgium), the Université Clermont-Auvergne (Clermont-Ferrand, France), and CHU Estaing (Clermont-Ferrand, France) published “Radioimmunotherapy in oncology: Overview of the last decade clinical trials” on November 7 in *Cancers (Basel)* (2021;13[21]:5570).

# A European Oncology Leader Looks at PSMA

A Conversation Between Silke Gillessen, Johannes Czernin, and Ken Herrmann

Silke Gillessen<sup>1,2</sup>, Johannes Czernin<sup>3</sup>, and Ken Herrmann<sup>4</sup>

<sup>1</sup>University of Southern Switzerland, Lugano, Switzerland; <sup>2</sup>Department of Oncology, Institute of Oncology of Southern Switzerland, Bellinzona, Switzerland; <sup>3</sup>David Geffen School of Medicine at UCLA, Los Angeles, California; and <sup>4</sup>Universitätsklinikum Essen, Essen, Germany

**J**ohannes Czernin, MD, editor in chief of *The Journal of Nuclear Medicine*, and Ken Herrmann, MD, MBA, a professor of nuclear medicine at the Universitätsklinikum Essen (Germany), talked with Silke Gillessen, MD, an internationally recognized oncologist whose practice and research focus on genitourinary cancer. She is a professor and head of the Department of Medical Oncology at the Università della Svizzera Italiana (Lugano, Switzerland) and director of the Istituto Oncologico della Svizzera Italiana (Bellinzona, Switzerland). She received her early medical training in Switzerland and completed her training at the Dana-Farber Cancer Institute (Boston, MA). After returning to Switzerland, she launched the medical oncology unit for genitourinary cancer and headed the clinical research unit for oncology/hematology at the Kantonsspital St. Gallen (Switzerland). From 2018 to 2020, she was Genitourinary Cancer Systemic Therapy Research Chair at the University of Manchester and Honorary Consultant at The Christie Hospital (Manchester, U.K.).

Dr. Gillessen has led numerous clinical trials. She cofounded the Advanced Prostate Cancer Consensus Conference (APCCC), served 2 terms as president of the Swiss Group for Clinical Cancer Research (SAKK) Genitourinary group, and chaired the European Organization for Research and Treatment of Cancer Genitourinary Cancers Group. She was the recipient of the prestigious SAKK/Pfizer award.

**Dr. Czernin:** *You were trained in medicine and oncology and went through extensive clinical training in Switzerland. You completed a postdoctoral fellowship at Dana-Farber and then came back to Switzerland to become a faculty member and then professor in medicine and oncology. Then you moved to Manchester for some time to lead a large cancer program. What did you do there, and what prompted you to return to Switzerland?*

**Dr. Gillessen:** I spent almost 20 years in St. Gallen, Switzerland, after I came back from Dana-Farber Cancer Institute. Thomas Cerny, MD, who was the leader of the team at St. Gallen (Kantonsspital St. Gallen), was a renaissance doctor, interested in sports, in classical music, in philosophy—interested in everything. It was a great pleasure working for and with him. I never considered leaving. But, because our children went to college, my husband and I were suddenly free to move. I received offers from all over the world. Because my parents were older, we decided to stay close to them in Europe. The University of Manchester wanted to build up a systemic therapy trial unit, and I accepted. It was really interesting to see the English system, which is very

different from the Swiss system. Clinicians see many more patients and, of special interest to me, many prostate and testicular cancer patients. They also had huge scientific potential there. Everything worked well for me, but it was not easy for my husband, who is an ecologic architect and could not find work in the United Kingdom. I was offered this position in Ticino, with my main office in Bellinzona, which is one of the most beautiful places in the world. We decided to move back home where there are also many more opportunities for my husband.

**Dr. Herrmann:** *When talking with you we want to immediately bring up the APCCC. This is one of your major achievements. Can you talk for a moment about how you created the APCCC?*

**Dr. Gillessen:** St. Gallen was the birthplace of a famous consensus conference for early breast cancer that had been taking place for more than 20 years. We came up with the idea of holding a consensus conference on advanced prostate cancer. I asked Johann De Bono, MD, PhD, and other friends, who all responded, “why not”? We started very small, with 250 participants, and had to rely mostly on the support of pharma sponsors (although they had no impact on topic questions or discussions). The most critical point in an effort like this is to frame the questions in such a way that they can be helpful for the professionals who subsequently consult the resulting consensus articles. The APCCC is held every second year, and so far we have doubled attendance at each conference, with satellite conferences to establish management paradigms all over the world.

**Dr. Czernin:** *One of the key topics of the 2021 APCCC was prostate-specific membrane antigen (PSMA) imaging. The landscape of prostate cancer diagnosis at various stages is changing. How do you see the role of PSMA PET/CT for staging and biochemical recurrence and also for later stage, progressive disease?*

**Dr. Gillessen:** PSMA-targeted imaging is a very good tool, and I do not think anyone is suggesting that we go back to bone scans. However, we need to stay critical. Most of the data that I have seen were based on <sup>68</sup>Ga-labeled PET probes. In Switzerland, we now see more and more <sup>18</sup>F-PSMA-1007 usage, where less data are available. And there is an issue with nonspecific bone uptake. I now see many high-risk patients who have undergone <sup>18</sup>F-PSMA-1007 imaging for primary staging, with, for example, 2 visualized



Silke Gillessen, MD

bone lesions. With conventional imaging these would be staged as M0, and we treat them like M0. We also have cases in which MRI locates bone lesions in different regions from those localized by PSMA PET—and then the bone biopsy is negative. As the treating physician, what am I supposed to do? Am I moving away from a curative to a palliative treatment? This is very, very difficult right now. What are your thoughts?

**Dr. Herrmann:** *In this case we would do a gallium PSMA scan, and then the majority of lesions are gone. Nonspecific bone uptake is much more frequent with PSMA-1007, requiring experience and involving a learning curve.  $^{18}\text{F}$ -DCFPyL is also fluorinated, but this problem is not encountered as frequently.*

**Dr. Gillessen:** It is no longer easy to get a gallium scan here. These unclear results are very stressful for patients. It makes us nervous, too, because we may overtreat these false-positives. I think the interaction between our nuclear medicine specialists and oncologists must become much closer in disease staging, because we all need to learn. The danger is that some physicians are going away from a curative intent to a palliative treatment because of false-positive bone lesions.

**Dr. Herrmann:** *Yes, we have to start a discussion. I am a PSMA believer. We tend to look at impact on management, which may not be a good endpoint. Could we still perform a randomized trial with the endpoints of progression-free and overall survival in PET versus conventional imaging based at initial staging in high-risk patients?*

**Dr. Czernin:** *Our combined University of California at Los Angeles/University of California San Francisco presurgical study showed detection of lymph node involvement in 40% of patients.*

versus a bad fluorinated compound and that one may require more experience than the other for interpretation. This is something you know very well, but 95% of clinicians won't know about differences between various PSMA PET probes. You need to teach us!

**Dr. Herrmann:** *You previously mentioned bone scans, which are still very widely available. Do you still see a role for bone scans?*

**Dr. Gillessen:** I sometimes do bone scans in patients with high-risk prostate cancer who were staged with  $^{18}\text{F}$ -PSMA-1007 PET CT and have, for example, 2 small lesions that might be false-positive. I do this to confirm M0 staging with conventional imaging, and I can then treat them with curative intent. I have to say that (except for a few patients with DNA repair defects or microsatellite instability) bone scans are the only predictive biomarker that we have for treatment of metastatic prostate cancer. We don't have other validated predictive biomarkers that we use for treatment decision making in hormone-sensitive disease. It is amazing that such an old and inexpensive method can help us decide on treatment management in hormone-sensitive disease, in the sense that fewer bone lesions (low-burden disease) predict an overall benefit for radiotherapy to the primary tumor in the metastatic setting.

**Dr. Czernin:** *Despite all of that, the new National Comprehensive Cancer Network (NCCN) guidelines now include PSMA PET/CT, limited to  $^{68}\text{Ga}$ -PSMA-11 and  $^{18}\text{F}$ -PYL. NCCN endorses PSMA PET/CT pretty much at every stage of disease. The NCCN panel noted that PSMA PET/CT can also be considered as front-line imaging before any other imaging test. What would you do with these new guidelines as a practicing urooncologist?*

---

“PSMA-targeted imaging is a very good tool, and I do not think anyone is suggesting that we go back to bone scans. However, we need to stay critical.”

---

*This is above and beyond what conventional imaging detects. The specificity is less of a problem, because the positive predictive value is very high, especially for lymph nodes (as long as you have fairly knowledgeable readers). People often simply lack clinical insights, and we do not know enough about pretest likelihoods. The other problem is the fundamental error of “Wow, I see more,” which is a trap leading to reduced specificity.*

**Dr. Gillessen:** It think it is a trap. Seeing more does not necessarily mean that we reach a better clinical outcome.

**Dr. Herrmann:** *You have responded in part to one of our questions already, namely what you expect from nuclear medicine consultations. Can you elaborate?*

**Dr. Gillessen:** Nuclear medicine physicians believe in their images. But I think we need that interaction. I adore what Michael Hofman, MD, has done, but I assume he is still working with  $^{68}\text{Ga}$ -PSMA and probably has not used  $^{18}\text{F}$ -PSMA-1007 much. At least in Switzerland,  $^{18}\text{F}$ -PSMA-1007 is logistically so much easier and is therefore used a lot. Even if I wanted to use  $^{68}\text{Ga}$ -PSMA more, it is not easily available. Many oncologists, urologists, and radiotherapists who are not specialized may just see that a PSMA PET/CT is available and order it. On Twitter, for example, “PSMA PET” is almost always referenced without specifying the tracer, or whether the scan is performed with a CT or a MRI, or whether iodine contrast media is given for the CT part. Not all clinicians realize that when we say “PSMA PET/CT,” this could mean different exams. Now you two tell me you can have a good

**Dr. Gillessen:** To be honest, I follow European guidelines more, because I'm also a member of the panel writing them. The 2021 European guidelines endorse PSMA imaging for biochemical recurrence or prostate-specific antigen (PSA) persistence. In Switzerland, it is approved for high-risk and even intermediate localized cancer and for biochemical recurrence. But we also use it in identifying metastatic castrate-resistant prostate cancer (mCRPC) patients for  $^{177}\text{Lu}$ -PSMA radioligand treatment.

**Dr. Czernin:** *That's pretty much the same as the NCCN guidelines.*

**Dr. Herrmann:** *What information would you want to see to implement PSMA PET/CT for treatment response assessments? We do not have any data making the case now, but, looking forward, what kind of data would you want to see?*

**Dr. Gillessen:** For me there are 2 items: For the hormone-sensitive stage, little data are available about the impact of hormone treatment on PSMA expression. This treatment works in 95% of men. The Australians have the feeling that androgen-deprivation therapy (ADT) decreases PSMA expression in most patients and increases it in a few. Not enough prospective data are available to determine what this means. The value of PSMA PET-based response assessments in castrate-resistant patients is also unknown. I have seen patients with hormone-sensitive advanced disease treated with abiraterone and ADT, in whom PSMA PET imaging shows a decreased size of the lesions but PSMA “activity” goes up. What does this “activity” mean?

**Dr. Herrmann:** More “active” meaning higher SUV or more lesions?

**Dr. Gillessen:** Higher SUV. Patients are getting nervous about reports like this. And I have to tell them that we don’t yet have enough experience with PSMA-based imaging in this situation, but we do have experience with reduction of lesion sizes (like lymph nodes). For the moment, we probably have to focus on the “old” response criteria in the hormone-sensitive setting, and these include reductions in lesion size and in PSA levels. This is what we know. Please, dear nuclear medicine community, develop a consistent nomenclature and help us by developing response criteria for PSMA PET/CT!

**Dr. Czernin:** *What is really being imaged is PSMA expression. In my view, that’s the term that should be used.*

**Dr. Gillessen:** It is your community, so you have to discuss this and homogenize.

**Dr. Herrmann:** *Another difficult area is metastasis-directed treatment based on PSMA PET. You have seen the EMPIRE-1 study with <sup>18</sup>F-fluciclovine PET/CT, which had impressive outcomes. Based on the EMPIRE-1 study, do you think that there’s room for PSMA PET-directed metastatic-directed treatment?*

**Dr. Gillessen:** The EMPIRE-1 study is a single-center, open-label, phase 2/3 study comparing conventional imaging plus <sup>18</sup>F-fluciclovine PET/CT versus conventional imaging alone to guide postprostatectomy salvage radiotherapy. The researchers included 165 patients, and the primary endpoint was 3-year event-free survival. I think it is a very important study, because it asked an imaging question not about accuracy but about clinical outcome. We urgently need more such studies, even if you could argue that a clinically more relevant endpoint like overall survival should be chosen. Multicenter larger trials are needed as well.

**Dr. Czernin:** *I agree; data on targeted approaches are very limited. In our presurgical staging study published in 2021, more than 30 patients underwent metastasis-targeted treatment. PSA declined by > 50% in 80% of patients in response to the intervention. The question is, of course, what does it mean for the outcome?*

**Dr. Gillessen:** In a patient treated with metastasis-directed therapy after prostatectomy, if the PSA does not go down to zero it is very likely that all the lesions have not been hit. There are lesions that won’t be visible, even on PSMA PET/CT. We know that generally the earlier you start hormonal treatment, the better the probable outcome. So what you are doing with that “zapping” may also be deferring the systemic treatment that could be beneficial. Do we really know that we are doing something good for our patients? Strong evidence is still missing.

**Dr. Czernin:** *Good argument.*

**Dr. Gillessen:** But I think some patients with oligometastatic metachronous disease may profit from radiotherapy of metastases, maybe with temporary systemic treatment. After that, they could be free of systemic treatment for some time—perhaps for a very long time. I totally agree with you both. But who are these patients? How do we select them? The goal here would be to defer continuous systemic treatment. We need prospective randomized trials to prove that there is a benefit. Another idea would be *not* to defer systemic treatment but to try to give “maximal” combined treatment at the beginning to “cure” (meaning to achieve long-term complete remission in) some patients. But we don’t have the data.

**Dr. Czernin:** *That brings us to the therapy portion of our discussion. We have all seen the results of the VISION trial of <sup>177</sup>Lu-PSMA-617 in mCRPC. Were they what you expected or maybe*

*just the first realistic information about what kind of impact this treatment has on survival?*

**Dr. Gillessen:** Can I say that this is a somewhat manipulative question? We have a new treatment with a new mechanism of action, which is always very good news. It means we have an additional treatment for our patients. It’s not just another hormonal treatment that can be used in place of another—it’s really something new. However, I was a bit disappointed by the trial results. It is not so different from cabazitaxel, and it’s not so different from the standard of care in these late-line mCRPC patients. I would assume there must be a better way to select patients who will benefit. I’m just hoping that the academics will try to go back and identify the patients who really profited and, perhaps more important, those who did not.

**Dr. Herrmann:** *I fully agree with your emphasis on better patient selection. There’s a vocal group of people in the United States who say we should not select patients for PSMA radioligand therapy at all because such a high proportion of prostate cancers exhibit PSMA expression. What is your take there?*

**Dr. Gillessen:** If we have a biomarker, we should use it, in my opinion. But evidence needs to develop. I am concerned about patients with PSMA imaging results that are only slightly positive in liver metastases. I would prefer to start with chemotherapy first, because we do not know if the patient is still chemotherapy-fit after the treatment with <sup>177</sup>Lu-PSMA. But this is a gut feeling, right? I have asked VISION investigators about liver involvement, degree of expression in liver lesions, and outcomes but have not seen the data. Another problem is that nuclear medicine PET/CT studies often don’t use intravenous contrast, which prevents appropriate liver imaging.

**Dr. Czernin:** *I completely agree with you, because not doing intravenous contrast with PET/CT to me is wrong. Why would you have a patient undergoing a suboptimal CT? We give intravenous contrast in pretty much every patient.*

**Dr. Herrmann:** *Even the guidelines say it. We do 90% of our PET/CTs with intravenous contrast.*

**Dr. Czernin:** *The group at Peter MacCallum Cancer Centre (Melbourne, Australia) adds <sup>18</sup>F-FDG PET/CT to stratify patients. When applying their criteria, we would probably exclude 25% of patients for <sup>177</sup>Lu-PSMA radioligand treatment.*

**Dr. Gillessen:** So they had excluded more patients because of their PET findings’ defined criteria. It would be interesting to know what the results of the VISION trial would have been using the criteria from the THERAP phase 2 trial of <sup>177</sup>Lu-PSMA-617 versus cabazitaxel in mCRPC progressing after docetaxel.

**Dr. Herrmann:** *We talked about PSMA-targeted imaging and therapy, current limitations, and unresolved issues. What would be your concluding remarks on the new era of PSMA-targeted theranostics? What would be the priorities for achieving integration with the practice of urologic oncology and be most relevant for optimal patient care?*

**Dr. Gillessen:** I would hope that we can intensify our collaborations and have more nuclear medicine specialists involved in our multidisciplinary tumor boards. This networking will be essential to facilitating the best outcomes for our patients.

**Dr. Czernin:** *Finally, can you provide some advice to our young colleagues in nuclear medicine, urology, and oncology? What should they focus on in making career choices?*

**Dr. Gillessen:** Collaboration and networking. We are all much more productive when we work together as a team.

# A Guide to ComBat Harmonization of Imaging Biomarkers in Multicenter Studies

Fanny Orlhac<sup>1</sup>, Jakoba J. Eertink<sup>2</sup>, Anne-Ségolène Cottreau<sup>1,3</sup>, Josée M. Zijlstra<sup>2</sup>, Catherine Thieblemont<sup>4,5</sup>, Michel Meignan<sup>6</sup>, Ronald Boellaard<sup>7</sup>, and Irène Buvat<sup>1</sup>

<sup>1</sup>LITO-UI288, Institut Curie, Université PSL, Université Paris-Saclay, Inserm, Orsay, France; <sup>2</sup>Amsterdam UMC, Vrije Universiteit Amsterdam, Department of Hematology, Cancer Center Amsterdam, Amsterdam, The Netherlands; <sup>3</sup>Department of Nuclear Medicine, Hôpital Cochin, Université Paris-Descartes, APHP, Paris, France; <sup>4</sup>Department of Hemato-Oncology, Hôpital Saint-Louis, DMU DHI, Université de Paris, APHP, Paris, France; <sup>5</sup>NF-kappaB, Différenciation et Cancer, Université de Paris, Paris, France; <sup>6</sup>Lysa Imaging, Hôpital Henri Mondor, Université Paris-Est, APHP, Créteil, France; and <sup>7</sup>Amsterdam UMC, Vrije Universiteit Amsterdam, Department of Radiology and Nuclear Medicine, Cancer Center Amsterdam, Amsterdam, The Netherlands

The impact of PET image acquisition and reconstruction parameters on SUV measurements or radiomic feature values is widely documented. This scanner effect is detrimental to the design and validation of predictive or prognostic models and limits the use of large multicenter cohorts. To reduce the impact of this scanner effect, the ComBat method has been proposed and is now used in various contexts. The purpose of this article is to explain and illustrate the use of ComBat based on practical examples. We also give examples in which the ComBat assumptions are not met and, thus, in which ComBat should not be used.

**Key Words:** radiomics; harmonization; texture analysis; multicenter studies

**J Nucl Med 2022; 63:172–179**

DOI: 10.2967/jnumed.121.262464

The emergence of radiomics in mid-2010 renewed interest in quantitative image analysis for prediction and classification tasks. Because radiomics requires large image datasets for designing and validating models, it would largely benefit from pooling images from different sites or from different scanners. However, many quantitative biomarkers and radiomic features are sensitive to a scanner or protocol effect (1–5), referred to here as the site effect, underlining the importance of harmonizing image acquisition and reconstruction procedures to reduce multicenter variability before pooling data from different sites. Similarly, when a new radiomic or quantitative image analysis method is developed at one site, its application to images from another site requires prior verification that the images from the 2 sites are comparable.

Much effort has been deployed in recent years to propose procedures to harmonize image quality (6), including the successful European Association of Nuclear Medicine Research Ltd. (EARL) accreditation program (7,8). However, in retrospective studies, many images have been reconstructed using protocols that did not follow these harmonization guidelines, for which it is impossible to

retrieve or perform phantom acquisitions that would be needed to harmonize them a posteriori. Often, the raw data are not stored, hampering any novel reconstruction to target a given image quality. The variability between scans resulting from different acquisition and reconstruction protocols can be reduced using image resampling or filtering (9,10), but these techniques require image postprocessing and most often yield a decrease in spatial resolution in the images acquired using the most recent devices, yielding suboptimal image quality for subsequent quantitative and radiomic studies.

To address these site effects, the ComBat harmonization method has been proposed (11–15) and has produced satisfactory results in various contexts. Since 2017, at least 51 papers have reported the use of ComBat in radiomic analysis of MRI (36%), CT (34%), or PET images (28%). Of these articles, 41% reported higher performance metrics after ComBat than before, and 41% presented only the results with harmonization. Only 18% of the articles did not report a benefit in using ComBat, without any detrimental effect.

ComBat directly applies to features already extracted from the images without the need to retrieve the images. However, as with any harmonization method, it is based on assumptions that have to be met for the method to generate valid results. The objective of this paper is to explain and demonstrate under which conditions ComBat can be used to harmonize image-derived biomarkers measured in different conditions and when it should be used with caution. We first summarize the theory behind ComBat and then illustrate several use cases to demonstrate its ability to compensate for site effects when properly used and to answer practical questions a ComBat user might have. We also give examples of situations in which the ComBat assumptions are not met and, thus, in which ComBat should not be used. Finally, we discuss the assets and limitations of ComBat.

All patient data used in the examples were obtained from previous retrospective studies approved by an institutional review board, and the requirement to obtain informed consent was waived.

## THEORY OF COMBAT

ComBat was initially introduced in the field of genomics (16) and has been widely used in this field (17). ComBat assumes that

$$y_{ij} = \alpha + \gamma_i + \delta_i \varepsilon_{ij} \quad \text{Eq. 1}$$

where  $j$  denotes the specific measurement of feature  $y$ ,  $i$  denotes the setting,  $\alpha$  corresponds to the average value of the feature of

Received Apr. 27, 2021; revision accepted Aug. 26, 2021.

For correspondence or reprints, contact Fanny Orlhac (orlhac@gmail.com).

Published online Sep. 16, 2021.

COPYRIGHT © 2022 by the Society of Nuclear Medicine and Molecular Imaging.

interest  $y$ ,  $\gamma_i$  is an additive batch effect affecting the measurement,  $\delta_i$  is a multiplicative batch effect and,  $\varepsilon_{ij}$  is an error term. Batch  $i$  corresponds to the experimental settings used for making the  $y$  measurement, including the possible observer effect, scanner effect, or even sample effect.

In medical imaging,  $y$  is an image feature (e.g., SUV);  $i$  denotes the scanner, protocol effect, or even observer effect (called the site effect); and  $j$  denotes the specific measurement, typically the volume of interest in which the measurement is made.

The model therefore assumes that the value of measurement  $i$  of a given feature  $y$  in volume of interest  $j$  is possibly affected by additive and multiplicative effects that depend on the scanner, protocol, or even observer who made the measurement. These effects are common to all measurements  $j$  of that same quantity  $y$  made using the same scanner, protocol, or observer. On the basis of multiple measurements  $y_{ij}$  of the same feature  $y$  made in volume of interest  $j$  in different images coming from different scanners  $i$ , the site effects  $\gamma_i$  and  $\delta_i$  can be estimated using conditional posterior means (16) and subsequently corrected using

$$y_{ij}^{\text{ComBat}} = \frac{y_{ij} - \hat{\alpha} - \hat{\gamma}_i}{\hat{\delta}_i} + \hat{\alpha} \quad \text{Eq. 2}$$

where  $\hat{\alpha}$ ,  $\hat{\gamma}_i$  and  $\hat{\delta}_i$  are estimators of  $\alpha$ ,  $\gamma_i$  and  $\delta_i$  and  $y_{ij}^{\text{ComBat}}$  is the transformed  $y_{ij}$  measurement devoid of the site  $i$  effect.

ComBat is a data-driven method that does not require any phantom acquisition to estimate the site effect but requires data from the different sites with sufficient sample size. The site effect can be estimated and corrected directly from the available image feature values measured at different sites without having to perform any image processing or any new measurements in the images. ComBat always theoretically improves the alignment of the mean and SD of the distributions given the criterion optimized by the method. A Kolmogorov–Smirnov test can be used to determine whether the statistical distributions of 2 sets of feature values are significantly different, in which case ComBat is needed, and to check the effectiveness of the applied transformation. A nonsignificant Kolmogorov–Smirnov test suggests that there is no evidence of differences in the 2 distributions, implying that any subsequent analysis should not be affected by a detectable difference between the distributions.

## EXAMPLE

We numerically generated 3,000 values drawn from 3 gaussian distributions with different means (8, 12, or 14) and SDs (3, 4, or 5) (Table 1), mimicking, for example,  $\text{SUV}_{\text{max}}$  measured in 3 sets of highly metabolic tumors but with 3 scanners of different generations, of which one had a much higher spatial resolution than the others (hence higher  $\text{SUV}_{\text{max}}$  due to reduced partial-volume effect (18)). As shown in Figure 1, ComBat can be

used in 2 ways: either to realign the distributions of the 3 sites to a virtual site (11), which is neither site A nor site B nor site C, or to realign the data from sites B and C to site A chosen as the reference site (or vice versa) (19). Contrary to what has been reported (20), both approaches lead to the same ranking of the patients and, hence, identical receiver-operating-characteristic curves for classification tasks, and only the absolute value of the feature changes. Aligning the data to a reference site may be preferable for feature value interpretation, but the reference site selection has no impact on the quality of the realignment. In the following, harmonization will always be performed with respect to a reference site.

## COMBAT TO COMPENSATE FOR PROTOCOL DIFFERENCES

The straightforward application of ComBat in medical imaging is to compensate for differences in radiomic feature values obtained from images acquired using different protocols. To illustrate, we performed an EARL experiment using PET images of 49 lesions from 15 lymphoma patients reconstructed according to the EARL1 and EARL2 standards (8). Without harmonization, we observed a systematic deviation in  $\text{SUV}_{\text{max}}$  between the 2 reconstructions (Kolmogorov–Smirnov,  $P = 0.0002$ ; Fig. 2). After applying ComBat considering the EARL2 reconstruction as a reference site, we observed a better concordance of  $\text{SUV}_{\text{max}}$  ( $P = 0.6994$ ).

## NEED FOR TISSUE-SPECIFIC AND TUMOR-SPECIFIC TRANSFORMATIONS

Since ComBat is a data-driven method, the realignment transformation (Eq. 2) is specific to the input data. It is therefore specific to the tissue or tumor type or patient population from which it is estimated. For example, in a previous publication (12), the ComBat transformation appropriate for  $\text{SUV}_{\text{max}}$  was different for liver tissue and breast tumors when pooling 63 patients from site A and 74 patients from site B (Fig. 3). In that example, values from site B were realigned to values measured at site A, and the resulting transformations were  $\text{SUV}_{\text{max}}(A) = 1.05 \times \text{SUV}_{\text{max}}(B) + 0.07$  for liver tissue and  $\text{SUV}_{\text{max}}(A) = 1.13 \times \text{SUV}_{\text{max}}(B) + 1.84$  for tumor tissue. This effect of the imaging protocols is different as a function of the structure of interest.  $\text{SUV}_{\text{max}}$  in the liver is not much impacted by the partial-volume effect, as the liver is a large region; hence, it is relatively robust to the difference in spatial resolution in the images produced by the 2 sites. Therefore, the slope of the transformation was close to 1, and the intercept was close to 0. In contrast, the  $\text{SUV}_{\text{max}}$  in breast tumors is affected by the partial-volume effect. This translates into a slope farther from 1 and an intercept farther from 0. Therefore, unlike what is stated in a previous publication (21), phantom measurements cannot be used to determine the transformations to be applied to feature values measured at one site to convert them to values that would have been obtained at the other site a priori. Given the ComBat assumptions, Equation 2 can be applied only to data affected by the site effect in the same way as the data used to estimate the  $\alpha$ ,  $\gamma$ , and  $\delta$  parameters of the model. This implies that, for example, a transformation derived for lung tumors should not be applied to lymphoma tumors unless the biomarker of interest is affected by the site effect in the same way in the 2 tumor types.

## NEED FOR A FEATURE-SPECIFIC TRANSFORMATION

Just as transformations are specific to each tissue, they are also specific to each index. For example, using the same data as in

### NOTEWORTHY

- Guidelines are proposed for using the ComBat harmonization method on SUVs, metabolic tumor volume, or any radiomic features illustrated with simulated and real data.
- Recommendations are made on the use of covariates within ComBat.
- The ComBat, EARL, and z score harmonization strategies are compared.

**TABLE 1**  
Description of Simulations

Experiment	Site A		Site B		Site C
	Limited stage	Advanced stage	Limited stage	Advanced stage	Limited stage
Experiment 1 (virtual site), reference site = A	$N = 1,000, \mu = 8,$ $SD = 3$	$\emptyset$	$N = 1,000, \mu = 12,$ $SD = 4$	$\emptyset$	$N = 1,000, \mu = 14,$ $SD = 5$
Experiment 2, reference site = A	$N = 1,000, \mu = 8,$ $SD = 3$	$N = 1,000, \mu = 10,$ $SD = 3$	$N = 1,000, \mu = 12,$ $SD = 4$	$N = 1,000, \mu = 14,$ $SD = 4$	$\emptyset$
Experiment 3, reference site = A, without and with covariate (=stage)	$N = 1,000, \mu = 8,$ $SD = 3$	$N = 1,000, \mu = 10,$ $SD = 3$	$N = 1,000, \mu = 12,$ $SD = 4$	$\emptyset$	$\emptyset$
Experiment 4, reference site = A, without and with covariate (=stage)	$N = 1,000, \mu = 8,$ $SD = 3$	$N = 1,000, \mu = 10,$ $SD = 3$	$N = 200, \mu = 12,$ $SD = 4$	$N = 1,800, \mu = 14,$ $SD = 4$	$\emptyset$
Experiment 5, reference site = A, without and with covariate (=stage)	$N = 1,000, \mu = 8,$ $SD = 3$	$N = 1,000, \mu = 10,$ $SD = 3$	$N = 1,000, \mu = 12,$ $SD = 4$	$N = 1,000, \mu = 12,$ $SD = 4$	$\emptyset$
Experiment 6, reference site = A, without and with covariate (=stage)	$N = 1,000, \mu = 8,$ $SD = 3$	$N = 1,000, \mu = 10,$ $SD = 3$	$N = 1,000, \mu = 12,$ $SD = 4$	$N = 1,000, \mu = 20,$ $SD = 4$	$\emptyset$

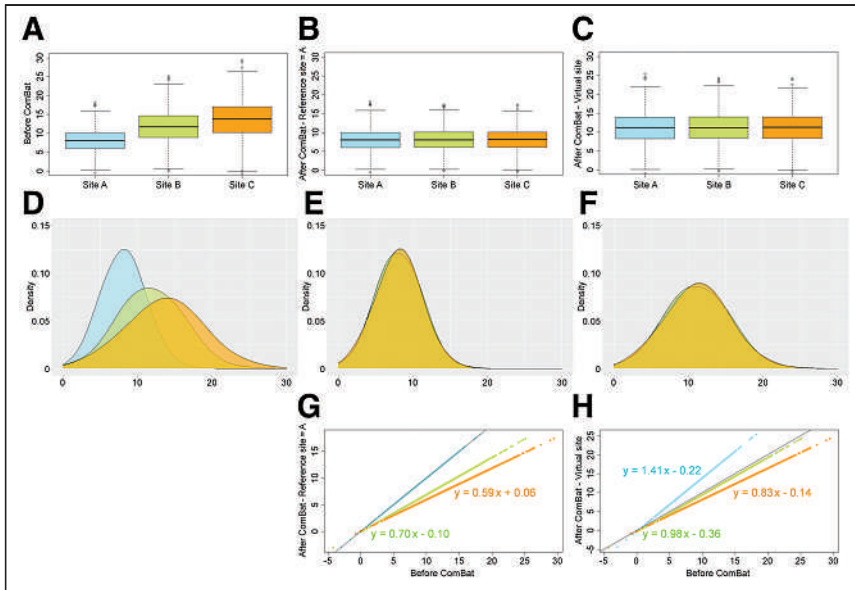
$N$  = number of simulated samples;  $\mu$  = mean of gaussian distribution;  $\emptyset$  = no simulation for this category.

Figure 3, the equations differ for  $SUV_{max}$  ( $SUV_{max}(A) = 1.05 \times SUV_{max}(B) + 0.07$  for liver tissue) and for the homogeneity feature ( $homog(A) = 1.06 \times homog(B) - 0.14$ ). The transformation has to be estimated for each feature independently because not all features are affected in the same way by the site effect. Some features are relatively immune to the site effect (e.g., shape features), unlike others (e.g.,  $SUV_{max}$  or metabolic tumor volume).

#### USE OF COMBAT TO ADJUST CUTOFFS BETWEEN DIFFERENT SITES

Aligning data from different sites might be extremely useful to adjust the cutoff used to distinguish between groups. Let us take the example of lymphoma patients, for whom it is well known that the total metabolic tumor volume (TMTV) calculated from  $^{18}F$ -FDG PET images is a valuable prognostic factor of progression-free and overall survival (22). However, the cutoff to identify patients with a poor prognosis depends on the segmentation method used for TMTV calculation, and there is no consensus on the optimal segmentation method (23). ComBat can thus be used to automatically determine how the cutoff appropriate for a segmentation method should be shifted to be applicable to TMTV measured using a different segmentation method. To illustrate, we studied a cohort of 280 patients with diffuse large

B-cell lymphoma from the REMARC trial (NCT01122472), for whom TMTV was calculated from  $^{18}F$ -FDG PET images using 2 segmentation methods (24). Method 1 (M1) used a threshold of 41% of  $SUV_{max}$  to segment lesions previously identified by a nuclear medicine physician. Method 2 (M2) used a convolutional neural network model (25). Using M1, the optimal TMTV cutoff was  $242 \text{ cm}^3$  to best distinguish between patients with short and long progression-free survival. Applying that cutoff to TMTVs measured with M2, the Youden index (sensitivity + specificity - 1) was 0.18 (sensitivity, 41%; specificity, 77%; Table 2). From the TMTV distributions obtained by the 2 methods (Supplemental Figs. 1A–1C; supplemental materials are available at <http://jnm.snmjournals.org>), ComBat identified the transformation needed to convert M1 TMTVs to TMTVs that would have been obtained if M2 segmentation had been used:  $TMTV_{M2} = 0.61 \times TMTV_{M1} - 28.64$ . This formula can be used to determine how the cutoff appropriate for M1 TMTV should be shifted to be applicable to TMTV measured with M2, which was  $119 \text{ cm}^3$  ( $= 0.61 \times 242 - 28.64$ ). With that cutoff, the Youden index was 0.22 (sensitivity, 64%; specificity, 58%), close to the performance obtained when optimizing the cutoff directly on the M2 TMTV (Youden index, 0.23). These results demonstrate the ability of ComBat to determine how a cutoff should be shifted to account for differences in the segmentation method.



**FIGURE 1.** Box plot and feature value distributions for experiment 1 (Table 1). (A and D) Plots before ComBat. (B, E, and G) Plots after ComBat by aligning data from sites B and C to site A. (C, F, and H) Plots after ComBat by aligning data on virtual site (intermediate between 3 sites). Bottom graphs show equations of transformations.

### CIRCUMSTANCES IN WHICH A COVARIATE IS NEEDED

Equation 1 corresponds to the simplest version of ComBat, which is applicable when the 2 distributions of features to be realigned are drawn from the same population and differ only because of a site effect. However, in many examples, each of these distributions is itself composed of 2 or more distributions. For example, a feature value distribution might be different in patients with different tumor stages. If the subcategories (patients with different stages) are not present with the same frequencies at the 2 sites, then the feature distributions observed at the 2 sites will differ in 2 respects: because of the site effect and because of the different frequencies of subcategories. Equation 1 will not apply unless the subcategory covariate is introduced. Equation 1 then becomes

$$y_{ij} = \alpha + X_{ij}\beta + \gamma_i + \delta_i\epsilon_{ij} \quad \text{Eq. 3}$$

where  $X$  is the design matrix for the covariates of interest, and  $\beta$  is the vector of regression coefficients corresponding to each covariate. The values after realignment are obtained using

$$y_{ij}^{\text{ComBat}} = \frac{y_{ij} - \hat{\alpha} - X_{ij}\hat{\beta} - \hat{\gamma}_i}{\hat{\delta}_i} + \hat{\alpha} \quad \text{Eq. 4}$$

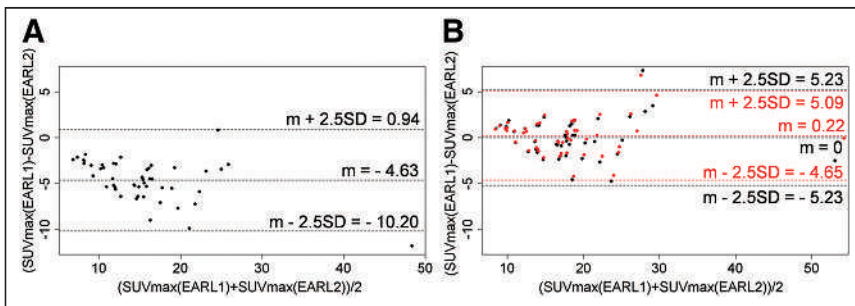


**FIGURE 2.** Bland-Altman plots for  $SUV_{\max}$  obtained using EARL1 and EARL2 reconstructions before ComBat (A) and after ComBat (B). Black = without covariate; red = with metabolic volume ( $\text{cm}^3$ ) as continuous covariate;  $m$  = mean.

To illustrate the impact of using a covariate, we performed 5 experiments, as listed in Table 1 (experiments 2–6). In all experiments, we assumed we had data from 2 different sites and that at each site there were patients with limited-stage or advanced-stage disease.

In experiment 2, the numbers of patients with limited-stage and advanced-stage disease were identical at both sites. Using ComBat with or without the stage covariate yields almost identical results (Fig. 4). The differences are because only 1 transformation is estimated without a covariate, compared with 2 transformations corresponding to each of the 2 stages in the version including a covariate. Because the proportion of patients in each stage is exactly the same, the stage covariate does not introduce confounding factors. The covariate is thus not necessary, but using it does not influence the ComBat results.

In experiment 3, the samples were the same as in experiment 2, but there were no advanced-stage patients at site B. Without the covariate stage, ComBat realigns patients at site A (limited and advanced stages) with patients at site B (limited stage only), as shown in Figure 5. Although the realignment of the 2 distributions seems to be satisfactory, a closer analysis shows that limited-stage patients are not well aligned between sites A and B because ComBat assumed that all site A patients were drawn from a single distribution, identical to that of the site B patients. When stage information is provided as a covariate, the distributions of limited-stage patients from site B are properly realigned with those of limited-stage patients from site A.

The frequency of the covariate may also differ between the 2 sites, such as in experiment 4 (Table 1). Similar to what was observed for experiment 3, the stage covariate must be introduced in the model to obtain a correct realignment for each stage (Fig. 4).

Applying ComBat with a covariate is different from performing ComBat for each subcategory separately. Using a covariate assumes that the site effect is identical for the 2 (or more) subcategories composing the sample and that only the proportion of individuals in the subcategories differs between the sites. The transformations associated with each subcategory are then constrained to have the same slope and will differ in their intercept only, as the intercept expression includes the design matrix  $X$  (Supplemental Fig. 2). If that assumption can be made, using ComBat with a covariate should be preferred to performing ComBat independently for each subcategory, as ComBat parameter estimates will benefit from a larger sample. If the site effect is expected to be different for the subcategories (e.g., for different tissue types), then ComBat should be performed for each subcategory independently. However, introducing covariates implies that the transformation will be determined from a smaller number of patients, which may lead to a less reliable

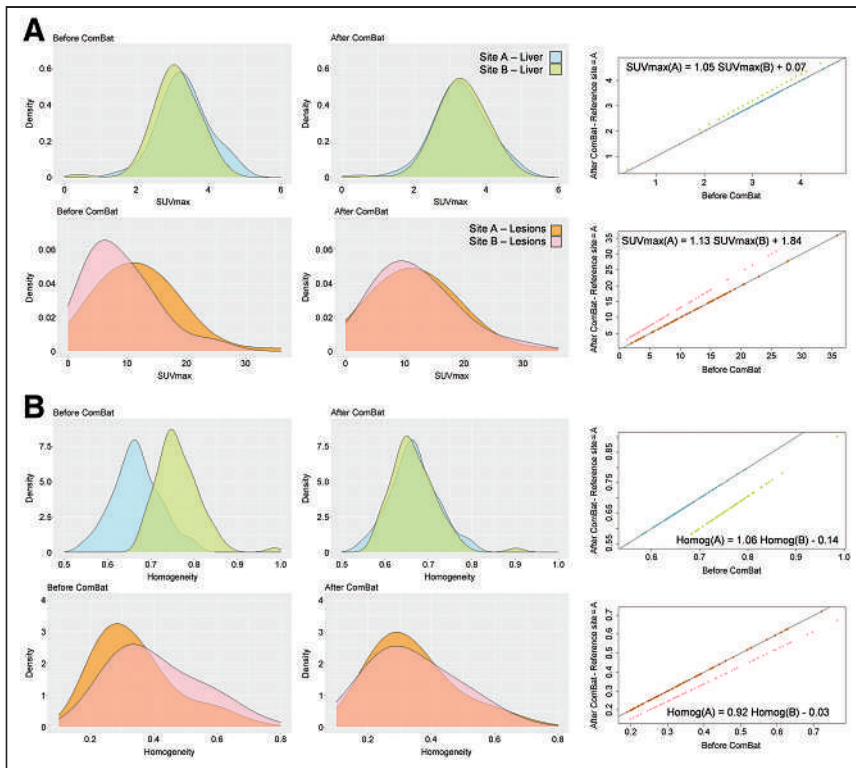


**FIGURE 3.** Application of ComBat in liver and tumor tissues for  $SUV_{max}$  (A) and homogeneity (B). (Left) Distributions at 2 sites before ComBat. (Center) Distributions after ComBat (site A = reference site). (Right) Values after ComBat plotted against value for same index and tissue before ComBat. Equation is transformation identified by ComBat to align data from site B to site A.

estimate. The need for a covariate must therefore be carefully considered.

### NO INTRODUCTION OF SPURIOUS INFORMATION FROM COMBAT COVARIATES

Introducing covariates does not artificially add information to the data, as demonstrated by experiment 5 (Fig. 4). In that setting, the data were the same as in experiment 4, except that at site B, limited- and advanced-stage patients yielded features with the exact same distribution. When ComBat is used with the stage covariate, limited-stage patients from both sites are realigned, advanced-stage patients from both sites are realigned, and the differences in limited- and advanced-stage patient feature distributions are reduced after pooling of the data from both sites, given that there was a real difference between the 2 stages at site A but not at site B. The stage covariate did not introduce any illegitimate differences between the 2 stages in patients scanned at site B (Fig. 4).

Similarly, when the difference between 2 categories (here, stages) is more detectable on feature values measured at one site

(here, site B) than at the other (site A), applying ComBat using a covariate will not corrupt the results (Fig. 4). In experiment 6, the gap between the limited and advanced stages is 4 times larger at site B than at site A. After realignment of the distributions with ComBat and the stage covariate, the gap between the 2 stages remains larger at site B (interquartile range of feature values from site B after ComBat with covariate, 7.5) than at site A (interquartile range, 4.2), thus preserving the original properties of the site B distributions (interquartile range, 8.4) compared with without covariate (interquartile range, 4.7).

The fact that ComBat does not introduce false-positives even with the addition of a covariate has been previously demonstrated using sham experiments (15).

The covariate can also take continuous values. In the EARL experiment, the addition of the metabolic tumor volume of the volume of interest in cubic centimeters as a covariate also slightly improved agreement in  $SUV_{max}$  between with the EARL1 and EARL2 reconstructions (Fig. 2), with a reduction in the SD of the Bland–Altman plot from 2.1 SUV to 1.9 SUV.

### COMBAT VERSUS Z SCORE

Another frequent harmonization method that can be applied a posteriori to feature values is the calculation of z scores at each site independently (26). The feature values at site A are converted into z scores using the average feature value and associated SD observed over all patients at site A. The same procedure is used for data from site B, using the mean and SD of all measurements made at site B. In doing so, values measured at the 2 sites become comparable. Supplemental Figure 3 shows the result after calculating a z score from the  $SUV_{max}$  in the lesions for centers A and B in comparison with Figure 3. Yet, this does not preserve the original range of values, since SUVs vary between  $-1.5$  and  $3.6$  when expressed in z scores, against  $1.2$  SUV and  $35.8$  SUV on the original data. A second limitation is that it is not possible to account for a covariate. Supplemental Figure 4 shows that the absence of the advanced stage at site B for experiment 3 did not allow the distributions of the limited stages in the 2 sites to be aligned correctly when using a z score, in comparison to Figure 5.

**TABLE 2**  
Summary of Results Obtained with ComBat to Adjust TMTV Cutoffs Between Different Sites

Parameter	Cutoff	Youden	Sensitivity	Specificity
Cutoff optimized for M1	242 $cm^3$	0.18	41%	77%
Based on M1 cutoff, estimated cutoff for M2 (ComBat without log transformation)	119 $cm^3$	0.22	64%	58%
Optimal cutoff for M2	112 $cm^3$	0.23	66%	57%

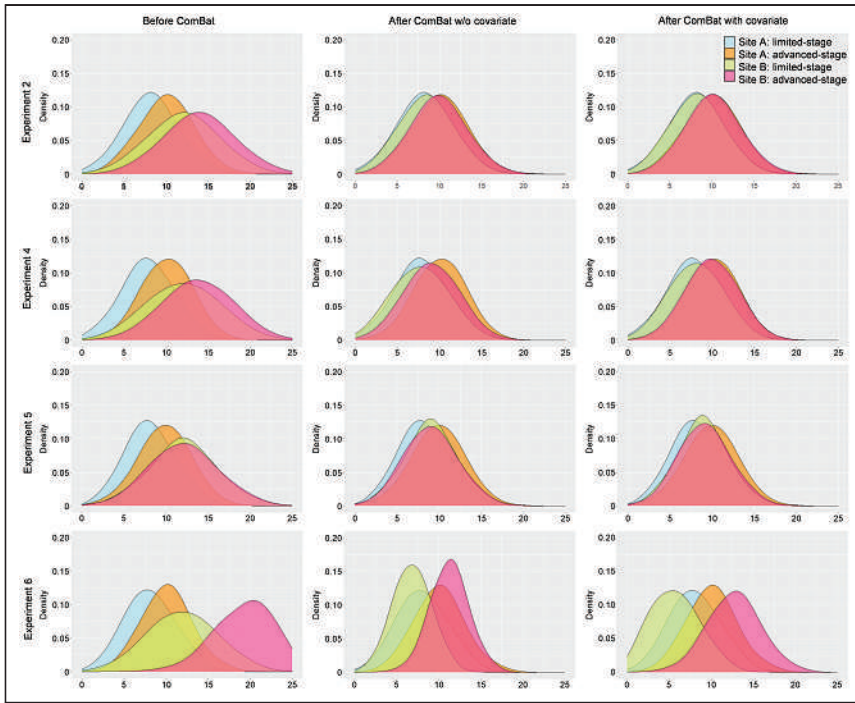


**FIGURE 4.** Value distributions for experiments 2, 4, 5, and 6 (Table 1). (Left) Distributions before ComBat. (Center) Distributions after ComBat (without covariates). (Right) Distributions after ComBat and specifying stage as covariate.

#### REQUIREMENTS TO PREVENT FAILURE OF COMBAT

For ComBat to be useful, some basic assumptions must be fulfilled. The first assumption is that the distributions of the features to be realigned must be similar except for shift (additive factor) and spread (multiplicative factor) effects. This assumption can be checked by plotting the distributions of the feature values from the 2 sites. ComBat can be used even for nongaussian distributions. A log transformation before applying ComBat (followed by exponentiation after ComBat) can further improve the effectiveness of ComBat for heavy-tailed distributions, as shown in Supplemental Figure 1D.

The second assumption is that covariates (if any) that might explain different distributions at the 2 sites (see the first assumption) have to be identified and considered using the design matrix of Equation 3.

Third, the different sets of feature values to be realigned have to be independent. If not, it is unlikely that the first assumption will be met; hence, ComBat will not provide any sound result. A practical example is the realignment of TMTVs as described in this paper but between 2 segmentation methods, M1 and M2, where M2 produces the same result as M1 in some examples and produces a different result in others. Unless the cases for which the 2 methods produce the same segmentation can be predicted and coded as a covariate (e.g., in small lesions), ComBat should not be used. To illustrate, we analyzed TMTV from 140 lymphoma patients. M1 corresponds to a threshold set to an SUV of 4, and M2

corresponds to a majority vote between 3 segmentation approaches, including M1. In 60 of 140 cases, M2 led to exactly the same TMTV as M1, and the TMTV was different for all other cases. The TMTVs to be aligned are not independent, thus resulting in a misalignment with ComBat (Supplemental Fig. 5), which should realign the cases in which the TMTVs are identical and different separately.

Fourth, determining a single transformation with ComBat from data with different tissue or tumor types does not always lead to satisfactory data realignments, because different texture patterns are not necessarily affected identically by the image acquisition and reconstruction protocols. It is therefore not appropriate to realign them all using a single ComBat transformation. This consideration fully explains why Ibrahim et al. (27) did not realign the data correctly with ComBat: the 10 patterns in the investigated phantom were affected differently by the pixel spacing. When ComBat was applied separately for each of the textural patterns, the realignments were correct (28).

#### AMOUNT OF DATA NEEDED TO USE COMBAT

The success of ComBat when only small datasets are available depends on the magnitude of the site effect and on the representativeness of the samples available for each site. In previous studies (13), ComBat was successful when the number of patients per site was as low as 20. To illustrate the impact of the number of patients, we reanalyzed previously published data (12) by aligning the feature distribution from site B (74 patients) to site A (63 patients) after estimating the ComBat transformation using only a subset of site B data (74 to 5 patients, 100 repeated random selections). Before ComBat, the distributions from the 2 sites were different (Kolmogorov–Smirnov,  $P < 5\%$ ) for  $SUV_{max}$  or homogeneity measured in the lesions (Supplemental Table 1). After ComBat, the distributions were not significantly different in at least 95 of 100

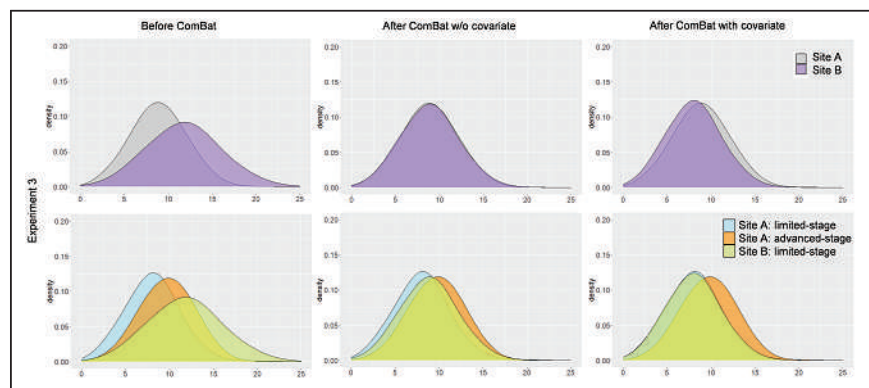


**FIGURE 5.** Distributions for experiment 3 (Table 1). (Left) Distributions before ComBat. (Center) Distributions after ComBat (without covariate). (Right) Distributions after ComBat and specifying stage as covariate. (Top) Pooling of data at each site. (Bottom) Data represented per site and stage.

**TABLE 3**  
Implementations of ComBat

Name	Details
neuroComBat (script)	<a href="https://github.com/Jfortin1/ComBatHarmonization">https://github.com/Jfortin1/ComBatHarmonization</a> ; language: R, Python, or MATLAB
M-ComBat (script)	<a href="https://github.com/SteinCK/M-ComBat">https://github.com/SteinCK/M-ComBat</a> ; language: R
ComBaTool (standalone web application)	<a href="https://forlhac.shinyapps.io/Shiny_ComBat/">https://forlhac.shinyapps.io/Shiny_ComBat/</a> ; language: R

tests when the transformation was estimated using 25 patients or more from site B for  $SUV_{max}$  (20 patients for homogeneity). Supplemental Figure 6 shows the increase in variability in estimating the intercept and slope of the ComBat transformation when the estimation is based on fewer and fewer patients. These results support the recommendation of using ComBat when at least 20–30 patients per batch are available. Use of a small sample size to estimate the transformations can also lead to a nonsignificant Kolmogorov–Smirnov test because the scanner effect becomes undetectable. In case a covariate is used, a minimum of 20–30 patients per covariate in each batch is also recommended.

A variant of ComBat named B-ComBat, which uses a bootstrap approach to determine the parameters of the transformation, has been proposed (20). However, the use of B-ComBat and the potential benefit of this more computationally demanding approach compared with ComBat have not yet been reported by independent groups.

#### USE OF COMBAT IN PRACTICE

Different implementations of ComBat are publicly available (R, Python, MATLAB [MathWorks]) and are summarized in Table 3. ComBat can also be used without any third-party software or programming skills using a free online application ([https://forlhac.shinyapps.io/Shiny\\_ComBat/](https://forlhac.shinyapps.io/Shiny_ComBat/)).

#### DISCUSSION

In this article, we provide a guide to understanding and using the ComBat harmonization method correctly. The main advantage of ComBat is that it can be used retrospectively and directly on image features that are already calculated without the need to perform phantom experiments. However, given that ComBat is a data-driven method, a highly recommended practice is to

scrutinize the distributions of the feature values from the sites to be pooled before using ComBat. This practice usually makes it possible to quickly determine whether the assumptions underlying ComBat are fulfilled, especially whether the distributions observed at the different sites are similar except for shift and spread effects. When this is the case, ComBat can be used; otherwise, the reason should first be identified. Often, the reason is the presence of one or more covariates, such as patient age, disease stage, treatment, molecular subtype, or metabolic volume. When covariates can be identified, it is easy to check whether ComBat assumptions are met for each dataset corresponding to a covariate value and whether the site effect impacts the sample corresponding to each covariate identically. If so, ComBat can be used by including that covariate. If the site effect impacts samples corresponding to each covariate differently, then a specific ComBat transformation should be estimated for each sample independently. Examination of feature distributions in tumors can sometimes be challenging, as the variability in the biologic signal associated with tumor heterogeneity can hide other sources of variability associated with the site effect. An easy check is to segment a reference region of fixed size in a nonpathologic tissue (e.g., healthy liver) and observe feature values within that region in images from different sites. This check is not sufficient, as it will not give precise information about site effects related to the spatial resolution in the images because the liver usually displays a low-frequency signal. However, we still find it useful to characterize how image quality differs between sites.

ComBat users should keep in mind that data can be grouped in the same batch if they were extracted from images obtained using the same setting on the same scanner. If the image acquisition and reconstruction protocols vary on a scanner, a careful check is needed to ensure that this variance does not affect the image properties. Otherwise, different batches should be used for the same scanner corresponding to different settings.

**TABLE 4**  
Opportunities and Limitations of Harmonization Using EARL and ComBat

Parameter	Upfront harmonization (like EARL)	ComBat
Opportunities	Applicable without restriction on number of patients; valid for any pathology and feature	Applicable directly to calculated radiomic feature values (no need to access images); no need for phantom acquisition; applicable retrospectively; applicable prospectively if data have already been acquired for same pathology with same acquisition and analysis protocols and settings; ability to realign data to particular site
Limitations	Not applicable retrospectively; requires acquisition of phantom images, optimization of reconstruction settings, and access to machine	Requirement for minimum number of patients (~20–30 per batch); specific transformation for each type of tissue, each type of tumor, each scanner, each material in phantom, each analysis method (e.g., segmentation approach) and each feature; not applicable prospectively if little or no previously acquired data

In prospective studies, the transformation to be applied with ComBat can be deduced from data acquired previously for the same patient population. The ComBat method is complementary to the EARL standardization approach. We have summarized the pros and cons of both approaches in Table 4. EARL and ComBat can be used together if differences in feature distributions remain even with an EARL-standardized imaging protocol.

Harmonization in medical imaging can also be seen as domain adaptation, where the goal would be to produce images belonging to a single domain (here, corresponding to the image quality or accuracy obtained with a specific scanner and protocol) from images recorded in different domains. Promising approaches for domain adaptation using, for example, generative adversarial networks have been developed in recent years (29–31). The role of such approaches in harmonizing PET and SPECT images remains to be studied. Unlike ComBat, generative adversarial networks act on the images and not on the already computed features; this requires access to the images, which could be a limitation.

## CONCLUSION

In this article, we provide a guide to using the ComBat method to compensate for multicenter effects affecting quantitative biomarkers extracted from nuclear medicine images and beyond. This harmonization method is largely used in medical imaging and should facilitate large-scale multicenter studies needed to translate radiomics to the clinics.

## DISCLOSURE

This work is partially supported by the Dutch Cancer Society (VU 2018-11648). The HOVON-84 study was supported by the Dutch Cancer Society (CKTO-2006-14) and by Roche Nederland. Michel Meignan has received funds from ROCHE for an educational program. Ronald Boellaard is an (unpaid) scientific advisor for the EARL PET/CT accreditation program. No other potential conflict of interest relevant to this article was reported.

## ACKNOWLEDGMENTS

We thank the patients and their families, the LYSARC team for management of the REMARC study, all the investigators, and Celgene/BMS for the financial support.

## REFERENCES

1. Yan J, Chu-Shern JL, Loi HY, et al. Impact of image reconstruction settings on texture features in <sup>18</sup>F-FDG PET. *J Nucl Med*. 2015;56:1667–1673.
2. Reuzé S, Orlhac F, Chargari C, et al. Prediction of cervical cancer recurrence using textural features extracted from <sup>18</sup>F-FDG PET images acquired with different scanners. *Oncotarget*. 2017;8:43169–43179.
3. Shiri I, Rahmim A, Ghaffarian P, Geramifar P, Abdollahi H, Bitarafan-Rajabi A. The impact of image reconstruction settings on <sup>18</sup>F-FDG PET radiomic features: multi-scanner phantom and patient studies. *Eur Radiol*. 2017;27:4498–4509.
4. Pfaehler E, van Sluis J, Merema BBJ, et al. Experimental multicenter and multi-vendor evaluation of the performance of PET radiomic features using 3-dimensionally printed phantom inserts. *J Nucl Med*. 2020;61:469–476.
5. Nyflot MJ, Yang F, Byrd D, Bowen SR, Sandison GA, Kinahan PE. Quantitative radiomics: impact of stochastic effects on textural feature analysis implies the need for standards. *J Med Imaging (Bellingham)*. 2015;2:041002.
6. Clarke LP, Nordstrom RJ, Zhang H, et al. The Quantitative Imaging Network: NCI's historical perspective and planned goals. *Transl Oncol*. 2014;7:1–4.

7. Boellaard R, Delgado-Bolton R, Oyen WJG, et al. FDG PET/CT: EANM procedure guidelines for tumour imaging—version 2.0. *Eur J Nucl Med Mol Imaging*. 2015;42:328–354.
8. Kaalep A, Sera T, Rijnsdorp S, et al. Feasibility of state of the art PET/CT systems performance harmonisation. *Eur J Nucl Med Mol Imaging*. 2018;45:1344–1361.
9. Shafiq-Ul-Hassan M, Latifi K, Zhang G, Ullah G, Gillies R, Moros E. Voxel size and gray level normalization of CT radiomic features in lung cancer. *Sci Rep*. 2018;8:10545.
10. Mackin D, Fave X, Zhang L, et al. Harmonizing the pixel size in retrospective computed tomography radiomics studies. *PLoS One*. 2017;12:e0178524.
11. Fortin J-P, Cullen N, Sheline YI, et al. Harmonization of cortical thickness measurements across scanners and sites. *Neuroimage*. 2018;167:104–120.
12. Orlhac F, Boughdad S, Philippe C, et al. A postreconstruction harmonization method for multicenter radiomics studies in PET. *J Nucl Med*. 2018;59:1321–1328.
13. Orlhac F, Frouin F, Nioche C, Ayache N, Buvat I. Validation of a method to compensate multicenter effects affecting CT radiomics. *Radiology*. 2019;291:53–59.
14. Mahon RN, Ghita M, Hugo GD, Weiss E. ComBat harmonization for radiomic features in independent phantom and lung cancer patient computed tomography datasets. *Phys Med Biol*. 2020;65:015010.
15. Orlhac F, Lecler A, Savatovski J, et al. How can we combat multicenter variability in MR radiomics? Validation of a correction procedure. *Eur Radiol*. 2021;31:2272–2280.
16. Johnson WE, Li C, Rabinovic A. Adjusting batch effects in microarray expression data using empirical Bayes methods. *Biostatistics*. 2007;8:118–127.
17. Chen C, Grennan K, Badner J, et al. Removing batch effects in analysis of expression microarray data: an evaluation of six batch adjustment methods. *PLoS One*. 2011;6:e17238.
18. Soret M, Bacharach SL, Buvat I. Partial-volume effect in PET tumor imaging. *J Nucl Med*. 2007;48:932–945.
19. Stein CK, Qu P, Epstein J, et al. Removing batch effects from purified plasma cell gene expression microarrays with modified ComBat. *BMC Bioinformatics*. 2015;16:63.
20. Da-Ano R, Masson I, Lucia F, et al. Performance comparison of modified ComBat for harmonization of radiomic features for multicenter studies. *Sci Rep*. 2020;10:10248.
21. Ibrahim A, Primakov S, Beuque M, et al. Radiomics for precision medicine: current challenges, future prospects, and the proposal of a new framework. *Methods*. 2021;188:20–29.
22. Meignan M, Cottreau AS, Versari A, et al. Baseline metabolic tumor volume predicts outcome in high-tumor-burden follicular lymphoma: a pooled analysis of three multicenter studies. *J Clin Oncol*. 2016;34:3618–3626.
23. Cottreau A-S, Hapdey S, Chartier L, et al. Baseline total metabolic tumor volume measured with fixed or different adaptive thresholding methods equally predicts outcome in peripheral T cell lymphoma. *J Nucl Med*. 2017;58:276–281.
24. Orlhac F, Capobianco N, Cottreau A-S, et al. Refining the stratification of diffuse large B-cell lymphoma patients based on metabolic tumor volume (MTV) by automatically adapting the MTV cut-off value to the segmentation method [abstract]. *J Nucl Med*. 2020;61(suppl 1):274.
25. Sibille L, Seifert R, Avramovic N, et al. <sup>18</sup>F-FDG PET/CT uptake classification in lymphoma and lung cancer by using deep convolutional neural networks. *Radiology*. 2020;294:445–452.
26. Chatterjee A, Vallières M, Dohan A, et al. Creating robust predictive radiomic models for data from independent institutions using normalization. *IEEE Trans Radiat Plasma Med Sci*. 2019;3:210–215.
27. Ibrahim A, Refaee T, Primakov S, et al. The effects of in-plane spatial resolution on CT-based radiomic features' stability with and without ComBat harmonization. *Cancers (Basel)*. 2021;13:1848.
28. Orlhac F, Buvat I. Comment on Ibrahim et al.: the effects of in-plane spatial resolution on CT-based radiomic features' stability with and without ComBat harmonization. *Cancers (Basel)*. 2021;13:3037.
29. Zhong J, Wang Y, Li J, et al. Inter-site harmonization based on dual generative adversarial networks for diffusion tensor imaging: application to neonatal white matter development. *Biomed Eng Online*. 2020;19:4.
30. Modanwal G, Vellal A, Buda M, Mazurkowski MA. MRI image harmonization using cycle-consistent generative adversarial network. In: *Medical Imaging 2020: Computer-Aided Diagnosis*. SPIE; 2020:1131413.
31. Marcadent S, Hofmeister J, Preti MG, Martin SP, Van De Ville D, Montet X. Generative adversarial networks improve the reproducibility and discriminative power of radiomic features. *Radiol Artif Intell*. 2020;2:e190035.

## Is It Too Soon to Know When It's LATE?

Angela C. Rieger and Daniel H.S. Silverman

*Department of Molecular and Medical Pharmacology, David Geffen School of Medicine at UCLA, Los Angeles, California*

**D**evelopments over the past 2 decades in neuronuclear imaging and cerebrospinal fluid biomarker technologies for detecting dementia-related proteinopathies have made it increasingly clear how commonly Alzheimer disease (AD) has been clinically diagnosed to explain cognitive decline in patients who turn out to lack biologic evidence of the traditional hallmarks of AD. Polymeric amyloid-containing senile plaques or hyperphosphorylated tau-comprised neurofibrillary tangles are the hallmarks that have come to define an illness estimated to affect senior citizens numbering 6 million in America and an order of magnitude greater globally (1). If, however, millions of patients worldwide meeting the clinical criteria for AD do not actually harbor its defining patterns of cerebral amyloidopathy and tauopathy—or when, for example, they turn out to have amyloid-positive scans but AD is excluded as the cause of their dementia (e.g., when significant tauopathy is absent)—what processes may then actually be underlying their evident cognitive decline?

Numerous such processes, involving various cell types and molecules, have been implicated. One such molecule, TAR DNA-binding protein 43 (TDP-43), plays roles under normal conditions in regulating RNA metabolism, messenger RNA transport, micro-RNA maturation, and stress granule formation. In the absence of neuropathology, TDP-43 is identified predominantly in its unphosphorylated state and located in cell nuclei. When hyperphosphorylated or ubiquitinated, TDP-43 can localize to the cytosol, with nuclear loss of function and cytoplasmic gains of function leading to a host of disorders including frontotemporal lobar degeneration, amyotrophic lateral sclerosis, and limbic-predominant age-related TDP-43 encephalopathy (LATE) (2).

Recently drafted consensus criteria (3) describe LATE as a neurodegenerative disease occurring in older adults (most commonly in their 80s) and clinically characterized by an amnesic dementia syndrome that mimics AD. It is associated with a TDP-43 proteinopathy affecting the amygdala and hippocampus structures in the anteromedial temporal lobe first, followed by measurable involvement of the prefrontal cortex and, especially, the middle frontal gyrus. This form of dementia previously escaped definition as a distinct diagnostic entity, in part because of its confusion with AD (along with more general effects of aging) in this population, with misdiagnoses having had little chance of being recognized as such in the absence of autopsy, before the advent of PET-based and cerebrospinal fluid–based biomarker testing for the presence of the relevant proteinopathies. Diagnostic clarity in this regard has been further confounded by the frequency with which there is

coexistence between proteinopathies serving as the primary pathologic hallmarks for each of several different dementia diagnoses with overlapping clinical profiles. Examples are the amyloidopathy and tauopathy of AD, with or without the synucleinopathy of dementia with Lewy bodies, and the TDP-43 cytoplasmic inclusions associated with frontotemporal lobar degeneration or LATE (4–6). Preceding the current conceptualization of LATE, several other descriptors for this and related conditions were used, such as TDP-43 pathologies in the elderly, TDP-43 proteinopathy associated with cognitive impairment, cerebral age-related TDP-43 with hippocampal sclerosis, hippocampal sclerosis of aging, and hippocampal sclerosis dementia (3,7,8). The last 3 of these reflect how often the pathologies of limbic-associated TDP-43 as a molecular finding, and hippocampal sclerosis on a more macro scale, are both found, but it is clear that either can exist in the absence of the other (9).

Clinically, LATE is distinguished by a less aggressive trajectory of cognitive and functional decline than is AD and by generally being diagnosed in older patients than is frontotemporal lobar degeneration with TDP-43. The relatively restricted neuroanatomic distribution of TDP-43 proteinopathy, particularly in its earlier stages, causes the hippocampus-dependent function of delayed recall to typically be more prominently affected than are other cognitive domains. This manifests as an amnesic syndrome resembling early stages of AD, which is neuropathologically characterized by a tauopathy also concentrated in medial temporal structures. Correspondingly, MRI studies most often identify, in early stages, volume loss associated with TDP-43 in medial temporal lobe structures and, in later stages, diminished volume in certain frontocortical regions (10). Apart from excluding AD as a likely cause of a patient's symptoms through imaging findings regarded as negative for the presence of frequent amyloid plaques or substantial tauopathy (11), published experience with PET in the evaluation of patients with LATE is sparse. A pioneering recent study in this regard compared  $^{18}\text{F}$ -FDG PET scans of patients diagnosed as having AD with and without coexisting TDP-43, suggesting that for a given magnitude of persisting inferior temporal metabolism, AD patients with TDP-43 had more severely diminished medial temporal metabolism than did AD patients unaffected by TDP-43, resulting in a higher inferior temporal-to-medial temporal metabolic ratio (6). Though quite some time will elapse before we will have the kind of data needed to establish the sensitivity and specificity of neuroimaging modalities for assessing patients for the TDP-43 proteinopathy characteristic of LATE—alone or in combination with other neuropathologic changes—there is a pressing need for physicians who interpret scans of patients with AD-like symptoms to consider a differential diagnosis encompassing all non-AD pathologies potentially contributing to their clinical presentation. This process entails

Received Nov. 5, 2021; revision accepted Nov. 16, 2021.

For correspondence or reprints, contact Daniel H. Silverman (dsilver@ucla.edu).

COPYRIGHT © 2022 by the Society of Nuclear Medicine and Molecular Imaging.  
DOI: 10.2967/jnumed.121.263229

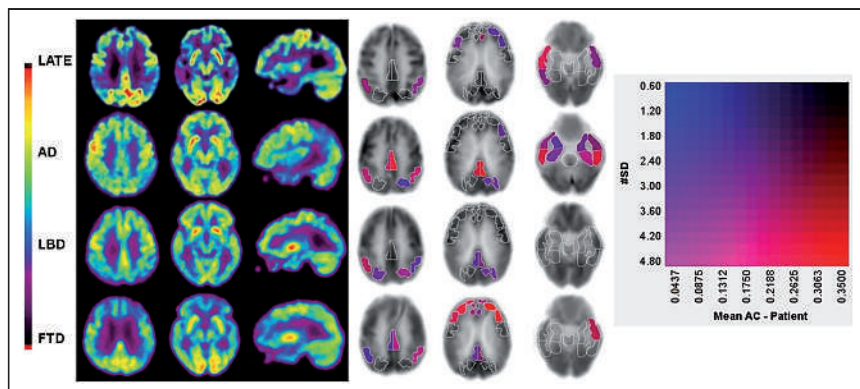


**FIGURE 1.** Some typical patterns of regional cerebral metabolism to be considered in differential diagnosis of patients presenting with dementia symptoms. First 3 columns are dedicated brain PET scans, and next 3 columns are standardized volume-of-interest analysis, as normalized to sensorimotor cortex, with NeuroQ software (Syntermed, Inc.). (First row) Scan of LATE patient is remarkable for moderately severe anterior temporal and parietotemporal hypometabolism, right somewhat worse than left, and milder hypometabolism of middle and posterior inferior frontal gyri, with pristine preservation of sensorimotor, posterior cingulate and occipital cortical metabolism. Volume-of-interest analysis quantified metabolism in this patient's temporal regions as falling approximately 3–5 SDs and 20%–30% below, and lateral prefrontal regions as falling approximately 2 SDs and 10%–15% below, corresponding regional mean values in database of 50 asymptomatic control scans. (Second row) In contrast to LATE patient, scan of AD patient reveals marked hypometabolism of posterior cingulate and posterior temporal cortex, whereas sensorimotor and occipital metabolism remain relatively preserved. (Third row) In contrast to scans of LATE and AD patients, scan of patient with dementia with Lewy bodies (LBD) shows moderately diminished occipital metabolism along with adjacent parietotemporal metabolism. (Fourth row) In contrast to scans of LATE, AD, and LBD patients, scan of patient with frontotemporal dementia (FTD) shows most severe hypometabolism in anterior temporal and multiple prefrontal regions, whereas metabolism of posterior temporal and occipital cortex remains preserved. AC = asymptomatic control.

extracting the most clinically relevant information from scans by piecing together 4 decades of existing PET experience along with emerging, more systematic investigations, while our field awaits more definitive tools and data to enable more scientifically secure conclusions. The following case attempts to illustrate this process.

## CASE

A 78-y-old woman presented with memory difficulties that she first noticed in January 2021, which her husband characterized as “COVID fog,” as her cognitive decline was preceded by infection with severe acute respiratory syndrome coronavirus 2. She complained of struggling with articulating her thoughts. Her serum thyroid-stimulating hormone and vitamin B12 levels were within normal limits, and she had no history of anxiety or depression. Neuropsychologic testing demonstrated diminished 5-min word recall and mild deficits in naming, language ability, attention, abstraction and visuospatial/executive function. An MRI study demonstrated evidence of only very mild microangiopathy and moderate generalized atrophy, whereas a PET study revealed a markedly abnormal distribution of <sup>18</sup>F-FDG in her forebrain, most compatible with LATE (Fig. 1).

## CONCLUDING REMARKS

LATE is an entity well suited for a molecular imaging–based diagnosis, perhaps more so than any other neurodegenerative disease except AD as traditionally defined, from which it must be distinguished. A definitive diagnosis of LATE will likely not be

possible in the premortem setting, however, without neuroimaging that specifically includes assessment of limbic structures with a clinically available tracer for TDP-43 that is sensitive and specific for localizing this protein in brain tissue. The development of such a tracer will require overcoming considerable challenges posed by the intracellular location and small pathologic burden of TDP-43 proteinopathy—challenges that limit signal intensity (3).

In the meantime, some neuropsychologic–biochemical bases for suspecting this neurodegenerative process are provided by a preponderance of diagnostic evidence built on an AD-like clinical picture in older adults. This evidence includes an amnesic component of cognitive dysfunction, coupled with a pattern of diminished regional cerebral metabolism that is posterior-predominant but nevertheless differs from AD in lacking as marked a defect of posterior cingulate or posterior/inferior parietotemporal activity in the face of more anterior temporal metabolic hypometabolism, as well as differing from dementia with Lewy bodies in lacking as marked a defect of occipital metabolism. In fact, even with the eventual availability of clinical TDP-43 imaging, the other 2 bases would remain valuable in ensuring

that TDP-43 not only has locally accumulated (particularly in this age group in which neurodegenerative-type proteinopathy is known to occur even among those who are cognitively normal) but also is associated with regional cerebral dysfunction that marks the presence of the LATE disease process. Ultimately, in the broader context of dementia evaluations, whereas <sup>18</sup>F-FDG PET serves as the neuroimaging modality with the single greatest specificity for distinguishing across the full spectrum of neurodegenerative etiologies, the differential diagnostic and prognostic power of neuroimaging tools will be expected to be optimized in evaluations for LATE (like other diagnostic entities) through application of available tools in combinations intelligently selected to match the needs of each clinical situation (12).

## DISCLOSURE

No potential conflict of interest relevant to this article was reported.

## REFERENCES

- 2021 Alzheimer's disease facts and figures. *Alzheimers Dement.* 2021;17:327–406.
- de Boer EMJ, Orié VK, Williams T, et al. TDP-43 proteinopathies: a new wave of neurodegenerative diseases. *J Neurol Neurosurg Psychiatry.* 2020;92:86–95.
- Nelson PT, Dickson DW, Trojanowski JQ, et al. Limbic-predominant age-related TDP-43 encephalopathy (LATE): consensus working group report. *Brain.* 2019; 142:1503–1527.
- Agrawal S, Yu L, Nag S, et al. The association of Lewy bodies with limbic-predominant age-related TDP-43 encephalopathy neuropathologic changes and their role in cognition and Alzheimer's dementia in older persons. *Acta Neuropathol Commun.* 2021;9:156.

5. Teylan MA, Mock C, Gauthreaux K, et al. Differences in symptomatic presentation and cognitive performance among participants with LATE-NC compared to FTL-D-TDP. *J Neuropathol Exp Neurol*, October 21, 2021 [Epub ahead of print].
6. Buciu M, Botha H, Murray ME, et al. Utility of FDG-PET in diagnosis of Alzheimer-related TDP-43 proteinopathy. *Neurology*. 2020;95:e23–e34.
7. Pelletier A, Bernard C, Dilharreguy B, et al. Patterns of brain atrophy associated with episodic memory and semantic fluency decline in aging. *Aging (Albany NY)*. 2017;9:741–752.
8. Amador-Ortiz C, Lin WL, Ahmed Z, et al. TDP-43 immunoreactivity in hippocampal sclerosis and Alzheimer's disease. *Ann Neurol*. 2007;61:435–445.
9. Power MC, Mormino E, Soldan A, et al. Combined neuropathological pathways account for age-related risk of dementia. *Ann Neurol*. 2018;84:10–22.
10. Kotrotsou A, Schneider JA, Bennett DA, et al. Neuropathologic correlates of regional brain volumes in a community cohort of older adults. *Neurobiol Aging*. 2015;36:2798–2805.
11. Botha H, Mantyh WG, Murray ME, et al. FDG-PET in tau-negative amnesic dementia resembles that of autopsy-proven hippocampal sclerosis. *Brain*. 2018; 141:1201–1217.
12. Raji CA, Torosyan N, Silverman DHS. Optimizing use of neuroimaging tools in evaluation of prodromal Alzheimer's disease and related disorders. *J Alzheimers Dis*. 2020;77:935–947.

# Visualizing T-Cell Responses: The T-Cell PET Imaging Toolbox

Chao Li<sup>1,2</sup>, Chaozhe Han<sup>1,2</sup>, Shao Duan<sup>1,2</sup>, Ping Li<sup>3</sup>, Israt S. Alam<sup>4</sup>, and Zunyu Xiao<sup>1,4</sup>

<sup>1</sup>Harbin Medical University, Harbin, China; <sup>2</sup>Department of Orthopedics, Second Affiliated Hospital of Harbin Medical University, Harbin, China; <sup>3</sup>Department of Radiology and Nuclear Medicine, Second Affiliated Hospital of Harbin Medical University, Harbin, China; and <sup>4</sup>Molecular Imaging Program at Stanford, Department of Radiology, Stanford University School of Medicine, Stanford, California

T lymphocytes are key mediators of the adaptive immune response. Inappropriate or imbalanced T-cell responses are underlying factors in cancer progression, allergy, and other immune disorders. Monitoring the spatiotemporal dynamics of T cells and their functional status has the potential to provide unique biologic insights into health and disease. Noninvasive PET imaging represents an ideal whole-body modality for achieving this goal. With the appropriate PET imaging probes, T-cell dynamics can be monitored in vivo with high specificity and sensitivity. Herein, we provide a comprehensive overview of the applications of this state-of-the-art T-cell PET imaging toolbox and the potential it has to improve the clinical management of cancer immunotherapy and T-cell-driven diseases. We also discuss future directions and prospects for clinical translation.

**Key Words:** T-cell PET imaging; graft-versus-host disease; inflammatory bowel disease; rheumatoid arthritis; cancer immunotherapy

**J Nucl Med 2022; 63:183–188**  
DOI: 10.2967/jnumed.121.261976

**T** lymphocytes play a central role in the adaptive immune response. The interplay between T cells and extracellular factors maintains a careful balance between activation, proliferation, survival, and inhibition. Dysregulation of T-cell responses can contribute to cancer progression, allergy, and immune disorders (1,2). Noninvasive PET imaging represents an ideal approach for visualizing T-cell dynamics in vivo, which could improve our understanding of their role in disease pathogenesis. This has motivated the development and evaluation of numerous T-cell imaging probes in both preclinical and clinical settings (Fig. 1). The T-cell PET imaging toolbox consists of a diverse set of approaches that include direct labeling of cells in vitro, proteins and peptides targeting endogenous T-cell surface and secreted biomarkers, small-molecule metabolic tracers, and engineering cells to express PET reporter genes (3). In direct cell labeling, immune cells are incubated with radiolabels ex vivo before adoptive transfer into a living subject for subsequent imaging. Although this is a relatively straightforward methodology for T-cell tracking, its wider clinical

use to date has been limited. Incorporation of radionuclides can cause toxicities, such as radiolysis, and can adversely impact T-cell function. The radiolabel itself becomes diluted as cells divide and proliferate in vivo, reducing the utility of this approach for longitudinal imaging (4). Given the drawbacks of this approach, we will focus our review on the alternative approaches mentioned above, which are summarized in Table 1.

## UTILITY OF T-CELL PET IMAGING FOR DIAGNOSIS OF ALLOGENIC AND AUTOIMMUNE DISEASES

Inappropriate T-cell activation and trafficking are seen in a range of pathologies, including acute graft-versus-host disease (GVHD) in the allogeneic transplant setting, and autoimmune diseases such as rheumatoid arthritis (RA) and inflammatory bowel disease. It is well documented that early diagnosis and timely therapeutic intervention in these scenarios can lead to better outcomes and minimize organ damage (5,6), illustrating the urgent need to develop more reliable diagnostic tools. T-cell PET imaging represents an ideal approach for achieving noninvasive, early detection of disease, before the onset of clinical symptoms.

T-cell imaging with 2'-deoxy-2'-<sup>18</sup>F-fluoro-9-β-D-arabinofuranosylguanine (<sup>18</sup>F-AraG) has successfully detected activated T cells in secondary lymphoid organs at both early and late stages of disease in a murine acute-GVHD model (Fig. 2A) (7) and is now being evaluated clinically in hematopoietic stem cell transplant recipients (NCT03367962). Imaging of the T-cell surface lineage marker CD3 successfully visualized the total T-cell compartment in vivo in a humanized GVHD model (8). However, downregulation of CD3 expression during T-cell activation poses a limitation to this approach. A <sup>64</sup>Cu-labeled OX40 monoclonal antibody demonstrated excellent diagnostic potential in a murine acute-GVHD model, detecting T-cell activation early in disease and before presentation of overt clinical symptoms (Fig. 2B) (9). However, the agonist OX40 monoclonal antibody clone used in this model also accelerated acute GVHD lethality, even when administered at the relatively low mass doses used for imaging. These findings highlight the importance of testing for biologic perturbations and overall safety before clinical translation. Given the utility of OX40 as a biomarker of GVHD, using an OX40 antagonist clone may be a safer imaging approach for GVHD and other indications for which T-cell activation may be deleterious.

Imaging activated T cells also represents a promising strategy for early diagnosis of RA. Although <sup>18</sup>F-FDG was tested in preclinical and clinical RA studies, the glucose metabolism pathway is shared by multiple tissues, which results in a high rate of

Received Jul. 16, 2021; revision accepted Dec. 6, 2021.  
For correspondence or reprints, contact Zunyu Xiao (xiao\_zunyu@hrbmu.edu.cn) or Israt S. Alam (israt@stanford.edu).  
Published online Dec. 9, 2021.  
COPYRIGHT © 2022 by the Society of Nuclear Medicine and Molecular Imaging.

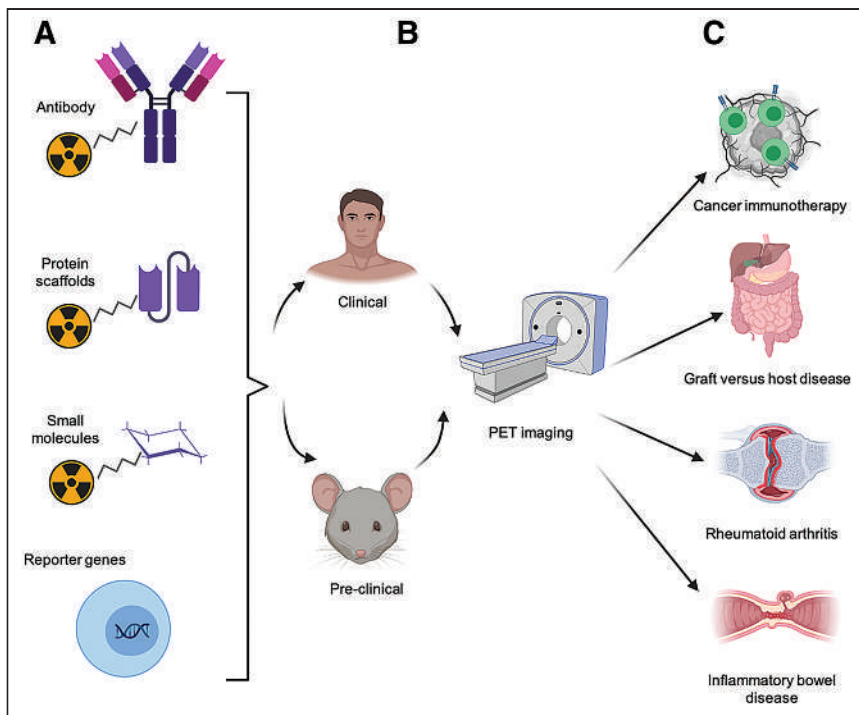


**FIGURE 1.** Approaches to PET imaging of T cells. T-cell PET imaging toolbox expanded rapidly over last decade. (A) Numerous T-cell-specific PET tracers have been developed, including radiolabeled antibodies and antibody fragments, protein scaffolds, small molecules, and tracers complementary to reporter genes that can be used to track engineered T cells. (B) These approaches have been evaluated in both preclinical and clinical studies. (C) Noninvasive PET imaging of T cells has potential to be highly useful, allowing preclinical researchers and clinicians to predict or monitor therapeutic response to cancer immunotherapy. This modality also enables early diagnosis of inflammatory diseases, such as GVHD, RA, and inflammatory bowel disease, for timely and effective intervention.

false-positives, especially when the region of interest is adjacent to metabolically active tissues (10). Evaluation of  $^{18}\text{F}$ -AraG in a pre-clinical adjuvant-induced arthritis model (Fig. 2C) (11) showed significantly higher accumulation of  $^{18}\text{F}$ -AraG in RA-affected paws in both the acute and the chronic phases of disease, demonstrating its potential utility for RA diagnosis. Because of the enormous challenge of developing small-molecule binders, antibody-based PET tracers known as immuno-PET probes are favored as a reliable tool for immune cell imaging given their robust and facile radiolabeling protocols. Immuno-PET tracers targeting T-cell surface or secreted biomarkers should also warrant evaluation for RA detection in future studies (12).

For inflammatory bowel disease detection, an anti-CD4 monoclonal antibody labeled with  $^{111}\text{In}$  was previously evaluated for SPECT imaging of CD4-positive T cells. More recently, an  $^{89}\text{Zr}$ -labeled CD4-specific GK1.5 cys-diabody was developed and evaluated in a mouse model of dextran sulfate sodium-induced colitis (Fig. 2D) (13). Increased accumulation of  $^{89}\text{Zr}$ -maleimide-deferoxamine-GK1.5 cDb was detected in the distal colon of colitis mice and further corroborated by increased CD4-positive immunohistochemistry staining, demonstrating the sensitivity of this probe for CD4-positive T cells *in vivo*. Whether PET quantification correlated with disease severity was not discussed in this study; further evaluation is therefore required to explore the feasibility of this approach for determining disease severity. Additionally, naïve CD4-positive T cells residing in the gut may raise the background signal in CD4-targeted imaging. Since

activated T cells are the true mediators of inflammatory bowel disease pathogenesis, PET tracers specific to activated T cells may be preferred.

### T-CELL PET IMAGING FOR PREDICTING AND MONITORING IMMUNE RESPONSE TO CANCER IMMUNOTHERAPIES

Immunooncology has rapidly evolved over the last decade (14), with numerous clinical trials demonstrating the unprecedented success of cancer immunotherapies in treating late-stage and recurrent malignancies, including relapsed or refractory B-cell malignancies, melanoma, bladder cancer, and non-small cell lung carcinoma (15–18). Despite the meteoric rise of these innovative therapies, only a small fraction of patients exhibits durable responses, highlighting the urgent need for reliable tools to monitor and predict therapeutic response (19). Anatomic imaging often lacks sensitivity and does not collect direct molecular or functional information about the T-cell compartment. Biopsies are invasive, risk iatrogenic complications, fail to capture whole-body information, and do not assess tumor heterogeneity (20,21). Longitudinal PET imaging and quantitative analysis of T-cell distribution in tumors or secondary lymphoid organs before and after treatment may correlate with therapeutic response, helping clinicians to identify patients most likely to benefit from treatment (22). With this motivation, a wide

range of T-cell-specific PET tracers has been developed and evaluated in preclinical studies and clinical trials.

Endogenous T-cell biomarkers include those specifically expressed on the cell surface, such as T-cell lineage markers (CD4, CD8); those secreted by certain T-cell subsets, such as granzyme B; and activation markers, such as CD278 and CD134 (Figs. 3A and 3B). A major advantage of using immuno-PET probes is their high specificity and affinity toward their homologous target, generating high signal-to-noise ratios and high-contrast images. Neutral binders without agonistic and antagonistic functions have the potential to be widely applicable without concern about perturbative effects. However, because of their large size, intact antibodies (150 kDa) can suffer from poor penetration into target tissues and slow clearance. Additionally, the crystallizable fragment regions of whole antibodies can bind nonspecifically to crystallizable fragment receptors on other cells, such as macrophages and natural killer cells (23). To overcome these challenges, antibody fragments such as the minibody, diabody, and single-domain antibody formats and other engineered protein scaffolds have been evaluated as radiotracers (24,25). These smaller vectors are likely to exhibit better tissue penetration and faster clearance and are more suited to radiolabeling with PET isotopes with shorter half-lives, making same-day imaging more feasible (26).

Radiolabeled small molecules are usually designed to target specific intracellular metabolic pathways, such as carbohydrate metabolism and DNA synthesis. The most widely used clinical PET tracer for cancer diagnosis and staging,  $^{18}\text{F}$ -FDG, has also

**TABLE 1**  
Candidate Biomarkers for PET Imaging of T-Cell Responses

Target	Type	Stage	Application
OX40	Surface biomarker	Preclinical	TILs, GVHD
CTLA-4	Surface biomarker	Preclinical	TILs, GVHD
CD3	Surface biomarker	Preclinical	TILs
CD4	Surface biomarker	Preclinical	TILs, IBD, HSCT, lymphoid organs
CD8	Surface biomarker	Preclinical/clinical	TILs, lymphoid organs
ICOS	Surface biomarker	Preclinical	TILs, CAR-T
PD-1	Surface biomarker	Preclinical/clinical	TILs
IL-2R	Surface biomarker	Preclinical/clinical	TILs, ONNV, lymphoid organs
TCRmu	Surface biomarker	Preclinical	CAR-T
VLA4	Surface biomarker	Preclinical	Tuberculosis
Granzyme B	Secreted biomarker	Preclinical	TILs
dCK	Intracellular enzyme	Preclinical/clinical	TILs, autoimmune hepatitis
dGK	Intracellular enzyme	Preclinical/clinical	GVHD, TILs, RA
HSV1-tk	Reporter gene/encoded protein size (46 kDa)	Preclinical/clinical	CAR-T
HSV1-sr39tk	Reporter gene/encoded protein size (42 kDa)	Preclinical	RA
PSMA	Reporter gene/encoded protein size (100 kDa)	Preclinical	CAR-T
NET	Reporter gene/encoded protein size (69 kDa)	Preclinical	TILs
SSTR2	Reporter gene/encoded protein size (41 kDa)	Preclinical	CAR-T
DHFR	Reporter gene/encoded protein size (18 kDa)	Preclinical	CAR-T
NIS	Reporter gene/encoded protein size (69 kDa)	Preclinical	CAR-T
2D12.5/G54C	Reporter gene/encoded protein size (52 kDa)	Preclinical	CAR-T

TIL = tumor infiltrating lymphocytes; CTLA-4 = cytotoxic T-lymphocyte antigen-4; IBD = inflammatory bowel disease; HSCT = hematopoietic stem cell transplantation; IL-2R = interleukin-2 receptors; ONNV = o'nyong-nyong virus; TCRmu = murine T-cell receptor  $\beta$ -domain; VLA4 = very late antigen-4; dCK = deoxycytidine kinase; dGK = deoxyguanosine kinase; PSMA = prostate-specific membrane antigen; NET = norepinephrine transporter; SSTR2 = somatostatin receptor 2; DHFR = dihydrofolate reductase enzyme; NIS = sodium iodide symporter; 2D12.5/G54C = antilanthanoid-DOTA antibody.

PET tracers targeting biomarkers listed here are also discussed in references 3, 22, and 35.

been explored for monitoring immune responses (27). Since the glycolytic pathway is shared by both activated immune cells and cancer cells, its specificity for the interrogation of T-cell responses is low. Rapidly proliferating T cells rely heavily on the nucleoside salvage pathway for DNA synthesis. Deoxycytidine kinase and deoxyguanosine kinase are key enzymes that regulate this pathway, motivating the development of radiolabeled small molecules targeting each. The first deoxycytidine kinase-targeting PET tracer, 1-2'-deoxy-2'-<sup>18</sup>F-fluoroarabinofuranosyl cytosine, was able to distinguish proliferating CD8-positive T cells from naïve T cells (28), but rapid catabolism in vivo impeded its clinical translation. Another deoxycytidine kinase tracer with improved metabolic stability, 2-chloro-2'-deoxy-2'-<sup>18</sup>F-fluoro-9-b-D-arabinofuranosyl-adenine, was subsequently developed and evaluated in glioblastoma patients treated with PD-1 blockade. Increased accumulation of this tracer was observed in secondary lymphoid organs and tumor tissue, and the PET signal in the latter strongly correlated with the concentration of tumor-infiltrating lymphocytes (Fig. 3C) (29). <sup>18</sup>F-AraG, a guanosine analog with high specificity for deoxyguanosine kinase, was successfully used to detect activated T cells induced by anti-PD-1 therapy in mouse models, enabling early prediction of therapeutic response (30). Given its favorable imaging characteristics,

several clinical trials are currently evaluating the feasibility of monitoring T-cell responses with <sup>18</sup>F-AraG (NCT04186988, NCT04726215).

Engineering cells to express reporter genes encoding proteins that can be detected with complementary PET tracers is a promising approach suited to tracking adoptively transferred T cells (31). The most extensively evaluated PET reporter gene is the herpes simplex virus type 1 thymidine kinase (*HSV1-tk*) and its mutant version *HSV1-sr39tk*. In a pilot clinical study, CD8-positive cytotoxic T lymphocytes were engineered to express both *HSV1-tk* and interleukin-13 zetakine chimeric antigen receptor (CAR) and then adoptively transferred into recurrent high-grade glioblastoma patients. <sup>18</sup>F-FHGB was subsequently administered to monitor the trafficking and proliferation of the engineered cytotoxic T lymphocytes in the brain (Fig. 3D) (32). This landmark study demonstrated the feasibility of using the *HSV1-tk* system to clinically track engineered immune cells. The *HSV1-sr39tk* system can also act as a suicide gene on treatment with the prodrug ganciclovir, enabling ablation of CAR-T cells for safe control of potential toxicities (33). Human PET reporter genes including sodium iodide symporter, norepinephrine transporter, and somatostatin receptor 2 have also been developed to overcome the potential

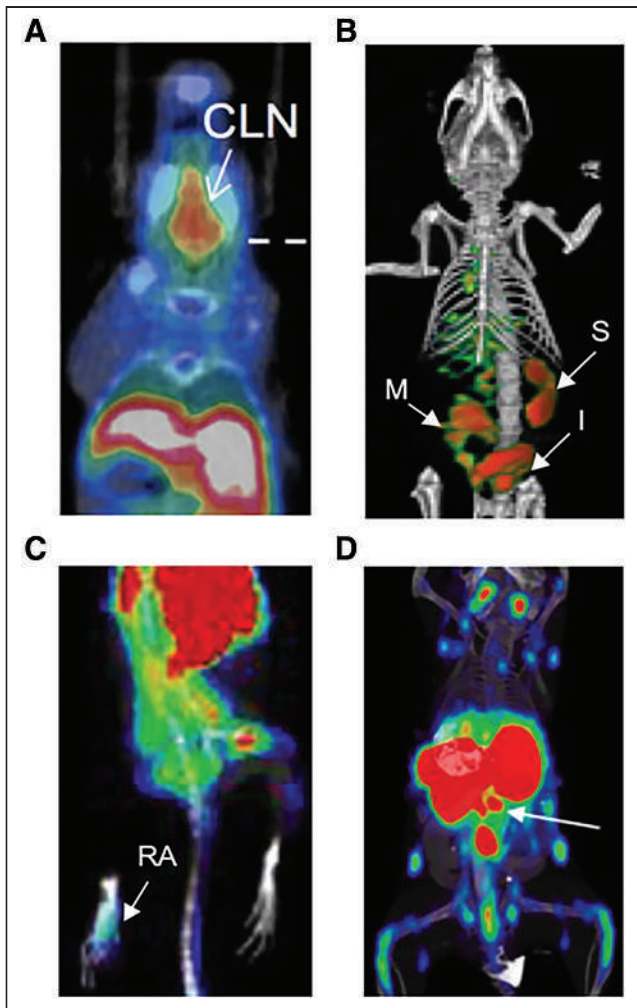


**FIGURE 2.** PET imaging of T cells for early detection of inflammatory diseases. (A)  $^{18}\text{F}$ -AraG enables detection of T-cell activation in cervical lymph nodes during acute GVHD (7). (B) OX40 immuno-PET allows early diagnosis of acute GVHD, before overt clinical symptoms (9). (C)  $^{18}\text{F}$ -AraG imaging detects RA in mouse model of adjuvant-induced arthritis (11). (D)  $^{89}\text{Zr}$ -labeled CD4-targeting cys-diabody allows detection of inflammatory bowel disease (white arrow indicating mesenteric lymph nodes) (13). CLN = cervical lymph nodes; I = intestine; M = mesenteric lymph node, S = spleen.

immunogenicity of *HSV1-tk* and evaluated for CAR-T-cell imaging. However, because of their endogenous expression, as well as the internalization of hNET and somatostatin receptor 2, their application has been limited (34). Recently, a highly promising prostate-specific membrane antigen/ $^{18}\text{F}$ -DCFPyL reporter system was evaluated for CD19-positive CAR-T-cell imaging (35). To specifically prevent the internalization of prostate-specific membrane antigen, human CD19-targeted CAR-T cells were transduced with an N-terminally modified variant, tPSMA<sup>(N9del)</sup>.  $^{18}\text{F}$ -DCFPyL, a prostate-specific membrane antigen-specific PET tracer, subsequently allowed detection of these cells with high sensitivity and specificity in vivo. Importantly, quantification of the  $^{18}\text{F}$ -DCFPyL PET signal from CD19-positive CAR-T cells in these tumors led to more accurate assessment of therapeutic response than that from measurement of CAR-T cells in peripheral blood.

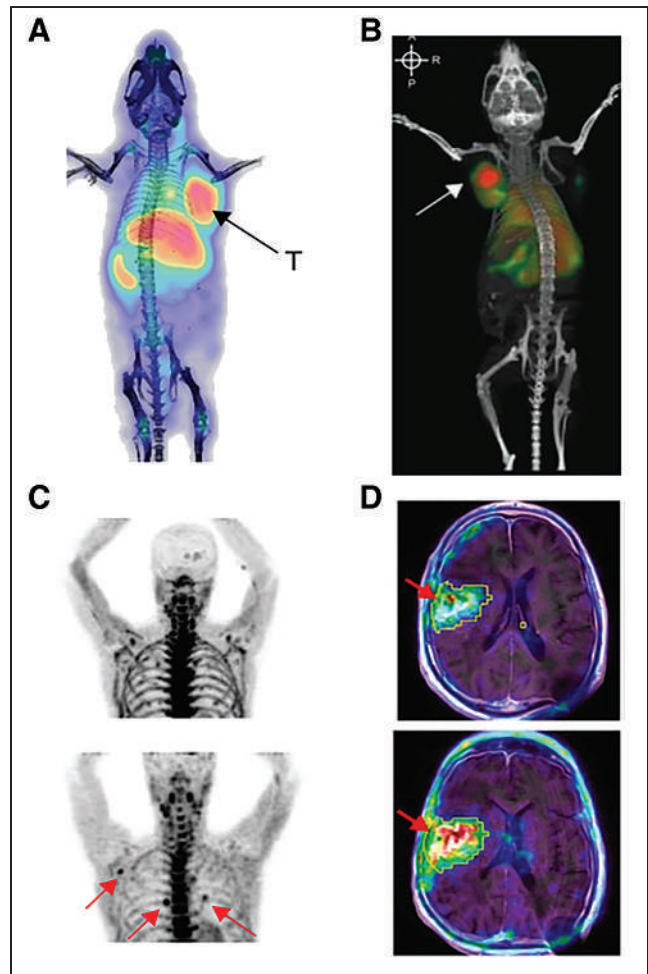


**FIGURE 3.** PET imaging of T cells enables monitoring of treatment response in cancer immunotherapy. (A) ICOS immuno-PET with  $^{89}\text{Zr}$ -DFO-ICOS monoclonal antibody visualizes and predicts therapeutic response in mouse model of Lewis lung cancer treated intratumorally with STING agonist and PD-1 blockade (37). (B) OX40 immuno-PET imaging enables visualization of activated T cells in A20 tumor-bearing mouse treated intratumorally with CpG (arrow represents CpG-treated tumor) (44). (C) Elevated uptake of 2-chloro-2'-deoxy-2'- $^{18}\text{F}$ -fluoro-9-b-d-arabino-furanosyl-adenine was observed in several lymph nodes (arrows) of recurrent glioblastoma patient after treatment with tumor lysate-pulsed DCVax and PD-1 blockade (bottom), compared with before treatment (top) (29). (D)  $^{18}\text{F}$ -FHBG enables visualization of HSV-TK1 reporter gene-modified interleukin-13 CAR-T cells (arrows) in recurrent glioblastoma patients (top, before CAR-T infusion; bottom, after CAR-T infusion) (32). T = treated tumor.

### CONCLUDING REMARKS

Here, we have reviewed state-of-the-art PET imaging approaches for in vivo T-cell visualization and their applications in T-cell-mediated diseases and cancer immunotherapy. Noninvasive PET imaging has the potential to provide comprehensive information about the distribution and abundance of immune cell subsets in real time (36,37). With these imaging approaches, physicians and research scientists can be better informed about the adaptive immune response and T-cell behaviors in different settings, which would greatly facilitate personalized medicine.

For novel T-cell PET tracers to translate from bench to bedside, lessons learned in the clinic should be brought back to the bench

to facilitate probe optimization. Although many T-cell–targeted PET tracers have yielded promising preclinical results, only a few candidates are currently under clinical investigation, and they have yet to be approved for routine clinical use. This imbalance may be attributed to redundant preclinical studies. To streamline PET tracer development, unsupervised analysis of prospective biomarkers using both preclinical and clinical “omic” datasets would help identify the optimal target for a given application. In a recent study, we used RNAseq to compare several candidate T-cell activation markers expressed on activated CD19-positive human CAR-T cells, and inducible costimulator was identified as a promising imaging biomarker that was specifically and consistently upregulated; subsequent PET imaging was focused accordingly (38). In the future, advanced techniques such as Slide-seq and CODEX (CO-Detection by indEXing) should be incorporated to identify the most relevant biomarker for T-cell imaging in a given scenario (39,40). Another reason for the imbalance is the slow adoption of novel molecular imaging techniques in the clinic. In conventional clinical workflow, anatomic imaging remains the gold standard for therapeutic response evaluation and monitoring; novel immunotherapy adjuvants are also approved by the Food and Drug Administration under certain criteria. Future clinical studies need to demonstrate that these PET approaches provide actionable insights for improved patient management. In a recent landmark study, PD-L1 imaging in cancer patients indicated that noninvasive immuno-PET outperformed RNA and immunohistochemistry-based biomarker measurements from tissue biopsies in the selection of patients most likely to benefit from PD-L1 blockade (41). These are compelling reasons to accelerate the clinical evaluation of new probes and the selection of the most promising candidates for further consideration.

To optimize the T-cell PET imaging toolbox, we should carefully compare different biomarkers, pathways, and probe formats. For example, intact antibodies exhibit higher binding affinity than small molecules but lower tissue penetration. Although the reporter gene strategy has the advantage of low background, immunogenicity usually limits its wider applications. Thus, among all the potential candidates, we should consider their affinity, specificity, sensitivity, immunogenicity, tissue penetration, and clearance and then select the best candidate for further investigation. Moreover, with current imaging probes, although we can visualize the in vivo distribution of distinct T-cell populations, we are unable to delineate their antigen specificity. A recent published study reported a novel engineered PET imaging probe—<sup>64</sup>Cu-labeled synTac (synapse for T-cell activation)—which was able to distinguish antigen-specific CD8-positive T cells from bystander CD8-positive T cells (42). This powerful approach could allow the detection of cytotoxic CD8-positive T cells specific for invading pathogens or tumor cells, which would provide more precise assessment of cancer immunotherapy efficacy or disease severity. Finally, the groundbreaking total-body PET will substantially improve sensitivity, enabling enhanced detection of T cells while also lowering the radioactive dose typically required to acquire high-resolution images, allowing for safer repeat imaging (43).

In summary, the T-cell PET imaging toolbox has great potential for improving clinical management of cancer immunotherapy and diagnosis of T-cell–driven immunopathology. Further optimization of these approaches is still needed to overcome limitations in their specificity, sensitivity, and safety. We hope that our discussion will highlight the utility of the T-cell PET imaging toolbox to both researchers and physicians and encourage the translation and wider adoption of these tools in clinical practice.

## DISCLOSURE

This work was supported by Heilongjiang Postdoctoral funding (LBH-Z18197). Israt Alam was supported by NIH/NCI (R01 CA201719-05). No other potential conflict of interest relevant to this article was reported.

## ACKNOWLEDGMENTS

We thank our colleagues in the fields of molecular imaging, immunology, and oncology, among others, for their contributions toward the development of T-cell PET imaging strategies and probes discussed in this review.

## REFERENCES

1. Waldman AD, Fritz JM, Lenardo MJ. A guide to cancer immunotherapy: from T cell basic science to clinical practice. *Nat Rev Immunol.* 2020;20:651–668.
2. Alcover A, Alarcón B, Di Bartolo V. Cell biology of T cell receptor expression and regulation. *Annu Rev Immunol.* 2018;36:103–125.
3. Wei W, Jiang D, Ehlerding EB, et al. Noninvasive PET imaging of T cells. *Trends Cancer.* 2018;4:359–373.
4. Pittet MJ, Grimm J, Berger CR, et al. In vivo imaging of T cell delivery to tumors after adoptive transfer therapy. *Proc Natl Acad Sci USA.* 2007;104:12457–12461.
5. Rheumatoid arthritis. *Nat Rev Dis Primers.* 2018;4:18002.
6. Narkhede M, Rybicki L, Abounader D, et al. The association of histologic grade with acute graft-versus-host disease response and outcomes. *Am J Hematol.* 2017;92:683–688.
7. Ronald JA, Kim BS, Gowrishankar G, et al. A PET imaging strategy to visualize activated T cells in acute graft-versus-host disease elicited by allogeneic hematopoietic cell transplant. *Cancer Res.* 2017;77:2893–2902.
8. Pektor S, Schlöder J, Klasen B, et al. Using immuno-PET imaging to monitor kinetics of T cell-mediated inflammation and treatment efficiency in a humanized mouse model for GvHD. *Eur J Nucl Med Mol Imaging.* 2020;47:1314–1325.
9. Alam IS, Simonetta F, Scheller L, et al. Visualization of activated T cells by OX40-ImmunoPET as a strategy for diagnosis of acute graft-versus-host disease. *Cancer Res.* 2020;80:4780–4790.
10. Narayan N, Owen DR, Taylor PC. Advances in positron emission tomography for the imaging of rheumatoid arthritis. *Rheumatology (Oxford).* 2017;56:1837–1846.
11. Franc BL, Goth S, MacKenzie J, et al. In vivo PET imaging of the activated immune environment in a small animal model of inflammatory arthritis. *Mol Imaging.* 2017;16:1536012117712638.
12. van der Krogt JMA, van Binsbergen WH, van der Laken CJ, et al. Novel positron emission tomography tracers for imaging of rheumatoid arthritis. *Autoimmun Rev.* 2021;20:102764.
13. Freise AC, Zettlitz KA, Salazar FB, et al. Immuno-PET in inflammatory bowel disease: imaging CD4-positive T cells in a murine model of colitis. *J Nucl Med.* 2018;59:980–985.
14. Hiam-Galvez KJ, Allen BM, Spitzer MH. Systemic immunity in cancer. *Nat Rev Cancer.* 2021;21:345–359.
15. Heppt MV, Steeb T, Schlager JG, et al. Immune checkpoint blockade for unresectable or metastatic uveal melanoma: a systematic review. *Cancer Treat Rev.* 2017;60:44–52.
16. Tabchi S, Kassouf E, Rassy EE, et al. Management of stage III non-small cell lung cancer. *Semin Oncol.* 2017;44:163–177.
17. Wołaczewicz M, Hryniewicz R, Grywalska E, et al. Immunotherapy in bladder cancer: current methods and future perspectives. *Cancers (Basel).* 2020;12:1181.
18. Stenger D, Stief TA, Kaeuferle T, et al. Endogenous TCR promotes in vivo persistence of CD19-CAR-T cells compared to a CRISPR/Cas9-mediated TCR knockout CAR. *Blood.* 2020;136:1407–1418.
19. Valero C, Lee M, Hoen D, et al. Response rates to anti-PD-1 immunotherapy in microsatellite-stable solid tumors with 10 or more mutations per megabase. *JAMA Oncol.* 2021;7:739–743.
20. Tazdait M, Mezquita L, Lahmar J, et al. Patterns of responses in metastatic NSCLC during PD-1 or PDL-1 inhibitor therapy: comparison of RECIST 1.1, irRECIST and iRECIST criteria. *Eur J Cancer.* 2018;88:38–47.
21. Borcoman E, Nandikolla A, Long G, et al. Patterns of response and progression to immunotherapy. *Am Soc Clin Oncol Educ Book.* 2018;38:169–178.
22. Krekorian M, Fruhwirth GO, Srinivas M, et al. Imaging of T-cells and their responses during anti-cancer immunotherapy. *Theranostics.* 2019;9:7924–7947.
23. Vivier D, Sharma SK, Adumeau P, et al. The impact of FcγRI binding on immuno-PET. *J Nucl Med.* 2019;60:1174–1182.

24. Zhao H, Wang C, Yang Y, et al. ImmunoPET imaging of human CD8<sup>+</sup> T cells with novel <sup>68</sup>Ga-labeled nanobody companion diagnostic agents. *J Nanobiotechnology*. 2021;19:42.
25. Freise AC, Wu AM. In vivo imaging with antibodies and engineered fragments. *Mol Immunol*. 2015;67:142–152.
26. Wu AM. Engineered antibodies for molecular imaging of cancer. *Methods*. 2014;65:139–147.
27. Valentinuzzi D, Vrankar M, Boc N, et al. [<sup>18</sup>F]FDG PET immunotherapy radiomics signature (iRADIOMICS) predicts response of non-small-cell lung cancer patients treated with pembrolizumab. *Radiol Oncol*. 2020;54:285–294.
28. Radu CG, Shu CJ, Nair-Gill E, et al. Molecular imaging of lymphoid organs and immune activation by positron emission tomography with a new [<sup>18</sup>F]-labeled 2'-deoxycytidine analog. *Nat Med*. 2008;14:783–788.
29. Antonios JP, Soto H, Everson RG, et al. Detection of immune responses after immunotherapy in glioblastoma using PET and MRI. *Proc Natl Acad Sci USA*. 2017;114:10220–10225.
30. Levi J, Lam T, Goth SR, et al. Imaging of activated T cells as an early predictor of immune response to anti-PD-1 therapy. *Cancer Res*. 2019;79:3455–3465.
31. Iafrate M, Fruhwirth GO. How non-invasive in vivo cell tracking supports the development and translation of cancer immunotherapies. *Front Physiol*. 2020;11:154.
32. Keu KV, Witney TH, Yaghoubi S, et al. Reporter gene imaging of targeted T cell immunotherapy in recurrent glioma. *Sci Transl Med*. 2017;9:eaag2196.
33. Murty S, Labanieh L, Murty T, et al. PET reporter gene imaging and ganciclovir-mediated ablation of chimeric antigen receptor T cells in solid tumors. *Cancer Res*. 2020;80:4731–4740.
34. Abousaway O, Rakhshandehroo T, Van den Abbeele AD, et al. Noninvasive imaging of cancer immunotherapy. *Nanotheranostics*. 2021;5:90–112.
35. Minn I, Huss DJ, Ahn HH, et al. Imaging CAR T cell therapy with PSMA-targeted positron emission tomography. *Sci Adv*. 2019;5:eaaw5096.
36. Mayer AT, Gambhir SS. The immunoimaging toolbox. *J Nucl Med*. 2018;59:1174–1182.
37. Xiao Z, Mayer AT, Nobashi TW, et al. ICOS is an indicator of T-cell-mediated response to cancer immunotherapy. *Cancer Res*. 2020;80:3023–3032.
38. Simonetta F, Alam IS, Lohmeyer JK, et al. Molecular imaging of chimeric antigen receptor T cells by ICOS-immunoPET. *Clin Cancer Res*. 2021;27:1058–1068.
39. Rodrigues SG, Stickels RR, Goeva A, et al. Slide-seq: a scalable technology for measuring genome-wide expression at high spatial resolution. *Science*. 2019;363:1463–1467.
40. Goltsev Y, Samusik N, Kennedy-Darling J, et al. Deep profiling of mouse splenic architecture with CODEX multiplexed imaging. *Cell*. 2018;174:968–981.e15.
41. Bensch F, van der Veen EL, Lub-de Hooge MN, et al. <sup>89</sup>Zr-atezolizumab imaging as a non-invasive approach to assess clinical response to PD-L1 blockade in cancer. *Nat Med*. 2018;24:1852–1858.
42. Woodham AW, Zeigler SH, Zeyang EL, et al. In vivo detection of antigen-specific CD8<sup>+</sup> T cells by immuno-positron emission tomography. *Nat Methods*. 2020;17:1025–1032.
43. Cherry SR, Jones T, Karp JS, et al. Total-body PET: maximizing sensitivity to create new opportunities for clinical research and patient care. *J Nucl Med*. 2018;59:3–12.
44. Alam IS, Mayer AT, Sagiv-Barfi I, et al. Imaging activated T cells predicts response to cancer vaccines. *J Clin Invest*. 2018;128:2569–2580.

# Management of Differentiated Thyroid Cancer: The Standard of Care

Anca M. Avram<sup>1,2</sup>, Katherine Zukotynski<sup>3-5</sup>, Helen Ruth Nadel<sup>6</sup>, and Luca Giovanella<sup>7,8</sup>

<sup>1</sup>Division of Nuclear Medicine, Department of Radiology, University of Michigan, Ann Arbor, Michigan; <sup>2</sup>Division of Endocrinology, Department of Internal Medicine, University of Michigan, Ann Arbor, Michigan; <sup>3</sup>Departments of Medicine and Radiology, McMaster University, Hamilton, Ontario, Canada; <sup>4</sup>Department of Medical Imaging, Schulich School of Medicine and Dentistry, Western University, London, Ontario, Canada; <sup>5</sup>Department of Radiology, University of British Columbia, Vancouver, British Columbia, Canada; <sup>6</sup>Lucile Packard Children's Hospital at Stanford, Stanford University School of Medicine, Stanford, California; <sup>7</sup>Clinic for Nuclear Medicine and Competence Center for Thyroid Diseases, Imaging Institute of Southern Switzerland, Bellinzona, Switzerland; and <sup>8</sup>Clinic for Nuclear Medicine, University Hospital and University of Zurich, Zurich, Switzerland

In the past decade, the management of differentiated thyroid cancer (DTC) underwent a paradigm shift toward the use of risk stratification with the goal of maximizing the benefit and minimizing the morbidity of radioiodine (<sup>131</sup>I) therapy. <sup>131</sup>I therapy is guided by information derived from surgical histopathology, molecular markers, postoperative diagnostic radioiodine scintigraphy, and thyroglobulin levels. <sup>131</sup>I is used for diagnostic imaging and therapy of DTC based on physiologic sodium-iodine symporter expression in normal and neoplastic thyroid tissue. We summarize the essential information at the core of multidisciplinary DTC management, which emphasizes individualization of <sup>131</sup>I therapy according to the patient's risk for tumor recurrence.

**Key Words:** differentiated thyroid cancer; state of the art; guidelines; clinical management

**J Nucl Med 2022; 63:189–195**  
DOI: 10.2967/jnumed.121.262402

**S**tandard-of-care management for differentiated thyroid cancer (DTC) is risk-adapted and typically includes surgery, <sup>131</sup>I therapy, and thyroid hormone therapy. In rare cases of radioiodine-refractory disease, symptomatic relief and slowing of metastatic disease progression may be provided by external radiotherapy, radiofrequency ablation, and multikinase or tyrosine kinase inhibitors.

## EPIDEMIOLOGY AND CLASSIFICATION

Thyroid neoplasms are the most common endocrine tumors (annual incidence, 8–9 cases/100,000 people), and DTC accounts for more than 90% of cases. The rising DTC incidence in recent years may reflect a combination of increased imaging and a concomitant true rise in incidence (1). DTC is biologically and functionally heterogeneous, with different molecular pathways impacting cancer cell biology. In particular, BRAF V600E mutation is associated with reduced expression of all thyroid-specific genes involved in iodine

metabolism, resulting in variable decreased responsiveness to <sup>131</sup>I therapy (2). The clinical, pathologic, and molecular characteristics of DTC are summarized in Supplemental Table 1 (supplemental materials are available at <http://jnm.snmjournals.org>) (3).

## DIAGNOSIS

The most common clinical presentation of DTC is as an incidental thyroid nodule. Neck ultrasound, serum thyroid-stimulating hormone (TSH), and thyroid scintigraphy are used to select high-risk nodules for fine-needle aspiration. Sonomorphologic nodule features are used in the Thyroid Imaging Reporting and Data System, a standardized risk assessment for thyroid malignancy. In the absence of suggestive cervical lymph nodes, fine-needle aspiration is discouraged for nodules smaller than 1 cm, and the decision to aspirate larger nodules is guided by the Thyroid Imaging Reporting and Data System score in the context of nodule size.

## SURGICAL TREATMENT

Traditionally, total or near-total thyroidectomy was performed on most DTC patients, with lobectomy reserved for cytologically indeterminate nodules or patients with unifocal microcarcinoma (i.e., papillary thyroid carcinoma ≤ 1 cm). Currently, lobectomy is suggested for patients with unifocal intrathyroidal low-risk DTC up to 4 cm in the absence of additional risk factors (i.e., no clinical evidence of nodal metastases, cN0) (4). The management of low-risk DTC between 2 and 4 cm remains a topic of debate, and total thyroidectomy is still frequently advised (5). Active surveillance is an alternative to lobectomy for unifocal papillary thyroid microcarcinoma with no extracapsular extension or lymph node metastases (6). The decision for active surveillance is based primarily on age-related risk of progression, individual surgical risk factors, and patient preference (7).

Cervical lymph nodal metastases occur in 20%–60% of patients with DTC, and this nodal involvement varies from clinically relevant macrometastases to seemingly clinically irrelevant micrometastases (8,9). When lymph nodal metastases are diagnosed preoperatively, central or lateral neck compartment dissection reduces the risk of locoregional recurrence. Prophylactic central neck dissection may improve regional control for invasive tumors (T3–T4) but is discouraged for low-risk DTC because potentially associated morbidities (i.e., hypoparathyroidism and recurrent

Received Apr. 4, 2021; revision accepted Aug. 5, 2021.  
For correspondence or reprints, contact Anca M. Avram ([ancaa@umich.edu](mailto:ancaa@umich.edu)).

Published online Aug. 19, 2021.  
COPYRIGHT © 2022 by the Society of Nuclear Medicine and Molecular Imaging.

laryngeal nerve damage) are not justified by a significant clinical benefit (10).

## POSTOPERATIVE MANAGEMENT

Postoperative evaluation includes thyroglobulin measurement, neck ultrasound, and diagnostic radioiodine ( $^{131}\text{I}$  or  $^{123}\text{I}$ ) whole-body scanning (WBS), which is helpful to identify persistent disease and characterize tumor  $^{131}\text{I}$  avidity. Tumor biology information encrypted in the molecular profile may also help determine indications for  $^{131}\text{I}$  treatment and modulate treatment intensity; however, further studies are required before molecular profiling can be incorporated into clinical practice. Institutional management protocols are established by multidisciplinary teams based on the local availability and expertise of the surgical, pathology, radiology, and laboratory components integral to the DTC treatment algorithm (11).

### Postoperative $^{131}\text{I}$ Therapy

The goal of  $^{131}\text{I}$  therapy is determined on integration of clinical–pathologic, laboratory, and imaging information, using standardized definitions as follows (12).

**Remnant Ablation.** Remnant ablation is intended to eliminate postoperative normal thyroid tissue remnants in low-risk DTC in order to achieve an undetectable serum thyroglobulin level, facilitating follow-up and early detection of relapse. Thyroid remnant ablation also enables high-sensitivity posttherapy WBS for diagnosis and localization of any residual disease after surgery, such as unsuspected regional cervical metastases or distant metastatic disease.

**Adjuvant Treatment.** Adjuvant  $^{131}\text{I}$  treatment in patients with suspected microscopic metastatic disease is based on histopathologic risk factors that predict tumor spread beyond the thyroid gland, with the intention of irradiating and eliminating occult infradiologic residual disease in the neck or other occult micro-metastases to improve recurrence-free survival.

**Treatment of Known Disease.**  $^{131}\text{I}$  treatment in patients with known residual or metastatic disease has the goal of eliminating iodine-avid regional or distant metastases in order to achieve cure or remission, reduce persistent or recurrent disease, and improve overall prognosis.

### Preparation for $^{131}\text{I}$ Therapy

Evaluation with radioiodine scintigraphy and  $^{131}\text{I}$  therapy is scheduled to take place at a minimum of 4 wk after surgery, which allows time to prepare the patient and reach the necessary postoperative thyroglobulin plateau levels, used as a marker for residual thyroid tissue or metastatic thyroid cancer after total thyroidectomy. Thyroglobulin levels must always be interpreted in the context of concomitant TSH level (unstimulated vs. stimulated thyroglobulin) and type of TSH stimulation (endogenous vs. exogenous) (13). Patient preparation for optimal  $^{131}\text{I}$  uptake by residual thyroid tissue and metastatic disease includes 1–2 wk of a low-iodine diet (Supplemental Table 2) and adequate TSH stimulation (TSH  $\geq$  30 mIU/L, measured 1–3 d before  $^{131}\text{I}$  administration) by either thyroid hormone withdrawal (THW) or recombinant human TSH (rhTSH) stimulation (14). For female patients of childbearing age (12–50 y), a negative pregnancy test is required within 72 h of  $^{131}\text{I}$  administration or before the first rhTSH injection (if used), unless the patient has undergone hysterectomy or is postmenopausal.

There are 2 main approaches to TSH stimulation, which is necessary for increasing Na-I symporter expression and function in

metastatic lesions (and residual thyroid tissue), with the goal of increasing the diagnostic sensitivity of  $^{131}\text{I}$  scintigraphy and absorbed radiation dose to target lesions.

**Endogenous TSH Stimulation.** Endogenous TSH stimulation is through thyroid hormone deprivation after total thyroidectomy, thus inducing a hypothyroid state: the hypothyroid stimulation protocol (THW) has 2 variants: levothyroxine withdrawal for 4 wk or levothyroxine/liothyronine substitution for the first 2 wk.

**Exogenous TSH Stimulation.** For exogenous TSH stimulation, the patient continues levothyroxine treatment, and TSH is elevated through administration of rhTSH (thyrotropin alfa [Thyrogen; Genzyme] stimulation protocol): 0.9 mg of rhTSH administered intramuscularly on 2 consecutive days, followed by  $^{131}\text{I}$  therapy administered at 48–72 h.

The choice of preparation method (THW vs. rhTSH) needs to be individualized for each patient. There is general agreement that for normal thyroid tissue (i.e., thyroid remnant), rhTSH and THW stimulation are equivalent, because normal thyroid tissue has constitutive high expression of highly functional Na-I symporter and does not require prolonged TSH stimulation for adequate  $^{131}\text{I}$  uptake and retention. However, metastatic thyroid cancer is less dense and has poorer functionality of the Na-I symporter; therefore, TSH elevation over time (area under the curve of TSH stimulation) is important to promote increased  $^{131}\text{I}$  uptake and retention in tumors (15,16). In the setting of distant metastases, THW preparation and dosimetry-guided  $^{131}\text{I}$  therapy are favored, when clinically safe and feasible (17–19).

## $^{131}\text{I}$ THERAPY

There are 2 approaches to delivering  $^{131}\text{I}$  therapy: the theranostic approach, which integrates the information obtained with postoperative diagnostic radioiodine ( $^{123}\text{I}$  or  $^{131}\text{I}$ ) scans in the management algorithm, and the risk-based approach based on clinical–pathologic factors and institutional protocols. Which of these 2 approaches is chosen depends on local factors, including the quality of surgery; the availability of, and expertise with, various imaging modalities; and physician and patient preferences. Each approach has strengths and limitations, and no conclusive evidence regarding primary outcome measures is available for recommending one strategy over the other.

### Management of the Integration of Functional Diagnostic Radioiodine Imaging

This theranostic approach to  $^{131}\text{I}$  administration involves the acquisition of a postoperative diagnostic radioiodine ( $^{123}\text{I}$ ,  $^{131}\text{I}$ , or  $^{124}\text{I}$ ) scan for planning  $^{131}\text{I}$  therapy. Diagnostic WBS is performed to identify and localize regional and distant metastatic disease and to determine the capacity of metastatic deposits to concentrate  $^{131}\text{I}$ . Depending on institutional protocols, the findings on diagnostic WBS may alter management, such as providing guidance for additional surgery; altering the prescribed  $^{131}\text{I}$  therapy, either by adjusting conventional  $^{131}\text{I}$  activity or by performing dosimetry calculations to determine the maximum tolerated therapeutic  $^{131}\text{I}$  activity for treatment of distant metastases; and avoiding unnecessary  $^{131}\text{I}$  therapy when diagnostic WBS finds no evidence of residual thyroid tissue or metastatic disease and the stimulated thyroglobulin is less than 1 ng/mL in the absence of interfering antithyroglobulin antibodies (the thyroglobulin cutoff should be adapted locally depending on the stimulation protocol and thyroglobulin assay) (17). Information acquired from the diagnostic WBS may also lead to additional functional metabolic imaging

with  $^{18}\text{F}$ -FDG PET/CT when non-iodine-avid metastatic disease is suspected (on the basis of thyroglobulin elevation out of proportion to the findings on the diagnostic WBS). It is preferable for postoperative diagnostic scanning to be performed using integrated multimodality imaging (i.e., SPECT/CT), whenever available. SPECT/CT is relevant for assessing focal radioiodine uptake in the neck, for differentiating thyroid remnant from nodal metastasis, and for detecting metastases in normal-sized cervical lymph nodes (not appreciated on postoperative neck ultrasound). Scintigraphic evaluation with diagnostic WBS can identify pulmonary micrometastases (which are too small to be detected on routine chest radiographs and may remain undetected on CT; Fig. 1) and bone metastases at an early stage (i.e., before cortical disruption is visible on bone radiographs or CT; Fig. 2). Most importantly, since  $^{131}\text{I}$  therapy is most effective for smaller metastatic deposits, early identification of regional and distant metastases is important for successful therapy (20,21). In a group of 320 thyroid cancer patients referred for postoperative  $^{131}\text{I}$  therapy, diagnostic WBS with SPECT/CT detected regional metastases in 35% of patients and distant metastases in 8% of patients. This scintigraphy information changed staging in 4% of younger, and 25% of older, patients (22). Clinical management was changed in 29% of patients when information from diagnostic WBS and stimulated thyroglobulin was integrated into the decision algorithm, as

compared with a management strategy based on clinical and histopathology information alone (23). In 350 patients at intermediate and high risk of recurrence, a single  $^{131}\text{I}$  therapeutic administration guided by postoperative diagnostic WBS information resulted in a complete response in 88% of patients with locoregional disease and 42% of patients with distant metastases (median follow-up of 3 y) (24). The information obtained with the diagnostic WBS reasonably predicts  $^{131}\text{I}$  therapeutic localization and can be used for  $^{131}\text{I}$  therapy planning in the paradigm of thyroid cancer radiotherapeutics (22,25,26).

$^{124}\text{I}$  is a positron emitter isotope with a 4.2-d half-life that has imaging characteristics superior to those of  $^{123}\text{I}$  and  $^{131}\text{I}$  scintigraphy.  $^{124}\text{I}$  is expensive, with limited accessibility, and is not widely available; however, on the basis of its PET imaging capability,  $^{124}\text{I}$  is the ideal agent for pretherapy tumor and organ dosimetry calculations (27). A standardized protocol for  $^{124}\text{I}$  PET/CT acquisition, analysis, and quantification remains to be established.

#### Risk-Adapted $^{131}\text{I}$ Therapy Followed by $^{131}\text{I}$ Scans with Diagnostic Intent

The conventional approach, in which the nuclear medicine physician chooses an  $^{131}\text{I}$  activity based on local protocols, availability, experience with various imaging modalities, and patient-related parameters, is widely used for thyroid remnant ablation, adjuvant treatment, and curative therapy of known structural disease. With this therapeutic approach, the prescribed  $^{131}\text{I}$  activity depends on the goal of  $^{131}\text{I}$  therapy as determined by the estimated risk for persistent or recurrent disease. Thyroid remnant ablation in low-risk patients is typically performed with a low  $^{131}\text{I}$  activity (i.e., 1.1–1.85 GBq [30–50 mCi]). Adjuvant  $^{131}\text{I}$  therapy is performed with a slightly higher activity (i.e., 1.85–3.7 GBq [50–100 mCi], with some institutions extending this range to 5.55 GBq [150 mCi]). Treatment of known disease is performed by administering a high activity (i.e., 3.7–5.56 GBq [100–150 mCi] for advanced locoregional disease and 5.6–7.4 GBq [150–200 mCi] for distant metastatic disease) (28). However, when diagnostic scintigraphy demonstrates diffuse homogeneous uptake throughout the lungs, simplified whole-body dosimetry should be performed to adjust the prescribed  $^{131}\text{I}$  activity so that pulmonary  $^{131}\text{I}$  retention does not exceed 3 GBq (80 mCi) after 48 h, with the goal of minimizing the risk of radiation-induced lung toxicity (29). Administration of therapeutic  $^{131}\text{I}$  activities of at least 7.4 GBq (200 mCi) for treatment of diffuse distant metastatic disease requires full whole-body or blood dosimetry calculations (24). Table 1 shows a suggested  $^{131}\text{I}$  therapy framework in DTC.

Posttherapy WBS is performed at 2–7 d after  $^{131}\text{I}$  administration to localize the therapeutic  $^{131}\text{I}$  and assess for regional and distant

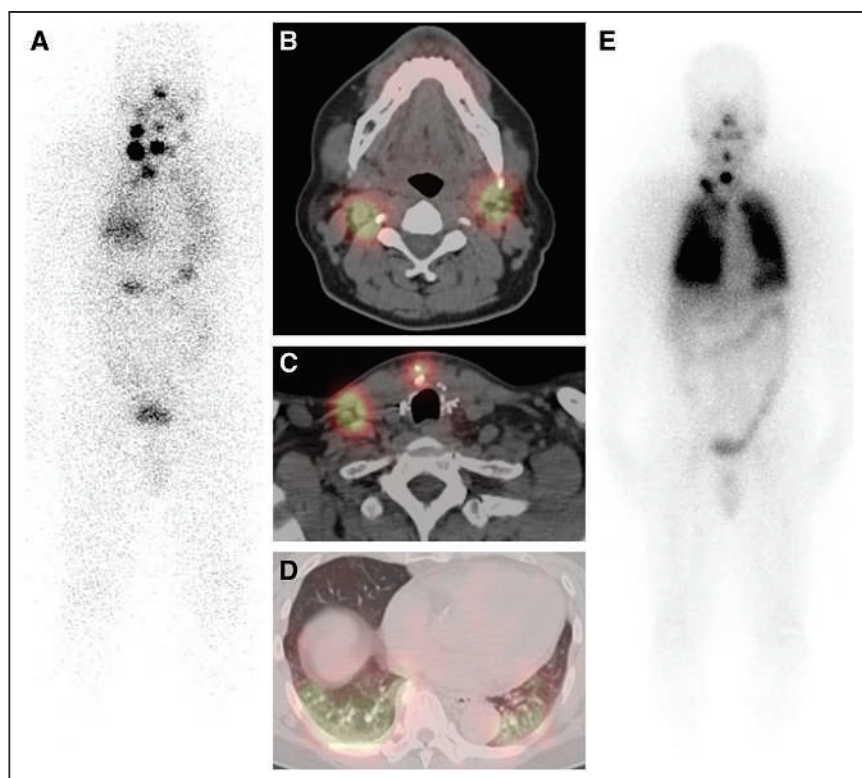


**FIGURE 1.** Radiiodine theranostics for 63-y-old man with 2.2-cm regionally advanced papillary thyroid carcinoma and of 11 lymph nodes dissected, all 11 were positive for metastasis, in surgical specimen of total thyroidectomy. (A) Diagnostic 37-MBq (1 mCi)  $^{131}\text{I}$  WBS, anterior projection, depicts multifocal neck activity and diffuse lung activity. (B and C, different anatomic levels within the neck, depicting lymph nodal metastases located in different cervical compartments) Neck SPECT/CT demonstrates iodine-avid soft-tissue nodules consistent with cervical nodal metastases. (D) Chest SPECT/CT demonstrates diffuse lung activity and branching pulmonary vasculature without definite lung nodules identified. Patient received dosimetry-guided 12.6-GBq (340 mCi)  $^{131}\text{I}$  treatment. (E) On posttherapy WBS at 3 d, anterior projection demonstrates therapeutic  $^{131}\text{I}$  localization to cervical lymph nodal metastases and diffuse miliary pulmonary metastatic disease.

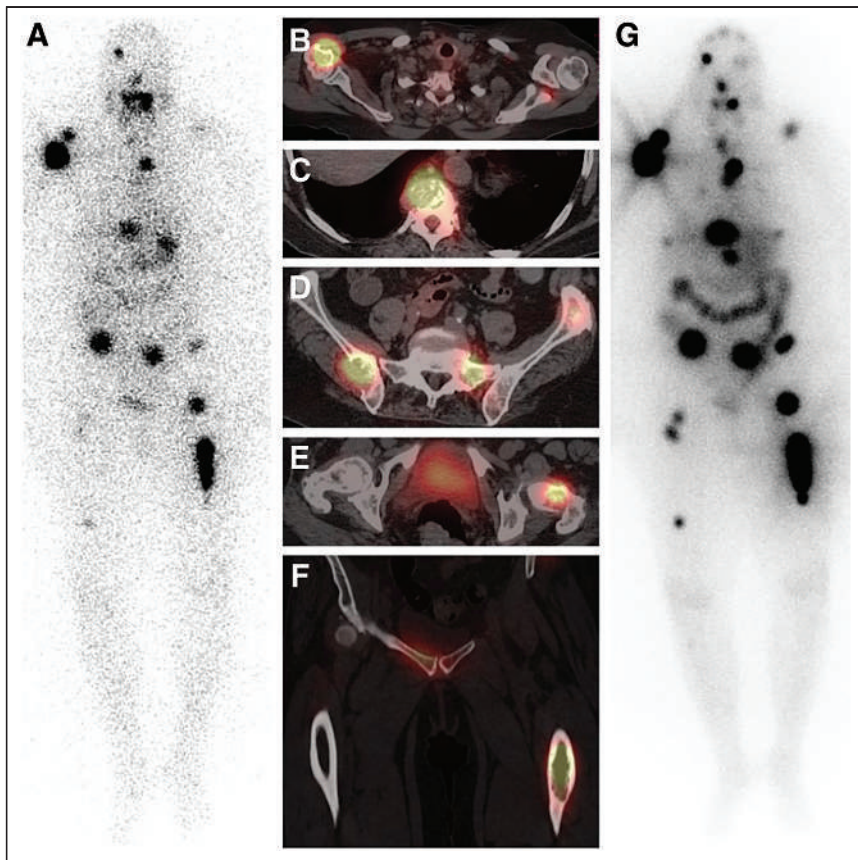


**FIGURE 2.** Radioiodine theranostics for 66-y-old woman with 2.5-cm widely invasive follicular thyroid carcinoma with osseous metastatic disease. (A–F) Diagnostic 37-MBq (1 mCi)  $^{131}\text{I}$  WBS, anterior projection (A), depicts multifocal skeletal activity, which is further characterized on SPECT/CT as iodine-avid lytic osseous metastases involving right humerus (B), vertebrae (C), pelvis (D) left femoral neck (E), and left femoral diaphysis (F). Patient received dosimetry-guided 12-GBq (325 mCi)  $^{131}\text{I}$  treatment. (G) Posttherapy WBS, anterior projection, obtained at 2 d demonstrates therapeutic  $^{131}\text{I}$  targeting of extensive iodine-avid multifocal osseous metastatic disease involving axial and proximal appendicular skeleton, with increased lesion conspicuity and numerous new foci detected as compared with diagnostic scan.

metastases. Campenni et al. reported in a cohort of 570 DTC patients at low risk or low-to-intermediate risk (pT1–pT3) that posttherapy WBS with SPECT/CT demonstrated metastases in 82 (14.4%), of whom 73 (90.2%) had a postsurgical nonstimulated thyroglobulin level of no more than 1 ng/mL (30). Furthermore, in 44 patients (54%), stimulated thyroglobulin remained at no more than 1 ng/mL, despite the presence of metastases on posttreatment scans (30). Therefore, postsurgical nonstimulated thyroglobulin levels cannot be used independently in deciding whether to pursue therapeutic  $^{131}\text{I}$  administration, mainly in patients assigned as low risk on the basis of surgical pathology alone.

#### THYROID HORMONE REPLACEMENT THERAPY

After thyroidectomy, DTC patients require thyroid hormone (levothyroxine) replacement. The TSH target for levothyroxine therapy is based on a dynamic risk classification, thyroglobulin level, thyroglobulin trend over time, antithyroglobulin antibodies, and potential adverse effects of TSH suppression. For patients with a structurally incomplete response, the serum TSH is suppressed to less than 0.1 mU/L. In the excellent treatment response category, the serum TSH is maintained at 0.5–2 mU/L for intermediate-risk

patients and at 0.1–0.5 mU/L for high-risk patients. For patients with biochemically indeterminate or incomplete responses, the recommended serum TSH target is 0.1–0.5 mU/L (6).

#### DTC MANAGEMENT IN CHILDREN

DTC represents 1.8% of all cases of cancer in individuals less than 20 y old. The incidence of pediatric thyroid cancer has increased, in part because of better techniques for diagnosis. A 4.43% increase in all stages of primarily papillary histology in 10- to 19-y-old non-Hispanic white patients, non-Hispanic black patients, and Hispanic patients was reported in a study that included 39 U.S. cancer registries (31).

Although 50% of adults older than 60 y have thyroid nodules, only 5%–7% of children and young adults are diagnosed with thyroid nodules. However, thyroid cancer is diagnosed in 25% of thyroid nodules in the pediatric population (as compared with 10%–15% of thyroid nodules in adults). Assessment using the Thyroid Imaging Reporting and Data System is not applied in pediatric patients, as one study of 314 patients younger than 18 y showed that 22% of cancers would be missed (32). Children with thyroid cancer have an increased incidence of regional and distant metastatic disease at presentation, as compared with adults, with cervical lymph nodal metastases diagnosed in 50% of cases and lung metastases in 20%.

The recommended treatment for pediatric thyroid cancer is total thyroidectomy because of the higher incidence of bilateral and multifocal disease (30% and 65%, respectively) than in adults, as well as the greater likelihood for regional and distant metastasis at presentation (33). Central node dissection is recommended in the presence of locoregional cervical disease diagnosed by imaging and confirmed on fine-needle aspiration or identified during surgery. Although some have approached disease in a single lobe with lobectomy or a phased approach, a recent study by Zong et al. suggested that because of large lesions often involving both thyroid lobes in the pediatric age group, there is increased morbidity in staged resection (34). Lobectomy may be indicated in cases of follicular thyroid carcinoma that have certain characteristics, including a size of less than 4 cm and invasion of fewer than 3 vessels (minimally invasive follicular thyroid carcinoma).

The American Thyroid Association pediatric guidelines identify 3 risk categories dependent on risk of persistent disease: low risk, or disease confined to the thyroid with few central nodes and no macroscopic metastases; medium risk, or significant central and minimal lateral node involvement; and high risk, or either distant metastases or locally invasive tumor with extensive involvement of lateral neck lymph nodes (33).

Postoperatively, the use of diagnostic WBS and 24-h neck uptake at 6–12 wk after surgery and thyroglobulin testing is

**TABLE 1**  
Suggested Framework for <sup>131</sup>I Therapy for DTC (28)

Strategy	Prescribed <sup>131</sup> I activity	Clinical context
Risk-adapted <sup>131</sup> I therapy	1.11–1.85 GBq (30–50 mCi)	Remnant ablation
	1.85–3.7 GBq (50–100 mCi)	Adjuvant treatment
	3.7–5.6 GBq (100–150 mCi)	Treatment of small-volume locoregional disease
	5.6–7.4 GBq (150–200 mCi)	Treatment of advanced locoregional disease or small-volume distant metastatic disease
Whole-body/blood dosimetry	≥7.4 GBq (≥200 mCi), maximum tolerable safe activity	Treatment of diffuse distant metastatic disease

All pediatric therapeutic <sup>131</sup>I activities are adjusted as multiplier based on 70-kg adult body weight.

recommended. Although the American Thyroid Association guidelines suggest this for intermediate- and high-risk groups, many pediatric centers extend it to all risk groups. Apart from the fact that low-risk disease is less common in children, children have a higher risk of recurrence of DTC (35). Diagnostic WBS is now routinely performed with SPECT/CT (unenhanced CT) to evaluate for cervical, upper mediastinal, and pulmonary metastatic disease. Depending on the diagnostic WBS findings, the child may be referred back to surgery for resection of unsuspected bulky residual nodal metastases in unexplored neck compartments or may proceed with <sup>131</sup>I therapy for remnant ablation or treatment of locoregional or pulmonary metastatic disease, if present.

There is controversy as to how the <sup>131</sup>I treatment activity is determined. Some suggest an empiric dosing for initial <sup>131</sup>I therapy in pediatrics, with dosimetry possibly relegated if follow-up <sup>131</sup>I therapy is needed. A weight-based dose calculated by multiplying a 70-kg adult by a 1–1.5 mCi/kg (37–56 MBq/kg) activity has been used (36). American Thyroid Association guidelines do not specify recommended therapeutic <sup>131</sup>I activities. Parisi et al. presented this algorithm: low-risk disease, 1.1–1.85 GBq (30–50 mCi); higher-risk locoregional disease, 5.6–6.5 GBq (150–175 mCi); and known or suspected pulmonary metastatic disease, 6.5–7.4 GBq (175–200 mCi). All these therapeutic <sup>131</sup>I activities are adjusted for body weight based on a 70-kg adult weight (Table 1) (35). As with adults, routine posttherapy WBS is performed at 5–7 d after therapy.

The overall prognosis for pediatric DTC is good, with greater than a 98% 10-y survival rate (37). In the small subset of children with refractory disease or disease that is not responsive to <sup>131</sup>I treatment, newer molecular therapies that target the known genetic alterations and molecular mutations may be used (38).

#### RESPONSE ASSESSMENT AFTER PRIMARY TREATMENT AND FOLLOW-UP

The combination of thyroglobulin measurement, neck ultrasound, and follow-up diagnostic WBS performed at 1–2 y after primary therapy is used to reclassify the risk of recurrence according to the patient's response to initial therapy. This process of risk reassignment is called dynamic risk stratification and is predictive of long-term clinical outcome. The criteria for treatment response evaluation are summarized in Table 2 (4).

In patients with an excellent (complete) response, the risk of disease recurrence is 1%–4%, which for intermediate-risk patients (whose initial recurrence risk is 36%–43%) and for high-risk patients (whose initial recurrence risk is 68%–70%) represents a major change in risk. The clinical outcome in patients with a biochemically incomplete response is usually good: approximately 60% of patients have no evidence of disease over long-term follow-up; 20% of patients have persistently abnormal thyroglobulin without a structural correlate, and 20% of patients develop structurally identifiable disease over 5–10 y of follow-up. Patients with a biochemically indeterminate response generally do well: in 80%–90% of patients, nonspecific biochemical findings either remain stable or resolve over time with levothyroxine suppression therapy alone; however, up to 20% of these patients will eventually develop functional or structural evidence of disease progression and require additional therapy. Patients with a structurally incomplete response require multidisciplinary management tailored to their disease status (e.g., regional vs. distant metastases and iodine-avid vs. non-iodine-avid disease) (4); depending on the results of additional treatment, patients are reclassified according to the criteria above.

#### TREATMENT OF ADVANCED DISEASE

Distant metastases develop in about 10% of DTC patients, commonly in the lungs, bone, brain, liver, and skin, and are the main cause of death (i.e., overall mortality of 65% at 5 y and 75% at 10 years) (39).

The prognosis of metastatic DTC is variable, with 2 distinct phenotypes identified: indolent and aggressive (40). Patients with iodine-avid metastatic DTC tend to have a better prognosis, with 10-y survival greater than 90%, whereas non-iodine-avid metastatic DTC has a dire 10-y survival of 10% (41). Younger patients and those with single-organ metastases and a low disease burden have the best outcome. The mainstay of treatment is TSH suppression and <sup>131</sup>I therapy as long as the disease remains radioiodine-avid. About two thirds of patients have radioiodine-avid distant metastases, and one third of them will achieve remission after multiple radioiodine treatments (20). Approximately 15%–20% of patients with metastatic DTC and most patients with Hürthle cell thyroid cancer are refractory to radioiodine, and overall survival for these patients ranges between 2.5 and 4.5 y (20,42).

**TABLE 2**  
Response to Treatment in DTC Patients: Assessment Criteria (4)

Response	Criteria
Excellent (complete)	No clinical, biochemical, or structural evidence of disease; definition: negative imaging and either suppressed thyroglobulin < 0.2 ng/mL or stimulated thyroglobulin < 1 ng/mL
Biochemically incomplete	Abnormal thyroglobulin (suppressed thyroglobulin > 1 ng/mL or stimulated thyroglobulin > 10 ng/mL or rising anti-thyroglobulin antibody levels in absence of localizable disease [i.e., negative imaging])
Structurally incomplete	Persistent or new locoregional or distant metastases (any thyroglobulin)
Indeterminate	Nonspecific biochemical findings (suppressed thyroglobulin = 0.2–1 ng/mL or stimulated thyroglobulin = 1–10 ng/mL or stable/declining anti-thyroglobulin antibody levels) or structural findings that cannot be confidently classified as benign or malignant

Determining when a patient no longer responds to <sup>131</sup>I can be challenging. Factors impacting the specific clinical situation such as age, tumor histology, stage, residual radioiodine avidity, and <sup>18</sup>F-FDG avidity should be evaluated (43). <sup>18</sup>F-FDG PET/CT is particularly useful for identifying and localizing non-iodine-avid metastases and is used to evaluate patients with elevated thyroglobulin along with negative results on diagnostic WBS (44). In this setting, if lack of <sup>131</sup>I uptake has already been established on diagnostic WBS, a positive <sup>18</sup>F-FDG PET/CT result strongly supports the suspicion of <sup>131</sup>I-negative or <sup>131</sup>I-refractory disease, leading to changes in management by identifying patients who are unlikely to benefit from additional <sup>131</sup>I therapy and instead qualify for alternative therapy (45). In addition, <sup>18</sup>F-FDG PET/CT has shown prognostic value in metastatic DTC, predicting the course of disease as aggressive or indolent (46). In radioiodine-refractory metastatic DTC, there is a survival disadvantage for patients with positive PET results as compared with those with negative PET results (42).

Ablative treatment for locoregional disease control (i.e., resection, vertebroplasty, external-beam radiation therapy, and thermal ablation) can provide symptomatic relief and delay the initiation of systemic therapy, whereas bisphosphonate or denosumab can delay the time to skeleton-related events (47). In cases of confirmed radioiodine-resistant metastatic disease progression, treatment with multikinase inhibitors (e.g., lenvatinib, sorafenib, vandetanib, cabozantinib, vemurafenib, dabrafenib/trametinib, and others) may induce periods of progression-free survival (rarely remission) without evidence of increased cancer-specific survival, and these drugs may be associated with side effects, such as hypertension, diarrhea, hand or foot skin reactions, rash, fatigue, mucositis, loss of appetite, and weight loss (48). The optimal time to start therapy, especially in asymptomatic patients, is unclear, nor is it clear which patients are likely to benefit in terms of increased quality-adjusted life years. As a rule, the decision to start molecular targeted therapies is based on a multidisciplinary team discussion. Such therapies are more likely to be used in patients who have negative findings on diagnostic WBS and symptoms that are not amenable to local therapy or who have progression of measurable lesions as defined by RECIST over the previous 12 mo, taking into consideration the tumor burden and the risk of local complications (49). The biologic mechanisms implicated in radioiodine refractoriness involve gain-of-function mutations in the MAPK signaling pathway, resulting in reduced Na-I symporter and other iodine-metabolizing gene expression. Experimental data showed that MAPK signaling pathway inhibition using MEK or

BRAF inhibitors restored radioiodine avidity. Subsequent clinical studies demonstrated that mutation-guided treatment using selective MEK inhibitors (selumetinib, trametinib), BRAF inhibitors (dabrafenib, vemurafenib), or a combination of BRAF inhibitor and MEK inhibitor is feasible and promising for redifferentiating radioiodine-refractory DTC, thereby permitting reapplication of <sup>131</sup>I therapy. Preliminary data obtained on a small clinical series of 13 patients demonstrated restoration of <sup>131</sup>I avidity in 62% of patients who subsequently received <sup>131</sup>I treatment (median activity, 7.6 GBq [204.4 mCi]; range, 5.5–9.4 GBq [150–253 mCi]), resulting in durable disease control (median duration > 1 y) while not receiving chronic, expensive multikinase inhibitor therapy (50). <sup>131</sup>I therapy remains the only known cure for metastatic radioiodine-sensitive DTC, and the use of a redifferentiating strategy to permit additional <sup>131</sup>I treatment for patients with radioiodine-refractory metastatic disease represents a promising therapeutic approach while minimizing exposure to kinase inhibitor therapy.

## CONCLUSION

DTC is the most common endocrine malignancy. Although standard management including surgery and radioiodine therapy is successful in most cases, therapy should be tailored according to a risk stratification integrating the information from histopathology, molecular markers, postoperative thyroglobulin levels, and imaging studies. Ultimately, local multidisciplinary teams consider the availability of surgical, pathologic, nuclear medicine, and laboratory expertise and take into account individual patient preferences to guide appropriate therapy.

## DISCLOSURE

No potential conflict of interest relevant to this article was reported.

## ACKNOWLEDGMENT

We thank Vanessa Allen for preparing composite figures for this article.

## REFERENCES

- Davies L, Morris LG, Haymart M, et al. American Association of Clinical Endocrinologists and American College of Endocrinology disease state clinical review: the increasing incidence of thyroid cancer. *Endocr Pract.* 2015;21:686–696.

2. Gulec SA, Ahuja S, Avram A, et al. A joint statement from the American Thyroid Association, the European Association of Nuclear Medicine, the European Thyroid Association, the Society of Nuclear Medicine and Molecular Imaging on current diagnostic and theranostic approaches in the management of thyroid cancer. *Thyroid*. 2021;31:1009–1019.
3. Rossi ED, Fadda G. Pathology and immunohistochemistry in thyroid tumors. In: *Atlas of Thyroid and Neuroendocrine Tumor Markers*. Giovanella L, ed. Springer; 2018:3–12.
4. Haugen BR, Alexander EK, Bible KC, et al. 2015 American Thyroid Association management guidelines for adult patients with thyroid nodules and differentiated thyroid cancer: the American Thyroid Association Guidelines task force on thyroid nodules and differentiated thyroid cancer. *Thyroid*. 2016;26:1–133.
5. Bilimoria KY, Bentrem DJ, Ko CY, et al. Extent of surgery affects survival for papillary thyroid cancer. *Ann Surg*. 2007;246:375–381.
6. Ito Y, Miyauchi A, Oda H. Low-risk papillary microcarcinoma of the thyroid: a review of active surveillance trials. *Eur J Surg Oncol*. 2018;44:307–315.
7. Davies L, Roman BR, Fukushima M, Ito Y, Miyauchi A. Patient experience of thyroid cancer active surveillance in Japan. *JAMA Otolaryngol Head Neck Surg*. 2019;145:363–370.
8. Miller JE, Al-Attar NC, Brown OH, et al. Location and causation of residual lymph node metastasis after surgical treatment of regionally advanced differentiated thyroid cancer. *Thyroid*. 2018;28:593–600.
9. Roh JL, Park JY, Park CI. Total thyroidectomy plus neck dissection in differentiated papillary thyroid carcinoma patients: pattern of nodal metastasis, morbidity, recurrence, and postoperative levels of serum parathyroid hormone. *Ann Surg*. 2007;245:604–610.
10. Barczyński M, Konturek A, Stopa M, Nowak W. Prophylactic central neck dissection for papillary thyroid cancer. *Br J Surg*. 2013;100:410–418.
11. Tuttle RM, Ahuja S, Avram AM, et al. Controversies, consensus, and collaboration in the use of <sup>131</sup>I therapy in differentiated thyroid cancer: a joint statement from the American Thyroid Association, the European Association of Nuclear Medicine, the Society of Nuclear Medicine and Molecular Imaging, and the European Thyroid Association. *Thyroid*. 2019;29:461–470.
12. Van Nostrand D. The benefits and risks of I-131 therapy in patients with well-differentiated thyroid cancer. *Thyroid*. 2009;19:1381–1391.
13. Mazzaferri EL, Kloos RT. Clinical review 128: current approaches to primary therapy for papillary and follicular thyroid cancer. *J Clin Endocrinol Metab*. 2001;86:1447–1463.
14. Xiao J, Yun C, Cao J, et al. A pre-ablative thyroid-stimulating hormone with 30-70 mIU/L achieves better response to initial radioiodine remnant ablation in differentiated thyroid carcinoma patients. *Sci Rep*. 2021;11:1348.
15. Pötzi C, Moameni A, Karanikas G, et al. Comparison of iodine uptake in tumour and nontumour tissue under thyroid hormone deprivation and with recombinant human thyrotropin in thyroid cancer patients. *Clin Endocrinol (Oxf)*. 2006;65:519–523.
16. Freudenberg LS, Jentzen W, Petrich T, et al. Lesion dose in differentiated thyroid carcinoma metastases after rhTSH or thyroid hormone withdrawal: <sup>124</sup>I PET/CT dosimetric comparisons. *Eur J Nucl Med Mol Imaging*. 2010;37:2267–2276.
17. Giovanella L, Duntas LH. Management of endocrine disease: the role of rhTSH in the management of differentiated thyroid cancer—pros and cons. *Eur J Endocrinol*. 2019;181:R133–R145.
18. Zanotti-Fregonara P, Hindie E. On the effectiveness of recombinant human TSH as a stimulating agent for <sup>131</sup>I treatment of metastatic differentiated thyroid cancer. *Eur J Nucl Med Mol Imaging*. 2010;37:2264–2266.
19. Plyku D, Hobbs RF, Huang K, et al. Recombinant human thyroid-stimulating hormone versus thyroid hormone withdrawal in <sup>124</sup>I PET/CT-based dosimetry for <sup>131</sup>I therapy of metastatic differentiated thyroid cancer. *J Nucl Med*. 2017;58:1146–1154.
20. Durante C, Haddy N, Baudin E, et al. Long-term outcome of 444 patients with distant metastases from papillary and follicular thyroid carcinoma: benefits and limits of radioiodine therapy. *J Clin Endocrinol Metab*. 2006;91:2892–2899.
21. Schmidt D, Linke R, Uder M, Kuwert T. Five months' follow-up of patients with and without iodine-positive lymph node metastases of thyroid carcinoma as disclosed by <sup>131</sup>I-SPECT/CT at the first radioablation. *Eur J Nucl Med Mol Imaging*. 2010;37:699–705.
22. Avram AM, Fig LM, Frey KA, Gross MD, Wong KK. Preablation <sup>131</sup>I scans with SPECT/CT in postoperative thyroid cancer patients: what is the impact on staging? *J Clin Endocrinol Metab*. 2013;98:1163–1171.
23. Avram AM, Esfandiari NH, Wong KK. Preablation <sup>131</sup>I scans with SPECT/CT contribute to thyroid cancer risk stratification and <sup>131</sup>I therapy planning. *J Clin Endocrinol Metab*. 2015;100:1895–1902.
24. Avram AM, Rosculet N, Esfandiari NH, et al. Differentiated thyroid cancer outcomes after surgery and activity-adjusted <sup>131</sup>I theragnostics. *Clin Nucl Med*. 2019;44:11–20.
25. McDougall IR. 74 MBq radioiodine <sup>131</sup>I does not prevent uptake of therapeutic doses of <sup>131</sup>I (i.e. it does not cause stunning) in differentiated thyroid cancer. *Nucl Med Commun*. 1997;18:505–512.
26. Avram AM, Dewaraja YK. Thyroid cancer radiotheragnostics: the case for activity adjusted <sup>131</sup>I therapy. *Clin Transl Imaging*. 2018;6:335–346.
27. Jentzen W, Freudenberg L, Bockisch A. Quantitative imaging of <sup>124</sup>I with PET/CT in pretherapy lesion dosimetry: effects impairing image quantification and their corrections. *Q J Nucl Med Mol Imaging*. 2011;55:21–43.
28. Luster M, Clarke SE, Dietlein M, et al. Guidelines for radioiodine therapy of differentiated thyroid cancer. *Eur J Nucl Med Mol Imaging*. 2008;35:1941–1959.
29. Sisson JC. Practical dosimetry of <sup>131</sup>I in patients with thyroid carcinoma. *Cancer Biother Radiopharm*. 2002;17:101–105.
30. Campenni A, Giovanella L, Pignata SA, et al. Undetectable or low (<1 ng/ml) postsurgical thyroglobulin values do not rule out metastases in early stage differentiated thyroid cancer patients. *Oncotarget*. 2018;9:17491–17500.
31. Bernier MO, Withrow DR, Berrington de Gonzalez A, et al. Trends in pediatric thyroid cancer incidence in the United States, 1998–2013. *Cancer*. 2019;125:2497–2505.
32. Richman DM, Benson CB, Doubilet PM, et al. Assessment of American College of Radiology thyroid imaging reporting and data system (TI-RADS) for pediatric thyroid nodules. *Radiology*. 2020;294:415–420.
33. Francis GL, Waguespack SG, Bauer AJ, et al. Management guidelines for children with thyroid nodules and differentiated thyroid cancer. *Thyroid*. 2015;25:716–759.
34. Zong Y, Li K, Dong K, Yao W, Liu G, Xiao X. The surgical choice for unilateral thyroid carcinoma in pediatrics: lobectomy or total thyroidectomy? *J Pediatr Surg*. 2018;53:2449–2453.
35. Parisi MT, Eslamy H, Mankoff D. Management of differentiated thyroid cancer in children: focus on the American Thyroid Association pediatric guidelines. *Semin Nucl Med*. 2016;46:147–164.
36. Machac J. Thyroid cancer in pediatrics. *Endocrinol Metab Clin North Am*. 2016;45:359–404.
37. Suginio K, Nagahama M, Kitagawa W, et al. Papillary thyroid carcinoma in children and adolescents: long-term follow-up and clinical characteristics. *World J Surg*. 2015;39:2259–2265.
38. Remiker AS, Chuang J, Corathers S, et al. Differentiated thyroid cancer in the pediatric/adolescent population: evolution of treatment. *J Pediatr Hematol Oncol*. 2019;41:532–536.
39. Cabanillas ME, McFadden DG, Durante C. Thyroid cancer. *Lancet*. 2016;388:2783–2795.
40. Ain KB. Papillary thyroid carcinoma: etiology, assessment, and therapy. *Endocrinol Metab Clin North Am*. 1995;24:711–760.
41. Xing M, Haugen BR, Schlumberger M. Progress in molecular-based management of differentiated thyroid cancer. *Lancet*. 2013;381:1058–1069.
42. Robbins RJ, Wan Q, Grewal RK, et al. Real-time prognosis for metastatic thyroid carcinoma based on 2-[<sup>18</sup>F]fluoro-2-deoxy-D-glucose-positron emission tomography scanning. *J Clin Endocrinol Metab*. 2006;91:498–505.
43. Giovanella L, van Nostrand D. Advanced differentiated thyroid cancer: when to stop radioiodine? *Q J Nucl Med Mol Imaging*. 2019;63:267–270.
44. Silberstein EB. The problem of the patient with thyroglobulin elevation but negative iodine scintigraphy: the TENIS syndrome. *Semin Nucl Med*. 2011;41:113–120.
45. Schlepner MC, Riemann B, Schafers M, Backhaus P, Vrachimis A. Impact of FDG-PET on therapy management and outcome of differentiated thyroid carcinoma patients with elevated thyroglobulin despite negative iodine scintigraphy. *Nuklearmedizin*. 2020;59:356–364.
46. Wang W, Larson SM, Fazzari M, et al. Prognostic value of [<sup>18</sup>F]fluorodeoxyglucose positron emission tomographic scanning in patients with thyroid cancer. *J Clin Endocrinol Metab*. 2000;85:1107–1113.
47. Giovanella L, Scappaticcio L. Radioiodine therapy of advanced differentiated thyroid cancer: clinical considerations and multidisciplinary approach. *Q J Nucl Med Mol Imaging*. 2019;63:229–234.
48. Porter A, Wong DJ. Perspectives on the treatment of advanced thyroid cancer: approved therapies, resistance mechanisms, and future directions. *Front Oncol*. 2021;10:592202.
49. Sabra MM, Sherman EJ, Tuttle RM. Tumor volume doubling time of pulmonary metastases predicts overall survival and can guide the initiation of multikinase inhibitor therapy in patients with metastatic, follicular cell-derived thyroid carcinoma. *Cancer*. 2017;123:2955–2964.
50. Jaber T, Waguespack SG, Cabanillas ME, et al. Targeted therapy in advanced thyroid cancer to resensitize tumors to radioactive iodine. *J Clin Endocrinol Metab*. 2018;103:3698–3705.

# Managing a High-Specific-Activity Iobenguane Therapy Clinic: From Operations to Reimbursement

Sophia R. O'Brien<sup>1</sup> and Daniel A. Pryma<sup>2</sup>

<sup>1</sup>Division of Nuclear Medicine, Department of Radiology, Hospital of the University of Pennsylvania, Philadelphia, Pennsylvania; and <sup>2</sup>Division of Nuclear Medicine, Department of Radiology, Perelman School of Medicine at the University of Pennsylvania, Philadelphia, Pennsylvania

**M**etaiodobenzylguanidine (MIBG, iobenguane) is a guanethidine analog that targets the norepinephrine transporter and, when radiolabeled with the  $\beta$ -emitter <sup>131</sup>I, has been used with varying protocols to treat neuroendocrine tumors, including pheochromocytoma/paraganglioma (PPGL), neuroblastoma, and carcinoid, in adults and children around the globe for more than 35 y (1). In 2018, a high-specific-activity (HSA) formulation (Azedra; Molecular Insight Pharmaceuticals, Inc.) became the first, and is currently the only, Food and Drug Administration–approved drug to treat unresectable, locally advanced, or metastatic PPGL (2). Multiple clinical trials are currently investigating other applications of <sup>131</sup>I-MIBG, such as for children with metastatic neuroblastoma and in combination with PRRT for patients with carcinoid tumor (3,4). We will likely see increasing Food and Drug Administration–approved and off-label use of <sup>131</sup>I-MIBG in the coming years. This editorial will discuss the operational aspects of clinical implementation and use of HSA <sup>131</sup>I-MIBG in advanced-PPGL patients. In addition to reviewing the literature, this editorial is supported by our experience in performing over 150 PPGL treatments over the last 10 y in both the inpatient and the outpatient setting.

## PRETREATMENT EVALUATION AND TREATMENT OVERVIEW

Since HSA <sup>131</sup>I-MIBG is the only Food and Drug Administration–approved treatment for advanced PPGL, all patients with advanced PPGL for whom systemic anticancer therapy is being considered should undergo diagnostic <sup>123</sup>I-MIBG imaging, and HSA <sup>131</sup>I-MIBG therapy should be considered first-line in those with <sup>123</sup>I-MIBG–avid disease. Systemic therapy is not considered in patients solely on the basis of metastatic disease but is reserved for patients with clear evidence of disease progression or who have disease symptoms not controlled by supportive treatment. For example, poorly controlled catecholamine-mediated symptoms (such as hypertension or anxiety) or disease-related pain can be an indication for therapy in the absence of objective progression.

Authorized user physicians evaluate prospective patients in the clinic to ensure they meet the criteria for treatment with <sup>131</sup>I-MIBG, to explain the treatment protocol and goals of therapy, and to engage

in shared decision making regarding whether and when to move forward with treatment. Patients are counseled that therapy is intended to halt progression of their disease or decrease their symptoms, hopefully for many years, but is not a disease cure (5,6). Diagnostic <sup>123</sup>I-MIBG scintigraphy is obtained to confirm <sup>123</sup>I-MIBG–avid disease and to demonstrate the patient's baseline disease burden.

In patients pursuing <sup>131</sup>I-MIBG therapy, baseline bloodwork is obtained to confirm that certain safety metrics are met, notably that platelets are greater than 80,000/ $\mu$ L, absolute neutrophil count is greater than 1,200/ $\mu$ L, and estimated glomerular filtration rate is greater than 30. A negative pregnancy test is confirmed in women of childbearing potential, and all patients are counseled to use effective contraception during treatment and for approximately 6 mo after their final therapy. Recent baseline biochemical tumor markers (chromogranin A, catecholamines, metanephrines) and anatomic imaging are important for subsequent response assessment (noting that anatomic imaging may be unhelpful in patients with bone-dominant disease). To protect patients' thyroid function, inorganic iodine is given starting the day before and for 10 d after each treatment. A complete discussion of pretreatment patient preparation can be found in the HSA <sup>131</sup>I-MIBG prescribing information (2).

The recommended dosing regimen includes planar dosimetry with 3 anterior and posterior whole-body scans done over 3–5 d after intravenous administration of about 185 MBq of HSA <sup>131</sup>I-MIBG. The maximum cumulative administered activity without exceeding organ limits is calculated. For on-label indications, there is no cost for the dosimetry dose. If a site does not have the expertise or software for dosimetry, third-party services are available.

The recommended administered activity for therapy is 296 MBq/kg (8 mCi/kg) up to a maximum of 18.5 GBq (500 mCi) in each of 2 treatment cycles given at least 90 d apart. For dosimetry revealing a maximum cumulative activity of less than 37 GBq, the prescribed activity for each cycle should be decreased equally. Most patients will require inpatient therapy; however, in patients with more indolent disease, lower administered activities can be given in an outpatient setting with reported efficacy. A common approach is 74 MBq/kg (2 mCi/kg)  $\times$  4 cycles at 3-mo intervals; 7.4 GBq (200 mCi) per cycle has also been used.

Between cycles, bloodwork is obtained to ensure that the absolute values and overall trends are safe before proceeding to the next therapy. Myelosuppression, specifically thrombocytopenia, is the most common toxicity of Azedra (5). Recovery from nadir levels is usually seen by 4–6 wk after treatment. Febrile neutropenia, grade 4 thrombocytopenia (<25,000/ $\mu$ L), or neutropenia

Received Jun. 11, 2021; revision accepted Nov. 9, 2021.  
For correspondence or reprints, contact Daniel A. Pryma (dpryma@pennmedicine.upenn.edu).  
Published online Dec. 2, 2021.  
COPYRIGHT © 2022 by the Society of Nuclear Medicine and Molecular Imaging.  
DOI: 10.2967/jnumed.121.262306

(<500/ $\mu$ L) lasting more than 1 wk should prompt a 15% reduction in prescribed activity for subsequent treatment.

Scintigraphic imaging is performed about 5–7 d after therapy (or earlier on the day of hospital discharge for inpatients) to confirm successful radiotracer tumor targeting and sometimes reveals sites of disease not well seen on the lower-dose  $^{123}\text{I}$ -MIBG diagnostic imaging. Delayed posttreatment imaging, largely focused on anatomic imaging with CT or MRI (ideally matching baseline imaging) with  $^{123}\text{I}$ -MIBG scintigraphy as an adjunct, is performed 3 mo or more after the completion of therapy. Response to therapy is usually best assessed with anatomic imaging, biochemical tumor markers, and patient symptoms. A follow-up visit in the nuclear medicine clinic is scheduled to discuss the posttreatment imaging results, bloodwork results, symptoms, and next steps. Frequently, the authorized user physician transfers primary oversight of the patient to the patient's medical oncologist, endocrinologist, or nephrologist, depending on local expertise.

### SYSTEM INFRASTRUCTURE AND INPATIENT STAY

Most HSA  $^{131}\text{I}$ -MIBG administrations will require an inpatient stay for radiation isolation. Patients will be given a private hospital room that is wrapped—that is, with the floor and surfaces covered with impervious materials for easy cleaning and disposal after the patient's stay.

Rolling shields may be required to minimize radiation exposure to adjacent rooms. Depending on room size, administered activity, and adjacent room occupancy (including above and below), shielding requirements can vary greatly. Therapy is infused intravenously by a trained nuclear medicine technologist or authorized user. Many methods for infusion have been described, but a simple lead-shielded syringe pump is believed to be the most straightforward method with the least potential for contamination. The recommended infusion duration in adults is 30 min, but as pharmacologic effects from  $^{131}\text{I}$ -MIBG have not been observed with the HSA preparation (in contrast to low-specific-activity  $^{131}\text{I}$ -MIBG), more rapid infusions can be cautiously considered. To decrease exposure, staff should enter the patient's room no more than necessary but can attend to all of a patient's medical needs. A Geiger–Mueller counter with hand and foot monitoring attachments outside the patient room is helpful to assess for potential contamination each time a member of the staff leaves the room. Additionally, providing instant-read dosimeters to the health-care staff reassures that exposures are low and can spur immediate staffing changes in the unlikely event of higher exposures. We have found that with these measures in place, nursing care for our admitted patients is straightforward and often welcomed by the nurses, as our patients tend to be far less sick than the typical oncology inpatient.

Nausea and vomiting are almost ubiquitous with high-dose therapy, and scheduled antiemetics are recommended for all patients. Intravenous fluids are also recommended for all patients to minimize nausea and improve clearance of unbound radiotracer. Intravenous fluids are continued for as long as the patient can tolerate, limited either by patient preference or by signs or symptoms of volume overload. Since most  $^{131}\text{I}$ -MIBG is excreted intact in the urine, bladder catheterization is recommended for young children and incontinent adults during hospitalization. Continent patients are encouraged to empty their bladder frequently to decrease bladder exposure. To reduce potential contamination, patients should sit when urinating, double flush the toilet, and carefully wash their hands.

Damaged and dying neuroendocrine cells can paroxysmally release large amounts of catecholamines, leading to blood pressure lability or a hypertensive crisis. Although most common within 2 d of treatment, lability can persist for weeks, and titration of anti-hypertensives may be needed (in many patients the optimal antihypertensive regimen will decrease after therapy) (2). Additionally, in patients with catecholamine-induced hyperglycemia, hypoglycemic drugs may require decreasing doses after therapy.

Radiation safety personnel will assess inpatients' radiation levels daily. In most of the United States, patients can be discharged when the exposure rate at 1 m from the patient is less than 70  $\mu\text{Sv/h}$  (7 mrem/h). The hospital stay for radiation isolation typically lasts 3–5 d after an 18.5-GBq administration but varies on the basis of multiple factors, including total administered activity, overall tumor burden, organ function, the patient's home living situation, and local regulations. Because the kinetics of MIBG are similar to those of sodium iodide, the radiation precautions and outpatient dose limits used for thyroid cancer patients treated with sodium  $^{131}\text{I}$  can also be applied to PPGL patients treated with  $^{131}\text{I}$ -MIBG.

### MULTIDISCIPLINARY STAFF

Like other therapeutic and diagnostic nuclear medicine agents, HSA  $^{131}\text{I}$ -MIBG must be handled and administered by a well-trained multidisciplinary staff. A licensed authorized user as defined by the U.S. Nuclear Regulatory Commission is responsible for the overall safe handling of radiopharmaceuticals, including  $^{131}\text{I}$ -MIBG. Nuclear medicine technologists accept, store, and handle  $^{131}\text{I}$ -MIBG according to standard Nuclear Regulatory Commission and agreement state operating procedures.

Health or medical physicists collaborate with authorized users to quantify safe levels of administered activities for each patient. Nurses, radiation safety officers, and environmental service employees work in patient-facing roles and non-patient-facing roles to ensure the safety of patients, their families, and hospital staff.

Institutions that currently administer other nuclear therapies likely have this multidisciplinary staff in place, and typically, no new resources are needed to initiate an HSA  $^{131}\text{I}$ -MIBG therapy program. If needed, training given to nuclear medicine staff can easily be adapted to nursing and other health-care staff. Periodic in-service training programs and written standard operating procedures are recommended since PPGL patients are rare. Easy accessibility to a health physicist is recommended for any staff questions or concerns.

### PURCHASING AND REIMBURSEMENT

Each HSA  $^{131}\text{I}$ -MIBG patient will require a dosimetry dose and, usually, multiple therapy doses. The HSA  $^{131}\text{I}$ -MIBG manufacturer provides a list of dates on which doses are available. There is no charge for the dosimetric dose for PPGL patients treated according to the approved indication, though the site will want to bill for the imaging acquisition. Billing for dosimetry calculations themselves is potentially feasible; guidelines are currently being created by an SNMMI Dosimetry Task Force and will be published separately. It can be helpful to provisionally place an order for a patient's expected treatment dose at the time that the dosimetry dose is ordered.

Most insurance providers have national coverage decisions for HSA  $^{131}\text{I}$ -MIBG therapy; however, given the rarity of the disease, the coverage decision may not be included in individual center

contracts. Preauthorization is required. Additionally, working with a site's billing staff to create single-case agreements with the insurance provider is recommended as a best practice. Given the rarity of the disease, this process is a straightforward one with most payers. Although standard coverage policies or contracts will provide adequate reimbursement for most outpatient therapies, single-case agreements help to ensure that the full drug acquisition cost is added to the standard inpatient reimbursement.

The "Azedra Service Connection" is a manufacturer program designed to help providers order therapy and to help patients and providers navigate treatment logistics and payment. Financial assistance is available for eligible uninsured patients and may cover the entirety of the treatment costs. Because HSA  $^{131}\text{I}$ -MIBG can be ordered at a per-millicurie cost, scaling of a prescription to a lower outpatient administered activity is easily done. The Centers for Medicare and Medicaid Services have granted a temporary new-technology add-on payment to increase reimbursement for inpatient Azedra therapy for Medicare beneficiaries. With preauthorization and single-case agreements, we have found providing this unique treatment to this ultra-orphan patient population to be economically viable.

## CONCLUSION

A  $^{131}\text{I}$ -MIBG therapy clinic is easily managed from both an operational and a financial aspect and serves an important role in

the multidisciplinary care for PPGL patients and potentially other neuroendocrine tumor patient populations.

## DISCLOSURE

Daniel A. Pryma discloses research grants from Siemens AG, 511 Pharma, and Progenics Pharmaceuticals, Inc; research consultant positions with 511 Pharma, Progenics Pharmaceuticals, Inc., Ipsen, and Actinium Pharmaceuticals, Inc; and Clinical Trial Funding from Nordic Nanovector ASA. No other potential conflict of interest relevant to this article was reported.

## REFERENCES

1. Tobes MC, Jaques S, Wieland DM, Sisson JC. Effect of uptake-one inhibitors on the uptake of norepinephrine and metaiodobenzylguanidine. *J Nucl Med.* 1985;26:897–907.
2. Azedra. Package insert. Progenics Pharmaceuticals, Inc.; 2018.
3.  $^{131}\text{I}$ -MIBG alone vs.  $^{131}\text{I}$ -MIBG with vincristine and irinotecan VS1311-MIBG with vorinostat (N2011-01). ClinicalTrials.gov website. <https://clinicaltrials.gov/ct2/show/NCT02035137>. Published January 14, 2014. Updated January 20, 2021. Accessed December 2, 2021.
4. Bushnell DL, Bodeker KL, O'Dorisio TM, et al. Addition of  $^{131}\text{I}$ -MIBG to PRRT ( $^{90}\text{Y}$ -DOTATOC) for personalized treatment of selected patients with neuroendocrine tumors. *J Nucl Med.* 2021;62:1274–1277.
5. Pryma DA, Chin BB, Noto RB, et al. Efficacy and safety of high-specific-activity  $^{131}\text{I}$ -MIBG therapy in patients with advanced pheochromocytoma or paraganglioma. *J Nucl Med.* 2019;60:623–630.
6. Azedra. Patient brochure. Progenics Pharmaceuticals, Inc.; 2019.

---

---

# <sup>18</sup>F-FDG PET/CT Imaging Biomarkers for Early and Late Evaluation of Response to First-Line Chemotherapy in Patients with Pancreatic Ductal Adenocarcinoma

Matthias R. Benz<sup>\*1-3</sup>, Wesley R. Armstrong<sup>\*1</sup>, Francesco Ceci<sup>4</sup>, Giulia Polverari<sup>5</sup>, Timothy R. Donahue<sup>6</sup>, Zev A. Wainberg<sup>7</sup>, Andrew Quon<sup>1</sup>, Martin Auerbach<sup>1</sup>, Mark D. Girgis<sup>6</sup>, Ken Herrmann<sup>3</sup>, Johannes Czernin<sup>1</sup>, and Jeremie Calais<sup>1</sup>

<sup>1</sup>Ahmanson Translational Theranostics Division, Department of Molecular and Medical Pharmacology, UCLA, Los Angeles, California; <sup>2</sup>Clinic of Radiology and Nuclear Medicine, University Hospital of Basel, Basel, Switzerland; <sup>3</sup>Department of Nuclear Medicine, University of Duisburg–Essen and German Cancer Consortium, University Hospital Essen, Essen, Germany; <sup>4</sup>Division of Nuclear Medicine, IEO European Institute of Oncology IRCCS, Milan, Italy; <sup>5</sup>PET Center, Affidea IRMET, Turin, Italy; <sup>6</sup>Department of Surgery, UCLA, Los Angeles, California; and <sup>7</sup>Department of Medical Oncology, UCLA, Los Angeles, California

---

The purpose of this study was to evaluate <sup>18</sup>F-FDG PET/CT as an early and late interim imaging biomarker in patients with pancreatic ductal adenocarcinoma who undergo first-line systemic therapy.

**Methods:** This was a prospective, single-center, single-arm, open-label study (IRB12-000770). Patient receiving first-line chemotherapy were planned to undergo baseline <sup>18</sup>F-FDG PET/CT, early interim <sup>18</sup>F-FDG PET/CT, and late interim <sup>18</sup>F-FDG PET/CT. Cutoffs for metabolic and radiographic tumor response assessment as selected and established by receiver-operating-characteristic analysis were applied (modified PERCIST/RECIST1.1). Patients were followed to collect data on further treatments and overall survival. **Results:** The study population consisted of 28 patients who underwent baseline <sup>18</sup>F-FDG PET/CT. Twenty-three of these (82%) underwent early interim <sup>18</sup>F-FDG PET/CT, and 21 (75%) underwent late interim <sup>18</sup>F-FDG PET/CT. Twenty-three deaths occurred during a median follow-up period of 14 mo (maximum follow-up, 58.3 mo). The median overall survival was 36.2 mo (95% CI, 28 mo to not yet reached [NYR]) in early metabolic responders (6/23 [26%],  $P = 0.016$ ) and 25.4 mo (95% CI, 19.6 mo–NYR) in early radiographic responders (7/23 [30%],  $P = 0.16$ ). The median overall survival was 27.4 mo (95% CI, 21.4 mo–NYR) in late metabolic responders (10/21 [48%],  $P = 0.058$ ) and 58.2 mo (95% CI, 21.4 mo–NYR) in late radiographic responders (7/21 [33%],  $P = 0.008$ ). **Conclusion:** <sup>18</sup>F-FDG PET may serve as an early interim imaging biomarker (at ~4 wk) for evaluation of response to first-line chemotherapy in patients with pancreatic ductal adenocarcinoma. Radiographic changes might be sufficient for response evaluation after the completion of first-line chemotherapy.

**Key Words:** <sup>18</sup>F-FDG PET; pancreas; adenocarcinoma; response

**J Nucl Med 2022; 63:199–204**

DOI: 10.2967/jnumed.121.261952

**P**ancreatic ductal adenocarcinoma (PDAC) typically has a tumor microenvironment characterized by a dense desmoplastic stroma. Extensive desmoplasia results in decreased stromal vascularization and altered immune cell infiltration but also represents an imaging challenge in differentiating between viable tumor and desmoplasia. In addition, CT and MRI have been reported to be imperfect in discriminating between viable tumor, desmoplastic stroma, and dead scar tissue even after successful therapy (1).

The preferred chemotherapy regimens in the neoadjuvant or adjuvant setting and the first-line therapy for metastatic disease are FOLFIRINOX (fluorouracil, leucovorin, irinotecan, and oxaliplatin), modified FOLFIRINOX, or gemcitabine/nab-paclitaxel. New second-line approaches and specific treatments, such as poly(adenosine diphosphate-ribose) polymerase inhibitors in cancer related to BRCA1 or BRCA2 mutations, have broadened the spectrum of PDAC therapies. The considerable genetic heterogeneity among patients, however, results in a limited number of patients benefiting from a selected treatment.

Currently, multiple biomarkers are under investigation for their ability to predict treatment responses (2). The best validated and most widely used prognostic biomarker in PDAC is CA 19-9, which has shown value as a prognostic and predictive biomarker in PDAC in various settings (3–5).

Current imaging criteria for tumor response assessment focus on changes in tumor size, which were described as an imperfect predictor of response of PDAC to therapy in a white paper from the Society of Abdominal Radiology (6). Other imaging biomarkers, such as diffusion-weighted MRI (7–9) and <sup>18</sup>F-FDG PET/CT (10–15), have been proposed for treatment response assessment in PDAC but are not specifically supported by current society guidelines because of inconsistent and limited data, even more so when investigating early response.

In this exploratory prospective study, we investigated whether metabolic response assessment measured by <sup>18</sup>F-FDG PET can predict survival early after the start of first-line chemotherapy in patients with PDAC. The hypothesis was that early <sup>18</sup>F-FDG PET response is a better intermediate endpoint biomarker of overall survival (OS) than are early radiographic size changes.

---

Received Jan. 20, 2021; revision accepted May 5, 2021.  
For correspondence or reprints, contact Matthias R. Benz (mbenz@mednet.ucla.edu).

\*Contributed equally to this work.  
Guest Editor: Todd E. Peterson, Vanderbilt University  
Published online Jul. 16, 2021.

COPYRIGHT © 2022 by the Society of Nuclear Medicine and Molecular Imaging.

## MATERIALS AND METHODS

### Study Design and Patients

This was a single-center, single-arm, open-label, prospective exploratory study. Patients with biopsy-proven PDAC who were scheduled to undergo first-line chemotherapy were offered participation in this study. Exclusion criteria were an inability to tolerate a PET/CT scan or the presence of another concurrent malignant condition.

Patients were planned to undergo baseline  $^{18}\text{F}$ -FDG PET/CT (PET1), early interim  $^{18}\text{F}$ -FDG PET/CT (PET2), and late interim  $^{18}\text{F}$ -FDG PET/CT (PET3) during first-line treatment. Patients were then followed to obtain further clinical data and OS.

The study was approved by the UCLA Institutional Review Board (August 1, 2012), and all patients provided written informed consent for their participation (IRB12-000770). The study was initiated, planned, funded, conducted, analyzed, and published by the investigators.

### $^{18}\text{F}$ -FDG PET/CT Imaging and Analysis

Images were acquired in accordance with  $^{18}\text{F}$ -FDG PET/CT guidelines (16). In total, 72  $^{18}\text{F}$ -FDG PET/CT studies were conducted (on a Siemens Biograph 64 TruePoint [ $n = 41$ ], Siemens Biograph 64 mCT [ $n = 27$ ], or Siemens Biograph 16 [ $n = 4$ ]). PET images were acquired from mid thigh to vertex (whole-body scan) with a time of 2–4 min per bed position using a weight-based protocol. All PET images were reconstructed using attenuation, dead-time, random-event, and scatter corrections. PET images were reconstructed with an iterative algorithm (ordered-subset expectation maximization) in an axial  $168 \times 168$  matrix (2-dimensional, 2 iterations, 8 subsets, gaussian filter of 5.0) or  $200 \times 200$  matrix (3-dimensional, 2 iterations, 24 subsets, gaussian filter of 5.0).

Patients fasted for a minimum of 6 h. The median serum glucose level was 104 mg/dL (interquartile range [IQR], 97–118 mg/dL). Patients received 7.77 MBq (0.21 mCi)/kg of  $^{18}\text{F}$ -FDG intravenously. The median injected activity of  $^{18}\text{F}$ -FDG was 372 MBq (IQR, 308–424.6 MBq). The median uptake time was 60 min (IQR, 57–67 min). Intravenous and oral contrast media were administered in 71 of 72 and 71 of 72 scans, respectively. The PET and CT image acquisition was performed as reported previously (17,18).

$^{18}\text{F}$ -FDG PET images were interpreted by 3 readers: 2 certified nuclear medicine physicians and 1 dual-certified radiologist/nuclear medicine physician. All 3 readers were aware of the PDAC diagnosis but not of the treatment regimen, other clinical data, or outcome data. The 3 readers independently quantified the  $^{18}\text{F}$ -FDG uptake of the primary pancreatic tumor site at each time point by placing a volume of interest to record the  $\text{SUV}_{\text{max}}$ . The choice of the size and location of the volume of interest was left to the reader. If there was agreement in  $\text{SUV}_{\text{max}}$  measurements between 2 readers but disagreement with the third reader, the  $\text{SUV}$  measurement of the third reader was neglected. Tumor size was evaluated by 1 radiologist at each time point.

For early and late metabolic and size response,  $\text{SUV}_{\text{max}}$  and size cutoffs as selected by modified PERCIST (mPERCIST) (19), RECIST1.1 (20), and receiver-operating-characteristic analysis were evaluated.

### Statistics

The primary objective of the study was to assess metabolic and radiographic response during first-line chemotherapy as early and late imaging biomarkers of OS in patients with PDAC. Quantitative variables are presented as median and IQR or as mean and SD. Statistics were performed using R, version 3.6.1 (R Core Team).

The study was initially powered for a total of 70 patients with the following parameters: expected survival of responders, 20 mo; expected survival of nonresponders, 10 mo; hazard ratio, 2.0; power, 0.8.

Cutoffs for early and late metabolic tumor response assessment were delineated using optimally selected cutoffs and by mPERCIST ( $\geq 30\%$  decrease in tumor  $\text{SUV}_{\text{max}}$ ) (19). Receiver-operating-characteristic analysis–selected cutoffs, plotting  $\text{SUV}_{\text{max}}$  against OS dichotomized by median OS, were  $\text{SUV}_{\text{max}}$  decreases of at least 15% and at least 38% for early and late metabolic response, respectively. Cutoffs were increased to at least 20% and at least 40%, respectively, because of considerations related to clinical relevance and reproducibility (21).

The cutoff for early assessment of size response was also optimally selected to be at least a 13% decrease in size but was increased to at least a 20% decrease because of considerations related to clinical relevance and reproducibility. Late size response was defined according to RECIST1.1 ( $\geq 30\%$  decrease in tumor size) (20).

OS was calculated from the date of subject consent to the date of death or last follow-up. All deaths included in the survival analysis were cancer-related. OS was estimated using the method of Kaplan and Meier. A  $P$  value of less than 0.05 was considered to indicate statistical significance.

## RESULTS

### Patient Characteristics

Between February 2013 and February 2019, 33 patients with histologically proven PDAC were enrolled. Five patients were excluded: 3 patients never underwent PET1, in 1 patient chemotherapy was initiated before PET1, and 1 patient was enrolled in another trial investigating nivolumab. Therefore, the study population consisted of 28 patients who underwent PET1; 23 of these (82%) underwent PET2, and 21 (75%) underwent PET3, (Fig. 1).

The median time between PET1 and PET2 and between PET1 and PET3 was 4.6 wk (IQR, 3.8–5 wk) and 12.6 wk (IQR, 11.4–14.9 wk), respectively. The median interval between PET1 and treatment initiation was 0.7 wk (IQR, 0.5–1.3 wk). PET2 and PET3 were performed 3.6 wk (IQR, 3–4.3 wk) and 11.4 wk (IQR, 10.5–14.4 wk) after initiation of treatment, respectively (Fig. 1).

The baseline characteristics are summarized in Table 1. The study cohort consisted of 11 men (39%) and 17 women (61%), with a mean age of  $65 \pm 12$  y (median, 65 y; range, 40–86 y). The primary tumor was located in the pancreatic head in 18 patients (64%). Twenty-two patients (79%) had at least clinical stage 3 disease.

### Treatment

First-line treatments were FOLFIRINOX ( $n = 12$ ; 43%), gemcitabine/nab-paclitaxel ( $n = 7$ ; 25%), FOLFIRINOX plus gemcitabine/nab-paclitaxel ( $n = 4$ ; 14%), FOLFOX (folinic acid, fluorouracil, and oxaliplatin) ( $n = 1$ ; 4%), and gemcitabine ( $n = 1$ ; 4%). Fourteen patients underwent second-line chemotherapy, and 8 patients received at least 3 lines of chemotherapy. Eight patients (29%) underwent curative surgical excision after PET3. Thirteen patients (46%) received additional local radiation therapy. Three patients (11%) died after PET1 before initiation of treatment.

### Outcome Assessment

The cutoff for the last follow-up was October 14, 2020. Twenty-three deaths occurred during a median follow-up of 14 mo (maximum follow-up, 58.3 mo). The median follow-up time in patients alive at the last follow-up date was 25.4 mo (IQR, 14.7–36.2 mo). The median OS was 14 mo (95% CI, 9.8–27.6 mo).

### Imaging Characteristics

Primary tumor  $\text{SUV}_{\text{max}}$  averaged  $6.9 \pm 3$  (median, 6.3; range, 3.5–17.7),  $6.3 \pm 3.4$  (median, 5.7; range, 2.6–15.1), and  $4.7 \pm 3.2$  (median, 4.2; range, 0–15.2) at PET1, PET2, and PET3, respectively.

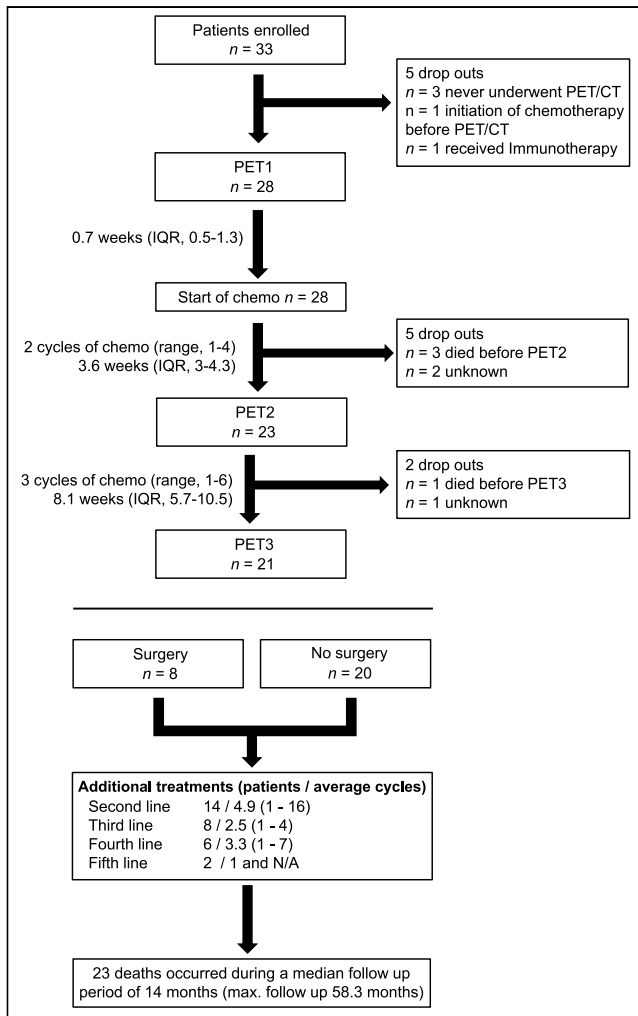


**FIGURE 1.** Flowchart.

Primary tumor size averaged  $4.1 \pm 1.7$  cm (median, 3.8 cm; range, 2.0–8.4 cm),  $3.6 \pm 1.5$  cm (median, 3.6 cm; range, 1.6–8.7 cm), and  $2.8 \pm 1.3$  cm (median, 2.7 cm; range, 0–5.6 cm) at PET1, PET2, and PET3, respectively.

#### Baseline Imaging Biomarkers

Survival did not differ significantly in patients with tumors with high versus low  $SUV_{max}$  (dichotomized by median  $SUV_{max} \geq 6.3$  vs.  $< 6.3$ :  $n = 15/28$  [54%] vs.  $n = 13/28$  [46%] at PET1; median OS, 16.8 mo vs. 14 mo [ $P = 0.62$ ]).

Baseline primary tumor size did not affect survival (dichotomized by median size  $\geq 3.8$  cm vs.  $< 3.8$  cm:  $n = 14/28$  [50%] vs.  $n = 14/28$  [50%]); median OS 12 mo vs. 19.6 mo [ $P = 0.32$ ]).

#### PET2 Imaging Biomarkers

Six of 23 patients (26%) were defined as early metabolic responders (Fig. 2A), and 7 of 23 (30%), as early radiographic responders (Fig. 2B). The median OS was 36.2 mo (95% CI, 28 mo–not yet reached [NYR]) in early metabolic responders ( $P = 0.016$ ) (Fig. 3A) and 25.4 mo (95% CI, 19.6 mo–NYR) in early radiographic responders ( $P = 0.16$ ) (Fig. 3B).

Tumor metabolic response as defined by mPERCIST showed a strong trend but did not reach statistical significance at PET2 (median OS was 32.1 mo (95% CI, 28 mo–NYR) in early

**TABLE 1**  
Patient Characteristics ( $n = 28$ )

Characteristic	Data
Age (y)	
Mean	65
Range	40–86
Sex	
Male	11
Female	17
Site	
Head	18
Body	6
Tail	4
Clinical stage	
Ib	2
II	4
III	16
IV	6
Died of disease	23
Lost to follow-up	1
Alive with disease	4
CA 19-9	
Median	101 (IQR, 5.95–592)
Range	5–1,432
Carcinoembryonic antigen ( $n = 13$ )	
Median	3.7 (IQR, 2.7–59.1)
Range	1.4–39.7
Surgery	
Yes	8
No	20
Radiation therapy	
Yes	13
No	15
Initial chemotherapy	
FOLFIRINOX	12
Gemcitabine/nab-paclitaxel	7
FOLFOX	1
FOLFORINOX+	4
Gemcitabine/nab-paclitaxel	
Gemcitabine	1
No treatment	3
Initial treatment, average cycles	6.0 (range, 2–12)
Additional treatments	
Second line	14 (average cycles, 4.9; range, 1–16)
Third line	8 (average cycles, 2.5; range, 1–4)
Fourth line	6 (average cycles, 3.3; range, 1–7)
Fifth line	2 (average cycles, 1; range, NA)

NA = not applicable.

Qualitative data are number of patients; continuous data are as individually indicated.

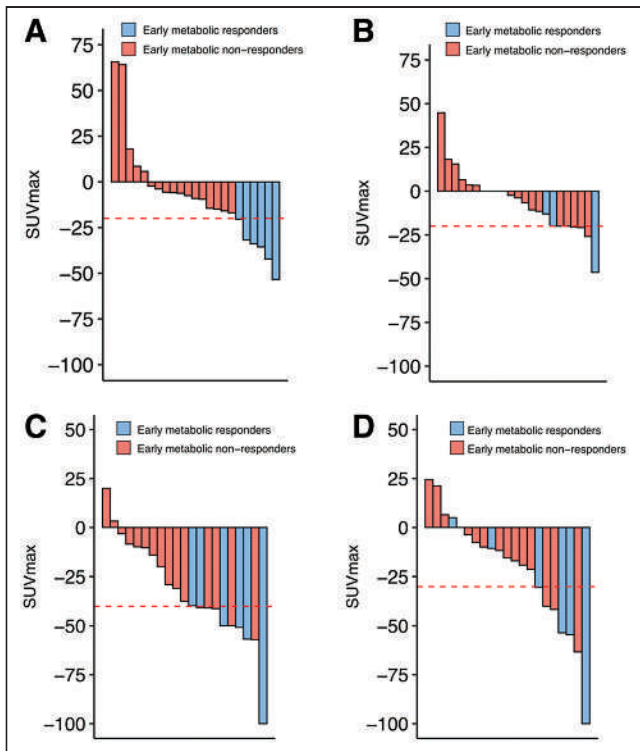


**FIGURE 2.** Waterfall plot depicting per-patient changes in early metabolic responders (A), early size responders (B), late metabolic responders (C), and late size responders (D).

metabolic responders (5/23 [22%],  $P = 0.052$ ) (Supplemental Fig. 1A; supplemental materials are available at <http://jnm.snmjournals.org>).

### PET3 Imaging Biomarkers

Ten of 21 (48%) and 7 of 21 (33%) patients were defined as late metabolic (Fig. 2C) and radiographic (Fig. 2D) responders,

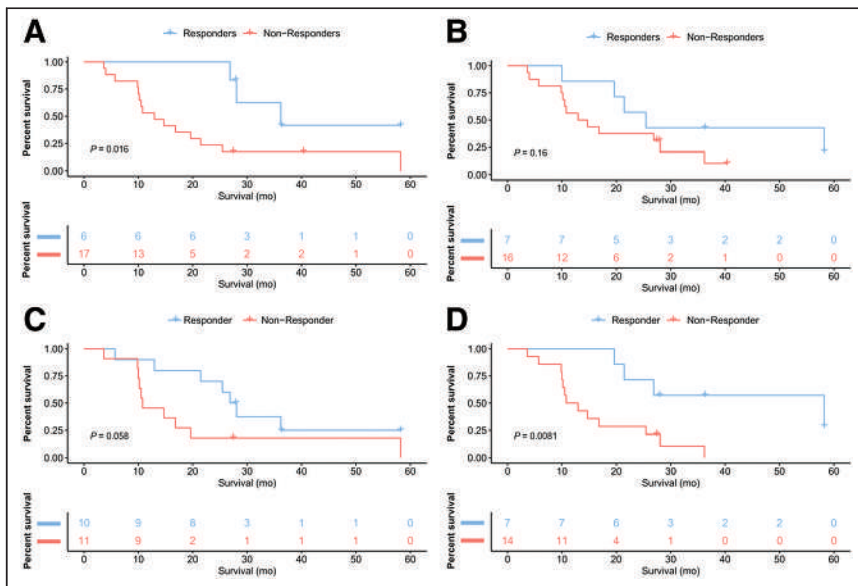


**FIGURE 3.** Kaplan-Meier curves showing OS in early metabolic responders ( $\geq 20\%$  decrease in  $SUV_{max}$ ) (A), early size responders ( $\geq 20\%$  decrease in tumor size) (B), late metabolic responders ( $\geq 40\%$  decrease in  $SUV_{max}$ ) (C), and late size responders ( $\geq 30\%$  decrease in tumor size) (D).

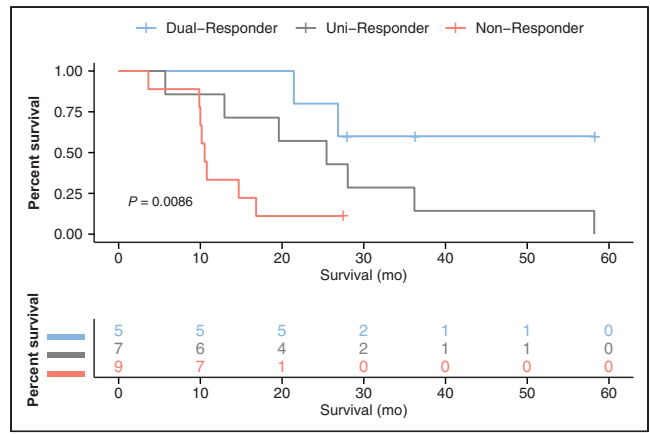


**FIGURE 4.** Kaplan-Meier curves showing OS in dual-modality responders (metabolic and size response), unimodality responders (either metabolic or size response), and nonresponders (neither metabolic nor size response) at PET3 (11 wk).

respectively. The median OS was 27.4 mo (95% CI, 21.4 mo–NYR) in late metabolic responders ( $P = 0.058$ ) (Fig. 3C) and 58.2 mo (95% CI, 21.4 mo–NYR) in late radiographic responders ( $P = 0.008$ ) (Fig. 3D).

Five of 21 patients (24%) were classified as late metabolic and size responders (dual-modality responders), whereas 7 of 21 patients (33%) were either metabolic or size responders (unimodality responders) (Fig. 4). The median OS was not yet reached in dual-modality responders and was 25.4 mo (95% CI, 12.3 mo–NYR) in unimodality responders ( $P = 0.108$ ). Dual-modality responders showed significantly improved survival when compared with nonresponders (median OS, NYR vs. 10.5;  $P = 0.042$ ), whereas unimodality responders showed a trend toward improved survival (median OS, 25.4 vs. 10.5,  $P = 0.09$ ).

Tumor metabolic response as defined by mPERCIST was not predictive of survival (median OS was 26.1 mo [95% CI, 19.6 mo–NYR]) in late metabolic responders (12/21 [57%],  $P = 0.18$ ) (Supplemental Fig. 1B).

Six of 6 early metabolic responders were also classified as late metabolic responders.

### DISCUSSION

In this prospective study,  $SUV_{max}$  changes assessed 4 wk after initiation of first-line chemotherapy served as a PET2 imaging biomarker of OS in patients with PDAC. After 11 wk from initiation of treatment, tumor size measurements by CT were superior to  $SUV_{max}$  in predicting survival. Dual-modality late responders (metabolic and size) trended toward a prolonged survival in comparison to unimodality late responders (either metabolic or size); nonresponders (neither metabolic nor size) exhibited the shortest survival.

According to RECIST1.1, the frequency of tumor reevaluation while on treatment should be protocol-specific and adapted to

the type and schedule of treatment (20). However, since tumor metabolic changes precede changes in tumor size in response to cytotoxic treatments (18), there is a broad consensus that tumor size measurements are not suitable as an early imaging biomarker. Therefore, the superiority of early  $SUV_{max}$  changes in comparison to early size changes in predicting OS are consistent with reports in other cancers (18,22,23). In fact, only 1 of 23 patients exhibited an early size response according to the RECIST1.1 cutoff of 30%. An early size cutoff of 20%, which classified 7 of 23 patients as early size responders, showed a trend toward improved survival ( $P = 0.16$ ).

Even late changes in tumor size have been described as an imperfect predictor of response of PDAC to therapy (6), as is explained mainly by the challenge in differentiating between viable tumor, the desmoplastic stroma, and dead scar tissue as a result of the treatment. However, a cutoff of 30% for late size response, as suggested by RECIST1.1, significantly predicted OS ( $P = 0.008$ ), whereas a selected cutoff of 40% for late metabolic response only tended to be predictive ( $P = 0.058$ ).

Although our patient cohort was too small for a robust statistical analysis, a response classification system that considers hybrid imaging components for both metabolic and radiographic responses (dual-modality vs. unimodality vs. nonresponder) warrants further investigation. This then could be expanded to investigate the role of changes in diffusion-weighted MRI findings, and size and metabolic changes using PET/MRI, in response assessments of PDAC. Diffusion-weighted MRI has been proposed as an imaging biomarker of therapy response; however, previous studies lack data on progression-free survival and OS (7,8) or investigate post-neoadjuvant therapy changes (9).

The selected early and late metabolic response cutoffs of at least a 20% and at least a 40% decrease in  $SUV_{max}$ , respectively, improved outcome predictions in comparison to the mPERCIST cutoff of 30%. A single cutoff, as proposed by PERCIST, to longitudinally assess cytotoxic treatment effects might not entirely reflect the treatment-induced metabolic changes of a responding or nonresponding tumor. Therefore, future guidelines might need to address the need for subcategorization of metabolic response criteria depending on time of assessment.

Our findings support the notion that  $^{18}F$ -FDG PET/CT may be used as an early predictive imaging biomarker to assess the effectiveness of new cytotoxic or potentially specific treatments in phase II clinical trials. Further studies will be needed to determine whether adaptive treatment protocols in early nonresponders could lead to improved outcomes in PDAC (24).

Several potential limitations of our study merit consideration. First, the statistically powered patient accrual target—70 patients—was not met. Although the study was designed as a 2-center study, enrollment occurred primarily at UCLA. Even though the statistical sample size was small and reduced the power of this study, we still observed significance and trends in our analysis, in line with our hypothesis. Second, cutoffs for early and late metabolic response were not predefined but optimally selected. However, the optimally selected early metabolic response cutoff of at least 20% fell within the early partial metabolic response criteria evaluated after 1 cycle of chemotherapy given by the European Organization for Research and Treatment of Cancer (25,26).

Third, patients with various tumor stages and therefore outcomes and treatment regimens, which might have affected  $^{18}F$ -FDG tumor uptake differently, were included in this study (Supplemental Table 1).

## CONCLUSION

The current study suggests that  $^{18}F$ -FDG PET allows survival predictions early after the initiation of first-line therapy (~4 wk) in patients with PDAC and might, therefore, potentially serve as an early interim endpoint biomarker in research and the clinic. At approximately 11 wk, radiographic changes might be sufficient for response evaluation after the completion of first-line therapy.

## DISCLOSURE

No potential conflict of interest relevant to this article was reported.

## KEY POINTS

**QUESTION:** Is metabolic response, assessed by  $^{18}F$ -FDG-PET, better than radiographic response as an intermediate endpoint biomarker of OS early and late after the start of first-line chemotherapy in patients with PDAC?

**PERTINENT FINDINGS:** Metabolic response assessed 4 wk after initiation of first-line chemotherapy served as a PET2 imaging biomarker of OS in patients with PDAC. After 11 wk from the initiation of treatment, tumor size measurements by CT were superior to  $SUV_{max}$  in predicting survival. Dual-modality late responders (metabolic and size) trended toward a prolonged survival in comparison to unimodality late responders (either metabolic or size); nonresponders (neither metabolic nor size) exhibited the shortest survival.

**IMPLICATIONS FOR PATIENT CARE:**  $^{18}F$ -FDG PET allows survival predictions early after the initiation of first-line therapy in patients with PDAC and might therefore potentially serve as an early interim endpoint biomarker in research and the clinic.

## REFERENCES

1. Donahue TR, Isacoff WH, Hines OJ, et al. Downstaging chemotherapy and alteration in the classic computed tomography/magnetic resonance imaging signs of vascular involvement in patients with pancreaticobiliary malignant tumors: influence on patient selection for surgery. *Arch Surg*. 2011;146:836–843.
2. Iovanna J. Implementing biological markers as a tool to guide clinical care of patients with pancreatic cancer. *Transl Oncol*. 2021;14:100965.
3. Tzeng CW, Balachandran A, Ahmad M, et al. Serum carbohydrate antigen 19-9 represents a marker of response to neoadjuvant therapy in patients with borderline resectable pancreatic cancer. *HPB (Oxford)*. 2014;16:430–438.
4. Berger AC, Garcia M Jr, Hoffman JP, et al. Postresection CA 19-9 predicts overall survival in patients with pancreatic cancer treated with adjuvant chemoradiation: a prospective validation by RTOG 9704. *J Clin Oncol*. 2008;26:5918–5922.
5. Hess V, Glimelius B, Grawe P, et al. CA 19-9 tumour-marker response to chemotherapy in patients with advanced pancreatic cancer enrolled in a randomised controlled trial. *Lancet Oncol*. 2008;9:132–138.
6. Kulkarni NM, Mannelli L, Zins M, et al. White paper on pancreatic ductal adenocarcinoma from Society of Abdominal Radiology's disease-focused panel for pancreatic ductal adenocarcinoma: part II, update on imaging techniques and screening of pancreatic cancer in high-risk individuals. *Abdom Radiol (NY)*. 2020;45:729–742.
7. Bali MA, Pullini S, Metens T, et al. Assessment of response to chemotherapy in pancreatic ductal adenocarcinoma: comparison between diffusion-weighted MR quantitative parameters and RECIST. *Eur J Radiol*. 2018;104:49–57.
8. Dalah E, Erickson B, Oshima K, et al. Correlation of ADC with pathological treatment response for radiation therapy of pancreatic cancer. *Transl Oncol*. 2018;11:391–398.
9. Panda A, Garg I, Truty MJ, et al. Borderline resectable and locally advanced pancreas cancer: FDG PET/MRI and CT tumor metrics for assessment of neoadjuvant therapy pathologic response and prediction of survival. *AJR*. 2021;217:730–740.

10. Bjerregaard JK, Fischer BM, Vilstrup MH, et al. Feasibility of FDG-PET/CT imaging during concurrent chemo-radiotherapy in patients with locally advanced pancreatic cancer. *Acta Oncol.* 2011;50:1250–1252.
11. Choi M, Heilbrun LK, Venkatramanamoorthy R, Lawhorn-Crews JM, Zalupski MM, Shields AF. Using  $^{18}\text{F}$ -fluorodeoxyglucose positron emission tomography to monitor clinical outcomes in patients treated with neoadjuvant chemo-radiotherapy for locally advanced pancreatic cancer. *Am J Clin Oncol.* 2010;33:257–261.
12. Heinrich S, Schafer M, Weber A, et al. Neoadjuvant chemotherapy generates a significant tumor response in resectable pancreatic cancer without increasing morbidity: results of a prospective phase II trial. *Ann Surg.* 2008;248:1014–1022.
13. Kittaka H, Takahashi H, Ohigashi H, et al. Role of  $^{18}\text{F}$ -fluorodeoxyglucose positron emission tomography/computed tomography in predicting the pathologic response to preoperative chemoradiation therapy in patients with resectable T3 pancreatic cancer. *World J Surg.* 2013;37:169–178.
14. Patel M, Hoffe S, Malafa M, et al. Neoadjuvant GTX chemotherapy and IMRT-based chemoradiation for borderline resectable pancreatic cancer. *J Surg Oncol.* 2011;104:155–161.
15. Topkan E, Parlak C, Kotek A, Yapar AF, Pehlivan B. Predictive value of metabolic  $^{18}\text{F}$ -FDG-PET response on outcomes in patients with locally advanced pancreatic carcinoma treated with definitive concurrent chemoradiotherapy. *BMC Gastroenterol.* 2011;11:123.
16. Boellaard R, Delgado-Bolton R, Oyen WJ, et al. FDG PET/CT: EANM procedure guidelines for tumour imaging: version 2.0. *Eur J Nucl Med Mol Imaging.* 2015;42:328–354.
17. Polverari G, Ceci F, Passera R, et al. [ $^{18}\text{F}$ ]FDG PET/CT for evaluating early response to neoadjuvant chemotherapy in pediatric patients with sarcoma: a prospective single-center trial. *EJNMMI Res.* 2020;10:122.
18. Benz MR, Herrmann K, Walter F, et al.  $^{18}\text{F}$ -FDG PET/CT for monitoring treatment responses to the epidermal growth factor receptor inhibitor erlotinib. *J Nucl Med.* 2011;52:1684–1689.
19. Wahl RL, Jacene H, Kasamon Y, Lodge MA. From RECIST to PERCIST: evolving considerations for PET response criteria in solid tumors. *J Nucl Med.* 2009;50(suppl 1):122S–150S.
20. Eisenhauer EA, Therasse P, Bogaerts J, et al. New response evaluation criteria in solid tumours: revised RECIST guideline (version 1.1). *Eur J Cancer.* 2009;45:228–247.
21. Weber WA, Gatsonis CA, Mozley PD, et al. Repeatability of  $^{18}\text{F}$ -FDG PET/CT in advanced non-small cell lung cancer: prospective assessment in 2 multicenter trials. *J Nucl Med.* 2015;56:1137–1143.
22. Benz MR, Czernin J, Allen-Auerbach MS, et al. FDG-PET/CT imaging predicts histopathologic treatment responses after the initial cycle of neoadjuvant chemotherapy in high-grade soft-tissue sarcomas. *Clin Cancer Res.* 2009;15:2856–2863.
23. Ott K, Weber WA, Lordick F, et al. Metabolic imaging predicts response, survival, and recurrence in adenocarcinomas of the esophagogastric junction. *J Clin Oncol.* 2006;24:4692–4698.
24. Lordick F, Ott K, Krause BJ, et al. PET to assess early metabolic response and to guide treatment of adenocarcinoma of the oesophagogastric junction: the MUNICON phase II trial. *Lancet Oncol.* 2007;8:797–805.
25. Pinker K, Riedl C, Weber WA. Evaluating tumor response with FDG PET: updates on PERCIST, comparison with EORTC criteria and clues to future developments. *Eur J Nucl Med Mol Imaging.* 2017;44(suppl 1):55–66.
26. Young H, Baum R, Cremerius U, et al. Measurement of clinical and subclinical tumour response using [ $^{18}\text{F}$ ]-fluorodeoxyglucose and positron emission tomography: review and 1999 EORTC recommendations. European Organization for Research and Treatment of Cancer (EORTC) PET Study Group. *Eur J Cancer.* 1999;35:1773–1782.

---

---

# <sup>131</sup>I-GD2-ch14.18 Scintigraphy to Evaluate Option for Radioimmunotherapy in Patients with Advanced Tumors

Ying Zhang<sup>1</sup>, Juergen Kupferschlaeger<sup>1</sup>, Peter Lang<sup>2</sup>, Gerald Reischl<sup>3,4</sup>, Rupert J. Handgretinger<sup>2</sup>, Christian la Fougère<sup>1,4,5</sup>, and Helmut Dittmann<sup>1</sup>

<sup>1</sup>Department of Nuclear Medicine and Clinical Molecular Imaging, University Hospital Tuebingen, Tuebingen, Germany; <sup>2</sup>Clinic for Paediatric Hematology and Oncology, University Hospital Tuebingen, Tuebingen, Germany; <sup>3</sup>Department of Preclinical Imaging and Radiopharmacy, University Hospital Tuebingen, Tuebingen, Germany; <sup>4</sup>Cluster of Excellence iFIT (EXC 2180) "Image Guided and Functionally Instructed Tumor Therapies," University of Tuebingen, Tuebingen, Germany; and <sup>5</sup>German Cancer Consortium, Partner Site Tuebingen, Tuebingen, Germany

The tumor-selective ganglioside antigen GD2 is frequently expressed on neuroblastomas and to a lesser extent on sarcomas and neuroendocrine tumors. The aim of our study was to evaluate the tumor targeting and biodistribution of <sup>131</sup>I-labeled chimeric GD2-antibody clone 14/18 (<sup>131</sup>I-GD2-ch14.18) in patients with late-stage disease in order to identify eligibility for radioimmunotherapy. **Methods:** Twenty patients (neuroblastoma, *n* = 9; sarcoma, *n* = 9; pheochromocytoma, *n* = 1; and neuroendocrine tumor, *n* = 1) were involved in this study. A 21- to 131-MBq dose (1–2 MBq/kg) of <sup>131</sup>I-GD2-ch14.18 (0.5–1.0 mg) was injected intravenously. Planar scintigraphy was performed within 1 h from injection (day 0) and on days 1, 2, 3, and 6 or 7 to analyze tumor uptake and tracer biodistribution. Serial blood samples were collected in 4 individuals. Absorbed dose to tumor lesions and organs was calculated using OLINDA software. **Results:** The tumor-targeting rate on a per-patient base was 65% (13/20), with 6 of 9 neuroblastomas showing uptake of <sup>131</sup>I-GD2-ch14.18. Tumor lesions showed maximum uptake at 20–64 h after injection (effective half-life in tumors, 33–192 h). The tumor-absorbed dose varied between 0.52 and 30.2 mGy/MBq (median, 9.08 mGy/MBq; *n* = 13). Visual analysis showed prominent blood-pool activity up to day 2 or 3 after injection. No pronounced uptake was observed in the bone marrow compartment or in the kidneys. Bone marrow dose was calculated at 0.09–0.18 mGy/MBq (median, 0.12 mGy/MBq), whereas blood dose was 1.1–4.7 mGy/MBq. Two patients (1 neuroblastoma and 1 pheochromocytoma) with particularly high tumor uptake underwent radioimmunotherapy using 2.3 and 2.9 GBq of <sup>131</sup>I-GD2-ch14.18, both achieving stable disease. Overall survival was 17 and 6 mo, respectively. **Conclusion:** <sup>131</sup>I-GD2-ch14.18 is cleared slowly from blood, not resulting in good tumor-to-background contrast until 2 d after application. With acceptable red marrow and organ dose, radioimmunotherapy is an option for patients with high tumor uptake. However, because of the variable GD2 expression, the decision should depend on pretherapeutic dosimetry.

**Key Words:** <sup>131</sup>I-GD2; neuroblastoma; dosimetry; tumor dose; radioimmunotherapy

**J Nucl Med 2022; 63:205–211**  
DOI: 10.2967/jnumed.120.261854

**T**he disialoganglioside GD2 is a sialic acid-containing glycosphingolipid physiologically expressed on cell surfaces in the central nervous system, peripheral sensory nerve fibers, and skin melanocytes at low levels (1–3). High GD2 expression has been recognized in tumors such as neuroblastoma, in bone and soft-tissue sarcoma, in neuroendocrine tumors, and in some brain tumors (1,4). Antibodies targeting GD2 have been shown to exert antibody-dependent and complement-dependent cytotoxicity in tumor cells (1,5,6). For tumor-specific therapy, the chimeric antibody dinutuximab (ch14.18) received approval for an orphan drug designation in 2015 from the U.S. Food and Drug Administration at a dose of 17.5 mg/m<sup>2</sup>/d. It is the first monoclonal antibody specifically approved for maintenance treatment of pediatric patients with high-risk neuroblastoma who have achieved at least a partial response to first-line multimodal therapy. In patients with neuroblastoma, dinutuximab was shown to increase the 2-y event-free survival rate from approximately 46% with standard treatment to 66% (6–8). Similar to this result, some patients with refractory or recurrent disease achieved benefit from an anti-GD2 therapy (9–11).

Radioimmunotherapy also involves selective targeting of cancer-associated cell antigens, primarily using the antibody as a carrier vehicle for radionuclides that deliver irradiation to tumor areas (12). Thus, the anticancer activity of radioimmunotherapy is predominantly due to irradiation rather than antibody- or complement-dependent cytotoxicity. As a result, radiation-sensitive tumors such as leukemia and lymphomas are good candidates for radioimmunotherapy. In particular, CD20-targeted radioimmunotherapy using <sup>131</sup>I (<sup>131</sup>I-tositumomab) (13) and <sup>90</sup>Y-labeled antibodies (<sup>90</sup>Y-ibritumomab tiuxetan) (14) have demonstrated durable remission of B-cell lymphoma. GD2-targeting radioimmunotherapy in high-risk neuroblastoma patients was first evaluated using the murine antibody 3F8 labeled with <sup>131</sup>I (15). In the subgroup of patient receiving <sup>131</sup>I-3F8, the engraftment of autologous bone marrow transplantation was successful, and long-term progression-free survival was comparable to a combination therapy with 3F8 and granulocyte-macrophage colony-stimulating factor for patients in a first complete response (16).

Accurate patient stratification is of the upmost interest, and there are several criteria that might help to identify eligibility for radioimmunotherapy (12). Besides tumor specificity and high target antigen expression, low uptake of the radiolabeled antibody in organs such as the liver, spleen, and kidneys is crucial (17).

---

Received Dec. 17, 2020; revision accepted Apr. 21, 2021.  
For correspondence or reprints, contact: Ying Zhang (ying.zhang@med.uni-tuebingen.de).  
Published online May 28, 2021.  
COPYRIGHT © 2022 by the Society of Nuclear Medicine and Molecular Imaging.

Thus, evaluation of in vivo biodistribution is a key step toward considering new applications of radioimmunotherapy (18).

For immunotherapies such as dinutuximab, with regard to potential adverse effects—for example, neuropathic pain, infusion reactions such as hypersensitivity, hypotension, and occasionally capillary leak syndrome (7,19)—it is highly desirable to identify eligibility (for immunotherapy and radioimmunotherapy) before making a decision about further treatment. Therefore, the aim of this pilot study was to evaluate the tumor targeting and biodistribution of the <sup>131</sup>I-labeled GD2-antibody ch14.18 (<sup>131</sup>I-GD2-ch14.18) in patients with late-stage disease and ultimately identify candidates for radioimmunotherapy.

## MATERIALS AND METHODS

### Antibody Preparation and Radiolabeling

<sup>131</sup>I for labeling in sodium hydroxide solution was purchased from GE Healthcare Buchler. The antibody GD2-mAb (ch14.18) in sterile aqueous solution (~4–5 mg/mL) was provided by the children's hospital of our institution in a quality suitable for clinical trials. As an iodination reagent, Iodo-Gen (Thermo Fisher Scientific) was used. All other chemicals and materials were provided by commercial suppliers. According to supplier instructions, 200 μL of a solution (1 mg/mL) of Iodo-Gen in CH<sub>2</sub>Cl<sub>2</sub> were introduced per vial, followed by evaporation at room temperature. Coated vials were stored for a maximum of 1 wk under inert gas in the dark.

For diagnostic application, 1–2 mg of antibody (200–400 μL of antibody solution) were added to a coated vial, followed by the acquired amount of <sup>131</sup>I (25–100 μL) corresponding to 50–175 MBq. For therapeutic application, 5 mg of GD2-ch14.18 and 3,000–4,000 MBq of <sup>131</sup>I were used for the otherwise identical labeling procedure.

### Patients and Clinical Characteristics

The need for written informed consent for this study was waived by the institutional review board (registry 821/2020BO2). Following the stipulations of the German medicinal products act (“Arzneimittelgesetz”; AMG §13[2b]), <sup>131</sup>I-GD2-ch14.18 was used in patients with late-stage disease and in order to identify candidates for radioimmunotherapy.

In total, 20 patients were included in this retrospective analysis (Table 1). All patients had a history of surgical tumor resection and systemic chemotherapy. Neuroblastoma patients (8 children and 1 adult) had stage IV disease and had previously been treated by myeloablative chemotherapy with autologous hematopoietic stem cell rescue. Four of 9 patients additionally received external-beam irradiation, and 5 of 9 received nonradioactive GD2-antibody therapy. All neuroblastoma patients underwent <sup>123</sup>I-metaiodobenzylguanidine (<sup>123</sup>I-MIBG) scintigraphy, which demonstrated tumor uptake in only 3 of 9 cases. Individuals with <sup>123</sup>I-MIBG-positive tumors had earlier received <sup>131</sup>I-MIBG therapy. Patients with metastatic sarcoma were predominantly adults (*n* = 6/9; age range, 18–51 y). One of the remaining 2 patients had advanced neuroendocrine tumor, and the other had malignant pheochromocytoma. MRI or CT imaging was used as the reference standard for detection of tumor manifestations on <sup>131</sup>I-GD2-ch14.18 scans.

### Protocol for Scintigraphy

A 21- to 131-MBq dose (1–3 MBq/kg) of <sup>131</sup>I-GD2-ch14.18 (0.5–1.0 mg of antibody) was diluted in 100 mL of 0.9% NaCl and infused intravenously over 45–60 min. Premedication included antihistamines and prednisolone. Whole-body (WB) planar scintigraphy was performed using a double-head γ-camera (Hawkeye/Millennium VG; GE Healthcare) with a high-energy general-purpose collimator and a matrix size of 1,024 × 256 pixels. The energy window was set at 364 ± 36 keV for <sup>131</sup>I. Acquisitions were performed at 1, 24, 48, and 72 h after injection, as well as, if possible, 5–6 d after injection. Additional

SPECT/CT of tumor regions was performed for some patients. Serial blood samples were collected from 4 patients (3 adults and 1 child).

### <sup>131</sup>I-GD2-ch14.18 Treatment

Two adult patients (1 neuroblastoma and 1 pheochromocytoma) received treatment with <sup>131</sup>I-GD2-ch14.18 (2,275 MBq with 1.7 mg of GD2-Ab and 2,942 MBq with 1.6 mg of GD2-Ab, respectively). Comedications included dexamethasone, 8 mg to 16 mg daily for 5 d; antihistamines; and analgesia, if required. The patients were hospitalized for 4–5 d after the infusion. Posttreatment evaluations included clinical status, vital signs, neurologic examination, blood for serum chemistries, and electrocardiography. The hemogram was checked 0.5, 1, 2, and 3 mo after treatment. WB CT imaging was performed 2 and 5 mo after treatment.

### Normalized Blood Tracer Concentration

Activity concentrations (Bq/mL) from blood samples (0.1–0.5 mL of full blood) were determined using an automatic γ-counter (Wizard 1480; Wallac). Data were corrected for background radiation, cross over, dead time, and decay due to the collection times of the individual samples. A final normalization of the injected activity was calculated with the normalized blood tracer concentration and expressed as percentage injected activity per milliliter.

### Biodistribution

Distribution of radioactivity in various organs was measured using count rates in regions of interest defined on serial planar scans. A baseline scan was performed within 1 h from activity infusion before the first urination. Data were expressed as percentage WB count fraction of injected activity.

Since data from 1 patient were not eligible for biodistribution measurement, the statistics were based on 19 patients. Time-activity curves were drawn for visually well-defined GD2-positive tumors (fraction of injected activity per cubic centimeter of tumor, *n* = 12 patients).

### Bone Marrow Dose

The bone marrow dose was calculated using the following equation (20):

$$\text{Bone marrow dose} \left[ \frac{\text{mGy}}{\text{MBq}} \right] = 0.058 \times \tilde{A}_{\text{blood}} \times m_{\text{RM}} \times \frac{\text{RMECFF}}{(1 - \text{HCT}) \times A_{\text{injected}}}$$

where  $A_{\text{blood}}$  denotes the accumulated blood activity concentration (MBq × h/g),  $m_{\text{RM}}$  denotes the mass of red bone marrow (g), and  $A_{\text{injected}}$  denotes the injected activity (MBq). RMECFF is red marrow extracellular fluid fraction, and HCT denotes hematocrit.

The red bone marrow mass was calculated from the total body weight (g) multiplied by 1.37% in male patients and 1.16% in female patients (21). The dose conversion factor RMECFF/(1 – HCT) was assumed to be 0.32 (20).

### Dosimetry

Radiation doses absorbed by WB, heart, lung, liver, spleen, and kidney were calculated from the <sup>131</sup>I time-integrated activity coefficient (TIAC) in the defined region of interest. Organ radioactivity content was estimated from the geometric mean of anterior and posterior region-of-interest counts. A standard marker of <sup>131</sup>I-GD2-ch14.18 (~1 MBq) was placed in each WB scan as a reference to ensure constancy of γ-camera electronics and scan speed. These data were fitted to a rising and falling exponential function:

$$Y(t) = A[1 - \exp(-\alpha t)] \cdot \exp(-\beta t)$$

Integration of the equation for  $Y(t)$  yields the cumulative activity in counts × h (or fraction of injected activity × h). Finally, OLINDA

**TABLE 1**  
Patient Characteristics, <sup>131</sup>I-GD2-ch14.18 Activity, and Tumor Detectability on GD2 Scans

Patient no.	Sex	Age (y)	BMI	Histology	Prior treatments	Histology and MIBG scan	Tumor sites	Activity (MBq)	Tumor detection
1	M	23	21	Neuroblastoma	S, chemo, RT	G3, MIBG neg	Bone, hep, lym	82.3	Pos
2	M	32	23	Pheochromocytoma	S, chemo, RT, PRRT	Chromogranine pos	Bone, hep, pul	89.7	Pos
3	F	50	21	Neuroendocrine tumor	Chemo, RT	Chromogranine pos	Bone, hep, lym, pul	87.2	Pos
4	M	7	13	Neuroblastoma	S, chemo, RT, ABMT	MIBG neg, VMA/HVA neg, MYCN pos	Bone	50.8	Pos
5	F	8	16	Neuroblastoma	S, chemo, RT, ABMT	MIBG, NSE, VMA, MYCN neg	Bone, BM	32.6	Pos
6	M	8	16	Neuroblastoma	S, chemo, RT, ABMT	MYCN neg, no chromosome aberration 1 (p36)	Bone	27	Pos
7*	M	7	14	Neuroblastoma	S, chemo, RT, ABMT, GD2	MYCN neg, MIBG pos	Bone, BM	24.7	Neg
8*	M	4	16	Neuroblastoma	S, chemo, MIBG-T, ABMT	MYCN neg, imbalance chromosome 1 (p36)	Bone, BM	21.2	Neg
9	F	4	13	Neuroblastoma	S, chemo, RT, ABMT	MIBG neg	Bone, lym	22.3	Pos
10	F	13	15	Neuroblastoma	S, chemo, MIBG-T, ABMT, GD2	MYCN neg, 1 p-deletion pos, catecholamine pos, MIBG pos	Bone, BM	46.8	Pos
11	M	51	29	Ewing sarcoma	S, chemo, RT, ABMT	Ewing sarcoma	Cerebral, pul	83.2	Neg
12	F	20	19	Ewing sarcoma	S, chemo, RT, ABMT	Ewing sarcoma	Hep, pul	59	Neg
13	M	18	30	Ewing sarcoma	S, chemo	Ewing sarcoma	Pul	130.8	Neg
14	M	13	25	Ewing sarcoma	S, chemo, RT, ABMT	Ewing sarcoma	Bone, pul	76.5	Pos
15	M	17	18	Ewing sarcoma	S, chemo, ABMT	Ewing sarcoma	Bone, lym	80.5	Pos
16	F	18	27	Ewing sarcoma	S, chemo, RT, ABMT	Ewing sarcoma	Bone	79.5	Pos
17	M	19	19	Osteosarcoma	S, chemo	Osteosarcoma	Bone, lym, pul, soft	82.1	Pos
18	M	11	19	Osteosarcoma	S, GD2	Osteosarcoma	No metastasis	84	Pos
19	M	22	17	Osteosarcoma	S, chemo	Osteosarcoma	GI, pul	105	Neg
20*	M	5	17	Neuroblastoma	S, chemo, RT, ABMT	MYCN and MIBG neg, no chromosome aberration 1 (p36)	Bone, BM, lym	59.3	Neg

\*Not suitable for dosimetric analysis.

BMI = body mass index; MIBG-T = <sup>131</sup>I-MIBG therapy; S = surgery; chemo = chemotherapy; RT = focal radiotherapy; neg = negative; bone = skeletal metastases; hep = hepatic metastases; lym = lymph node metastases; pos = positive; PRRT = peptide receptor radiotherapy; pul = pulmonary metastases; ABMT = myeloablative chemotherapy with stem-cell rescue; VMA = vanillylmandelic acid; HVA = homovanillic acid; MYCN = N-myc proto-oncogene protein; NSE = neuron-specific enolase; BM = bone marrow metastases; GD2 = nonradioactive GD2-antibody therapy; soft = soft-tissue metastases; GI = gastrointestinal tract metastases.

software (Vanderbilt University) was used for dosimetric analysis of all patients.

### Tumor Uptake and Tumor TIACs

Absorbed doses of tumors were calculated from regions of interest, with background correction and tumor volumes measured from CT or MRT scans. In patients presenting with multiple tumor lesions, a reference tumor site was defined on the basis of the CT or MRI data comprising the best-delineated or largest lesion. Because time–activity curves showed increasing uptake in tumor regions during the examination cycle, the above equation could not be applied for tumor TIAC. For this reason, we used the following formulas for TIAC in tumor regions:

$$\tau_{\text{tumor}} = \tilde{A}_{\text{tumor}} / A_{\text{injected}}$$

and

$$\tilde{A}_{\text{tumor}} = \int_0^{\infty} dt A(t) = \int_0^T dt A(t) + \int_T^{\infty} dt A(t)$$

where the first integral was approximated from experimental data using the trapezoidal rule and the second integral was analytically solved using the last measured value and a monoexponential decay with physical half-life time.

### Statistics

Results are shown as means  $\pm$  SDs. Data were calculated using Microsoft Excel software. Statistical testing (1-way ANOVA) was performed using SigmaStat software (version 3.5; Systat Software). For analyzing the significance of the results, a *t* test based on range was used. A *P* of less than 0.05 was regarded as significant.

## RESULTS

### Biodistribution

Application of  $^{131}\text{I}$ -GD2-ch14.18 was accompanied by a sensation of mild to moderate malaise and tightness in the chest during infusion in most patients (18/20). In addition, grade 3 generalized pain was observed in 2 patients (patients 3 and 17). These side effects were completely resolved right after the end of infusion in all cases. All patients underwent a sequential WB scintigraphy scan up to day 4. Data from 3 patients were not sufficient for dosimetry—in one (patient 7), because of a missing scan on day 1, and in two (patients 8 and 20), because there were only 2 consecutive scans. Thus, scans from 17 individuals were used for dosimetric analyses. The tumor-targeting rate on a per-patient base was 65% (13/20). In particular, 6 of 9 investigated patients with neuroblastoma showed uptake of  $^{131}\text{I}$ -GD2-ch14.18. Clinical characteristics and tumor detectability on GD2 scans are depicted in Table 1. The liver and spleen were visualized in all patients, except for one with a history of splenectomy. The urinary bladder showed pronounced radioactivity in most patients, usually on days 1 and 2. No remarkable uptake was seen in the bone marrow compartment or in the kidneys at any time point.

The blood activity concentration in 3 adults indicated nearly complete retention of  $^{131}\text{I}$ -GD2-ch14.18 in the blood compartment up to 2 h after infusion ( $0.0174\% \pm 0.0018\%$  injected activity/mL at 0.1 h after injection), followed by a decrease with an effective blood half-life of approximately 24 h (Fig. 1A). Data from a single pediatric patient (Fig. 1B) showed a higher blood activity right

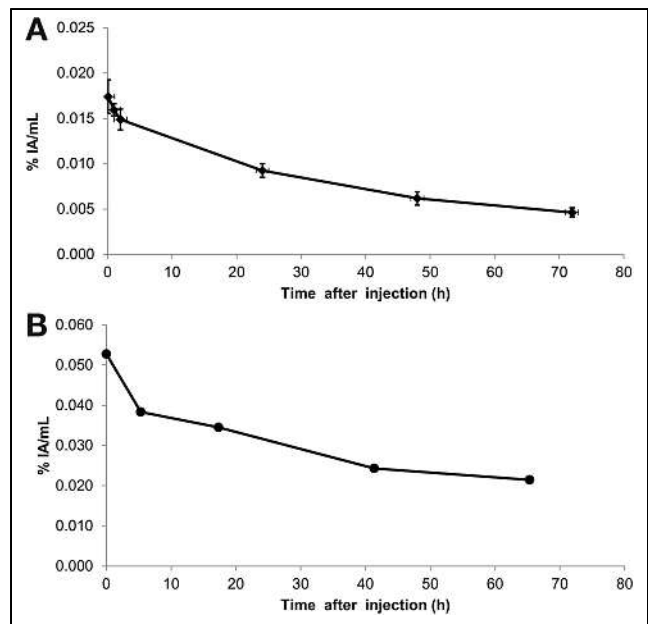


**FIGURE 1.** Normalized blood tracer concentrations at different time points (percentage injected activity [IA] of  $^{131}\text{I}$ -GD2-ch14.18 per milliliter of blood). (A) Mean  $\pm$  SD from 3 adults (patients 1–3). (B) Values from 1 pediatric patient (6-y-old boy, patient 4).

after the tracer application (0.053% injected activity/mL) and an effective blood half-life of 41 h.

A typical example of sequential planar WB scans is depicted in Figure 2. Analysis of biodistribution (Fig. 3) demonstrated that the activity of  $^{131}\text{I}$ -GD2-ch14.18 in organs peaked within the first hour and continually declined thereafter (lung,  $8.02\% \pm 1.17\%$ ; liver,  $9.33\% \pm 1.63\%$ ; spleen,  $2.07\% \pm 0.64\%$ ; and kidney,  $2.24\% \pm 0.91\%$ , at 1 h after injection, vs. lung,  $5.20\% \pm 1.24\%$ ; liver,  $5.39\% \pm 1.42\%$ ; spleen,  $1.25\% \pm 0.42\%$ ; and kidney,  $1.21\% \pm 0.61\%$ , at 24 h after injection). Tumor lesions showed uptake in 13 of 20 patients, but a sole pelvic tumor lesion in patient 16 was partly superimposed by the urinary bladder. Hence, tumor dosimetry could be performed for 12 patients.

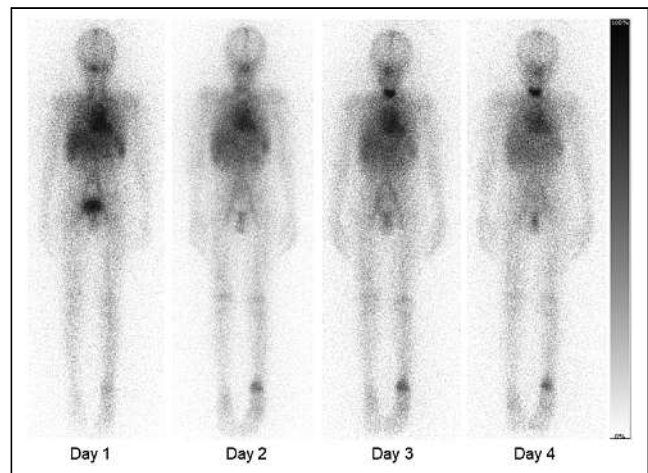


**FIGURE 2.** Sequential planar WB  $^{131}\text{I}$ -GD2-ch14.18 scans (anterior view) demonstrating increased targeting of tumor lesion in left distal tibia on days 2–4 in patient 18, with osteosarcoma.

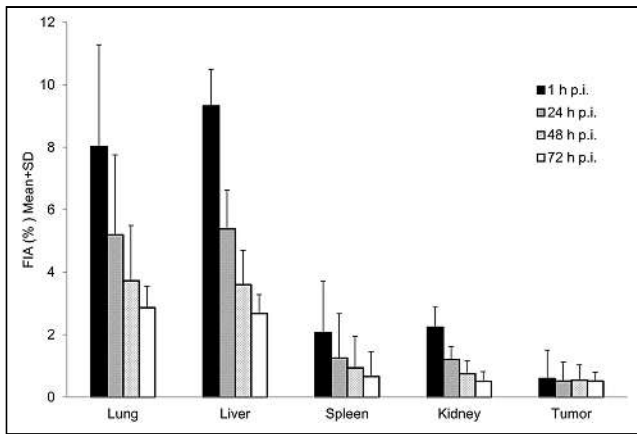


**FIGURE 3.** Biodistribution as calculated from region-of-interest analysis of planar scintigraphy ( $n = 19$ ).  $^{131}\text{I}$ -GD2-ch14.18 uptake in organ and tumor lesions is expressed as fraction of injected activity (FIA) (mean  $\pm$  SD) at different time points after injection (p.i.).

In contrast, GD2-expressing tumors showed no early peak but a more stable activity level, with maximum uptake between 1 and 3 d after injection ( $0.60\% \pm 0.85\%$  at 1 h after injection,  $0.52\% \pm 0.65\%$  at 24 h after injection,  $0.54\% \pm 0.69\%$  at 48 h after injection, and  $0.52\% \pm 0.63\%$  at 72 h after injection) (Fig. 3). Of note, the tumoral activity varied over a wide range between individuals (Fig. 4). Because of the high blood-pool activity level on early scans, tumor-to-background contrast was best on day 2 or later.

#### Dosimetry

Quantification of the absorbed radiation dose is presented in Table 2. The calculated median and mean doses to tumor lesions were 9.08 and 11.83 mGy/MBq, respectively. The ratios of median tumor-to-organ doses were 10.32 for lungs, 15.93 for liver, 7.90 for spleen, 15.93 for kidneys, and 75.67 for red bone marrow. The individual absorbed tumor dose varied over a range between 0.52

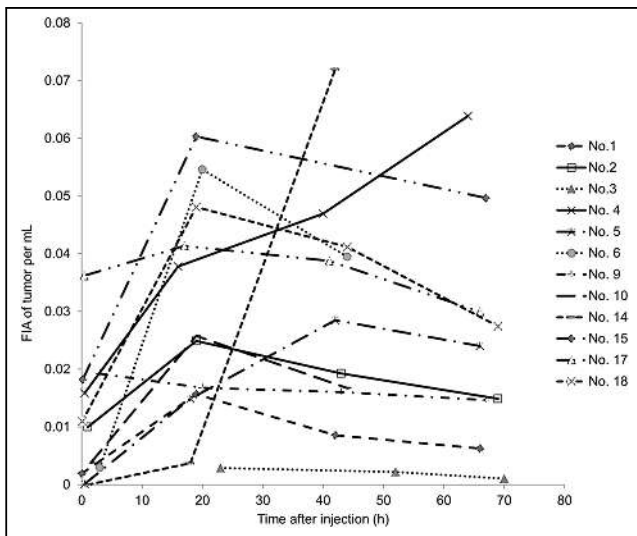


**FIGURE 4.** Time-activity curves for GD2-positive tumors (fraction of injected activity [FIA] of tumor volume per cubic centimeter). Data represent uptake of reference tumor lesions in 12 patients. Because of overlapping of tumor lesion with urinary bladder, patient 16 was excluded.

**TABLE 2**  
 $^{131}\text{I}$ -GD2-ch14.18 Absorbed Dose (mGy/MBq)

Target organ	Median	Minimum	Maximum	<i>n</i>	Mean	SD
Red marrow	0.12	0.09	0.18	4	0.12	0.03
Lung	0.88	0.29	3.31	17	1.20	0.86
Liver	0.57	0.23	1.70	17	0.70	0.41
Spleen	1.15	0.40	4.41	16	1.51	1.13
Kidney	0.57	0.19	1.89	17	0.72	0.48
Total body	0.30	0.09	1.46	17	0.41	0.34
Tumor	9.08	0.52	30.20	12	11.83	8.10
Effective dose	0.43	0.12	2.68	17	0.61	0.59

and 30.20 mGy/MBq. The noticeably highest and lowest values were both from Ewing sarcoma patients. All 6 GD2-positive neuroblastoma patients showed intense uptake, with a median tumor dose of 8.50 mGy/MBq.

#### Radioimmunotherapy

Two adult patients (patient 1, with neuroblastoma, and patient 2, with pheochromocytoma) who showed intense tumor uptake (tumor dose, 6.7 and 8.2 mGy/MBq) were selected to receive radioimmunotherapy with I-GD2-ch14.18. The bone marrow dose was calculated at 0.11 and 0.18 mGy/MBq, respectively. An activity of 2.3 and 2.9 GBq (30–40 MBq/kg) of I-GD2-ch14.18 was applied for radioimmunotherapy. Treatment was well tolerated in both cases. Both patients received posttherapeutic imaging with WB scans and additional SPECT/CT. Figure 5 depicts intense targeting of bone and liver tumor lesions in the patient with neuroblastoma on day 2 after radioimmunotherapy.

Follow-up imaging after 2 mo (CT or MRI) showed stable disease with metastases in the patient with neuroblastoma. Moderate thrombocytopenia was observed in this patient 4 wk after radioimmunotherapy and spontaneously recovered after another 4 wk. However, the patient with pheochromocytoma presented with progression of metastases in the bone, bone marrow, liver, and lung 2 mo after radioimmunotherapy. Pancytopenia with severe thrombocytopenia ( $19,000/\mu\text{L}$ ) occurred in this patient 6 wk after radioimmunotherapy. The improvement thereafter indicates that the radioimmunotherapy was the possible cause. Underlying limited hematopoiesis due to heavy pretreatment, as well as bone marrow tumor involvement, were likely cofactors. The overall survival of these patients was 17 and 6 mo from radioimmunotherapy, respectively.

#### DISCUSSION

Even though radionuclide therapies such as MIBG or peptide receptor radionuclide therapy are readily available for neuroblastoma or neuroendocrine tumor, patients with insufficient targeting or refractory disease may be candidates for GD2-directed radioimmunotherapy. Immunotherapy targeting GD2 using the chimeric antibody ch14.18 has been studied extensively, but its use as a radiolabeled compound and thus dosimetry in humans as a prerequisite for radioimmunotherapy have been lacking so far. Our results confirmed significant GD2 targeting in most tumors investigated. In particular, most patients with advanced neuroblastoma showed intense tumor uptake. These results correspond to the

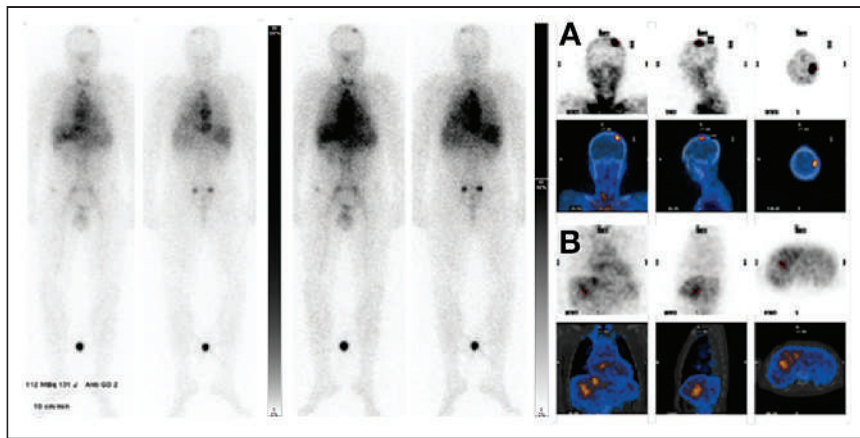


**FIGURE 5.**  $^{131}\text{I}$ -GD2-ch14.18 scan (left) with additional SPECT/CT on day 2 from application demonstrates intense targeting of bone (A) and liver (B) tumor lesions in patient 1, with neuroblastoma.

findings of Reuland et al. (22), who revealed GD2 targeting in a cohort of largely MIBG-negative neuroblastomas using the same antibody but labeled with  $^{99\text{m}}\text{Tc}$ . GD2 targeting was currently also demonstrated in 2 individuals with osteosarcoma and 3 of 6 patients with Ewing sarcomas, as is in line with the variable expression of the target antigen in these malignancies (23). Overall, our study revealed that the ch14.18 antibody retains its antigen-binding ability after labeling with  $^{131}\text{I}$ .

Serial WB scans showed a slow but continuous decline of organ and blood radioactivity, whereas GD2-positive tumor lesions demonstrated relatively stable radiotracer retention over time. This resulted in good tumor-to-background contrast from 2 d after tracer injection. Slow clearance of radioactivity from the blood is common for radiopharmaceuticals based on full-size monoclonal antibodies (24) and has in fact been observed previously with  $^{64}\text{Cu}$ -labeled GD2-ch14.18 antibody in an animal model (25,26). The prolonged blood residence of the antibody conjugate will contribute to absorbed dose in blood-bearing organs such as the liver, spleen, heart, kidneys, and bone marrow. Nevertheless, dosimetry in GD2-positive tumors revealed 10-fold higher or even better tumor-to-organ dose ratios—that is, therapeutic indices—thus meeting published criteria for radioimmunotherapy (12).

Despite premedication, mild to moderate antigen reactions were observed under infusion of I-GD2-ch14.18 in most of our patients, whereas 2 individuals additionally experienced diffuse pain. Such antigen toxicity is well known from therapeutic application of nonradioactive GD2-targeting antibodies (27) and has been shown to be dose-dependent (28). However, the amount of antibody injected for scintigraphy (maximum, 1 mg) was less than 10% of the approved dose in nonradioactive immunotherapy with dinutuximab.

Our study had some limitations. Only planar scintigraphy was available for sequential imaging, and SPECT/CT was added in only selected cases, aiming to better delineate tumor sites. As a result, dose estimations are based on planar scans alone and have to be considered merely semiquantitative, as the combined uncertainties are considered a factor of 2 or even greater (29). Moreover, overlap of lesions and blood pool or organs may prevent precise identification of tumor lesions. A dual integral formula was used to estimate tumor TIAC. Because effective half-life after the last measured time point was

unknown, physical decay was used for the second integral. As a result, the true tumor-absorbed dose might be considerably lower. Obviously, an elaborate dosimetry will be needed for volume-of-interest analyses using quantitative SPECT/CT (30) or PET/CT (25). Serial blood samples were available for only 4 of 20 patients; thus, analyses of  $^{131}\text{I}$ -GD2-ch14.18 blood kinetics and red marrow dose are to be regarded as preliminary. Finally, because of the small number of patients in this retrospective analysis, tumor targeting and, especially, the safety and efficacy of  $^{131}\text{I}$ -GD2-ch14.18 radioimmunotherapy will have to be further evaluated in prospective studies.

## CONCLUSION

Sequential scintigraphy demonstrated slow clearance of  $^{131}\text{I}$ -GD2-ch14.18 from blood, resulting in favorable tumor-to-background contrast from 2 d after application. With an acceptable red marrow dose, radioimmunotherapy may be considered an option for patients with high tumor uptake. Because of the variable GD2 expression, pretherapeutic imaging and dosimetry are recommended. Development of GD2-targeting fragments might accelerate blood clearance and may improve radioimmunotherapy in the future.

## DISCLOSURE

This work was funded by the Deutsche Forschungsgemeinschaft (DFG, German Research Foundation) under Germany's Excellence Strategy (EXC 2180-390900677). No other potential conflict of interest relevant to this article was reported.

## KEY POINTS

**QUESTION:** What are the tumor targeting and biodistribution of  $^{131}\text{I}$ -GD2-ch14.18 in patients with late-stage disease who are potentially eligible for radioimmunotherapy?

**PERTINENT FINDINGS:** In this retrospective study, sequential scintigraphy demonstrated a favorable tumor-to-background contrast for  $^{131}\text{I}$ -GD2-ch14.18 from 2 d after application. Moreover, dosimetry in planar scintigraphy in GD2-positive tumors revealed up to 10-fold higher tumor-to-organ dose ratios—that is, therapeutic indices.

**IMPLICATIONS FOR PATIENT CARE:** With an acceptable red marrow dose, radioimmunotherapy may be an option for patients with high tumor uptake. Because of the variable GD2 expression, pretherapeutic imaging and dosimetry are recommended.

## REFERENCES

- Mujoo K, Cheresch DA, Yang HM, Reisfeld RA. Disialoganglioside GD2 on human neuroblastoma cells: target antigen for monoclonal antibody-mediated cytotoxicity and suppression of tumor growth. *Cancer Res.* 1987;47:1098–1104.
- Schulz G, Cheresch DA, Varki NM, Yu A, Staffileno LK, Reisfeld RA. Detection of ganglioside GD2 in tumor tissues and sera of neuroblastoma patients. *Cancer Res.* 1984;44:5914–5920.
- Svennerholm L, Bostrom K, Fredman P, et al. Gangliosides and allied glycosphingolipids in human peripheral nerve and spinal cord. *Biochim Biophys Acta.* 1994; 1214:115–123.

4. Chang HR, Cordon-Cardo C, Houghton AN, Cheung NK, Brennan MF. Expression of disialogangliosides GD2 and GD3 on human soft tissue sarcomas. *Cancer*. 1992;70:633–638.
5. Navid F, Santana VM, Barfield RC. Anti-GD2 antibody therapy for GD2-expressing tumors. *Curr Cancer Drug Targets*. 2010;10:200–209.
6. Ploessl C, Pan A, Maples KT, Lowe DK. Dinutuximab: an anti-GD2 monoclonal antibody for high-risk neuroblastoma. *Ann Pharmacother*. 2016;50:416–422.
7. Ladenstein R, Potschger U, Valteau-Couanet D, et al. Interleukin 2 with anti-GD2 antibody ch14.18/CHO (dinutuximab beta) in patients with high-risk neuroblastoma (HR-NBL1/SIOPEN): a multicentre, randomised, phase 3 trial. *Lancet Oncol*. 2018;19:1617–1629.
8. Yu AL, Gilman AL, Ozkaynak MF, et al. Anti-GD2 antibody with GM-CSF, interleukin-2, and isotretinoin for neuroblastoma. *N Engl J Med*. 2010;363:1324–1334.
9. Dinutuximab approved for high-risk neuroblastoma. *Cancer Discov*. 2015;5:OF5.
10. Ehlert K, Hansjuergens I, Zinke A, et al. Nivolumab and dinutuximab beta in two patients with refractory neuroblastoma. *J Immunother Cancer*. 2020;8:e00540.
11. Gohil K. Pharmaceutical approval update. *P&T*. 2015;40:327–360.
12. Larson SM, Carrasquillo JA, Cheung NK, Press OW. Radioimmunotherapy of human tumours. *Nat Rev Cancer*. 2015;15:347–360.
13. Kaminski MS, Zelenetz AD, Press OW, et al. Pivotal study of iodine I 131 tositumomab for chemotherapy-refractory low-grade or transformed low-grade B-cell non-Hodgkin's lymphomas. *J Clin Oncol*. 2001;19:3918–3928.
14. Witzig TE, Gordon LI, Cabanillas F, et al. Randomized controlled trial of yttrium-90-labeled ibritumomab tiuxetan radioimmunotherapy versus rituximab immunotherapy for patients with relapsed or refractory low-grade, follicular, or transformed B-cell non-Hodgkin's lymphoma. *J Clin Oncol*. 2002;20:2453–2463.
15. Cheung NK, Kushner BH, LaQuaglia M, et al. N7: a novel multi-modality therapy of high risk neuroblastoma (NB) in children diagnosed over 1 year of age. *Med Pediatr Oncol*. 2001;36:227–230.
16. Cheung NK, Cheung IY, Kushner BH, et al. Murine anti-GD2 monoclonal antibody 3F8 combined with granulocyte-macrophage colony-stimulating factor and 13-cis-retinoic acid in high-risk patients with stage 4 neuroblastoma in first remission. *J Clin Oncol*. 2012;30:3264–3270.
17. Maxon HR, Thomas SR, Hertzberg VS, et al. Relation between effective radiation dose and outcome of radioiodine therapy for thyroid cancer. *N Engl J Med*. 1983;309:937–941.
18. Press OW, Eary JF, Appelbaum FR, et al. Radiolabeled-antibody therapy of B-cell lymphoma with autologous bone marrow support. *N Engl J Med*. 1993;329:1219–1224.
19. Ozkaynak MF, Gilman AL, London WB, et al. A comprehensive safety trial of chimeric antibody 14.18 with GM-CSF, IL-2, and isotretinoin in high-risk neuroblastoma patients following myeloablative therapy: Children's Oncology Group study ANBL0931. *Front Immunol*. 2018;9:1355.
20. Stabin MG, Siegel JA, Sparks RB. Sensitivity of model-based calculations of red marrow dosimetry to changes in patient-specific parameters. *Cancer Biother Radiopharm*. 2002;17:535–543.
21. Woodard HQ. The relation of weight of haematopoietic marrow to body weight. *Br J Radiol*. 1984;57:903–907.
22. Reuland P, Geiger L, Thelen MH, et al. Follow-up in neuroblastoma: comparison of metaiodobenzylguanidine and a chimeric anti-GD2 antibody for detection of tumor relapse and therapy response. *J Pediatr Hematol Oncol*. 2001;23:437–442.
23. Dobrenkov K, Ostrovskaya I, Gu J, Cheung IY, Cheung NK. Oncotargets GD2 and GD3 are highly expressed in sarcomas of children, adolescents, and young adults. *Pediatr Blood Cancer*. 2016;63:1780–1785.
24. Lewis MR, Wang M, Axworthy DB, et al. In vivo evaluation of pretargeted <sup>64</sup>Cu for tumor imaging and therapy. *J Nucl Med*. 2003;44:1284–1292.
25. Dearling JL, Voss SD, Dunning P, et al. Imaging cancer using PET: the effect of the bifunctional chelator on the biodistribution of a <sup>64</sup>Cu-labeled antibody. *Nucl Med Biol*. 2011;38:29–38.
26. Maier FC, Schmitt J, Maurer A, et al. Correlation between positron emission tomography and Cerenkov luminescence imaging in vivo and ex vivo using <sup>64</sup>Cu-labeled antibodies in a neuroblastoma mouse model. *Oncotarget*. 2016;7:67403–67411.
27. Dobrenkov K, Cheung NK. GD2-targeted immunotherapy and radioimmunotherapy. *Semin Oncol*. 2014;41:589–612.
28. Cheung NK, Kushner BH, Cheung IY, et al. Anti-G(D2) antibody treatment of minimal residual stage 4 neuroblastoma diagnosed at more than 1 year of age. *J Clin Oncol*. 1998;16:3053–3060.
29. Stabin MG. Uncertainties in internal dose calculations for radiopharmaceuticals. *J Nucl Med*. 2008;49:853–860.
30. Cheal SM, Xu H, Guo HF, et al. Theranostic pretargeted radioimmunotherapy of internalizing solid tumor antigens in human tumor xenografts in mice: curative treatment of HER2-positive breast carcinoma. *Theranostics*. 2018;8:5106–5125.

---

---

# Detecting Fibroblast Activation Proteins in Lymphoma Using $^{68}\text{Ga}$ -FAPI PET/CT

Xiao Jin<sup>\*1</sup>, Maomao Wei<sup>\*1</sup>, Shuailiang Wang<sup>\*1</sup>, Guochang Wang<sup>\*1</sup>, Yumei Lai<sup>2</sup>, Yunfei Shi<sup>2</sup>, Yan Zhang<sup>1</sup>, Zhi Yang<sup>1</sup>, and Xuejuan Wang<sup>1</sup>

<sup>1</sup>Key Laboratory of Carcinogenesis and Translational Research (Ministry of Education) and NMPA Key Laboratory for Research and Evaluation of Radiopharmaceuticals (National Medical Products Administration), Department of Nuclear Medicine, Peking University Cancer Hospital and Institute, Beijing, China; and <sup>2</sup>Department of Pathology, Peking University Cancer Hospital and Institute, Beijing, China

---

Cancer-associated fibroblasts that overexpress fibroblast activation protein (FAP) are enriched in many epithelial carcinomas and in hematologic neoplasms. PET/CT with radiolabeled FAP inhibitor (FAPI) is a new diagnostic tool for visualizing the tumor stroma. This prospective study aimed to profile FAPs in different subtypes of lymphomas and explore the potential utility of  $^{68}\text{Ga}$ -FAPI PET/CT in lymphomas.

**Methods:** In this prospective study, we recruited 73 lymphoma patients who underwent  $^{68}\text{Ga}$ -FAPI PET/CT and recorded and measured semiquantitative parameters and ratios of their scan results. FAPI expression was assessed by immunochemistry in samples obtained from 22 of the lymphoma patients. **Results:** We evaluated 11 patients with Hodgkin lymphoma and 62 with non-Hodgkin lymphoma (NHL). Significantly elevated FAP uptake was observed in Hodgkin lymphoma lesions, correlating with the intensity of FAP immunostaining (score, 3+). A positive association was found between the corresponding clinical classification of NHL and the  $^{68}\text{Ga}$ -FAPI uptake activity of the lesion. Aggressive NHL lesions, with moderate to strong FAP immunostaining (score, 2+ to 3+), exhibited intense to moderate  $^{68}\text{Ga}$ -FAPI uptake. Indolent NHL lesions showed weak FAP staining and mild to moderate  $^{68}\text{Ga}$ -FAPI uptake. No statistically significant correlation emerged between the sum of the product of the diameters and the corresponding  $\text{SUV}_{\text{max}}$  ( $P = 0.424$ ). The tumor-to-liver ratios were  $6.26 \pm 4.17$  in indolent NHL and more than 9 in other subtypes. **Conclusion:**  $^{68}\text{Ga}$ -FAPI imaging can be used to detect FAP expression in lymphoma lesions and may be an alternate method for characterizing lymphoma profiles.

**Key Words:**  $^{68}\text{Ga}$ -FAPI PET; lymphoma; cancer-associated fibroblasts; fibroblast activation protein; tumor stroma

**J Nucl Med 2022; 63:212–217**  
DOI: 10.2967/jnumed.121.262134

---

**L**ymphomas are a heterogeneous group of malignancies arising from lymphocytes and typically involve lymphoid organs. They account for approximately 3.5% of new malignant cases worldwide, with B-cell lymphomas (BCLs) and Hodgkin lymphoma (HL) accounting for 80% and 10% of all lymphoma cases,

respectively. Lymphoma pathogenesis is well understood, and there is increasing focus on nonmalignant cells residing in the tumor, primarily immune and stromal cells, which constitute the so-called tumor microenvironment (1).

Recent studies have suggested that the outcome of patients with lymphoma is entwined with the remarkable heterogeneity of both the malignant clone and the cellular/extracellular microenvironment and unveiled fibroblasts in the microenvironment that might exhibit both a protumorigenic and an antitumorigenic phenotype (2,3). A stromal gene signature representing fibroblasts has been shown to correlate with poor survival in carcinomas, including breast, ovarian, pancreatic, and colorectal cancer. Paradoxically, a closely related gene signature has been associated with good survival in BCLs (4,5). This contradictory result has generated lots of interest and effort in elucidating fibroblast-mediated effects. Even though these studies indicated that stromal signatures of BCLs could predict survival, they were clinically restrained by the lack of robust and reproducible biomarkers (6,7). Additionally, to support histopathologic and genic evidence, the tumor stroma needs to be visualized and monitored, and imaging is an essential aspect of the diagnostic workup.

Nonhematopoietic (CD45-negative) tumor stroma in lymphoid tissues comprise cells of mesenchymal origin and vascular endothelial cells (8). Cancer-associated fibroblasts (CAFs) belong to the CD45-negative-reprogrammed myelofibroblastic network and play a crucial role in the development and progression of solid tumors (9). CAFs and activated fibroblasts selectively overexpress a growth factor, fibroblast activation protein (FAP). Molecular PET/CT imaging with radiolabeled FAP inhibitor (FAPI) has been evaluated in various diseases but not in lymphoma (10,11). Recently, we incidentally found a mild  $^{68}\text{Ga}$ -FAPI uptake in a primary gastric diffuse large BCL (DLBCL) lesion. Thus, we hypothesize that CAFs in lymphoma can be imaged using  $^{68}\text{Ga}$ -FAPI PET/CT (12).

The aim of this prospective study was to identify FAPs with  $^{68}\text{Ga}$ -FAPI-04 PET/CT in different subtypes of lymphomas (especially T-cell lymphoma), quantify  $^{68}\text{Ga}$ -FAPI-04 accumulations in nodal and extranodal lesions, and explore the potential utility of  $^{68}\text{Ga}$ -FAPI-04 PET/CT in lymphomas.

## MATERIALS AND METHODS

### Patients

This prospective study was approved by the Institutional Review Board of our hospital (approval 2019KT95) and registered with ClinicalTrials.gov (NCT04367948). Written informed consent was obtained from the patients for receiving  $^{68}\text{Ga}$ -FAPI PET/CT examinations and

---

Received Feb. 15, 2021; revision accepted Apr. 21, 2021.  
For correspondence or reprints, contact Xuejuan Wang (xuejuan\_wang@hotmail.com).

\*Contributed equally to this work.

Published online May 28, 2021.

COPYRIGHT © 2022 by the Society of Nuclear Medicine and Molecular Imaging.

the publication of their anonymous data accompanying the imaging results. Study enrollment was performed from December 2019 to August 2020. The patient inclusion criteria were a pathologic diagnosis of lymphoma, an age of 18–75 y, expected survival of at least 12 wk, and a minimum of 1 target lesion with <sup>68</sup>Ga-FAPI uptake. The exclusion criteria were severe liver or kidney dysfunction, pregnancy or lactation, inability of the patient to lie on the scanner bed for less than 0.5 h, and inability or unwillingness of the patient or legal representative to provide written informed consent. The final study cohort comprised 73 patients with lymphoma. The study flowchart of patient enrollment is presented as Supplemental Figure 1 (supplemental materials are available at <http://jnm.snmjournals.org>).

### Radiopharmaceuticals

Synthesis and radiolabeling of <sup>68</sup>Ga-FAPI-04 were performed as previously described. Briefly, <sup>68</sup>Ga was chelated after pH adjustment with sodium acetate. Then, a reaction mixture of 25 µg (28.6 nmol) of FAPI-04 and 1.7 GBq of <sup>68</sup>Ga solution was heated to 100°C for 10 min. Next, the reaction solution was diluted to 5 mL and passed through a preconditioned Sep-Pak C18 Plus Light Cartridge (Waters), and the cartridge was eluted with 0.5 mL of 75% ethanol to obtain the final product. Quality control of the radiosynthesis was performed by ultraviolet and radio-high-performance liquid chromatography, and the radiochemical purity was more than 95%. The <sup>68</sup>Ga-FAPI injections were filtered through a 0.22-µm Millex-LG filter (EMD Millipore) before clinical use.

### PET/CT Imaging

The radiopharmaceutical was administered intravenously at a dose of 1.8–2.2 MBq/kg. At approximately 60 ± 10 min after injection, a torso acquisition (*n* = 52) of 6–8 bed positions (1 min/bed position) commenced using a hybrid system (Philips Gemini TF PET/CT scanner) that covered from the base of the skull to the upper thigh. Non-contrast-enhanced CT was performed using 100-mA modulation, 120 kV, and a slice thickness of 3 mm for attenuation correction and anatomic localization purposes. The dedicated head acquisition was separately performed at 1 bed position (8–10 min/bed position). Acquisitions from the top of the skull to the upper thigh or the tip of the toes were performed on the remaining 21 patients. The emission data were corrected for random, scatter, and decay. The data were reconstructed using the ordered-subset expectation maximum algorithm to obtain coronal, sagittal, and cross-sectional PET and PET/CT images. The total scan time was approximately 19 min. The patients were asked to self-report any abnormalities at 30 min after the PET/CT scans.

### Image Interpretation

Three experienced nuclear physicians were assigned to independently interpret each patient's PET images with knowledge of the clinicopathologic data on a Philips EBW workstation. The presence and sites of lymphoma involvement and the intensity of the <sup>68</sup>Ga-FAPI uptake in the lesions were recorded for each PET scan. Increased radioactivity compared with the background uptake was considered positive and was measured and calculated via the region-of-interest technique. Any discordant results were resolved by consensus. Up to 6 of the largest or highest SUV<sub>max</sub> lymphoma lesions were identified from different body regions for each PET/CT scan. The product of the diameters was calculated by multiplying the longest diameter by the shortest diameter for each lesion. Then, the products of the diameters were added to assess the sum of products of the diameters (SPD), which was representative of the patient's overall disease burden. The nonspecific background in the liver was quantified with a circular 2-cm-diameter sphere, and the tumor-to-liver ratio was calculated.

### Immunohistochemistry

FAP expression in lymphoma lesions was determined using post-surgical histology samples from 7 patients and biopsy samples from

**TABLE 1**  
Clinical Features of 73 Patients with Lymphoma

Parameters	No. of patients
<b>Sex</b>	
Male	37 (50.68%)
Female	36 (49.32%)
<b>Age</b>	
>60 y	26 (35.62%)
≤60 y	47 (64.38%)
<b>Treatment type</b>	
Initial assessment	48 (65.75%)
Progressed	17 (23.29%)
Relapsed	8 (10.96%)
<b>Lesion distribution</b>	
Nodal only	15 (20.55%)
Extranodal, primary	19 (26.03%)
Both	39 (53.42%)
<b>Histologic subtype</b>	
HL	11 (15.07%)
NHL	62 (84.93%)
DLBCL	34 (46.57%)
ENKTCL	5 (6.85%)
AITL	4 (5.48%)
PMBL	2 (2.74%)
BL	1 (1.37%)
MCL	1 (1.37%)
B-LBL	1 (1.37%)
C-ALCL	1 (1.37%)
CD8 <sup>+</sup> AECTCL	1 (1.37%)
FL	9 (12.33%)
MALT lymphoma	2 (2.74%)
CLL/SLL	1 (1.37%)

ENKTCL = extranodal natural killer/T-cell lymphoma; AITL = angioimmunoblastic T-cell lymphoma; PMBL = primary mediastinal large BCL; BL = Burkitt lymphoma; MCL = mantle cell lymphoma; B-LBL = B lymphoblastic leukemia/lymphoma; C-ALCL = primary cutaneous anaplastic large-cell lymphoma; CD8<sup>+</sup> AECTCL = cutaneous CD8-positive aggressive epidermotropic cytotoxic T-cell lymphoma; FL = follicular lymphoma; CLL/SLL = chronic lymphocytic leukemia/small lymphocytic lymphoma.

15 patients via immunohistochemistry performed as per a previous report. Before immunohistochemistry staining, the tissue sections were stained with hematoxylin and eosin and reviewed by 2 experienced pathologists. FAP was detected using a rabbit monoclonal antibody against FAP (BM5121; Boster). Briefly, formalin-fixed, paraffin-embedded blocks were cut into 4-µm-thick sections, deparaffinized in xylene, and rehydrated. Antigen was retrieved using ethylenediaminetetraacetic acid (pH 8.0; Santa Cruz Biotechnology) in a pressure cooker for 3 min. Then, the sections were incubated in 3% H<sub>2</sub>O<sub>2</sub> solution for 10 min at room temperature to block endogenous peroxidase activity. Immunohistochemistry was performed with anti-FAP antibody at a dilution of 1:400 for 12 h at 4°C. Subsequently,

**TABLE 2**  
SUV<sub>max</sub> of Nodal and Extranodal Lymphoma Lesions

Lymphoma group	Histology	Patients (n)	Nodal			Extranodal			P
			Average	Median	Range	Average	Median	Range	
Initial	HL	6	11.78 ± 4.03	11.8	7.3–18.1	7.20 ± 2.55	7.2	5.4–9.0	0.18
	DLBCL	22	8.52 ± 4.57	8.4	2.3–20.2	10.14 ± 4.33	10.9	3.7–17.1	0.08
	ENKTCL	3	5.40 ± 3.14	6.8	1.8–7.6	7.93 ± 1.12	8.2	6.7–8.9	0.29
	AITL	3	6.57 ± 2.40	6	4.5–9.2	2.4	2.4	NA	NA
	PMBL	2	18.40 ± 6.01	20.2	11.7–23.3	NA	NA	NA	NA
	BL	1	NA	NA	NA	19.1	19.1	NA	NA
	B-LBL	1	2.3	2.3	NA	6.5	6.5	NA	NA
	MCL	1	NA	NA	NA	5.1	5.1	NA	NA
	FL	7	5.60 ± 2.71	5.4	1.7–9.8	7.95 ± 3.68	8.05	4.2–11.5	0.47
	MALT lymphoma	1	NA	NA	NA	1.8	1.8	NA	NA
CLL/SLL	1	5.9	5.9	NA	4.5	4.5	NA	NA	
Total		48	8.35 ± 4.87	7.6	1.7–23.3	8.92 ± 6.08	8.2	1.8–19.1	0.11
Progressed	HL	3	9.63 ± 4.05	8.6	6.2–14.1	5.90 ± 5.44	3.7	1.9–12.1	0.29
	DLBCL	8	7.87 ± 1.89	8.7	4.3–9.7	9.40 ± 6.40	6.8	2.8–21.0	0.36
	CD8+ AECTCL	1	NA	NA	NA	8.4	8.4	NA	NA
	ENKTCL	1	NA	NA	NA	7.5	7.5	NA	NA
	AITL	1	4.9	4.9	NA	NA	NA	NA	NA
	MALT	1	4.9	4.9	NA	5.6	5.6	NA	NA
	FL	2	5.5	5.5	4.3–6.7	12.3	12.3	NA	NA
Total		17	7.49 ± 2.68	7.05	4.3–14.1	8.38 ± 5.23	7.15	1.9–21.0	0.60
Relapsed	HL	2	7.45 ± 3.75	7.45	4.8–10.1	6.75 ± 2.62	6.75	4.9–8.6	NA
	DLBCL	4	5.67 ± 5.23	3.7	1.7–11.6	7.63 ± 3.68	6.65	4.4–12.8	0.96
	ENKTCL	1	NA	NA	NA	8.7	8.7	NA	NA
	C-ALCL	1	NA	NA	NA	5.2	5.2	NA	NA
	Total		8	6.38 ± 4.26	4.8	1.7–11.6	7.24 ± 2.80	6.65	4.4–12.8

ENKTCL = extranodal natural killer/T-cell lymphoma; AITL = angioimmunoblastic T-cell lymphoma; NA = not applicable; PMBL = primary mediastinal large BCL; BL = Burkitt lymphoma; B-LBL = B lymphoblastic leukemia/lymphoma; MCL = mantle cell lymphoma; FL = follicular lymphoma; CLL/SLL = chronic lymphocytic leukemia/small lymphocytic lymphoma; CD8<sup>+</sup> AECTCL = cutaneous CD8-positive aggressive epidermotropic cytotoxic T-cell lymphoma; C-ALCL = primary cutaneous anaplastic large-cell lymphoma.

antirabbit IgG-horseradish peroxidase-linked secondary antibody was applied for 30 min at 37°C. Then, the sections were developed with 3,3'-diaminobenzidine tetrahydrochloride. Mayer hematoxylin was applied for 5 min as a counterstain. Photographs of representative fields were taken using an N-Achroplan objective (Zeiss). The FAP expression was assessed visually and quantitatively. Stromal cell staining was scored as 0 (absence of FAP immunostaining), 1+ (weak FAP staining in <10% of stromal cells), 2+ (positive FAP immunostaining in 10%–50% of stromal cells), and 3+ (moderate to strong FAP immunostaining in >50% of stromal cells) (13).

#### Statistical Analysis

All statistical analyses were conducted using SPSS software (version 20.0; IBM Corp.). SUVs were presented as the mean ± SD. The Kolmogorov–Smirnov test was used to determine whether the data were normally distributed. Comparisons between the average SUV<sub>max</sub> were made using the *t* test or Mann–Whitney *U* test. The correlation between SUV<sub>max</sub> and histologic subtypes was evaluated by the

Pearson correlation coefficient. A *P* value of less than 0.05 was considered statistically significant.

## RESULTS

### Patient Characteristics

We enrolled 73 patients (36 women and 37 men; age, 51.6 ± 14.2 y; range, 21–74 y) in our study. Of them, 48 had newly diagnosed lymphoma, 17 had progressive disease, and 8 had relapses. Non-Hodgkin lymphoma (NHL; *n* = 62, 84.93%) was the most prevalent pathologic subtype, including DLBCL (*n* = 34, 46.57%), follicular lymphoma (*n* = 9, 12.33%), extranodal natural killer/T-cell lymphoma (*n* = 5, 6.85%), angioimmunoblastic T-cell lymphoma (*n* = 4, 5.48%), primary mediastinal large BCL (*n* = 2, 2.74%), and mucosa-associated lymphoid tissue (MALT) lymphoma (*n* = 2, 2.74%). The other enrolled subtypes had 1 case each. Fifteen cases (20.55%) involved only lymph nodes, and 19 (26.02%) were primary extranodal lymphomas (Table 1).

**TABLE 3**  
Size and SPD of Lymphoma Lesions

Histologic subtype	Patients (n)	Node size (cm)			SPD		
		Median	Average	Range	Median	Average	Range
HL	11	10.07	14.14 ± 13.22	2.53–47.23	27.13	41.44 ± 32.10	8.28–95.00
DLBCL	34	7.88	9.93 ± 12.12	3.55–58.83	35.43	43.51 ± 47.78	11.99–229.49
ENKTCL	5	2.53	2.29 ± 0.81	1.39–2.95	10.55	14.12 ± 7.86	7.09–24.47
AITL	4	4.60	4.58 ± 1.69	2.56–6.58	26.55	25.76 ± 18.36	2.56–47.36
PMBL	2	7.99	9.06 ± 4.99	3.55–19.35	39.61	38.02 ± 17.45	15.49–67.02
BL	1	NA	NA	NA	18.18	18.18	18.18
MCL	1	NA	NA	NA	15.89	15.89	15.89
B-LBL	1	2.71	2.71	2.71	43.03	43.03	43.03
C-ALCL	1	NA	NA	NA	2.10	2.10	2.10
CD8 <sup>+</sup> AECTCL	1	NA	NA	NA	8.96	8.96	8.96
FL	9	5.40	8.23 ± 8.49	2.78–39.99	31.35	31.89 ± 18.40	5.56–70.88
MALT lymphoma	2	2.17	2.17	2.17	3.22	3.22 ± 1.57	2.11–4.33
CLL/SLL	1	8.84	8.84	8.84	32.6	32.6	32.6

ENKTCL = extranodal natural killer/T-cell lymphoma; AITL = angioimmunoblastic T-cell lymphoma; PMBL = primary mediastinal large BCL; BL = Burkitt lymphoma; NA = not applicable; MCL = mantle cell lymphoma; B-LBL = B lymphoblastic leukemia/lymphoma; C-ALCL = primary cutaneous anaplastic large-cell lymphoma; CD8<sup>+</sup> AECTCL = cutaneous CD8-positive aggressive epidermotropic cytotoxic T-cell lymphoma; FL = follicular lymphoma; CLL/SLL = chronic lymphocytic leukemia/small lymphocytic lymphoma.

#### Quantifying <sup>68</sup>Ga-FAPI-04 Uptake in Lymphoma Lesions

The <sup>68</sup>Ga-FAPI-04 PET/CT scans were visually positive for detecting lymphoma in 72 of 73 (98.6%) patients because of the low background, except a patient with primary gastric MALT lymphoma. The average SUV<sub>max</sub>, median SUV<sub>max</sub>, and SUV<sub>max</sub> range of the lymphoma lesions were 9.46 ± 4.61, 8.9, and 1.7–23.3, respectively. The average SUV<sub>max</sub> of the initial assessment,

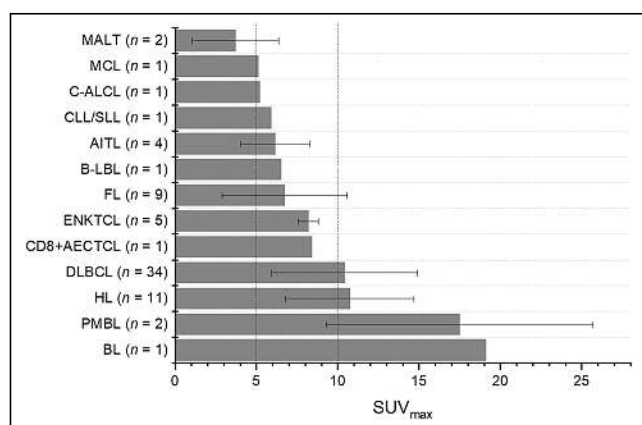


**FIGURE 1.** Average SUV<sub>max</sub> of <sup>68</sup>Ga-FAPI PET/CT in various histologic subtypes. MCL = mantle cell lymphoma; C-ALCL = primary cutaneous anaplastic large-cell lymphoma; CLL/SLL = chronic lymphocytic leukemia/small lymphocytic lymphoma; AITL = angioimmunoblastic T-cell lymphoma; B-LBL = B lymphoblastic leukemia/lymphoma; FL = follicular lymphoma; ENKTCL = extranodal natural killer/T-cell lymphoma; CD8+AECTCL = cutaneous CD8-positive aggressive epidermotropic cytotoxic T-cell lymphoma; PMBL = primary mediastinal large BCL; BL = Burkitt lymphoma.

progressed, and relapsed groups was 9.74 ± 4.88, 9.37 ± 5.03, and 8.35 ± 2.57, respectively ( $P = 0.769$ ). The overall SUV<sub>max</sub> (7.98 ± 4.39 vs. 8.49 ± 4.45), median SUV<sub>max</sub> (7.3 vs. 7.5) and SUV<sub>max</sub> range (1.7–23.0 vs. 1.8–21.0) of <sup>68</sup>Ga-FAPI in nodal and extranodal lesions did not differ ( $P > 0.05$ ). Similar results were found in various histologic subtypes ( $P > 0.05$ ) (Table 2).

The lymph node sizes and SPDs in different histologic subtypes are shown in Table 3. The mean SPD, median SPD, and SPD range of lymphoma lesions were 34.22 ± 34.46, 25.54, and 2.10–229.49, respectively. No statistically significant correlation emerged between the SPD and corresponding SUV<sub>max</sub> ( $r = 0.107$ ,  $P = 0.424$ ).

All tumor entities exhibited a high interindividual and intraleisional SUV variation (Fig. 1). The highest average SUV<sub>max</sub> (>10) was found in primary mediastinal large BCL, Burkitt lymphoma, HL, and DLBCL. The lowest <sup>68</sup>Ga-FAPI intensity (average SUV<sub>max</sub> < 5) was observed in MALT lymphoma. Other subtypes showed moderate <sup>68</sup>Ga-FAPI uptake (average SUV<sub>max</sub>, 5–10). No statistically significant difference was found between the SUV<sub>max</sub> of HL (10.74 ± 3.95) and NHL (9.23 ± 4.71) ( $P = 0.323$ ). SUV<sub>max</sub> was significantly higher for BCLs (9.97 ± 4.68) than for T-cell lymphomas (7.19 ± 1.73) ( $P = 0.002$ ). Figure 2 exhibits various extranodal sites in the enrolled patients.

According to the clinical classification for NHL, the average SUV<sub>max</sub> of <sup>68</sup>Ga-FAPI in aggressive ( $n = 50$ ) lymphoma was significantly higher than in indolent ( $n = 12$ ) lesions (9.97 ± 4.68 vs. 6.16 ± 3.57;  $P = 0.008$ ). Correlation analysis revealed a moderate correlation between the clinical classification and SUV<sub>max</sub> ( $r = 0.338$ ,  $P = 0.007$ ). Because of the low background activity (average SUV<sub>mean</sub> of liver, 1.11 ± 0.36), the tumor-to-liver ratios were 9.89 ± 6.08, 10.03 ± 5.12, and 6.26 ± 4.17 in HL, aggressive NHL, and indolent NHL, respectively.

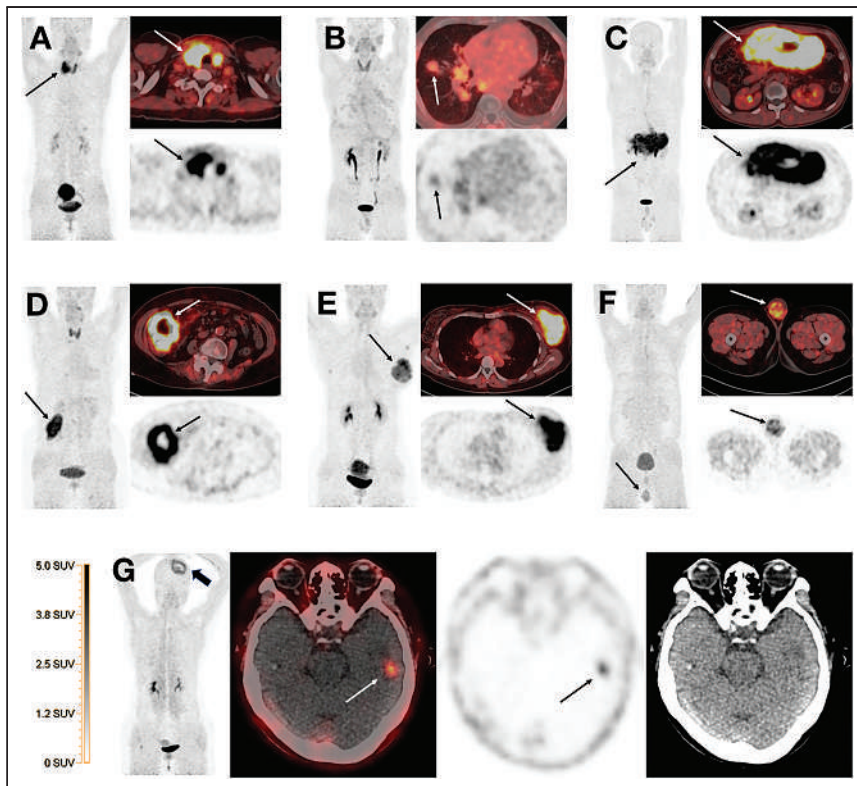


**FIGURE 2.** Maximum-intensity projections, axial  $^{68}\text{Ga}$ -FAPI PET, and fused images (left, top right, and bottom right, respectively, in each panel) of various extranodal sites in enrolled patients. (A) Primary thyroid Burkitt lymphoma (arrows). (B) HL with lung involvement (arrows). (C) Primary gastric DLBCL (arrows). (D) Ileum DLBCL (arrows). (E) Left breast DLBCL (arrows). (F) Left testicle DLBCL (arrows). (G) Left temporal lobe DLBCL lesion (thin arrows) after left frontal lymphoma resection (thick arrow).

### Immunohistochemistry

To further characterize FAP as a target structure within lymphoma, we performed FAP immunohistochemistry in 22 of the included cases. There were 4 patients with HL and 18 patients with NHL (9 DLBCL, 2 extranodal natural killer/T-cell lymphoma, 1 angioimmunoblastic T-cell lymphoma, 1 mantle cell lymphoma, 3 follicular lymphoma, 1 MALT lymphoma, and 1 chronic lymphocytic leukemia/small lymphocytic lymphoma).

The pathologic examinations showed intense FAP expression (score, 3+) in all HL lesions (4/4). For NHL, 7 of 12 aggressive lesions scored 3+ for FAP immunostaining, 4 of 5 indolent lesions showed weak FAP expression (score, 1+), and 5 of 9 DLBCL lesions overexpressed FAP (score, 3+). Weak FAP expression (score, 1+) was detected in MALT lymphoma lesions. Surprisingly, chronic lymphocytic leukemia/small lymphocytic lymphoma lesions showed moderate FAP expression (score, 2+). Furthermore, lesions with intense FAP expression exhibited an higher  $\text{SUV}_{\text{max}}$  than lesions that scored 1+, and a statistically significant correlation was unmasked between the  $\text{SUV}_{\text{max}}$  of lymphoma lesions and FAP expression ( $b = 0.551$ ,  $P < 0.001$ ). Figure 3 shows representative examples of the FAP immunostaining results.

### DISCUSSION

The most crucial contribution of our study is the first visualization of FAPs in malignant lymphoid tumors, particularly in T-cell

lymphomas. Moreover, we quantified the accumulation of  $^{68}\text{Ga}$ -FAPI ligand in different subtypes of lymphoma lesions.

Fibroblastic reticular cells are specialized myofibroblasts that create the lymph node skeleton with its conduit system (14). Malignant cells recruit and reeducate their surrounding cells to establish a tumor-supportive milieu that also affects the biology and function of fibroblastic reticular cells. Once reprogrammed to CAFs, they can induce extracellular matrix remodeling (15). There is increasing evidence that CAFs can potentially regulate tumor progression in hematologic neoplasms. Lenz et al. (3) and Haro et al. (4) reported that the stromal-1 gene signature was associated with good survival in patients with DLBCL and several other BCLs. Paradoxically, Bankov et al. (7) and Aronovich et al. (16) demonstrated that fibroblasts in classic HL and mycosis fungoides promoted tumor cell migration and drug resistance. These conflicting results indicate that there is still much to learn about the biologic and clinical significance of CAFs in different lymphoma subtypes. Thus, a new strategy is necessary to depict tumor–stroma interaction in lymphoma that does not involve visualization using morphologic or metabolic imaging.

Biologically,  $^{68}\text{Ga}$ -FAPI PET/CT is an excellent imaging modality to visualize FAP expression in the tumor stroma (10,17).

Most false-positive results occur in wound healing and inflammatory or fibrosis conditions caused by the activation, proliferation,

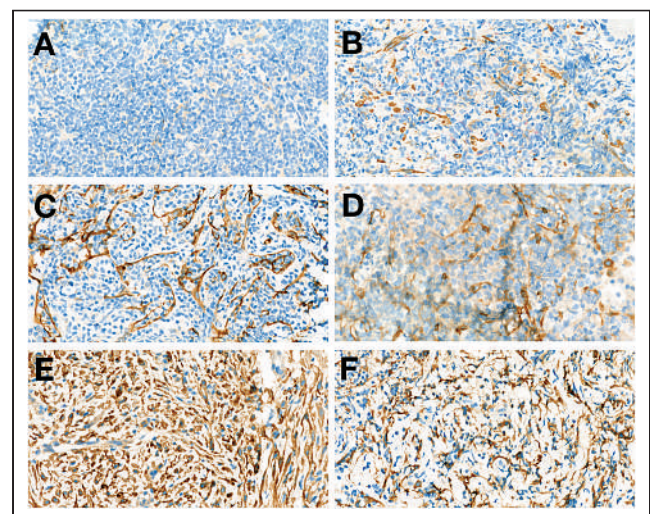


**FIGURE 3.** FAP immunohistochemistry of 6 exemplary cases of lymphoma. (A and B) Follicular lymphoma (A) and MALT with mild stromal FAP expression and FAP-negative neoplastic cells (B). (C and D) Chronic lymphocytic leukemia/small lymphocytic lymphoma (C) and DLBCL with moderate stromal FAP expression (D). (E and F) DLBCL (E) and HL with intense stromal FAP expression (F).

and accumulation of fibroblasts (11). Although clinical evaluations of  $^{68}\text{Ga}/^{18}\text{F}$ -FAPI PET have been performed in a spectrum of cancers, there are none involving lymphomas. In our study, 72 lymphoma patients referred for  $^{68}\text{Ga}$ -FAPI PET imaging showed FAPI-positive lesions in most subtypes of lymphoma, including both BCLs and T-cell lymphomas, except a patient with MALT lymphoma.

Since the origin, number, and distribution of FAP-expressing CAFs, as well as the number of FAP molecules per cell, may differ in tumors, we expect variations in tumor uptake and in the intratumoral tracer distribution. HL, especially the nodular sclerosing subtype of classic HL, is characterized by fibroblast proliferation in the tumor microenvironment, leading to fibrotic bands surrounding the lymphoma infiltrate. In our study, we found intense FAP immunostaining and significantly elevated FAPI uptake in HL lesions. Regarding NHL, there was a positive association between the clinical classification of NHL and the  $^{68}\text{Ga}$ -FAPI uptake activity of the lesion in PET/CT imaging. Aggressive NHL, especially DLBCL, exhibited intermediate to intense  $^{68}\text{Ga}$ -FAPI uptake and showed moderate to strong FAP immunostaining. These results were consistent with Haro and Orsulic's findings, who reported a high proportion of CAFs in B-cell lymphomas via a stromal gene signature analysis (4). Less common aggressive NHL subtypes, such as mantle cell lymphoma, B-lymphoblastic leukemia/lymphoma, primary cutaneous anaplastic large-cell lymphoma, and angioimmunoblastic T-cell lymphoma, with moderate FAP expression (score, 2+), exhibited moderate  $^{68}\text{Ga}$ -FAPI avidities. Surprisingly, we noted that follicular lymphoma, which showed the lowest desmoplastic reaction by histopathology, had intermediate  $^{68}\text{Ga}$ -FAPI uptake ( $\text{SUV}_{\text{max}}$ ,  $6.69 \pm 3.85$ ). MALT lymphoma, which showed weak FAP staining, exhibited mild  $^{68}\text{Ga}$ -FAPI uptake, as expected. However, we did not expect that T-cell lymphoma would accumulate less  $^{68}\text{Ga}$ -FAPI, even though the lesions expressed moderate to intense FAP expression.

Because of the very low background activity for  $^{68}\text{Ga}$ -FAPI, especially in the brain, liver, and peritoneal cavity, the high tumor-to-background ratios resulted in high contrast ratios for lymphoma lesions, particularly in the brain, liver, and oropharynx. These may be advantageous for the detection of cerebral, hepatic, or oropharyngeal involvement. As previous studies have reported, we also easily identified a DLBCL lesion in the left temporal lobe in our study.

Because of the limitations of this report, such as a heterogeneous patient collective and a low case number for some subtypes, further studies are necessary. Furthermore, because of the lack of follow-up, analysis of the long-term prognosis regarding disease-free and overall survival is currently unfeasible. Therefore, larger prospective clinical studies are needed for further evaluation.

## CONCLUSION

Our study results showed that  $^{68}\text{Ga}$ -FAPI PET/CT is an extremely useful technique for profiling FAP expression status in lymphoma lesions. HL and aggressive NHL may possess more CAFs in tumor stroma than does indolent disease.

## DISCLOSURE

This work was financially supported by the National Natural Science Foundation of China (no. 82071957), special funding from the Beijing Hospitals Authority Clinical Medicine Development (code XMLX202120), and Capital's Funds for Health Improvement and Research (no. 2018-2-1024). No other potential conflict of interest relevant to this article was reported.

## KEY POINTS

**QUESTION:** Can  $^{68}\text{Ga}$ -FAPI PET/CT detect FAPs in lymphoma?

**PERTINENT FINDINGS:** In this prospective study of 73 lymphoma patients, we found that  $^{68}\text{Ga}$ -FAPI PET/CT could be used to profile FAP expression status in lymphoma lesions. Furthermore, HL and aggressive NHL may possess more FAPs in tumor stroma than does indolent disease.

**IMPLICATIONS FOR PATIENT CARE:**  $^{68}\text{Ga}$ -FAPI imaging may be an alternate method for characterizing lymphoma profiles.

## REFERENCES

1. Höpken UE, Rehm A. Targeting the tumor microenvironment of leukemia and lymphoma. *Trends Cancer*. 2019;5:351–364.
2. Augsten M. Cancer-associated fibroblasts as another polarized cell type of the tumor microenvironment. *Front Oncol*. 2014;4:62.
3. Lenz G, Wright G, Dave SS, et al. Stromal gene signatures in large-B-cell lymphomas. *N Engl J Med*. 2008;359:2313–2323.
4. Haro M, Orsulic S. A paradoxical correlation of cancer-associated fibroblasts with survival outcomes in B-cell lymphomas and carcinomas. *Front Cell Dev Biol*. 2018;6:98.
5. Ciavarella S, Vegliante MC, Fabbri M, et al. Dissection of DLBCL microenvironment provides a gene expression-based predictor of survival applicable to formalin-fixed paraffin-embedded tissue. *Ann Oncol*. 2018;29:2363–2370.
6. Staiger AM, Duppel J, Dengler MA, et al. An analysis of the role of follicular lymphoma-associated fibroblasts to promote tumor cell viability following drug-induced apoptosis. *Leuk Lymphoma*. 2017;58:1922–1930.
7. Bankov K, Döring C, Ustaszewski A, et al. Fibroblasts in nodular sclerosing classical Hodgkin lymphoma are defined by a specific phenotype and protect tumor cells from brentuximab-vedotin induced injury. *Cancers (Basel)*. 2019;11:1687.
8. Roozendaal R, Mebius RE. Stromal cell-immune cell interactions. *Annu Rev Immunol*. 2011;29:23–43.
9. Kalluri R. The biology and function of fibroblasts in cancer. *Nat Rev Cancer*. 2016;16:582–598.
10. Kratochwil C, Flechsig P, Lindner T, et al.  $^{68}\text{Ga}$ -FAPI PET/CT: tracer uptake in 28 different kinds of cancer. *J Nucl Med*. 2019;60:801–805.
11. Altmann A, Haberkorn U, Sivek J. The latest developments in imaging of fibroblast activation protein. *J Nucl Med*. 2021;62:160–167.
12. Wang G, Jin X, Zhu H, et al.  $^{68}\text{Ga}$ -NOTA-FAPI-04 PET/CT in a patient with primary gastric diffuse large B cell lymphoma: comparisons with [ $^{18}\text{F}$ ] FDG PET/CT. *Eur J Nucl Med Mol Imaging*. 2021;48:647–648.
13. Serfling S, Zhi Y, Schirbel A, et al. Improved cancer detection in Waldeyer's tonsillar ring by  $^{68}\text{Ga}$ -FAPI PET/CT imaging. *Eur J Nucl Med Mol Imaging*. 2021;48:1178–1187.
14. Roozendaal R, Mebius RE, Kraal G. The conduit system of the lymph node. *Int Immunol*. 2008;20:1483–1487.
15. Öhlund D, Elyada E, Tuveson D. Fibroblast heterogeneity in the cancer wound. *J Exp Med*. 2014;211:1503–1523.
16. Aronovich A, Moyal L, Gorovitz B, et al. Cancer-associated fibroblasts in mycosis fungoides promote tumor cell migration and drug resistance through CXCL12/CXCR4. *J Invest Dermatol*. 2021;141:619–627.e2.
17. Lindner T, Loktev A, Altmann A, et al. Development of quinoline-based theranostic ligands for the targeting of fibroblast activation protein. *J Nucl Med*. 2018;59:1415–1422.

---

---

# Efficacy and Safety of <sup>177</sup>Lu-DOTATATE in Lung Neuroendocrine Tumors: A Bicenter study

Lamiaa Zidan<sup>\*1</sup>, Amir Iravani<sup>\*1-3</sup>, Kira Oleinikov<sup>4</sup>, Simona Ben-Haim<sup>5,6</sup>, David J. Gross<sup>4</sup>, Amichay Meirovitz<sup>7</sup>, Ophra Maimon<sup>7</sup>, Tim Akhurst<sup>1,2</sup>, Michael Michael<sup>2,8</sup>, Rodney J. Hicks<sup>1,2</sup>, Simona Grozinsky-Glasberg<sup>\*4</sup>, and Grace Kong<sup>\*1,2</sup>

<sup>1</sup>Molecular Imaging and Therapeutic Nuclear Medicine, Peter MacCallum Cancer Centre, Melbourne, Victoria, Australia; <sup>2</sup>Sir Peter MacCallum Department of Oncology, The University of Melbourne, Melbourne, Victoria, Australia; <sup>3</sup>Washington University School of Medicine, Mallinckrodt Institute of Radiology, St. Louis, Missouri; <sup>4</sup>Neuroendocrine Tumor Unit, ENETS Center of Excellence, Department of Endocrinology and Metabolism, Hadassah-Hebrew University Medical Center, Jerusalem, Israel; <sup>5</sup>Department of Nuclear Medicine, Hadassah-Hebrew University Medical Center, Jerusalem, Israel; <sup>6</sup>Institute of Nuclear Medicine, University College London and UCL Hospitals NHS Trust, London United Kingdom; <sup>7</sup>Sharett Institute of Oncology, Hadassah-Hebrew University Medical Center, Jerusalem, Israel; and <sup>8</sup>Division of Oncology, Peter MacCallum Cancer Centre, Melbourne, Victoria, Australia

The purpose of this study was to assess the efficacy and safety of <sup>177</sup>Lu-DOTATATE in patients with somatostatin receptor (SSR)-positive lung neuroendocrine tumors (NETs). **Methods:** This is a retrospective review of the outcome of patients with typical carcinoid (TC) and atypical carcinoid (AC), treated with <sup>177</sup>Lu-DOTATATE at 2 ENETS Centers of Excellence. Morphologic imaging (RECIST 1.1) and <sup>68</sup>Ga-DOTATATE PET/CT responses were assessed at 3 mo after completion of <sup>177</sup>Lu-DOTATATE. Concordance between 2 response assessment methods was evaluated by  $\kappa$  statistics. Progression-free survival (PFS) and overall survival (OS) were estimated by Kaplan–Meier analysis and compared by Log-rank test. Treatment-related adverse events (AEs) were graded based on Common Terminology Criteria for Adverse Events, version 5. **Results:** Of 48 patients (median age, 63 y; 13 women), 43 (90%) had AC and 5 (10%) TC. Almost all patients (47, 98%) were treated due to progression. Most patients (40, 83%) received somatostatin analogs, and 10 patients (20%) had prior everolimus, chemotherapy, or both. All patients had high SSR expression ( $\geq$  modified Krenning score 3) on pretreatment <sup>68</sup>Ga-DOTATATE PET/CT. Patients received a median 4 (range, 1–4) cycles of <sup>177</sup>Lu-DOTATATE (33% with concurrent radiosensitizing chemotherapy) to a median cumulative activity of 27 GBq (range, 6–43GBq). At a median follow-up of 42 mo, the median PFS and OS were 23 mo (95% CI, 18–28 mo) and 59 mo (95% CI, 50–not reached [NR]), respectively. Of 40 patients with RECIST-measurable disease and 39 patients with available <sup>68</sup>Ga-DOTATATE PET/CT, response categories were partial response, 20% (95% CI, 10%–35%) and 44% (95% CI, 30%–59%); stable disease, 68% (95% CI, 52%–80%) and 44% (95% CI, 30%–59%); and progressive disease, 12% (95% CI, 5%–27%) by both, respectively. There was a moderate concordance between response categories by RECIST and <sup>68</sup>Ga-DOTATATE PET/CT, weighted  $\kappa$  of 0.51 (95% CI, 0.21–0.68). Of patients with stable disease by RECIST, those with partial response on <sup>68</sup>Ga-DOTATATE PET/CT had a longer OS than those with no response, NR versus 52 mo (95% CI, 28–64), hazard ratio 0.2 (95% CI, 0.1–0.6),  $P < 0.001$ . Most grade 3/4 AEs were reversible and the most common was lymphopenia (14%) with no incidence of myelodysplasia or leukemia. **Conclusion:** In patients with advanced progressive lung

NET and satisfactory SSR expression, <sup>177</sup>Lu-DOTATATE is effective and safe with a high disease control rate and encouraging PFS and OS.

**Key Words:** lung neuroendocrine tumor; bronchial carcinoid; peptide receptor radionuclide therapy; somatostatin receptor

**J Nucl Med 2022; 63:218–225**  
DOI: 10.2967/jnumed.120.260760

**W**ell-differentiated lung neuroendocrine tumor (NET) or “lung carcinoid,” classified into typical carcinoid (TC) and atypical carcinoid (AC), is a heterogeneous disease with variable clinical behavior and prognosis (1). TC rarely metastasizes and generally has a favorable prognosis, whereas AC is more likely to be metastatic at presentation and has a worse prognosis (1).

Surgery is the treatment of choice in patients with localized disease, whereas management of inoperable locally advanced and metastatic disease is complex and requires a multidisciplinary approach (1). For metastatic disease, the European Neuroendocrine Tumors Society (ENETS) guidelines recommend the mammalian target of rapamycin inhibitor everolimus as the first-line therapy for progressive lung NET; however, in patients with tumor of a low proliferative index, a somatostatin analog (SSA) can be considered as first-line therapy, especially when the uptake on somatostatin receptor (SSR) imaging is strongly positive (2). In the LUNA phase 2 trial, pasireotide (an agonist for SSR subtypes 1–3 and 5) alone or in combination with everolimus showed evidence of activity and safety (3). Chemotherapy is only considered in rapidly progressive metastatic pulmonary carcinoids and when no other treatment options are available. According to the National Comprehensive Cancer Network guidelines, platinum-based regimens or temozolomide can be used in stage IV AC with a high proliferation index (4).

Although lung NET frequently expresses SSR subtype 2 (SSR-2), the role of SSR-2-targeted peptide receptor radionuclide therapy (PRRT) with <sup>177</sup>Lu DOTA-0-Tyr3-Octreotate (<sup>177</sup>Lu-DOTATATE) remains to be determined (5). Limited retrospective studies showed the efficacy of PRRT in lung NET, comparable to the results of the NETTER-1 trial, reflecting the generalizability of PRRT for any SSR-positive NET (6–8). Because of the lack of comparative

---

Received Nov. 21, 2020; revision accepted Apr. 21, 2021.  
For correspondence or reprints, contact Amir Iravani (Amir.iravani@wustl.edu).  
<sup>\*</sup>Contributed equally to this work.  
Published online May 28, 2021.  
COPYRIGHT © 2022 by the Society of Nuclear Medicine and Molecular Imaging.

studies, after progression on SSA the selection of the next systemic treatment modality including everolimus, chemotherapy, or PRRT is at the discretion of physicians and depends on the access, expertise, and practice patterns of different institutions in the world. Besides, the efficacy of  $^{177}\text{Lu}$ -DOTATATE in patients previously untreated with either chemotherapy or everolimus is unclear. This dual-center study aims to assess the safety and efficacy of patients with lung NET who received  $^{177}\text{Lu}$ -DOTATATE.

## MATERIALS AND METHODS

### Patients

This is a retrospective review of all consecutive patients with biopsy-proven, well-differentiated lung NET (TC or AC), who received PRRT. Data are extracted from 2 ENETS centers of excellence—Peter MacCallum Cancer Centre (PMCC) in Melbourne, Australia, and Hadassah-Hebrew University Medical Center (HHUMC), Jerusalem, Israel—during the period from 2006 to 2019. This series shares a single patient with the series of Lim et al. (8). This shared patient underwent PRRT at PMCC but was managed at another institution involved in that publication. We consider it valuable to include this patient's data given the additional response assessment analyses and longer follow-up in our series.

Eligibility criteria for  $^{177}\text{Lu}$ -DOTATATE therapy included positive SSR imaging in all lesions, with either imaging progression or uncontrolled symptoms related to the unresectable disease. Positive  $^{68}\text{Ga}$  DOTA-0-Tyr3-Octreotate ( $^{68}\text{Ga}$ -DOTATATE) PET/CT or SSR imaging was defined as lesion uptake higher than liver and subgrouped to less than spleen or higher than spleen on the basis of tomographic imaging (modified Krenning score 3 and 4, respectively). Further eligibility criteria are listed in the supplemental materials (supplemental materials are available at <http://jnm.snmjournals.org>).

This study was conducted after receiving approval from the institutional ethics committee at the PMCC (Peter Mac project no. 19/214R) and the HHUMC (approval no. 0072-16). Details of access to PRRT at respective institutions are summarized in the supplemental materials.

### Therapy

Each cycle of  $^{177}\text{Lu}$ -DOTATATE was administered with premedication granisetron (2 mg), dexamethasone (8 mg), and renoprotective amino-acid infusion (25 g lysine and 25 g arginine in 1 L of normal saline) commencing 30 min before  $^{177}\text{Lu}$ -DOTATATE and continuing for 3 h thereafter (9). Dexamethasone was used as an antiemetic medication per institutional protocol only at PMCC. The treatment regimen typically included up to 4 cycles of  $^{177}\text{Lu}$ -DOTATATE given 6–10 wk apart. At PMCC,  $^{177}\text{Lu}$ -DOTATATE was usually given with radiosensitizing chemotherapy unless contraindicated, based on prior experiences showing enhanced efficacy without additional toxicity (10–12). Further details of radiosensitizing chemotherapy are described in the supplemental materials. Patients at HHUMC did not receive concurrent chemotherapy.

### Follow-up

Patients were clinically reviewed before, and after, each cycle of  $^{177}\text{Lu}$ -DOTATATE and typically at 3 mo after the last cycle of treatment. Evaluation at 3 mo included assessment of symptoms; laboratory tests including full blood counts, renal function, hepatic function, and serum chromogranin A (supplemental materials); and imaging by CT or  $^{68}\text{Ga}$ -DOTATATE PET/CT with or without  $^{18}\text{F}$ -FDG PET/CT. Ongoing follow-up occurred at intervals of 3 to 6 mo. CT response was defined by RECIST 1.1 (13). Where available, contrast-enhanced CT images were directly compared. Otherwise, nonenhanced CT from the PET/CT component of the study was assessed, using  $^{68}\text{Ga}$ -DOTATATE uptake as a guide to follow the dominant lesions. RECIST response was used to define the main outcomes and  $^{68}\text{Ga}$ -DOTATATE PET/CT and  $^{18}\text{F}$ -FDG PET response were used for exploratory outcome measures. Response assessments were performed blinded to the patient outcome.

A descriptor for pathologic uptake on  $^{68}\text{Ga}$ -DOTATATE PET/CT was adapted from a semiquantitative visual scoring system originally designed for planar  $^{111}\text{In}$  octreotide imaging known as the Krenning score. Scores were from 0 to 4 as follows: 0 = no uptake; 1 = uptake < liver; 2 = lesion uptake similar to liver;

**TABLE 1**  
 $^{68}\text{Ga}$ -DOTATATE PET/CT Response Criteria

Response category	Description
Complete response	Disappearance of all tracer-avid lesions or If residual anatomic abnormality on CT with tracer uptake indistinguishable or less than background physiologic uptake
Partial response	Reduction in intensity of uptake by one modified Krenning score* in at least 1 tumor site associated with decrease/stable in size on CT (if measurable) or PET (if nonmeasurable on CT) or Reduction in size of tracer-avid lesions on CT (if measurable) regardless of intensity of uptake
Stable disease	Not partial response or progressive disease
Progressive disease	Development of new tracer-avid lesions or Increase in the size of the tracer-avid lesions on CT (if measurable) or on PET (if nonmeasurable on CT) regardless of intensity of uptake <sup>†</sup>

\*Modified Krenning score, 0 = no uptake; 1 = uptake < liver; 2 = lesion uptake similar to liver; 3 = uptake > liver but < spleen; 4 = uptake  $\geq$  spleen.

<sup>†</sup>Rarely an increase in the size of the lesion can be seen in responsive lesions. This may be associated with an increase in central hypodensity/necrosis on CT and a decrease in peripheral tracer uptake on PET. In this circumstance, a confirmatory follow-up study or correlation with other imaging modalities may be required.

3 = uptake > liver and < spleen; 4 = uptake ≥ spleen (14). Response by <sup>68</sup>Ga-DOTATATE PET/CT is described in Table 1.

In patients who underwent baseline <sup>18</sup>F-FDG PET/CT, positive lesion was defined as uptake above the liver, and metabolic responses were assessed on the <sup>18</sup>F-FDG PET images qualitatively according to the PMCC criteria (supplemental materials) (15,16).

Time to next treatment has been included to capture the timing of the next treatment from start of <sup>177</sup>Lu-DOTATATE. All hematologic and renal toxicities occurring from the time of the first <sup>177</sup>Lu-DOTATATE administration were recorded and defined according to the Common Terminology Criteria for Adverse Events (CTCAE; version 5.0).

### Statistical Analysis

The continuous variables are summarized using the median (interquartile range [IQR] or range), and categoric variables are summarized using basic proportions. The concordance between RECIST and <sup>68</sup>Ga-DOTATATE PET/CT response was assessed by Cohen's κ statistics. Fisher's exact was used to evaluate the difference between response rates in different groups. Progression-free survival (PFS) was calculated from the start of <sup>177</sup>Lu-DOTATATE to clinical or imaging progression, new oncologic treatment, or death. Overall survival (OS) was recorded as the duration from the start of <sup>177</sup>Lu-DOTATATE to last follow-up or death. The patients who were alive at the last follow-up were censored on that date. The cutoff follow-up date was August 31, 2019. The Log-rank test and Cox regression model were used to compare survival of different groups. A Kaplan–Meier curve was used to depict the survival. Statistical analysis was performed using GraphPad Prism 8 (GraphPad Software).

## RESULTS

### Patient Characteristics

Of 51 consecutive patients with lung NET (22 from PMCC and 29 from HHUMC), 3 patients were removed from the analysis as they received at least 1 cycle of <sup>90</sup>Y-DOTATATE. Forty-eight patients were included for final analysis, including 43 (90%) with AC and 5 (10%) with TC. The median Ki-67 of the entire population was 10% (range, 1%–30%), and most patients (90%) had metastatic disease in the liver, bone, or multiorgan involvement. Most patients (83%) received SSAs, and 10 (20%) had prior everolimus, chemotherapy, or both. Almost all patients (47/48, 98%) were treated due to radiographic disease progression and 1 patient for uncontrolled symptoms (back pain correlated to sites of osseous metastasis). Most (94%) demonstrated high avidity on SSR imaging, with a Krenning score of 4. Of 25 patients who underwent baseline <sup>18</sup>F-FDG PET/CT, 16 (64%) had concurrent <sup>18</sup>F-FDG-avid disease (Table 2). The median cumulative activity of <sup>177</sup>Lu-DOTATATE was 27.4 GBq (range, 7.1–43.4 GBq) administered over a median of 4 cycles (range, 1–4). Sixteen patients (33%) had radiosensitizing chemotherapy (5FU or capecitabine with or without temozolomide) (Table 3).

### Imaging Response

Of 40 patients with RECIST-measurable disease at 3 mo, 8 patients (20%; 95% CI, 10%–35%) had partial response and 27 patients (68%; 95% CI, 52%–80%) had stable disease resulting in a disease control rate (DCR) of 88% (95% CI, 73%–95%). Five patients (12%; 95% CI, 5–27) had progressive disease (Fig. 1). Five patients were lost to follow-up, 1 died early, and 2 had no available follow-up CT data (Supplemental Table 1).

**TABLE 2**  
Patient Characteristics

Characteristic	Number (%)
Sex, male:female	35:13 (73:27)
Median age (y)	63 (range, 25–84)
Type	
Typical carcinoid	5 (10)
Atypical carcinoid	43 (90)
Ki-67	
≤2%	3 (6)
3%–20%	34 (71)
>20%	3 (6)
Unknown	8 (17)
Dominant site of disease	
Local/locoregional	5 (10)
Liver	10 (21)
Bone	3 (6)
Multiorgan	30 (63)
SSR expression by <sup>68</sup> Ga-DOTATATE (modified Krenning score)	
Score 3	3 (6)
Score 4	45 (94)
Baseline <sup>18</sup> F-FDG PE/CT	
No uptake	3 (6)
≤liver	6 (12)
>liver	16 (33)
Not available	23 (48)
Prior treatments	
SSA	40 (83)
Surgery	25 (52)
Chemotherapy	5 (10)
Everolimus	3 (6)
Everolimus and chemotherapy	2 (4)
Radiotherapy	2 (4)
Liver-directed therapy	2 (4)
None	1 (2)

Data in parentheses are percentages, unless otherwise noted. SSR = somatostatin receptor; SSA = somatostatin analog.

Of 39 patients with available <sup>68</sup>Ga-DOTATATE PET/CT at 3 mo, 17 patients (44%; 95% CI, 30%–59%) had partial response and 17 patients (44%; 95% CI, 30%–59%) had stable disease with a DCR of 88% (95% CI, 73%–95%) (Table 4 and Fig. 2). Five of those 39 patients (12%; 95% CI, 5%–27%) had progressive disease. Of the 9 patients with no available <sup>68</sup>Ga-DOTATATE PET/CT, 5 were lost to follow-up, 1 died, and 3 had Octreoscan as their posttreatment molecular imaging. In 39 patients with both RECIST-assessable disease and available <sup>68</sup>Ga-DOTATATE PET/CT results, only a moderate concordance in response categories of the 2 modalities was noted, weighted κ of 0.51 (95% CI, 0.21–0.68).

**TABLE 3**  
Treatment Parameters

Parameter	Number
<b>Indication of <sup>177</sup>Lu-DOTATATE (n = 48)</b>	
Disease progression	47
Uncontrolled symptoms	1
<b>No. of cycles</b>	
1	3
2	6
3	13
4	26
Cumulative <sup>177</sup> Lu-DOTATATE activity in GBq	27 (range, 6–43)
<b>Radiosensitizing chemotherapy (n = 16)</b>	
1 cycle	3
2 cycles	3
3 cycles	4
4 cycles	6
<b>Chemotherapy regimen</b>	
5FU	4
Capecitabine	8
Combined capecitabine and temozolomide	4

Most patients with partial response or progressive disease by RECIST were also categorized similarly by <sup>68</sup>Ga-DOTATATE PET/CT, 4 of 5 (80%) and 7 of 8 (87%) patients, respectively. The discordant response categories were noted in stable disease by RECIST: in this category, 10 of 26 patients were classified as

partial response and 1 patient as progressive disease by <sup>68</sup>Ga-DOTATATE PET/CT due to the development of new avid lesions.

Follow-up <sup>18</sup>F-FDG PET/CT was available in 12 of 48 patients. Although RECIST and <sup>18</sup>F-FDG PET/CT responses were in agreement in most cases, 3 cases with stable disease by RECIST were grouped as partial response by <sup>18</sup>F-FDG PET/CT.

In 30 patients from the AC cohort, although the rate of partial response was numerically higher in patients with a Ki-67 of >10% than in those with a Ki-67 of ≤10%, the difference did not reach statistical significance (36% and 16%, respectively; *P* = 0.4). Similarly, there was no significant difference in the rate of partial response in patients who received radiosensitizing chemotherapy, although a trend toward higher response rate was noted (36% and 12%, respectively; *P* = 0.1).

### Survival Outcome

At a median follow-up of 42 mo, there were 16 (33%) deaths. The median PFS and OS of the entire cohort were 23 mo (95% CI, 18–28 mo) and 59 mo (95% CI, 50–not reached [NR]), respectively (Figs. 3A and 3B). The OS was not significantly different between the 2 institutions. The OS of the AC patients with Ki-67 ≤ 10% versus Ki-67 >10% and patients who received radiosensitizing chemotherapy versus those who did not receive chemotherapy were not significantly different (*P* = 0.7 and 0.4, respectively) (Supplemental Figs. 1A and 1B).

Of patients with stable disease by RECIST, those with partial response on <sup>68</sup>Ga-DOTATATE PET/CT had longer OS than those with no response (NR vs. 52 mo [95% CI, 28–65]; hazard ratio, 0.2 [95% CI, 0.1–0.6]; *P* < 0.001) (Fig. 4). Baseline <sup>18</sup>F-FDG PET/CT–positive disease (available for 25/48 patients) and follow-up <sup>18</sup>F-FDG PET/CT response (available for 12/48 patients) did not correlate with OS (*P* = 0.2 and 0.3, respectively).

During follow-up, 27 patients received further treatment. The median time to next treatment was 23 mo (range, 7–56). Fifteen patients received further PRRT, and 12 patients received other treatments, including everolimus (*n* = 4), liver-directed therapy (*n* = 3), or change or increase in the dosage of SSA (*n* = 3) or chemotherapy (*n* = 2). One patient who did show progressive disease at 3 mo after PRRT received no treatment but did not show any further progression up to 24 mo, possibly indicating pseudoprogression.

### Toxicity

<sup>177</sup>Lu-DOTATATE was well tolerated with acceptable toxicity, and most CTCAE grade 3/4 hematologic toxicity during treatment reversed to CTCAE grade 1/2 or baseline (Table 5). The most common hematologic toxicity included thrombocytopenia and lymphopenia. There was no incidence of myelodysplasia/leukemia or renal toxicity on long-term follow-up.

### DISCUSSION

PRRT is an effective treatment option for patients with advanced gastroenteropancreatic NET, with sufficient SSR expression after progression on SSA (4,7). We have recently reported that only a proportion of lung NET expresses SSR at sufficient levels

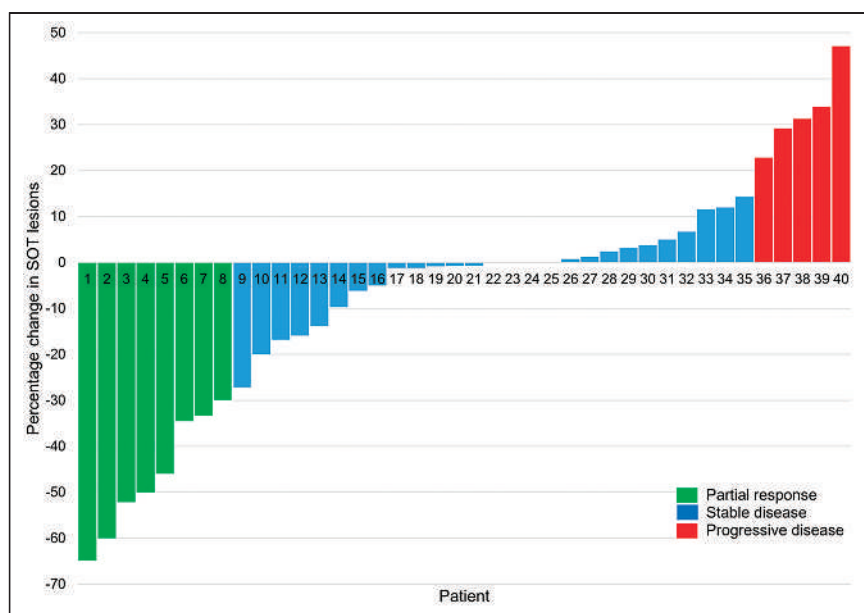


**FIGURE 1.** Waterfall plot of RECIST response at 3 mo after completion of PRRT. SOT lesions = sum of target lesions diameters.

**TABLE 4**  
Response to Treatment

Modality	Response	Number (% [95% CI]*)
CT-RECIST	Complete response	0
	Partial response	8/40 (20 [10–35])
	Stable disease	27/40 (67.5 [52–80])
	Progressive disease	5/40 (12.5 [5–27])
	Not available	8
<sup>68</sup> Ga-DOTATATE PET/CT	Complete response	0
	Partial response	17/39 (43.5 [30–59])
	Stable disease	17/39 (43.5 [30–59])
	Progressive disease	5/39 (13 [5–27])
	Not available	9
<sup>18</sup> F-FDG PET/CT	Complete response	0
	Partial response	5/12 (42)
	Stable disease	3/12 (25)
	Progressive disease	4/12 (33)
	Not available	36

\*Not calculated for the sample sizes of <30.

to potentially benefit from PRRT (17). Although lung NETs were not included in the NETTER-1 trial, limited clinical studies have shown promising results (6,7). By pooling the patients from 2 ENETs centers of excellence, we have shown that <sup>177</sup>Lu-DOTATATE is an effective and safe treatment modality in lung NETs with high SSR expression after progression on SSA with a radiographic response of 20%, DCR of 88%, and favorable median PFS and OS of 23 and 59 mo, respectively. These results are largely consistent with those of previous studies, indicating the efficacy of this treatment (Supplemental Table 2) (8,18–27).

Effective treatment options for advanced progressive lung NET are limited, with no available data to guide the sequencing of therapy. Furthermore, the limited patient tolerability remains of serious consideration when deciding on further lines of treatment with the aim of preserving the quality of life. In the subcohort of 90 patients with lung NET in the RADIANT 4 trial, in 57 patients randomized to the everolimus arm a 50% reduction in risk of disease progression or death was reported compared with placebo (28). Although 58% of the patients achieved any tumor shrinkage, only 2% were evaluated as partial response by RECIST. The median PFS was 9.2 mo (95% CI, 6.8–10.9), with a 5.6-mo improvement compared with placebo (28). The phase II LUNA trial involving 112 patients, the majority with lung NET, supported the efficacy of pasireotide, everolimus, or their combination, with a radiographic DCR at 9 mo of 39%, 33%, and 58%, respectively (3). In line with the RADIANT-4 trial, the rate of partial response in the LUNA trial was 2% in all 3 groups. Adverse events (AEs) requiring dose adjustment or interruption were reported in 24%, 52%, and 61% of patients in the pasireotide, everolimus, and the combination arm, respectively (3). Chemotherapy remains an option as palliative therapy in lung NET, with a combination of various chemotherapeutic drugs showing a <30% objective response and median OS of 24.3 mo in a small retrospective series (29). Although PRRT is usually considered after progression on everolimus or

chemotherapy, most patients (80%) in this study were untreated with either of those treatments. Although our result cannot be compared with prior trials or extrapolated to all patients with lung NET, the stringent patient selection based on sufficient SSR expression on pretreatment scanning remains a major advantage of this targeted treatment. Furthermore, attention to tumor heterogeneity of SSR expression is important as we have recently shown that up to 50% of patients with lung NET may demonstrate inter- and inpatient heterogeneity on dual imaging by <sup>68</sup>Ga-DOTATATE and <sup>18</sup>F-FDG PET/CT (17).

PRRT has also shown an acceptable safety profile, with largely reversible short-term and limited long-term treatment-related AEs, with no cases of myelodysplasia or renal toxicity in our cohort, which is consistent with other studies (18–21). In a study by Sabet et al., grade 3 hematotoxicity was reported in 13.6% of patients at 3–10 wk after at least 1 cycle of PRRT with no grade 3 or higher nephrotoxicity (19). Mariniello et al. reported a <5% hematotoxicity after <sup>90</sup>Y-DOTATOC and no hematologic or renal AEs after <sup>177</sup>Lu-DOTATATE (21). In an Australian multicenter study, Lim et al. reported 2 of 48 (4%) patients with acute myeloid leukemia after PRRT; 1 patient was heavily pretreated including alkylating chemotherapy and the other patient was treated with SSA only (8).

Although previous studies and clinical trials have typically used CT or MRI for response assessment, it appears that the outcome of the patients with NET may not be adequately captured by RECIST 1.1 alone (19–22,26,27,30). In addition to standard RECIST, by combining the functional information provided by PET and morphologic change by CT, we also explored the use of <sup>68</sup>Ga-DOTATATE PET/CT for response assessment and found a moderate concordance between 2 modalities. Interestingly, the response by <sup>68</sup>Ga-DOTATATE PET/CT further stratified the OS of the patients who were otherwise grouped as stable disease by RECIST (Fig. 4). Such patients constituted almost two thirds of our cohort. The recent update on appropriate-use criteria indicated

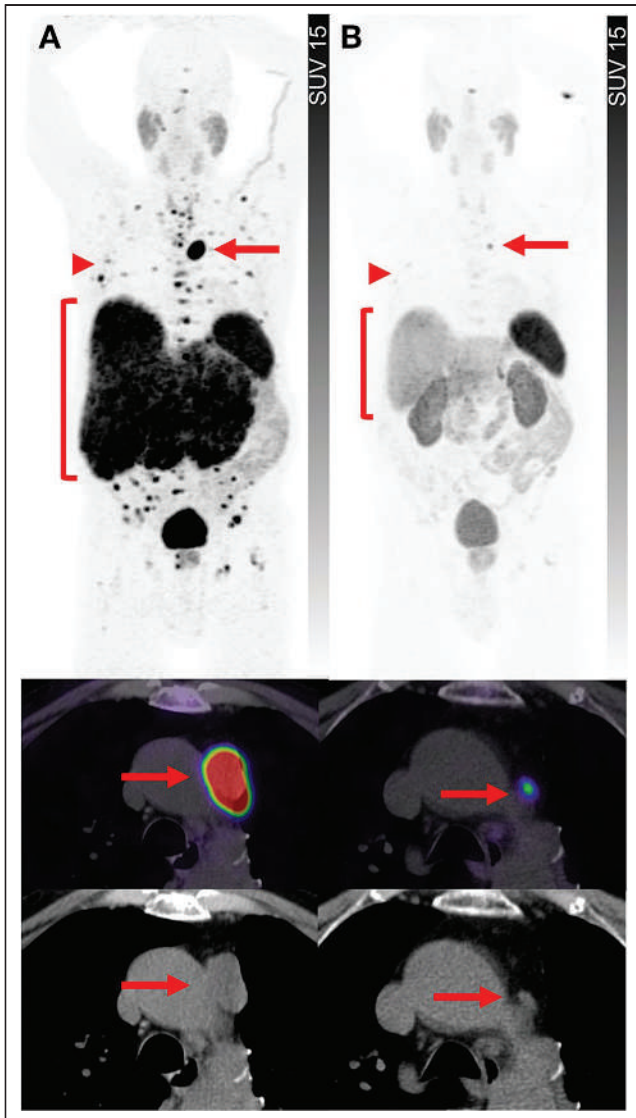


**FIGURE 2.** A representative patient with metastatic atypical lung carcinoma with partial response on  $^{68}\text{Ga}$ -DOTATATE PET/CT and CT at 3 mo after PRRT. Maximum-intensity-projection PET (top), PET/CT (middle), and CT (bottom) at baseline (A) and 3-mo follow-up (B) show marked response to treatment in liver (brackets), bones (arrowheads), and lymph nodes (arrows).

the use of SSR PET as appropriate for restaging after completion of PRRT(31). On the basis of our experience, response should include the disappearance or significant reduction of  $^{68}\text{Ga}$ -DOTATATE avidity such as a decline in the Krenning score of the

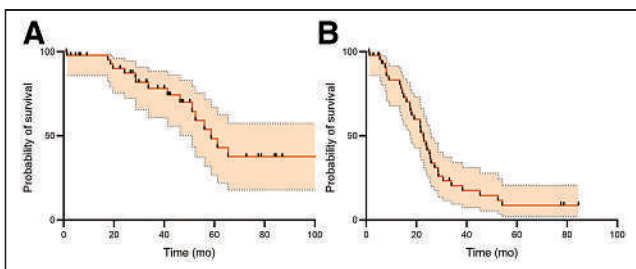


**FIGURE 3.** Kaplan-Meier plot depiction of OS (A) and PFA (B) of entire cohort.

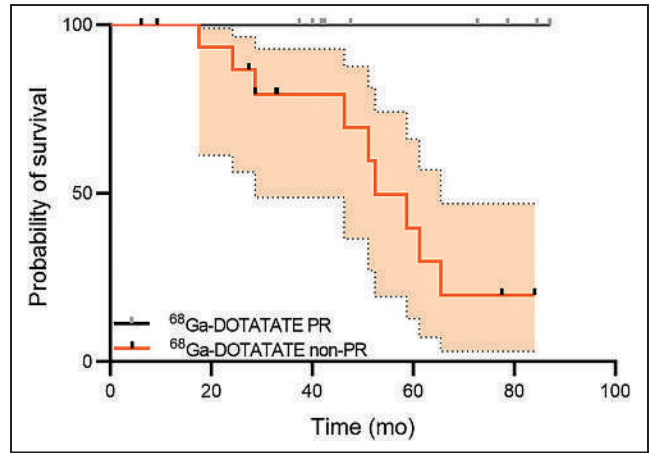


**FIGURE 4.** Of the patients with stable disease by RECIST, those with partial response (PR) on  $^{68}\text{Ga}$ -DOTATATE PET/CT had longer OS than nonresponders (non-PR) on  $^{68}\text{Ga}$ -DOTATATE PET/CT, as demonstrated by Kaplan-Meier plot.

known lesions without structural progression on CT or MRI. The response monitoring of nonmeasurable lesions such as osseous disease is also another advantage of SSR PET/CT. However, the exact role of  $^{68}\text{Ga}$ -DOTATATE PET/CT in response monitoring remains to be determined without currently established or validated criteria but warrants further evaluation.

The retrospective methodology of this study imposes some limitations, including potential selection bias, which we hope has been mitigated by combining the patients from the 2 institutions. Despite a relatively long follow-up time, death occurred only in around one third of patients, limiting the statistical power to robustly evaluate the prognostic implications of multiple clinical and imaging factors. In addition, the relatively low number of patients included further restricted the strength of statistical inference and precluded multivariate analysis. The use of different treatment protocols between the sites is also another limitation. For instance, dexamethasone was used as an antiemetic, and most patients at PMCC also received concurrent radiosensitizing chemotherapy. However, use of different procedures appears not to have had a major impact on outcomes, with comparable survival demonstrated at both centers. Lastly, 10% of patients had only locoregional disease, which may have better outcomes compared with those with bone, liver, or multiorgan involvement. We did not remove these patients from the analysis as this may have further reduced the statistical power of this study.

## CONCLUSION

In patients with advanced progressive lung NET and satisfactory SSR expression,  $^{177}\text{Lu}$ -DOTATATE is effective and safe, with a high DCR and encouraging PFS and OS. Further prospective studies comparing  $^{177}\text{Lu}$ -DOTATATE with other systemic options are warranted.

## DISCLOSURE

Grace Kong is supported by a Clinical Fellowship Award from the Peter MacCallum Foundation. Rodney J. Hicks is recipient of a National Health and Medical Research Council Practitioner Fellowship (APP1108050). No other potential conflict of interest relevant to this article was reported.

**TABLE 5**  
Hematologic Adverse Events of <sup>177</sup>Lu-DOTATATE

Adverse event	During treatment (%)				3-mo after treatment (%)			
	1	2	3	4	1	2	3	4
CTCAE grade								
Anemia	22 (43)	4 (8)			26 (51)	1 (2)		
Leukopenia	10 (20)		1 (2)	1 (2)	8 (16)	1 (2)	1 (2)	
Neutropenia	5 (10)	2 (4)		1 (2)	4 (8)			
Lymphopenia	9 (18)	13 (25)	6 (12)	1 (2)	11 (22)	12 (24)	1 (2)	
Thrombocytopenia	13 (25)	1 (2)		1 (2)	12 (24)			

## ACKNOWLEDGMENTS

We thank the nuclear medicine and nursing staff at the Peter MacCallum Cancer Centre and Hadassah-Hebrew University Medical Center for their commitment to providing excellent care for the patients.

## KEY POINTS

**QUESTION:** What is the role of <sup>177</sup>Lu-DOTATATE in patients with SSR-positive metastatic lung NET?

**PERTINENT FINDINGS:** In this retrospective study of 48 patients from 2 ENETS centers of excellence, <sup>177</sup>Lu-DOTATATE was safe and achieved a high disease control rate, with an objective response in one fifth of patients. In patients who achieved stable disease by RECIST at 3 mo after completion of <sup>177</sup>Lu-DOTATATE, the response by <sup>68</sup>Ga-DOTATATE PET/CT may have prognostic implication.

**IMPLICATIONS FOR PATIENT CARE:** In patients with advanced progressive lung NET and satisfactory SSR expression, <sup>177</sup>Lu-DOTATATE should be considered as an early effective and safe treatment modality.

## REFERENCES

- Caplin ME, Baudin E, Ferolla P, et al. Pulmonary neuroendocrine (carcinoid) tumors: European Neuroendocrine Tumor Society expert consensus and recommendations for best practice for typical and atypical pulmonary carcinoids. *Ann Oncol*. 2015;26:1604–1620.
- Pavel M, O'Toole D, Costa F, et al. ENETS consensus guidelines update for the management of distant metastatic disease of intestinal, pancreatic, bronchial neuroendocrine neoplasms (NEN) and NEN of unknown primary site. *Neuroendocrinology*. 2016;103:172–185.
- Ferolla P, Brizzi MP, Meyer T, et al. Efficacy and safety of long-acting pasireotide or everolimus alone or in combination in patients with advanced carcinoids of the lung and thymus (LUNA): an open-label, multicentre, randomised, phase 2 trial. *Lancet Oncol*. 2017;18:1652–1664.
- Shah MH, Goldner WS, Halfdanarson TR, et al. NCCN guidelines insights: neuroendocrine and adrenal tumors, version 2.2018. *J Natl Compr Canc Netw*. 2018;16:693–702.
- Reubi JC, Waser B. Concomitant expression of several peptide receptors in neuroendocrine tumours: molecular basis for in vivo multireceptor tumour targeting. *Eur J Nucl Med Mol Imaging*. 2003;30:781–793.
- Naraev BG, Ramirez RA, Kendi AT, Halfdanarson TR. Peptide receptor radionuclide therapy for patients with advanced lung carcinoids. *Clin Lung Cancer*. 2019;20:e376–e392.
- Strosberg J, El-Haddad G, Wolin E, et al. Phase 3 trial of <sup>177</sup>Lu-Dotatate for mid-gut neuroendocrine tumors. *N Engl J Med*. 2017;376:125–135.
- Lim LE, Chan DL, Thomas D, et al. Australian experience of peptide receptor radionuclide therapy in lung neuroendocrine tumours. *Oncotarget*. 2020;11:2636–2646.
- Kong G, Grozinsky-Glasberg S, Hofman MS, et al. Efficacy of peptide receptor radionuclide therapy for functional metastatic paraganglioma and pheochromocytoma. *J Clin Endocrinol Metab*. 2017;102:3278–3287.
- Kong G, Johnston V, Ramdave S, Lau E, Rischin D, Hicks RJ. High-administered activity In-111 octreotide therapy with concomitant radiosensitizing 5FU chemotherapy for treatment of neuroendocrine tumors: preliminary experience. *Cancer Biother Radiopharm*. 2009;24:527–533.
- Hubble D, Kong G, Michael M, Johnson V, Ramdave S, Hicks RJ. <sup>177</sup>Lu-octreotate, alone or with radiosensitising chemotherapy, is safe in neuroendocrine tumour patients previously treated with high-activity <sup>111</sup>In-octreotide. *Eur J Nucl Med Mol Imaging*. 2010;37:1869–1875.
- Claringbold PG, Brayshaw PA, Price RA, Turner JH. Phase II study of radiolabeled <sup>177</sup>Lu-octreotate and capecitabine therapy of progressive disseminated neuroendocrine tumours. *Eur J Nucl Med Mol Imaging*. 2011;38:302–311.
- Eisenhauer EA, Therasse P, Bogaerts J, et al. New response evaluation criteria in solid tumours: revised RECIST guideline (version 1.1). *Eur J Cancer*. 2009;45:228–247.
- Krenning EP, Valkema R, Kooij PP, et al. Scintigraphy and radionuclide therapy with [indium-111-labelled-diethyl triamine penta-acetic acid-D-Phe1]-octreotide. *Ital J Gastroenterol Hepatol*. 1999;31(suppl 2):S219–S223.
- Wahl RL, Jacene H, Kasamon Y, Lodge MA. From RECIST to PERCIST: evolving considerations for PET response criteria in solid tumors. *J Nucl Med*. 2009;50(suppl 1):122S–150S.
- Hicks RJ. The role of PET in monitoring therapy. *Cancer Imaging*. 2005;5:51–57.
- Zidan L, Irvani A, Kong G, Akhurst T, Michael M, Hicks RJ. Theranostic implications of molecular imaging phenotype of well-differentiated pulmonary carcinoid based on <sup>68</sup>Ga-DOTATATE PET/CT and <sup>18</sup>F-FDG PET/CT. *Eur J Nucl Med Mol Imaging*. 2021;48:204–216.
- Ianniello A, Sansovini M, Severi S, et al. Peptide receptor radionuclide therapy with <sup>177</sup>Lu-DOTATATE in advanced bronchial carcinoids: prognostic role of thyroid transcription factor 1 and <sup>18</sup>F-FDG PET. *Eur J Nucl Med Mol Imaging*. 2016;43:1040–1046.
- Sabet A, Haug AR, Eiden C, et al. Efficacy of peptide receptor radionuclide therapy with <sup>177</sup>Lu-octreotate in metastatic pulmonary neuroendocrine tumors: a dual-centre analysis. *Am J Nucl Med Mol Imaging*. 2017;7:74–83.
- Parghane RV, Talole S, Prabhaskar K, Basu S. Clinical response profile of metastatic/advanced pulmonary neuroendocrine tumors to peptide receptor radionuclide therapy with <sup>177</sup>Lu-DOTATATE. *Clin Nucl Med*. 2017;42:428–435.
- Mariniello A, Bodei L, Tinelli C, et al. Long-term results of PRRT in advanced bronchopulmonary carcinoid. *Eur J Nucl Med Mol Imaging*. 2016;43:441–452.
- Brabander T, van der Zwan WA, Teunissen JJM, et al. Long-term efficacy, survival, and safety of [<sup>177</sup>Lu-DOTA(0),Tyr(3)]octreotate in patients with gastroenteropancreatic and bronchial neuroendocrine tumors. *Clin Cancer Res*. 2017;23:4617–4624.
- van Essen M, Krenning EP, Bakker WH, de Herder WW, van Aken MO, Kwekkeboom DJ. Peptide receptor radionuclide therapy with <sup>177</sup>Lu-octreotate in patients with foregut carcinoid tumours of bronchial, gastric and thymic origin. *Eur J Nucl Med Mol Imaging*. 2007;34:1219–1227.

24. Filice A, Fraternali A, Frasoldati A, et al. Radiolabeled somatostatin analogues therapy in advanced neuroendocrine tumors: a single centre experience. *J Oncol*. 2012;2012:320198.
25. Bodei L, Cremonesi M, Grana CM, et al. Peptide receptor radionuclide therapy with <sup>177</sup>Lu-DOTATATE: the IEO phase I-II study. *Eur J Nucl Med Mol Imaging*. 2011;38:2125–2135.
26. Pfeifer AK, Gregersen T, Gronbaek H, et al. Peptide receptor radionuclide therapy with Y-DOTATOC and <sup>177</sup>Lu-DOTATOC in advanced neuroendocrine tumors: results from a Danish cohort treated in Switzerland. *Neuroendocrinology*. 2011;93:189–196.
27. Garske-Román U, Sandström M, Fröss Baron K, et al. Prospective observational study of <sup>177</sup>Lu-DOTA-octreotate therapy in 200 patients with advanced metastasized neuroendocrine tumours (NETs): feasibility and impact of a dosimetry-guided study protocol on outcome and toxicity. *Eur J Nucl Med Mol Imaging*. 2018;45:970–988.
28. Fazio N, Buzzoni R, Delle Fave G, et al. Everolimus in advanced, progressive, well-differentiated, non-functional neuroendocrine tumors: RADIANT-4 lung subgroup analysis. *Cancer Sci*. 2018;109:174–181.
29. Tsoukalas N, Baxevanos P, Aravantinou-Fatorou E, et al. Advances on systemic treatment for lung neuroendocrine neoplasms. *Ann Transl Med*. 2018;6:146.
30. Bodei L, Cremonesi M, Kidd M, et al. Peptide receptor radionuclide therapy for advanced neuroendocrine tumors. *Thorac Surg Clin*. 2014;24:333–349.
31. Hope TA. Updates to the appropriate-use criteria for somatostatin receptor PET [editorial]. *J Nucl Med*. 2020;61:1764.

# Tumor Sink Effect in $^{68}\text{Ga}$ -PSMA-11 PET: Myth or Reality?

Andrei Gafita<sup>1,2\*</sup>, Hui Wang<sup>2\*</sup>, Andrew Robertson<sup>2</sup>, Wesley R. Armstrong<sup>1</sup>, Raphael Zaum<sup>2</sup>, Manuel Weber<sup>3</sup>, Farid Yagubayli<sup>2</sup>, Clemens Kratochwil<sup>4</sup>, Tristan R. Grogan<sup>5</sup>, Kathleen Nguyen<sup>1</sup>, Fernando Navarro<sup>2,6</sup>, Rouzbeh Esfandiari<sup>7</sup>, Isabel Rauscher<sup>2</sup>, Bjoern Menze<sup>6,8</sup>, David Elashoff<sup>5</sup>, Ebrahim S. Delpassand<sup>7</sup>, Ken Herrmann<sup>3</sup>, Johannes Czernin<sup>1</sup>, Michael S. Hofman<sup>9</sup>, Jeremie Calais<sup>1</sup>, Wolfgang P. Fendler<sup>3</sup>, and Matthias Eiber<sup>2</sup>

<sup>1</sup>Ahmanson Translational Theranostics Division, Department of Molecular and Medical Pharmacology, UCLA, Los Angeles, California; <sup>2</sup>Department of Nuclear Medicine, Klinikum rechts der Isar, Technical University Munich, Munich, Germany; <sup>3</sup>Department of Nuclear Medicine, University of Duisburg–Essen and German Cancer Consortium–University Hospital Essen, Essen, Germany; <sup>4</sup>Department of Nuclear Medicine, Heidelberg University Hospital, Heidelberg, Germany; <sup>5</sup>Department of Medicine Statistics Core, David Geffen School of Medicine, UCLA, Los Angeles, California; <sup>6</sup>Department of Informatics, Technical University Munich, Munich, Germany; <sup>7</sup>Excel Diagnostics and Nuclear Oncology Center, Houston, Texas; <sup>8</sup>Department of Quantitative Biomedicine, University of Zurich, Zurich, Switzerland; and <sup>9</sup>Prostate Cancer Theranostics and Imaging Centre of Excellence, Molecular Imaging and Therapeutic Nuclear Medicine, Peter MacCallum Cancer Centre, and Sir Peter MacCallum Department of Oncology, University of Melbourne, Melbourne, Victoria, Australia

We aimed to systematically determine the impact of tumor burden on  $^{68}\text{Ga}$ -prostate-specific membrane antigen-11 ( $^{68}\text{Ga}$ -PSMA) PET biodistribution by the use of quantitative measurements. **Methods:** This international multicenter, retrospective analysis included 406 men with prostate cancer who underwent  $^{68}\text{Ga}$ -PSMA PET/CT. Of these, 356 had positive findings and were stratified by quintiles into a very low (quintile 1,  $\leq 25\text{ cm}^3$ ), low (quintile 2,  $25\text{--}189\text{ cm}^3$ ), moderate (quintile 3,  $189\text{--}532\text{ cm}^3$ ), high (quintile 4,  $532\text{--}1,355\text{ cm}^3$ ), or very high (quintile 5,  $\geq 1,355\text{ cm}^3$ ) total PSMA-positive tumor volume (PSMA-VOL). PSMA-VOL was obtained by semiautomatic segmentation of total tumor lesions using qPSMA software. Fifty prostate cancer patients with no PSMA-positive lesions (negative scan) served as a control group. Normal organs, which included salivary glands, liver, spleen, and kidneys, were semiautomatically segmented using  $^{68}\text{Ga}$ -PSMA PET images, and  $\text{SUV}_{\text{mean}}$  was obtained. Correlations between the  $\text{SUV}_{\text{mean}}$  of normal organs and PSMA-VOL as continuous and categorical variables by quintiles were evaluated. **Results:** The median PSMA-VOL was  $302\text{ cm}^3$  (interquartile range [IQR],  $47\text{--}1,076\text{ cm}^3$ ). The median  $\text{SUV}_{\text{mean}}$  of salivary glands, kidneys, liver, and spleen was 10.0 (IQR,  $7.7\text{--}11.8$ ), 26.0 (IQR,  $20.0\text{--}33.4$ ), 3.7 (IQR,  $3.0\text{--}4.7$ ), and 5.3 (IQR,  $4.0\text{--}7.2$ ), respectively. PSMA-VOL showed a moderate negative correlation with the  $\text{SUV}_{\text{mean}}$  of the salivary glands ( $r = -0.44$ ,  $P < 0.001$ ), kidneys ( $r = -0.34$ ,  $P < 0.001$ ), and liver ( $r = -0.30$ ,  $P < 0.001$ ) and a weak negative correlation with the spleen  $\text{SUV}_{\text{mean}}$  ( $r = -0.16$ ,  $P = 0.002$ ). Patients with a very high PSMA-VOL (quintile 5,  $\geq 1,355\text{ cm}^3$ ) had a significantly lower PSMA uptake in the salivary glands, kidneys, liver, and spleen than did the control group, with an average difference of  $-38.1\%$ ,  $-40.0\%$ ,  $-43.2\%$ , and  $-34.9\%$ , respectively ( $P < 0.001$ ). **Conclusion:** Tumor sequestration affects  $^{68}\text{Ga}$ -PSMA biodistribution in normal organs. Patients with a very high tumor load showed a significantly lower uptake of  $^{68}\text{Ga}$ -PSMA in normal organs, confirming a tumor sink effect. As similar effects might occur with PSMA-targeted radioligand therapy, these

patients might benefit from increased therapeutic activity without exceeding the radiation dose limit for organs at risk.

**Key Words:** PET; tumor sink effect; prostate cancer; PSMA; Ga-PSMA; radioligand therapy

**J Nucl Med 2022; 63:226–232**  
DOI: 10.2967/jnumed.121.261906

**T**he biodistribution of radiolabeled prostate-specific membrane antigen (PSMA) ligands in prostate cancer patients reflects a complex interaction between tracer uptake, retention, and excretion in pathologic and normal tissues. Accumulation of PSMA ligands is also observed in nontumoral tissues, such as liver, spleen, kidneys and salivary glands, which have been shown to exhibit a high variability in tracer uptake (1). In clinical practice, it is observed that the relative accumulation of PSMA ligands in normal tissue is inversely related to the PSMA-positive tumor burden. This phenomenon is commonly referred to as the tumor sink effect, in which high tracer uptake in extensive tumor masses reduces tracer accumulation in normal tissues (2–4).

PSMA-targeted radioligand therapy with  $^{177}\text{Lu}$  ( $^{177}\text{Lu}$ -PSMA-RLT) demonstrated positive results in phase II trials of men with metastatic castration-resistant prostate cancer (5–7) and is currently being investigated in the metastatic hormone-sensitive prostate cancer setting (8). If confirmed, a tumor sink effect might have implications for  $^{177}\text{Lu}$ -PSMA-RLT by providing the rationale for individual adaptation of therapeutic dosages to the patient tumor load (9). Patients with a high tumor load might benefit from a higher injected activity per cycle without exceeding radiation dose limit in organs at risk, particularly the salivary glands and the kidneys, which are considered dose-limiting organs (10).

Besides their therapeutic use, PSMA ligands have also been applied for diagnostic purposes using tumor-specific whole-body PET imaging (e.g.,  $^{68}\text{Ga}$ -PSMA-11 [ $^{68}\text{Ga}$ -PSMA]) (11).  $^{68}\text{Ga}$ -PSMA PET imaging provides reliable estimates of the biodistribution of therapeutic PSMA ligands (12). Several reports have previously investigated the sink effect in PSMA-targeted PET; however, the data reported are contradictory (13,14).

Received Jan. 4, 2021; revision accepted May 4, 2021.  
For correspondence or reprints, contact Andrei Gafita (agafita@mednet.ucla.edu).  
\*Contributed equally to this work.  
Guest editor: Todd Peterson, Vanderbilt University  
Published online May 28, 2021.  
COPYRIGHT © 2022 by the Society of Nuclear Medicine and Molecular Imaging.

To address this question, we aimed here to quantify the effect of tumor burden on  $^{68}\text{Ga}$ -PSMA PET organ biodistribution by the use of quantitative measurements. We hypothesized that the tumor sequestration of the injected radiopharmaceutical in patients with a high disease burden leads to a significant decrease in uptake in nontumoral tissue.

## MATERIALS AND METHODS

### Study Design and Patient Population

Data of men with histologically proven prostate cancer who underwent  $^{68}\text{Ga}$ -PSMA PET imaging at 6 institutions were screened retrospectively. This international multicenter study was designed to include patients with both PSMA-positive and PSMA-negative PET scans. First, 2 preestablished databases of patients with known metastatic disease on  $^{68}\text{Ga}$ -PSMA PET were screened: the first was a dataset of men with metastatic hormone-sensitive prostate cancer who received  $^{68}\text{Ga}$ -PSMA PET in the setting of initial staging or biochemical recurrence ( $n = 100$ ), and the second was a dataset of men with metastatic castration-resistant prostate cancer who received  $^{68}\text{Ga}$ -PSMA PET before initiation of  $^{177}\text{Lu}$ -PSMA-RLT (15,16) ( $n = 285$ ). Next, 50 men with biochemical recurrence after definitive treatment of prostate cancer who had no tumor lesions on  $^{68}\text{Ga}$ -PSMA PET were randomly selected from the institution database (17) to serve as a control group. The flowchart of this study is displayed in Figure 1. Inclusion criteria were imaging with  $^{68}\text{Ga}$ -PSMA PET/CT and data evaluable by the segmentation software. Patients who underwent  $^{18}\text{F}$ -labeled PSMA PET/CT or PSMA-targeted PET/MRI were excluded.

Of 435 screened men with prostate cancer, 406 were eligible and were included in the study. Overall, 162 (40%) patients underwent the scan in a prospective setting (NCT02940262, NCT03042312, and ACTRN12615000912583), whereas 244 (60%) underwent the scan under compassionate-access programs. In a subanalysis, we identified 20 patients from the metastatic castration-resistant prostate cancer cohort who had a high disease burden on the baseline  $^{68}\text{Ga}$ -PSMA PET at the initiation of  $^{177}\text{Lu}$ -PSMA-RLT and received a follow-up scan after 2 treatment cycles, as previously described (Fig. 1) (18).

All scans were performed between October 2014 and August 2019. All patients gave written consent to undergo a clinical  $^{68}\text{Ga}$ -PSMA

PET scan. The need for study-specific consent was waived by the Ethics Committee.

### Outcomes

The primary objective of this study was to determine the impact of total tumor burden on  $^{68}\text{Ga}$ -PSMA uptake in normal organs on PET imaging. On the basis of reproducibility data that showed a normal variability of up to 30% between 2 SUV measurements of normal organs (19,20), the tumor sink effect was a priori defined as a 30% or greater decline in  $^{68}\text{Ga}$ -PSMA uptake in normal organs, compared with the control group.

The secondary objective was to determine the impact of changes in tumor volume on normal-organ  $^{68}\text{Ga}$ -PSMA uptake and the appearance of new lesions on the interim PET scan after 2 cycles of  $^{177}\text{Lu}$ -PSMA-RLT. Patients were stratified into responders versus nonresponders to  $^{177}\text{Lu}$ -PSMA-RLT on the basis of a PSMA tumor volume decline of 30% on the interim PET scan, as previously described (18).

### Imaging Protocol

Patients received an average ( $\pm$ SD) of  $155 \pm 53$  MBq of  $^{68}\text{Ga}$ -PSMA-HBED-CC (PSMA-11) via complete intravenous injection. Image acquisition was started after an average of  $64 \pm 17$  min after injection. Static, whole-body images were used (mid thighs to skull vertex). All scans were corrected for decay, scatter, and random coincidences. Data from the CT scan were used for attenuation correction. Images were acquired using GE Healthcare Discovery 710 ( $n = 50$ ), Siemens Biograph mCT ( $n = 244$ ), Siemens Biograph 64 ( $n = 92$ ), and Siemens Biograph 16 ( $n = 20$ ) scanners. All images were obtained in accordance with the  $^{68}\text{Ga}$ -PSMA PET joint guideline of the European Association of Nuclear Medicine and the Society of Nuclear Medicine and Molecular Imaging, ensuring harmonized quantification (21). Standard vendor-provided image reconstructions were used. The applied reconstruction parameters are summarized in Supplemental Table 1 (supplemental materials are available at <http://jnm.snmjournals.org>).

### Image Analyses

Tumor segmentation was performed centrally by a nuclear medicine physician using qPSMA software (22) to obtain total PSMA-positive tumor volume (PSMA-VOL). PSMA-VOL was categorized into 5 groups based on quintiles: very low (quintile 1:  $\leq 20$ th percentile), low (quintile 2: 20th–40th percentiles), moderate (quintile 3: 40th–60th percentiles), high (quintile 4: 60th–80th percentiles), and very high (quintile 5:  $\geq 80$ th percentile). Organs that typically exhibit moderate to high PSMA-ligand uptake were assessed: salivary glands, kidneys, liver, and spleen (23). The entire volume of each normal organ was segmented automatically using an in-house algorithm. The annotations obtained using the automatic algorithm were reviewed by a nuclear medicine physician using PET images and adjusted manually when necessary.  $\text{SUV}_{\text{mean}}$  and  $\text{SUV}_{\text{max}}$  not corrected for lean body mass or body surface area were obtained to measure  $^{68}\text{Ga}$ -PSMA uptake in normal organs. The liver was not analyzed in patients with PSMA-positive liver metastases. Salivary glands not entirely included in the PET field of view were excluded from the analysis.

### Statistical Analyses

Values were reported as mean  $\pm$  SD or median and interquartile range (IQR). Correlations between PSMA-VOL and normal-organ tracer uptake were evaluated using the Spearman correlation coefficient ( $\rho$ ) with a 2-tailed test for significance. Kruskal–Wallis testing was performed to compare the degree of  $^{68}\text{Ga}$ -PSMA uptake in normal organs among the 6 tumor-burden groups (control, very low, low, moderate, high, and very high). Differences among groups were tested

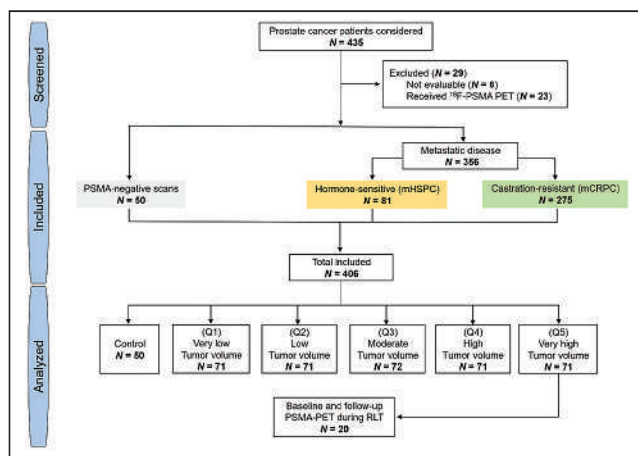


**FIGURE 1.** Study flowchart. mCRPC = metastatic castration-resistant prostate cancer; mHSPC = metastatic hormone-sensitive prostate cancer; Q = quintile.

for significance against no difference. A *P* value of 0.05 or less was considered statistically significant. The *P* values were not adjusted for multiple testing. Analyses were performed using SPSS Statistics, version 26.0 (IBM Corp.), and R Statistics (version 3.4.0).

## RESULTS

Population characteristics are summarized in Table 1. Liver uptake was not analyzed in 40 patients because of PSMA-positive liver metastases. The salivary glands of 2 patients could not be delineated and were excluded from the analysis.

### Tumor Volume and Organ SUV Measurements

The median  $SUV_{mean}$  of salivary glands, kidneys, liver, and spleen was 10.0 (IQR, 7.7–11.8), 26.0 (IQR, 20.0–33.4), 3.7 (IQR, 3.0–4.7), and 5.3 (IQR, 4.0–7.2), respectively (Fig. 2), whereas the median  $SUV_{max}$  was 21.3 (IQR, 16.9–27.0), 51.8 (IQR, 37.8–67.9), 9.7 (IQR, 7.8–11.8), and 10.1 (IQR, 8.0–12.8), respectively (Supplemental Fig. 1). The median PSMA-VOL was 302  $cm^3$  (IQR, 47–1,076  $cm^3$ ). The 20th, 40th, 60th, and 80th percentile of PSMA-VOL was 25, 189, 532, and 1,355  $cm^3$ , respectively. The median PSMA-VOL in the very low ( $n = 71$ ), low ( $n = 71$ ), moderate ( $n = 71$ ), high ( $n = 72$ ), and very high ( $n = 71$ ) groups was 5  $cm^3$  (IQR, 2–11  $cm^3$ ), 76  $cm^3$  (IQR, 46–123  $cm^3$ ), 302  $cm^3$  (IQR, 235–387  $cm^3$ ), 899  $cm^3$  (IQR, 685–1,078  $cm^3$ ), and 2,336  $cm^3$  (IQR, 1,852–3,080  $cm^3$ ), respectively. Examples of  $^{68}Ga$ -PSMA PET studies for each tumor volume group are presented in Figure 3.

### Correlations of Tumor Volume with Normal-Organ Uptake

PSMA-VOL showed a statistically significant moderate negative correlation with the  $SUV_{mean}$  of salivary glands ( $r = -0.44$ ,  $P < 0.001$ ), kidneys ( $r = -0.34$ ,  $P < 0.001$ ), and liver ( $r = -0.30$ ,  $P < 0.001$ ) and a statistically significant weak negative correlation

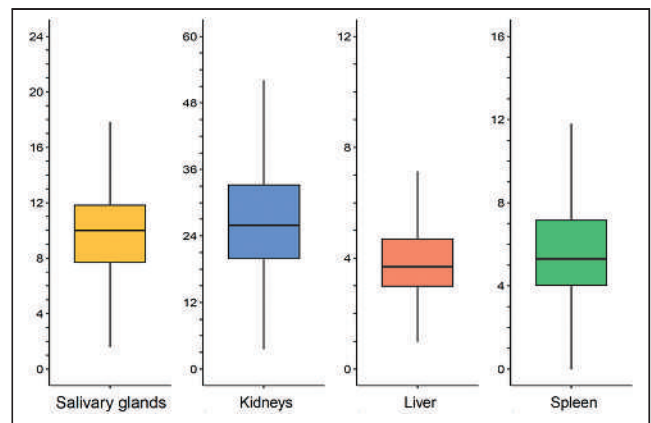


**FIGURE 2.**  $SUV_{mean}$  of normal organs. Horizontal lines represent median value.

with spleen  $SUV_{mean}$  ( $r = -0.16$ ,  $P = 0.002$ ). PSMA-VOL showed a statistically significant moderate negative correlation with the  $SUV_{max}$  of salivary glands ( $r = -0.35$ ,  $P < 0.001$ ) and a statistically significant weak negative correlation with kidneys ( $r = -0.26$ ,  $P < 0.001$ ), liver ( $r = -0.23$ ,  $P < 0.001$ ), and spleen  $SUV_{max}$  ( $r = -0.19$ ,  $P < 0.001$ ).

### Normal-Organ Uptake Stratified by Tumor Volume Groups

The absolute values and differences in SUVs of normal organs in the very low, low, moderate, high, and very high PSMA-VOL groups compared with the control group are given in Table 2, Figure 4, and Supplemental Figure 2. In general, a higher PSMA-VOL was associated with lower  $^{68}Ga$ -PSMA uptake in normal organs.

The  $SUV_{mean}$  of salivary glands, kidneys, liver, and spleen was significantly lower in patients with a very high PSMA-VOL

**TABLE 1**  
Characteristics of Patients

Characteristics	Control ( $n = 50$ )	mHSPC ( $n = 81$ )	mCRPC ( $n = 275$ )
Age (y)	71 (69–74)	69 (63–72)	72 (66–76)
Weight (kg)	86 (80–99)	81 (75–92)	80 (72–92)
Injected activity (MBq)	185 (183–196)	128 (96–153)	155 (112–195)
Acquisition time (min)	60 (55–66)	65 (59–82)	60 (53–67)
PSA (ng/mL)*	0.4 (0.2–0.8)	4.0 (1–11)	130 (37–431)
PSMA-VOL ( $cm^3$ )	0	7 (2–37)	563 (194–1,358)
Site of disease on PSMA-PET			
Bone	0	70 (86%)	256 (93%)
Lymph nodes	0	34 (42%)	202 (74%)
Bone + lymph nodes	0	27 (33%)	183 (67%)
Viscera <sup>†</sup>	0	10 (12%)	82 (30%)
Bone + lymph nodes + viscera	0	1 (1%)	59 (22%)

\*Data missing for 10 patients.  
<sup>†</sup>Viscera include lung, liver, rectum, pancreas, peritoneal, brain and adrenal.  
 mHSPC = metastatic hormone-sensitive prostate cancer; mCRPC = metastatic castration-resistant prostate cancer; PSA = prostate-specific antigen.  
 Qualitative data are number and percentage; continuous data are median and IQR.

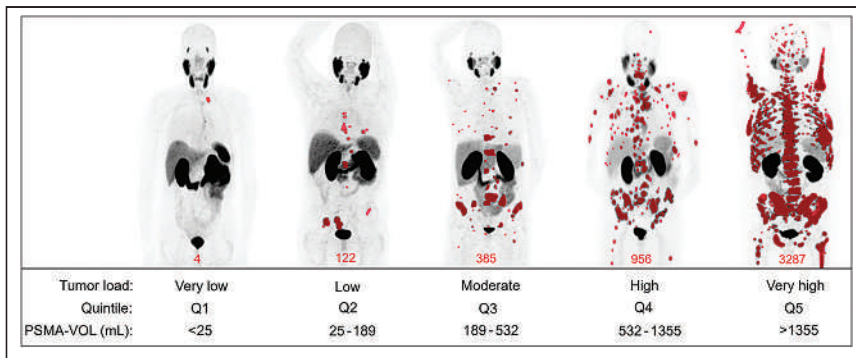


**FIGURE 3.** Examples of maximum-intensity-projection images of PSMA PET for each tumor load group. PSMA-positive tumor segmentation is highlighted in red.

than in the control group ( $P < 0.001$ ), with an average difference of  $-38.1\%$  (95% CI,  $-47.8\%$ ,  $-29.7\%$ ),  $-40.0\%$  (95% CI,  $-50.3\%$ ,  $-31.1\%$ ),  $-43.2\%$  (95% CI,  $-55.6\%$ ,  $-30.8\%$ ), and  $-34.9\%$  (95% CI,  $-49.8\%$ ,  $-21.3\%$ ), respectively.

The  $SUV_{max}$  of salivary glands, kidneys, and liver was significantly lower in patients with a very high PSMA-VOL than in the control group ( $P < 0.05$ ), with an average difference of  $-26.6\%$  (95% CI,  $-38.9\%$ ,  $-15.1\%$ ),  $-28.4\%$  (95% CI,  $-39.4\%$ ,  $-18.0\%$ ), and  $-17.9\%$  (95% CI,  $-30.0\%$ ,  $-4.2\%$ ), respectively.

#### Changes in Tumor Volume and Normal Uptake

Of 20 patients included in this analysis, 10 (50%) were responders achieving a PSMA-VOL decline of at least 30% on the interim scan relative to baseline. The average change in PSMA-VOL in responders was  $-47.0\%$  (95% CI,  $-55.7\%$ ,  $-38.4\%$ ), whereas in nonresponders it was  $+6.3\%$  (95% CI,  $-14.4\%$ ,  $+26.9\%$ ). The average difference in  $SUV_{mean}$  of salivary glands, liver, kidneys and spleen in responders was  $+61.1\%$  (95% CI,  $-3.5\%$ ,  $+125.7\%$ ;  $P = 0.06$ ),  $+33.4\%$  (95% CI,  $-17.2\%$ ,  $+83.9\%$ ;  $P = 0.17$ ),  $+74.0\%$  (95% CI,  $+8.7\%$ ,  $+139.2\%$ ;  $P = 0.03$ ), and  $+61.8\%$  (95% CI,  $+21.4\%$ ,  $+102.2\%$ ;  $P = 0.007$ ), respectively. In nonresponders, the average change in salivary glands, kidneys, liver and spleen was  $-2.5\%$  (95% CI,  $-15.3\%$ ,  $+10.3\%$ ;  $P = 0.67$ ),  $+10.7\%$  (95% CI,  $-6.1\%$ ,  $+28.3\%$ ;  $P = 0.07$ ),  $+12.1\%$  (95% CI,  $-6.1\%$ ,  $+30.3\%$ ;  $P = 0.16$ ), and  $+23.8\%$  (95% CI,  $-18.9\%$ ,  $+66.5\%$ ;  $P = 0.24$ ), respectively. Individual changes in PSMA-VOL,  $SUV_{mean}$ , and  $SUV_{max}$  for normal organs in  $^{68}\text{Ga}$ -PSMA PET are given in Supplemental Table 2. The appearance of new PSMA-positive lesions on interim scans was observed in 1 (10%) responder and 7 (70%) nonresponders.

#### DISCUSSION

In this multicenter retrospective analysis, patients with a high tumor burden demonstrated significantly lower normal-organ uptake on  $^{68}\text{Ga}$ -PSMA PET. Our primary endpoint of an SUV difference numerically greater than 30% in salivary glands and kidneys compared with the control group was met in patients with a very high tumor volume ( $\geq 1,355 \text{ cm}^3$ ).

Controversial results on the tumor sink effect in PSMA-targeted PET have been reported. Gaertner et al. (13) found a decline of 36%–43%, 45%, 25%, and 19% of  $^{68}\text{Ga}$ -PSMA uptake in salivary glands, kidneys, liver, and spleen, respectively, in metastatic castration-resistant prostate cancer patients who were classified

visually as having a high PSMA-positive tumor burden on PET. In contrast, Werner et al. (14) found in  $^{18}\text{F}$ -DCFPyL PET a significant correlation only for kidney uptake with PSMA-VOL. However, these results are not surprising, since only patients with early-stage prostate cancer having a low tumor burden were included (median PSA, 3.2 ng/mL) whereas a sink effect is expected to occur at high tumor volume levels. Limitations of these studies also include the small sample size, which was not powered for uptake correlation, use of a small region of interest for measuring tracer uptake in large organs (e.g., liver or spleen), and visual assessment of disease burden. To overcome these, in the present analysis we segmented semiautomatically on  $^{68}\text{Ga}$ -PSMA PET the total disease burden and the entire volume of normal organs. Moreover, for a complete understanding of the associations between disease burden and normal uptake, we included patients from the entire spectrum of prostate cancer and categorized them into 6 subgroups: PSMA-negative, very low, low, moderate, high, and very high tumor volume.

The highest correlation of normal-organ uptake with tumor burden was noticed in salivary glands, followed by kidneys, liver, and, to a lower degree, spleen. However, the  $SUV_{mean}$  of kidneys and liver was significantly lower beginning with patients with a low tumor volume (25–189  $\text{cm}^3$ ), whereas for salivary glands it was significantly lower only in patients with high (532–1,355  $\text{cm}^3$ ) and very high ( $\geq 1,355 \text{ cm}^3$ ) tumor volumes.  $SUV_{mean}$  of normal organs had a weaker correlation with SUV. This observation underlines the importance of using  $SUV_{mean}$  over  $SUV_{max}$  for measuring tracer uptake in normal organs in PET imaging, which captures the entire organ uptake and does not limit the uptake to 1 voxel. Two limitations of  $SUV_{max}$  are worth mentioning here: the variability when structures with heterogeneous uptake are measured (e.g., liver) and the dependence on the reconstruction parameters (e.g., potential use of point-spread function). These limitations can have important implications, particularly in a multicentric setting in which the harmonization protocol can affect  $SUV_{max}$  findings.

Our study has clinical implications. When performing PSMA-targeted RLT, the therapeutic activity is limited because of potential toxicity to organs at risk. Salivary glands and kidneys are the main critical organs with the highest absorbed dose (10). Moreover, xerostomia was reported as the main reason for treatment discontinuation during  $^{225}\text{Ac}$ -PSMA-RLT (24). Our findings suggest that candidates for  $^{177}\text{Lu}$ -PSMA-RLT with a very high tumor volume ( $\geq 1,355 \text{ cm}^3$  for our analysis defined by quintiles) on the screening PSMA-PET have a significantly lower normal-organ uptake and might benefit from an increased therapeutic activity without exceeding the radiation dose limit for organs at risk.

A first attempt toward individualizing therapeutic activity for  $^{177}\text{Lu}$ -PSMA-RLT was made by Hofman et al. (5), in a study in which  $^{177}\text{Lu}$ -PSMA-617 activity was increased by up to 20% in heavily metastasized patients. Dosimetry data from the same cohort showed that a higher absorbed dose to tumor was associated with higher rates of PSA response and that tumor volume delineated on pretherapeutic  $^{68}\text{Ga}$ -PSMA PET is inversely correlated with salivary gland and kidney absorbed radiation dose (25). Hence, the sink effect may represent a great opportunity for

**TABLE 2**  
Comparison of PSMA-VOL Groups and <sup>68</sup>Ga-PSMA Uptake in Normal Organs

Organ	Tumor load group	PSMA-VOL (cm <sup>3</sup> )	SUV <sub>mean</sub>			SUV <sub>max</sub>		
			Median	Difference from control (%)	P	Median	Difference from control (%)	P
Salivary gland	Control	0	11.0 (10.0–12.4)	–	–	21.8 (19.3–26.2)	–	–
	Very low	<25	10.3 (8.3–13.7)	–6.4 (–15.2, +3.4)	0.189	22.9 (18.3–29.5)	+5.0 (–4.0, +14.2)	0.585
	Low	25–189	11.0 (9.1–12.9)	+0.5 (–9.8, +10.5)	0.239	21.9 (18.1–29.2)	+0.5 (–9.1, +9.9)	0.768
	Moderate	189–532	10.8 (9.1–12.0)	–1.8 (–9.8, +5.1)	0.195	23.4 (20.1–29.0)	+7.3 (–2.5, +18.0)	0.352
	High	532–1,355	8.3 (6.6–10.3)	–24.5 (–33.3, –17.0)	<0.001	18.3 (13.8–22.5)	–16.0 (–7.2, –25.5)	<0.001
Kidney	Very high	>1,355	6.8 (5.5–9.4)	–38.1 (–47.8, –29.7)	<0.001	16.0 (11.2–23.0)	–26.6 (–15.1, –38.9)	<0.001
	Control	0	34.7 (26.4–37.8)	–	–	59.8 (49.5–68.1)	–	–
	Very low	<25	30.3 (23.0–35.8)	–12.6 (–22.0, +2.2)	0.125	55.4 (43.8–69.5)	–7.4 (–17.8, +3.1)	0.394
	Low	25–189	26.7 (20.0–33.9)	–23.0 (–34.1, –13.5)	0.001	52.6 (37.3–69.7)	–12.0 (–22.9, –1.4)	0.054
	Moderate	189–532	26.5 (19.3–32.8)	–23.6 (–32.0, –15.2)	<0.001	54.2 (37.4–71.2)	–9.4 (–12.5, +3.0)	0.085
Liver	High	532–1,355	24.0 (18.9–31.4)	–30.8 (–42.1, –20.3)	<0.001	47.7 (35.2–65.3)	–20.2 (–30.5, –9.8)	0.005
	Very high	>1,355	20.8 (15.1–23.6)	–40.0 (–50.3, –31.1)	<0.001	42.8 (31.4–52.8)	–28.4 (–39.4, –18.0)	<0.001
	Control	0	4.4 (3.6–5.5)	–	–	9.5 (8.2–11.2)	–	–
	Very low	<25	3.8 (3.2–5.2)	–13.6 (–25.0, +1.6)	0.070	11.0 (8.5–12.4)	15.8 (+2.4, +25.9)	0.073
	Low	25–189	3.9 (3.1–4.5)	–11.4 (–20.3, –3.0)	0.010	10.1 (7.5–11.6)	+6.3 (–4.1, +15.2)	0.886
Spleen	Moderate	189–532	3.9 (3.3–4.8)	–11.4 (–22.0, –1.7)	0.033	9.9 (8.5–12.2)	+4.2 (–9.8, +17.1)	0.451
	High	532–1,355	3.7 (3.0–4.9)	–15.9 (–25.9, –16.1)	0.008	9.3 (7.6–11.6)	–2.1 (–11.8, +7.9)	0.842
	Very high	>1,355	2.5 (1.8–3.5)	–43.2 (–55.6, –30.8)	<0.001	7.8 (6.4–10.6)	–17.9 (–30.0, –4.2)	0.017
	Control	0	6.3 (4.6–8.2)	–	–	10.3 (8.2–13.4)	–	–
	Very low	<25	5.5 (4.2–6.8)	–12.7 (–25.5, +1.2)	0.074	10.9 (9.3–12.6)	+5.8 (–6.1, +17.6)	0.384
Spleen	Low	25–189	5.3 (4.5–7.6)	–14.9 (–30.0, +2.4)	0.175	10.2 (8.2–13.7)	–1.0 (–9.8, +8.0)	0.888
	Moderate	189–532	5.9 (4.4–7.8)	–6.3 (–18.9, +6.2)	0.422	11.0 (8.4–13.9)	+6.8 (–6.2, +19.3)	0.492
	High	532–1,355	4.8 (3.9–7.2)	–23.8 (–37.3, –6.8)	0.012	9.2 (7.5–12.9)	–10.7 (–23.9, +3.4)	0.271
	Very high	>1,355	4.1 (3.3–6.0)	–34.9 (–49.8, –21.3)	<0.001	9.1 (6.4–12.2)	–11.7 (–24.4, +1.9)	0.068

Data are median and IQR, or difference and 95% CI.

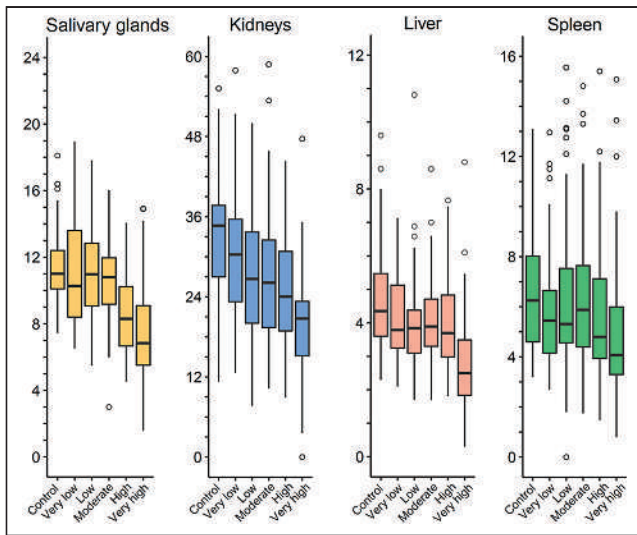


**FIGURE 4.** SUV<sub>mean</sub> of normal organs stratified by tumor load.

<sup>177</sup>Lu-PSMA-RLT to safely increase therapeutic activity in order to improve antitumor efficacy. Besides toxicity, it might also be logical to administer a higher treatment activity when the tumor load is higher, in order to avoid undertreatment.

Overall, the present study establishes tumor sequestration as a major factor affecting <sup>68</sup>Ga-PSMA biodistribution in patients with a high disease burden, which leads to a sink effect that decreases activity concentrations in normal organs. In addition, we found that changes in tumor volume during <sup>177</sup>Lu-PSMA-RLT impact the normal uptake on follow-up <sup>68</sup>Ga-PSMA PET images. This finding emphasizes the potential utility of repeated dosimetry studies during <sup>177</sup>Lu-PSMA-RLT when individualizing therapeutic dosage. Only 1 patient (without a decrease in <sup>68</sup>Ga-PSMA uptake in normal organs; Supplemental Table 2) had new lesions on the follow-up scan, suggesting that new lesions on PSMA posttreatment scans are likely to be treatment-related. Nevertheless, additional studies investigating the impact of the sink effect on intratumor heterogeneity are warranted to provide additional insights on this phenomenon.

Strengths of this study include the multicenter setting, large patient population, and use of full quantitative measurements for tumor burden assessment. The major limitation of this study is the use of a single static PET image protocol, and thus, our results should be interpreted with caution in the framework of <sup>177</sup>Lu-PSMA-RLT. In addition, we are unable to analyze the influence of potential effects arising from different specific activities. However, given the low half-life of <sup>68</sup>Ga and a standardized production, no large-scale (>10<sup>2</sup>) difference might be present. Further, we used only SUV normalized to body weight as a quantitative parameter of PET signal. Alternative quantitative parameters have been described in the literature, that is, SUV normalized to lean body mass (26) or the ratio of tumor uptake to blood-pool uptake (27), although only at a research level. Further studies to support their implementation in clinical practice are awaited. Correlations with dosimetry data with multiple time points are warranted to establish pretherapeutic PSMA-targeted PET as a quantitative tool for individualizing therapeutic doses.

## CONCLUSION

Tumor sequestration affects <sup>68</sup>Ga-PSMA biodistribution by decreasing the activity concentration in normal organs, confirming the tumor sink effect. A relevant sink effect was noticed in patients with a very high tumor burden ( $\geq 1,355 \text{ cm}^3$ ). Because of favorable uptake ratios, PSMA-targeted RLT with increased activity regimens should be assessed in patients with a very high tumor volume. Repeated dosimetry during PSMA-targeted RLT should be considered, in order not to miss the impact of changes in tumor burden on dose distribution. Further studies are warranted to establish pretherapeutic PSMA-targeted PET as a tool for individual activity adaptation in PSMA-targeted RLT.

## DISCLOSURE

This work was partially supported by the Jonsson Comprehensive Cancer Center fellowship award. Andrei Gafita is the recipient of the Jonsson Comprehensive Cancer Center fellowship award and the Dr. Christiaan Schiepers postdoctoral fellowship award. Jeremie Calais is supported by the Prostate Cancer Foundation (2020 Young Investigator Award 20YOUN05, 2019 Challenge Award 19CHAL02) and the Society of Nuclear Medicine and Molecular Imaging (2019 Molecular Imaging Research Grant for Junior Academic Faculty) and reports prior consulting activities outside the submitted work for Advanced Accelerator Applications, Blue Earth Diagnostics, Curium Pharma, GE Healthcare, Janssen Pharmaceuticals, Progenics Pharmaceuticals, Radiomedix, and Telix Pharmaceuticals. Michael Hofman is supported by grants from the Prostate Cancer Foundation, Movember Foundation, Australian Government Medical Research Future Fund, Prostate Cancer Foundation of Australia, and U.S. Department of Defence and reports honoraria for lectures from Astellas, Janssen, Mundipharma and advisory fees from Merck/MSD. Wolfgang Fendler received financial support from the German Research Foundation (Deutsche Forschungsgemeinschaft grant FE1573/3-1/659216), Mercator Research Center Ruhr (MERCUR, An-2019-0001), IFORES (D/107-81260, D/107-30240), Doktor Robert Pflieger-Stiftung, and Wiedenfeld-Stiftung/Stiftung Krebsforschung Duisburg; was a consultant for Endocyte and BTG; and received fees from Radio-Medix and Bayer outside the submitted work. Hui Wang received financial support from the China Scholarship Council. Fernando Navarro received financial support from the German Research Foundation (Deutsche Forschungsgemeinschaft research training group grant GRK 2274). Matthias Eiber reports prior consulting activities for Blue Earth Diagnostics, Progenics Pharmaceuticals, and Point Biopharma and a patent application for rhPSMA outside the submitted work. Johannes Czernin is a founder and board member of, and holds equity in, Sofie Biosciences and Trethera Therapeutics and was a consultant for Endocyte Inc. (VISION trial steering committee), Actinium Pharmaceuticals, and Point Biopharma outside the submitted work. Intellectual property is patented by the University of California and licensed to Sofie Biosciences and Trethera Therapeutics. Ken Herrmann reports personal fees from Bayer, Sofie Biosciences, SIRTEX, Adacap, Curium, Endocyte, BTG, IPSEN, Siemens Healthineers, GE Healthcare, Amgen, Novartis, ymabs, Bain Capital, and MPM Capital outside the submitted work; other fees from Sofie Biosciences; nonfinancial support from ABX; and grants from BTG. No other potential conflict of interest relevant to this article was reported.

## KEY POINTS

**QUESTION:** Does the tumor burden impact the biodistribution of  $^{68}\text{Ga}$ -PSMA PET?

**PERTINENT FINDINGS:** In this international multicenter, retrospective study, we observed a significant negative correlation between PSMA-positive tumor burden and  $^{68}\text{Ga}$ -PSMA PET uptake in normal organs—that is, salivary glands, kidneys, liver, and spleen. Patients with a very high tumor burden ( $\geq 1,355\text{ cm}^3$  for our analysis defined by quintiles) had a significantly lower uptake of  $^{68}\text{Ga}$ -PSMA in normal organs.

**IMPLICATIONS FOR PATIENT CARE:** Our findings suggest that candidates for  $^{177}\text{Lu}$ -PSMA-RLT with a very high tumor volume on screening PSMA-PET have significantly lower normal-organ uptake and might benefit from an increased therapeutic activity without exceeding the radiation dose limit for organs at risk.

## REFERENCES

1. Pfob CH, Ziegler S, Graner FP, et al. Biodistribution and radiation dosimetry of  $^{68}\text{Ga}$ -PSMA HBED CC: a PSMA specific probe for PET imaging of prostate cancer. *Eur J Nucl Med Mol Imaging*. 2016;43:1962–1970.
2. Beauregard JM, Hofman MS, Kong G, Hicks RJ. The tumour sink effect on the biodistribution of  $^{68}\text{Ga}$ -DOTA-octreotate: implications for peptide receptor radionuclide therapy. *Eur J Nucl Med Mol Imaging*. 2012;39:50–56.
3. Viglianti BL, Wale DJ, Wong KK, et al. Effects of tumor burden on reference tissue standardized uptake for PET imaging: modification of PERCIST criteria. *Radiology*. 2018;287:993–1002.
4. Love C, Din AS, Tomas MB, Kalapparambath TP, Palestro CJ. Radionuclide bone imaging: an illustrative review. *Radiographics*. 2003;23:341–358.
5. Hofman MS, Violet J, Hicks RJ, et al. [ $^{177}\text{Lu}$ ]-PSMA-617 radionuclide treatment in patients with metastatic castration-resistant prostate cancer (LuPSMA trial): a single-centre, single-arm, phase 2 study. *Lancet Oncol*. 2018;19:825–833.
6. Emmett L, Crumbaker M, Ho B, et al. Results of a prospective phase 2 pilot trial of  $^{177}\text{Lu}$ -PSMA-617 therapy for metastatic castration-resistant prostate cancer including imaging predictors of treatment response and patterns of progression. *Clin Genitourin Cancer*. 2019;17:15–22.
7. Violet J, Sandhu S, Irvani A, et al. Long-term follow-up and outcomes of retreatment in an expanded 50-patient single-center phase II prospective trial of  $^{177}\text{Lu}$ -PSMA-617 theranostics in metastatic castration-resistant prostate cancer. *J Nucl Med*. 2020;61:857–865.
8. Privé BM, Janssen MJR, van Oort IM, et al. Lutetium-177-PSMA-I&T as metastases directed therapy in oligometastatic hormone sensitive prostate cancer, a randomized controlled trial. *BMC Cancer*. 2020;20:884.
9. Hofman MS, Hicks RJ. Peptide receptor radionuclide therapy for neuroendocrine tumours: standardized and randomized, or personalized? *Eur J Nucl Med Mol Imaging*. 2014;41:211–213.
10. Okamoto S, Thieme A, Allmann J, et al. Radiation dosimetry for  $^{177}\text{Lu}$ -PSMA I&T in metastatic castration-resistant prostate cancer: absorbed dose in normal organs and tumor lesions. *J Nucl Med*. 2017;58:445–450.
11. Hofman MS, Lawrentschuk N, Francis RJ, et al. Prostate-specific membrane antigen PET-CT in patients with high-risk prostate cancer before curative-intent surgery or radiotherapy (proPSMA): a prospective, randomised, multicentre study. *Lancet*. 2020;395:1208–1216.
12. Wang J, Zang J, Wang H, et al. Pretherapeutic  $^{68}\text{Ga}$ -PSMA-617 PET may indicate the dosimetry of  $^{177}\text{Lu}$ -PSMA-617 and  $^{177}\text{Lu}$ -EB-PSMA-617 in main organs and tumor lesions. *Clin Nucl Med*. 2019;44:431–438.
13. Gaertner FC, Halabi K, Ahmadzadehfard H, et al. Uptake of PSMA-ligands in normal tissues is dependent on tumor load in patients with prostate cancer. *Oncotarget*. 2017;8:55094–55103.
14. Werner RA, Bundschuh RA, Bundschuh L, et al. Semiquantitative parameters in PSMA-targeted PET imaging with [ $^{18}\text{F}$ ]DCFPyL: impact of tumor burden on normal organ uptake. *Mol Imaging Biol*. 2020;22:190–197.
15. Gafita A, Fendler WP, Hui W, et al. Efficacy and safety of  $^{177}\text{Lu}$ -labeled prostate-specific membrane antigen radionuclide treatment in patients with diffuse bone marrow involvement: a multicenter retrospective study. *Eur Urol*. 2020;78:148–154.
16. Gafita A, Calais J, Grogan TR, et al. Nomograms to predict outcome after LuPSMA radionuclide therapy in men with metastatic castration resistant prostate cancer: an international multicenter retrospective study. *Lancet Oncol*. 2021;22:1115–1125.
17. Fendler WP, Calais J, Eiber M, et al. Assessment of  $^{68}\text{Ga}$ -PSMA-11 PET accuracy in localizing recurrent prostate cancer: a prospective single-arm clinical trial. *JAMA Oncol*. 2019;5:856–863.
18. Gafita A, Weber W, Tauber R, Eiber M. Predictive value of interim PSMA PET during  $^{177}\text{Lu}$ -PSMA radioligand therapy for overall survival in patients with advanced prostate cancer [abstract]. *J Nucl Med*. 2019;60(suppl 1):73.
19. Pollard JH, Raman C, Zakharia Y, et al. Quantitative test-retest measurement of  $^{68}\text{Ga}$ -PSMA-HBED-CC in tumor and normal tissue. *J Nucl Med*. 2020;61:1145–1152.
20. olde Heuvel J, de Wit-van der Veen BJ, Donswijk ML, Slump CH, Stokkel MPM. Day-to-day variability of [ $^{68}\text{Ga}$ ]Ga-PSMA-11 accumulation in primary prostate cancer: effects on tracer uptake and visual interpretation. *EJNMMI Res*. 2020;10:132.
21. Fendler WP, Eiber M, Beheshti M, et al.  $^{68}\text{Ga}$ -PSMA PET/CT: joint EANM and SNMMI procedure guideline for prostate cancer imaging—version 1.0. *Eur J Nucl Med Mol Imaging*. 2017;44:1014–1024.
22. Gafita A, Bieth M, Krönke M, et al. qPSMA: semiautomatic software for whole-body tumor burden assessment in prostate cancer using  $^{68}\text{Ga}$ -PSMA11 PET/CT. *J Nucl Med*. 2019;60:1277–1283.
23. Pfob CH, Ziegler S, Graner FP, et al. Biodistribution and radiation dosimetry of  $^{68}\text{Ga}$ -PSMA HBED CC: a PSMA specific probe for PET imaging of prostate cancer. *Eur J Nucl Med Mol Imaging*. 2016;43:1962–1970.
24. Feuerecker B, Tauber R, Knorr K, et al. Activity and adverse events of actinium-225-PSMA-617 in advanced metastatic castration-resistant prostate cancer after failure of lutetium-177-PSMA. *Eur Urol*. 2021;79:343–350.
25. Violet J, Jackson P, Ferdinandus J, et al. Dosimetry of  $^{177}\text{Lu}$ -PSMA-617 in metastatic castration-resistant prostate cancer: correlations between pretherapeutic imaging and whole-body tumor dosimetry with treatment outcomes. *J Nucl Med*. 2019;60:517–523.
26. Gafita A, Calais J, Franz C, et al. Evaluation of SUV normalized by lean body mass (SUL) in  $^{68}\text{Ga}$ -PSMA11 PET/CT: a bi-centric analysis. *EJNMMI Res*. 2019;9:103.
27. Jansen BHE, Kramer GM, Cysouw MCF, et al. Healthy tissue uptake of  $^{68}\text{Ga}$ -prostate specific membrane antigen (PSMA),  $^{18}\text{F}$ -DCFPyL,  $^{18}\text{F}$ -fluoromethylcholine (FCH) and  $^{18}\text{F}$ -dihydrotestosterone (FDHT). *J Nucl Med*. 2019;60:1111–1117.

---

---

# aPROMISE: A Novel Automated PROMISE Platform to Standardize Evaluation of Tumor Burden in <sup>18</sup>F-DCFPyL Images of Veterans with Prostate Cancer

Nicholas Nickols<sup>1-4</sup>, Aseem Anand<sup>5-7</sup>, Kerstin Johnsson<sup>7</sup>, Johan Brynolfsson<sup>7</sup>, Pablo Borrelli<sup>8</sup>, Neil Parikh<sup>2</sup>, Jesus Juarez<sup>2</sup>, Lida Jafari<sup>9</sup>, Mattias Eiber<sup>10</sup>, and Matthew Rettig<sup>2,3,11</sup>

<sup>1</sup>Radiation Oncology Service, VA Greater Los Angeles Healthcare System, Los Angeles, California; <sup>2</sup>Department of Radiation Oncology, David Geffen School of Medicine, UCLA, Los Angeles, California; <sup>3</sup>Department of Urology, David Geffen School of Medicine, UCLA, Los Angeles, California; <sup>4</sup>Institute of Urologic Oncology, Jonsson Comprehensive Cancer Center, UCLA, Los Angeles, California; <sup>5</sup>Department of Translational Medicine, Division of Urological Cancer, Lund University, Malmö, Sweden; <sup>6</sup>Department of Medicine, Memorial Sloan Kettering Cancer Center, New York, New York; <sup>7</sup>Department of Data Science and Machine Learning, EXINI Diagnostic AB, Lund, Sweden; <sup>8</sup>Department of Clinical Physiology, Sahlgrenska University Hospital, Gothenburg, Sweden; <sup>9</sup>Imaging Service, VA Greater Los Angeles Healthcare System, Los Angeles, California; <sup>10</sup>Department of Nuclear Medicine, Klinikum Rechts der Isar, Technical University of Munich, Munich, Germany; and <sup>11</sup>Division of Hematology-Oncology, VA Greater Los Angeles Healthcare System, Los Angeles, California

Standardized staging and quantitative reporting are necessary to demonstrate the association of <sup>18</sup>F-DCFPyL PET/CT imaging with clinical outcome. This work introduces an automated platform, aPROMISE, to implement and extend the Prostate Cancer Molecular Imaging Standardized Evaluation (PROMISE) criteria. The objective is to validate the performance of aPROMISE in staging and quantifying disease burden in patients with prostate cancer who undergo prostate-specific antigen (PSMA) imaging. **Methods:** This was a retrospective analysis of 109 veterans with intermediate- or high-risk prostate cancer who underwent PSMA imaging. To validate the performance of aPROMISE, 2 independent nuclear medicine physicians conducted aPROMISE-assisted reads, resulting in standardized reports that quantify individual lesions and stage the patients. Patients were staged as having local disease only (miNOM0), regional lymph node disease only (miN1M0), metastatic disease only (miNOM1), or both regional and distant metastatic disease (miN1M1). The staging obtained from aPROMISE-assisted reads was compared with the staging by conventional imaging. Cohen pairwise  $\kappa$ -agreement was used to evaluate interreader variability. Correlation coefficients and intraclass correlation coefficients were used to evaluate the interreader variability of the quantitative assessment (molecular imaging PSMA [miPSMA] index) at each stage. Kendall tau and *t* testing were used to evaluate the association of miPSMA index with prostate-specific antigen and Gleason score. **Results:** All PSMA images of 109 veterans met the DICOM conformity and the requirements for the aPROMISE analysis. Both independent aPROMISE-assisted analyses demonstrated significant upstaging in patients with localized (23%, *n* = 20/87) and regional (25%, *n* = 2/8) tumor burden. However, a significant number of patients with bone metastases identified on conventional imaging (<sup>18</sup>F-NaF PET/CT) were downstaged (29%, *n* = 4/14). The comparison of the 2 independent aPROMISE-assisted reads demonstrated a high  $\kappa$ -agreement: 0.82 for miNOM0, 0.90 for miN1M0, and 0.77 for miNOM1. The Spearman correlation of quantitative miPSMA index was 0.93, 0.96, and 0.97, respectively. As a

continuous variable, miPSMA index in the prostate was associated with risk groups defined by prostate-specific antigen and Gleason score. **Conclusion:** We demonstrated the consistency of the aPROMISE platform between readers and observed substantial upstaging in PSMA imaging compared with conventional imaging. aPROMISE may contribute to broader standardization of PSMA imaging assessment and to its clinical utility in the management of prostate cancer patients.

**Key Words:** <sup>18</sup>F-DCFPyL; PSMA; aPROMISE; segmentation; quantification; standardization

**J Nucl Med 2022; 63:233–239**

DOI: 10.2967/jnumed.120.261863

**P**rostate cancer is the most common solid tumor in men, with an incidence of nearly 192,000 cases and nearly 30,000 deaths in the United States annually. Accurate staging of a patient with prostate cancer is critical for selection of appropriate treatment strategies, especially as applied to differentiating between those with localized or regional disease who can be treated with curative intent and those with metastatic disease. Whether surgery, radiation, and systemic hormone therapy or chemotherapy are appropriate for a given patient is driven largely by the clinical stage (1). According to the recently updated National Comprehensive Cancer Network guidelines, <sup>99m</sup>Tc-phosphonate bone scintigraphy (bone scanning) and CT or MRI remain the standard imaging modalities for prostate cancer staging. However, bone and CT scans have demonstrated limited diagnostic accuracy in earlier disease settings (2,3), in turn limiting the accurate staging necessary for optimal prostate cancer management.

Accurate detection of metastatic disease is a particularly important goal because metastatic prostate cancer requires a different treatment approach and carries a significantly worse prognosis than local disease. PET is a noninvasive technique that can image bone and soft tissue in a single modality, evaluate high-grade tumors that may not produce prostate-specific antigen (PSA), and

---

Received Dec. 23, 2020; revision accepted Apr. 23, 2021.  
For correspondence or reprints, contact: Matthew Rettig (mrettig@mednet.ucla.edu).  
Published online May 28, 2021.  
COPYRIGHT © 2022 by the Society of Nuclear Medicine and Molecular Imaging.

provide quantifiable data using the SUV. However, in prostate cancer, PET tracers that image metabolic pathways, such as  $^{11}\text{C}$ -choline,  $^{11}\text{C}$ -acetate, and  $^{18}\text{F}$ -FDG, suffer from suboptimal sensitivity and specificity in the detection of regional and distant metastatic disease. Recently, small ligands for PET imaging have been developed that target the cell-surface protein prostate-specific membrane antigen (PSMA), which is overexpressed in prostate cancer cells but is also expressed to some extent in other organs and blood vessels (4). Radiopharmaceuticals based on PSMA ligands have demonstrated high diagnostic accuracy for the detection of both regional and distant metastatic prostate cancer. The proPSMA trial demonstrated that PSMA PET/CT has greater staging accuracy than conventional imaging consisting of bone scanning and CT for initial staging of patients with high-risk prostate cancer (5). This supports the use of a single PSMA PET/CT scan rather than 2 conventional imaging modalities in this setting.

Recent efforts in standardizing the assessment of PSMA scans have resulted in several PSMA PET evaluation and reporting systems, including the PSMA Reporting and Data System, the system of the European Association of Nuclear Medicine, and the Prostate Cancer Molecular Imaging Standardized Evaluation (PROMISE) (6–8). Although all the proposed criteria are focused on the characterization of individual PSMA lesions based on the location and on the definition of significant uptake, the PROMISE standard is also proposing a patient-level staging (molecular imaging TNM), which is based on the detection and location of the disease in the PSMA PET/CT image. A recent study comparing such standardized assessments has shown that they have a high interreader reproducibility (9,10).

However, the adoption of PROMISE criteria in routine clinical practice and investigational studies is limited by the fact that it must be done manually and is labor-intensive. The manual work can be greatly facilitated through automation by deep-learning image analysis. The structural radiologic processes, including the segmentation of anatomic structures (from CT), can be automated to contextualize and characterize the functional imaging. The application of deep learning in automating the whole-body segmentation in PET/CT is the foundational framework for automating the PROMISE criteria. In this study, we introduce and evaluate the analysis of PSMA PET images through aPROMISE, a deep-learning platform to both automate standardized staging and generate a fully quantitative assessment of PSMA-defined disease burden at the lesion and patient levels.

## MATERIALS AND METHODS

### Patient Population

The purpose of our study was to evaluate the performance of the aPROMISE technology in standardizing the staging and quantification of prostate cancer. This investigation was a retrospective analysis of 109 veterans with unfavorable intermediate- and high-risk primary prostate cancer who underwent  $^{18}\text{F}$ -DCFPyL PET/CT under clinical trial NCT03852654, a single-arm trial of PSMA PET/CT on veterans who also underwent conventional imaging with bone scanning, CT, or MRI. The study was approved by the local institutional review board at a Veterans

Affairs hospital (PCC 2018-100989), with a waiver of individual informed consent.

### Study Design

To validate the performance of aPROMISE, 2 independent board-certified nuclear medicine physicians (3 y of clinical experience) reviewed the PSMA images with the assistance of aPROMISE. No prior instructions were given, and the readers solely and independently relied on the aPROMISE workflow. aPROMISE provides the reader with automated segmentation and quantification of lesions with a pre-selected molecular imaging TNM type. The reader can choose to accept or override the aPROMISE automated selections at the level of each individual lesion. A final report is autogenerated on the basis of the aPROMISE-assisted read.

First, the aPROMISE-assisted staging was evaluated against conventional-imaging staging obtained from the routine clinical reports. Conventional imaging in every patient included  $^{99\text{m}}\text{Tc}$ -methylenediphosphonate bone scanning or  $^{18}\text{F}$ -NaF PET/CT, and CT or MRI of the pelvis. Second, we evaluated the reproducibility of the staging and lesion quantification between the 2 independent aPROMISE-assisted reads. Finally, we evaluated the clinical association of quantitative PSMA uptake (molecular imaging PSMA [miPSMA] index) with 2 baseline clinical variables: Gleason score and PSA value. All patients were staged into 1 of 4 distinct categories: miN0M0 (localized disease and absence of regional lymph node or distant metastatic disease), miN1M0 (regional lymph node disease but absence of distant metastatic disease), miN0M1 (absence of regional lymph node but presence of distant metastatic disease), and miN1M1 (presence of both regional lymph node and distant metastatic disease).

### aPROMISE and miPSMA Index

aPROMISE (version 1.1), a class II software as a medical device, is a web application developed by EXINI Diagnostics AB to standardize and quantify PSMA imaging in prostate cancer. aPROMISE is enabled with deep learning that automatically analyzes the CT image to segment anatomic regions in detail, including individual vertebrae, ribs, pelvic bones, and soft-tissue organs such as the prostate (Fig. 1). The anatomic contextualization of the molecular image is used to stage the patient on the basis of the location and extent of the primary tumor in the prostate and of the disease in the local or regional pelvic lymph nodes and in the distant metastases. Subsequently, the PET image is analyzed to detect target lesions. aPROMISE technology enables implementation of standard guidelines such as PROMISE in

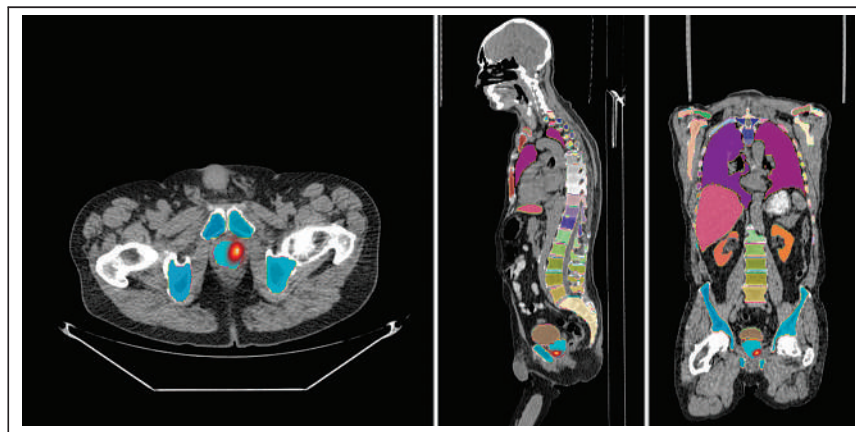


**FIGURE 1.** Deep-learning-enabled segmentation of anatomic context in low-dose CT component of PET/CT. Individual color represents respective segmented organ. aPROMISE technology enables automated segmentation of reference organs and anatomic delineation of disease in prostate tumor, regional lymph node, and distant metastases.

standardizing PSMA assessment (6). Merging the target lesion information with the anatomic location, the technology quantifies each target lesion in terms of both intensity and volume and summarizes by tissue type to generate the miPSMA index. The aPROMISE report is created automatically, with both aggregated information and detailed information on a per-lesion basis. Manual controls are provided as fallback to augment automatic analysis.

In the PROMISE criteria, Eiber et al. (6) defined the miPSMA score of a lesion as 0 when uptake is below the level in the aorta, 1 when uptake is between the levels in the aorta and liver, 2 when uptake is between the levels in the liver and the parotid gland, and 3 when uptake is above the level in the parotid gland. The miPSMA lesion index is a continuous extension of these criteria, defined by linear interpolation from the lesion  $SUV_{mean}$  and from the aorta and liver SUV references as follows:

$$\text{Lesion } SUV_{mean} \leq \text{aorta } SUV_{ref}:$$

$$\text{Lesion index} = \frac{\text{lesion } SUV_{mean}}{\text{aorta } SUV_{ref}}$$

$$\text{Aorta } SUV_{ref} \leq \text{lesion } SUV_{mean} \leq \text{liver } SUV_{ref}:$$

$$\text{Lesion index} = 1 + \frac{\text{lesion } SUV_{mean} - \text{aorta } SUV_{ref}}{\text{aorta } SUV_{ref}}$$

$$\text{Liver } SUV_{ref} \leq \text{lesion } SUV_{mean} \leq 2 \times \text{liver } SUV_{ref}:$$

$$\text{Lesion index} = 2 + \frac{\text{lesion } SUV_{mean} - \text{liver } SUV_{ref}}{\text{liver } SUV_{ref}}$$

$$2 \times \text{liver } SUV_{ref} \leq \text{lesion } SUV_{mean}: \text{lesion index} = 3.$$

The use of the parotid gland as a threshold has been replaced by 2 times the liver reference since it is not certain that the parotid glands are included in all PSMA PET/CT scans. For each molecular imaging TNM type, lesion uptake is aggregated into the intensity-weighted total lesion uptake volume. This PSMA index is defined as

$$\sum_{\text{lesion type}} \text{lesion index} \times \text{lesion uptake volume}$$

for extent of disease in any lesion type (primary tumor [T stage], local or regional pelvic nodes [N stage], or distant metastases [M stage, which is further denoted as “a” for metastatic lymph nodes, “b” for bone metastases, and “c” for visceral organ metastases]).

### Statistical Analysis

Descriptive statistics were used to compare the aPROMISE staging with conventional-imaging staging. Cohen pairwise  $\kappa$ -agreement was used to evaluate the interreader variability of aPROMISE-assisted staging (miN0M0, miN1M0, and miN0M1). Spearman and Kendall correlation coefficients were used to evaluate the interreader variability of the quantitative assessment (miPSMA index) of each stage. Student *t* testing was used to evaluate the miPSMA index values (in tumor) in the risk groups defined by PSA and Gleason score. All statistical analyses were performed using R, version 4.0.2.

### RESULTS

The analysis included 109 consecutive patients, whose baseline characteristics are detailed in Table 1. Conventional imaging staged 87 of the 109 patients as having N0M0 disease, 8 patients as having N1M0 disease, 14 patients as having N0M1 disease, and no patients as having N1M1 disease. All 14 of the N0M1 patients were found to have bone metastasis (N0M1b) on conventional staging by  $^{18}\text{F}$ -NaF PET/CT and did not undergo  $^{99\text{m}}\text{Tc}$ -methylene diphosphonate bone scanning.

The duration of the aPROMISE-assisted read, from selecting a patient to generating a complete report, was recorded to be a mean

**TABLE 1**  
Patient Characteristics ( $n = 109$ )

Characteristic	Data
<b>Age (y)</b>	
Average	70
Median	69
Minimum	55
Maximum	86
<b>Race (n)</b>	
White	54 (49%)
African American	44 (41%)
Hispanic	7 (7%)
Asian Pacific Islander	3 (2%)
Native American	1 (1%)
<b>Clinical T stage (n)</b>	
cT1/2	62 (57%)
cT3	47 (43%)
<b>Gleason score (n)</b>	
3 + 3	13 (7%)
3 + 4	28 (23%)
4 + 3	24 (18%)
$\geq 4 + 4$	49 (36%)
<b>PSA at diagnosis (ng/mL)</b>	
Average	20.4 ng/mL
Median	13.55 ng/mL
Minimum	3.03 ng/mL
Maximum	167.92 ng/mL
<b>Percentage positive core (n)</b>	
<25%	18 (17%)
25%–50%	28 (26%)
51%–75%	14 (13%)
>75%	28 (26%)
Unknown	11 (10%)

of 3.2 min (range, 1.8–5.1 min) per scan for reader 1 and 3.4 min (range, 2.3–5.8 min) for reader 2. The comparative assessment of conventional against aPROMISE-assisted PSMA staging is detailed in Table 2. Both aPROMISE-assisted PSMA analyses demonstrated significant upstaging in patients with localized and regional tumor burden and downstaging in patients who were positive for distant bone metastasis by  $^{18}\text{F}$ -NaF PET/CT. In aPROMISE-assisted read 1, of the 87 patients who were determined to be negative for local (N1) or distant (M1) metastatic disease by conventional imaging, 20 (23%) were upstaged in the PSMA imaging assessment to having regional lymph node disease ( $n = 13$ ) or distant metastatic disease ( $n = 6$ ). Similarly, of the 8 patients staged as having local pelvic nodal disease only (N1), 2 (25%) were upstaged to having distant metastatic disease also. Notably, a significant population (4/14, 29%) with bone metastatic disease by conventional imaging were downstaged by aPROMISE-assisted PSMA imaging. Examples of downstaged aPROMISE-assisted PSMA reads against  $^{18}\text{F}$ -NaF reads are

**TABLE 2**  
aPROMISE-PSMA Staging Reads vs. Local and Distant Metastatic Staging by Conventional Imaging

Read no.	Parameter	Conventional imaging			
		NOM0 ( <i>n</i> = 87)	N1M0 ( <i>n</i> = 8)	NOM1a/b ( <i>n</i> = 14)	N1M1a/b ( <i>n</i> = 0)
1	miNOM0 ( <i>n</i> = 71)	67	0	4	0
	miN1M0 ( <i>n</i> = 19)	13	6	0	0
	miN0 M1a/b ( <i>n</i> = 15)	6	0	9	0
	miN1M1a/b ( <i>n</i> = 4)	1	2	1	0
2	miNOM0 ( <i>n</i> = 72)	68	0	4	0
	miN1M0 ( <i>n</i> = 18)	12	6	0	0
	miNOM1a/b ( <i>n</i> = 15)	6	0	9	0
	miN1M1a/b ( <i>n</i> = 4)	1	2	1	0

*n* = 109.

demonstrated in Figure 2. aPROMISE-assisted read 2 had observations similar to those on conventional imaging (Table 2).

**Interobserver Reproducibility of aPROMISE Reads**

The 2 independent aPROMISE-assisted read are compared in Table 3. The  $\kappa$ -agreement between them was 0.82 for categorization of patients with miNOM0, 0.90 for patient with miN1M0, and 0.77 for patients with miNOM1b. Among all stages, the relatively

modest discrepancy in aPROMISE-associated reads was most notable for isolated low-intensity bone lesions. The quantitative reproducibility of miPSMA index in the cases that were categorized the same in the 2 independent aPROMISE-assisted reads—miNOM0 (*n* = 66), miN1M0 (*n* = 17), miNOM1 (*n* = 12)—is illustrated in Figure 3. The Spearman correlation was 0.93, 0.96, and 0.97, respectively.

**aPROMISE miPSMA Index**

As a continuous variable, miPSMA index in the prostate tumor of all patients (*n* = 109) was correlated with PSA value ( $t = 0.30$ ;  $P < 0.0001$ ). Figure 4 shows the miPSMA index values in the prostate, stratified in risk groups defined by PSA and separately by Gleason score. There was a significant difference in values between patients with a PSA of 10 ng/mL or lower (median, 17.61; interquartile range, 8.75–44.63) and patients with a PSA of 20 ng/mL or higher (median, 54.63; interquartile range, 27.55–80.79) ( $P = 0.05$ ). Similarly, the PSMA index values of prostate tumors with a Gleason score of 3 + 3 (median, 19.45; interquartile range, 9.97–23.54) was significantly lower than that of tumors with a Gleason score of at least 4 + 3 (median, 32.74; interquartile range, 15.38–54.63) ( $P = 0.01$ ).

**DISCUSSION**

The aPROMISE-assisted independent staging and the quantitative assessments of total disease burden were found to be consistent and reproducible between readers. Integrating PSMA assessment tools into the clinical workflow could allow for automation to provide efficiency, consistency, and accuracy in the staging and quantification of PSMA PET/CT. This study also demonstrated that aPROMISE-assisted reads for PSMA PET/CT detected significantly more regional and metastatic suggestive lesions than were identified by conventional imaging.

The ability of PSMA imaging to detect a greater number of suspected metastatic lesions than can be detected by conventional bone scanning or CT has been evident across multiple studies (11–14). The frequency of upstaging in nodal and distant metastasis by PSMA PET/CT, compared with conventional imaging, in this cohort of patients with intermediate- or high-risk prostate cancer was in line with previous reports. Notably, the biologic

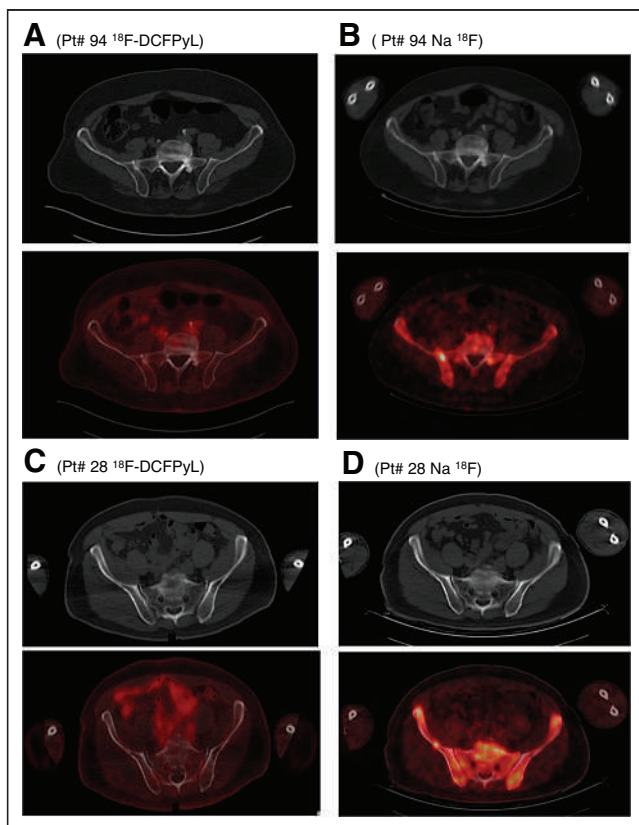


**FIGURE 2.** Example of patients who were negative in aPROMISE-assisted reads of  $^{18}\text{F}$ -DCFPyL scans (A and C, axial images) compared with  $\text{Na}^{18}\text{F}$  (B and D, axial images) and were downstaged from NOM1 to NOM0.

**TABLE 3**  
Local and Distant Metastatic Staging by aPROMISE-PSMA Read 1 Against aPROMISE-PSMA Read 2

Read 2	Read 1			
	miNOM0 ( <i>n</i> = 71)	miN1M0 ( <i>n</i> = 19)	miNOM1a/b ( <i>n</i> = 15)	miN1M1a/b ( <i>n</i> = 4)
miNOM0 ( <i>n</i> = 72)	67	2	3	0
miN1M0 ( <i>n</i> = 18)	1	17	0	0
miNOM1a/b ( <i>n</i> = 15)	3	0	12	0
miN1M1a/b ( <i>n</i> = 4)	0	0	0	4

*n* = 109.

dimension of PSMA in evaluating suspected metastatic disease was particularly apparent when comparing findings from <sup>18</sup>F-NaF with those from PSMA imaging. Of the 14 patients categorized as M1b through <sup>18</sup>F-NaF scans, 4 (29%) were called negative in aPROMISE-assisted reads of their respective PSMA scans. As a bone metabolic scan, <sup>18</sup>F-NaF imaging is known to be susceptible to nonpathophysiologic features in bone such as trauma, degenerative changes, and fibrous dysplasia. Of these 4 patients with lesions seen on <sup>18</sup>F-NaF imaging but not on PSMA PET/CT, 2 demonstrated lesions that appeared more likely to be benign on PSMA PET/CT but were called positive on the corresponding <sup>18</sup>F-NaF imaging. The other 2 patients with discordant findings between <sup>18</sup>F-NaF and PSMA imaging had suggestive sclerotic bone lesions that were not seen on the aPROMISE reads because of low PSMA intensity in the lesions. One of these 2 patients underwent curative-intent radical prostatectomy and remains free of biochemical recurrence almost 1 y after surgery, without additional therapy. The other patients delayed treatment and instead underwent a repeat <sup>18</sup>F-NaF examination 6 mo later that showed no interval change in the bone lesion but did show progression within soft tissue. In these 2 cases, clinical follow-up was more consistent with the PSMA PET staging than with the <sup>18</sup>F-NaF imaging. A more comprehensive comparison of PSMA and <sup>18</sup>F-NaF imaging is beyond the scope of this study but will be done in a separate follow-up analysis.

Interreader agreement on the interpretation of PSMA PET/CT has been evaluated mostly using <sup>68</sup>Ga-PSMA11 PET/CT. Fendler et al. evaluated interreader agreements in 50 patients with primary disease and after biochemical recurrence and found  $\kappa$  values of 0.62 for primary tumor, 0.74 for nodes, and 0.88 for bone lesions (15). In a more homogeneous biochemically recurrent population consisting of patients with PSA levels of up to 0.6 ng/mL, Miksch et al. demonstrated  $\kappa$  values of 0.76 for primary tumor, 0.73 for nodes, and 0.58 for bone lesions (16). In a study focused exclusively on 50 patients who underwent <sup>18</sup>F-DCFPyL PET, an intraclass correlation coefficient of 0.79 was derived for nodal disease (17). Similarly, the manual reproducibility of following the PROMISE classification has been reviewed and reported by Torihara et al., who demonstrated moderate interreader agreement (0.67) for molecular imaging TNM classification in PSMA PET/CT (9). The agreement between the aPROMISE-assisted reads in our study compares favorably against these prior evaluations (Cohen  $\kappa$  > 0.75), with a notably quick reading time (mean, 3.2 and 3.4 min per scan). One reader in our study had considerably more prior experience in the interpretation of PSMA PET/CT than

did the other. Still, a high degree of agreement was noted. The readers in our study did not get any strict guidance on lesion detection, nor did they receive any formal training on the PROMISE criteria. The findings may suggest that an aPROMISE-assisted read that involves automated segmentation, localization, and lesion preselection may nudge readers toward a moderately high agreement irrespective of their prior experience. This hypothesis warrants a multicenter, multireader study for validation.

Quantitative metrics of disease burden may further enhance the prognostic and predictive power of imaging. Currently, the automated bone scan index (aBSI) is the only Food and Drug Administration–cleared software as a medical device that has been prospectively validated in a registration study as a prognostic imaging biomarker for metastatic prostate cancer (18). The STAMPEDE trial investigated the addition of radiation to the primary tumor in M1 patients. In a post hoc analysis that used aBSI to assess disease burden, aBSI was predictive of response to prostate radiotherapy (19). aBSI uses a machine-learning algorithm that preselects and segments the lesions in bone and automatically computes a quantitative total tumor burden in <sup>99m</sup>Tc planar bone scans (20). In some sense, the miPSMA index for quantification of disease burden defined by PSMA PET/CT can be considered a 3-dimensional analog of aBSI.

However, the automated miPSMA index offers a far more comprehensive assessment of disease burden. The miPSMA index is a continuous extension of the miPSMA score proposed in the PROMISE criteria. Like the miPSMA score, the miPSMA index is the PSMA quantification of an individual lesion in relation to the mean uptake in reference organs. The result, for each lesion, is a linear PSMA-burden quantification that can be summarized by each tissue type (primary tumor [T stage], local or regional pelvic nodes [N stage], or distant metastases [M stage, which is further denoted as “a” for metastatic lymph nodes, “b” for bone metastases, and “c” for visceral organ metastases]). Our study showed an association between miPSMA index in the primary tumor and both Gleason grade and PSA value. This finding is consistent with prior studies reporting that PSMA expression in the primary tumor is associated with a higher Gleason grade and recurrence risk (21,22). We hypothesize that the miPSMA index may be useful for selecting patients for PSMA-targeted radiotherapy, with current trials largely using qualitative assessments of PSMA expression as inclusion criteria. Moreover, there is a potential role for the miPSMA index in conjunction with morphologic findings as a quantitative method of response assessment after treatment.

The purpose of our hypothesis-generating study was to evaluate the performance of the aPROMISE technology for subsequent

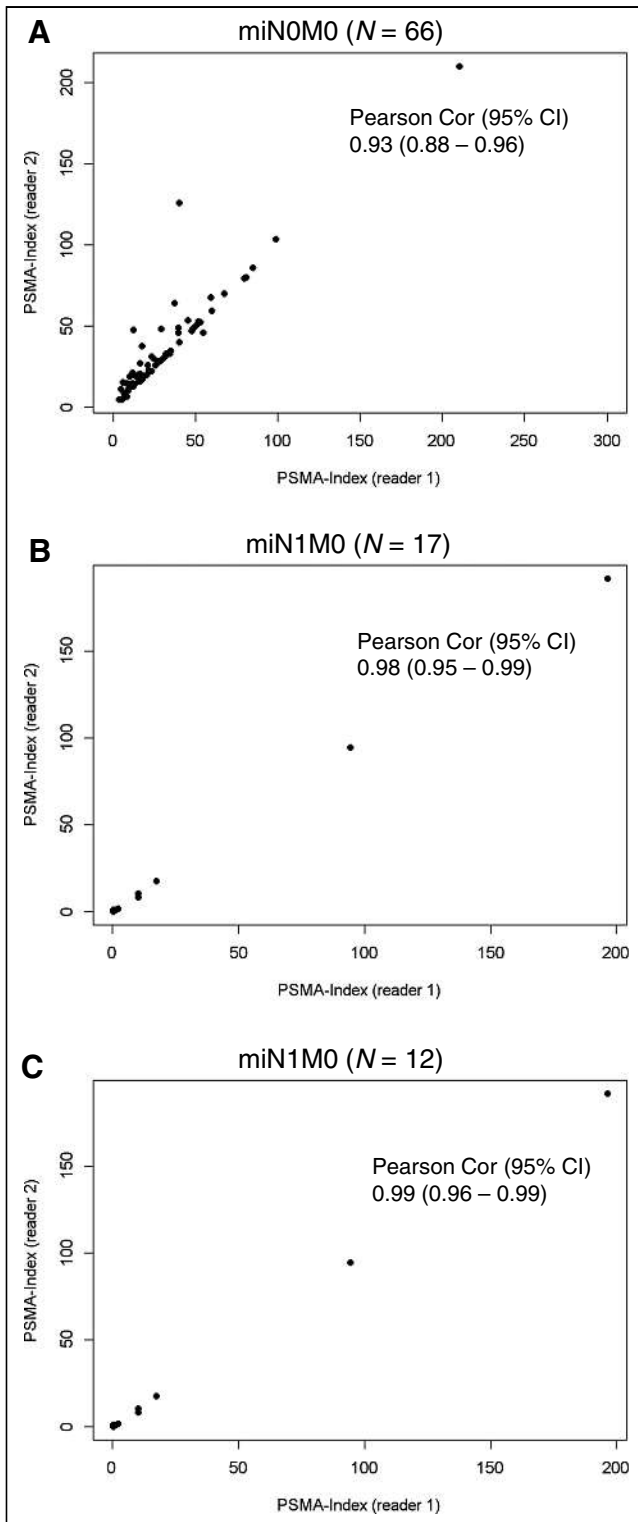


**FIGURE 3.** Quantitative reproducibility of miPSMA index in patients who were categorized the same in 2 independent aPROMISE-assisted reads: miNOM0 (A), miN1M0 (B), and miNOM1(C). In A, 1 patient was excluded because of a manual segmentation error that incorporated bladder. Cor = correlation.

prospective clinical investigations. The findings here enable future investigations to evaluate any additive benefits of aPROMISE-assisted reads over manual reads of PSMA PET/CT and to assess

whether the diagnostic performance of PSMA PET/CT is enhanced when using the aPROMISE software. Our study was limited in the number of independent reads and in its retrospective design. Therefore, the findings and the hypothesis presented here should be validated in a prospectively designed multireader and multiinstitutional

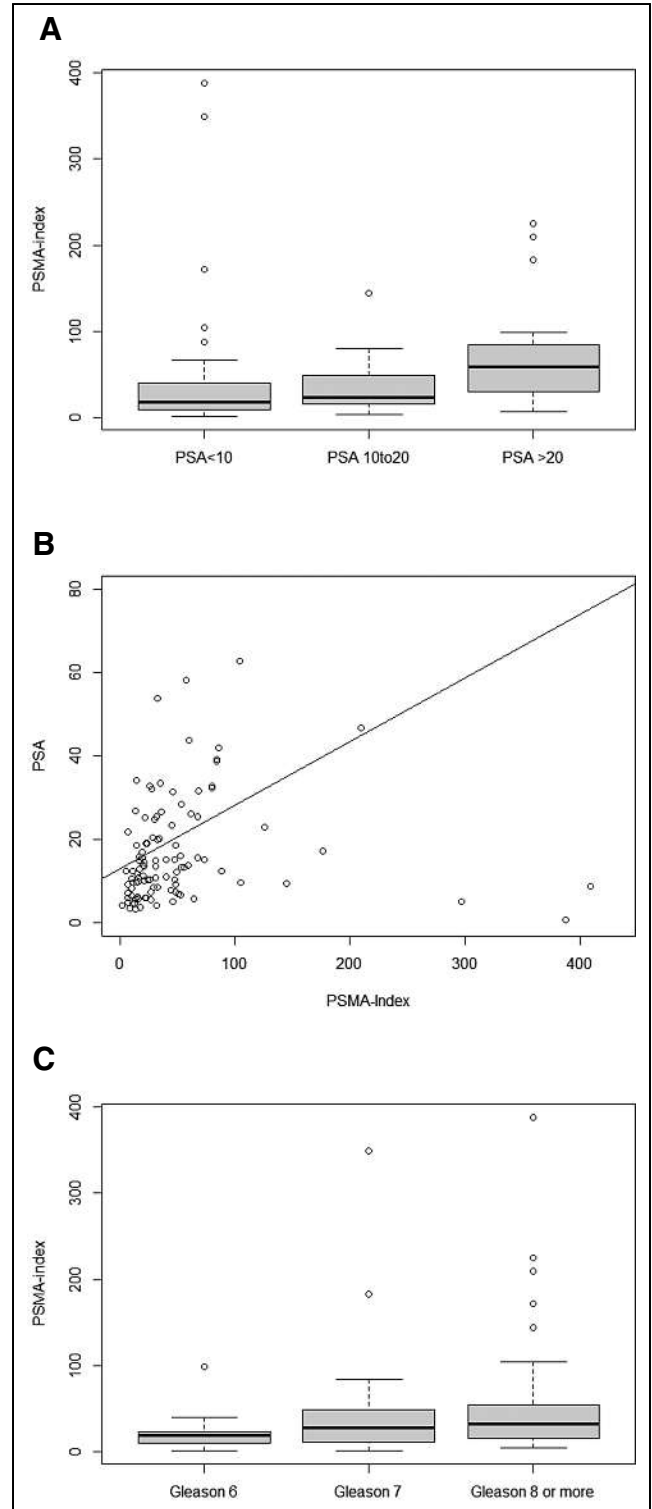


**FIGURE 4.** miPSMA index values in prostate, stratified by PSA (A and B) and separately by Gleason grade (C).

study design. In addition, lesions selected by aPROMISE have not been histopathologically validated. However, PSMA PET was shown to have high specificity in several recent studies (23).

Despite these limitations, our study demonstrated the performance of aPROMISE in an independent assessment. Incorporation of aPROMISE and the miPSMA index into subsequent clinical investigations can allow further exploration of the clinical context of their use for prospective validation.

## CONCLUSION

aPROMISE-assisted PSMA PET/CT reads generate detailed imaging reports at the whole-patient and lesion levels within minutes. Compared with conventional imaging, aPROMISE assistance upstages patients and reduces interreader variability, even among readers with differing baseline levels of experience. Moreover, aPROMISE-assisted reads may standardize PSMA evaluation. Prospective studies and direct manual comparison studies are required to validate these findings. The miPSMA index is a quantitative measure of lesion volume and relative intensity, is associated with Gleason grade and PSA, and describes overall and tissue-specific tumor burden. Evaluation of the miPSMA index as an imaging biomarker of disease burden is warranted in order to assess prognostic value.

## DISCLOSURE

This work was supported by EXINI Diagnostics AB (a wholly owned subsidiary of Progenics Pharmaceuticals Inc.). Nicholas Nickols is a PCF Young Investigator. Johan Brynlofsson and Kerstin Johnsson are employees of EXINI Diagnostics AB. Aseem Anand and Pablo Borelli have received honorary support from EXINI Diagnostics AB. No other potential conflict of interest relevant to this article was reported.

## KEY POINTS

**QUESTION:** Can the aPROMISE platform generate a consistent and standardized evaluation of PSMA scans?

**PERTINENT FINDINGS:** The comparison of the 2 independent aPROMISE-assisted reads demonstrated a high  $\kappa$  agreement in staging of patients. As a continuous variable, miPSMA index in the prostate was associated with risk groups defined by PSA values and Gleason scores.

**IMPLICATIONS FOR PATIENT CARE:** aPROMISE-assisted reads may standardize PSMA evaluation and reduce interreader variability, even among readers with differing baseline levels of experience. The miPSMA index is a quantitative measure of lesion volume and relative intensity, is associated with Gleason grade and PSA, and describes overall and tissue-specific tumor burden.

## REFERENCES

- Mohler JL, Antonarakis ES, Armstrong AJ, et al. Prostate cancer, version 2.2019, NCCN clinical practice guidelines in oncology. *J Natl Compr Canc Netw*. 2019; 17:479–505.
- Abuzalouf S, Dayes I, Lukka H. Baseline staging of newly diagnosed prostate cancer: a summary of the literature. *J Urol*. 2004;171:2122–2127.
- Golimbu M, Morales P, Al-Askari S, Shulman Y. CAT scanning in staging of prostatic cancer. *Urology*. 1981;18:305–308.
- Budäus L, Leyh-Bannurah SR, Salomon G, et al. Initial experience of  $^{68}\text{Ga}$ -PSMA PET/CT imaging in high-risk prostate cancer patients prior to radical prostatectomy. *Eur Urol*. 2016;69:393–396.
- Hofman MS, Lawrentschuk N, Francis RJ, et al. Prostate-specific membrane antigen PET-CT in patients with high-risk prostate cancer before curative-intent surgery or radiotherapy (proPSMA): a prospective, randomised, multicentre study. *Lancet*. 2020;395:1208–1216.
- Eiber M, Herrmann K, Calais J, et al. Prostate Cancer Molecular Imaging Standardized Evaluation (PROMISE): proposed miTNM classification for the interpretation of PSMA-ligand PET/CT. *J Nucl Med*. 2018;59:469–478.
- Fanti S, Minozzi S, Morigi JJ, et al. Development of standardized image interpretation for  $^{68}\text{Ga}$ -PSMA PET/CT to detect prostate cancer recurrent lesions. *Eur J Nucl Med Mol Imaging*. 2017;44:1622–1635.
- Rowe SP, Pienta KJ, Pomper MG, Gorin MA. PSMA-RADS version 1.0: a step towards standardizing the interpretation and reporting of PSMA-targeted PET imaging studies. *Eur Urol*. 2018;73:485–487.
- Toriihara A, Nobashi T, Baratto L, et al. Comparison of 3 interpretation criteria for  $^{68}\text{Ga}$ -PSMA11 PET based on inter- and intrareader agreement. *J Nucl Med*. 2020; 61:533–539.
- Demirci E, Akyel R, Caner B, et al. Interobserver and intraobserver agreement on prostate-specific membrane antigen PET/CT images according to the miTNM and PSMA-RADS criteria. *Nucl Med Commun*. 2020;41:759–767.
- Calais J, Czernin J, Cao M, et al.  $^{68}\text{Ga}$ -PSMA-11 PET/CT mapping of prostate cancer biochemical recurrence after radical prostatectomy in 270 patients with a PSA level of less than 1.0 ng/mL: impact on salvage radiotherapy planning. *J Nucl Med*. 2018;59:230–237.
- Calais J, Kishan AU, Cao M, et al. Potential impact of  $^{68}\text{Ga}$ -PSMA-11 PET/CT on the planning of definitive radiation therapy for prostate cancer. *J Nucl Med*. 2018; 59:1714–1721.
- Maurer T, Gschwend JE, Rauscher I, et al. Diagnostic efficacy of  $^{68}\text{Ga}$ -PSMA positron emission tomography compared to conventional imaging for lymph node staging of 130 consecutive patients with intermediate to high risk prostate cancer. *J Urol*. 2016;195:1436–1443.
- van Leeuwen PJ, Emmett L, Ho B, et al. Prospective evaluation of  $^{68}\text{Ga}$ -PSMA-specific membrane antigen positron emission tomography/computed tomography for preoperative lymph node staging in prostate cancer. *BJU Int*. 2017;119: 209–215.
- Fendler WP, Calais J, Allen-Auerbach M, et al.  $^{68}\text{Ga}$ -PSMA-11 PET/CT interobserver agreement for prostate cancer assessments: an international multicenter prospective study. *J Nucl Med*. 2017;58:1617–1623.
- Miksch J, Bottke D, Krohn T, et al. Interobserver variability, detection rate, and lesion patterns of  $^{68}\text{Ga}$ -PSMA-11-PET/CT in early-stage biochemical recurrence of prostate cancer after radical prostatectomy. *Eur J Nucl Med Mol Imaging*. 2020; 47:2339–2347.
- Werner RA, Bundschuh RA, Bundschuh L, et al. Interobserver agreement for the standardized reporting system PSMA-RADS 1.0 on  $^{18}\text{F}$ -DCFPyL PET/CT imaging. *J Nucl Med*. 2018;59:1857–1864.
- Armstrong AJ, Anand A, Edenbrandt L, et al. Phase 3 assessment of the automated bone scan index as a prognostic imaging biomarker of overall survival in men with metastatic castration-resistant prostate cancer: a secondary analysis of a randomized clinical trial. *JAMA Oncol*. 2018;4:944–951.
- Ali A, Hoyle AP, Parker CC, et al. The automated bone scan index as a predictor of response to prostate radiotherapy in men with newly diagnosed metastatic prostate cancer: an exploratory analysis of STAMPEDE's "M1RT comparison." *Eur Urol Oncol*. 2020;3:412–419.
- Ulmert D, Kaboteh R, Fox JJ, et al. A novel automated platform for quantifying the extent of skeletal tumour involvement in prostate cancer patients using the bone scan index. *Eur Urol*. 2012;62:78–84.
- Hupe MC, Philippi C, Roth D, et al. Expression of prostate-specific membrane antigen (PSMA) on biopsies is an independent risk stratifier of prostate cancer patients at time of initial diagnosis. *Front Oncol*. 2018;8:623.
- Demirci E, Kabasakal L, Sahin OE, et al. Can SUVmax values of Ga-68-PSMA PET/CT scan predict the clinically significant prostate cancer? *Nucl Med Commun*. 2019;40:86–91.
- Pienta KJ, Gorin MA, Rowe SP, et al. A phase 2/3 prospective multicenter study of the diagnostic accuracy of prostate specific membrane antigen PET/CT with  $^{18}\text{F}$ -DCFPyL in prostate cancer patients (OSPPEY). *J Urol*. 2021;206:52.

---

---

# Diagnostic Performance and Clinical Impact of <sup>68</sup>Ga-PSMA-11 PET/CT Imaging in Early Relapsed Prostate Cancer After Radical Therapy: A Prospective Multicenter Study (IAEA-PSMA Study)

Juliano J. Cerci<sup>1</sup>, Stefano Fanti<sup>2</sup>, Enrique E. Lobato<sup>3</sup>, Jolanta Kunikowska<sup>4</sup>, Omar Alonso<sup>5</sup>, Sevastian Medina<sup>6</sup>, Fuad Novruzov<sup>7</sup>, Thabo Lengana<sup>8</sup>, Carlos Granados<sup>9</sup>, Rakesh Kumar<sup>10</sup>, Venkatesh Rangarajan<sup>11</sup>, Akram Al-Ibraheem<sup>12</sup>, Mukbil Hourani<sup>13</sup>, Nor S. Ali<sup>14</sup>, Azra Ahmad<sup>15</sup>, Zohar Keidar<sup>16</sup>, Ozlem Küçük<sup>17</sup>, Umut Elboga<sup>18</sup>, Mateos Bogoni<sup>1</sup>, and Diana Paez<sup>3</sup>

<sup>1</sup>Quanta Diagnóstico e Terapia, Curitiba, Brazil; <sup>2</sup>IRCCS Azienda Ospedaliero-Universitaria di Bologna, Bologna, Italy; <sup>3</sup>Division of Human Health, International Atomic Energy Agency, Vienna, Austria; <sup>4</sup>Nuclear Medicine Department, Medical University of Warsaw, Warsaw, Poland; <sup>5</sup>Centro Uruguayo de Imagenología Molecular (CUDIM), Montevideo, Uruguay; <sup>6</sup>Instituto Nacional de Cancerología, Tlalpan, Mexico; <sup>7</sup>Nuclear Medicine Department, National Centre of Oncology, Baku, Azerbaijan; <sup>8</sup>University of Pretoria, Pretoria, South Africa; <sup>9</sup>Instituto Nacional de Cancerología, Bogotá, Colombia; <sup>10</sup>All India Institute of Medical Sciences, New Delhi, India; <sup>11</sup>Tata Memorial Centre, Mumbai, India; <sup>12</sup>King Hussein Cancer Center, Amman, Jordan; <sup>13</sup>American University of Beirut Medical Center, Beirut, Lebanon; <sup>14</sup>Institute Kanser Negara, Putrajaya, Malaysia; <sup>15</sup>Pakistan Atomic Energy Commission (PAEC), Islamabad, Pakistan; <sup>16</sup>Rambam Medical Centre, Haifa, Israel; <sup>17</sup>Ankara University, Ankara, Turkey; and <sup>18</sup>University of Gaziantep, Gaziantep, Turkey

---

Biochemical recurrence (BCR) is a clinical challenge in prostate cancer (PCa) patients, as recurrence localization guides subsequent therapies. The use of PET with prostate-specific membrane antigen (PSMA) provides better accuracy than conventional imaging practice. This prospective, multicenter, international study was performed to evaluate the diagnostic performance and clinical impact of PSMA PET/CT for evaluating BCR in PCa patients in a worldwide scenario.

**Methods:** Patients were recruited from 17 centers in 15 countries. Inclusion criteria were histopathologically proven prostate adenocarcinoma, previous primary treatment, clinically established BCR, and negative conventional imaging (CT plus bone scintigraphy) and MRI results for patients with PSA levels of 4–10 ng/mL. All patients underwent PET/CT scanning with <sup>68</sup>Ga-PSMA-11. Images and data were centrally reviewed. Multivariate logistic regression analysis was applied to identify the independent predictors of PSMA-positive results. Variables were selected for this regression model on the basis of significant associations in the univariate analysis and previous clinical knowledge: Gleason score, the PSA level at the time of the PET scan, PSA doubling time, and primary treatment strategy. All patients were monitored for a minimum of 6 mo. **Results:** From a total of 1,004 patients, 77.7% were treated initially with radical prostatectomy and 22.3% were treated with radiotherapy. Overall, 65.1% had positive PSMA PET/CT results. PSMA PET/CT positivity was correlated with the Gleason score, PSA level at the time of the PET scan, PSA doubling time, and radiotherapy as the primary treatment ( $P < 0.001$ ). Treatment was modified on the basis of PSMA PET/CT results in

56.8% of patients. PSMA PET/CT positivity rates were consistent and not statistically different among countries with different incomes.

**Conclusion:** This multicenter, international, prospective trial of PSMA PET/CT confirmed its capability for detecting local and metastatic recurrence in most PCa patients in the setting of BCR. PSMA PET/CT positivity was correlated with the Gleason score, PSA level at the time of the PET scan, PSA doubling time, and radiotherapy as the primary treatment. PSMA PET/CT results led to changes in therapeutic management in more than half of the cohort. The study demonstrated the reliability and worldwide feasibility of PSMA PET/CT in the workup of PCa patients with BCR.

**Key Words:** PSMA; PET/CT; prostate cancer; biochemical relapse

**J Nucl Med 2022; 63:240–247**

DOI: 10.2967/jnumed.120.261886

---

**P**rostate cancer (PCa) is the second most common cancer in men, accounting for 7.8% of all cancers in this population (1). Greater life expectancy worldwide and improved access to screening and diagnostic methods in developing nations are mainly responsible for the current trend of increasing incidence (2).

Initial treatment with curative intent is feasible, with radical prostatectomy or radiotherapy; nevertheless, early recurrence occurs in up to 50% of patients within 10 y (3–5). Biochemical recurrence (BCR) is defined as increasing serum prostate-specific antigen (PSA) levels after initial treatment, under specific criteria (6–8).

The key question for proper treatment planning in BCR remains whether the rise in PSA levels is reflective of local, regional, or distant recurrence. With increasing rates of success of early salvage therapy, the diagnosis of local tumor recurrence at the earliest possible stage has become pertinent. Salvage radiotherapy after radical prostatectomy has been shown to be most effective—reaching a

---

Received Dec. 28, 2020; revision accepted May 20, 2021.

For correspondence or reprints, contact Juliano J. Cerci (cercijuliano@hotmail.com).

Published online Jul. 2, 2021.

Immediate Open Access: Creative Commons Attribution 4.0 International License (CC BY) allows users to share and adapt with attribution, excluding materials credited to previous publications. License: <https://creativecommons.org/licenses/by/4.0/> Details: <http://jnm.snmjournals.org/site/misc/permission.xhtml>.

COPYRIGHT © 2022 by the Society of Nuclear Medicine and Molecular Imaging.

urable response—when the postoperative PSA level is preferably below 0.5 ng/mL, with better outcomes when the PSA level is below 0.2 ng/mL (4,9).

Despite guidelines indicating that prostate-specific membrane antigen (PSMA) PET/CT is the imaging modality of choice in BCR (10–17), in some countries—especially those with lower incomes—conventional imaging with CT and bone scintigraphy are still being used, even if the diagnostic yield of these techniques is low, especially for patients with low PSA levels (11).

Most PSMA PET/CT studies have been performed at a single institution or were retrospectively planned. Furthermore, most reported studies have been conducted at academic centers in highly developed countries; thus, to our knowledge, there are no data from large prospective international trials. The International Atomic Energy Agency initiated a Coordinated Research Project to evaluate the feasibility and usefulness of PSMA PET/CT for studying PCa patients with BCR in 15 countries to inform international practice.

The primary aim of this prospective study was to evaluate the diagnostic performance of PSMA PET/CT in PCa patients with BCR worldwide, through an international multicenter effort, and the impact of PSMA PET/CT on clinical management.

## MATERIALS AND METHODS

### Study Design

Two investigators' meetings were held, in 2017 and 2019. The first defined the study protocol, whereas in the second, an interim evaluation was performed, together with image and data review. The study followed a prospective, multicenter, international design, encompassing 17 centers in 15 countries (Azerbaijan, Brazil, Colombia, India, Israel, Italy, Jordan, Lebanon, Malaysia, Mexico, Pakistan, Poland, South Africa, Turkey, and Uruguay). Standard forms for data registration were developed and agreed on by the investigators. Data were collected for PSMA PET/CT positivity rate, localization of positive findings, and impact on patient management (Supplemental Fig. 1) (supplemental materials are available at <http://jnm.snmjournals.org>). All centers obtained local ethics clearance for prospective recruitment of patients and data collection, according to national regulations. All subjects signed an informed consent form.

### Patients

Patients who had histopathologically proven prostate adenocarcinoma, who had undergone primary definitive treatment (radical prostatectomy or radiotherapy), and who had BCR were recruited. All patients were monitored for a minimum of 6 mo after PSMA PET/CT.

The 6 inclusion criteria were an age of greater than 18 y; histopathologically proven prostatic adenocarcinoma; previous primary treatment for PCa (radical prostatectomy or radiotherapy); BCR, defined as a PSA level above 0.2 ng/mL, confirmed by 2 subsequent consecutive measurements, after radical prostatectomy, or as an absolute increase in the PSA level of 2 ng/mL above the nadir after radiotherapy; negative conventional imaging (CT plus bone scintigraphy) and MRI results for patients with PSA levels of 4–10 ng/mL; and written informed consent.

The 3 exclusion criteria were a history of any malignancy other than PCa; a history of Paget disease; and BCR and PSA levels of greater than or equal to 10 ng/mL.

### PET/CT Imaging

All patients underwent PSMA PET/CT with the same radiopharmaceutical, <sup>68</sup>Ga-PSMA-11 (18–21), which was synthesized at the radiopharmaceutical laboratory of each participating center. PET studies

were performed on dedicated PET/CT scanners, and image quality was evaluated by board-certified nuclear medicine physicians.

According to the methodology proposed in the medical literature (10), patients were administered <sup>68</sup>Ga-PSMA-11 (2 MBq/kg; a minimum of 125 MBq) by slow intravenous injection. At 60 to 90 min after injection, standard image acquisition was performed. Low-dose (diagnostic) CT images were obtained from the midthigh to above the orbitomeatal line. Three-dimensional PET images were acquired for the same body extension, for at least 2 min/bed position. Real true-body images (images from head to toes), contrast-enhanced CT, and diuretic and late images were allowed.

PET/CT studies were assessed by 2 board-certified nuclear medicine physicians with extensive experience in PSMA PET/CT oncologic imaging at each center, and all scans were later centrally reviewed. Discordant findings were addressed at consensus meetings, and final results were used for analysis.

### PET/CT Image Analysis

The studies were classified as either positive or negative with regard to the identification of findings suggestive of recurrence on the basis of procedure guidelines for PCa imaging (Fig. 1) (10). The anatomic sites of the lesions were registered.

PSMA PET/CT findings were compared with histology (when necessary, in the judgment of the clinician); correlative imaging methods, such as CT with contrast, MRI, whole-body MRI, and bone scanning; and clinical and laboratory data (PSA behavior). All data were obtained in the normal care pathway.

Given the composite nature of the standard of reference, we could not calculate sensitivity or specificity; furthermore, a proper evaluation of negative findings was beyond the scope of the present study, which focused on assessing the PSMA PET/CT detection rate (positivity rate), defined as the proportion of patients with positive PSMA PET/CT results.

### Intention to Treat

Before PSMA PET/CT, an intention-to-treat questionnaire was completed by the assistant urooncology teams by the time of referral for evaluation; the treatment categories were radiotherapy only, radiotherapy and antiandrogenic therapy (ADT), salvage lymphadenectomy, ADT only, active surveillance, bilateral orchiectomy, second-generation ADT (abiraterone or enzalutamide), radionuclide therapy, and chemotherapy (taxane).

After the PSMA PET/CT results were made available, the assistant urooncology teams completed the same questionnaire on the basis of the actual treatments used.

### Statistical Analyses

The demographic and clinical variables were tabulated using descriptive analysis. Continuous variables were assessed for the gaussian distribution of the data and presented as mean  $\pm$  SD, if normally distributed, or median (25th percentile, 75th percentile) if not normally distributed. Comparisons of patients with positive PSMA results and those with negative PSMA results were performed using the *t* test or Wilcoxon–Mann–Whitney test. Discrete variables were presented as proportions and compared between groups using the  $\chi^2$  test. A multivariate logistic regression analysis was performed to identify the independent predictors of positive PSMA results. Variables were selected for the regression model on the basis of significant associations in the univariate analysis and previous clinical knowledge. The level of significance was set at a *P* value of less than 0.05. Analyses were performed using Stata version 15.1 (Stata Corp.).

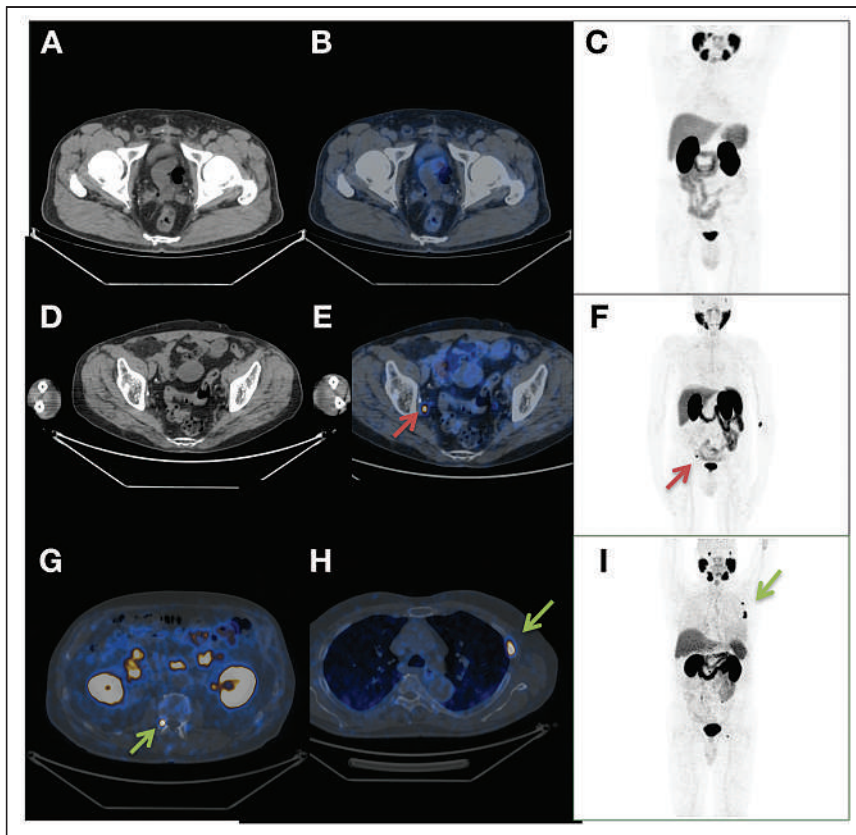


**FIGURE 1.** (A–C) Negative PSMA PET/CT results for 65-y-old patient who had undergone radical prostatectomy plus PNLN and had T3bN0 BCR (PSA, 0.55 ng/mL). Treatment plan was not altered by PSMA PET/CT results (radiotherapy) (A: axial CT; B: axial fusion; C: maximum-intensity projection [MIP]). (D–F) Positive PSMA PET/CT results for 67-y-old patient who had undergone radical prostatectomy plus PNLN and who had T2aN1 BCR (PSA, 0.4 ng/mL). Treatment plan was modified from radiotherapy to ADT (D: axial CT; E: axial fusion; F: MIP) for 0.4-cm lymph nodes (red arrows). (G–I) Positive PSMA PET/CT results for 65-y-old patient who had undergone radical prostatectomy plus PNLN and who had T3aN0 BCR (PSA, 0.2 ng/mL). Treatment plan was modified from radiotherapy to chemotherapy (G: axial CT; H: axial fusion; I: MIP) for metastatic bone lesions (green arrows). PNLN = pelvic lymph node dissection.

## RESULTS

### Patient Characteristics

A total of 1,198 PCa patients referred for PSMA PET/CT because of BCR between November 2017 and December 2019 were enrolled; 194 were subsequently excluded because of missing information or loss of follow-up data. Therefore, a cohort of 1,004 patients could be analyzed, here divided by country: Azerbaijan (48), Brazil (165), Colombia (29), India (86), Israel (16), Italy (172), Jordan (26), Lebanon (65), Malaysia (35), Mexico (91), Pakistan (19), Poland (111), South Africa (42), Turkey (57), and Uruguay (42). For 2 nations (India and Turkey), data from 2 contributing centers were pooled together for the present study (see the list of participant centers and contributors in the supplemental materials). The distribution of patients according to the Gleason score (GS) was as follows: for a GS of 7, there were 613 patients (61.1%); for a GS of 8, there were 196 patients (19.5%); for a GS of 9, there were 180 patients (17.9%); and for a GS of 10, there were 15 patients (1.5%). The distribution of patients according to PSA levels at PET/CT was as follows: for PSA levels of less than 0.2 ng/mL, there were 41 patients (4.1%); for PSA levels between greater than or equal to 0.2 ng/mL and less than 0.5 ng/mL, there were 188 patients (18.7%); for PSA

levels between greater than or equal to 0.5 ng/mL and less than 1 ng/mL, there were 232 patients (23.1%); for PSA levels between greater than or equal to 1 ng/mL and less than 2 ng/mL, there were 235 patients (23.4%); for PSA levels between greater than or equal to 2 ng/mL and less than 4 ng/mL, there were 206 patients (20.5%); and for PSA levels between greater than or equal to 4 ng/mL and less than 10 ng/mL, there were 102 patients (10.2%). The mean PSA doubling time was 11.18 mo (SD, 13.15 mo) (Table 1). Overall, 780 patients (77.7%) were treated initially with radical prostatectomy and 224 (22.3%) were treated with radiotherapy. At the time of the PET scan, the mean time from PCa diagnosis to BCR was 15.6 mo (range, 0.6–43.7 mo); 248 patients (24.7%) were receiving ongoing ADT; and 630 patients (62.7%) had a PSA doubling time of less than or equal to 10 mo.

The mean age of patients was 67.3 y (range, 45–87 y); 908 men (90.4%) met the eligibility requirement because they had PSA levels of less than 4 ng/mL, whereas 96 men (9.6%) had PSA concentrations of 4–10 ng/mL and negative MRI, CT, and bone scintigraphy results. The mean PSA level at the time of the PET scan was 1.55 ng/mL. Regarding the stage at presentation, 443 men (44.1%) had clinical stages T1–T2 and 341 (34.0%) had clinical stages T3–T4; in 220 men (21.9%), the T stage was unknown. The mean duration of follow-up after PSMA PET/CT was 16.8 mo (SD, 9.3 mo).

Regarding income, 105, 509, and 390 patients were in the lower middle-income, upper middle-income, and high-income groups, respectively. PSA differences were not significant among them ( $P = 0.94$ ). Of note, there were statistically significant differences regarding PSA doubling time, ongoing ADT, and radiotherapy as the primary treatment among the different income groups. For these 3 groups, the mean PSA doubling times were 9.14, 9.98, and 13.3 mo ( $P < 0.001$ ). There were 40 patients (38.1%), 131 patients (25.7%), and 77 patients (19.7%) receiving ongoing ADT ( $P < 0.001$ ). Radiotherapy was the primary treatment in 42 patients (40.0%), 129 patients (25.3%), and 53 patients (13.6%) ( $P < 0.001$ ).

### PSMA PET/CT

At least 1 malignant lesion was found in 65.1% of the patients (654/1,004), whereas 34.9% (350/1,004) had negative PSMA PET/CT results, with no detectable disease. A summary of the PSMA PET/CT results is shown in Table 1.

There was a correlation between PSMA PET/CT and the GS ( $P < 0.001$ ). Detection rates were 60.5% (371/613) for patients with a GS of 7; 66.3% (130/196) for those with a GS of 8; 77.8% (140/180) for those with a GS of 9; and 86.7% (13/15) for those with a GS of 10 (Fig. 2).

**TABLE 1**  
Patient Characteristics Based on PSMA PET Results

Characteristic	All patients (n = 1,004)*	Patients with negative PSMA PET/CT results (n = 350)*	Patients with positive PSMA PET/CT results (n = 654)*	P
Age <sup>†</sup>	67.29 ± 7.48	66.37 ± 7.36	67.77 ± 7.51	0.005
PSA level at time of PET scan				<0.001
<0.2	41 (4.1)	20 (5.7)	21 (3.2)	
0.2–0.5	188 (18.7)	104 (29.7)	84 (12.8)	
0.5–1.0	232 (23.1)	108 (30.9)	124 (19.0)	
1–2	235 (23.4)	77 (22.0)	158 (24.2)	
2–4	206 (20.5)	35 (10.0)	171 (26.1)	
>4	102 (10.2)	6 (1.7)	96 (14.7)	
PSA doubling time <sup>†</sup>	11.18 ± 13.15	12.97 ± 14.04	10.22 ± 12.56	0.002
Initial PSA before therapy <sup>†</sup>	17.27 ± 22.10	14.63 ± 17.69	18.69 ± 24.02	0.006
TNM				<0.001
T1	4 (0.5)	2 (0.6)	2 (0.4)	
T2	439 (56.0)	208 (65.8)	231 (49.4)	
T3	333 (42.5)	103 (32.6)	230 (49.1)	
T4	8 (1.0)	3 (0.9)	5 (1.1)	
Ongoing ADT	248 (24.7)	62 (17.7)	186 (28.4)	<0.001
Radiotherapy as first treatment	224 (22.3)	35 (10.0)	189 (28.9)	<0.001
Time to relapse <sup>‡</sup>	23.0 (8.0, 49.0)	22.5 (8.0, 48.0)	24.0 (9.0, 51.0)	0.57
GS				<0.001
7	613 (61.1)	242 (69.1)	371 (56.7)	
8	196 (19.5)	66 (18.9)	130 (19.9)	
9	180 (17.9)	40 (11.4)	140 (21.4)	
10	15 (1.5)	2 (0.6)	13 (2.0)	
Country income				0.07
High income	390 (38.8)	149 (42.6)	241 (36.9)	
Upper middle income	509 (50.7)	160 (45.7)	349 (53.4)	
Lower middle income	105 (10.5)	41 (11.7)	64 (9.8)	
Continent				0.73
Africa	42 (4.2)	18 (5.1)	24 (3.7)	
Asia	182 (18.1)	64 (18.3)	118 (18.0)	
Europe	388 (38.6)	132 (37.7)	256 (39.1)	
Latin America	392 (39.0)	136 (38.9)	256 (39.1)	

\*Data are reported as numbers of patients, with percentages of patients in parentheses, unless otherwise indicated.

<sup>†</sup>Data are reported as mean ± SD.

<sup>‡</sup>Data are reported as median (25th percentile, 75th percentile).

We also found a significant correlation between PSMA PET/CT positivity and PSA values ( $P < 0.001$ ). Detection rates were 51.2% (21/41) for PSA values of less than 0.2; 44.7% (84/188) for PSA values between greater than or equal to 0.2 and less than 0.5; 53.4% (124/232) for PSA values between greater than or equal to 0.5 and less than 1; 67.2% (158/235) for PSA values between greater than or equal to 1 and less than 2; 83.0% (171/206) for

PSA values between greater than or equal to 2 and less than 4; and 94.1% (96/102) for PSA values between greater than or equal to 4 and less than 10 (Fig. 3).

PSMA PET/CT results were positive for 69.4% of the patients (437/630) whose PSA doubling times were less than or equal to 10 mo and for 58.0% of the patients (217/374) whose PSA doubling times were greater than 10 mo ( $P = 0.003$ ) (Fig. 4).

The PSMA PET/CT positivity rates per anatomic site were 13.7% (138/1,004) in the prostate or prostatic bed only; 3.9% (39/1,004) in the prostate or prostatic bed and pelvic lymph nodes; 20.5% (206/1,004) in the pelvic lymph nodes only; and 27.0% (271/1,004) in a metastasis at any site (bone only in 10.0% [100/1,004]) (Table 2). In a univariate analysis, factors associated with positive PSMA PET/CT results were age, the PSA level at the time of the PET scan, PSA doubling time, the initial PSA level before therapy, TNM, GS, ongoing ADT, and radiotherapy as the first treatment. Logistic regression showed that PSMA PET/CT positivity was associated with the GS, the PSA level at the time of the PET scan, decreasing PSA doubling time, and radiotherapy as the primary treatment (Table 3).

Of the 1,004 cases included in the present study, 12.4% (124 patients) had doubtful PET findings (as reported by local readers). Of these, 90 patients had other positive findings, regardless of the indeterminate one(s); thus, their scans were already defined as positive PSMA PET/CT scans. Of the remaining 34 patients (3.4%) in whom the indeterminate lesion at PSMA PET/CT was the sole finding, 3 were confirmed to have true-positive results on the basis of follow-up data, whereas 31 (3.1%) were regarded as having false-positive results (encompassing reactive lymph nodes, bone fractures, trauma, and benign pulmonary lesions).

#### Impact of PSMA PET/CT on Clinical Management

Disease management changed in 56.8% of our cohort (570/1,004) after PSMA PET/CT information was obtained. The following changes occurred as a result of PSMA PET/CT: 77 patients underwent active surveillance, 35 underwent radiotherapy only, 55 underwent radiotherapy and ADT, 152 underwent ADT only, 48 underwent salvage lymphadenectomy, 5 underwent bilateral orchiectomy, 140 underwent second-generation ADT (abiraterone or enzalutamide), 10 underwent radionuclide therapy, and 48 (patients with polymetastatic disease) started taxane chemotherapy.

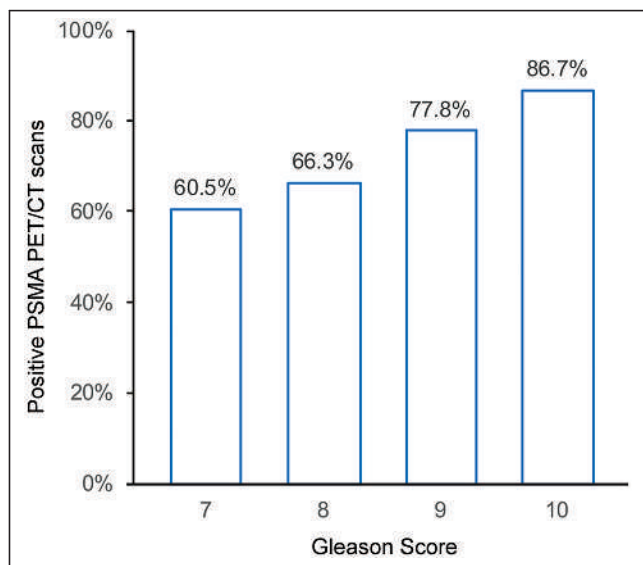


FIGURE 2. Correlation between PSMA PET/CT positivity and GS.

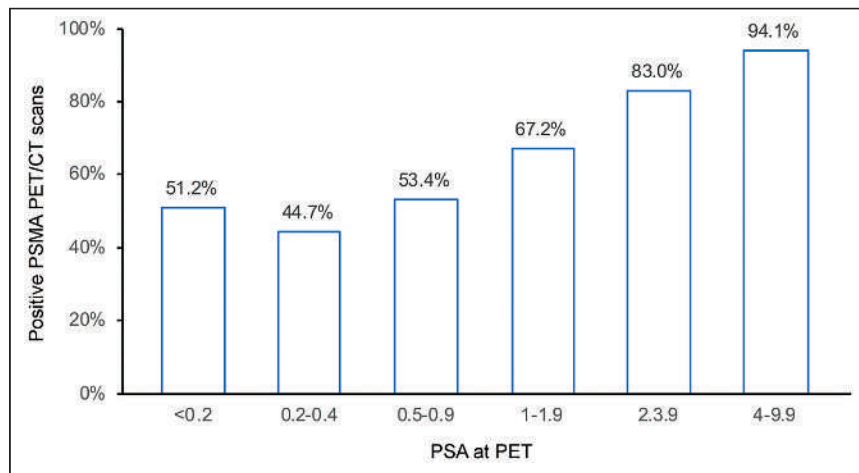


FIGURE 3. Correlation between PSMA PET/CT positivity and PSA values.

Of the patients for whom there was no management change motivated by PSMA PET/CT results (434/1,004; 43.2%), 118 remained under active surveillance, 57 underwent radiotherapy only, 48 underwent radiotherapy and ADT, 5 underwent salvage lymphadenectomy, 155 underwent ADT, 2 underwent bilateral orchiectomy, 32 underwent second-generation ADT (abiraterone or enzalutamide), and 17 (patients with polymetastatic disease) started taxane chemotherapy (Fig. 4).

#### PSMA PET/CT Worldwide

The centers were grouped in 2 distinct ways: by country income (high income: Israel, Italy, Poland, and Uruguay; upper middle income: Azerbaijan, Brazil, Colombia, Jordan, Lebanon, Malaysia, Mexico, South Africa, and Turkey; and lower middle income: India and Pakistan) and by continent (Africa, America, Asia, and Europe). There were no significant differences in PSMA PET/CT positivity by lower middle income, upper middle income, and high income (61%, 69%, and 62%, respectively) or by continent (Africa: 57%; Asia: 65%; Europe: 66%; and Latin America: 65%) ( $P = 0.07$  and  $P = 0.73$ , respectively) (Table 1).

#### DISCUSSION

Our findings resonate with the available literature on the use of PSMA PET/CT in the evaluation of PCa patients in the scenario of BCR (3–8,10,20–44). We analyzed 4 main aspects of PSMA PET/CT in this setting: positivity rate, clinical factors associated with PSMA positivity, differences in performance with regard to continents and incomes, and impact on clinical management. The PSMA PET/CT positivity rate was 65.1%, similar to the positivity rates reported in other studies, ranging overall from 63% to 75% (10,14,16,21,22). Also, increasing PSA levels at the time of the scan were associated with higher PSMA PET/CT positivity, with rates similar to those previously reported (Supplemental Table 1); the exception was higher PSMA PET/CT positivity in the group with PSA levels of less than 0.2 ng/mL compared with the mean in the available literature: 51.2% versus 36.8% (3–8,10,20–44). This difference might be explained by the small number of patients in this group in our cohort (41) but also by the small number of patients evaluated in the cohort of all patients (316). Nevertheless, 51.2% falls into the range observed in the literature (11.3%–58.3%). In the other scenarios (PSA levels of <0.5, <1.0,

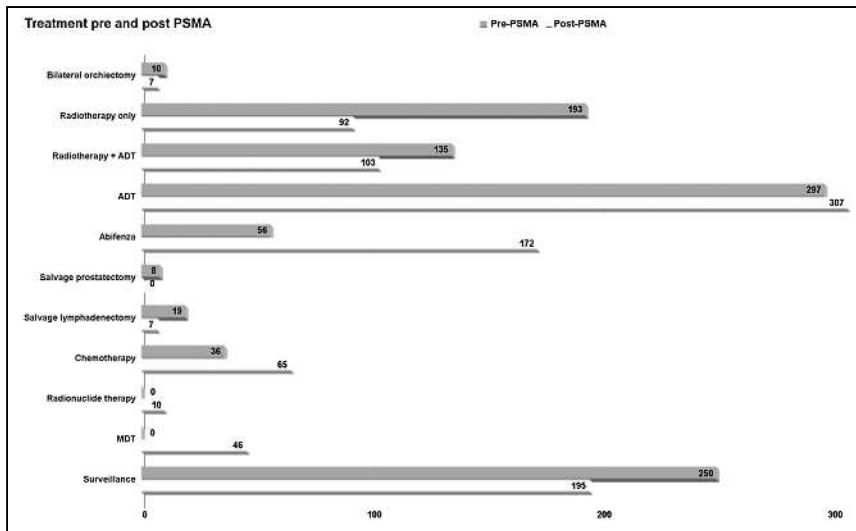


**FIGURE 4.** Impact of PSMA PET/CT on clinical management. MDT = metastasis-directed therapy.

and  $<2.0$  ng/mL), the positivity rates were quite similar (44.7% vs. 43.3%; 53.4% vs. 52.2%, and 67.2% vs. 58.9%, respectively).

The observed location of malignant lesions is in agreement with those in previous reports, with lymph nodes being the principal site of recurrence (24.4%), followed by local recurrence in the prostate bed (17.6%), and with any metastatic disease in 27.0% (9,45).

**TABLE 2**

Positive PSMA PET/CT Studies per Anatomic Site

Anatomic site	Result for positive PSMA PET/CT studies*
Prostate or prostatic bed only	138 (13.7)
Prostate or prostatic bed + lymph nodes	39 (3.9)
Lymph nodes only	206 (20.5)
Metastasis at any site	271 (27.0)
Bone only	100 (10.0)

\*Data are reported as numbers of patients, with percentages of patients in parentheses.

**TABLE 3**

Association of Clinical Covariates with Likelihood of Detection by PSMA PET/CT

Covariate	Odds ratio	z	P	95% CI	
				Lower	Upper
Age	1.01	1.69	0.091	0.99	1.03
PSA level at PCa diagnosis	0.99	-0.05	0.958	0.99	1.01
GS	1.37	3.30	0.001	1.25	1.65
at time of PSMA PET/CT	1.72	7.57	0.001	1.47	1.97
PSA doubling time	0.98	-3.30	0.001	0.97	0.99
Ongoing ADT	1.23	1.14	0.255	0.93	1.76
Radiotherapy first	2.17	3.56	0.001	1.42	3.34

Furthermore, higher positivity rates were also associated with features of advanced or aggressive disease other than increasing PSA levels: a shorter PSA doubling time ( $\leq 10$  mo) and a higher GS. These findings are also in line with the current available literature (42,46) and are likely due to the presence of more neoplastic lesions and to higher tumoral cell turnover, which provide more available sites for PSMA ligand binding and, thus, lead to positive PET/CT results.

One interesting finding was the association of radiotherapy as a primary radical treatment with PSMA PET/CT positivity in the BCR setting. Although patients receiving radiotherapy represented only 22.3% of all patients, they comprised 28.9% of patients with positive PSMA PET/CT results ( $P < 0.001$ ). It is already known that, in comparison to radical prostatectomy, radiotherapy is associated with higher BCR rates (46). Our results suggest that in addition to having more frequent residual/recurrent disease, these patients are also more likely to have positive PSMA PET/CT scans in the BCR setting.

The most relevant finding is that there were no statistically significant differences in PSMA PET/CT performance among continents or among the different income categories in which the participants were distributed. This finding is important because it highlights the fact that the great heterogeneities among nations do not seem to interfere with each country's capacity to provide high-quality PSMA PET/CT studies in the appropriate medical centers.

PSMA PET/CT affected clinical management in more than half of our cohort, as the therapeutic strategy was altered by PSMA PET/CT results 56.8% of the time, similar to previous reports in different studies (13,16,21).

Regarding the limitations of the present study, a major one is that histopathology as a gold standard was available only in a few cases. It is well known that histopathologic confirmation in all patients is not feasible because of practical and ethical issues.

Hence, in most patients, a composite standard of reference (histopathology and clinical and laboratory evaluations) was used. Another important limitation is the relatively small percentage of patients included in low-income countries and in Africa. Furthermore,

South Africa's income and PSMA PET/CT availability are not representative of the continent. Moreover, regarding the impact of PSMA PET/CT on clinical management, the available data unfortunately do not permit an evaluation of its effects on survival rates.

The endeavor of performing this multicenter, international study, enrolling more than 1,000 patients from many countries was made possible only through the combined efforts of several different researchers and the support of the International Atomic Energy Agency, a nonprofit agency, which enabled gathering of this large and diverse cohort.

## CONCLUSION

This multicenter, international, prospective trial of PSMA PET/CT confirms its capability for detecting local and metastatic recurrences in most PCa patients in the setting of BCR. PSMA PET/CT positivity was correlated with the GS, the PSA level at the time of the PET scan, PSA doubling time, and radiotherapy as the primary treatment. PSMA PET/CT results led to changes in therapeutic management in more than half of the cohort. The present study demonstrates the reliability and feasibility of PSMA PET/CT in the workup of PCa patients with BCR.

## DISCLOSURE

This research was partially funded by IAEA. No personal grants, consulting fees, or honoraria were involved in the present work. No other potential conflict of interest relevant to this article was reported.

## ACKNOWLEDGMENTS

We thank the following individuals for their contributions: from the National Centre of Oncology, Baku, Azerbaijan—Jamil A. Aliyev, Fuad Guliyev, Elnur Mehdi, Mirsaleh Valiyev, and Leyla Mehmetbeyli; from Brazil—Margaret Masukawa, Jonatas L. Pereira, Murilo A. Luz, Rodrigo J. Cerci, and Miguel Morita; from Azienda Ospedaliero-Universitaria di Bologna, Bologna, Italy—Andrea Farolfi, Paolo Castellucci, Veronica Cervati, Francesca Serani, and Riccardo Schiavina; from King Hussein Cancer Center, Amman, Jordan—Ula Al-Rasheed and Samer Salah; from the University of Pretoria, Pretoria, South Africa—Mike Sathekge; from Ankara University Medical school—Çiğdem Soydal; and from the Centro Uruguayo de Imagenología Molecular, Montevideo, Uruguay—G. dos Santos, E. Silvera, and M. Rodríguez.

## KEY POINTS

**QUESTION:** In a large international cohort of PCa patients in the setting of BCR, how similar are PSMA PET/CT positivity rates and impact on clinical management among countries on different continents and with different incomes?

**PERTINENT FINDINGS:** PSMA PET/CT positivity was correlated with the GS, serum PSA levels, and radiotherapy as the primary treatment. An impact of PSMA PET/CT results on clinical management was observed in most cases, and all findings were similarly consistent regardless of the country.

**IMPLICATIONS FOR PATIENT CARE:** Our results confirm the worldwide feasibility and usefulness of PSMA PET/CT in the setting of PCa BCR.

## REFERENCES

1. Ferlay JEM, Lam F, Colombet M, et al. Global cancer observatory: cancer tomorrow. Lyon, France: International Agency for Research on Cancer. <https://gco.iarc.fr/today/data/factsheets/cancers/40-All-cancers-excluding-non-melanoma-skin-cancer-fact-sheet.pdf>. Accessed December 21, 2021.
2. Rawla P. Epidemiology of prostate cancer. *World J Oncol*. 2019;10:63–89.
3. Gupta SK, Watson T, Denham J, et al. Prostate-specific membrane antigen positron emission tomography-computed tomography for prostate cancer: distribution of disease and implications for radiation therapy planning. *Int J Radiat Oncol Biol Phys*. 2017;99:701–709.
4. Meredith G, Wong D, Yaxley J, et al. The use of  $^{68}\text{Ga}$ -PSMA PET CT in men with biochemical recurrence after definitive treatment of acinar prostate cancer. *BJU Int*. 2016;118(suppl 3):49–55.
5. Morigi JJ, Stricker PD, van Leeuwen PJ, et al. Prospective comparison of  $^{18}\text{F}$ -fluoromethylcholine versus  $^{68}\text{Ga}$ -PSMA PET/CT in prostate cancer patients who have rising psa after curative treatment and are being considered for targeted therapy. *J Nucl Med*. 2015;56:1185–1190.
6. Afshar-Oromieh A, Avtzi E, Giesel FL, et al. The diagnostic value of PET/CT imaging with the  $^{68}\text{Ga}$ -labelled PSMA ligand HBED-CC in the diagnosis of recurrent prostate cancer. *Eur J Nucl Med Mol Imaging*. 2015;42:197–209.
7. Afshar-Oromieh A, Holland-Letz T, Giesel FL, et al. Diagnostic performance of  $^{68}\text{Ga}$ -PSMA-11 (HBED-CC) PET/CT in patients with recurrent prostate cancer: evaluation in 1007 patients. *Eur J Nucl Med Mol Imaging*. 2017;44:1258–1268.
8. Calais J, Czernin J, Cao M, et al.  $^{68}\text{Ga}$ -PSMA-11 PET/CT mapping of prostate cancer biochemical recurrence after radical prostatectomy in 270 patients with a PSA level of less than 1.0 ng/mL: impact on salvage radiotherapy planning. *J Nucl Med*. 2018;59:230–237.
9. Dietlein F, Kobe C, Neubauer S, et al. PSA-stratified performance of  $^{18}\text{F}$ - and  $^{68}\text{Ga}$ -PSMA PET in patients with biochemical recurrence of prostate cancer. *J Nucl Med*. 2017;58:947–952.
10. Fendler WP, Eiber M, Beheshti M, et al.  $^{68}\text{Ga}$ -PSMA PET/CT: joint EANM and SNMMI procedure guideline for prostate cancer imaging—version 1.0. *Eur J Nucl Med Mol Imaging*. 2017;44:1014–1024.
11. Eiber M, Maurer T, Souvatzoglou M, et al. Evaluation of hybrid  $^{68}\text{Ga}$ -PSMA ligand PET/CT in 248 patients with biochemical recurrence after radical prostatectomy. *J Nucl Med*. 2015;56:668–674.
12. Hofman MS, Hicks RJ, Maurer T, Eiber M. Prostate-specific membrane antigen PET: clinical utility in prostate cancer, normal patterns, pearls, and pitfalls. *Radiographics*. 2018;38:200–217.
13. Han S, Woo S, Kim YJ, Suh CH. Impact of  $^{68}\text{Ga}$ -PSMA PET on the management of patients with prostate cancer: a systematic review and meta-analysis. *Eur Urol*. 2018;74:179–190.
14. Bashir U, Tree A, Mayer E, et al. Impact of  $^{68}\text{Ga}$ -PSMA PET/CT on management in prostate cancer patients with very early biochemical recurrence after radical prostatectomy. *Eur J Nucl Med Mol Imaging*. 2019;46:901–907.
15. Albisinni S, Artigas C, Aoun F, et al. Clinical impact of  $^{68}\text{Ga}$ -prostate-specific membrane antigen (PSMA) positron emission tomography/computed tomography (PET/CT) in patients with prostate cancer with rising prostate-specific antigen after treatment with curative intent: preliminary analysis of a multidisciplinary approach. *BJU Int*. 2017;120:197–203.
16. Mattioli AB, Santos A, Vicente A, et al. Impact of  $^{68}\text{Ga}$ -PSMA PET/CT on treatment of patients with recurrent/metastatic high risk prostate cancer - a multicenter study. *Int Braz J Urol*. 2018;44:892–899.
17. Matushita CS, da Silva AMM, Schuck PN, et al.  $^{68}\text{Ga}$ -prostate-specific membrane antigen (PSMA) positron emission tomography (PET) in prostate cancer: a systematic review and meta-analysis. *Int Braz J Urol*. 2021;47:705–729.
18. National Cancer Institute. Cancer reference information. <https://www.cancer.gov/publications/dictionaries/cancer-drug/def/gallium-ga-68-labeled-psma-11>. Accessed September 24, 2020.
19. Ceci F, Oprea-Lager DE, Emmett L, et al. E-PSMA: the EANM standardized reporting guidelines v1.0 for PSMA-PET. *Eur J Nucl Med Mol Imaging*. 2021;48:1628–1640.
20. Markowski MC, Chen Y, Feng Z, et al. PSA doubling time and absolute PSA predict metastasis-free survival in men with biochemically recurrent prostate cancer after radical prostatectomy. *Clin Genitourin Cancer*. 2019;17:470–475.e1.
21. Hope TA, Aggarwal R, Chee B, et al. Impact of  $^{68}\text{Ga}$ -PSMA-11 PET on management in patients with biochemically recurrent prostate cancer. *J Nucl Med*. 2017;58:1956–1961.
22. Tan N, Bavadian N, Calais J, et al. Imaging of prostate specific membrane antigen targeted radiotracers for the detection of prostate cancer biochemical recurrence after definitive therapy: a systematic review and meta-analysis. *J Urol*. 2019;202:231–240.

23. Fendler WP, Calais J, Eiber M, et al. Assessment of <sup>68</sup>Ga-PSMA-11 PET accuracy in localizing recurrent prostate cancer: a prospective single-arm clinical trial. *JAMA Oncol*. 2019;5:856–863.
24. Sachpekidis C, Eder M, Kopka K, et al. <sup>68</sup>Ga-PSMA-11 dynamic PET/CT imaging in biochemical relapse of prostate cancer. *Eur J Nucl Med Mol Imaging*. 2016;43:1288–1299.
25. Schmuck S, Nordlohne S, von Klot CA, et al. Comparison of standard and delayed imaging to improve the detection rate of [<sup>68</sup>Ga]PSMA I&T PET/CT in patients with biochemical recurrence or prostate-specific antigen persistence after primary therapy for prostate cancer. *Eur J Nucl Med Mol Imaging*. 2017;44:960–968.
26. Kranzbühler B, Nagel H, Becker AS, et al. Clinical performance of <sup>68</sup>Ga-PSMA-11 PET/MRI for the detection of recurrent prostate cancer following radical prostatectomy. *Eur J Nucl Med Mol Imaging*. 2018;45:20–30.
27. Miksch J, Bottke D, Krohn T, et al. Interobserver variability, detection rate, and lesion patterns of <sup>68</sup>Ga-PSMA-11-PET/CT in early-stage biochemical recurrence of prostate cancer after radical prostatectomy. *Eur J Nucl Med Mol Imaging*. 2020;47:2339–2347.
28. Sonni I, Eiber M, Fendler WP, et al. Impact of <sup>68</sup>Ga-PSMA-11 PET/CT on staging and management of prostate cancer patients in various clinical settings: a prospective single-center study. *J Nucl Med*. 2020;61:1153–1160.
29. Sanli Y, Kuyumcu S, Sanli O, et al. Relationships between serum PSA levels, Gleason scores and results of <sup>68</sup>Ga-PSMA PET/CT in patients with recurrent prostate cancer. *Ann Nucl Med*. 2017;31:709–717.
30. Lengana T, van de Wiele C, Lawal I, et al. <sup>68</sup>Ga-PSMA-HBED-CC PET/CT imaging in black versus white South African patients with prostate carcinoma presenting with a low volume, androgen dependent biochemical recurrence: a prospective study. *Nucl Med Commun*. 2018;39:179–185.
31. Rauscher I, Düwel C, Haller B, et al. Efficacy, predictive factors, and prediction nomograms for <sup>68</sup>Ga-labeled prostate-specific membrane antigen-ligand positron-emission tomography/computed tomography in early biochemical recurrent prostate cancer after radical prostatectomy. *Eur Urol*. 2018;73:656–661.
32. Berliner C, Tienken M, Frenzel T, et al. Detection rate of PET/CT in patients with biochemical relapse of prostate cancer using [<sup>68</sup>Ga]PSMA I&T and comparison with published data of [<sup>68</sup>Ga]PSMA HBED-CC. *Eur J Nucl Med Mol Imaging*. 2017;44:670–677.
33. Derlin T, Schmuck S, Juhl C, et al. PSA-stratified detection rates for [<sup>68</sup>Ga]THP-PSMA, a novel probe for rapid kit-based <sup>68</sup>Ga labeling and PET imaging, in patients with biochemical recurrence after primary therapy for prostate cancer. *Eur J Nucl Med Mol Imaging*. 2018;45:913–922.
34. Grubmüller B, Baltzer P, D'Andrea D, et al. <sup>68</sup>Ga-PSMA 11 ligand PET imaging in patients with biochemical recurrence after radical prostatectomy: diagnostic performance and impact on therapeutic decision-making. *Eur J Nucl Med Mol Imaging*. 2018;45:235–242.
35. Deandreis D, Guarneri A, Ceci F, et al. <sup>68</sup>Ga-PSMA-11 PET/CT in recurrent hormone-sensitive prostate cancer (HSPC): a prospective single-centre study in patients eligible for salvage therapy. *Eur J Nucl Med Mol Imaging*. 2020;47:2804–2815.
36. Farolfi A, Ceci F, Castellucci P, et al. <sup>68</sup>Ga-PSMA-11 PET/CT in prostate cancer patients with biochemical recurrence after radical prostatectomy and PSA <0.5 ng/mL: efficacy and impact on treatment strategy. *Eur J Nucl Med Mol Imaging*. 2019;46:11–19.
37. Hoffmann MA, Buchholz HG, Wieler HJ, et al. PSA and PSA kinetics thresholds for the presence of <sup>68</sup>Ga-PSMA-11 PET/CT-detectable lesions in patients with biochemical recurrent prostate cancer. *Cancers (Basel)*. 2020;12:398.
38. Krafl P, Maurer T, Gafita A, et al. Pre-test <sup>68</sup>Ga-PSMA-ligand PET/CT positivity in early biochemical recurrent prostate cancer after radical prostatectomy: validation of a prediction model. *EJNMMI Res*. 2020;10:6.
39. Bianchi L, Borghesi M, Schiavina R, et al. Predictive accuracy and clinical benefit of a nomogram aimed to predict <sup>68</sup>Ga-PSMA PET/CT positivity in patients with prostate cancer recurrence and PSA < 1 ng/ml external validation on a single institution database. *Eur J Nucl Med Mol Imaging*. 2020;47:2100–2105.
40. Calais J, Ceci F, Eiber M, et al. <sup>18</sup>F-fluciclovine PET-CT and <sup>68</sup>Ga-PSMA-11 PET-CT in patients with early biochemical recurrence after prostatectomy: a prospective, single-centre, single-arm, comparative imaging trial. *Lancet Oncol*. 2019;20:1286–1294.
41. McCarthy M, Francis R, Tang C, Watts J, Campbell A. A multicenter prospective clinical trial of <sup>68</sup>gallium PSMA HBED-CC PET-CT restaging in biochemically relapsed prostate carcinoma: oligometastatic rate and distribution compared with standard imaging. *Int J Radiat Oncol Biol Phys*. 2019;104:801–808.
42. Verburg FA, Pfister D, Heidenreich A, et al. Extent of disease in recurrent prostate cancer determined by [<sup>68</sup>Ga]PSMA-HBED-CC PET/CT in relation to PSA levels, PSA doubling time and Gleason score. *Eur J Nucl Med Mol Imaging*. 2016;43:397–403.
43. Fourquet A, Aveline C, Cussenot O, et al. <sup>68</sup>Ga-PSMA-11 PET/CT in restaging castration-resistant nonmetastatic prostate cancer: detection rate, impact on patients' disease management and adequacy of impact. *Sci Rep*. 2020;10:2104.
44. Treglia G, Annunziata S, Pizzuto DA, Giovannella L, Prior JO, Ceriani L. Detection rate of <sup>18</sup>F-labeled PSMA PET/CT in biochemical recurrent prostate cancer: a systematic review and a meta-analysis. *Cancers (Basel)*. 2019;11:710.
45. Barbosa FG, Queiroz MA, Nunes RF, et al. Revisiting prostate cancer recurrence with PSMA PET: atlas of typical and atypical patterns of spread. *Radiographics*. 2019;39:186–212.
46. Perera M, Papa N, Christidis D, et al. Sensitivity, specificity, and predictors of positive <sup>68</sup>Ga-prostate-specific membrane antigen positron emission tomography in advanced prostate cancer: a systematic review and meta-analysis. *Eur Urol*. 2016;70:926–937.

# The European Association of Urology Biochemical Recurrence Risk Groups Predict Findings on PSMA PET in Patients with Biochemically Recurrent Prostate Cancer After Radical Prostatectomy

Liang Dong<sup>1,2</sup>, Yun Su<sup>3</sup>, Yinjie Zhu<sup>2</sup>, Mark C. Markowski<sup>4</sup>, Mei Xin<sup>5</sup>, Michael A. Gorin<sup>1</sup>, Baijun Dong<sup>2</sup>, Jiahua Pan<sup>2</sup>, Martin G. Pomper<sup>6</sup>, Jianjun Liu<sup>5</sup>, Kenneth J. Pienta<sup>1</sup>, Wei Xue<sup>2</sup>, and Steven P. Rowe<sup>6</sup>

<sup>1</sup>James Buchanan Brady Urological Institute and Department of Urology, Johns Hopkins University School of Medicine, Baltimore, Maryland; <sup>2</sup>Department of Urology, Renji Hospital, Shanghai Jiao Tong University School of Medicine, Shanghai, China; <sup>3</sup>Bloomberg School of Public Health, Johns Hopkins University, Baltimore, Maryland; <sup>4</sup>Department of Oncology, Sidney Kimmel Comprehensive Cancer Center, Johns Hopkins University School of Medicine, Baltimore, Maryland; <sup>5</sup>Department of Nuclear Medicine, Renji Hospital, Shanghai Jiao Tong University School of Medicine, Shanghai, China; and <sup>6</sup>Russell H. Morgan Department of Radiology and Radiological Science, Johns Hopkins University School of Medicine, Baltimore, Maryland

Our purpose was to evaluate the association of a new biochemical recurrence (BCR) risk stratification system with PSMA-targeted PET/CT findings. **Methods:** Two prospective studies that included patients with BCR were pooled. Findings on PSMA PET were catalogued. Patients were characterized according to the European Association of Urology BCR risk categories. Univariable and multivariable analyses were performed by logistic regression. **Results:** In total, 145 patients were included (45 low-risk and 100 high-risk). High-risk BCR patients had a higher positive rate than low-risk patients (82.0% vs. 48.9%;  $P < 0.001$ ) and reached independent predictor status for positive PSMA PET/CT scan results on multivariable logistic regression (odds ratio, 6.73; 95% CI, 2.41–18.76;  $P < 0.001$ ). The area under the curve using the combination of BCR risk group and prostate-specific antigen was higher than that using prostate-specific antigen alone (0.834 vs. 0.759,  $P = 0.015$ ). **Conclusion:** The European Association of Urology BCR risk groups define the candidates who can most benefit from a PSMA PET/CT scan when BCR occurs.

**Key Words:** prostate cancer; BCR; prostate-specific membrane antigen; PET

**J Nucl Med 2022; 63:248–252**  
DOI: 10.2967/jnumed.121.262411

**P**rostate cancer is the second most common cancer type and the fifth leading cause of cancer death in men worldwide (1). In patients who receive either radical prostatectomy (RP) or radiotherapy to treat their primary tumors, approximately 30% will develop biochemical recurrence (BCR) (2). Since, by definition, prostate cancer at this stage is invisible on conventional imaging, it is of importance to stratify BCR patients into different risk groups in order to give intensive treatment to patients with aggressive disease phenotypes.

The European Association of Urology (EAU) BCR risk stratification system was proposed by the EAU prostate cancer guideline update, which defines low-risk BCR after RP as patients with a prostate-specific antigen (PSA) doubling time of more than 12 mo and a Gleason score of less than 8; high-risk BCR after RP is defined as patients with a PSA doubling time of no more than 12 mo or a Gleason score of at least 8 (3). Validation of this risk stratification system in 1,125 patients demonstrated that the 5-y metastatic progression-free and prostate cancer-specific mortality-free survival rates were significantly higher among patients with low-risk BCR. Multivariable analysis confirmed the EAU risk stratification as an independent predictor of metastatic progression and prostate cancer-specific mortality (4).

With the recent advances in prostate-specific membrane antigen (PSMA) PET/CT, our current definition of BCR may soon be obsolete. We may need to begin rephrasing our clinical questions in the context of PSMA positivity. We previously reported that more than 60% of post-RP BCR patients had positive findings on PSMA PET/CT, and according to a metaanalysis, the positive predictive value of PSMA PET/CT was 0.99 based on a histopathologic gold standard (5–7).

The aim of the current study was to compare the detection rates and the localization of PSMA-avid lesions in low-risk versus high-risk BCR patients after RP and to evaluate the association of this new risk stratification system with PSMA PET/CT findings.

## MATERIALS AND METHODS

### Patients

We pooled cohorts of patients with BCR from 2 prospective studies at tertiary referral centers (Johns Hopkins Hospital and Renji Hospital). The inclusion criteria of the patients in each cohort, as well as technical details of the PSMA PET/CT scan (e.g., scanner, scan protocol, and scan interpretation) have been previously reported (5,6). Risk stratification was performed as proposed by Van den Broeck et al. (3).

Pelvis-confined disease was defined by uptake of the radiotracer in the prostate bed, pelvic soft tissue, or pelvic lymph nodes. PSA doubling time was calculated as previously described (6), using the 3 most recent PSA values before PSMA PET/CT. If the slope of the

Received Apr. 7, 2021; revision accepted May 20, 2021.  
For correspondence or reprints, contact Steven P. Rowe (srowe8@jhmi.edu) or Wei Xue (uroxuewei@163.com).  
Published online Jul. 29, 2021.  
COPYRIGHT © 2022 by the Society of Nuclear Medicine and Molecular Imaging.

linear regression was 0 (elevated but constant PSA) or negative (decreasing PSA after initial increase), the PSA doubling time was set as at least 12 mo.

### Statistical Analysis

Logistic regression models were conducted for univariable and multivariable analyses, calculating odds ratios with 95% CIs to estimate the associations between BCR risk stratification and outcomes, adjusting for potential confounders. The predictive value of BCR risk stratification was assessed using the receiver-operating-characteristic curve and the area under the curve. Statistical testing was based on 2-sided tests at the 5% level of significance. SAS software (version 9.4; SAS Institute) was used.

## RESULTS

### Patients

In total, 145 patients were enrolled; 94 were scanned with <sup>18</sup>F-DCFPyL PET/CT (Johns Hopkins Hospital), and 51 were scanned with <sup>68</sup>Ga-PSMA-11 PET/CT (Renji Hospital). Low-risk BCR was present in 45 patients, and high-risk BCR in 100. Table 1 summarizes the clinical and pathologic characteristics of these patients.

### Imaging Findings

Of the 145 patients, 104 (71.7%) had at least one PSMA-positive lesion on the PSMA PET/CT scan. High-risk BCR patients had a significantly higher positive rate than the low-risk

BCR group (82.0% vs. 48.9%;  $P < 0.001$ ; Fig. 1A). On multivariable logistic regression analyses adjusted for age, PSA at the time of the scan, disease-free time, pathologic tumor stage (pT stage), and cohort (Johns Hopkins Hospital or Renji Hospital), the BCR risk group was an independent predictor for a positive PSMA PET/CT result (odds ratio, 6.73; 95% CI, 2.41–18.76;  $P < 0.001$ ; Table 2). The median number of PSMA-positive lesions is 0 (interquartile range, 0–1) for low-risk BCR and 1 (interquartile range, 1–3) for high-risk BCR. The multivariable linear regression model was used to estimate the associations between BCR risk group and lesion number. The model parameter  $\beta$  is 0.85, with statistical significance ( $P = 0.037$ ).

In PSA subgroups, the positive rates of patients with low-risk BCR remained the same (40%) in groups with a PSA of less than 0.5 ng/mL and with a PSA of 0.5–1.0 ng/mL, whereas higher positive rates were observed with increasing PSA values in patients with high-risk BCR. Nearly 95% of patients with a PSA of more than 1.0 ng/mL in the high-risk group had detectable disease on PSMA PET/CT, whereas the positive rate was 66.7% for low-risk patients in the same PSA subgroup (Fig. 1B).

Of the 104 scan-positive patients, 56 (53.8%) had pelvis-confined disease. The BCR risk group was not associated with pelvis-confined disease (Table 2; Fig. 1C). Receiver-operating-characteristic curves were generated to demonstrate the ability of the BCR risk group and PSA to predict positive PSMA PET/CT results. The areas under the curve using the BCR risk group or

**TABLE 1**  
Demographics and Clinical Data for Study Cohort

Parameter	BCR low risk	BCR high risk	<i>P</i>
Median age (y)	71 (IQR, 65–76)	69 (IQR, 63–73)	0.426
Cohort			0.288
Johns Hopkins Hospital	32 (71.1)	62 (62.0)	
Renji Hospital	13 (28.9)	38 (38.0)	
Median disease-free time (y)	5.1 (IQR, 3–8)	2.2 (IQR, 1.3–5.3)	0.012
Adjuvant therapy	44 (97.8)	86 (86.0)	0.242
Salvage therapy	36 (80.0)	85 (85.0)	0.688
PSA (ng/mL) at time of scan			0.195
<0.5	20 (44.4)	31 (31.0)	
0.5–1	10 (22.2)	22 (22.0)	
>1	15 (33.4)	47 (47.0)	
PSADT (mo)*			<0.001
<12	0 (0.0)	87 (89.7)	
≥12	45 (100.0)	10 (10.3)	
Gleason score			<0.001
<8	45 (100.0)	54 (54.0)	
≥8	0 (0.0)	46 (46.0)	
pT stage			0.005
<pT3	33 (73.3)	48 (48.0)	
≥pT3	12 (26.7)	52 (52.0)	

\*PSA doubling time data of 3 Johns Hopkins Hospital patients are not available; however, all were high-risk based on Gleason scores. BCR = biochemical recurrence; IQR = interquartile range; PSADT = PSA doubling time. Data are number followed by percentage in parentheses, unless specified otherwise.

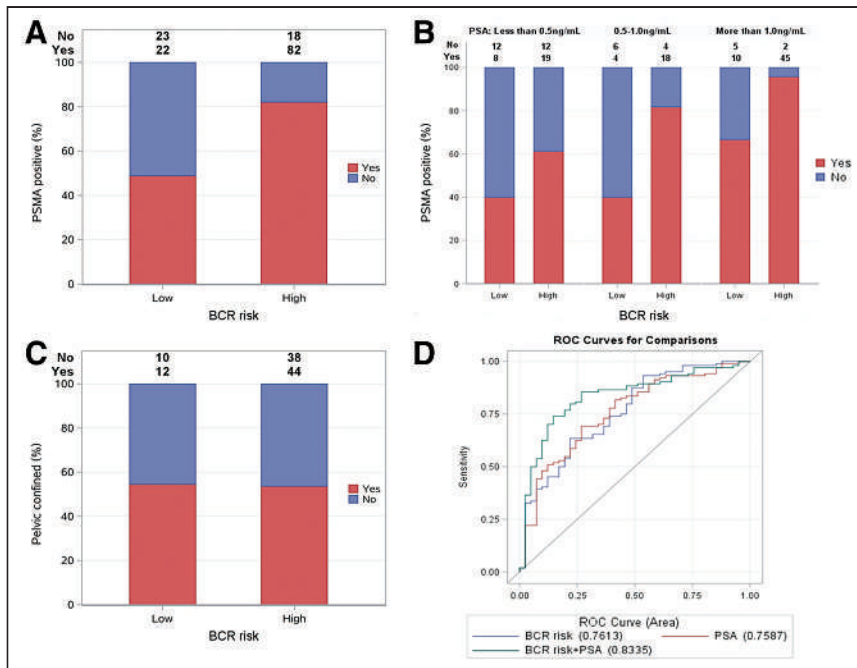


**FIGURE 1.** (A and B) Percentage of positive PSMA PET/CT scans among all patients (A) and among PSA subgroups (B). (C) Prevalence of pelvis-confined disease in each risk group. (D) Area under curve for detection of prostate cancer stratified by BCR risk group, PSA, and combination of BCR risk group and PSA. Each receiver-operating-characteristic multivariable analysis model also includes age, disease-free time, and pT stage. LN = lymph node; PB = prostate bed; ROC = receiver operating characteristic.

PSA alone were comparable (0.761 vs. 0.759,  $P = 0.96$ ; Fig. 1D), whereas the area under the curve using the combination of BCR risk group and PSA was higher than PSA alone (0.834 vs. 0.759,  $P = 0.015$ ; Fig. 1D).

Of the 145 total patients, 68 (46.9%) had recurrence or metastasis in lymph nodes, 28 (19.3%) had bone metastasis, and 31 (21.4%) had prostate bed recurrence. On multivariable logistic regression analyses, the BCR risk group was independently

associated with lymph node involvement on PSMA PET/CT in all patients, including those with negative scan results (odds ratio, 2.38; 95% CI, 1.04–5.49;  $P = 0.041$ ; Table 2). However, in 104 patients with positive scan results, the BCR group was not associated with the location of PSMA-avid lesions (Fig. 2; Table 2).

## DISCUSSION

We demonstrated that patients with EAU high-risk BCR were more likely to have PSMA PET/CT-detectable disease, suggesting that tumor volume and distribution may help to explain the worse prognosis of those patients. Notably, even patients with low-risk BCR had relatively high detection rates on PSMA PET/CT, and the rates of extrapelvic disease on positive scans was similar between high- and low-risk groups, suggesting that patients across the BCR spectrum may be good candidates for PSMA PET/CT imaging.

Previously, PSA has been reported as the strongest predictor of a positive PSMA PET/CT result (8). In this study, the added value of the EAU BCR risk groups has been demonstrated in a diverse population. It further stratifies the patients in each PSA subgroup, defining the patients who are most likely to have a positive PSMA

PET/CT result. Use of EAU risk groups can serve as a simple and clinically applicable nomogram for predicting whether patients will have a positive scan result. The survival benefits from salvage pelvic radiation or focal treatment of oligometastases in different BCR risk groups in the context of PSMA PET/CT should be further explored.

The EAU BCR risk groups are associated with meaningful oncologic outcomes such as metastatic progression-free and

**TABLE 2**

Univariable and Multivariable Logistic Regression Models Stratified According to EAU BCR Risk Groups Predicting Positive Findings, Pelvis-Confined Disease, and Disease Location on PSMA PET/CT Imaging

Outcome	Univariable analysis			Multivariable analysis		
	Odds ratio	95% CI	<i>P</i>	Odds ratio*	95% CI	<i>P</i>
Positive PSMA PET/CT scan	4.76	2.19–10.35	0.000	6.73	2.41–18.76	0.000
Pelvis-confined disease	0.96	0.38–2.48	0.941	1.31	0.43–3.96	0.631
Lymph node involvement in all patients	2.60	1.24–5.47	0.012	2.38	1.04–5.49	0.041
Bone metastasis in all patients	3.24	1.05–9.96	0.041	2.50	0.76–8.24	0.133
Prostate bed recurrence in all patients	1.71	0.68–4.33	0.255	1.91	0.69–5.32	0.216
Lymph node involvement in PSMA-positive patients	1.10	0.41–2.94	0.846	0.97	0.31–3.01	0.960
Bone metastasis in PSMA-positive patients	1.86	0.57–6.08	0.303	1.44	0.38–5.48	0.594
Prostate bed recurrence in PSMA-positive patients	0.89	0.32–2.45	0.816	0.93	0.29–3.02	0.902

\*Adjusted for age, PSA, disease-free time, pT stage, and cohort.

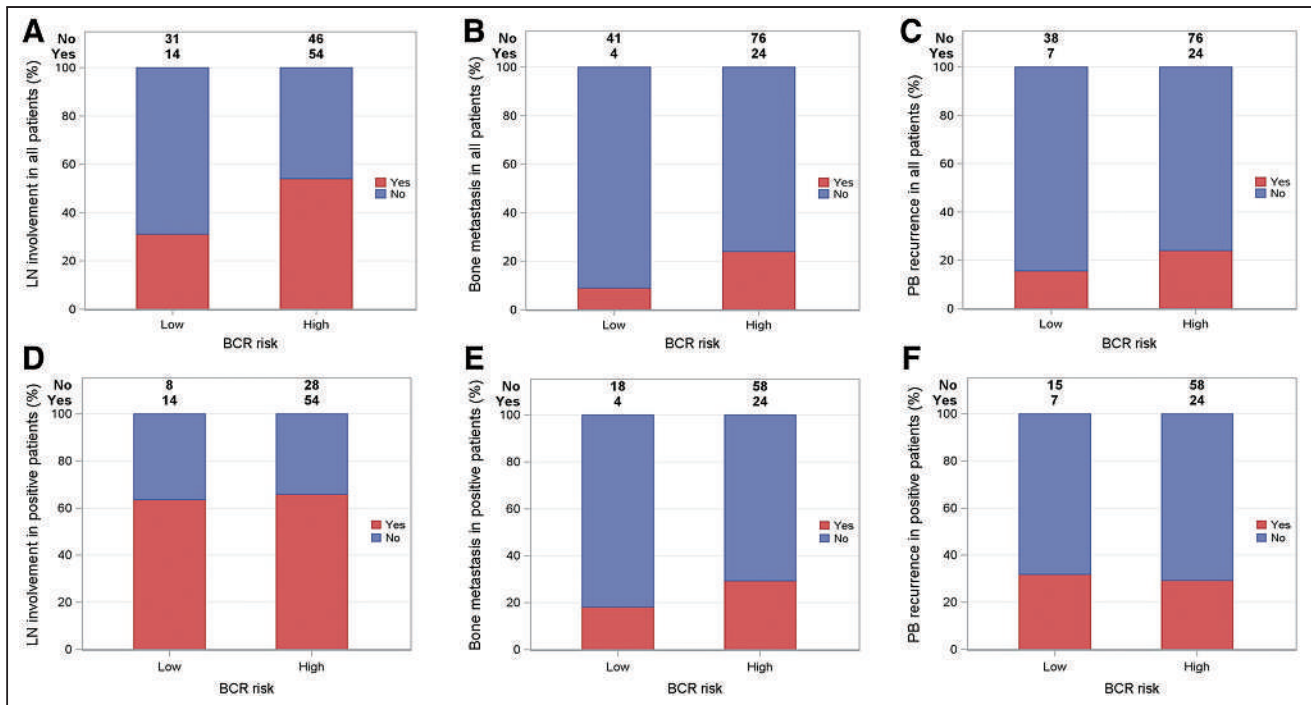


**FIGURE 2.** Percentage of all patients with lymph node involvement (A), bone metastasis (B), and prostate bed recurrence (C) ( $n = 145$ ), and percentage of PSMA scan-positive patients with lymph node involvement (D), bone metastasis (E), and prostate bed recurrence (F) ( $n = 104$ ).

prostate cancer-specific mortality-free survival rates (4), suggesting that PSMA-targeted PET imaging will yield imaging biomarkers. Imaging specialists, urologists, and oncologists working with PSMA imaging should focus on the design of prospective trials that can discover and validate the prognostic significance of findings.

The limitations of this work include the relatively small number of cases, post hoc evaluation of prospectively acquired data, use of more than one PSMA-targeted radiotracer, and lack of central review or a specific read paradigm. Future work is needed to confirm these findings in multicenter, larger prospective cohorts.

## CONCLUSION

The EAU BCR risk groups define the candidates who can most benefit from a PSMA PET/CT scan when BCR occurs.

## DISCLOSURE

Martin Pomper is a coinventor on a U.S. patent covering  $^{18}\text{F}$ -DCFPyL and as such is entitled to a portion of any licensing fees and royalties generated by this technology. This arrangement has been reviewed and approved by the Johns Hopkins University in accordance with its conflict-of-interest policies. Michael Gorin has served as a consultant to Progenics Pharmaceuticals, the licensee of  $^{18}\text{F}$ -DCFPyL. Steven Rowe is a consultant to Progenics Pharmaceuticals. Kenneth Pienta, Martin Pomper, Michael Gorin, and Steven Rowe have received research funding from Progenics Pharmaceuticals. Funding was received from Progenics Pharmaceuticals, the Prostate Cancer Foundation Young Investigator Award, the National Institutes of Health (grants CA134675, CA183031, CA184228, and EB024495), Program of Shanghai

Subject Chief Scientist (19XD1402300), and Program for Outstanding Medical Academic Leader (2019LJ11). No other potential conflict of interest relevant to this article was reported.

## ACKNOWLEDGMENTS

We thank Meghan Pienta and Morgan D. Kuczler for their kind help in data collection.

## KEY POINTS

**QUESTION:** Are the EAU BCR risk groups associated with findings on PSMA PET?

**PERTINENT FINDINGS:** In men with BCR after RP, the EAU high-risk group is more likely to have visible sites of recurrent disease on PSMA PET. However, low-risk and high-risk men have the same likelihood of having non-pelvis-confined disease.

**IMPLICATIONS FOR PATIENT CARE:** Risk stratification using the EAU BCR risk groups can help select men who are most likely to benefit from imaging with PSMA PET.

## REFERENCES

- Bray F, Ferlay J, Soerjomataram I, Siegel RL, Torre LA, Jemal A. Global cancer statistics 2018: GLOBOCAN estimates of incidence and mortality worldwide for 36 cancers in 185 countries. *CA Cancer J Clin.* 2018;68:394-424.
- Han M, Partin AW, Zahurak M, Piantadosi S, Epstein JI, Walsh PC. Biochemical (prostate specific antigen) recurrence probability following radical prostatectomy for clinically localized prostate cancer. *J Urol.* 2003;169:517-523.

3. Van den Broeck T, van den Bergh RC, Briers E, et al. Biochemical recurrence in prostate cancer: the European Association of Urology prostate cancer guidelines panel recommendations. *Eur Urol Focus*. 2020;6:231–234.
4. Tilki D, Preisser F, Graefen M, Huland H, Pompe RS. External validation of the European Association of Urology biochemical recurrence risk groups to predict metastasis and mortality after radical prostatectomy in a European cohort. *Eur Urol*. 2019;75:896–900.
5. Dong L, Zhu Y, Xin M, et al. Prospective evaluation of <sup>68</sup>Ga-PSMA-11 PET/CT in Chinese men with biochemical recurrence after radical prostatectomy for prostate cancer: relationships between location of recurrence, time after prostatectomy, and serum PSA level. *Med Oncol*. 2020;37:89.
6. Markowski MC, Sedhom R, Fu W, et al. Prostate specific antigen and prostate specific antigen doubling time predict findings on <sup>18</sup>F-DCFPyL positron emission tomography/computerized tomography in patients with biochemically recurrent prostate cancer. *J Urol*. 2020;204:496–502.
7. Hope TA, Goodman JZ, Allen IE, Calais J, Fendler WP, Carroll PR. Metaanalysis of <sup>68</sup>Ga-PSMA-11 PET accuracy for the detection of prostate cancer validated by histopathology. *J Nucl Med*. 2019;60:786–793.
8. Perera M, Papa N, Roberts M, et al. Gallium-68 prostate-specific membrane antigen positron emission tomography in advanced prostate cancer: updated diagnostic utility, sensitivity, specificity, and distribution of prostate-specific membrane antigen-avid lesions—a systematic review and meta-analysis. *Eur Urol*. 2020;77:403–417.

## Erratum

In the article “Comparative Prognostic and Diagnostic Value of Myocardial Blood Flow and Myocardial Flow Reserve After Cardiac Transplantation,” by Miller et al. (*J Nucl Med*. 2020 Feb;61(2):249–255), Figures 1 and 4 contain errors.

In Figure 1, the AUC for corrected MFR should be 0.714, as noted in the manuscript text as follows: “There were no significant differences in the ability of stress MBF (AUC, 0.713), MFR (AUC, 0.749), or *corrected MFR* (AUC, 0.714) to identify patients with significant CAV (Fig. 1).” In Figure 4, the labels for corrected and uncorrected MFR have been switched. *The correct AUC for uncorrected MFR should be 0.748 and for correct MFR should be 0.724.* This is consistent with the current manuscript text as follows: “*Uncorrected MFR* showed improved discrimination for all-cause mortality compared with stress MBF (AUC, 0.748 vs. 0.639;  $P = 0.048$ ).”

Due to these significant errors, we have re-reviewed the manuscript for any discrepancies between the manuscript text and tables/figures. Additionally, we have repeated all analyses to ensure accuracy. During this process, we have not identified any additional errors.

Corrected versions of Figures 1 and 4 appear below; the authors sincerely regret these errors.

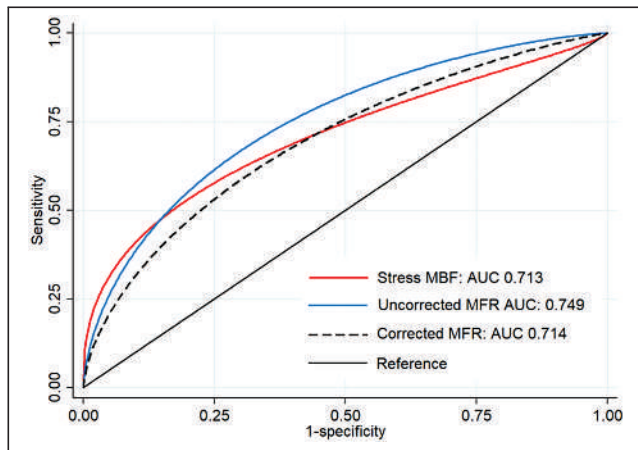


FIGURE 1.

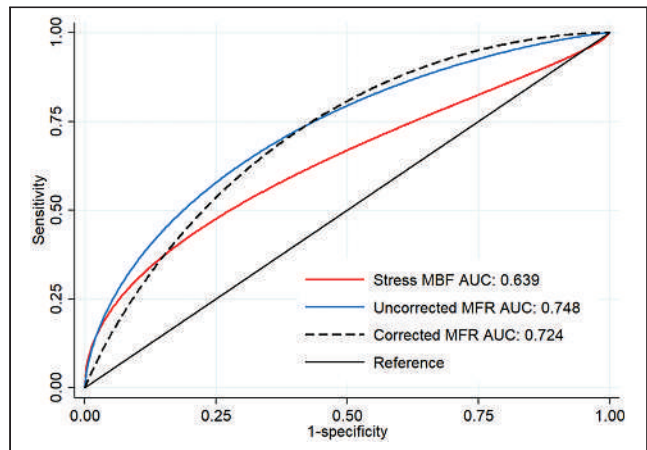


FIGURE 4.

---

---

# Kidney Doses in $^{177}\text{Lu}$ -Based Radioligand Therapy in Prostate Cancer: Is Dose Estimation Based on Reduced Dosimetry Measurements Feasible?

Michael Mix<sup>1-3</sup>, Tobias Renaud<sup>1</sup>, Felix Kind<sup>1</sup>, Ursula Nemer<sup>1</sup>, Elham Yousetzadeh-Nowsha<sup>1</sup>, Tumelo C.G. Moalosi<sup>3</sup>, Aymen M. Ormrane<sup>1</sup>, Philipp T. Meyer<sup>1,2</sup>, and Juri Ruf<sup>1,2</sup>

<sup>1</sup>Department of Nuclear Medicine, Faculty of Medicine, University of Freiburg Medical Center, University of Freiburg, Freiburg, Germany; <sup>2</sup>German Cancer Consortium, Partner Site Freiburg, German Cancer Research Center, Freiburg, Germany; and <sup>3</sup>Nuclear Medicine Division, Department of Medical Imaging and Clinical Oncology, Faculty of Medicine and Health Science, Stellenbosch University, Cape Town, South Africa

---

J Nucl Med 2022; 63:253–258

DOI: 10.2967/jnumed.121.262245

---

The radiation dose to the kidneys should be monitored in prostate cancer patients treated with radioligand therapy (RLT) targeting the prostate-specific membrane antigen (PSMA). We analyzed whether pretherapeutic kidney function is predictive of subsequent kidney dose and to what extent the cumulative kidney dose at the end of multiple therapy cycles can be predicted from a dosimetry based on the first cycle. **Methods:** Data of 59 patients treated with at least 2 cycles of  $^{177}\text{Lu}$ -PSMA-617 (PSMA RLT) were analyzed. Treatment (median, 6 GBq/cycle) was performed at 6- to 8-wk intervals, accompanied by voxel-based 3-dimensional dosimetry (measured kidney dose) with SPECT/CT on each of days 0–3 and once during days 6–9. Pretherapeutic kidney function (estimated glomerular filtration rate, mercaptoacetyltryglycine clearance) was correlated to the kidney doses. Cumulative kidney doses at the end of treatment were compared with a dose estimated from the population-based mean kidney dose, individual first-cycle kidney dose, and mean kidney doses of cycles 1, 3, and 5 per administered activity. **Results:** In total, 176 PSMA RLT cycles were performed, with a median of 3 cycles per patient. The average kidney dose per administered activity of all 176 cycles was  $0.67 \pm 0.24$  Gy/GBq (range, 0.21–1.60 Gy/GBq). Mercaptoacetyltryglycine clearance and estimated glomerular filtration rate were no reliable predictors of subsequent absorbed kidney dose and showed only small effect sizes ( $R^2 = 0.080$  and  $0.014$  [ $P = 0.039$  and  $0.375$ ], respectively). All simplified estimations of cumulative kidney dose correlated significantly ( $P < 0.001$ ) with measured kidney doses: estimations based on the individual first-cycle dose were more accurate than the use of the population-based average kidney dose ( $R^2 = 0.853$  vs.  $0.560$ ). Dose estimation was best when the doses of cycles 3 and 5 were included as well ( $R^2 = 0.960$ ). **Conclusion:** Pretherapeutic renal function was not predictive of subsequent kidney dose during therapy. Extrapolation of individual data from dosimetry of the first cycle was highly predictive of the cumulative kidney dose at the end of treatment. This prediction was further improved by the integration of dose information from every other cycle. In any case, because of a high interindividual variance, an individual dosimetry is advisable.

**Key Words:** prostate-specific membrane antigen; radioligand therapy;  $^{177}\text{Lu}$ ; renal toxicity; kidney dosimetry

**P**rostate-specific membrane antigen (PSMA) is frequently over-expressed in prostate cancer. Aside from imaging with PET with ligands targeting this antigen,  $^{177}\text{Lu}$ -based radioligand therapies (PSMA RLTs) are an emerging and promising treatment option in patients with metastatic castration-resistant prostate cancer (1). The potential of PSMA RLT has been demonstrated in recent phase II trials (2–4), and the effectiveness is currently under investigation in a multicenter phase III trial (NCT03511664).

Although PSMA RLT is generally well tolerated and shows only mild side effects, the bone marrow, salivary glands, and kidneys are considered to be potentially dose-limiting organs (5). In this respect, PSMA RLT shares similarities with peptide-receptor radionuclide therapy (PRRT) for neuroendocrine tumors, which also show an overall good tolerability, with renal and hematopoietic toxicity being the main side effects. As the kidney dose has been a major concern for PRRT, various protocols for nephroprotection by coinfusion of amino acids have been developed over the years (6). Traditionally, a tolerance dose of 23 Gy for the kidneys is assumed in PRRT, based on external-beam radiation therapy data (7). As a consequence, meticulous renal dosimetry is recommended in RLTs and should be thoroughly integrated into treatment protocols (8).

Although the kidney dose in  $^{177}\text{Lu}$ -based PSMA RLT is in a range similar to that when using PRRT with  $^{177}\text{Lu}$ -DOTATATE, no protocol for nephroprotection has been established yet. Especially, there is no evidence that an amino acid coinfusion results in a lower radiation exposure to the kidneys. On the basis of more recent data on  $^{177}\text{Lu}$ -based therapies, a higher renal tolerability of up to a 40-Gy cumulative kidney dose is assumed in PSMA RLT in the absence of risk factors, also taking prognostic aspects of the treated patient into account (5).

To accurately assess kidney doses in PSMA RLT, various procedures for dosimetry have been developed, ranging from simple planar imaging (9) to more complex SPECT/CT-based protocols (10). In this study, the kidney dose per cycle was determined on the basis of a dosimetry protocol that includes 5 intratherapeutically acquired SPECT/CT scans. Using these data, we assessed whether the cumulative kidney dose at the end of multiple therapy

---

Received Mar. 5, 2021; revision accepted May 5, 2022.

For correspondence or reprints, contact Michael Mix (michael.mix@uniklinik-freiburg.de).

Published online Jun. 4, 2021.

COPYRIGHT © 2022 by the Society of Nuclear Medicine and Molecular Imaging.

cycles can reliably be predicted from the dosimetry of the first therapy cycle only.

## MATERIALS AND METHODS

### Patients

In this retrospective analysis, data of patients with metastasized castration-resistant prostate cancer who had been treated with  $^{177}\text{Lu}$ -labeled PSMA-617 between July 2015 and July 2020 were analyzed. Patients were eligible for this analysis if 2 or more cycles of PSMA RLT had been performed and complete 3-dimensional (3D) SPECT/CT dosimetry data were available, including a late SPECT/CT image from at least 6 d after injection.

Treatment eligibility and pretherapeutic examinations had been done in accordance with the recommendations of the German Society of Nuclear Medicine (11). Mercaptoacetyltriglycine (MAG3) renal scintigraphy was used to determine pretherapeutic MAG3 clearance, especially to exclude active ureter obstruction. Patients with proven, treated previous obstruction and an inconspicuous MAG3 scan were eligible for therapy.

According to the aforementioned guideline, a standard activity of 6 GBq of  $^{177}\text{Lu}$ -DOTA-PSMA-617 was applied. A reduced activity of 4 GBq was used only in cases of reduced bone marrow function or strongly impaired renal function.

The institutional review board (vote no. 326/18) approved this study, and all subjects gave written informed consent.

### Synthesis of $^{177}\text{Lu}$ -DOTA-PSMA-617

$^{177}\text{Lu}$ -DOTA-PSMA-617 was produced in compliance with good manufacturing practices using an automated radiosynthesis device (Modular-Lab PharmTracer) with low-bioburden single-use cassettes. The commercially available precursor (ABX) and reagents were prepared and sampled according to standard operating procedures. No-carrier-added  $^{177}\text{LuCl}_3$  was purchased from ITM, and the cassettes were supplied by Eckert and Ziegler Eurotope GmbH. Before the synthesis was started,  $^{177}\text{LuCl}_3$  (~8 GBq), ammonium acetate buffer (0.5 M, pH 5.4), 50% ethanol, and isotonic saline vials were connected to the cassette. The Sep-Pak Light C-18 cartridge (Waters) was preconditioned with 4 mL of 50% ethanol and 6 mL of isotonic saline. The synthesis was started by transferring  $^{177}\text{LuCl}_3$  (~8 GBq) into the reaction vessel preloaded with 70  $\mu\text{g}$  (67 nmol) of DOTA-PSMA-617 and 100  $\mu\text{L}$  of ethanol to prevent radiolysis. The ammonium acetate buffer (700  $\mu\text{L}$ ) was transferred through the radioactive vial into the reaction vessel. The radiosynthesis was performed at 75°C for 40 min in ammonium acetate buffer. The mixture was subsequently passed through the preconditioned Sep-Pak Light C-18 cartridge and washed with isotonic saline. The final product was eluted with 50% ethanol, diluted with isotonic saline and passed through a 0.22- $\mu\text{m}$  sterile membrane filter into a presterilized product vial prefilled with 100–200  $\mu\text{L}$  of Ditriventat-Heyl (diethylenetriaminepentaacetic acid, solution for injection). The quality control was conducted in adherence with European Pharmacopeia standards, including filter integrity and pH testing, limulus amoebocyte lysate testing, radionuclide identity testing, and purity testing by determining the half-life and energy spectrum. Chemical and radiochemical purity ( $\geq 97\%$ ) were identified by radio-high-performance liquid chromatography, and the residual solvent was identified by gas chromatography. Finally, after release, a sample of the product formulation was tested for sterility by an independent institution (Biochem) according to the recommendations of the European Pharmacopoeia and U.S. Pharmacopoeia using the direct inoculation method.

### SPECT/CT Imaging and Dosimetry

At each therapy cycle, imaging for dosimetry was performed on days 0–3, consisting of planar whole-body scans and abdominal SPECT/CT (including kidneys, liver, and spleen) at 1, 24, 48, and 72 h

after injection. Moreover, 1 late SPECT/CT scan was acquired on an outpatient basis in the following week on day 6, 7, 8, or 9 after injection (Fig. 1).

All acquisitions were performed on a SPECT/CT scanner (Bright-View XCT; Philips Healthcare) equipped with medium-energy general-purpose collimators. Measurements were done with an energy window of  $\pm 10\%$  around the 208-keV peak. SPECT was measured with 40 projections per head on a body-contour trajectory with a  $128 \times 128$  matrix and a 20-s acquisition duration per projection. Attenuation correction was based on a cone-beam CT scan (30 mAs at 120 kV); SPECT was reconstructed iteratively with the ordered-subsets expectation maximization algorithm (4 iterations and 16 subsets; postreconstruction filter, Butterworth; cutoff, 0.4; order, 1.4). Whole-body scans were performed with a velocity of 20 cm/min and an imaging matrix of  $256 \times 1,024$  to document the tracer distribution.

The SPECT/CT system was calibrated for  $^{177}\text{Lu}$  by phantom measurements with a National Electrical Manufacturers Association image-quality phantom using the aforementioned imaging protocol. The phantom body was filled with water, and two 500-mL volumes simulating kidneys were inserted, one filled with 100 MBq of  $^{177}\text{Lu}$  and the other with 200 MBq of  $^{177}\text{Lu}$ . Calibration measurements were done 4 times, at an interval of every other day. The resulting calibration factor was  $9.9 \pm 0.4$  cps/MBq. 3D dose maps were calculated using STRATOS, which is part of the IMALYTICS Research Workstation (Philips Technology). The software package is based on the MIRD formalism for voxel-based dose calculation by voxel S values (12). The original SPECT images of each cycle were coregistered to the CT portion of the last scan in STRATOS and resampled to a voxel size of  $4.42 \times 4.42 \times 4.42$  mm in accordance with STRATOS' voxel S-value sizes. The integral of the time-activity curve for each image voxel was calculated by the trapezoidal integration method until the last imaging time points, followed by an exponential tail fit using the physical half-life of  $^{177}\text{Lu}$ . Because of the late time point of SPECT/CT after 6–9 d, the dose contribution of the tail fit is very low and there is only a slight difference between the use of the physical half-life or the individual effective half-life.

The software package Rover (ABX) was used for kidney segmentation and 3D dose-map analysis (13).

In accordance with current guidelines (5), pretherapeutic kidney function before the first cycle was assessed using the estimated glomerular filtration rate according to the Chronic Kidney Disease Epidemiology Collaboration (14) ( $\text{eGFR}_{11}$ ) and MAG3 clearance derived from renal scintigraphy performed before therapy in order to rule out obstructions. Estimated glomerular filtration rate was again determined approximately 2 wk before the third cycle ( $\text{eGFR}_{12}$ ).

### Statistics

For all patients and all cycles, the absorbed doses by the kidneys were calculated using voxel-based 3D dosimetry (measured kidney dose).

$\text{eGFR}_{11}$  and MAG3 clearance were correlated with the respective kidney dose of the first cycle for every patient, and if applicable,  $\text{eGFR}_{12}$  was correlated to the third-cycle dose.

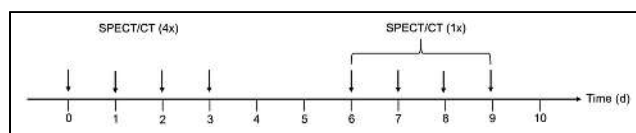


**FIGURE 1.** Schematic overview of SPECT/CT measurements performed on days 0–3 (on inpatient basis) and on days 6, 7, 8, or 9 (on outpatient basis).

**TABLE 1**  
Kidney Dose per Administered Activity at Each Cycle

Kidney dose (Gy/GBq)	Cycle 1 (n = 59 patients)	Cycle 2 (n = 59 patients)	Cycle 3 (n = 31 patients)	Cycle 4 (n = 20 patients)	Cycle 5 (n = 4 patients)	Cycle 6 (n = 3 patients)
Mean	0.68	0.70	0.65	0.66	0.43	0.58
SD	0.24	0.23	0.26	0.31	0.04	0.18
Minimum	0.28	0.21	0.33	0.29	0.39	0.39
Maximum	1.29	1.44	1.32	1.60	0.48	0.74

In all patients, the measured cumulative kidney dose was correlated with the estimated cumulative dose, based on our cohort's mean kidney dose per administered activity (Gy/GBq) and on the individually calculated first-cycle kidney dose per administered activity. Moreover, to account for potential changes during therapy in patients receiving 4 or more therapy cycles, the extrapolation of the cumulative dose at the end of the treatment was done with the individual kidney dose per administered activity of every other cycle. In this case, the kidney dose of even-numbered cycles (cycles 2, 4, and 6) was estimated from the measured kidney dose of the therapy cycles taking place immediately beforehand (cycles 1, 3, and 5, respectively).

Correlations were based on linear regression using ANOVA for significance analysis. Paired *t* tests were used for comparisons of eGFR<sub>t1/2</sub> and kidney doses at different cycles. All analyses were performed using IBM SPSS statistics software, version 27. Arithmetic mean values were calculated from the individual measurements and expressed at a precision of 1 SD (mean ± SD).

## RESULTS

### Patient Treatment and Measured Kidney Doses

The data of 59 patients (aged 72.8 ± 8.5 y; median, 74.6 y) with advanced metastatic castration-resistant prostate cancer were eligible for analysis. The patients had received a median of 3 cycles of <sup>177</sup>Lu-PSMA-617 (2 cycles, n = 28; 3 cycles, n = 11; 4 cycles, n = 16; 5 cycles, n = 1; 6 cycles, n = 3) at 6- to 8-wk intervals (total, 176 cycles). Average activity per cycle over all patients and cycles was 5.7 ± 0.8 GBq (median, 6.0 GBq) of <sup>177</sup>Lu-PSMA-617 (cycle 1, 5.6 ± 0.9 GBq; cycle 2, 5.8 ± 0.7 GBq; cycle 3, 5.6 ± 1.0 GBq; cycle 4, 6.0 ± 0.2 GBq; cycle 5, 5.9 ± 0.3 GBq; and cycle 6, 5.9 ± 0.4 GBq). The cumulative measured kidney doses in all 59 patients after PSMA RLT ranged from 3.4 to 25.3 Gy. Average kidney dose per administered activity over all patients and cycles (n = 176) was 0.67 ± 0.24 Gy/GBq (range, 0.21–1.60 Gy/GBq). The respective kidney dose for each cycle is shown in Table 1. Average kidney doses per cycle did not differ significantly (P = 0.217; Fig. 2). Details on kidney doses depending on the number of cycles administered can be found in Supplemental Table 1 (total kidney dose) and Supplemental Table 2 (left and right kidney separately assessed) (supplemental materials are available at <http://jnm.snmjournals.org>).

### Renal Function and Kidney Dose

The eGFR<sub>t1</sub> ranged from 29.4 to 116.7 mL/min/1.73 m<sup>2</sup> (76.5 ± 14.4 mL/min/1.73 m<sup>2</sup>). According to Kidney Disease Improving Global Outcomes (KDIGO) criteria (15), 13 patients presented with normal (KDIGO G1), 39 with mildly decreased (KDIGO G2), and 5 with a mildly to moderately decreased (KDIGO G3a) kidney function. One patient each presented with moderately to severely decreased (KDIGO G3b) and severely decreased (KDIGO G4)

kidney function. MAG3 clearance ranged from 115 to 307 mL/min/1.73 m<sup>2</sup> (202.8 ± 28.3 mL/min/1.73 m<sup>2</sup>) and correlated poorly with eGFR<sub>t1</sub> (R<sup>2</sup> = 0.167, P = 0.002). The kidney dose per administered activity (Gy/GB) observed after the first cycle correlated neither with eGFR<sub>t1</sub> (R<sup>2</sup> = 0.014, P = 0.375) nor with MAG3 clearance (R<sup>2</sup> = 0.080, P = 0.039), with small effects of determination only. Similarly, the kidney dose per administered activity (Gy/GBq) of the first cycle did not correlate (R<sup>2</sup> < 0.001, P = 0.85) with the amount of activity used (2.09–6.47 GBq). In particular, the 2 patients with more severely reduced kidney function did not receive higher kidney doses per gigabecquerel than did the other patients (0.69 and 0.48 Gy/GBq for KDIGO G3b and KDIGO G4, respectively). In 31 patients, eGFR<sub>t2</sub> was determined; it ranged from 41.5 to 95.80 mL/min/1.73 m<sup>2</sup> (72.3 ± 17.0 mL/min/1.73 m<sup>2</sup>). There was no correlation between eGFR<sub>t2</sub> and the kidney dose (Gy/GBq) of the third cycle (R<sup>2</sup> = 0.001, P = 0.993), and no significant change between eGFR<sub>t1</sub> and eGFR<sub>t2</sub> was observed (P = 0.96).

### Predicted and Measured Kidney Doses

In all 59 patients, correlations between the measured and estimated cumulative kidney dose at the end of treatment were significant (P < 0.001). However, the use of the population-based mean kidney dose of 0.67 Gy/GBq for the prediction of the kidney doses at the end of treatment resulted in a greater variance (R<sup>2</sup> = 0.560) than did the use of the individual first-cycle dose per administered activity (Gy/GBq) (R<sup>2</sup> = 0.853). As expected, the approach using an individual dosimetry at every second cycle resulted in the best prediction (R<sup>2</sup> = 0.960; Fig. 3).

Twenty patients received 4 or more cycles. Using the same dose estimation methods in this subgroup, the use of the mean kidney

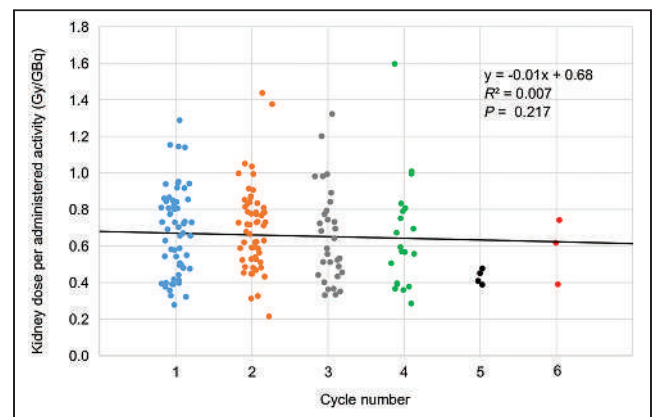


**FIGURE 2.** Comparing kidney dose per administered activity (Gy/GBq) distribution per cycle (59 patients); no significant changes in any of 6 cycles were observed (P = 0.217).

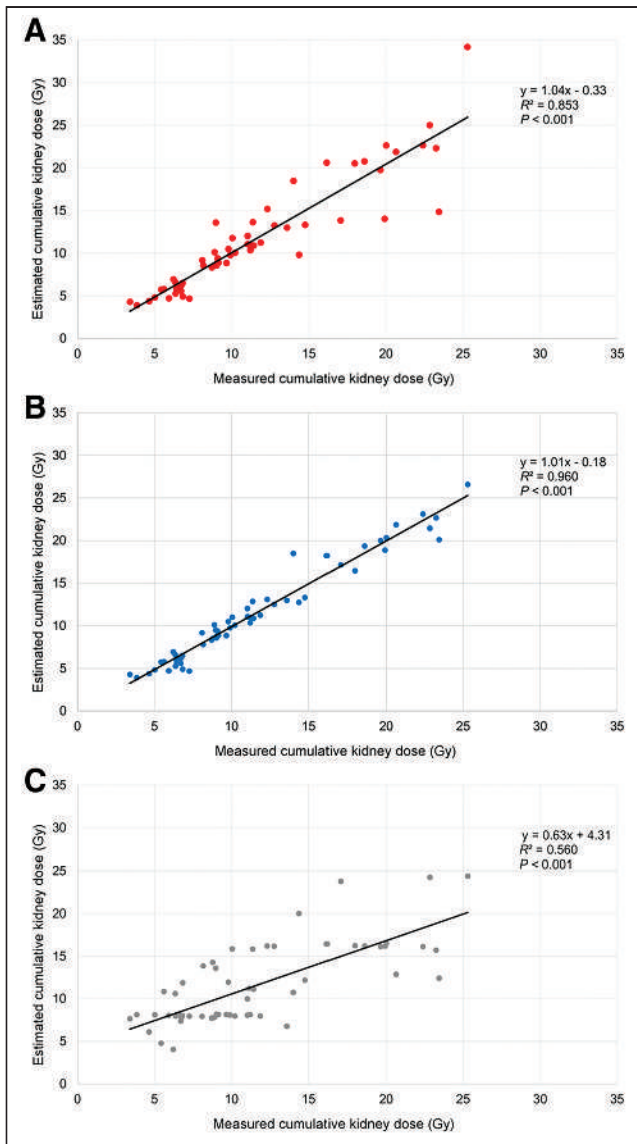


**FIGURE 3.** Correlations of estimated and measured cumulative kidney dose in all 59 patients based on 3 models. The good correlation and coefficient of determination that were seen when extrapolation was done using individual dose per administered activity from first-cycle dosimetry (A) can be further improved when data of cycles 3 and 5 are also considered (B). In contrast, poorest coefficient of determination was observed using population-based average kidney dose only (C), in which estimation resulted in systematic dose underestimation, as can be seen in slopes.

dose of  $0.67 \text{ Gy/GBq}$  did not result in a meaningful prediction ( $R^2 = 0.166$ ,  $P = 0.074$ ). In contrast, the individual-based dosimetry estimations still correlated significantly with the measured cumulative kidney dose ( $P < 0.001$ ). Dosimetry relying only on the first cycle showed a lower coefficient of determination than the approach using every other cycle ( $R^2 = 0.630$  vs.  $R^2 = 0.947$ ; Fig. 4).

## DISCUSSION

In the present study, the average kidney dose per administered activity was  $0.67 \pm 0.24 \text{ Gy/GBq}$  of activity when performing a treatment with  $6.0 \text{ GBq}$  of  $^{177}\text{Lu-PSMA-617}$ . In comparison to the kidney doses reported in the European Association of Nuclear

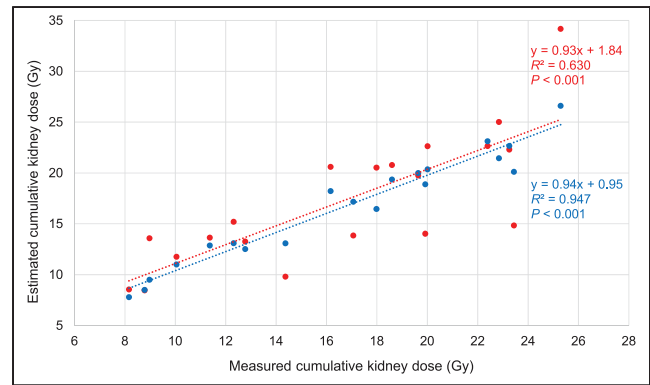


**FIGURE 4.** Correlation of estimated and measured cumulative kidney dose in 20 patients receiving 4 or more therapy cycles based on dosimetry of cycle 1 only (red) and cycles 1, 3, and 5 (blue). Use of individual average kidney dose from every second cycle greatly improves associated coefficient of determination.

Medicine procedure guideline for PSMA-based RLT (5), this dose average is in the upper range of the reported dose of  $0.4 \pm 0.2$  to  $0.8 \pm 0.3 \text{ Gy/GBq}$ . This finding is not surprising, as we used recommended late-time-point measurements in the week after therapy (16) to avoid dose underestimation. In that sense, our results were consistent with the results of SPECT/CT-based dosimetry protocols also using late time points (5).

In accordance with the kidney dosimetry results reported by Okamoto et al. (9), who also included the important late time points in their dose calculations, we observed an intraindividually relatively constant development of kidney dose in our patients using fixed activities. Especially in responders to therapy, we did not observe postulated tumor sink effects (17), such as a reciprocal increase in intraindividual kidney dose per cycle due to decreasing tumor burden.

With a state-of-the-art multi-SPECT/CT 3D dosimetry approach, the high coefficients of determination in cumulative kidney dose based on personalized dosimetry show the feasibility of a linear extrapolation of the individual kidney dose within the bounds of a rigid treatment setting (i.e., activity and time intervals). Our data suggest that an individual dosimetry of the first cycle sufficiently predicts the cumulated kidney dose at the end of treatment. Obviously, we see a higher coefficient of determination for the estimated cumulative kidney dose when also including dosimetry data from cycles 3 and 5 (if applicable). Considerations comparable to our results in the prediction of kidney dose have been reported for PRRT in neuroendocrine tumors based on the dosimetry of the first 2 cycles (18). In addition to these dose prediction approaches, measures such as a reduction in the number of CT or SPECT/CT acquisitions per cycle (18,19) have been suggested to simplify often-elaborate dosimetry protocols (20). These simplifications would not only free scanner and staff capacities at the nuclear medicine facility but also improve patient comfort (21,22). Considering this, our approach of a thorough dosimetry of the first cycle followed by extrapolation appears to be a viable option, again provided that crucial late measurement time points are also included in such protocols to avoid potential underestimation (16,23). However, especially when aiming at a more streamlined dosimetry or larger dosimetry intervals, the high interindividual variation of the resulting kidney dose after PSMA RLT ( $0.28\text{--}1.29 \text{ Gy/GBq}$  at the first cycle in our cohort), likewise observed in PRRT (23,24), must

be considered. The poor cumulative dose estimation using a population-based mean kidney dose only, especially if patients received 4 or more cycles, shows that a reliable individual dosimetry is essential. Accordingly, one should refrain from using average kidney dose values from the literature for the prediction.

Our results showed that the pretherapeutic renal function was not predictive of the subsequent kidney dose during therapy. In our cohort, 57 of 59 patients had normal or only slightly impaired renal function before PSMA RLT. Even taking the 2 patients with more severely impaired kidney function, KDIGO G3b and G4, into account, we observed neither an association between pretherapeutic kidney function (eGFR<sub>1</sub>) and the first-cycle kidney dose nor an association between kidney function after 2 cycles (eGFR<sub>2</sub>) and kidney dose at the third therapy cycle. Although the association between the kidney dose of the first cycle and MAG3 clearance was significant, the associated effect size was very small ( $R^2 = 0.062$ ). These observations imply that kidney function alone is not sufficient for the prediction of the resulting kidney dose.

Although the role of potential risk factors for kidney damage (25), such as age, arterial hypertension, or previous renal impairment, still remains to be determined, retrospective PSMA RLT series have reported mild renal toxicity of grade 1 or 2 only (25,26). Safe administration of PSMA RLT is also possible even in patients with only a single kidney (27). These observations were confirmed by the updated analysis of the prospective phase II <sup>177</sup>Lu-PSMA trial indicating that approximately 4 cycles of RLT are well tolerated and that renal impairment is to be expected only after a higher number of cycles (3). Similarly, nephrotoxicity was not a major adverse event in the recently published phase II TheraP trial (4). These observations on renal tolerance in <sup>177</sup>Lu-PSMA RLT are partly comparable to data on renal tolerance of <sup>177</sup>Lu-DOTATATE, as the phase III NETTER-1 trial did not show higher-grade (3 or 4) renal toxicity during the median 14 mo of follow-up (28). Even secondary salvage PRRT is sufficiently tolerated by the kidneys, whereas high-grade hematotoxicity is a more relevant issue (29). In this aspect, hematotoxicity may also be a more relevant side effect in patients with renal impairment, as a slower renal excretion might result in a longer exposure of the bone marrow due to circulating radioligand.

Although long-term data on the renal safety of PSMA RLT are still warranted, observations from PRRT suggest that the development of renal impairment is gradual and occurs over many years (30). Considering the often poorer prognosis of advanced metastatic castration-resistant prostate cancer than of neuroendocrine tumor disease, the individual risk of actually experiencing late kidney damage also has to be taken critically into account (5). Additionally, the risk of premature discontinuation of therapy in PSMA RLT due to disease progression and development of resistance to therapy must be heeded. Only one third of our patients received 4 or more therapy cycles, and as a consequence, only 6 patients had a cumulated kidney dose that came close to or even slightly surpassed the aforementioned conservative threshold of 23 Gy. Thus, in our cohort with a limited number of patients, kidney dose was not a reason for discontinuation of therapy.

## CONCLUSION

For a current standard PSMA RLT treatment protocol, the resulting kidney doses were independent from pretherapeutic kidney function. Because of the observed almost linear correlation between

treatment activity and the cumulative kidney dose in individual patients, a prediction of the cumulative kidney dose with dosimetry results from only the first cycle seems to be feasible. On the basis of our findings for patients with more than 4 therapy cycles, we recommend that dedicated dosimetry be performed during every other therapy cycle; this schedule offers a good compromise between effort, patient comfort, and accuracy in determining the estimated cumulative kidney dose.

## DISCLOSURE

No potential conflict of interest relevant to this article was reported.

## KEY POINTS

**QUESTION:** Is an accurate prediction of kidney dose in <sup>177</sup>Lu-PSMA RLT in prostate cancer patients feasible with reduced SPECT/CT measurements for dosimetry?

**PERTINENT FINDINGS:** A simplification of intratherapeutic imaging protocols by performing dosimetry only at the first or every other therapy cycle is feasible.

**IMPLICATIONS FOR PATIENT CARE:** A reduction of dosimetry measurements improves patient comfort and frees scanner and staff capacities, but an individual kidney dosimetry is essential for accurate dose estimation.

## REFERENCES

1. Afshar-Oromieh A, Babich JW, Kratochwil C, et al. The rise of PSMA ligands for diagnosis and therapy of prostate cancer. *J Nucl Med*. 2016;57(suppl 3):79S–89S.
2. Hofman MS, Violet J, Hicks RJ, et al. [<sup>177</sup>Lu]-PSMA-617 radionuclide treatment in patients with metastatic castration-resistant prostate cancer (LuPSMA trial): a single-centre, single-arm, phase 2 study. *Lancet Oncol*. 2018;19:825–833.
3. Violet J, Jackson P, Ferdinandus J, et al. Dosimetry of <sup>177</sup>Lu-PSMA-617 in metastatic castration-resistant prostate cancer: correlations between pretherapeutic imaging and whole-body tumor dosimetry with treatment outcomes. *J Nucl Med*. 2019;60:517–523.
4. Hofman MS, Emmett L, Sandhu S, et al. [<sup>177</sup>Lu]Lu-PSMA-617 versus cabazitaxel in patients with metastatic castration-resistant prostate cancer (TheraP): a randomised, open-label, phase 2 trial. *Lancet*. 2021;397:797–804.
5. Kratochwil C, Fendler WP, Eiber M, et al. EANM procedure guidelines for radionuclide therapy with <sup>177</sup>Lu-labelled PSMA-ligands (<sup>177</sup>Lu-PSMA-RLT). *Eur J Nucl Med Mol Imaging*. 2019;46:2536–2544.
6. Bodei L, Mueller-Brand J, Baum RP, et al. The joint IAEA, EANM, and SNMMI practical guidance on peptide receptor radionuclide therapy (PRRT) in neuroendocrine tumours. *Eur J Nucl Med Mol Imaging*. 2013;40:800–816.
7. Emami B, Lyman J, Brown A, et al. Tolerance of normal tissue to therapeutic irradiation. *Int J Radiat Oncol Biol Phys*. 1991;21:109–122.
8. Garske-Román U, Sandström M, Fröss Baron K, et al. Prospective observational study of <sup>177</sup>Lu-DOTA-octreotate therapy in 200 patients with advanced metastasized neuroendocrine tumours (NETs): feasibility and impact of a dosimetry-guided study protocol on outcome and toxicity. *Eur J Nucl Med Mol Imaging*. 2018;45:970–988.
9. Okamoto S, Thieme A, Allmann J, et al. Radiation dosimetry for <sup>177</sup>Lu-PSMA I&T in metastatic castration-resistant prostate cancer: absorbed dose in normal organs and tumor lesions. *J Nucl Med*. 2017;58:445–450.
10. Delker A, Fendler WP, Kratochwil C, et al. Dosimetry for <sup>177</sup>Lu-DKFZ-PSMA-617: a new radiopharmaceutical for the treatment of metastatic prostate cancer. *Eur J Nucl Med Mol Imaging*. 2016;43:42–51.
11. Fendler WP, Kratochwil C, Ahmadzadehfar H, et al. <sup>177</sup>Lu-PSMA-617 therapy, dosimetry and follow-up in patients with metastatic castration-resistant prostate cancer [in German]. *Nuklearmedizin*. 2016;55:123–128.
12. Berker Y, Goedicke A, Kemerink GJ, Aach T, Schweizer B. Activity quantification combining conjugate-view planar scintigraphies and SPECT/CT data

- for patient-specific 3-D dosimetry in radionuclide therapy. *Eur J Nucl Med Mol Imaging*. 2011;38:2173–2185.
13. Hofheinz F, Pöttsch C, Oehme L, et al. Automatic volume delineation in oncological PET: evaluation of a dedicated software tool and comparison with manual delineation in clinical data sets. *Nuklearmedizin*. 2012;51:9–16.
  14. Levey AS, Stevens LA, Schmid CH, et al. A new equation to estimate glomerular filtration rate. *Ann Intern Med*. 2009;150:604–612.
  15. Fraser SD, Blakeman T. Chronic kidney disease: identification and management in primary care. *Pragmat Obs Res*. 2016;7:21–32.
  16. Hohberg M, Eschner W, Schmidt M, et al. Lacrimal glands may represent organs at risk for radionuclide therapy of prostate cancer with [<sup>177</sup>Lu]DKFZ-PSMA-617. *Mol Imaging Biol*. 2016;18:437–445.
  17. Begum NJ, Thieme A, Eberhardt N, et al. The effect of total tumor volume on the biologically effective dose to tumor and kidneys for <sup>177</sup>Lu-labeled PSMA peptides. *J Nucl Med*. 2018;59:929–933.
  18. Chicheportiche A, Grozinsky-Glasberg S, Gross DJ, et al. Predictive power of the post-treatment scans after the initial or first two courses of [<sup>177</sup>Lu]-DOTA-TATE. *EJNMMI Phys*. 2018;5:36.
  19. Chicheportiche A, Artoul F, Schwartz A, et al. Reducing the number of CTs performed to monitor personalized dosimetry during peptide receptor radionuclide therapy (PRRT). *EJNMMI Phys*. 2018;5:10.
  20. Sundlöv A, Gustafsson J, Brolin G, et al. Feasibility of simplifying renal dosimetry in <sup>177</sup>Lu peptide receptor radionuclide therapy. *EJNMMI Phys*. 2018;5:12.
  21. Chicheportiche A, Ben-Haim S, Grozinsky-Glasberg S, et al. Dosimetry after peptide receptor radionuclide therapy: impact of reduced number of post-treatment studies on absorbed dose calculation and on patient management. *EJNMMI Phys*. 2020;7:5.
  22. Jackson PA, Hofman MS, Hicks RJ, Scalzo M, Violet J. Radiation dosimetry in <sup>177</sup>Lu-PSMA-617 therapy using a single posttreatment SPECT/CT scan: a novel methodology to generate time- and tissue-specific dose factors. *J Nucl Med*. 2020; 61:1030–1036.
  23. Larsson M, Bernhardt P, Svensson JB, Wängberg B, Ahlman H, Forssell-Aronsson E. Estimation of absorbed dose to the kidneys in patients after treatment with <sup>177</sup>Lu-octreotate: comparison between methods based on planar scintigraphy. *EJNMMI Res*. 2012;2:49.
  24. Sandström M, Garske-Román U, Granberg D, et al. Individualized dosimetry of kidney and bone marrow in patients undergoing <sup>177</sup>Lu-DOTA-octreotate treatment. *J Nucl Med*. 2013;54:33–41.
  25. Yordanova A, Becker A, Eppard E, et al. The impact of repeated cycles of radioligand therapy using [<sup>177</sup>Lu]Lu-PSMA-617 on renal function in patients with hormone refractory metastatic prostate cancer. *Eur J Nucl Med Mol Imaging*. 2017;44: 1473–1479.
  26. Rahbar K, Ahmadzadehfar H, Kratochwil C, et al. German multicenter study investigating <sup>177</sup>Lu-PSMA-617 radioligand therapy in advanced prostate cancer patients. *J Nucl Med*. 2017;58:85–90.
  27. Zhang J, Kulkarni HR, Singh A, et al. <sup>177</sup>Lu-PSMA-617 radioligand therapy in metastatic castration-resistant prostate cancer patients with a single functioning kidney. *J Nucl Med*. 2019;60:1579–1586.
  28. Strosberg J, El-Haddad G, Wolin E, et al.; NETTER-1 trial investigators. Phase 3 trial of <sup>177</sup>Lu-Dotatate for midgut neuroendocrine tumors. *N Engl J Med*. 2017; 376:125–135.
  29. Rudisile S, Gosewisch A, Wenter V, et al. Salvage PRRT with <sup>177</sup>Lu-DOTA-octreotate in extensively pretreated patients with metastatic neuroendocrine tumor (NET): dosimetry, toxicity, efficacy, and survival. *BMC Cancer*. 2019;19:788.
  30. Bergsma H, Konijnenberg MW, van der Zwan WA, et al. Nephrotoxicity after PRRT with <sup>177</sup>Lu-DOTA-octreotate. *Eur J Nucl Med Mol Imaging*. 2016;43: 1802–1811.

# An Improved $^{211}\text{At}$ -Labeled Agent for PSMA-Targeted $\alpha$ -Therapy

Ronnie C. Mease<sup>1</sup>, Choong Mo Kang<sup>2</sup>, Vivek Kumar<sup>1</sup>, Sangeeta Ray Banerjee<sup>1</sup>, Il Minn<sup>1</sup>, Mary Brummet<sup>1</sup>, Kathleen L. Gabrielson<sup>3</sup>, Yutian Feng<sup>2</sup>, Andrew Park<sup>1</sup>, Ana P. Kiess<sup>4</sup>, George Sgouros<sup>1,4</sup>, Ganesan Vaidyanathan<sup>2</sup>, Michael R. Zalutsky<sup>2</sup>, and Martin G. Pomper<sup>1,4</sup>

<sup>1</sup>Russell H. Morgan Department of Radiology and Radiological Science, Johns Hopkins University School of Medicine, Baltimore, Maryland; <sup>2</sup>Department of Radiology, Duke University Medical Center, Durham, North Carolina; <sup>3</sup>Department of Molecular and Comparative Pathobiology, Johns Hopkins University School of Medicine, Baltimore, Maryland; and <sup>4</sup>Department of Radiation Oncology and Molecular Radiation Sciences, Johns Hopkins University School of Medicine, Baltimore, Maryland

$\alpha$ -Particle emitters targeting the prostate-specific membrane antigen (PSMA) proved effective in treating patients with prostate cancer who were unresponsive to the corresponding  $\beta$ -particle therapy.  $^{211}\text{At}$  is an  $\alpha$ -emitter that may engender less toxicity than other  $\alpha$ -emitting agents. We synthesized a new  $^{211}\text{At}$ -labeled radiotracer targeting PSMA that resulted from the search for a pharmacokinetically optimized agent. **Methods:** A small series of  $^{125}\text{I}$ -labeled compounds was synthesized from tin precursors to evaluate the effect of the location of the radiohalogen within the molecule and the presence of lutetium in the chelate on biodistribution. On that basis,  $^{211}\text{At}$ -**3**-Lu was selected and evaluated in cell uptake and internalization studies, and biodistribution and PSMA-expressing (PSMA+) PC3 PIP tumor growth control were evaluated in experimental flank and metastatic (PC3-ML-Luc) models. A long-term (13-mo) toxicity study was performed for  $^{211}\text{At}$ -**3**-Lu, including tissue chemistries and histopathology. **Results:** The radiochemical yield of  $^{211}\text{At}$ -**3**-Lu was  $17.8\% \pm 8.2\%$ . Lead compound  $^{211}\text{At}$ -**3**-Lu demonstrated total uptake within PSMA+ PC3 PIP cells of  $13.4 \pm 0.5\%$  of the input dose after 4 h of incubation, with little uptake in control cells. In SCID mice,  $^{211}\text{At}$ -**3**-Lu provided uptake that was  $30.6 \pm 4.8$  percentage injected dose per gram (%ID/g) in PSMA+ PC3 PIP tumor at 1 h after injection, and this uptake decreased to  $9.46 \pm 0.96$  %ID/g by 24 h. Tumor-to-salivary gland and tumor-to-kidney ratios were  $129 \pm 99$  at 4 h and  $130 \pm 113$  at 24 h, respectively. Deastatination was not significant (stomach,  $0.34 \pm 0.20$  %ID/g at 4 h). Dose-dependent survival was demonstrated at higher doses ( $>1.48$  MBq) in both flank and metastatic models. There was little off-target toxicity, as demonstrated by hematopoietic stability, unchanged tissue chemistries, weight gain rather than loss throughout treatment, and favorable histopathologic findings. **Conclusion:** Compound  $^{211}\text{At}$ -**3**-Lu or close analogs may provide limited and acceptable toxicity while retaining efficacy in management of prostate cancer.

**Key Words:** prostate cancer;  $\alpha$ -emitter; radiopharmaceutical therapy;  $^{211}\text{At}$ ; PSMA; murine models

J Nucl Med 2022; 63:259–267

DOI: 10.2967/jnumed.121.262098

Received Feb. 6, 2021; revision accepted May 5, 2021.  
For correspondence or reprints, contact Martin G. Pomper (mpomper@jhmi.edu).  
Published online Jun. 4, 2021.  
COPYRIGHT © 2022 by the Society of Nuclear Medicine and Molecular Imaging.

**R**adiopharmaceutical therapy targeting prostate-specific membrane antigen (PSMA) using low-molecular-weight agents is becoming viable for metastatic prostate cancer (1–3). Such treatments have used  $\beta$ -particle emitters, including  $^{131}\text{I}$  and  $^{177}\text{Lu}$ , or  $\alpha$ -particle emitters such as  $^{213}\text{Bi}$ ,  $^{212}\text{Pb}$ ,  $^{227}\text{Th}$ , and  $^{225}\text{Ac}$  (4–10). To date, most clinical trials have used  $^{177}\text{Lu}$ . In one such trial, PSA levels decreased by over 50% in 57% of patients (11). PSMA-targeted  $\alpha$ -particle emitters may be even more promising, as evidenced by treatment with an  $^{225}\text{Ac}$ -labeled agent producing a significant tumor response in patients who were unresponsive to prior  $\beta$ -emitter therapy (12,13). However, the side effect of xerostomia from uptake of the agents in the salivary glands, and the potential of long-term renal toxicity, remain possible limitations.

A possible issue with  $\alpha$ -emitters such as  $^{225}\text{Ac}$  is that multiple  $\alpha$ -emitting daughters are generated from  $\alpha$ -emitting parents, and in each case the energy imparted by the nuclear recoil effect is orders of magnitude greater than chemical bonds. That energy makes the release of the radioactive daughters from the targeting vector extremely likely, which can then lead to unintended irradiation of nontarget tissues (14,15). Our approach has been to use the radiohalogen  $^{211}\text{At}$ , which emits a single  $\alpha$ -particle per decay. That strategy may permit greater control on the targeting of the therapeutic radiation, thereby reducing the chance of off-target effects. It should be noted that 58% of the  $\alpha$ -particles emitted during  $^{211}\text{At}$  decay do involve a chemical transformation of astatine to polonium before  $\alpha$ -emission. In that case, the parent decays by electron capture, not  $\alpha$ -emission; the  $\alpha$ -emitting 0.52-s half-life  $^{211}\text{Po}$  daughter is therefore not nuclear-recoil-afflicted. Even with worst-possible-case assumptions—that  $^{211}\text{Po}$  escapes immediately from the cell surface and can freely diffuse—nearly 100% of  $^{211}\text{Po}$  atoms should decay within 2 cell diameters from the original cell surface (16). The second  $^{211}\text{At}$  decay branch (42%) is by direct  $\alpha$ -particle emission to  $^{207}\text{Bi}$ , which has a 32.9-y half-life. That long-lived radioactive daughter is not of concern because about 100,000 decays of  $^{211}\text{At}$  are needed to produce a single decay of  $^{207}\text{Bi}$ . Accordingly, a 370-MBq (10 mCi) hypothetical patient dose of an  $^{211}\text{At}$ -labeled PSMA agent would yield approximately 3.7 kBq ( $\sim 0.1$   $\mu\text{Ci}$ ) of  $^{207}\text{Bi}$ , a level that is only 0.1% of the annual limit of intake recommended for  $^{207}\text{Bi}$  by the Nuclear Regulatory Commission (3.7 MBq [100  $\mu\text{Ci}$ ]) (17). Despite these issues, we believe  $^{211}\text{At}$  remains the best option for  $\alpha$ -therapy.

Our previous studies used the following compounds, shown in Figure 1: DCABzL, HS-549, GV-620, GV-904, and YC-550. The initial compound studied,  $^{211}\text{At}$ -DCABzL, showed high and prolonged uptake in PSMA-expressing (PSMA+) tumor xenografts and renal cortex, with moderate uptake in thyroid and stomach, likely from dehalogenation (18). Despite that suboptimal biodistribution, we were able to demonstrate a treatment-related increase in survival in both flank tumor xenograft and micrometastatic models with a single dose of 0.74 MBq (20  $\mu\text{Ci}$ ) and 0.11–0.37 MBq (3–10  $\mu\text{Ci}$ ), respectively (18). From long-term toxicity studies, we determined that the dose-limiting toxicity was late radiation nephropathy (18). Using the  $^{211}\text{At}$ -labeled analogs YC-550, HS-549, GV-904, and GV-620 (Fig. 1), we observed faster renal clearance in mice than was seen with  $^{211}\text{At}$ -DCABzL. However, in vivo dehalogenation or off-target organ uptake remained an issue (19).

Here, we describe a new  $^{211}\text{At}$ -labeled PSMA-targeted compound with high stability in vivo and rapid clearance from off-target tissues (including kidneys, salivary and lacrimal glands) in mice. We also demonstrate a dose-dependent therapeutic effect in flank xenograft and metastatic tumor models of prostate cancer.

## MATERIALS AND METHODS

### Reagents, Cell Lines, and Animal Models

**Chemistry.** The syntheses of compounds 4 (Fig. 1) and its tin precursor, 15, as well as of unlabeled compounds 3, 3-Lu, and their tin precursor, 9, are outlined in Figures 2 and 3 and are described in detail in the supplemental materials (available at <http://jnm.snmjournals.org> [20–22]). The PSMA-binding affinity of compounds 3 and 4 was determined using a fluorescence-based assay we have previously reported (18).

**Radiochemistry.** Sodium  $^{125}\text{I}$ -iodide in 10  $\mu\text{M}$  NaOH (pH 8–11) was purchased from Perkin Elmer.  $^{211}\text{At}$  was produced on the Duke University CS-30 cyclotron via the  $^{209}\text{Bi}(\alpha, 2n)^{211}\text{At}$  reaction on natural bismuth targets (23,24).

We investigated 2 methods (A and B) for the preparation of  $^{125}\text{I}$ -3-Lu and  $^{211}\text{At}$ -3-Lu (Fig. 2). Method A included purification of

$^{125}\text{I}/^{211}\text{At}$ -3 before complexation with  $^{175}\text{Lu}$ (III), whereas in method B lutetium complexation was performed in situ without purification of the intermediate. In both methods, the final compound was purified by high-performance liquid chromatography. Radiosynthesis of  $^{211}\text{At}$ -3-Lu by method B began with a solution of  $^{211}\text{At}$  in 0.02% N-chlorosuccinimide in methanol (600  $\mu\text{L}$ ; 638 MBq [17.3 mCi]) that was added to 310  $\mu\text{g}$  (204 nmol) of compound 9 in a borosilicate screw cap vial followed by 12  $\mu\text{L}$  of glacial acetic acid. The vial was capped, shaken, and allowed to stand at room temperature for 10 min. The reaction mixture was concentrated to dryness using a stream of nitrogen at 60°C. A 95:5 mixture of trifluoroacetic acid:water (200  $\mu\text{L}$ ) was added, and the vial was heated at 60°C for 30 min. Volatiles were evaporated using a stream of nitrogen at 60°C. Sodium acetate buffer (0.1 M), pH 4.5 (500  $\mu\text{L}$ ), and a solution of  $\text{Lu}(\text{NO}_3)_3$  in 0.1 M HCl (65  $\mu\text{L}$ ; 325 nmol) were added to the residue, and the solution was mixed with a micropipette. That solution was heated at 60°C for 20 min, 100  $\mu\text{L}$  of 5 mM ethylenediaminetetraacetic acid was added, and the reaction mixture was diluted with 600  $\mu\text{L}$  of water. The final product was purified by high-performance liquid chromatography. For this, a Phenomenex Luna C18 column (250  $\times$  4.6 mm, 10  $\mu\text{m}$ ) was eluted at a flow rate of 1 mL/min with a gradient consisting of 0.1% trifluoroacetic acid in both water (solvent A) and acetonitrile (solvent B). The proportion of B was linearly increased from 15% to 40% over 30 min. Under those conditions,  $^{211}\text{At}$ -3-Lu [54 MBq (1.47 mCi)] eluted at 22.5 min. Pooled high-performance liquid chromatography fractions containing  $^{211}\text{At}$ -3-Lu were diluted to 20 mL with water and were loaded onto a Waters Oasis HLB Light Sep-Pak. The cartridge was washed with 5 mL of water and dried under a stream of nitrogen, and the product was eluted with 0.5 mL of ethanol. The eluate was concentrated using a stream of nitrogen, and the activity was reconstituted in saline. Detailed radiosyntheses of  $^{211}\text{At}$ -3-Lu by method A, and syntheses of  $^{125}\text{I}$ -3,  $^{125}\text{I}$ -3-Lu,  $^{125}\text{I}$ -4, and  $^{125}\text{I}$ -4-Lu, are presented in the supplemental materials. Radiolabeling yields for  $^{125}\text{I}/^{211}\text{At}$ -3 and  $^{125}\text{I}/^{211}\text{At}$ -3-Lu are summarized in Tables 1 and 2.

**Cell Lines and Culture Conditions.** PSMA+ PC3 PIP and PSMA-negative (PSMA-) PC3 flu cells were maintained as previously described (25–27). For the experimental metastatic model, parental PC3-ML-Luc cells were obtained from Dr. Mauricio Reginato (Drexel University). Those cells are characterized in Supplemental Figure 1. Cell lines were maintained *Mycoplasma*-free through biweekly testing with the MycoAlert *Mycoplasma* detection kit (Lonza).

**Animals.** Animal studies conformed to protocols approved by the Johns Hopkins Animal Care and Use Committee. Johns Hopkins University has an approved Public Health Service Policy, and the approved protocols follow this and Animal Welfare Act regulations. NSG (NOD/SCID/IL2R $\gamma$ null) mice were obtained from the Animal Resources Core of the Johns Hopkins Sydney Kimmel Comprehensive Cancer Center.

### In Vitro Studies

PSMA+ PC3 PIP cells were plated at 5  $\times$  10<sup>5</sup> cells per well and incubated overnight. Cells were then incubated with  $^{211}\text{At}$ -3 in medium ( $\sim$ 3.7 kBq/100  $\mu\text{L}$ ) at 37°C for 0.5, 1.0, 2.0, and 4.0 h. Cell culture supernatant was removed, and the cells were processed as before (18). Cell-associated radioactivity was calculated as percentage of input dose. The

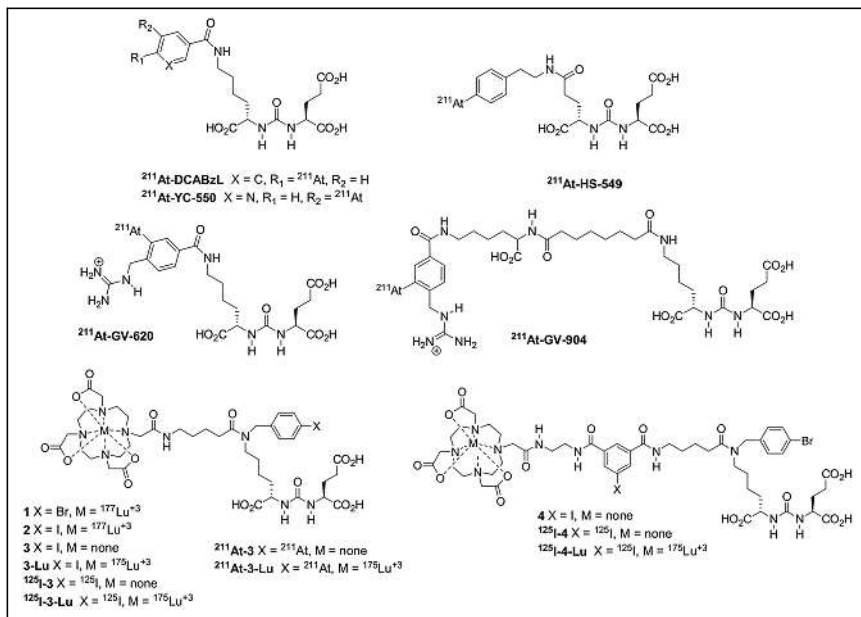
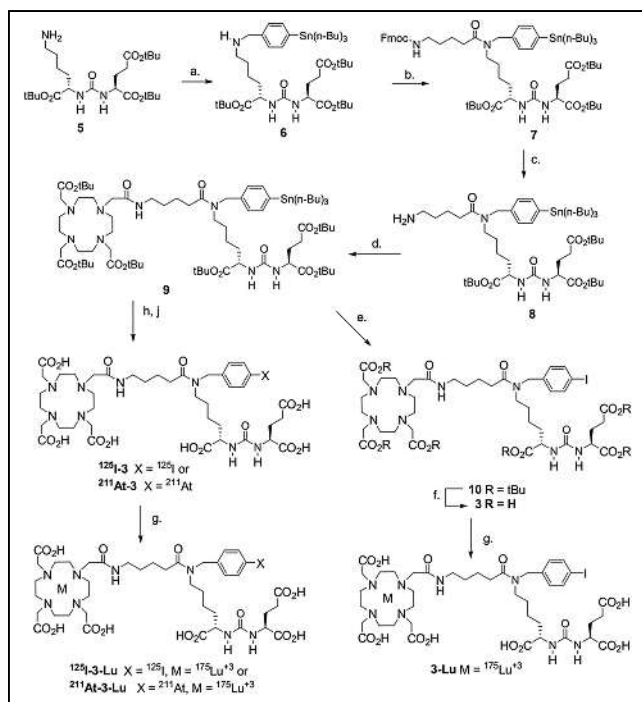


FIGURE 1. PSMA-targeted agents.



**FIGURE 2.** Synthesis of compound **3**, **3-Lu**, radiolabeling of precursor **9**,  $^{125}\text{I}$ -**3**,  $^{125}\text{I}$ -**3-Lu**, and  $^{211}\text{At}$ -**3-Lu**. Reagents and conditions: 4-(tributylstannyl)benzaldehyde, methanol, sodium cyanoborohydride (a); 5-(Fmoc-amino)valeric acid, *O*-(*N*-succinimidy)-*N,N,N,N'*-tetramethyluronium tetrafluoroborate, *N,N*-diisopropylethylamine, dimethylformamide (b); 20% piperidine in dimethylformamide (c); DOTA-*N*-hydroxysuccinimide tri-*tert*-butylester, *N,N*-diisopropylethylamine, dimethylsulfoxide (d);  $\text{I}_2$ ,  $\text{CH}_2\text{Cl}_2$  (e); 1/1 trifluoroacetic acid/ $\text{CH}_2\text{Cl}_2$  (f); 0.2 M  $\text{NH}_4\text{OAc}$ , dimethylsulfoxide, 5 mM  $^{175}\text{Lu}(\text{NO}_3)_3 \cdot \text{H}_2\text{O}$  in 0.1N HCl,  $70^\circ\text{C}$ , 20 min (g, step i), ethylenediaminetetraacetic acid (g, step ii); Na $^{125}\text{I}$  or  $^{211}\text{At}$ , methanol, glacial acetic acid, room temperature, 20 min (h); and trifluoroacetic acid,  $60\text{--}70^\circ\text{C}$ , 30–45 min (j).

internalized fraction of radioactivity was determined by solubilizing cells with 1% SDS cell lysis buffer after removing the unbound fractions and cell surface-bound fractions (by washing with glycine-HCl buffer). To determine binding specificity, PSMA+ PC3 PIP cells were coincubated with  $^{211}\text{At}$ -**3** and the known PSMA inhibitor (*R,S*)-2-(phosphonomethyl)pentanedioic acid (100  $\mu\text{M}$ ) (28).

### In Vivo Studies

**Biodistribution.** Six- to 8-wk-old male NSG mice were implanted subcutaneously with PSMA+ PC3 PIP ( $1.5 \times 10^6$ ) and PSMA– PC3 flu cells ( $1 \times 10^6$ ) in 100  $\mu\text{L}$  of Hanks balanced salt solution (Cellgro; Corning) at the forward right and left flanks, respectively. Mice were used in *ex vivo* biodistribution assays when the xenografts reached 5–7 mm in diameter. Biodistribution experiments were performed in the above mice bearing both PSMA+ PC3 PIP and PSMA– PC3 flu flank xenografts after an intravenous bolus of 37 kBq (1  $\mu\text{Ci}$ ) of  $^{125}\text{I}$ -**4**,  $^{125}\text{I}$ -**4-Lu**,  $^{125}\text{I}$ -**3**,  $^{125}\text{I}$ -**3-Lu**, or  $^{211}\text{At}$ -**3-Lu**. Tissues harvested at 1, 4, and 24 h after injection ( $n = 5$  per time point) included blood, heart, lung, liver, spleen, pancreas, stomach, small intestine, large intestine, fat, muscle, salivary gland, lacrimal gland, kidney, bladder, PSMA+ PC3 PIP tumor, and PSMA– PC3 flu tumor. Each tissue was weighed, and the associated radioactivity was measured with an automated  $\gamma$ -counter (2480 Wizard; Perkin Elmer). The percentage injected dose (%ID) was calculated using a known dilution of %ID. All measurements were corrected for decay. Data are expressed as

%ID/g of tissue or per organ (%ID) for organs that were too small for accurate dissection. All data are expressed as mean  $\pm$  SD.

**Antitumor Efficacy in Subcutaneous Xenograft Model.** PSMA+ PC3 PIP and PSMA– PC3 flu cells were implanted subcutaneously in male NSG mice as described above. When tumor diameter reached 5–7 mm, a single intravenous injection was performed with saline or with 0.24 MBq (6.6  $\mu\text{Ci}$ ), 0.74 MBq (20  $\mu\text{Ci}$ ), 1.48 MBq (40  $\mu\text{Ci}$ ), or 3.7 MBq (100  $\mu\text{Ci}$ ) of  $^{211}\text{At}$ -**3-Lu** ( $n = 5$  per group). Tumor progression was monitored by measuring subcutaneous tumor volume [(width $^2 \times$  length)/2 mm $^3$ ] using a caliper. A tumor volume increase of more than 4-fold was scored as death of the animal, at which point it was euthanized.

**Antitumor Efficacy in Metastatic Model.** Four- to 6-wk-old NSG mice were injected intravenously with  $1 \times 10^6$  PC3-ML-Luc cells suspended in 200  $\mu\text{L}$  of Hanks balanced salt solution to form micrometastatic deposits. One week after injection of cells, the mice were injected intravenously with 0 MBq (0  $\mu\text{Ci}$ ; saline), 0.185 MBq (5  $\mu\text{Ci}$ ), 0.37 MBq (10  $\mu\text{Ci}$ ), 0.74 MBq (20  $\mu\text{Ci}$ ), 1.48 MBq (40  $\mu\text{Ci}$ ), or 3.7 MBq (100  $\mu\text{Ci}$ ) of  $^{211}\text{At}$ -**3-Lu** ( $n = 5$  per group). Metastatic tumor progression was monitored by *in vivo* bioluminescence imaging and survival of injected animals. Weekly bioluminescence imaging was performed using the IVIS Spectrum *in vivo* imager (Perkin-Elmer). Mice were sacrificed and scored as death if they lost more than 20% of body weight or had signs of discomfort, such as hunched posture, anorexia, or dehydration. For both animal models, the probability of survival was characterized by Kaplan–Meier curves using Prism software (GraphPad Software).

**Long-Term Toxicity.** Healthy 11-wk-old male CD1 mice (Charles River) weighing 35–40 g received intravenous injections of 0 MBq (0  $\mu\text{Ci}$ ; saline), 0.24 MBq (6.6  $\mu\text{Ci}$ ), 0.74 MBq (20  $\mu\text{Ci}$ ), or 1.48 MBq (40  $\mu\text{Ci}$ ) of  $^{211}\text{At}$ -**3-Lu** ( $n = 5$  per group). Mice were monitored for 13 mo with a health inspection daily and a weight measurement twice per week. Monthly urinalysis was performed for specific gravity and urine protein content using Chemstrip test strips (Roche Diagnostics). After 13 mo, the mice were euthanized in a  $\text{CO}_2$  chamber, and blood, kidney, salivary glands, and lacrimal glands were collected. Complete blood counts, including white blood cells, red blood cells, hemoglobin, hematocrit, mean corpuscular volume, mean corpuscular hemoglobin, mean corpuscular hemoglobin concentration, and platelets, were measured using the scil Vet ABC hematology analyzer (scil Animal Care Co.). Blood chemistry testing for blood urea nitrogen, glucose, alkaline phosphatase, total protein, alanine aminotransferase, and creatinine was performed using a Spotchem EZ chemistry analyzer (Arkray USA). Histopathologic evaluation was performed by a certified veterinary pathologist for kidneys, salivary glands, and lacrimal glands with hematoxylin and eosin-stained slides of each tissue.

### Statistics

Survival analyses for the metastatic and subcutaneous models were performed using Prism software (version 9; GraphPad Software). *P* values were calculated by the log-rank (Mantel–Cox) test and were considered significant if less than 0.05.

## RESULTS

### Chemistry

Because of the promising results obtained with  $^{177}\text{Lu}$ -**1** and  $^{177}\text{Lu}$ -**2**, our strategy was to replace the nonradioactive bromine or iodine atom with  $^{125}\text{I}$  and evaluate their biodistribution in tumor-bearing animals with or without chelated nonradioactive lutetium ( $^{125}\text{I}$ -**3** and  $^{125}\text{I}$ -**3-Lu** [inhibition constant, 0.09–34 nM (29)]; Fig. 2). For comparison, we also synthesized and evaluated  $^{125}\text{I}$ -**4** and  $^{125}\text{I}$ -**4-Lu** (Fig. 3), where the radioiodine was

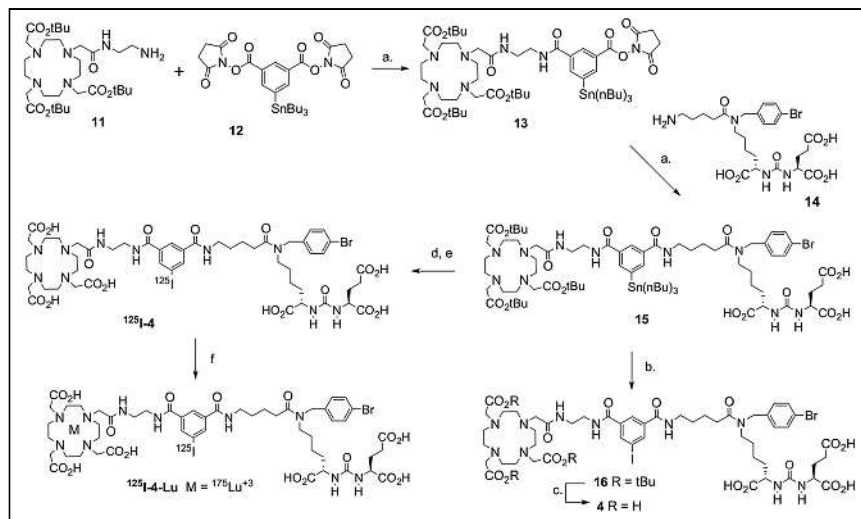


**FIGURE 3.** Synthesis of radiolabeling precursor 15, 4,  $^{125}\text{I}$ -4, and  $^{125}\text{I}$ -4-Lu. Reagents and conditions: triethylamine, dimethylsulfoxide, room temperature, 2 h (a);  $\text{I}_2$ ,  $\text{CH}_2\text{Cl}_2$ , room temperature, 2 h (b); 1/1 trifluoroacetic acid/ $\text{CH}_2\text{Cl}_2$ , room temperature, 2 h (c);  $\text{Na}^{125}\text{I}$ , *N*-chlorosuccinimide, glacial acetic acid, methanol, room temperature, 20 min (d); concentrated formic acid,  $60^\circ\text{C}$ , 1 h (e); 0.1 M sodium acetate, pH 4.5, 5 mM  $^{175}\text{Lu}(\text{NO}_3)_3$  in 0.1 M HCl,  $60^\circ\text{C}$ , 20 min (f, step i); and 5 mM ethylenediaminetetraacetic acid (f, step ii).

incorporated into the linking group, and each contained a 4-bromobenzyl moiety as in compound 1. The  $^{211}\text{At}$ -labeled analog of the most promising iodinated compound was synthesized and evaluated. The binding affinity of unlabeled compounds 3 and 4 was as follows: half-maximal inhibitory concentration, 1.51 nM (95% CI, 0.62–3.64 nM); inhibition constant, 0.30 nM (95% CI,

0.13–0.73 nM), and half-maximal inhibitory concentration, 7.82 nM (95% CI, 6.16–9.94 nM); inhibition constant, 0.30 nM (95% CI, 1.23–1.99 nM), respectively.

### Radiochemistry

Syntheses of  $^{125}\text{I}$ -4 and  $^{125}\text{I}$ -4-Lu were each performed once. The yield of  $^{125}\text{I}$ -4 from  $^{125}\text{I}$ -iodide was 14%, and that for the conversion of  $^{125}\text{I}$ -4 to  $^{125}\text{I}$ -4-Lu was 82%. Radiolabeling conditions and yields for  $^{125}\text{I}/^{211}\text{At}$ -3 and  $^{125}\text{I}/^{211}\text{At}$ -3-Lu are given in Tables 1 and 2, respectively. In general, fresh batches of  $^{211}\text{At}$  provided higher overall yields of either compound. Purification of the nonmetallated intermediate ( $^{125}\text{I}/^{211}\text{At}$ -3) did not enhance yield and actually provided lower overall yields of the final product ( $^{125}\text{I}/^{211}\text{At}$ -3-Lu).

### Cell Uptake and Internalization

In vitro studies of  $^{211}\text{At}$ -3-Lu demonstrated total uptake within PSMA+ PC3 PIP cells of  $13.4\% \pm 0.5\%$  of the input dose after 4 h of incubation and an increasing internalized fraction over time, namely,  $15.8\% \pm 0.7\%$ ,  $19.0\% \pm 0.7\%$ ,  $24.5\% \pm 1.0\%$ , and  $27.7\% \pm 2.2\%$  at 0.5, 1.0, 2.0, and 4.0 h, respectively. Coincubation with (*R,S*)-2-(phosphonome-thyl)pentanedioic acid showed an average of 0.6% uptake at all time points, confirming PSMA-specific uptake (Supplemental Fig. 2) (18).

**TABLE 1**  
Radiolabeling Yields for  $^{125}\text{I}/^{211}\text{At}$ -3

Radionuclide	Starting radioactivity	Age of $^{211}\text{At}$	<i>n</i>	% yield*
$^{125}\text{I}$	0.036–0.266 GBq (0.96–7.2 mCi)	Not applicable	3	$56.1 \pm 13.7$
$^{211}\text{At}$	0.1628–0.3145 GBq (4.4–8.5 mCi)	Fresh	3	$49.6 \pm 6.8$
$^{211}\text{At}$	0.444–0.6623 GBq (12.0–17.9 mCi)	$\geq 9$ h	2	$20.8\% \pm 8.2\%$

\*After preparative high-performance liquid chromatography purification.

**TABLE 2**  
Radiolabeling Yields for  $^{125}\text{I}/^{211}\text{At}$ -3-Lu

Radionuclide	Starting radioactivity	Age of $^{211}\text{At}$	Method of preparation	<i>n</i>	% yield*
$^{125}\text{I}$	0.170–0.266 GBq (4.6–7.2 mCi)	Not applicable	A	2	$46.5 \pm 7.7$
$^{125}\text{I}$	0.054–0.518 GBq (1.47–14 mCi)	Not applicable	B	4	$62.8 \pm 9.0$
$^{211}\text{At}$	0.16–0.31 GBq (4.4–8.5 mCi)	Fresh	A	3	$6.3 \pm 1.8$
$^{211}\text{At}$	0.126–0.34 GBq (3.4–9.2 mCi)	Fresh	B	2	$17.8 \pm 8.2$
$^{211}\text{At}$	0.44–0.66 GBq (12.0–17.0 mCi)	$\geq 9$ h	A	2	$8.6 \pm 3.6$
$^{211}\text{At}$	0.115–0.877 GBq (3.1–23.7 mCi)	$\geq 9$ h	B	4	$13.6 \pm 8.4$

\*After preparative high-performance liquid chromatography purification.

A = separate preparative high-performance liquid chromatography purification of  $^{125}\text{I}/^{211}\text{At}$ -3 and  $^{125}\text{I}/^{211}\text{At}$ -3-Lu. B = preparative high-performance liquid chromatography purification of  $^{125}\text{I}/^{211}\text{At}$ -3-Lu only.

## Biodistribution

Detailed biodistribution data, represented as %ID/g for all radiolabeled compounds, are given in Supplemental Tables 1–6. There was little deastination of  $^{211}\text{At-3-Lu}$  in vivo as evidenced by low uptake of radioactivity in stomach ( $0.39 \pm 0.12$  %ID/g), salivary glands ( $0.47 \pm 0.19$  %ID/g), and spleen ( $2.51 \pm 0.94$  %ID/g) at 1 h after administration, which decreased further by 4 h for stomach and salivary glands ( $<0.05$  %ID/g in spleen) (Supplemental Table 3). Uptake in PSMA+ PC3 PIP tumor and selected nontarget organs is shown in Figure 4. All compounds had high tumor uptake at 1 h (30–60 %ID/g). Although tumor activity remained at that high level out to 24 h for  $^{125}\text{I-4}$ ,  $^{125}\text{I-4-Lu}$ , and  $^{125}\text{I-3}$ , 50% and 67% of  $^{125}\text{I-3-Lu}$  and  $^{211}\text{At-3-Lu}$  activity, respectively, cleared from the tumor by 24 h. Importantly,  $^{211}\text{At-3-Lu}$  was nearly undetectable in normal organs at 24 h. Renal uptake of  $^{211}\text{At-3-Lu}$  at 1 h ( $89.5 \pm 42.7$  %ID/g) was 30%–50% lower than that seen for other compounds. By 4 h, renal activity levels for  $^{125}\text{I-3-Lu}$  and  $^{211}\text{At-3-Lu}$  decreased to  $18.2 \pm 3.9$  and  $2.1 \pm 0.6$  %ID/g, respectively, whereas activity in kidneys for the other compounds remained high (162–199 %ID/g). By 24 h, activity in kidneys from  $^{125}\text{I-3-Lu}$  and  $^{211}\text{At-3-Lu}$  decreased to  $3.30 \pm 1.15$  %ID/g and  $0.02 \pm 0.20$  %ID/g, respectively. On the other hand, renal activity was  $141 \pm 18$ ,  $50.4 \pm 25.9$ , and  $30.6 \pm 14.0$  %ID/g for  $^{125}\text{I-4}$ ,  $^{125}\text{I-4-Lu}$ , and  $^{125}\text{I-3}$ , respectively. Despite the lower %ID/g values of  $^{211}\text{At-3-Lu}$  in tumor, its considerably faster renal clearance resulted in tumor-to-kidney ratios of 8 and 130 at 4 and 24 h, respectively (Fig. 5). Those values are roughly 5- and 16-fold higher than achieved with  $^{125}\text{I-3-Lu}$  and 20- to 200-fold higher than achieved with the other compounds. The uptake in spleen at 1 h was much lower for  $^{125}\text{I-3-Lu}$  and  $^{211}\text{At-3-Lu}$  ( $7.41 \pm 2.57$  and  $2.51 \pm 0.94$  %ID/g, respectively) than for the other compounds (40–70 %ID/g). Radioactivity from spleen cleared rapidly for all agents, resulting in tumor-to-spleen ratios at 4 h of 1.3, 4.4, 6.8, 43, and 97 for  $^{125}\text{I-4}$ ,  $^{125}\text{I-4-Lu}$ ,  $^{125}\text{I-3}$ ,  $^{125}\text{I-3-Lu}$ , and  $^{211}\text{At-3-Lu}$ , respectively. The uptake of  $^{125}\text{I-3-Lu}$  and  $^{211}\text{At-3-Lu}$  in salivary and lacrimal glands was lower than observed for any other compound at any time point, resulting in tumor-to-salivary gland ratios of 58 and 75 and tumor-to-lacrimal gland

ratios of 13 and 44 at 1 h after injection, respectively (Supplemental Tables 5 and 6, respectively). At 4 h, those values were 365 and 129 for salivary gland and 92 and 164 for lacrimal gland.

## $\alpha$ -Therapy with $^{211}\text{At-3-Lu}$

We first evaluated the efficacy of  $^{211}\text{At-3-Lu}$  by scoring growth inhibition of subcutaneous xenograft tumors of both PSMA+ PC3 PIP and PSMA– PC3 flu cells implanted in the same animal. A single intravenous injection of 4 different doses (0 MBq [0  $\mu\text{Ci}$ ; saline], 0.24 MBq [6.5  $\mu\text{Ci}$ ], 0.74 MBq [20  $\mu\text{Ci}$ ], 1.48 MBq [40  $\mu\text{Ci}$ ], or 3.7 MBq [100  $\mu\text{Ci}$ ]) did not affect tumor growth of PSMA– PC3 flu tumors, as the median survival of the tumor-bearing mice was 9, 14, 11, 11, and 13 d, respectively. On the other hand, median survival compared with untreated controls for animals harboring PSMA+ PC3 PIP tumors at doses of 0 MBq (0  $\mu\text{Ci}$ ; saline), 0.24 MBq (6.5  $\mu\text{Ci}$ ), 0.74 MBq (20  $\mu\text{Ci}$ ), 1.48 MBq (40  $\mu\text{Ci}$ ), or 3.7 MBq (100  $\mu\text{Ci}$ ) were 11 (not statistically significant), 27 ( $P = 0.0015$ ), 39 ( $P = 0.0005$ ), 29 ( $P = 0.0005$ ), and not reached ( $P = 0.0005$ ), respectively, indicating that  $^{211}\text{At-3-Lu}$  was capable of PSMA-specific tumor growth control and enhancement of survival (Fig. 6). We also tested the efficacy of a single dose of intravenously administered  $^{211}\text{At-3-Lu}$  for treating metastatic deposits of PSMA-expressing tumors. Higher doses (1.48 and 3.7 MBq) provided survival benefits compared with the untreated group (Fig. 6B). Median survival for animals treated with 0 MBq (0  $\mu\text{Ci}$ ; saline), 0.186 MBq (5  $\mu\text{Ci}$ ), 0.373 MBq (10  $\mu\text{Ci}$ ), 0.74 MBq (20  $\mu\text{Ci}$ ), 1.48 MBq (40  $\mu\text{Ci}$ ), or 3.7 MBq (100  $\mu\text{Ci}$ ) were 48, 49 (not statistically significant), 48 ( $P = 0.5769$ , not statistically significant), 52 ( $P = 0.0699$ , not statistically significant), 57, ( $P = 0.0286$ ), and 58.5 d ( $P = 0.2718$ , due to an early mouse death), respectively.

## Long-Term Radiotoxicity

Eleven-week-old male CD1 mice were injected with 0.24 MBq (6.6  $\mu\text{Ci}$ ), 0.74 MBq (20  $\mu\text{Ci}$ ), or 1.48 MBq (40  $\mu\text{Ci}$ ) of  $^{211}\text{At-3-Lu}$  as a single intravenous injection. We also included an untreated group for the entire duration of the study as an age-matched control. All groups of mice consistently gained weight for the 13-mo period of monitoring (Supplemental Fig. 3). Blood chemistry data

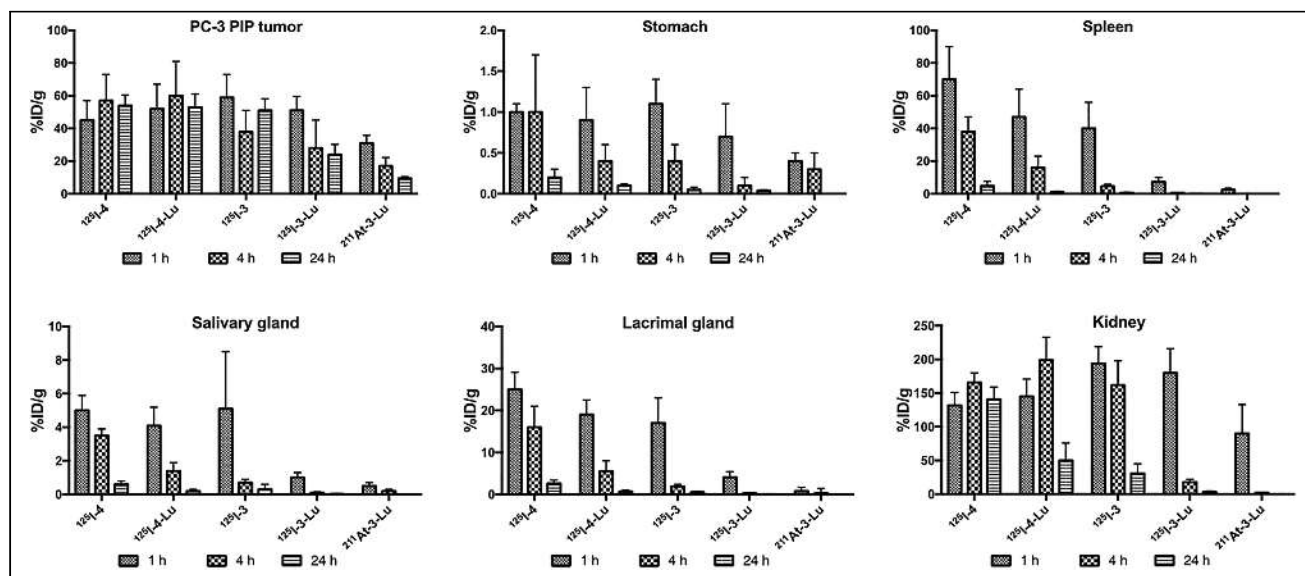
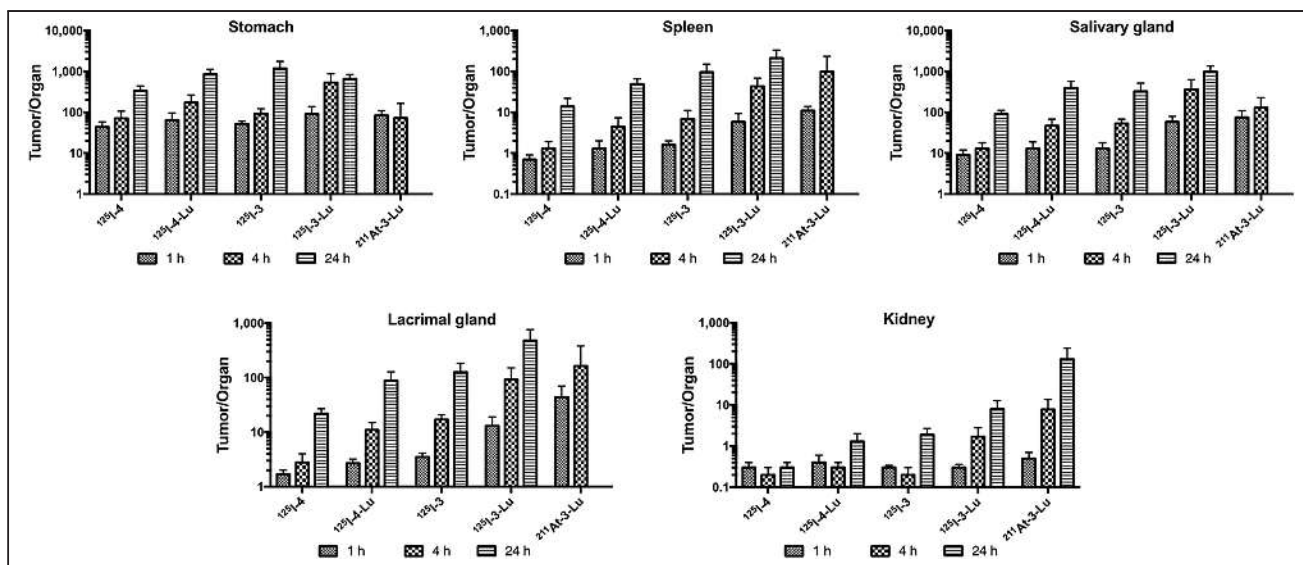


FIGURE 4. Biodistribution (%ID/g) of radiolabeled compounds of Figures 2 and 3 in selected tissues.



**FIGURE 5.** Biodistribution (ratios of tumor to selected organs) of compounds of Figures 2 and 3 in selected tissues.

for creatinine, blood urea nitrogen, glucose, alkaline phosphatase, alanine aminotransferase, and total protein for all treated groups were similar to those for age-matched untreated controls (Supplemental Fig. 4). A complete blood count also indicated that treated groups remained within normal limits (Supplemental Fig. 4). Monthly evaluation of urine protein level (Supplemental Table 7) and specific gravity (Supplemental Table 8) showed no sign of renal impairment compared with untreated controls for the duration of the study. Histopathologic examination of kidneys, salivary glands, and lacrimal glands revealed no treatment-specific pathologic abnormalities at any dose studied (Fig. 7). We observed mild inflammation, a few dilated tubules with protein deposits, and mild multifocal fibrosis in kidneys from all groups (including controls), which were age-related phenomena. Mild age-related inflammation was also observed in salivary and lacrimal glands from all groups.

## DISCUSSION

Banerjee et al. reported a series of 4-halobenzyl derivatives of Lys-Glu-urea inhibitors of PSMA containing a linking group that connects the PSMA-targeting urea pharmacophore with a metal chelator (29). Two of the most promising compounds were 1 and 2 (Fig. 1). When  $^{177}\text{Lu}$ -1 and  $^{177}\text{Lu}$ -2 were administered intravenously to tumor-bearing mice, they exhibited high uptake in PSMA+ PC3 PIP tumor xenografts (29), low uptake in the

salivary glands, rapid renal clearance, and dose-dependent tumor growth delay. We previously demonstrated in a head-to-head preclinical study that our scaffold bearing the  $\beta$ -particle emitter  $^{177}\text{Lu}$  was inferior to that delivering  $^{225}\text{Ac}$ , an  $\alpha$ -emitter, providing a rationale for our focus on PSMA-targeted compounds bearing an  $\alpha$ -emitting warhead (30).

Reports of PSMA-targeted therapy with the  $\alpha$ -emitter  $^{225}\text{Ac}$ -PSMA-617 have been encouraging, even in late-stage disease. Some trials reported PSA declines of at least 90% in roughly half of patients (31) and overall survival of more than 15 mo (32). Such results may exceed those of new chemo- or hormonal therapies. However, those results have come at the costs of decreased quality of life, including nontransient, treatment-halting xerostomia and substantial hematologic toxicity, according to 1 retrospective trial (33). A greater mitigation of off-target effects, which has proved challenging to date, is needed for PSMA-targeted radiopharmaceutical therapy to develop a niche in the management of prostate cancer. Two ways to do so are by optimizing the pharmacokinetics and choosing the correct  $\alpha$ -particle emitter. We have attempted both by focusing on the type II Lys-Glu-urea scaffold we have previously reported (29), a close structural analog of which is currently under investigation in a phase 1–2 clinical trial (NCT0349083800), and on using  $^{211}\text{At}$ , which produces only 1  $\alpha$ -particle per decay and has a tractable physical half-life of 7.2 h (34–37).

For convenience of handling, we initially studied the  $^{125}\text{I}$ -labeled surrogates of the intended  $^{211}\text{At}$  compounds to gauge pharmacokinetics and in vivo stability. Compounds of the 4 series (Fig. 3) enabled us to explore the effect of halogen location in the molecule on pharmacokinetics, as well as the influence of a metal within the chelator, which we previously showed enhanced affinity for PSMA (29). Although  $^{125}\text{I}$ -4 and  $^{125}\text{I}$ -4-Lu behaved similarly in PSMA+ PC3 PIP tumor,  $^{125}\text{I}$ -4-Lu in kidney substantially decreased by 24 h, indicating a

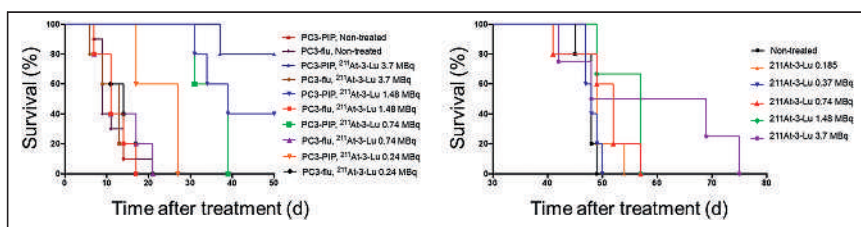


**FIGURE 6.** Kaplan–Meier curves showing survival in flank (A) and PC3-ML-Luc experimental metastatic (B) models at dose provided. PC3-PIP = PSMA+ PC3 PIP tumors; PC3-flu = PSMA– PC3 flu cell-derived tumors.

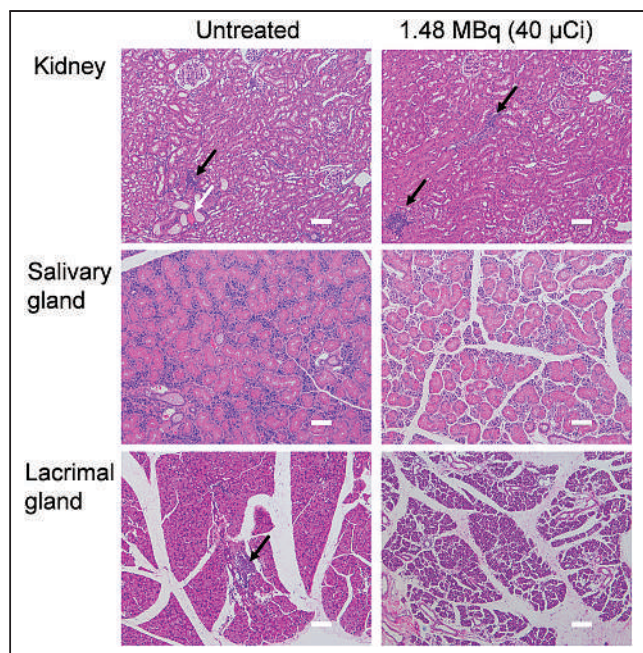


**FIGURE 7.** Representative microscopic images of kidney, salivary gland, and lacrimal gland (size bar, 100  $\mu\text{m}$ ). Black arrows indicate inflammation; white arrow indicates dilated tubule with protein deposit.

positive effect of the presence of lutetium in the chelator on renal clearance. Because even higher tumor-to-kidney ratios were observed for  $^{125}\text{I}$ -3-Lu than for  $^{125}\text{I}$ -4-Lu, we continued with the former for further in vivo testing. Relative to  $^{125}\text{I}$ -3-Lu,  $^{211}\text{At}$ -3-Lu demonstrated lower tumor uptake but also lower off-target uptake. There was also moderate uptake within stomach, consistent with some deastatination (38); however, levels remained below 0.5 %ID/g and tumor-to-stomach ratios were approximately 100 (Figs. 4 and 5). By contrast,  $^{211}\text{At}$ -DCABzL never had tumor-to-stomach ratios that rose above a few percentage points out to 18 h (18), and a recently published  $^{211}\text{At}$ -labeled minibody targeting prostate cancer had a ratio that only exceeded 1 on treatment with perchlorate at 5 h (1.2) and 9 h (1.4) after injection (39).

The lack of uptake within stomach and salivary glands of  $^{211}\text{At}$ -3-Lu could in part be due to the stability of the low-molecular-weight, Lys-Glu-urea-based targeting scaffold (40). There was also little radioactivity in blood (Supplemental Table 3) and no significant change in white blood cell counts (Supplemental Fig. 4). Accordingly, neither treatment with perchlorate (39) nor blocking agents were required to mitigate off-target effects. In vivo,  $^{211}\text{At}$ -3-Lu treatment caused a PSMA- and dose-dependent increase in survival compared with control animals in both the flank and metastatic models (Fig. 6). Comparison of this result with other reported compounds is challenging because of the different model systems used. If we focus on our own earlier therapy studies, we find that  $^{211}\text{At}$ -3-Lu provided survival effects at much lower doses than  $^{211}\text{At}$ -DCABzL (18), which had a maximum tolerated dose (MTD) of 37 kBq (1  $\mu\text{Ci}$ ). However, that study was performed on nude rather than SCID mice, which we used here. We did not reach the MTD for  $^{211}\text{At}$ -3-Lu, as the highest dose administered in the long-term (13 mo) toxicity study with normal mice was only 1.48 MBq (40  $\mu\text{Ci}$ ). Nonetheless, even at a dose up to 40 times higher than the MTD for  $^{211}\text{At}$ -DCABzL in the same mouse strain, our toxicity data showed only mild changes at all

doses and in all organs studied (Fig. 7). Perhaps a more relevant comparison is to  $^{225}\text{Ac}$ -L1 (30), which demonstrated an MTD of 9.3 kBq (0.25  $\mu\text{Ci}$ ) (fractionated  $\times 4$ ) because the scaffold is the same as that of  $^{211}\text{At}$ -3-Lu. Compound  $^{212}\text{Pb}$ -L2 (41), which has a similar scaffold, demonstrated an MTD of 1.5 MBq ( $\sim 40$   $\mu\text{Ci}$ ). For that compound, there were concerns of long-term renal toxicity, which may be due to the  $^{212}\text{Bi}$  daughter released and localized to the kidney, which is not a problem with  $^{211}\text{At}$ -based agents.

Our goal in this work was to find a suitable  $\alpha$ -particle-emitting agent to treat PSMA+ prostate and other cancers that had minimal off-target toxicity, namely, an agent that would be more effective than the corresponding  $\beta$ -particle emitter but not as toxic as those radiolabeled with  $^{225}\text{Ac}$ . We have achieved that with  $^{211}\text{At}$ -3-Lu, attesting to the potential benefits of this potentially tamer  $\alpha$ -emitter. As with  $^{212}\text{Pb}$ ,  $^{211}\text{At}$  emits only 1  $\alpha$ -particle per decay. As such, these 2 radionuclides do not produce daughter  $\alpha$ -emissions outside the intended target site and will not be expected to have the toxicity—for example, in liver—attendant on such emissions, such as those seen with  $^{225}\text{Ac}$ . However, there are differences between  $^{212}\text{Pb}$  and  $^{211}\text{At}$  that make us favor the latter. The therapeutic potential of  $^{212}\text{Pb}$  will be diminished if the daughter nuclei do not remain at the target site so that their energy can also be captured (7). For example, Ackerman et al. have calculated that migration of daughters with  $^{212}\text{Pb}$  could reduce its relative biological effectiveness to that of conventional external-beam radiation and  $\beta$ -particle emitters (42). Furthermore,  $^{211}\text{At}$  can be introduced to targeting ligands using chemistry very similar to that for other halogens to minimize perturbation of the targeting scaffold if a fastidious cellular target is sought, or a chelator can be deliberately introduced to enhance pharmacokinetics, as in this case (36,37). Lack of off-target toxicity, including to salivary and lacrimal glands, would obviate cumbersome coadministration of blocking agents. However, although the natural bismuth target material is inexpensive and widely available,  $^{211}\text{At}$  requires a 28-MeV  $\alpha$ -particle cyclotron beam for efficient production—a requirement that has curtailed its use (43). There are concerted efforts under way to increase the supply of  $^{211}\text{At}$  worldwide at academic institutions and research institutes, with commercial sources emerging in the not-too-distant future (<https://ionetix.com/why-alpha-therapy>).

A limitation of this study was the use of cells that may not reflect the natural abundance and heterogeneity of PSMA in human cancer. That issue has been discussed in detail elsewhere (44). However, PSMA+ PC3 PIP and PSMA- PC3 flu cells have the advantage of being isogenic, except for PSMA expression, enabling us to answer questions about pharmacokinetics with a minimum of variables present. The superior performance of  $^{211}\text{At}$ -3-Lu in the flank model rather than the metastatic model may reflect, in part, the supraphysiologic and 10-fold higher PSMA expression in the PSMA+ PC3 PIP cells relative to the PSMA+ PC3-ML-Luc cells used to generate the metastatic deposits (18), which express PSMA at about the same level of LNCaP cells (27).

## CONCLUSION

In this small series,  $^{211}\text{At}$ -3-Lu proved to have an excellent combination of properties: a pharmacokinetic profile matching the physical half-life of  $^{211}\text{At}$ , the ability to improve survival in tumor-bearing animals, and lack of off-target toxicity as demonstrated by hematopoietic stability, unchanged tissue chemistries, weight gain rather than loss throughout treatment, and favorable

histopathology. This compound or close analogs are promising for translation if and when an  $\alpha$ -particle emitter is to be considered in the therapeutic journey of the patient.

## DISCLOSURE

Financial support was received from CA184228, EB024495, CA134675, and the Commonwealth Foundation. Under a license agreement between D&D Pharmatech and Johns Hopkins and Duke Universities, the Universities' Ronnie Mease, Martin Pomper, Sangeeta Banerjee, Ganesan Vaidyanathan and Michael Zalutsky are entitled to royalty distributions related to the technology described in the study discussed in this publication. Martin Pomper, Sangeeta Banerjee, and Michael Zalutsky hold equity in D&D Pharmatech; Martin Pomper and Sangeeta Banerjee are cofounders. They and Michael Zalutsky are also paid consultants to the company. This arrangement has been reviewed and approved by Johns Hopkins University and Duke University in accordance with their conflict-of-interest policies. No other potential conflict of interest relevant to this article was reported.

## KEY POINTS

**QUESTION:** Can a PSMA-targeted,  $\alpha$ -emitting small molecule be designed with few off-target toxic effects while retaining therapeutic efficacy?

**PERTINENT FINDINGS:** Lead compound  $^{211}\text{At-3-Lu}$  was able to control tumor growth and enhance survival in animals treated at doses of 1.48 MBq or greater and did so without toxicity.

**IMPLICATIONS FOR PATIENT CARE:** Compounds such as  $^{211}\text{At-3-Lu}$  provide a further rationale for the use of  $^{211}\text{At}$  in targeted  $\alpha$ -emitting radiopharmaceuticals.  $^{211}\text{At}$  may be an effective and nontoxic alternative to other  $\alpha$ -emitters in use for management of prostate and other PSMA-expressing cancers. Its ease of incorporation in a variety of cancer affinity agents, including small molecules, as well as its convenient physical half-life could provide a safe, practical, and new method to treat a variety of intractable malignancies.

## REFERENCES

- Miyahira AK, Pienta KJ, Babich JW, et al. Meeting report from the Prostate Cancer Foundation PSMA Theranostics State of the Science meeting. *Prostate*. 2020; 80:1273–1296.
- Jones W, Griffiths K, Barata PC, Paller CJ. PSMA theranostics: review of the current status of PSMA-targeted imaging and radioligand therapy. *Cancers (Basel)*. 2020;12:1367.
- O'Dwyer E, Bodei L, Morris MJ. The role of theranostics in prostate cancer. *Semin Radiat Oncol*. 2021;31:71–82.
- Zechmann CM, Afshar-Oromieh A, Armor T, et al. Radiation dosimetry and first therapy results with a  $^{124}\text{I}/^{131}\text{I}$ -labeled small molecule (MIP-1095) targeting PSMA for prostate cancer therapy. *Eur J Nucl Med Mol Imaging*. 2014;41:1280–1292.
- Kratochwil C, Giesel FL, Stefanova M, et al. PSMA-targeted radionuclide therapy of metastatic castration-resistant prostate cancer with  $^{177}\text{Lu}$ -labeled PSMA-617. *J Nucl Med*. 2016;57:1170–1176.
- Morgenstern A, Apostolidis C, Kratochwil C, Sathekge M, Krolicki L, Bruchertseifer F. An overview of targeted alpha therapy with  $^{225}\text{Ac}$  and  $^{213}\text{Bi}$ . *Curr Radiopharm*. 2018;11:200–208.
- Dos Santos JC, Schafer M, Bauder-Wust U, et al. Development and dosimetry of  $^{203}\text{Pb}/^{212}\text{Pb}$ -labelled PSMA ligands: bringing "the lead" into PSMA-targeted alpha therapy? *Eur J Nucl Med Mol Imaging*. 2019;46:1081–1091.
- Hammer S, Hagemann UB, Zitzmann-Kolbe S, et al. Preclinical efficacy of a PSMA-targeted thorium-227 conjugate (PSMA-TTC), a targeted alpha therapy for prostate cancer. *Clin Cancer Res*. 2020;26:1985–1996.
- Kratochwil C, Bruchertseifer F, Giesel FL, et al.  $^{225}\text{Ac}$ -PSMA-617 for PSMA-targeted alpha-radiation therapy of metastatic castration-resistant prostate cancer. *J Nucl Med*. 2016;57:1941–1944.
- Yadav MP, Ballal S, Sahoo RK, Tripathi M, Seth A, Bal C. Efficacy and safety of  $^{225}\text{Ac}$ -PSMA-617 targeted alpha therapy in metastatic castration-resistant prostate cancer patients. *Theranostics*. 2020;10:9364–9377.
- Hofman MS, Violet J, Hicks RJ, et al. [ $^{177}\text{Lu}$ ]-PSMA-617 radionuclide treatment in patients with metastatic castration-resistant prostate cancer (LuPSMA trial): a single-centre, single-arm, phase 2 study. *Lancet Oncol*. 2018;19:825–833.
- Zacherl MJ, Gildehaus FJ, Mittlmeier L, et al. First clinical results for PSMA-targeted  $\alpha$ -therapy using  $^{225}\text{Ac}$ -PSMA-I&T in advanced-mCRPC patients. *J Nucl Med*. 2021;62:669–674.
- Ilhan H, Gosewisch A, Boning G, et al. Response to  $^{225}\text{Ac}$ -PSMA-I&T after failure of long-term  $^{177}\text{Lu}$ -PSMA RLT in mCRPC. *Eur J Nucl Med Mol Imaging*. 2021; 48:1262–1263.
- de Kruijff RM, Wolterbeek HT, Denkova AG. A critical review of alpha radionuclide therapy: how to deal with recoiling daughters? *Pharmaceuticals (Basel)*. 2015;8:321–336.
- Kozempel J, Mokhodoeva O, Vlk M. Progress in targeted alpha-particle therapy: what we learned about recoils release from in vivo generators. *Molecules*. 2018; 23:581.
- Palm S, Humm JL, Rundqvist R, Jacobsson L. Microdosimetry of astatine-211 single-cell irradiation: role of daughter polonium-211 diffusion. *Med Phys*. 2004;31: 218–225.
- Bismuth-207. U.S. Nuclear Regulatory Commission website. <https://www.nrc.gov/reading-rm/doc-collections/cfr/part020/appb/bismuth-207.html>. Updated March 24, 2021. Accessed August 11, 2021.
- Kiess AP, Minn I, Vaidyanathan G, et al. (2S)-2-(3-(1-carboxy-5-(4- $^{211}\text{At}$ -astato-benzamido)pentyl)ureido)-pentanedioic acid for PSMA-targeted alpha-particle radiopharmaceutical therapy. *J Nucl Med*. 2016;57:1569–1575.
- Vaidyanathan G, Mease RC, Minn I, et al. Synthesis and preliminary evaluation of  $^{211}\text{At}$ -labeled inhibitors of prostate-specific membrane antigen for targeted alpha particle therapy of prostate cancer. *Nucl Med Biol*. 2021;94–95:67–80.
- Sessler JL, Wang B, Harriman A. Photoinduced energy transfer in associated but noncovalently linked Photosynthetic model system. *J Am Chem Soc*. 1995;117: 704–714.
- Maresca KP, Hillier SM, Femia FJ, et al. A series of halogenated heterodimeric inhibitors of prostate specific membrane antigen (PSMA) as radiolabeled probes for targeting prostate cancer. *J Med Chem*. 2009;52:347–357.
- Vaidyanathan G, White BJ, Affleck DJ, et al. SIB-DOXA: a trifunctional prosthetic group potentially amenable for multi-modal labeling that enhances tumor uptake of internalizing monoclonal antibodies. *Bioorg Med Chem*. 2012;20:6929–6939.
- Zalutsky MR, Zhao XG, Alston KL, Bigner D. High-level production of alpha-particle-emitting  $^{211}\text{At}$  and preparation of  $^{211}\text{At}$ -labeled antibodies for clinical use. *J Nucl Med*. 2001;42:1508–1515.
- Pozzi OR, Zalutsky MR. Radiopharmaceutical chemistry of targeted radiotherapeutics, part 3: alpha-particle-induced radiolytic effects on the chemical behavior of  $^{211}\text{At}$ . *J Nucl Med*. 2007;48:1190–1196.
- Chang SS, Reuter VE, Heston WD, Bander NH, Grauer LS, Gaudin PB. Five different anti-prostate-specific membrane antigen (PSMA) antibodies confirm PSMA expression in tumor-associated neovasculature. *Cancer Res*. 1999;59:3192–3198.
- Nakajima T, Mitsunaga M, Bander NH, Heston WD, Choyke PL, Kobayashi H. Targeted, activatable, in vivo fluorescence imaging of prostate-specific membrane antigen (PSMA) positive tumors using the quenched humanized J591 antibody-iodocyanine green (ICG) conjugate. *Bioconjug Chem*. 2011;22: 1700–1705.
- Kiess AP, Minn I, Chen Y, et al. Auger radiopharmaceutical therapy targeting prostate-specific membrane antigen. *J Nucl Med*. 2015;56:1401–1407.
- Jackson PF, Cole DC, Slusher BS, et al. Design, synthesis, and biological activity of a potent inhibitor of the neuropeptidase N-acetylated alpha-linked acidic dipeptidase. *J Med Chem*. 1996;39:619–622.
- Banerjee SR, Kumar V, Lisok A, et al.  $^{177}\text{Lu}$ -labeled low-molecular-weight agents for PSMA-targeted radiopharmaceutical therapy. *Eur J Nucl Med Mol Imaging*. 2019;46:2545–2557.
- Banerjee SR, Lisok A, Minn I, et al. Preclinical evaluation of  $^{213}\text{Bi}$ - and  $^{225}\text{Ac}$ -labeled low-molecular-weight compounds for radiopharmaceutical therapy of prostate cancer. *J Nucl Med*. 2021;62:980–988.
- Sathekge M, Bruchertseifer F, Knoesen O, et al.  $^{225}\text{Ac}$ -PSMA-617 in chemotherapy-naive patients with advanced prostate cancer: a pilot study. *Eur J Nucl Med Mol Imaging*. 2019;46:129–138.

32. Sathekge M, Bruchertseifer F, Vorster M, et al. Predictors of overall and disease-free survival in metastatic castration-resistant prostate cancer patients receiving  $^{225}\text{Ac}$ -PSMA-617 radioligand therapy. *J Nucl Med.* 2020;61:62–69.
33. Feurecker B, Tauber R, Knorr K, et al. Activity and adverse events of actinium-225-PSMA-617 in advanced metastatic castration-resistant prostate cancer after failure of lutetium-177-PSMA. *Eur Urol.* 2021;79:343–350.
34. Lindgren S, Albertsson P, Bäck T, Jensen H, Palm S, Aneheim E. Realizing clinical trials with astatine-211: the chemistry infrastructure. *Cancer Biother Radiopharm.* 2020;35:425–436.
35. Meyer GJ. Astatine. *J Labelled Comp Radiopharm.* 2018;61:154–164.
36. Vaidyanathan G, Zalutsky MR. Astatine radiopharmaceuticals: prospects and problems. *Curr Radiopharm.* 2008;1:177.
37. Guérard F, Gustin JF, Brechbiel MW. Production of [ $^{211}\text{At}$ ]-astatinated radiopharmaceuticals and applications in targeted alpha-particle therapy. *Cancer Biother Radiopharm.* 2013;28:1–20.
38. Larsen RH, Slade S, Zalutsky MR. Blocking [ $^{211}\text{At}$ ]astatide accumulation in normal tissues: preliminary evaluation of seven potential compounds. *Nucl Med Biol.* 1998;25:351–357.
39. Bäck TA, Jennbacken K, Hagberg Thulin M, et al. Targeted alpha therapy with astatine-211-labeled anti-PSCA A11 minibody shows antitumor efficacy in prostate cancer xenografts and bone microtumors. *EJNMMI Res.* 2020;10:10.
40. Pomper MG, Musachio JL, Zhang J, et al.  $^{11}\text{C}$ -MCG: synthesis, uptake selectivity, and primate PET of a probe for glutamate carboxypeptidase II (NAALADase). *Mol Imaging.* 2002;1:96–101.
41. Banerjee SR, Minn I, Kumar V, et al. Preclinical evaluation of  $^{203/212}\text{Pb}$ -labeled low-molecular-weight compounds for targeted radiopharmaceutical therapy of prostate cancer. *J Nucl Med.* 2020;61:80–88.
42. Ackerman NL, de la Fuente Rosales L, Falzone N, Vallis KA, Bernal MA. Targeted alpha therapy with  $^{212}\text{Pb}$  or  $^{225}\text{Ac}$ : change in RBE from daughter migration. *Phys Med.* 2018;51:91–98.
43. Zalutsky MR, Pruszynski M. Astatine-211: production and availability. *Curr Radiopharm.* 2011;4:177–185.
44. Current K, Meyer C, Magyar CE, et al. Investigating PSMA-targeted radioligand therapy efficacy as a function of cellular PSMA levels and intratumoral PSMA heterogeneity. *Clin Cancer Res.* 2020;26:2946–2955.

# Imaging in Post-COVID Lung Disease: Does $^{18}\text{F}$ -FDG PET/CT Have the Key?

Olivier Gheysens<sup>1</sup>, Leïla Belkhir<sup>2</sup>, and François Jamar<sup>1</sup>

<sup>1</sup>Department of Nuclear Medicine, Cliniques Universitaires St-Luc and Institute for Clinical and Experimental Research, Université Catholique de Louvain, Brussels, Belgium; and <sup>2</sup>Department of Internal Medicine and Infectiology, Cliniques Universitaires St-Luc and Institute for Clinical and Experimental Research, Université Catholique de Louvain, Brussels, Belgium

See the associated article on page 270.

In this issue of *The Journal of Nuclear Medicine*, Thornton et al. present  $^{18}\text{F}$ -FDG PET/CT data obtained on coronavirus disease 2019 (COVID-19) patients at several disease stages (1). The study includes predominantly oncology patients in whom the diagnosis of severe acute respiratory syndrome coronavirus 2 (SARS-CoV-2) infection was not known before the PET/CT procedure ( $n = 32$ ), as well as 18 patients with known infection and persistent shortness of breath 28 d after the onset of disease and who were previously admitted to the hospital for oxygen therapy. The latter group was categorized as potential post-COVID-19 lung disease (PCLD) (2). In this PCLD group, half the patients had ongoing corticosteroid treatment. Although retrospective, this study triggers an interesting discussion on the potential role of  $^{18}\text{F}$ -FDG PET/CT in patients with late COVID-19 infection.

After the initial outbreak of SARS-CoV-2 in December 2019, 3–4 waves of the pandemic have been observed worldwide. As of September 26, 2021, and according to the data of the Johns Hopkins University (<https://coronavirus.jhu.edu>), more than 230 million people were diagnosed worldwide, with a death toll close to 5 million, making it the largest and deadliest pandemic since the 1918 flu. Importantly, the disease presentation at the early phases ranged from asymptomatic contamination to mild symptoms over overt symptoms requiring hospitalization with oxygen therapy and, at the extreme, assisted ventilation or extracorporeal membrane oxygenation. Shah et al. defined 3 phases of the disease: acute COVID-19 infection with signs and symptoms up to 4 wk, ongoing symptomatic COVID-19 between 4 and 12 wk, and PCLD syndrome beyond 12 wk, when persisting symptoms cannot be attributed to alternative diagnoses (3). The term *long COVID* commonly refers to both ongoing symptomatic COVID-19 and PCLD as defined above. Several studies describe persistent symptoms in patients after acute COVID-19, with one third or more experiencing more than one symptom, including fatigue, abnormal breathing, chest or throat

pain, headache, and cognitive symptoms up to 3–6 mo after diagnosis. Such persistent symptoms are more frequently reported after COVID-19 than after influenza infection.

However, this perspective will focus on subacute and chronic lung disease, referred to as PCLD. Five percent of COVID-19 survivors evolve to chronic respiratory failure, manifested by breathlessness, cough, or even oxygen needs (4).

From the very beginning of the outbreak, multiple casuistic reports on  $^{18}\text{F}$ -FDG PET/CT were published, without emphasis on the time course, since the initial observations focused either on the most acute phase in severely ill patients or on serendipitous findings in asymptomatic oncology patients. Several studies indicated a 2- to 4-fold increased incidence of interstitial pneumonia detected on  $^{18}\text{F}$ -FDG PET/CT in the latter group during the early phase of the pandemic (5). Other authors identified a relationship between the structural changes as assessed using the COVID-19 Reporting and Data System and metabolic changes (6). Albeit informative, such reports did not take into account the temporal kinetics of the disease. It has become clear that  $^{18}\text{F}$ -FDG PET/CT has a limited role, if any, in establishing the diagnosis of active COVID-19 infection. From a logistic viewpoint, organizing a PET/CT scan in a nuclear medicine department had more drawbacks than advantages, as compared with dedicated CT-scan suites, with a rapid turnover even with the implementation of all necessary hygiene measures. Several reports indicate that  $^{18}\text{F}$ -FDG PET/CT results in the early phase of the disease were similar to those observed in the literature on pneumonia due to other aggressive viruses.

In this retrospective observational study, Thornton et al. were able to distinguish several temporal patterns in a limited number of subjects during the first 2 peaks of COVID-19. Using  $^{18}\text{F}$ -FDG PET/CT, they not only studied the functional and morphologic pattern at different disease stages but also demonstrated the time relationship between these changes. In asymptomatic patients, without any history or suggestion of a COVID-19 diagnosis, the authors identified 2 distinct groups: one group of acute patients in the early stage ( $n = 8$ ) with typical ground-glass changes on CT and relatively low  $^{18}\text{F}$ -FDG uptake (median  $\text{SUV}_{\text{max}}$ , 1.6, and median target-to-background ratio [ $\text{TBR}_{\text{lung}}$ ], 6.4, where the background refers to the lowest lung uptake) and a second group of acute patients in the late stage, with a more extensive consolidation pattern on CT and a significantly higher  $\text{SUV}_{\text{max}}$  (median, 4.0) and  $\text{TBR}_{\text{lung}}$  (median, 13.7) ( $P = 0.001$ ).  $\text{SUV}_{\text{max}}$  was similar in a small series of convalescing patients reported by Bai et al., but these were patients recovering from severe infection (7). Temporal data in the study of

Received Oct. 1, 2021; revision accepted Oct. 12, 2021.

For correspondence or reprints, contact François Jamar ([francois.jamar@uclouvain.be](mailto:francois.jamar@uclouvain.be)).

Published online Oct. 21, 2021.

COPYRIGHT © 2022 by the Society of Nuclear Medicine and Molecular Imaging.

DOI: 10.2967/jnumed.121.263166

Thornton et al. were retrieved from the electronic health record system, with the inherent limitations of such a retrospective approach. Notwithstanding, the authors demonstrated a significant positive correlation between  $TBR_{lung}$  and the estimated time since onset (Spearman  $r_s = 0.595$ ,  $P = 0.003$ ). These findings are in keeping with the current pathophysiologic hypotheses of COVID-19 infection—that it first presents as a viral infection, with no or moderate symptoms and seemingly low  $^{18}F$ -FDG uptake, and then is followed by an acute immune response, endothelial activation and inflammation, and variable levels of immune cell infiltration (including neutrophils, lymphocytes, and monocyte–macrophages), as well as angiogenesis. This second phase, characterized by the presence of many glucose-avid cells, is responsible for the increased  $^{18}F$ -FDG uptake. However, the responsible mechanisms of PCLD are not well understood and are probably numerous and intertwined as reflected by the wide diversity of the symptoms. The main hypotheses include a persisting chronic inflammatory process or a dysregulated immune phenomenon (8).

Although the study by Thornton et al. illustrates the temporal changes in  $^{18}F$ -FDG PET/CT patterns, it does not provide information on the severity of the disease because of the lack of clinical outcome data, as stated by the authors in their conclusions.

Nevertheless, in the group of 18 patients with PCLD, a condition that has hardly been studied with  $^{18}F$ -FDG PET/CT, a higher  $SUV_{max}$  (median, 5.8) was observed in patients who had not been treated with high-dose steroids for at least 10 d. Conversely, patients treated with steroids after discharge had a lower  $SUV_{max}$  (median, 2.4) and  $TBR_{lung}$  (median, 6.6 under steroids, vs. 18.1 without steroids), like those observed in the early stage of the acute phase. The RECOVERY study clearly demonstrated the benefit of 6 mg of dexamethasone in oxygen-dependent or ventilated patients with a lower 28-d mortality (9). To our knowledge, little is known about the benefit to pulmonary function and survival over the long term. In addition, an observational study by Myall et al. including 35 patients with lung functional deficit beyond 6 wk after the acute phase (due to interstitial disease and organizing pneumonia) demonstrated a morbidity benefit, defined by improvement in lung functional tests, in the 30 patients treated with steroids (4). Furthermore, a recent report on long COVID demonstrated not only increased residual lung  $^{18}F$ -FDG uptake (with similar  $SUV_{max}$  data) but also evidence of multi-systemic inflammation (10).

From the published data and long–COVID-19 perspectives, it may be wise to envision that metabolic imaging with  $^{18}F$ -FDG PET/CT may help identify patients with persistent symptoms after 6–12 wk, for whom additional therapy with, for example, corticosteroids could be proposed. This possibility is in keeping with previous observations that increased  $^{18}F$ -FDG uptake in chronic interstitial lung disease of other etiologies was reported as a marker of evolution toward lung fibrosis and poor prognosis. At this stage,

there is no evidence that such imaging may be justified, nor is information available on the optimal timing and dosing of steroids. Therefore, it is worth challenging this issue with, for instance, a 2-arm randomized study in which all patients with persistent pulmonary symptoms beyond 6 wk of a negative PCR test would undergo  $^{18}F$ -FDG PET/CT upfront but in which the interpreters would be masked to patient data before randomization. Patients could then receive either corticosteroids or placebo, and as the outcome, the clinical benefit results would be correlated with the  $^{18}F$ -FDG PET/CT results.

In conclusion, although it is agreed that  $^{18}F$ -FDG PET/CT has little role in diagnosing COVID-19 as such, its potential role in the later phases of the disease must be considered. Whether  $^{18}F$ -FDG PET/CT can help identify patients who will develop a severe or even dramatic course of lung fibrosis remains to be determined: prospective and, when possible, randomized therapeutic trials with masking of the  $^{18}F$ -FDG PET/CT results would be extremely helpful.

## DISCLOSURE

No potential conflict of interest relevant to this article was reported.

## REFERENCES

1. Thornton A, Fraioli F, Wan S, et al. Evolution of  $^{18}F$ -FDG PET/CT findings in patients after COVID-19: an initial investigation. *J Nucl Med*. 2022;63:270–273.
2. Carfi A, Bernabei R, Landi F, et al. Persistent symptoms in patients after acute COVID-19. *JAMA*. 2020;324:603–605.
3. Shah W, Hillman T, Playford ED, Hishmeh L. Managing the long term effects of covid-19: summary of NICE, SIGN and RCGP rapid guideline. *BMJ*. 2021;372:n136.
4. Myall KJ, Mukherjee B, Castanheira AM, et al. Persistent post-COVID-19 interstitial lung disease: an observational study of corticosteroid treatment. *Ann Am Thorac Soc*. 2021;18:799–806.
5. Setti L, Bonacina M, Meroni R, et al. Increased incidence of interstitial pneumonia detected on [ $^{18}F$ ]-FDG-PET/CT in asymptomatic cancer patients during COVID-19 pandemic in Lombardy: a casualty or COVID-19 infection. *Eur J Nucl Med Mol Imaging*. 2021;48:777–785.
6. Wakkie-Corieh CG, Ferrando-Castagnetto F, Blanes Garcia AM, et al. Incidental findings suggestive of COVID-19 pneumonia in oncological patients undergoing  $^{18}F$ -FDG PET/CT studies: association between metabolic and structural lung changes. *J Nucl Med*. June 4, 2021 [Epub ahead of print].
7. Bai Y, Xu J, Chen L, et al. Inflammatory response in lungs and extrapulmonary sites detected by [ $^{18}F$ ] fluorodeoxyglucose PET/CT in convalescing COVID-19 patients tested negative for coronavirus. *Eur J Nucl Med Mol Imaging*. 2021;48:2531–2542.
8. Anaya JM, Rojas M, Salinas ML, et al. Post-COVID syndrome: a case series and comprehensive review. *Autoimmun Rev*. 2021;20:102947.
9. Horby P, Lim WS, Emberson JR, et al. Dexamethasone in hospitalized patients with Covid-19. *N Engl J Med*. 2021;384:693–704.
10. Sollini M, Morbelli S, Ciccarelli M, et al. Long COVID hallmarks on [ $^{18}F$ ]-FDG-PET/CT: a case-control study. *Eur J Nucl Med Mol Imaging*. 2021;48:3187–3197.

# Evolution of $^{18}\text{F}$ -FDG PET/CT Findings in Patients After COVID-19: An Initial Investigation

Andrew Thornton<sup>1</sup>, Francesco Fraioli<sup>1</sup>, Simon Wan<sup>1</sup>, Helen S. Garthwaite<sup>2</sup>, Balaji Ganeshan<sup>1</sup>, Robert I. Shortman<sup>1</sup>, Raymond Endozo<sup>1</sup>, Stefan Vöö<sup>1</sup>, Irfan Kayani<sup>1</sup>, Deena Neriman<sup>1</sup>, Leon Menezes<sup>1</sup>, Jamshed Bomanji<sup>1</sup>, Toby Hillman<sup>3</sup>, Melissa Heightman<sup>3</sup>, Joanna C. Porter<sup>\*2</sup>, and Ashley M. Groves<sup>\*1</sup>

<sup>1</sup>Institute of Nuclear Medicine, UCLH/UCL, London, United Kingdom; <sup>2</sup>ILD Service, UCLH/UCL Respiratory, London, United Kingdom; and <sup>3</sup>Post-COVID Disease Service, UCLH, London, United Kingdom

See an invited perspective on this article on page 268.

The aim of this study was to assess the temporal evolution of pulmonary  $^{18}\text{F}$ -FDG uptake in patients with coronavirus disease 2019 (COVID-19) and post-COVID-19 lung disease (PCLD). **Methods:** Using our hospital's clinical electronic records, we retrospectively identified 23 acute COVID-19, 18 PCLD, and 9 completely recovered  $^{18}\text{F}$ -FDG PET/CT patients during the 2 peaks of the U.K. pandemic. Pulmonary  $^{18}\text{F}$ -FDG uptake was measured as a lung target-to-background ratio ( $\text{TBR}_{\text{lung}} = \text{SUV}_{\text{max}}/\text{SUV}_{\text{min}}$ ) and compared with temporal stage. **Results:** In acute COVID-19, less than 3 wk after infection,  $\text{TBR}_{\text{lung}}$  was strongly correlated with time after infection ( $r_s = 0.81$ ,  $P < 0.001$ ) and was significantly higher in the late stage than in the early stage ( $P = 0.001$ ). In PCLD,  $\text{TBR}_{\text{lung}}$  was lower in patients treated with high-dose steroids ( $P = 0.003$ ) and in asymptomatic patients ( $P < 0.001$ ). **Conclusion:** Pulmonary  $^{18}\text{F}$ -FDG uptake in COVID-19 increases with time after infection. In PCLD, pulmonary  $^{18}\text{F}$ -FDG uptake rises despite viral clearance, suggesting ongoing inflammation. There was lower pulmonary  $^{18}\text{F}$ -FDG uptake in PCLD patients treated with steroids.

**Key Words:** infectious disease; PET/CT; respiratory;  $^{18}\text{F}$ -FDG; COVID-19; PET/CT

J Nucl Med 2022; 63:270–273

DOI: 10.2967/jnumed.121.262296

Throughout the United Kingdom, during February and March 2020 there was a rapid spread of coronavirus disease 2019 (COVID-19), which may result in viral pneumonitis and acute respiratory distress syndrome (1). The median time from symptom onset to intensive care admission was 10 d, although only 5% of patients were admitted (1). This is when antiviral responses are at

a peak, suggesting that pneumonitis is a consequence of adaptive immunity (2).

Persistent respiratory symptoms affect at least one third of hospitalized COVID-19 patients, some of whom will have post-COVID-19 lung disease (PCLD) (3). Steroids are critical in reducing mortality from COVID-19, but their role in PCLD is less clear, and identifying those who might benefit may be difficult.

Currently,  $^{18}\text{F}$ -FDG PET/CT has no role in the management of patients with COVID-19 (4), and there has been little investigation into the quantification and evolution of  $^{18}\text{F}$ -FDG uptake in COVID-19 (Supplemental Table 1; supplemental materials are available at <http://jnm.snmjournals.org>). Given the growing role of  $^{18}\text{F}$ -FDG PET/CT in interstitial lung diseases, the primary aim of this preliminary study was to assess the temporal evolution of  $^{18}\text{F}$ -FDG uptake in COVID-19 and to correlate this evolution with clinical progression and recovery. A secondary aim was to investigate whether steroids could alter this evolution.

## MATERIALS AND METHODS

The Institutional Review Board approved this retrospective study and waived the requirement to obtain informed consent. The challenges of the pandemic constrained the methodologic design, necessitating a retrospective approach.

### Patient Selection

All studies performed in the department over the first U.K. peak of the coronavirus pandemic (March–April 2020) and from September 2020 to February 2021 (second peak) were assessed for acute COVID-19 by following the British Society of Thoracic Imaging guidelines or a confirmed history of COVID-19 in the electronic health record system (5). These studies included some of patients without positive polymerase chain reaction (PCR) test results, because of the poor availability of PCR tests in the early period. Also included were studies performed for persistent (>4 wk) respiratory symptoms, in keeping with PCLD, and studies of patients who had recovered from COVID-19 after the initial period. Ongoing treatment with steroids and other immunosuppressive drugs was recorded. Formal lung function tests were not performed because of infection risks. Acute studies between May and September 2020 were not examined because of the low prevalence and incidence of COVID-19 in London during that time (Supplemental Fig. 1; Supplemental Table 2).

### $^{18}\text{F}$ -FDG PET/CT Imaging Protocol

Patients fasted for at least 6 h, and blood glucose levels were recorded before injection of 400 MBq of  $^{18}\text{F}$ -FDG adjusted for weight in keeping with the guidelines of the Administration of Radioactive Substances Advisory Committee (6). After an uptake time of 63.1 ±

Received Mar. 11, 2021; revision accepted May 25, 2021.

For correspondence or reprints, contact Ashley Groves ([ashleygroves@nhs.net](mailto:ashleygroves@nhs.net)).

\*Contributed equally to this work.

Published online Jul. 16, 2021.

Immediate Open Access: Creative Commons Attribution 4.0 International License (CC BY) allows users to share and adapt with attribution, excluding materials credited to previous publications. License: <https://creativecommons.org/licenses/by/4.0/>. Details: <http://jnm.snmjournals.org/site/misc/permission.xhtml>.

COPYRIGHT © 2022 by the Society of Nuclear Medicine and Molecular Imaging.

10.9 min, whole-body PET scans of supine patients with their arms above their head were acquired at a rate of 2 min per bed position using a GE Healthcare Discovery 710 PET/CT scanner. A nonenhanced low-dose CT scan was acquired for anatomic coregistration and attenuation correction. Images were reconstructed using a resolution recovery iterative algorithm.

All images were reviewed by at least one dually accredited radiologist–nuclear medicine physician. Quantification was performed by investigators with at least 10 y of experience in quantifying PET/CT images of diffuse lung disease. PET analysis was performed with masking of clinical history and CT analysis.

### Determination of Temporal Stage

After review of the clinical, CT, and electronic health records, the number of days since disease onset was estimated, and the acute COVID-19 cases were assigned to 1 of 2 temporal groups: early or late COVID-19 (7). Early COVID-19 (approximately  $\leq 1$  wk after disease onset) was defined predominantly as CT findings of ground-glass opacities with or without associated interlobular thickening. Late COVID-19 ( $> 1$  wk to  $\leq 4$  wk after disease onset) was defined as CT findings of increasing consolidation and signs of resolution marked by subpleural sparing, development of a fibrous stripe, and crescentic consolidation or a reversed halo or atoll sign. Patients who were asymptomatic after 28 d were classed as recovered patients. In addition, patients who were imaged because of persistent symptoms after 28 d were described as having PCLD. The CT component was correlated with other cross-sectional images to reduce the likelihood of incorrect classification due to breathing artifacts.

### Quantitative $^{18}\text{F}$ -FDG PET Analysis

All images were processed using a standard protocol on a dedicated imaging workstation (ADW Volume Viewer, version 4.6; GE Healthcare), which calculated the lung target-to-background ratio ( $\text{TBR}_{\text{lung}} = \text{SUV}_{\text{max}}/\text{SUV}_{\text{mins}}$ ) following methods described previously (8–10).

### Statistics

The difference in  $^{18}\text{F}$ -FDG PET uptake measures within the lung against temporal staging and pretreatment with steroids were assessed using the nonparametric Mann–Whitney test. Results were depicted using box-and-whisker plots. All statistical analyses were performed using SPSS, version 25.0 (IBM).

## RESULTS

Of the 3,112  $^{18}\text{F}$ -FDG PET/CT studies screened, 50 met the criteria for study entry, including 18 patients referred for  $^{18}\text{F}$ -FDG PET/CT for investigation of PCLD. Of these 50 patients (median age, 61 y; range, 18–87 y), 32 were male (64%), 27 were of ethnic minority background (54%), and 23 (46%) had acute COVID-19. None were intentionally imaged for COVID-19. Nine patients had asymptomatic recovered COVID-19 as confirmed by the electronic health record system (Supplemental Tables 3–5).

In 18 of the 50 patients, imaging was performed because of persistent shortness of breath and respiratory symptoms in keeping with PCLD. All 18 had been admitted to the hospital and had required oxygen. Fifteen of these patients previously had PCR tests positive for COVID-19, and COVID-19 was clinically diagnosed in the others. Nine had ongoing treatment with steroids for PCLD; the other 9 were not receiving treatment for their PCLD. All PCLD patients underwent repeated PCR testing confirming that they were PCR-negative before PET imaging (Supplemental Table 5).

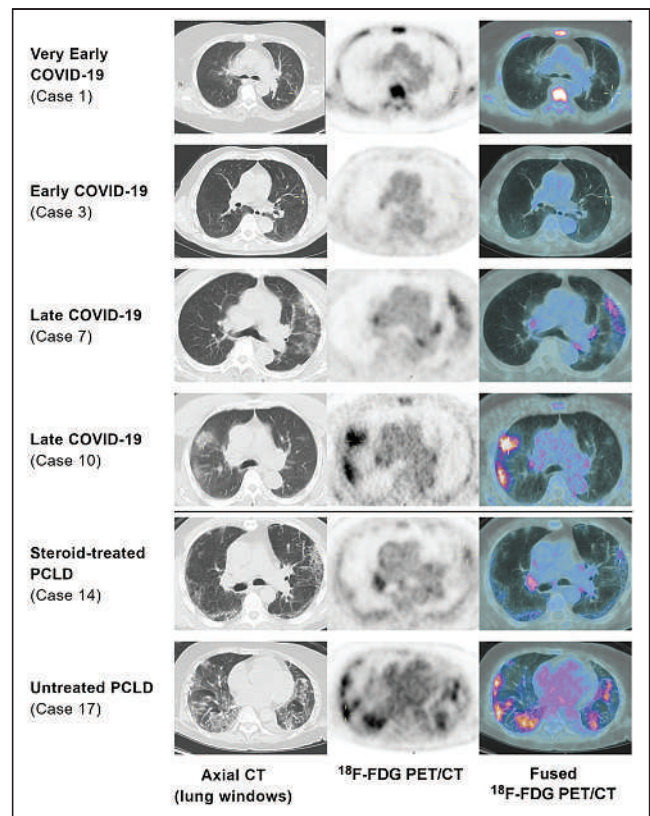


**FIGURE 1.** Exemplar images demonstrating increasing  $^{18}\text{F}$ -FDG uptake with temporal stage and lower  $^{18}\text{F}$ -FDG uptake in steroid-treated PCLD (lung-windowed axial CT,  $^{18}\text{F}$ -FDG PET [SUV 0–5], and  $^{18}\text{F}$ -FDG PET/CT images). Medullary uptake in case 1 was due to leukemia and not COVID-19.

### Temporal Stage

After review of the CT component of the PET/CT (lung windows) and available clinical history, 8 (35%) of the 23 acute COVID-19 patients were determined to represent early COVID-19 and 15 (65%) late (Fig. 1; Supplemental Table 5).

### Association of Pulmonary $^{18}\text{F}$ -FDG Uptake with Temporal Staging in Early- and Late-Stage Disease

$^{18}\text{F}$ -FDG uptake analysis of lung lesions in acute-disease patients demonstrated an increasing  $\text{TBR}_{\text{lung}}$  over time, with progression from low-avidity ground-glass changes in the early stage to avid consolidation during the late stage (median values in the early stage:  $\text{SUV}_{\text{max}}$ , 1.6, and  $\text{TBR}_{\text{lung}}$ , 6.4; median values in the late stage:  $\text{SUV}_{\text{max}}$ , 4.0, and  $\text{TBR}_{\text{lung}}$ , 13.7). In acute-disease patients,  $\text{TBR}_{\text{lung}}$  differed significantly between the early and late stages, with late-stage patients having a higher  $\text{TBR}_{\text{lung}}$  than early-stage patients ( $P = 0.001$ ; Fig. 2). Among these acute-disease patients, a significant positive correlation was observed between  $\text{TBR}_{\text{lung}}$  and estimated time since onset ( $r_s = 0.60$ ,  $P = 0.003$ ; Fig. 3). This correlation was stronger when limited to acute-disease patients estimated to be in the first 3 wk of infection ( $n = 18$ ,  $r_s = 0.81$ ,  $P < 0.001$ ).

### Pulmonary $^{18}\text{F}$ -FDG Uptake in PCLD

There was a lower  $\text{TBR}_{\text{lung}}$  in patients who had received treatment with high-dose steroids ( $P = 0.003$ ) (Fig. 2) (median values in steroid-treated patients:  $\text{SUV}_{\text{max}}$ , 2.4, and  $\text{TBR}_{\text{lung}}$ , 6.62; median values in untreated patients:  $\text{SUV}_{\text{max}}$ , 5.8, and  $\text{TBR}_{\text{lung}}$ , 18.1).

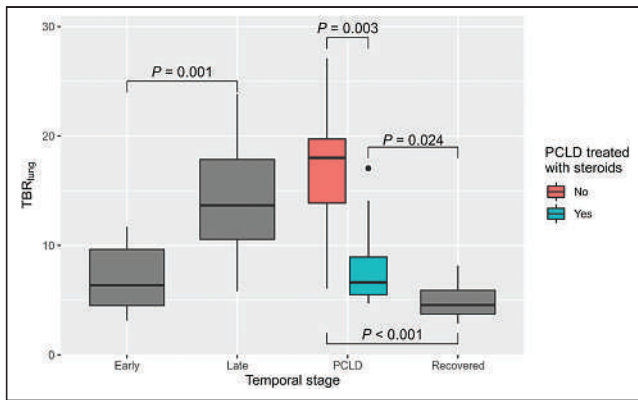


**FIGURE 2.**  $^{18}\text{F}$ -FDG uptake ( $\text{TBR}_{\text{lung}}$ ) by temporal stage.

$\text{TBR}_{\text{lung}}$  was lower in asymptotically recovered patients (median  $\text{SUV}_{\text{max}}$ , 1.2; median  $\text{TBR}_{\text{lung}}$ , 4.6) than in either untreated PCLD patients or those treated with steroids ( $P < 0.001$  and  $P = 0.020$ , respectively;  $P < 0.001$  on Kruskal–Wallis testing for all 3 groups).

## DISCUSSION

To our knowledge, this study was the first attempt to characterize the evolution of pulmonary  $^{18}\text{F}$ -FDG uptake in patients with COVID-19 assigned a temporal stage (early stage to late stage to PCLD) based on clinical context and CT findings.

The increase in lung avidity with time suggests increasing lung inflammation (11,12) in acute COVID-19. In most cases,  $^{18}\text{F}$ -FDG uptake would then be expected to decrease with viral clearance and establishment of immunity. There is, however, a subset of COVID-19 patients with delayed recovery who continue to show significant  $^{18}\text{F}$ -FDG uptake, reminiscent of our findings in interstitial lung disease (8,9,13,14), and raising the possibility that COVID-19 pneumonitis is associated with an activated host immune response rather than direct viral pathology (12,15,16). It

would be useful to understand the ability of lung avidity to predict the clinical course or the likelihood that post–COVID-19 interstitial lung disease will develop in this patient cohort.

The RECOVERY study (Randomized Evaluation of COVID-19 Therapy), which this study predates, demonstrated a survival benefit from steroid use in hypoxic patients with COVID-19 (15). In our study, several patients went on to develop an inflammatory organizing pneumonia characterized by persistent and increasing  $^{18}\text{F}$ -FDG uptake. Steroid therapy is a recognized treatment for organizing pneumonia and other inflammatory interstitial lung diseases (15), and  $^{18}\text{F}$ -FDG uptake was consistently lower in those cases treated with postdischarge steroids. Our findings raise the question of whether steroid administration has a role not just in acute hypoxia but in the later stages of COVID-19 and in PCLD. This question has been debated (15), with calls for a randomized, controlled trial to define the role of steroid therapy more widely. Although imaging may be useful, it is hard to determine from CT whether parenchymal changes indicate reversible inflammation or irreversible fibrosis. It is possible that  $^{18}\text{F}$ -FDG PET/CT may offer a sensitive and specific biomarker to guide and rationalize steroid treatment.

Given the challenges of nuclear medicine imaging in the pandemic, this study has methodologic limitations. They are directly related to the infectious and emergent epidemic, the workload and severe capacity restraints of PET/CT departments, the need to protect staff and sterilize equipment, and the medical instability of seriously ill COVID-19 patients. These challenges limit patient numbers, preventing the use of a control group and longitudinal  $^{18}\text{F}$ -FDG PET/CT imaging. Diagnostic CT will likely remain the most practical way to investigate acute COVID-19, although PET imaging may give potential mechanistic insights. However, PCLD patients are not currently believed to be an infection risk, and performing longitudinal  $^{18}\text{F}$ -FDG PET/CT studies in this population may thus be realistic and feasible. This study was not prospectively designed to examine the use of steroids in PCLD; however, statistically significant lower  $^{18}\text{F}$ -FDG uptake was observed in PCLD patients who received steroids than in those who did not. Finally, the lack of PCR testing in the first wave, as well as the

high incidence of asymptomatic cases throughout the pandemic, creates uncertainties about prevalence, and retrospective analyses may therefore suffer from selection bias. Despite the design limitations, the findings of this study offer some insight into the development of pulmonary disease in COVID-19 patients and can help provide the evidence to justify performing formal prospective studies on this topic in the future.

## CONCLUSION

$^{18}\text{F}$ -FDG uptake in COVID-19 patients increases with time after infection and correlates with severity. Persistent  $^{18}\text{F}$ -FDG uptake is seen in patients with PCLD disease. These findings suggest that future studies may be directed at the use of  $^{18}\text{F}$ -FDG PET/CT to clarify the disease trajectory and may aid management of those patients with persistent respiratory symptoms

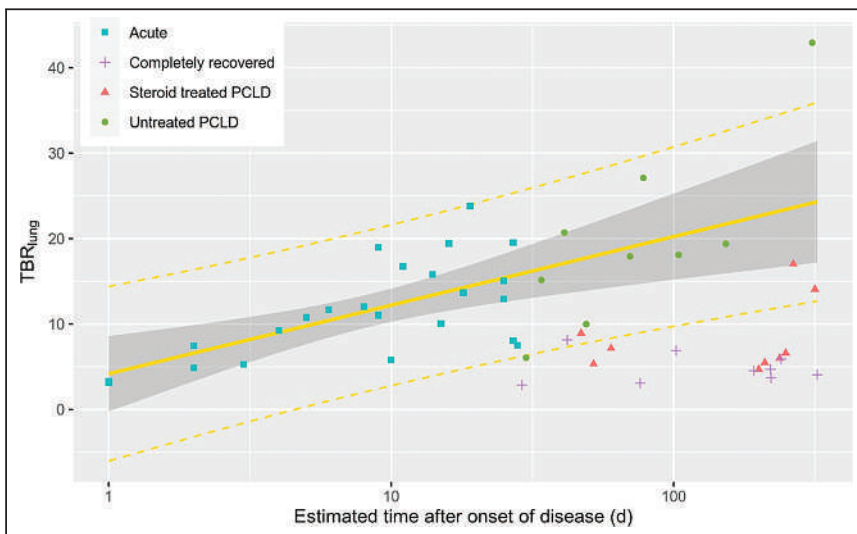


**FIGURE 3.**  $^{18}\text{F}$ -FDG uptake ( $\text{TBR}_{\text{lung}}$ ) against estimated time after onset of disease (on logarithmic scale), with superimposed regression using 23 acute (early and late) patients ( $F_{1,23} = 14.94$ ,  $P < 0.001$ ; Spearman  $r_s = 0.595$ ,  $P = 0.003$ ). Steroid treated = at least 10 d of high-dose steroid treatment.

## DISCLOSURE

Helen Garthwaite was funded by Breathing Matters. This work was undertaken at University College London Hospitals/University College London (UCLH/UCL), which receives funding from the U.K. Department of Health's National Institute for Health Research Biomedical Research Centre's funding scheme and the UCL Experimental Cancer Medicine Centre. No other potential conflict of interest relevant to this article was reported.

## KEY POINTS

**QUESTION:** What is the temporal evolution of  $^{18}\text{F}$ -FDG uptake in COVID-19 and in PCLD?

**PERTINENT FINDINGS:**  $^{18}\text{F}$ -FDG uptake was shown to increase with time after COVID-19 infection. Steroid treatment was associated with reduced uptake in PCLD.

**IMPLICATIONS FOR PATIENT CARE:**  $^{18}\text{F}$ -FDG PET/CT may help us understand the disease trajectory and aid in management of PCLD.

## REFERENCES

1. Huang C, Wang Y, Li X, et al. Clinical features of patients infected with 2019 novel coronavirus in Wuhan, China. *Lancet*. 2020;395:497–506.
2. Young BE, Ong SWX, Kalimuddin S, et al. Epidemiologic features and clinical course of patients infected with SARS-CoV-2 in Singapore. *JAMA*. 2020;323:1488–1494.
3. Carfi A, Bernabei R, Landi F, et al. Persistent symptoms in patients after acute COVID-19. *JAMA*. 2020;324:603–605.
4. Zhao Y, Shang Y-M, Song W-B, et al. Follow-up study of the pulmonary function and related physiological characteristics of COVID-19 survivors three months after recovery. *EClinicalMedicine*. 2020;25:100463.
5. **\*\*Updated\*\*** version 2 BSTI COVID-19 guidance for the reporting radiologist. The British Society of Thoracic Imaging website. <https://www.bsti.org.uk/standards-clinical-guidelines/clinical-guidelines/bsti-covid-19-guidance-for-the-reporting-radiologist/>. Updated March 16, 2020. Accessed September 21, 2021.
6. Notes for guidance on the clinical administration of radiopharmaceuticals and use of sealed radioactive sources. Gov.uk website. [https://assets.publishing.service.gov.uk/government/uploads/system/uploads/attachment\\_data/file/1018160/ARSAC\\_Notes\\_for\\_guidance\\_on\\_the\\_clinical\\_administration\\_of\\_radiopharmaceuticals\\_and\\_use\\_of\\_sealed\\_radioactive\\_sources.pdf](https://assets.publishing.service.gov.uk/government/uploads/system/uploads/attachment_data/file/1018160/ARSAC_Notes_for_guidance_on_the_clinical_administration_of_radiopharmaceuticals_and_use_of_sealed_radioactive_sources.pdf). Published September 2021. Accessed September 21, 2021.
7. Shi H, Han X, Jiang N, et al. Radiological findings from 81 patients with COVID-19 pneumonia in Wuhan, China: a descriptive study. *Lancet Infect Dis*. 2020;20:425–434.
8. Groves AM, Win T, Screaton NJ, et al. Idiopathic pulmonary fibrosis and diffuse parenchymal lung disease: implications from initial experience with  $^{18}\text{F}$ -FDG PET/CT. *J Nucl Med*. 2009;50:538–545.
9. Win T, Screaton NJ, Porter JC, et al. Pulmonary  $^{18}\text{F}$ -FDG uptake helps refine current risk stratification in idiopathic pulmonary fibrosis (IPF). *Eur J Nucl Med Mol Imaging*. 2018;45:806–815.
10. Giraudo C, Evangelista L, Fraia AS, et al. Molecular imaging of pulmonary inflammation and infection. *Int J Mol Sci*. 2020;21:894.
11. Braune A, Hofheinz F, Bluth T, et al. Comparison of static and dynamic  $^{18}\text{F}$ -FDG PET/CT for quantification of pulmonary inflammation in acute lung injury. *J Nucl Med*. 2019;60:1629–1634.
12. Bouadma L, Lescure F-X, Lucet J-C, Yazdanpanah Y, Timsit J-F. Severe SARS-CoV-2 infections: practical considerations and management strategy for intensivists. *Intensive Care Med*. 2020;46:579–582.
13. Sudre CH, Murray B, Varsavsky T, et al. Attributes and predictors of long-COVID: analysis of COVID cases and their symptoms collected by the Covid Symptoms Study App. medRxiv website. <https://www.medrxiv.org/content/10.1101/2020.10.19.20214494v1>. Published October 2020. Accessed September 21, 2021.
14. Win T, Screaton NJ, Porter J, et al. Novel positron emission tomography/computed tomography of diffuse parenchymal lung disease combining a labeled somatostatin receptor analogue and 2-deoxy-2[ $^{18}\text{F}$ ]fluoro-D-glucose. *Mol Imaging*. 2012;11:91–98.
15. Horby P, Lim WS, Emberson J, et al. Effect of dexamethasone in hospitalized patients with COVID-19: preliminary report. medRxiv website. <https://www.medrxiv.org/content/10.1101/2020.06.22.20137273v1>. Published June 2020. Accessed September 21, 2021.
16. Ackermann M, Verleden SE, Kuehnel M, et al. Pulmonary vascular endothelialitis, thrombosis, and angiogenesis in Covid-19. *N Engl J Med*. 2020;383:120–128.

---

---

# Incidental Findings Suggestive of COVID-19 Pneumonia in Oncologic Patients Undergoing $^{18}\text{F}$ -FDG PET/CT Studies: Association Between Metabolic and Structural Lung Changes

Cristina Gamila Wakfie-Corieh<sup>1,2</sup>, Federico Ferrando-Castagnetto<sup>3</sup>, Alba María Blanes García<sup>1,2</sup>, Marta García García-Esquinas<sup>2,4</sup>, Aída Ortega Candil<sup>1,2</sup>, Cristina Rodríguez Rey<sup>1,2</sup>, María Nieves Cabrera-Martín<sup>1,2</sup>, Ana Delgado Cano<sup>1,2</sup>, and José Luis Carreras Delgado<sup>1,2</sup>

<sup>1</sup>Department of Nuclear Medicine, Hospital Clínico San Carlos, Madrid, Spain; <sup>2</sup>Fundación Para la Investigación Biomédica del Hospital Clínico San Carlos, Madrid, Spain; <sup>3</sup>Department of Cardiology, Hospital de Clínicas Dr. Manuel Quintela, Montevideo, Uruguay; and <sup>4</sup>Department of Radiology, Hospital Clínico San Carlos, Madrid, Spain

---

Although the novel coronavirus disease 2019 (COVID-19) can present as nonspecific clinical forms, subclinical cases represent an important route of transmission and a significant source of mortality, mainly in high-risk subpopulations such as cancer patients. A deeper knowledge of the metabolic shift in cells infected with severe acute respiratory syndrome coronavirus 2 could provide new insights about its pathogenic and host response and help to diagnose pulmonary involvement. We explored the potential added diagnostic value of  $^{18}\text{F}$ -FDG PET/CT scans in asymptomatic cancer patients with suspected COVID-19 pneumonia by investigating the association between metabolic and structural changes in the lung parenchyma.

**Methods:**  $^{18}\text{F}$ -FDG PET/CT studies acquired between February 19 and May 29, 2020, were reviewed to identify those cancer patients with incidental findings suggestive of COVID-19 pneumonia. PET studies were interpreted through qualitative (visual) and semiquantitative (measurement of  $\text{SUV}_{\text{max}}$ ) analysis evaluating lung findings. Several characteristic signs of COVID-19 pneumonia on CT were described as COVID-19 Reporting and Data System (CO-RADS) categories (1–6). After comparing the  $\text{SUV}_{\text{max}}$  of pulmonary infiltrates among different CO-RADS categories, we explored the best potential cutoffs for pulmonary  $\text{SUV}_{\text{max}}$  against CO-RADS categories as the gold standard result to eliminate the possibility that the diagnosis of COVID-19 pneumonia exists. **Results:** On multimodal PET/CT imaging, CT signs classified as CO-RADS category 5 or 6 were found in 16 of 41 (39%) oncologic patients.  $\text{SUV}_{\text{max}}$  was higher in patients with categories 5 and 6 than in patients with category 4 ( $6.17 \pm 0.82$  vs.  $3.78 \pm 0.50$ ,  $P = 0.04$ ) or categories 2 and 3 ( $3.59 \pm 0.41$ ,  $P = 0.01$ ). A specificity of 93.8% (95% CI, 71.7%–99.7%) and an accuracy of 92.9% were obtained when combining a CO-RADS score of 5 or 6 with an  $\text{SUV}_{\text{max}}$  of 2.45 in pulmonary infiltrates. **Conclusion:** In asymptomatic cancer patients, the metabolic activity in lung infiltrates is closely associated with several combined tomographic changes characteristic of COVID-19 pneumonia. Multimodal  $^{18}\text{F}$ -FDG PET/CT imaging could provide additional information during early diagnosis in selected predisposed patients during the pandemic. The prognostic implications of simultaneous radiologic and molecular findings in

cancer patients and other subpopulations at high risk for COVID-19 pneumonia deserve further evaluation in prospective research.

**Key Words:** COVID-19; pneumonia; lung; cancer,  $^{18}\text{F}$ -FDG PET/CT

**J Nucl Med 2022; 63:274–279**

DOI: 10.2967/jnumed.121.261915

---

Since December 2019, severe acute respiratory syndrome coronavirus 2 (SARS-CoV-2) has quickly spread worldwide from a cluster of cases in Wuhan, China. Although the novel coronavirus disease 2019 (COVID-19) can present as different, nonspecific clinical forms, subclinical cases represent an important route of transmission and a significant source of morbidity and mortality.

Although COVID-19 is usually confirmed by real-time reverse-transcription polymerase chain reaction (rRT-PCR) in respiratory tract specimens, some imaging techniques may strongly suggest the diagnosis until laboratory results are available. In addition, many concerns have been raised about the low sensitivity of rRT-PCR tests (1). In this scenario, chest CT has been positioned as the most useful, noninvasive tool in the diagnosis of COVID-19 pneumonia. Moreover, some CT patterns observed in patients with COVID-19 pneumonia during the pandemic were even more sensitive than rRT-PCR. Despite the limitations of rRT-PCR, it is considered the best diagnostic tool to date.

Several clinical features of the novel infection are particularly challenging in cancer patients. In fact, cancer is a high-risk factor for viral infections, and oncologic patients usually demonstrate an indolent clinical course and a high COVID-19 case fatality rate (2,4). Unfortunately, differentiation among several respiratory virus and other causes of pneumonitis is difficult in this subpopulation (5). So, the rate of suspected infection in asymptomatic predisposed patients should consider the updated epidemiologic data, the risk of infection, and an individualized analytic, imaging, and rRT-PCR or gene sequencing assessment.

Only a few reports and small case series of cancer patients have documented the presence of incidental  $^{18}\text{F}$ -FDG uptake in the lungs suggestive of COVID-19 pneumonia on PET/CT. These data suggest a potential contribution of this technique to the differential diagnosis of complex or asymptomatic presentations of COVID-19

---

Received Feb. 8, 2021; revision accepted May 5, 2021.

For correspondence or reprints, contact Cristina Gamila Wakfie-Corieh (cristinagwc@gmail.com).

Published online Jun. 4, 2021.

Immediate Open Access: Creative Commons Attribution 4.0 International License (CC BY) allows users to share and adapt with attribution, excluding materials credited to previous publications. License: <https://creativecommons.org/licenses/by/4.0/>. Details: <http://jnm.snmjournals.org/site/misc/permission.xhtml>.

COPYRIGHT © 2022 by the Society of Nuclear Medicine and Molecular Imaging.

(6–10). In addition, a deeper knowledge of the metabolic shift in cells infected with SARS-CoV-2 could provide new insights about the pathogenesis of viral infection and host response and help to diagnose pulmonary and distant involvement in selected cases. However, a detailed characterization of combined clinical data, radiologic lung findings, and molecular lung findings in cancer patients with COVID-19 pneumonia is still lacking. With our experience, we aimed to explore the potential added diagnostic value of  $^{18}\text{F}$ -FDG PET/CT scans in asymptomatic cancer patients with suspected COVID-19 pneumonia by investigating the association between metabolic and structural changes in the lung parenchyma.

## MATERIALS AND METHODS

### Study Population

We analyzed 1,065 PET/CT scans acquired from February 19 to May 29, 2020 (Supplemental Figure 1, flowchart; supplemental materials are available at <http://jnm.snmjournals.org>). After exclusion of all subjects with a non- $^{18}\text{F}$ -FDG scan, a nononcologic indication, localized brain studies (functional or tumoral brain PET), or symptoms suggestive of respiratory tract infection (e.g., fever, cough, dyspnea, and sneezing), 967 subjects were included. The last exclusion criterion was the result of the updated European Association of Nuclear Medicine recommendations, in which all subjects undergoing PET/CT were questioned to detect any symptoms suggestive of COVID-19 infection or any personal contact with a confirmed case during the last 12–48 h (11). The Declaration of Helsinki was respected, and the study was approved by the local Ethical Committee. Because the study was retrospective and took place during the COVID-19 pandemic in Spain, the need for individual informed consent was waived (institutional review board approval 20/524-E).

### Clinical and Analytic Data

To identify patients with incidental findings suggestive of COVID-19 pneumonia, we reviewed the  $^{18}\text{F}$ -FDG PET/CT data, including clinical and demographic variables, oncologic indication, biochemical profile, and follow-up by clinical and imaging techniques after PET/CT.

### PET/CT Imaging

A usual preparation protocol for  $^{18}\text{F}$ -FDG PET/CT was followed, acquiring the images after 6 h of fasting in nondiabetic patients or 4 h in diabetic patients with a blood glucose level of less than 200 mg/dL. All patients remained at rest for 40–60 min after intravenous administration of  $^{18}\text{F}$ -FDG (5 MBq/kg). All studies were acquired following the European Association of Nuclear Medicine guidelines on a Siemens Biograph 6 True Point PET/CT multimodal device with a 6-ring detector CT component, performing diagnostic CT (Topogram Dose Modulation System, CARE Dose4D) with a slice thickness of 5 mm and a reconstruction interval of 3 mm. A first inspirational chest CT study was reconstructed as 2.5-mm slices, at 60 mAs and 110 kV, with a tube rotation time of 0.6 s and a pitch of 1.2. Then, another body CT study was performed from the base of the skull to the mid thigh in the craniocaudal direction, during free breathing. For patients who had not undergone contrast-enhanced CT during the previous month, and in the absence of contraindications such as iodine allergy or kidney failure, an intravenous dose of iodinated contrast medium (130 mL of iohexol, Omnipaque [GE Healthcare], 300 mg I/mL) was administered. In total, 782 of 967  $^{18}\text{F}$ -FDG PET/CT studies were performed after iodinated contrast administration. Finally, a PET study was performed at the same locations as the CT study. The acquisition time was 3 min per bed (stretcher) position. Data obtained from PET/CT were merged into a dedicated workstation using the Syngo software system (Siemens

Medical Imaging). Regions of interest were manually placed, and  $\text{SUV}_{\text{max}}$  was recorded in the lung parenchyma.

### Image Interpretation and Clinical Referral After PET/CT

PET/CT scans were reviewed by at least a nuclear medicine physician and a radiologist, reaching a consensus on the final interpretation of each study. The pulmonary findings for each PET/CT study were analyzed qualitatively (changes were interpreted as positive when the pulmonary infiltrates showed tracer uptake greater than normal lung activity) and semiquantitatively ( $\text{SUV}_{\text{max}}$ ). The presence of several diagnostic features in chest CT, such as opacity pattern, bilateralism, lobe involvement, multisegmentation, extension, proximity to visceral pleura and fissures, crazy-paving pattern, hilar lymphadenopathies, and pleural effusion were reported by an expert radiologist. Then, the tomographic changes were combined and characterized applying the COVID-19 Reporting and Data System (CO-RADS) criteria, categorized from 0 to 6 (12,13). In line with local and regional recommendations, all patients with CO-RADS 4 or 5 COVID-19-suggestive CT findings on PET/CT were sent to the emergency department immediately after contacting the referring oncology team. The emergency and oncology teams determined whether the patient would be admitted to the hospital or would stay in isolation at home, what preventive measures might be used, and what the clinical management plan would be. For patients categorized as CO-RADS 1–3, the PET/CT result was sent to the treating oncologist as usual.

### COVID-19 Diagnosis in the Real-Life Setting

Diagnostic rRT-PCR testing was performed on upper or lower respiratory specimens. When available, one or more serologic criteria were included as a surrogate for rRT-PCR, using a plate-based assay that detects antibodies obtained through enzyme-linked immunosorbent assay of serum from a peripheral vein. A confirmed case of COVID-19 was defined as CO-RADS category 5 or 6 findings (CO-RADS 5 with or without genetic or serologic confirmation by rRT-PCR or enzyme-linked immunosorbent assay techniques, respectively) in the absence of clinical or radiologic findings suggesting other, cancer-related, causes of lung infiltration (radiant or cytostatic pneumonitis, tumoral lymphadenopathies, carcinomatous lymphangitis, or secondary or newly primary tumoral lesions) (12). These differential diagnoses were made by at least 1 radiologist and 1 nuclear medicine physician working in consensus. Because of the design and the previously reported false-negative rate of rRT-PCR, the diagnosis could not be confirmed in all subjects in our study sample (14,15).

### Statistics

Normality of data was determined through Kolmogorov–Smirnov testing. Continuous data are presented as mean  $\pm$  SD or as median  $\pm$  interquartile range (25th–75th percentiles), when appropriate, and discrete or categorical variables are presented as frequencies. Discrete variables were compared through the Fisher exact test. A 1-way ANOVA followed by post hoc testing (Tukey) was applied to compare  $\text{SUV}_{\text{max}}$  among cancer patients with different combined tomographic signs included in the CO-RADS categories, grouped as CO-RADS 5 and 6 versus CO-RADS 4 versus CO-RADS 2 and 3. A second analysis was aimed at categorizing the chest CT pattern as being highly or very highly suggestive of COVID-19 pneumonia (group 1, CO-RADS 5 and 6) versus being suggestive at only an indeterminate or low level (group 2, CO-RADS 2–4). An unpaired *t* test was applied to compare pulmonary  $\text{SUV}_{\text{max}}$  between groups. Because the characteristic chest CT findings included in CO-RADS 5 category have less than optimal sensitivity, we added a second, masked, step to CT interpretation for diagnosis of COVID-19 pneumonia, constructing receiver-operating-characteristic curves to find the best cutoff for pulmonary  $\text{SUV}_{\text{max}}$  against these tomographic criteria (1,12). With this purpose,

sensitivity, specificity, likelihood ratio, and accuracy were calculated for different cutoffs. As the ratio of patients with the disease to patients without the disease does not reflect the true prevalence of the illness, we used the prevalence method to estimate accuracy for each cutoff. Accuracy was calculated considering a local COVID-19 pneumonia prevalence of 1.6% during the study period. A *P* value of less than 0.05 was considered significant (2-tailed). All analyses were performed and graphs created using GraphPad Prism software (version 9.0.0).

## RESULTS

In total, 41 of the 967 patients who underwent <sup>18</sup>F-FDG PET/CT for oncologic indications during the study period showed pulmonary infiltrates on CT, representing a frequency of 4.2% (41/967).

Lung cancer (*n* = 8), head and neck tumors (*n* = 7), and breast cancer (*n* = 6) were the most frequent oncologic indications for <sup>18</sup>F-FDG PET/CT, representing 51% (21/41) of patients. A serum biochemical profile was available in 20 of 41 patients, most of them with pulmonary infiltrates categorized as CO-RADS 5 on CT (*P* = 0.004). The clinical and analytic characteristics of the study population are provided in Table 1.

CT signs classified as CO-RADS category 5 or 6 were found in 39% (16/41) of our sample. Almost all of this group of patients (15/16, 94%) had ground-glass opacities on CT. Infiltrates were bilateral in 12 patients of this group and peripherally distributed in 10. The presence of subpleural fibrous bands was also frequent (9/16, 56%). A characteristic crazy-paving pattern was detected in 25% (4/16) of the patients. In contrast, no lymphadenopathies or pleural effusion was observed in any subject of this group. These lung changes in 2 patients are shown in Figures 1 and 2.

Tests for COVID-19 were available for 20 patients; the results were positive in 13 and negative in 7. Twenty-four percent (10/41) were CO-RADS category 6, 14% (6/41) were category 5, 27% (11/41) were category 4, 24% (10/41) were category 3, and 10% (4/41) were category 2. On the qualitative analysis, lung activity was interpreted as positive in 40 patients. After multiple comparisons of

SUV<sub>max</sub> among different CO-RADS categories, a higher SUV<sub>max</sub> was found for patients with CO-RADS category 5 and 6 than for patients with category 4 ( $6.17 \pm 0.82$  vs.  $3.78 \pm 0.50$ , *P* = 0.04) or categories 2 and 3 ( $3.59 \pm 0.41$ , *P* = 0.01) (Fig. 3). After we aggregated tomographic categories, SUV<sub>max</sub> was higher for group 1 than for group 2 ( $6.17 \pm 0.82$  vs.  $3.67 \pm 0.31$ , *P* = 0.002) (Fig. 3).

The area under the curve obtained for different cutoffs of SUV<sub>max</sub> was 0.73 (95% CI, 0.56–0.90; *P* = 0.015) (Fig. 4). The diagnostic yield aiming at eliminating the possibility that the diagnosis exists—estimated by comparing the specificity and likelihood ratio for different SUV<sub>max</sub> cutoffs against CO-RADS 5 and 6 as a gold standard—is presented in Table 2. An SUV<sub>max</sub> cutoff of 3.10 obtained a specificity of at least 75.0%. The best specificity (93.8%; 95% CI, 71.7%–99.7%) and a higher likelihood ratio and accuracy were obtained when combining CO-RADS categories 5 and 6 with an SUV<sub>max</sub> of 2.45 in pulmonary infiltrates.

A subtotal of 35 of 41 patients with pulmonary infiltrates on <sup>18</sup>F-FDG studies were followed by imaging techniques during the next few weeks after PET/CT (8 d to 8 mo). Pulmonary findings improved or resolved in 31 of 35 patients, worsened in 2 of 35, and evolved to post-COVID-19 sequelae in 2 of 35. Five patients (5/41) referred from other centers were lost during follow-up. Only 1 patient (1/41), a 78-y-old man with urothelial cancer without signs of recurrence on PET/CT, died after the PET/CT study (8 d afterward, as a result of severe respiratory failure). In this patient, COVID-19 pneumonia was confirmed by rRT-PCR, pulmonary changes were classified as CO-RADS 5 on CT, and SUV<sub>max</sub> was 6.0 on molecular imaging.

## DISCUSSION

Incidental changes suggesting COVID-19 pneumonia on the chest CT portion of <sup>18</sup>F-FDG PET/CT studies were found in 4.1% of cancer patients at our center, a lower proportion than previously reported (7.1%–9.2%) (7,8,16). These heterogeneous results could be explained by the differences in health-care facilities and policies in different medical centers and countries, the time-dependent

**TABLE 1**  
Clinical, Oncologic, and Biochemical Characterization of Study Population

Variable	Group 1 ( <i>n</i> = 16)	Group 2 ( <i>n</i> = 25)	<i>P</i>
<b>Clinical</b>			
Age (y)	69.8 ± 13.5	64.7 ± 14.9	0.28
Male sex	15 (60.0)	7 (43.8)	0.15
<b>Oncologic</b>			
Cancer staging	5 (12.2)	7 (17.1)	> 0.99
rt-PCR or serologic confirmation*	10 (24.4)	3 (7.3)	0.0014
<b>Biochemical†</b>			
Serum C reactive protein (mg/mL)	7.5 ± 8.7	4.4 ± 8.4	0.45
Lymphocyte blood count (per mm <sup>3</sup> )	1.4 ± 0.7	1.2 ± 0.6	0.44
Serum alanine aminotransferase (mg/mL)	18.6 ± 6.5	19.3 ± 4.8	0.82
Serum aspartate aminotransferase (mg/mL)	27.6 ± 12.8	22.3 ± 6.3	0.33
Serum lactate dehydrogenase (mg/mL)	586.1 ± 204.6	473.0 ± 163.8	0.22

\*One patient with diagnosis of COVID-19 infection was confirmed by serologic IgG test (enzyme-linked immunosorbent assay).

†Analytics were available for patients sent to emergency department with high or very high suspicion based on CO-RADS categories. Qualitative data are number and percentage; continuous data are mean ± SD.

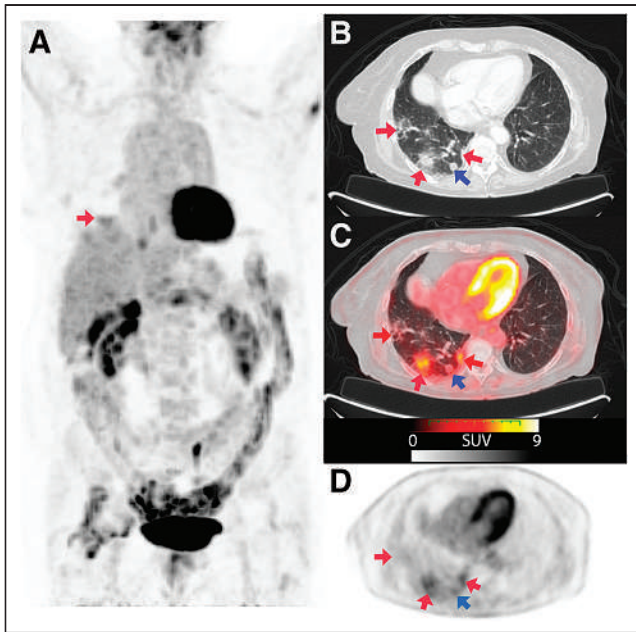


**FIGURE 1.** An 86-y-old woman with second primary lung tumor (B and C, blue arrow) referred for PET/CT to assess therapeutic response. Maximum-intensity projection (A) and axial sections with lung window (B) and fusion (C) images showed several pulmonary consolidations located mainly in right inferior lobe (red arrows, CO-RADS 5), with increased  $^{18}\text{F}$ -FDG uptake ( $\text{SUV}_{\text{max}}$ , 4.6). rRT-PCR was positive for COVID-19.

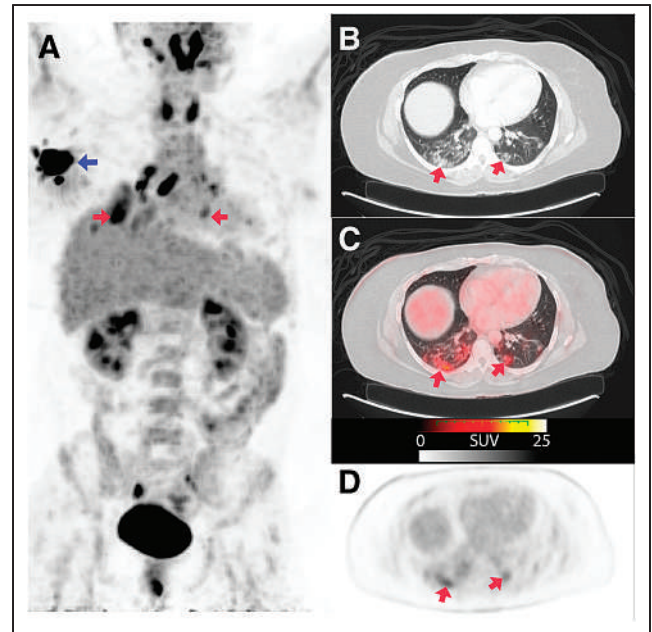


**FIGURE 2.** Staging PET/CT of 43-y-old woman with breast cancer (A, blue arrow). Maximum-intensity projection (A) and axial sections with lung window (B) and fusion (C) images show bilateral ground-glass pulmonary infiltrates (red arrows), some of them with pseudonodular morphology, located in both lower lobes and left middle lobe, with diffuse or peripheral distribution ( $\text{SUV}_{\text{max}}$ , 7.8). Early rRT-PCR obtained in emergency department was negative for COVID-19, and second test was not available.

transmissibility of the virus, or other factors related to the study sample (4,11,17).

Although the diagnostic potential of metabolic activity in pulmonary infiltrates of suggestive or confirmed COVID-19 pneumonia on PET/CT has recently been described, the correlation between the CO-RADS scale and the  $\text{SUV}_{\text{max}}$  of the lung parenchyma has not been evaluated in detail until now (6–10,16–21). Our preliminary results could provide a new perspective on the pathophysiology of SARS2-CoV-2 lung infection and even redefine the best diagnostic imaging criteria for several patient subpopulations.

The performance of chest CT for the diagnosis of COVID-19 pneumonia could be even better when applying several combined findings as in CO-RADS (22). However, the CO-RADS scale has been validated mainly in patients with moderate or severe symptoms and a minor incidence of cancer (21%) (18). The specificity obtained through our successive, diagnostic design ranged from 81.2% to 95.5%, considering an  $\text{SUV}_{\text{max}}$  cutoff of 2.25–3.10. Longitudinal investigation has confirmed that a high proportion of asymptomatic patients with COVID-19 pneumonia usually manifest symptoms during the next few days and weeks (23). A higher  $\text{SUV}_{\text{max}}$  obtained for those CT findings described as more specific for COVID-19 pneumonia (9,22) represents a new tool indicating the predictive value of different CO-RADS categories and also suggests its clinical contribution to discarding this viral pneumonia in cancer patients, even before the appearance of symptoms.

The methodologic approach of this study was aimed at exploring whether the  $\text{SUV}_{\text{max}}$  obtained in new pulmonary infiltrates could contribute to eliminating the possibility that the diagnosis of COVID-19 pneumonia exists, that is, improving the specificity obtained through isolated structural changes on chest CT. Not surprisingly, the best specificity was obtained with an  $\text{SUV}_{\text{max}}$  cutoff

of 2.25–2.55, a value that has been similarly reported as an indicator of benign etiology. This empiric cutoff and the relationship demonstrated between higher  $\text{SUV}_{\text{max}}$  and more suggestive CO-RADS category agree with observational research on other nonmalignant pulmonary processes (24). However, we confirmed that a higher  $\text{SUV}_{\text{max}}$  was observed predominately in the presence of several tomographic signs of COVID-19 pneumonia (Fig. 3). In addition to its diagnostic contribution, the close correlation between structural and metabolic findings could stimulate future research on the pathophysiology of COVID-19 lung injury in predisposed subjects to better characterize the local inflammatory component and its possible changes in response to new therapies.

However, the variation in  $\text{SUV}_{\text{max}}$  observed in lung changes related to COVID-19 pneumonia could also be influenced by

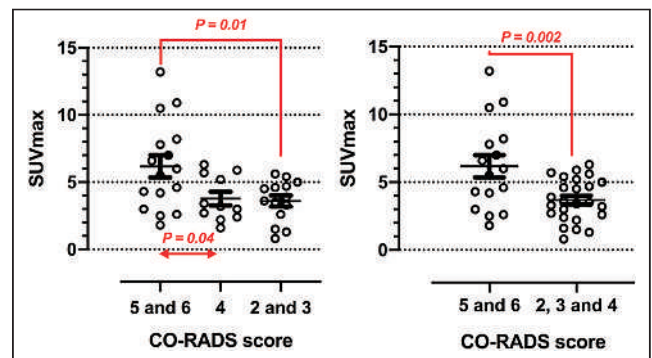


**FIGURE 3.** Association of molecular and structural findings observed on multimodal imaging.  $\text{SUV}_{\text{max}}$  is compared among cancer patients of different CO-RADS categories.

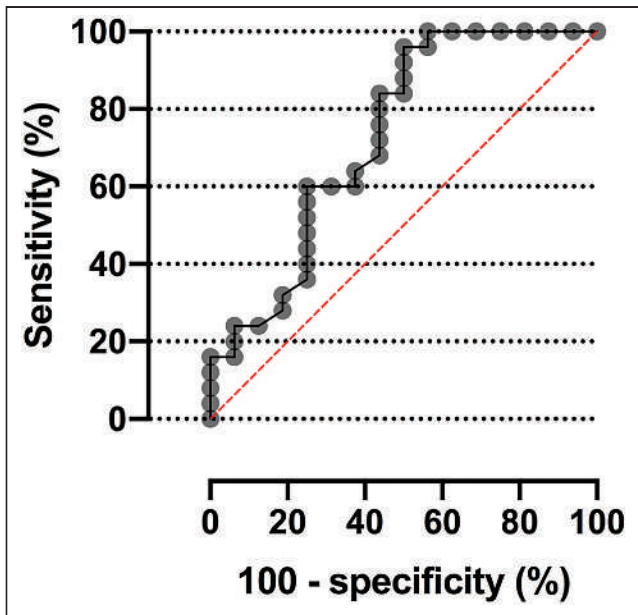


**FIGURE 4.** Receiver-operating-characteristic curve of  $SUV_{max}$  to detect COVID-19 pneumonia on basis of structural tomographic diagnosis (CO-RADS 5 and 6).

factors such as patient weight, motion artifacts, blood glucose levels, dose extravasation, the accuracy of dose calibration, and the time between injection and imaging. Previous reports on certain inflammatory pneumonias found that lung areas with consolidation are associated with a higher  $SUV_{max}$  than are areas with ground-glass opacity. Histopathologic examinations have revealed that the number of CD45-positive cells and CD8-positive T lymphocytes in parenchymal lung lesions correlates positively with  $SUV_{max}$  (25). As it is well known that there are noncellular components in ground-glass opacities (particularly in fluid-filled intraalveolar regions),  $SUV_{max}$  is lower in this pulmonary pattern. This supports the hypothesis that the higher the CO-RADS is, the highest will be the  $SUV_{max}$ , as CO-RADS 5 includes patterns of lung consolidation whereas CO-RADS 3–5 include patterns of ground-glass opacity (12,25,26). In addition, the pulmonary findings related to COVID-19 pneumonia may vary according to the phase of alveolar damage. In the end stage, with fully established fibrosis, the lung parenchyma is destroyed, potentially justifying the lower  $SUV_{max}$  found for lung fibrosis (CO-RADS 1) (12,26). Finally, the pulmonary findings in COVID-19 are not limited to a simple infiltrate of infectious and inflammatory cells but include possible

vessel-related damage such as capillary leaks and thrombosis (26,27). Although these findings are auspicious, the true and complete diagnostic value of different individual CT findings, combined with the local  $SUV_{max}$  on  $^{18}F$ -FDG PET/CT, should be explored in larger, multicenter experiences.

Several inflammatory lung diseases can be characterized by molecular findings similar to those of COVID-19 pneumonia in cancer patients (24). As a consequence, SARS-CoV-2 infection always needs to be distinguished from other viral or bacterial causes of pneumonia, as well as from noninfectious diseases such as pulmonary vasculitis, dermatomyositis, organizing pneumonia and from posttherapeutic changes. Finally, some patients with viral pneumonia may test positively to more than one virus, and the potential lethality of coinfection with SARS-CoV-2 and influenza should not be ignored. In diagnosing COVID-19 pneumonia during a local outbreak, we considered multiple CT findings and expert opinions, and not all patients underwent genetic testing or screening for other sources of infection. Our results should therefore be interpreted cautiously and should be considered as generating only a plausible hypothesis about the value of using PET/CT early to diagnose COVID-19 in cancer patients (28).

Our results should encourage all nuclear medicine physicians to pay special attention to incidental  $^{18}F$ -FDG PET/CT findings suggesting pneumonia and act as quickly as possible (29). During the COVID-19 outbreak in Spain, all nuclear medicine departments followed the safety and prevention protocols provided by the European Association of Nuclear Medicine, in a collective effort to allow for safer diagnosis and treatment procedures (11). Importantly,  $^{18}F$ -FDG PET/CT is a more complex procedure than chest CT and requires more time, leading a possible increased risk of viral spread. In addition, the probability of diagnosing at least some asymptomatic high-risk patients with COVID-19 infection by various common nuclear medicine procedures such as  $^{18}F$ -FDG PET/CT is not negligible (29). On the other hand, the oncology team needs to weigh the risk of death and morbidity from COVID-19 against the benefit of applying several therapies. Obtaining more detailed data through PET/CT could have a doubly positive impact by lowering the risk of spreading the infection while increasing the expected benefits of cancer therapy. This complex, critical clinical scenario requires maintaining an adequate balance for each individual.

The main limitation of our study is the small real-life sample of cancer patients with suspected COVID-19 pneumonia and use of only a single center. A second limitation is that the time since infection was not known, preventing us from evaluating the real impact of early diagnosis in predisposed patients. A third limitation is that

**TABLE 2**

Potential Usefulness of Different Cutoffs for  $^{18}F$ -FDG PET/CT  $SUV_{max}$  to Confirm or Eliminate Possibility That Tomographic Diagnosis of COVID-19 Exists

$SUV_{max}$ cutoff	Sensitivity (%)	95% CI (%)	Specificity (%)	95% CI (%)	LR	Accuracy (%)
<2.45	24.0	11.5–43.4	93.8	71.7–99.7	3.8	92.9
<2.55	24.0	11.5–43.4	87.5	64.0–97.8	1.9	86.7
<2.85	32.0	17.2–51.6	81.3	57.0–93.4	1.7	80.7
<3.10	36.0	20.3–55.5	75.0	50.5–89.8	1.4	74.5

LR = likelihood ratio.

only 1 examiner interpreted the CT images and that interrater variability in each CO-RADS category could therefore not be evaluated (22). Finally, the size of reference bias was not estimated.

## CONCLUSION

In asymptomatic cancer patients, the  $SUV_{max}$  of lung parenchyma infiltrates on  $^{18}F$ -FDG PET/CT studies is closely associated with several tomographic changes characteristic of COVID-19 pneumonia. Multimodal  $^{18}F$ -FDG PET/CT imaging could provide additional information during the diagnosis of COVID-19 in selected patients, even in early stages of the disease. Future prospective experiences are required to define the prognostic value of combining radiologic and molecular findings in cancer patients and other subpopulations at high risk for COVID-19 pneumonia.

## DISCLOSURE

Publication charges were funded by IdISSC. No other potential conflict of interest relevant to this article was reported.

## KEY POINTS

**QUESTION:** What is the association between metabolic and structural changes in lung parenchyma in asymptomatic cancer patients with suspected COVID-19 pneumonia?

**PERTINENT FINDINGS:** The  $SUV_{max}$  of lung parenchyma infiltrates is closely associated with several tomographic changes characteristic of COVID-19 pneumonia (CO-RADS categories) in asymptomatic cancer patients undergoing  $^{18}F$ -FDG PET/CT.

**IMPLICATIONS FOR PATIENT CARE:**  $^{18}F$ -FDG PET/CT may provide additional information about early diagnosis of COVID-19 pneumonia in cancer patients during the pandemic.

## REFERENCES

1. Ai T, Yang Z, Hou H, et al. Correlation of chest CT and RT-PCR testing for coronavirus disease 2019 (COVID-19) in China: a report of 1014 cases. *Radiology*. 2020;296:E32–E40.
2. Liang W, Guan W, Chen R, et al. Cancer patients in SARS-CoV-2 infection: a nationwide analysis in China. *Lancet Oncol*. 2020;21:335–337.
3. Xia Y, Jin R, Zhao J, et al. Risk of COVID-19 for patients with cancer. *Lancet Oncol*. 2020;21:e180.
4. Zhang X, Shao F, Lan X. Suggestions for safety and protection control in department of nuclear medicine during the outbreak of COVID-19. *Eur J Nucl Med Mol Imaging*. 2020;47:1632–1633.
5. Fang Y, Zhang H, Xie J, et al. Sensitivity of chest CT for COVID-19: comparison to RT-PCR. *Radiology*. 2020;296:E115–E117.
6. Qin C, Liu F, Yen TC, et al.  $^{18}F$ -FDG PET/CT findings of COVID-19: a series of four highly suspected cases. *Eur J Nucl Med Mol Imaging*. 2020;47:1281–1286.
7. Albano D, Bertagna F, Bertolia M, et al. Incidental findings suggestive of COVID-19 in asymptomatic patients undergoing nuclear medicine procedures in a high prevalence region. *J Nucl Med*. 2020;61:632–636.
8. Mucientes Rasilla J, Jimeno Pernet R, Cardona Arboniés J. Diagnosis of COVID-19 pneumonia in asymptomatic patients after an oncological PET/CT. *Rev Esp Med Nucl Imagen Mol*. 2020;39:299–302.
9. Setti L, Kirienko M, Dalto SC, et al. FDG-PET/CT findings highly suspicious for COVID-19 in an Italian case series of asymptomatic patients. *Eur J Nucl Med Mol Imaging*. 2020;47:1649–1656.
10. Albano D, Camoni L, Rinaldi R, Bertagna F, Giubbini R.  $^{18}F$ -FDG PET/CT metabolic behavior of COVID-19 pneumonia: a series of 4 patients with RT-PCR confirmation. *Clin Nucl Med*. 2020;45:e378–e380.
11. Paez D, Gnanasegaran G, Fanti S, et al. COVID-19 pandemic: guidance for nuclear medicine departments. *Eur J Nucl Med Mol Imaging*. 2020;47:1615–1619.
12. Prokop M, van Everdingen W, van Rees Vellinga T, et al.; COVID-19 standardized reporting working group of the Dutch Radiological Society. CO-RADS: a categorical CT assessment scheme for patients suspected of having COVID-19—definition and evaluation. *Radiology*. 2020;296:E97–E104.
13. Li K, Fang K, Li W, et al. CT image visual quantitative evaluation and clinical classification of coronavirus disease (COVID-19). *Eur Radiol*. 2020;30:4407–4416.
14. Xie X, Zhong Z, Zhao W, Zheng C, Wang F, Liu J. Chest CT for typical 2019-nCoV pneumonia: relationship to negative RT-PCR testing. *Radiology*. 2020;296:E41–E45.
15. Kucirka LM, Lauer SA, Laeyendecker O, Boon D, Lessler J. Variation in false-negative rate of reverse transcriptase polymerase chain reaction-based SARS-CoV-2 tests by time since exposure. *Ann Intern Med*. 2020;173:262–267.
16. Albano D, Bertagna F, Alongi P, et al. Prevalence of interstitial pneumonia suggestive of COVID-19 at  $^{18}F$ -FDG PET/CT in oncological asymptomatic patients in a high prevalence country during pandemic period: a national multi-centric retrospective study. *Eur J Nucl Med Mol Imaging*. 2021;48:2871–2882.
17. Annunziata S, Albano D, Laudicella R, Bauckneht M; Young Committee of the Italian Association of Nuclear Medicine (AIMN). Surveys on COVID-19 in nuclear medicine: what happened and what we learned. *Clin Transl Imaging*. September 24, 2020 [Epub ahead of print].
18. Polverari G, Arena V, Ceci F, et al.  $^{18}F$ -fluorodeoxyglucose uptake in patient with asymptomatic severe acute respiratory syndrome coronavirus 2 (coronavirus disease 2019) referred to positron emission tomography/computed tomography for NSCLC restaging. *J Thorac Oncol*. 2020;15:1078–1080.
19. Annunziata S, Delgado Bolton RC, Kamani CH, et al. Role of  $2-[^{18}F]FDG$  as a radiopharmaceutical for PET/CT in patients with COVID-19: a systematic review. *Pharmaceuticals (Basel)*. 2020;13:377.
20. Annunziata S, Bauckneht M, Albano D, et al. Impact of the COVID-19 pandemic in nuclear medicine departments: preliminary report of the first international survey. *Eur J Nucl Med Mol Imaging*. 2020;47:2090–2099.
21. Deng Y, Lei L, Chen Y, et al. The potential added value of FDG PET/CT for COVID-19 pneumonia. *Eur J Nucl Med Mol Imaging*. 2020;47:1634–1635.
22. Bellini D, Panvini N, Rengo M, et al. Diagnostic accuracy and interobserver variability of CO-RADS in patients with suspected coronavirus disease-2019: a multi-reader validation study. *Eur Radiol*. 2021;31:1932–1940.
23. Al-Shamsi HO, Coomes EA, Alrawi S. Screening for COVID-19 in asymptomatic patients with cancer in a hospital in the United Arab Emirates. *JAMA Oncol*. 2020;6:1627–1628.
24. Capitanio S, Nordin AJ, Noraini AR, et al. PET/CT in non oncological lung diseases: current applications and future perspectives. *Eur Respir Rev*. 2016;25:247–258.
25. Tateishi U, Hasegawa T, Seki K, et al. Disease activity and  $^{18}F$ -FDG uptake in organising pneumonia: semi-quantitative evaluation using computed tomography and positron emission tomography. *Eur J Nucl Med Mol Imaging*. 2006;33:906–912.
26. Schaller T, Hirschi K, Burkhardt K, et al. Postmortem examination of patients with COVID-19. *JAMA*. 2020;323:2518–2520.
27. Iba T, Levy JH, Levi M, et al. Coagulopathy of coronavirus disease 2019. *Crit Care Med*. 2020;48:1358–1364.
28. Zhu WJ, Wang J, He XH, et al. The differential diagnosis of pulmonary infiltrates in cancer patients during the outbreak of the 2019 novel coronavirus disease. *Chung Hua Chung Liu Tsai Chih*. 2020;42:305–311.
29. Tulchinsky M, Fotos JS, Slonimsky E. Incidental CT findings suspicious for COVID-19 associated pneumonia on nuclear medicine exams: recognition and management plan. *Clin Nucl Med*. 2020;45:531–533.

---

---

# Comparing Semiquantitative and Qualitative Methods of Vascular $^{18}\text{F}$ -FDG PET Activity Measurement in Large-Vessel Vasculitis

Himanshu R. Dashora<sup>1</sup>, Joel S. Rosenblum<sup>1</sup>, Kaitlin A. Quinn<sup>1</sup>, Hugh Alessi<sup>1</sup>, Elaine Novakovich<sup>1</sup>, Babak Saboury<sup>2</sup>, Mark A. Ahlman<sup>\*2</sup>, and Peter C. Grayson<sup>\*1</sup>

<sup>1</sup>Systemic Autoimmunity Branch, NIAMS, National Institutes of Health, Bethesda, Maryland; and <sup>2</sup>Radiology and Imaging Sciences, Clinical Center, National Institutes of Health, Bethesda, Maryland

---

The study rationale was to assess the performance of qualitative and semiquantitative scoring methods for  $^{18}\text{F}$ -FDG PET assessment in large-vessel vasculitis. **Methods:** Patients with giant cell arteritis or Takayasu arteritis underwent independent clinical and imaging assessments within a prospective observational cohort.  $^{18}\text{F}$ -FDG PET/CT scans were interpreted for active vasculitis by central reader assessment. Arterial  $^{18}\text{F}$ -FDG uptake was scored by qualitative visual assessment using the PET vascular activity score (PETVAS) and by semiquantitative assessment using SUVs and target-to-background ratios (TBRs) relative to liver or blood activity. The performance of each scoring method was assessed by intrarater reliability using the intraclass correlation coefficient (ICC) and areas under the receiver-operating-characteristic curve, applying physician assessment of clinical disease activity and reader interpretation of vascular PET activity as independent reference standards. The Wilcoxon signed-rank test was used to analyze change in arterial  $^{18}\text{F}$ -FDG uptake over time. **Results:** Ninety-five patients (giant cell arteritis, 52; Takayasu arteritis, 43) contributed 212  $^{18}\text{F}$ -FDG PET studies. The ICC for semiquantitative evaluation (0.99 [range, 0.98–1.00]) was greater than the ICC for qualitative evaluation (0.82 [range, 0.56–0.93]). PETVAS and target-to-background ratio metrics were more strongly associated with reader interpretation of PET activity than SUV metrics. All assessment methods were significantly associated with physician assessment of clinical disease activity, but the semiquantitative metric liver tissue-to-background ratio ( $\text{TBR}_{\text{Liver}}$ ) achieved the highest area under the receiver-operating-characteristic curve (0.66). Significant but weak correlations with C-reactive protein were observed for SUV metrics ( $r = 0.19$ ,  $P < 0.01$ ) and  $\text{TBR}_{\text{Liver}}$  ( $r = 0.20$ ,  $P < 0.01$ ) but not for PETVAS. In response to increased treatment in 56 patients, arterial  $^{18}\text{F}$ -FDG uptake was significantly reduced when measured by semiquantitative ( $\text{TBR}_{\text{Liver}}$ , 1.31–1.23; 6.1% change;  $P < 0.0001$ ) or qualitative (PETVAS, 22–18;  $P < 0.0001$ ) methods. Semiquantitative metrics provided information complementary to qualitative evaluation in cases of severe vascular inflammation. **Conclusion:** Both qualitative and semiquantitative methods of measuring arterial  $^{18}\text{F}$ -FDG uptake are useful in assessing and monitoring vascular inflammation in large-vessel vasculitis. Compared with qualitative metrics, semiquantitative methods have superior reliability and better discriminate treatment response in cases of severe inflammation.

**Key Words:** vasculitis; Takayasu arteritis; giant cell arteritis; PET; outcome measure

---

Received Mar. 19, 2021; revision accepted May 5, 2021.  
For correspondence or reprints, contact Peter C. Grayson (peter.grayson@nih.gov).

\*Contributed equally to this work.

Published online Jun. 4, 2021.

COPYRIGHT © 2022 by the Society of Nuclear Medicine and Molecular Imaging.

J Nucl Med 2022; 63:280–286

DOI: 10.2967/jnumed.121.262326

---

**L**arge-vessel vasculitis (LVV) refers to a class of rare diseases characterized by inflammation of the aorta and its primary branch arteries. Giant cell arteritis and Takayasu arteritis comprise the 2 major subtypes of LVV (1).  $^{18}\text{F}$ -FDG PET can detect metabolic activity in the walls of large arteries as a biomarker of vascular inflammation (2). Ample evidence supports the use of  $^{18}\text{F}$ -FDG PET as a diagnostic surrogate to histologic confirmation of vasculitis, which is advantageous because arterial biopsies are invasive and can be difficult to obtain (3,4). In contrast to diagnostic assessment, use of arterial  $^{18}\text{F}$ -FDG uptake to guide treatment decisions and monitor disease activity is less well defined (5–9), in part because of lack of prospective, longitudinal imaging studies on LVV (10,11). Reliance on clinical assessment alone may lead to underdetection of vascular pathology (12). Vascular inflammation with angiographic progression of disease can occur in patients with LVV who are otherwise completely asymptomatic, highlighting a need for vascular imaging to complement clinical assessment in these patients (13).

Uncertainty about the optimal method to evaluate  $^{18}\text{F}$ -FDG uptake in the large arteries remains a major barrier to the use of  $^{18}\text{F}$ -FDG PET to monitor vascular inflammation (11). Both visual/qualitative and semiquantitative methods of  $^{18}\text{F}$ -FDG PET assessment have been reported in LVV. Qualitative methods typically visually compare the amount of  $^{18}\text{F}$ -FDG uptake in the arterial wall relative to a background tissue, such as the liver (11,14), similar to the Deauville score used in lymphoma (15). In contrast, semiquantitative methods use regions of interest (ROIs) constructed on the PET image to determine  $\text{SUV}_{\text{max}}$  (16). Target-to-background ratios (TBRs), comprised of SUVs from arterial tissue referenced to background tissue (e.g., liver, blood pool), are also used to quantify arterial  $^{18}\text{F}$ -FDG uptake in atherosclerosis and vasculitis (17). Recent recommendations highlight that several methods of quantifying arterial  $^{18}\text{F}$ -FDG uptake are available, but the relevance of each method in evaluating patients requires further clarification (11). SUV metrics often overlap between patients with LVV and controls, and many patients with LVV have residual, and sometimes profound, arterial  $^{18}\text{F}$ -FDG uptake during periods of apparent clinical remission (18).

There is an unmet need to better understand the strengths and weaknesses of qualitative versus semiquantitative methods of

quantifying arterial  $^{18}\text{F}$ -FDG uptake in LVV. Semiquantitative assessment of arterial  $^{18}\text{F}$ -FDG uptake can be a time-consuming process, which may be difficult to apply in a contemporary clinical setting or be cost-prohibitive in research. In contrast, qualitative PET assessment may be easier to do with appropriate user training; however, qualitative assessment may be less reliable and accurate in quantifying arterial  $^{18}\text{F}$ -FDG uptake than are semiquantitative approaches (19,20).

This study aimed to compare the effectiveness of qualitative and semiquantitative scoring methods, with the goal of informing a standardized approach to  $^{18}\text{F}$ -FDG PET assessment in LVV for use in clinical care and research.

## MATERIALS AND METHODS

### Study Population

Patients with LVV who were at least 18 y old were recruited into a prospective, observational cohort at the National Institutes of Health. All patients provided written informed consent, and the study was approved by an institutional review board at the National Institutes of Health (NCT02257866; 14-AR-0200). All patients fulfilled the 1990 American College of Rheumatology Classification Criteria for Takayasu arteritis (21) or the modified 1990 American College of Rheumatology Criteria for giant cell arteritis (22,23). The patients were enrolled at various stages of the disease course. Treatment decisions were made at the discretion of each patient's local health-care provider rather than by the investigative research team.

### Clinical Assessment

Each patient's imaging assessment took place within 24 h after that same patient's clinical assessment at the National Institutes of Health Clinical Center. Repeat imaging studies and clinical assessments were performed at 6-mo intervals. A team of clinical rheumatologists with further specialist training and experience in LVV evaluated all cases. Physician assessment of clinical disease activity was recorded as active or remission on the basis of findings from the medical history, physical examination, and laboratory assessments. Active disease was defined as the presence of clinical disease features attributed to vasculitis (e.g., carotidynia) at the time of assessment. Remission was defined as the absence of clinical symptoms attributable to vasculitis at the time of assessment. Imaging study findings were not incorporated into the definition of clinical disease activity.

### $^{18}\text{F}$ -FDG PET Imaging Protocol

All patients underwent  $^{18}\text{F}$ -FDG PET CT on a 128-detector-row Biograph mCT (Siemens Medical Solutions). The patients were given detailed instructions to avoid carbohydrate-laden meals 1 d before imaging and to fast on the day of imaging. The  $^{18}\text{F}$ -FDG dose was fixed to 370 MBq for all patients. Images of the torso were acquired 2 h after injection. Postacquisition image reconstruction used CT attenuation correction and iterative reconstruction (point-spread function correction with time-of-flight correction, 3 iterations, 21 subsets, a 256 matrix, a final isotropic voxel resolution of 3.2 mm<sup>3</sup>, and no postreconstruction filtering).

### $^{18}\text{F}$ -FDG PET Imaging Assessment

**Qualitative Analysis.** One imaging specialist interpreted all PET studies without knowledge of the clinical data. A study was excluded if there were technical concerns about image quality per physician review. Each study was subjectively interpreted as PET-active or PET-inactive if, respectively, there was or was not at least 1 area of abnormal arterial  $^{18}\text{F}$ -FDG uptake felt to represent vascular inflammation. Intra- and interrater reproducibility of LVV PET image interpretation by our group has been previously reported to be excellent (18). Qualitative assessment of  $^{18}\text{F}$ -FDG uptake was also performed at the

territory level, which included 4 segments of the aorta (ascending, arch, descending thoracic, and abdominal) and 5 branch arteries (brachiocephalic, right and left carotid, and right and left subclavian). Scores between 0 and 3 were assigned to each territory, representing the visual degree of arterial  $^{18}\text{F}$ -FDG uptake relative to liver  $^{18}\text{F}$ -FDG uptake (0, no uptake; 1, less than liver; 2, similar to liver; and 3, greater than liver). Adding the qualitative arterial territory scores yields a summary score (termed the PET vascular activity score, or PETVAS) ranging from 0 to 27, with higher scores indicating a greater global burden of vascular inflammation (18).

**Semiquantitative Analysis.** ROIs were manually contoured in OsiriX DICOM Viewer (version 9.5.2) with respect to both CT anatomic location and coregistered PET activity to determine arterial  $^{18}\text{F}$ -FDG SUVs. ROIs were drawn in the axial dimension, encompassing both arterial wall and lumen. Five segments of the aorta (ascending aorta, aortic arch, descending thoracic aorta, suprarenal abdominal aorta, and infrarenal abdominal aorta) and 4 branch arteries (right and left common carotid and subclavian arteries) were segmented in this process to create 9 territories. The  $^{18}\text{F}$ -FDG SUV<sub>max</sub> per ROI of each territory was identified. A territory score was calculated by taking the average of the SUV<sub>max</sub> across all ROIs in the territory (17). A global summary metric (SUV<sub>Artery</sub>) was calculated by averaging all territory scores.

The volumetric SUV<sub>mean</sub> in the liver was measured in the dome of the right lobe. The volumetric SUV<sub>mean</sub> in the venous blood pool was measured within the right jugular, superior vena cava, right atrium, and inferior vena cava. SUV<sub>Artery</sub> was divided by the background tissue to generate 2 TBR metrics: liver TBR (TBR<sub>Liver</sub>) and blood TBR (TBR<sub>Blood</sub>).

### Statistical Analysis

**Intrarater Reliability.** Intrarater reliability, reflecting the variation in data measured by 1 rater over multiple trials, was quantified with a 2-way random effect (consistency) and a single-measurement intraclass correlation coefficient (ICC) (24). ICC estimates and their 95% CIs were calculated using R, package irr (version 0.84.1). ICCs lie between 0 and 1. Values less than 0.5, between 0.5 and 0.75, between 0.75 and 0.9, and greater than 0.9 are indicative of poor, moderate, good, and excellent reliability, respectively. The ICC for the qualitative approach was obtained by repeating PETVAS on a set of randomly selected patients. The ICC for the semiquantitative approach was obtained by recontouring ROIs to recalculate SUV<sub>Artery</sub> for a set of randomly selected patients representing 10% of the cohort.

**Receiver-Operating-Characteristic Curve.** Area under the receiver-operating-characteristic curve (AUC), along with the 95% CI, was used as a combined measure of sensitivity and specificity to evaluate the overall performance of the PET scoring metrics as classifiers of a binary outcome (25), either reader interpretation of vascular PET activity (PET-active vs. PET-inactive) or physician assessment of clinical disease activity (clinically active vs. clinical remission). AUCs lie between 0 and 1. Metrics with capability to distinguish between binary outcomes will result in an AUC above 0.5, with larger AUCs suggesting better diagnostic performance. The Youden J statistic was used to determine the optimal cutoff score that maximized the distance to the identity (diagonal) line.

**Mixed-Effects Logistic Regression.** To account for repeated imaging contributions from a single patient, generalized linear mixed models with logistic outcomes were constructed. The dependent variable was a binary classification of either reader interpretation of vascular PET activity (PET-active vs. PET-inactive) or physician assessment of clinical disease activity (clinically active vs. clinical remission). The PET scoring metric, either semiquantitative or qualitative, was used as the fixed effect, with patient identification used as a random effect. A "bound optimization by quadratic approximation" nonlinear optimizer and 10 points of integration for the adaptive gaussian Hermite

approximation were used as model control parameters. Independent generalized linear mixed models were created for each scoring method. The Akaike information criterion (AIC) estimates the information loss for a given model and is a means for model selection. Relative to the other models, the candidate model with the lowest AIC minimizes estimated information loss. All generalized linear mixed-model analysis was performed using R, package lme4 (version 1.1-21).

**Correlation Analysis.** Spearman rank-order correlation was used to measure the association between the PET scoring metrics and the acute-phase reactants (C-reactive protein and erythrocyte sedimentation rate). The Spearman *r*, ranging from 0 to 1, and the *P* value of the correlation are presented.

**Longitudinal PET Assessment in Response to Treatment.** The Wilcoxon matched-pairs signed-rank test was used to compare changes in PET assessment metrics between 2 time points for the same patient. When stratifying by treatment status, we placed initial and follow-up scan pairings into increased-treatment and no-change groups. Increased treatment was defined as the introduction of a glucocorticoid-sparing medication or an increase in daily prednisone dose by more than 5 mg. No change was defined as maintenance of biologic agent administration or a stable glucocorticoid dosage.

Semiquantitative metrics of <sup>18</sup>F-FDG PET activity exist on a continuous scale. In contrast, a qualitative metric such as PETVAS is ordinal, with a maximum score of 27 (18). In cases of severe inflammation in which PET activity may be reduced but remains in a range above the maximum PETVAS score, semiquantitative metrics may be better suited to demonstrate a change in PET activity. A subset of patients was selected who had, first, severe vascular inflammation defined by a baseline PETVAS score of 27 and, second, a reduction in <sup>18</sup>F-FDG uptake on the follow-up scan by visual assessment, as agreed on by 2 independent readers. The longitudinal change in PET activity measured by PETVAS versus TBR<sub>Liver</sub> metrics was compared in this subset of patients.

## RESULTS

### Study Population

In total, 95 patients (giant cell arteritis, 52; Takayasu arteritis, 43) contributed 212 imaging studies. Three imaging studies were

excluded because of concerns about image quality. Demographics were consistent with the expected age and sex distributions for giant cell arteritis and Takayasu arteritis (Table 1). The patients were seen, on average, 6.1 y into the disease course while taking, on average, 8.3 mg of daily prednisone.

### Intrarater Reliability

Intrarater reliability for repeat scoring of 34 imaging studies using the semiquantitative scoring protocol was excellent (ICC, 0.99; range, 0.98–1.00). Intrarater reliability for the qualitative assessment by PETVAS was good (ICC, 0.82; range, 0.56–0.93).

### Quantification of Arterial <sup>18</sup>F-FDG Uptake in Association with Reader Interpretation of PET Scan Activity

Of 209 <sup>18</sup>F-FDG PET imaging studies, 147 scans were interpreted as PET-active and 62 scans as PET-inactive. Compared with the use of SUV alone, discriminatory power (AUC) was greater and model quality was better (lower AIC) when TBR was used to differentiate PET-active from PET-inactive scans (Table 2). PETVAS performed similarly to TBR, with better performance characteristics than SUV. PETVAS achieved the highest AUC and lowest AIC relative to the other models, with an optimal cutoff of 19.5 (Table 2).

### Quantification of Arterial <sup>18</sup>F-FDG Uptake in Association with Physician Assessment of Clinical Disease Activity and Laboratory Tests

Complete clinical and imaging assessments were available for 206 study visits. Clinical disease activity was assessed as clinically active for 95 study visits and clinical remission for 131 study visits. Corresponding arterial <sup>18</sup>F-FDG uptake evaluated by any proposed method significantly discriminated active disease from clinical remission, but TBR metrics and PETVAS resulted in higher AUCs than did SUV metrics (Table 3). Within the proposed mixed models, the PETVAS-informed model had the lowest AIC when predicting the same clinical outcomes as the other models, suggesting the best model fit (26). Broadly, all AUCs were lower when <sup>18</sup>F-FDG metrics were compared with clinical

**TABLE 1**  
Baseline Demographics of Study Population

Demographic	Giant cell arteritis	Takayasu arteritis	Total
Patients	52	43	95
PET/CT studies per patient			
1 study	22	19	41
2 studies	11	14	25
≥3 studies	19	10	29
Age (y)	69.2 ± 8.9	34.3 ± 10.3	55.9 ± 19.4
Female	41 (78.8%)	33 (76.7%)	74 (77.9%)
BMI	27.3 ± 5.5	25.9 ± 6.7	26.8 ± 6.0
CRP	6.8 ± 14.1	10.7 ± 21.7	8.3 ± 17.4
ESR	17.3 ± 19.1	19.4 ± 16.6	18.1 ± 18.2
Daily prednisone (mg)	9.0 ± 13.9	7.2 ± 11.3	8.33 ± 12.9
Disease duration (y)	2.98 ± 2.41	10.9 ± 10.7	6.06 ± 7.94

BMI = body mass index; CRP = C-reactive protein; ESR = erythrocyte sedimentation rate  
Qualitative data are number; continuous data are mean ± SD.

**TABLE 2**

Performance Characteristics of Semiquantitative and Qualitative PET Assessment Methods in Association with Subjective Reader Interpretation of PET Activity

Parameter	Descriptive statistic				GLMM evaluation	
	PET active (mean ± SEM)	PET inactive (mean ± SEM)	AUC (95% CI)	Optimal cutoff	P	AIC
LVV (n)	147	62				
SUV <sub>Artery</sub>	3.41 ± 0.10	2.78 ± 0.08	0.67 (0.60–0.75)	3.36	< 0.0001	226.9
TBR <sub>Liver</sub>	1.45 ± 0.04	1.09 ± 0.02	0.85 (0.80–0.90)	1.22	< 0.0001	179.0
TBR <sub>Blood</sub>	2.59 ± 0.07	2.03 ± 0.03	0.80 (0.74–0.86)	2.31	< 0.0001	198.2
PETVAS	20.83 ± 0.41	12.87 ± 0.58	0.87 (0.83–0.92)	19.5	< 0.0001	165.2

GLMM = generalized linear mixed model.

**TABLE 3**

Performance Characteristics of Semiquantitative and Qualitative PET Assessment Methods in Association with Physician Assessment of Clinical Disease Activity

Parameter	Descriptive statistic				GLMM evaluation	
	Clinical active (mean ± SEM)	Clinical remission (mean ± SEM)	AUC (95% CI)	Optimal cutoff	P	AIC
LVV (n)	75	131				
SUV <sub>Artery</sub>	3.43 ± 0.13	3.11 ± 0.09	0.59 (0.51–0.68)	3.58	0.0293	255.2
TBR <sub>Liver</sub>	1.46 ± 0.06	1.27 ± 0.03	0.66 (0.58–0.73)	1.46	0.0002	253.1
TBR <sub>Blood</sub>	2.60 ± 0.09	2.31 ± 0.06	0.65 (0.57–0.73)	2.39	0.0003	254.7
PETVAS	20.6 ± 0.56	17.3 ± 0.55	0.65 (0.57–0.73)	22.5	0.0004	239.5

GLMM = generalized linear mixed model.

assessment than when reader interpretation of PET activity was used as the reference standard.

Significant but weak correlations with acute-phase reactants were observed for SUV<sub>Artery</sub> (C-reactive protein:  $r = 0.19$ ,  $P < 0.01$ ; erythrocyte sedimentation rate:  $r = 0.14$ ,  $P = 0.04$ ) and TBR<sub>Liver</sub> (C-reactive protein:  $r = 0.20$ ,  $P < 0.01$ ; erythrocyte

sedimentation rate:  $r = 0.15$ ,  $P = 0.03$ ). Neither TBR<sub>Blood</sub> nor PETVAS correlated significantly with C-reactive protein or erythrocyte sedimentation rate (Table 4).

**Longitudinal Treatment Response**

Treatment was increased over 56 interval study visits. Correspondingly, there was a significant reduction in vascular inflammation by the semiquantitative approach (median TBR<sub>Liver</sub>, 1.31 [IQR, 1.19–1.59] to 1.23 [IQR, 1.13–1.39];  $P < 0.001$ ) or the qualitative approach (median PETVAS, 22 [IQR, 17–25] to 18 [IQR, 15–22];  $P < 0.001$ ). Over 25 interval visits for which there was no change in treatment status between successive imaging studies, the degree of vascular inflammation remained similarly unchanged as measured by either semiquantitative assessment (median TBR<sub>Liver</sub>, 1.39 [IQR, 1.24–1.54] to 1.35 [IQR, 1.18–1.49];  $P = 0.22$ ) or qualitative assessment (median PETVAS, 21 [IQR, 18–25] to 21 [IQR, 18.5–25];  $P = 0.68$ ) (Figs. 1 and 2).

A subset of 9 patients with severe inflammation (baseline PETVAS of 27) who had a visually apparent reduction in arterial <sup>18</sup>F-FDG uptake on the follow-up imaging study were studied. PETVAS was significantly reduced from a score of 27 at baseline to a median score of 24 (IQR, 18.5–26;  $P < 0.01$ ) at the follow-up visit (Fig. 3). TBR<sub>Liver</sub> scores in these same patients were

**TABLE 4**

Correlation of Semiquantitative and Qualitative PET Assessment Methods to Acute-Phase Reactants (CRP and ESR)

	CRP		ESR	
	Spearman <i>r</i>	<i>P</i>	Spearman <i>r</i>	<i>P</i>
SUV <sub>Artery</sub>	0.19	<0.01	0.14	0.04
TBR <sub>Liver</sub>	0.20	<0.01	0.15	0.03
TBR <sub>Blood</sub>	0.11	0.14	0.02	0.78
PETVAS	0.08	0.29	0.08	0.27

CRP = C-reactive protein; ESR = erythrocyte sedimentation rate.

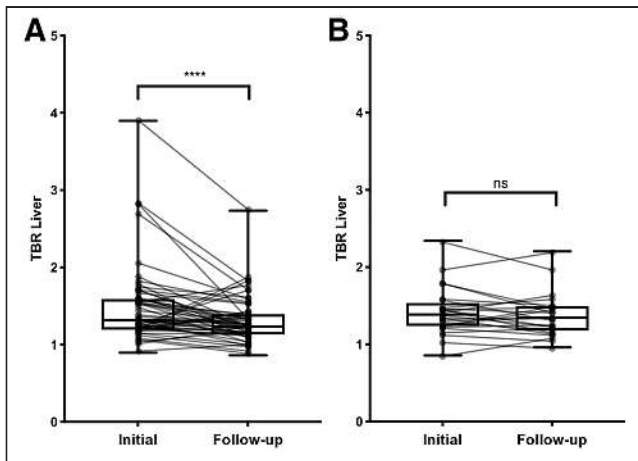


**FIGURE 1.** Response of qualitative  $^{18}\text{F}$ -FDG PET assessment scores to increased pharmacologic treatment (A) and to no change in pharmacologic treatment (B). Data are shown as box-and-whisker plots with paired comparisons. ns =  $P > 0.05$ . \*\*\*\* $P < 0.001$ .

a median of 1.86 (range, 1.55–2.63) at the baseline visit, with a significant reduction in scores at follow-up (median, 1.24 [range, 1.14–1.69];  $P < 0.01$ ). Although the baseline PETVAS scores were the same for all 9 patients, there was a corresponding dynamic range of baseline  $\text{TBR}_{\text{Liver}}$  scores, reflecting variability among these patients.  $\text{TBR}_{\text{Liver}}$  was reduced over time in every patient; however, in only 3 of 9 patients was there a reduction in PETVAS, and this reduction was minimal (i.e., change  $\leq 1$  point). Representative images from a patient with a visually apparent reduction in vascular PET activity are shown in Figure 4.

## DISCUSSION

Use of  $^{18}\text{F}$ -FDG PET to monitor vascular inflammation in LVV holds promise as a complement to clinical and laboratory-based assessment (10,18,27,28). Visualizing glucose metabolism within the arterial wall as a biomarker of vascular inflammation enables clinicians to noninvasively diagnose and track disease activity in

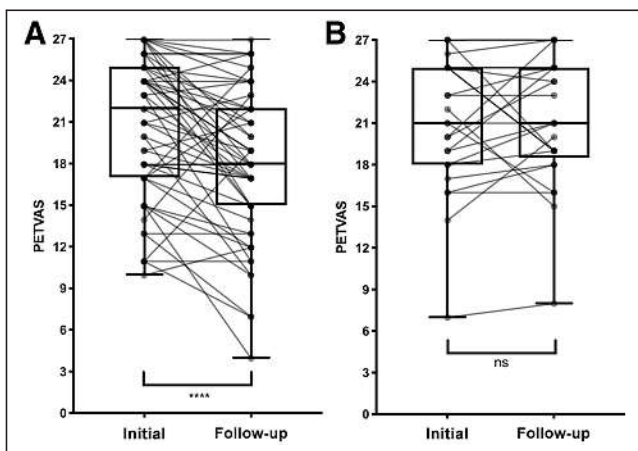


**FIGURE 2.** Response of semiquantitative  $^{18}\text{F}$ -FDG PET assessment scores to increased pharmacologic treatment (A) and to no change in pharmacologic treatment (B). Data are shown as box-and-whisker plots with paired comparisons. ns =  $P > 0.05$ . \*\*\*\* $P < 0.001$ .

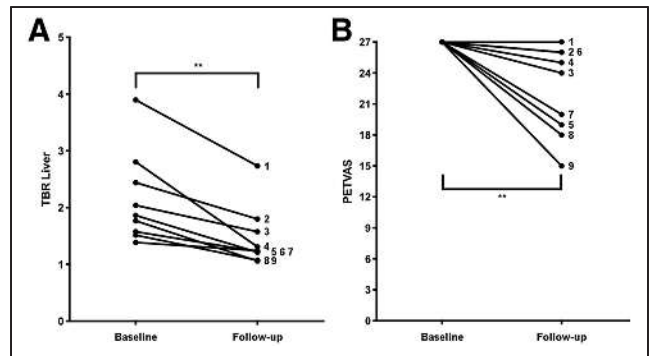


**FIGURE 3.** Change in  $^{18}\text{F}$ -FDG PET assessment metrics in subset of patients with maximum baseline PETVAS using qualitative metrics (A) and semiquantitative metrics (B). ns =  $P > 0.05$ . \*\* $P < 0.01$ .

LVV directly in the target tissue, in parallel with clinical and laboratory assessments (29). This ability is particularly important in LVV because patients can develop subclinical vascular inflammation that has no accompanying clinical symptoms or abnormal laboratory findings and can be detected and monitored only by vascular imaging (18,28,30). The present study advances our understanding of the strengths and weaknesses of different methodologic approaches to quantifying vascular inflammation.

Reassuringly, both qualitative and semiquantitative approaches performed well in detecting and monitoring arterial  $^{18}\text{F}$ -FDG PET uptake in patients with LVV. PETVAS, a qualitative scoring approach developed by our group, and semiquantitative methods had good-to-excellent intrarater reliability. Because some patients can show vascular inflammation on PET in the absence of clinical activity, we studied the performance characteristics of qualitative and semiquantitative metrics against 2 independent reference standards (31). As expected, SUV metrics, TBRs, and PETVAS were significantly associated with reader interpretation of vascular

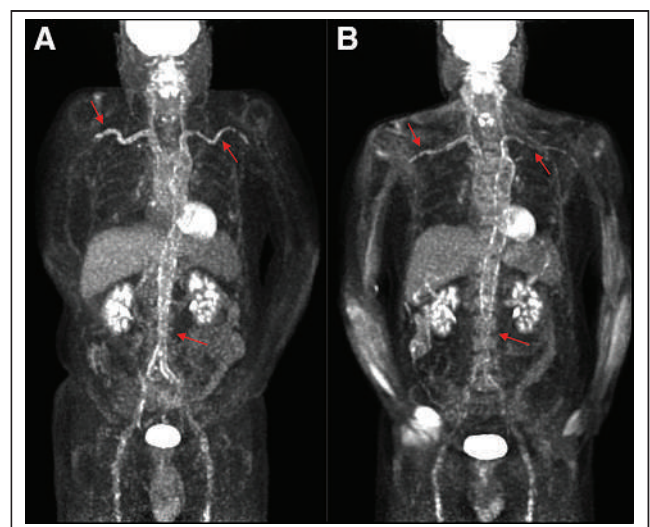


**FIGURE 4.** Improvement in  $^{18}\text{F}$ -FDG activity over time in patient with severe vascular inflammation. (A) Baseline imaging study with PETVAS of 27 (maximal score). (B) Follow-up imaging 6 mo later with continued PETVAS of 27 despite visual improvement in arterial  $^{18}\text{F}$ -FDG uptake and corresponding decrease in semiquantitative metrics ( $\text{TBR}_{\text{Liver}}$ ) from 3.90 to 2.73. Arrows show areas of increased  $^{18}\text{F}$ -FDG uptake in right and left subclavian/axillary arteries and abdominal aorta.

PET activity; however, TBRs and PETVAS outperformed SUV metrics as evidenced by a higher AUC in the models. When compared against physician assessment of clinical disease activity as the reference standard, all the metrics distinguished between active clinical disease and remission, with lower AUCs than when using reader interpretation of PET activity as the reference standard, showing that clinical assessment is not always linked to vascular inflammation. Both qualitative and semiquantitative approaches were useful in demonstrating a reduction in the burden of vascular inflammation in response to treatment, suggesting they have utility as outcome measures in future treatment trials on LVV.

The ease of implementation makes a qualitative strategy such as PETVAS an attractive option for clinical assessment; however, there are some limitations in comparison to semiquantitative approaches. Qualitative visual assessment requires reader experience and is subjective. Semiquantitative approaches, although more time-consuming and labor-intensive, are more reliable than PETVAS. The granularity and continuous scale of semiquantitative scoring systems leads to a better ability to discriminate change in PET activity across a wider range of values. Use of an ordinal scale such as PETVAS, with a ceiling limit of 27, may not capture important variability in patients with severe vascular inflammation, a situation in which semiquantitative metrics may be preferable or may provide an opportunity to investigate improvements in qualitative scoring.

Semiquantitative approaches correlated better than qualitative assessments with circulating markers of systemic inflammation; however, the correlation was weak. Future biomarker discovery studies on LVV that use  $^{18}\text{F}$ -FDG PET findings as a reference standard for disease activity should consider semiquantitative metrics rather than quantitative metrics of vascular inflammation, for greater precision in detecting candidate circulating biomarkers. In keeping with prior studies, the overall correlation of vascular inflammation with concentrations of acute-phase reactants was poor (28).

TBRs and PETVAS achieved better performance characteristics than SUV when compared with reader interpretation of vascular PET activity, as is in line with a recent study by an independent group (30).  $\text{TBR}_{\text{Liver}}$  and  $\text{TBR}_{\text{Blood}}$  displayed near-identical performance characteristics in association with clinical assessment of disease activity. However,  $\text{TBR}_{\text{Liver}}$  was more strongly associated with reader interpretation of vascular PET activity and with circulating acute-phase reactants.

There are several study strengths to highlight.  $^{18}\text{F}$ -FDG PET image acquisition and subsequent imaging interpretation were performed according to standardized protocols. Clinical and imaging assessments were performed independent of each other to enable unbiased comparisons. A prospective, longitudinal study design was used, which is uncommon in vascular imaging studies on LVV but are important in understanding the utility of  $^{18}\text{F}$ -FDG PET to detect changes in vascular inflammation and in avoiding bias inherent in retrospective study designs. The performance characteristics of PET assessment were tested against both reader interpretation of PET activity and physician assessment of clinical disease activity and performed well against both of these independent reference standards.

There are a few limitations to consider. This study was conducted at a single center using a specific imaging protocol, and these findings should be replicated in other cohorts. Specifically, the qualitative and quantitative imaging metrics reported here are a product of the methodology used for patient preparation, image

acquisition, and image reconstruction at a single institution. Thus, the performance characteristics of discrete cutoffs for metrics, as applied in this study, will vary if the same cutoffs are applied broadly. This study compared the performance of different methods of measuring arterial  $^{18}\text{F}$ -FDG uptake, as might be used in the clinical management of patients or in clinical trials of LVV. However, issues of feasibility and cost must be balanced against potential test utility.

## CONCLUSION

Qualitative and semiquantitative approaches to measuring arterial  $^{18}\text{F}$ -FDG uptake are useful in detecting and monitoring vascular inflammation in LVV. Qualitative metrics, such as PETVAS, can be used for  $^{18}\text{F}$ -FDG PET assessment when simplicity and ease of interpretation are a priority, as is often the case in clinical practice or observational studies. Semiquantitative metrics can be used for  $^{18}\text{F}$ -FDG PET assessment when there is a need for greater precision, such as in randomized clinical trials or translational research focused on biomarker discovery.

## DISCLOSURE

This work was supported through the intramural research program at the National Institute of Arthritis Musculoskeletal and Skin Disease (ZIA-AR-041199). No other potential conflict of interest relevant to this article was reported.

## KEY POINTS

**QUESTION:** How do the performance characteristics of qualitative versus semiquantitative metrics of arterial  $^{18}\text{F}$ -FDG uptake compare, in detecting and monitoring vascular inflammation by PET?

**PERTINENT FINDINGS:** In this prospective, observational cohort study of 95 patients with LVV, qualitative and semiquantitative measurements of arterial  $^{18}\text{F}$ -FDG uptake were useful in monitoring vascular inflammation.

**IMPLICATIONS FOR PATIENT CARE:** Assessment of vascular inflammation by  $^{18}\text{F}$ -FDG-PET should be studied as an outcome measure in clinical trials of LVV.

## REFERENCES

- Jennette JC, Falk RJ, Bacon PA, et al. 2012 revised International Chapel Hill Consensus Conference nomenclature of vasculitides. *Arthritis Rheum.* 2013;65:1–11.
- Rosenbaum D, Millon A, Fayad ZA. Molecular imaging in atherosclerosis: FDG PET. *Curr Atheroscler Rep.* 2012;14:429–437.
- Lee YH, Choi SJ, Ji JD, Song GG. Diagnostic accuracy of  $^{18}\text{F}$ -FDG PET or PET/CT for large vessel vasculitis. *Z Rheumatol.* 2016;75:924–931.
- Prieto-González S, Depetris M, García-Martínez A, et al. Positron emission tomography assessment of large vessel inflammation in patients with newly diagnosed, biopsy-proven giant cell arteritis: a prospective, case-control study. *Ann Rheum Dis.* 2014;73:1388–1392.
- Yamashita H, Kubota K, Mimori A. Clinical value of whole-body PET/CT in patients with active rheumatic diseases. *Arthritis Res Ther.* 2014;16:423.
- Blockmans D, de Ceuninck L, Vanderschueren S, et al. Repetitive  $^{18}\text{F}$ -fluorodeoxyglucose positron emission tomography in giant cell arteritis: a prospective study of 35 patients. *Arthritis Rheum.* 2006;55:131–137.
- Blockmans D, Bley T, Schmidt W. Imaging for large-vessel vasculitis. *Curr Opin Rheumatol.* 2009;21:19–28.
- Both M, Ahmadi-Simab K, Reuter M, et al. MRI and FDG-PET in the assessment of inflammatory aortic arch syndrome in complicated courses of giant cell arteritis. *Ann Rheum Dis.* 2008;67:1030–1033.

9. Lee K-H, Cho A, Choi Y-J, et al. The role of <sup>18</sup>F-fluorodeoxyglucose–positron emission tomography in the assessment of disease activity in patients with Takayasu arteritis. *Arthritis Rheum*. 2012;64:866–875.
10. Dejaco C, Ramiro S, Duftner C, et al. EULAR recommendations for the use of imaging in large vessel vasculitis in clinical practice. *Ann Rheum Dis*. 2018;77:636–643.
11. Slart RHJA, Glaudemans AWJM, Chareonthaitawee P, et al. FDG-PET/CT(A) imaging in large vessel vasculitis and polymyalgia rheumatica: joint procedural recommendation of the EANM, SNMMI, and the PET Interest Group (PIG), and endorsed by the ASNC. *Eur J Nucl Med Mol Imaging*. 2018;45:1250–1269.
12. Grayson PC, Tomasson G, Cuthbertson D, et al. Association of vascular physical examination findings and arteriographic lesions in large vessel vasculitis. *J Rheumatol*. 2012;39:303–309.
13. Kermani TA, Diab S, Sreih AG, et al. Arterial lesions in giant cell arteritis: a longitudinal study. *Semin Arthritis Rheum*. 2019;48:707–713.
14. Meller J, Strutz F, Siefker U, et al. Early diagnosis and follow-up of aortitis with [<sup>18</sup>F]FDG PET and MRI. *Eur J Nucl Med Mol Imaging*. 2003;30:730–736.
15. Meignan M, Gallamini A, Meignan M, et al. Report on the first international workshop on interim-PET-scan in lymphoma. *Leuk Lymphoma*. 2009;50:1257–1260.
16. Hautzel H, Sander O, Heinzl A, et al. Assessment of large-vessel involvement in giant cell arteritis with <sup>18</sup>F-FDG PET: introducing an ROC-analysis–based cutoff ratio. *J Nucl Med*. 2008;49:1107–1113.
17. Rosenblum JS, Quinn KA, Rimland CA, et al. Clinical factors associated with time-specific distribution of <sup>18</sup>F-fluorodeoxyglucose in large-vessel vasculitis. *Sci Rep*. 2019;9:15180.
18. Grayson PC, Alehashemi S, Bagheri AA, et al. <sup>18</sup>F-fluorodeoxyglucose–positron emission tomography as an imaging biomarker in a prospective, longitudinal cohort of patients with large vessel vasculitis. *Arthritis Rheumatol*. 2018;70:439–449.
19. Rudd JHF, Myers KS, Bansilal S, et al. Atherosclerosis inflammation imaging with <sup>18</sup>F-FDG PET: carotid, iliac, and femoral uptake reproducibility, quantification methods, and recommendations. *J Nucl Med*. 2008;49:871–878.
20. Zhuang H, Alavi A. <sup>18</sup>F-fluorodeoxyglucose positron emission tomographic imaging in the detection and monitoring of infection and inflammation. *Semin Nucl Med*. 2002;32:47–59.
21. Arend WP, Michel BA, Bloch DA, et al. The American College of Rheumatology 1990 criteria for the classification of Takayasu arteritis. *Arthritis Rheum*. 1990;33:1129–1134.
22. Hunder GG, Bloch DA, Michel BA, et al. The American College of Rheumatology 1990 criteria for the classification of giant cell arteritis. *Arthritis Rheum*. 1990;33:1122–1128.
23. Langford CA, Cuthbertson D, Ytterberg SR, et al. A randomized, double-blind trial of abatacept (CTLA-4Ig) for the treatment of giant cell arteritis. *Arthritis Rheumatol*. 2017;69:837–845.
24. Koo TK, Li MY. A guideline of selecting and reporting intraclass correlation coefficients for reliability research. *J Chiropr Med*. 2016;15:155–163.
25. Park SH, Goo JM, Jo C-H. Receiver operating characteristic (ROC) curve: practical review for radiologists. *Korean J Radiol*. 2004;5:11–18.
26. Ripplinger J, Sullivan J. Does choice in model selection affect maximum likelihood analysis? *Syst Biol*. 2008;57:76–85.
27. Banerjee S, Quinn KA, Gribbons KB, et al. Effect of treatment on imaging, clinical, and serologic assessments of disease activity in large-vessel vasculitis. *J Rheumatol*. 2020;47:99–107.
28. Quinn KA, Ahlman MA, Malayeri AA, et al. Comparison of magnetic resonance angiography and <sup>18</sup>F-fluorodeoxyglucose positron emission tomography in large-vessel vasculitis. *Ann Rheum Dis*. 2018;77:1165–1171.
29. Kerr GS, Hallahan CW, Giordano J, et al. Takayasu arteritis. *Ann Intern Med*. 1994;120:919–929.
30. Kang F, Han Q, Zhou X, et al. Performance of the PET vascular activity score (PETVAS) for qualitative and quantitative assessment of inflammatory activity in Takayasu’s arteritis patients. *Eur J Nucl Med Mol Imaging*. 2020;47:3107–3117.
31. Arnaud L, Haroche J, Malek Z, et al. Is <sup>18</sup>F-fluorodeoxyglucose positron emission tomography scanning a reliable way to assess disease activity in Takayasu arteritis? *Arthritis Rheum*. 2009;60:1193–1200.

---

---

# Dynamic Amyloid PET: Relationships to <sup>18</sup>F-Flortaucipir Tau PET Measures

Fabio Raman<sup>1-4</sup>, Yu-Hua Dean Fang<sup>1</sup>, Sameera Grandhi<sup>1,2</sup>, Charles F. Murchison<sup>2,5</sup>, Richard E. Kennedy<sup>2,3</sup>, John C. Morris<sup>6</sup>, Parinaz Massoumzadeh<sup>7</sup>, Tammie Benzinger<sup>7</sup>, Erik D. Roberson<sup>2-4</sup>, and Jonathan McConathy<sup>1,2</sup>

<sup>1</sup>Department of Radiology, University of Alabama at Birmingham, Birmingham, Alabama; <sup>2</sup>Alzheimer's Disease Center, University of Alabama at Birmingham, Birmingham, Alabama; <sup>3</sup>Department of Neurology, University of Alabama at Birmingham, Birmingham, Alabama; <sup>4</sup>Center for Neurodegeneration and Experimental Therapeutics, University of Alabama at Birmingham, Birmingham, Alabama; <sup>5</sup>Department of Medicine, University of Alabama at Birmingham, Birmingham, Alabama; <sup>6</sup>Department of Neurology, Washington University in St. Louis School of Medicine, St. Louis, Missouri; and <sup>7</sup>Mallinckrodt Institute of Radiology, Washington University in St. Louis School of Medicine, St. Louis, Missouri

---

Measuring amyloid and predicting tau status using a single amyloid PET study would be valuable for assessing brain AD pathophysiology. We hypothesized that early-frame amyloid PET (efAP) correlates with the presence of tau pathology because the initial regional brain concentrations of radioactivity are determined primarily by blood flow, which is expected to be decreased in the setting of tau pathology.

**Methods:** The study included 120 participants (63 amyloid-positive and 57 amyloid-negative) with dynamic <sup>18</sup>F-florbetapir PET and static <sup>18</sup>F-flortaucipir PET scans obtained within 6 mo of each other. These subjects were predominantly cognitively intact in both the amyloid-positive (63%) and the amyloid-negative (93%) groups. Parameters for efAP quantification were optimized for stratification of tau PET positivity, assessed by either a tauopathy score or Braak regions. The ability of efAP to stratify tau positivity was measured using receiver-operating-characteristic analysis of area under the curve (AUC). Pearson *r* and Spearman  $\rho$  were used for parametric and nonparametric comparisons between efAP and tau PET, respectively. Standardized net benefit was used to evaluate improvement in using efAP as an additional copredictor over hippocampal volume in predicting tau PET positivity. **Results:** Measuring efAP within the hippocampus and summing the first 3 min of brain activity after injection showed the strongest discriminative ability to stratify for tau positivity (AUC, 0.67–0.89 across tau PET Braak regions) in amyloid-positive individuals. Hippocampal efAP correlated significantly with a global tau PET tauopathy score in amyloid-positive participants ( $r = -0.57$ ,  $P < 0.0001$ ). Compared with hippocampal volume, hippocampal efAP showed a stronger association with tau PET Braak stage ( $\rho = -0.58$  vs.  $-0.37$ ) and superior stratification of tau PET tauopathy score (AUC, 0.86 vs. 0.66;  $P = 0.002$ ). **Conclusion:** Hippocampal efAP can provide additional information to conventional amyloid PET, including estimation of the likelihood of tau positivity in amyloid-positive individuals.

**Key Words:** <sup>18</sup>F-florbetapir PET; <sup>18</sup>F-flortaucipir PET; early-phase PET; early-frame amyloid PET

**J Nucl Med 2022; 63:287–293**  
DOI: 10.2967/jnumed.120.254490

**A**lzheimer disease (AD) is the primary cause of age-related dementia, affecting approximately 50 million people worldwide. AD pathophysiologic processes begin years before clinical symptoms. Established neuroimaging biomarkers include neurodegeneration with MRI and <sup>18</sup>F-FDG PET, as well as <sup>18</sup>F-florbetapir, <sup>18</sup>F-florbetaben, and <sup>18</sup>F-flutemetamol for amyloid plaques and <sup>18</sup>F-flortaucipir for tau tangles, respectively (1). These biomarkers can predict pathophysiologic progression and cognitive performance (1,2).

In standard amyloid PET studies, amyloid status is measured 30–120 min after injection, depending on the tracer (3,4). Dynamic acquisition allows collection of a second potential biomarker during the initial tracer flow–delivery phase (5–7), but the clinical role of these early uptake measures is not well defined. Several groups have shown strong correlations between early flow measures from dynamic amyloid PET and regional cerebral perfusion measured with <sup>15</sup>O-water PET (6,8) and between early flow measures from dynamic amyloid PET and regional cerebral glucose metabolism measured with <sup>18</sup>F-FDG (9–11). Other studies have shown that a higher tau burden as measured with PET correlates with regional hypometabolism observed with <sup>18</sup>F-FDG PET (12,13). This body of work led us to pursue the relationship between flow measures with dynamic amyloid PET and the presence of tau pathology.

The objectives of this study were to determine the relationship between early-frame amyloid PET (efAP) and tau PET in amyloid-positive individuals and to assess the potential of dynamic amyloid PET to predict tau PET status. We chose a relatively simple method to calculate efAP in order to increase the clinical relevance and ease of implementation. We hypothesized that reduced efAP would correlate with pathologic tau measured by PET in amyloid-positive individuals evaluated with both dynamic amyloid and tau PET scans within 6 mo of each other.

## MATERIALS AND METHODS

### Study Population

Participants were selected from a cohort at the Charles F. and Joanne Knight Alzheimer Disease Research Center at Washington University in St. Louis. The recruitment, assessment, and exclusion criteria methods have been published previously (14) and are available at <https://knightadrc.wustl.edu>. All studies were approved by the

---

Received Aug. 27, 2020; revision accepted Apr. 23, 2021.  
For correspondence or reprints, contact Jonathan McConathy (jmcconathy@uabmc.edu).  
Published online May 28, 2021.  
COPYRIGHT © 2022 by the Society of Nuclear Medicine and Molecular Imaging.

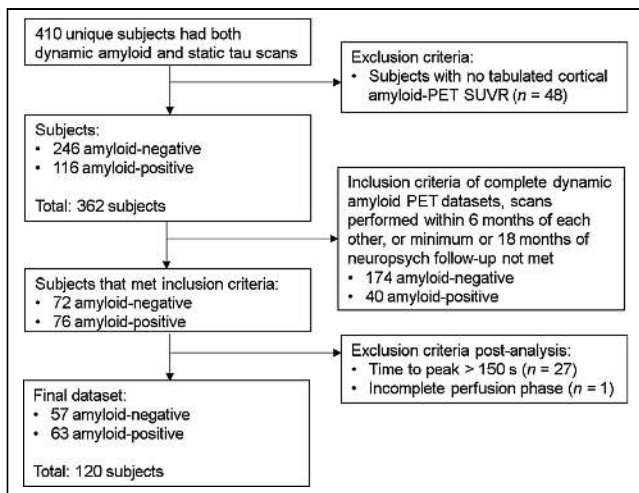


**FIGURE 1.** Flowchart for selection of 63 amyloid-positive and 57 amyloid-negative subjects for analysis in this study from retrospective cohort of 410 subjects.

Institutional Review Board at Washington University in St. Louis and the University of Alabama at Birmingham, indicating compliance with all ethical regulations; informed consent was obtained from all participants before study enrollment.

From the cohort of 410 unique participants, 63 amyloid-positive and 57 amyloid-negative participants who met the eligibility criteria were selected. Subjects had to have dynamic amyloid PET, tau PET, and brain MRI completed within 6 mo of each other and at least 18 mo of neuropsychologic evaluation after completion of imaging. Subjects were categorized as amyloid- and tau-positive or -negative on the basis of established cutoffs from the Charles F. and Joanne Knight Alzheimer Disease Research Center (15,16). Specifically, a mean cortical SUV ratio (SUVR) of 1.19 for amyloid PET (16) and a tauopathy SUVR of 1.22 for tau PET (15) were used to stratify amyloid and tau positivity and screen subjects on the basis of prior analyses. Subject selection and demographics, including cognitive measures, are presented in Figure 1 and Table 1, respectively.

### Image Sets Used for Analysis

$^{18}\text{F}$ -florbetapir PET was performed using an intravenous bolus of 274–418 MBq (7.4–11.3 mCi) on a Siemens Biograph mMR scanner. Data were acquired at the time of injection through 70 min, and reconstruction was performed with 26 frames ( $4 \times 15$  s,  $4 \times 30$  s,  $3 \times 60$  s,  $3 \times 120$  s,  $2 \times 240$  s, and  $10 \times 300$  s). Data from 50 to 70 min after injection were used for amyloid quantification (16). Amyloid SUVRs were calculated in brain regions of interest (ROIs), using the entire cerebellum as the reference ROI.

MRI and  $^{18}\text{F}$ -florbetapir PET acquisition and preprocessing were performed as previously reported (15). Tau PET was performed on a Siemens Biograph 40 PET/CT scanner using an intravenous bolus of 266–400 MBq (7.2–10.8 mCi) of  $^{18}\text{F}$ -florbetapir. Data from 80 to 100 min after injection were used for regional brain tau quantification (15). Tau SUVRs were calculated in brain ROIs, using cerebellar gray matter as the reference ROI.

### Calculation of Flow-Phase Parameters from Dynamic Amyloid PET

Regional dynamic amyloid and static tau PET data were measured using MRI-based FreeSurfer segmentation (17) with an algorithm (biomarker localization, analysis, visualization, extraction, and registration) developed by our group (18). Calculation of efAP from dynamic amyloid PET was performed in Matlab, version R2019b

(MathWorks). A set of time-averaged early-frame efAP intervals was generated in Matlab to test a range of different start points (5%–50% of peak cerebral cortex radioactivity) and endpoints of early-frame intervals (45–600 s from the start of acquisition). In total, 79 target ( $T$ ) ROIs based on FreeSurfer segmentation were integrated over each early-frame interval and subsequently normalized to the integrated time–activity curve of the appropriate reference ( $R$ ) ROI over the same period. Since we used discrete integrals based on the radioactivity ( $A$ ) and associated frame duration ( $D$ ) over the selected set of early frames, the equation could be simplified as follows:

$$\text{efAP}_{\text{SUVR}} = \frac{\sum_{i=\text{start}}^{\text{end}} (A_{Ti} D_{Ti})}{\sum_{i=\text{start}}^{\text{end}} (A_{Ri} D_{Ri})} \quad \text{Eq. 1}$$

### Tau Assessment in Tauopathy Summary Measure, Braak ROIs, and In Vivo Braak Staging

A tauopathy summary measure was previously experimentally derived using a sparse k-means clustering with resampling analysis to identify the ROIs most informative in dividing a cognitively normal population into high-tau and low-tau groups. The highest-weighted FreeSurfer ROIs separating these groups were the entorhinal cortex, amygdala, lateral occipital cortex, and inferior temporal cortex, and an average SUVR in these 4 ROIs was used as a summary metric for  $^{18}\text{F}$ -florbetapir uptake (15).

To replicate Braak neuropathologic staging, tau PET Braak ROIs were created from volume-weighted FreeSurfer subregions as defined by the algorithm our group developed (18). Braak ROIs refers to specific anatomic regions regardless of their tau status, whereas Braak staging refers to the presence of pathologic tau in these ROIs based on  $^{18}\text{F}$ -florbetapir PET. Similar to Schöll et al. 2016, tau PET Braak staging was performed by first categorizing the following volume-weighted, composite ROIs: transentorhinal (Braak stage I/II), limbic (Braak stage III/IV), and isocortical (Braak stage V/VI) (19). To maintain consistency across thresholding techniques, the same 1.22 cutoff (15) as was used to determine tau status was applied to the composite Braak ROIs as follows: subjects positive (SUVR > 1.22) across all 3 ROIs (Braak ROIs I/II, III/IV, and V/VI) were assigned Braak stages V and VI; subjects positive in Braak ROIs I/II and III/IV but negative in V/VI were assigned Braak stages III and IV; subjects positive in Braak ROI I/II but negative elsewhere were assigned Braak stages I and II; and subjects negative across all 3 composite ROIs were assigned Braak stage 0.

### Calculation of Normalized Hippocampal Volume

Hippocampal volume was reported as the percentage of the cerebral cortex to normalize across different participants, as calculated using the following equation (20):

$$\frac{\text{Volume of hippocampus}}{\text{Volume of cerebral cortex}} \times 100\% \quad \text{Eq. 2}$$

### Statistical Analyses

All statistical analyses were performed using SPSS Statistics, version 26.0 (IBM), and Matlab, version R2019b (MathWorks), to compare efAP values with tau PET positivity. All parametric analyses between Braak ROIs used the Pearson  $r$  correlation coefficient, whereas nonparametric analyses across all Braak stages used the Spearman  $\rho$  and nonparametric analyses between individual Braak stages used the Wilcoxon rank sum test. The significance level was a  $P$  value of less than 0.05 with a Bonferroni adjustment for multiple comparisons.

Intersubject, univariate Pearson correlations were performed between efAP and tau PET Braak ROIs I–VI across all 120 subjects, separating subjects by amyloid status. Because only 1 subject was positive in tau PET Braak ROI VI (SUVR > 1.22), this ROI was

**TABLE 1**  
Cohort Demographics

Demographic	Amyloid-positive	Amyloid-negative
Total number of subjects	63	57
Tauopathy*		
Positive	36	7
Negative	27	50
Age (y)	74.36 ± 7.95	69.67 ± 7.71
Sex		
Male	25	24
Female	33	31
Formal education (y)	15.97 ± 2.55	15.85 ± 2.19
Apolipoprotein E-ε4		
Non-carrier of ε4 alleles	24	44
ε4/ε*	27	10
ε4/ε4	7	1
Mini-Mental State Examination <sup>†</sup> (37)	28.10 ± 2.83 (range, 18–30)	29.38 ± 1.01 (range, 25–30)
Clinical Dementia Rating (36)		
0 (not demented)	40	53
0.5 (uncertain or very mild dementia)	14	2
1 (mild dementia)	4	0
Amyloid–tau scan interval (d)	63.17 ± 67.86	63.93 ± 60.84

\*Apolipoprotein E-ε4 (ApoE4) carriers represented as number of ε4 alleles where ε4/ε\* stands for heterozygotes.

<sup>†</sup>Scores range from 30 (best) to 0 (worst).

Qualitative data are number; continuous data are mean ± SD. Of subjects used in study, 5 amyloid-positive and 2 amyloid-negative were missing demographic data and not included in table.

excluded for optimization purposes. Additionally for optimization purposes, and to align with our hypothesis, only the 63 amyloid-positive subjects were used. Area under the curve (AUC) was used to test the performance of the receiver-operating-characteristic (ROC) curve, with efAP being used as the predictor variable and tau positivity (SUVR > 1.22) in tau PET Braak ROIs I–V being used as the outcome variable. The early-frame interval and target ROI corresponding to the maximum AUC (mean ± SD) was selected for the remainder of the study. Similarly, the following 6 reference ROIs for the calculation of efAP were compared for the ability to predict positive tau PET findings: the entire cerebellum, the cerebral white matter, the region pre- and postcentral gyri, the Braak VI tau ROI, the Braak V/VI composite ROI, and the basal ganglia.

Logistic regression models were used to examine the accuracy of efAP in distinguishing between tau-negative and tau-positive groups. The performance of efAP was assessed using ROC curves to compare sensitivity and specificity and to determine the optimal cutoff for efAP and the best time interval. For parameter optimization for the dataset, AUC was calculated and compared with a value of 0.5 (random agreement) using the methods of Obuchowski et al. (21). Sensitivity, specificity, positive predictive value (PPV), and negative predictive value (NPV) were reported at the optimal cutoff based on the maximum Youden index (22). To evaluate performance between biomarkers in stratifying for tau positivity, ROC curves were compared using the methods of DeLong et al. (23), with SE as calculated by SPSS. Additionally, standardized net benefit was used to measure the improvement in efAP as an additional predictor over hippocampal volume, with tau PET positivity set as the outcome variable (24,25).

## RESULTS

### The Hippocampus Is Selected as the Optimal Target ROI, and the Cerebral White Matter Is Selected as the Optimal Reference ROI

Our first objective was to determine which target ROI, reference ROI, and time frames would optimize the predictive performance of efAP. When evaluating efAP as the predictor variable for each of the 79 ROIs and tau positivity as the outcome variable, we found that efAP in tau PET Braak ROI II (hippocampus) showed the strongest AUC across Braak ROIs I–V when using a cerebral white matter reference ROI (0.79 ± 0.082), peaking at 0.89 for tau PET using Braak ROI III (Fig. 2; Supplemental Figs. 1 and 2; supplemental materials are available at <http://jnm.snmjournals.org>). Thus, the hippocampus was chosen as the target ROI and the cerebral white matter was chosen as the reference ROI for efAP calculations for the remainder of the study.

### The Optimal Early-Phase Interval Starts at 5% of Cerebral Cortex Peak Activity and Ends at 3 Minutes After Injection

Next, we determined which dynamic amyloid PET early time interval was most closely associated with tau PET. Using ROC analysis, we compared the AUCs when applying hippocampal efAP as the predictor variable and tau PET positivity across tau PET Braak ROIs I–V as the outcome variables (Supplemental Fig. 3). The endpoint of the early-phase interval was determined to be ideal at 3 min after injection, when the AUC was highest (0.79 ± 0.0042). Selection of the endpoint showed only a 3.3%

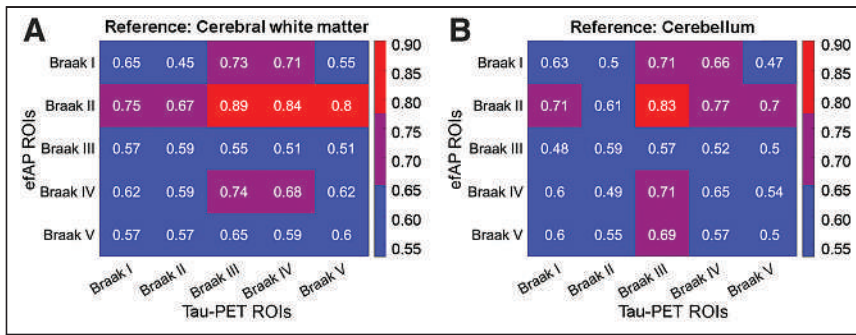


**FIGURE 2.** efAP Braak II ROI (hippocampus) and cerebral white matter chosen as target and reference ROIs, respectively. AUC was used to test performance of ROC curve. AUC between first 5 tau PET Braak ROIs shown for efAP was used as predictor variable, and tau PET was used as outcome variable. Different reference ROIs for calculation of efAP were compared with cerebral white matter (A) and cerebellum (B), showing strongest AUC across efAP in Braak II ROIs, also known as hippocampus. Color scale shows ranges of AUCs in tables, with blue being lowest, purple intermediate, and red highest.

decline from this peak AUC until 6 min after injection and a 8.5% decline until 10 min after injection, emphasizing the relative stability of efAP measurement to varying time intervals. Although altering the start point of the early-phase interval showed only marginal variations in the AUC (<5%), setting a higher threshold of peak cerebral cortex activity for selection of the first frame used in efAP measurement marginally decreased the AUC at all points (Supplemental Fig. 3). Thus, the early-phase interval starting at 5% of cerebral cortex peak activity and ending at 3 min after injection was deemed optimal.

**Hippocampal efAP Correlates with Tau PET Results in Amyloid-Positive Participants**

Next, we evaluated the relationships between hippocampal efAP and tau PET. A visual example of the inverse correlation between hippocampal efAP and tau PET for a cognitively normal subject (tau PET Braak stage 0) and for late-stage disease (tau PET Braak stages V and VI) is shown in Figure 3. Comparing hippocampal efAP with the tauopathy summary measure showed a significant Pearson correlation coefficient in amyloid-positive participants ( $r = -0.57, P < 0.0001$ ). As expected, this relationship was absent in amyloid-negative participants (Fig. 4). Significant

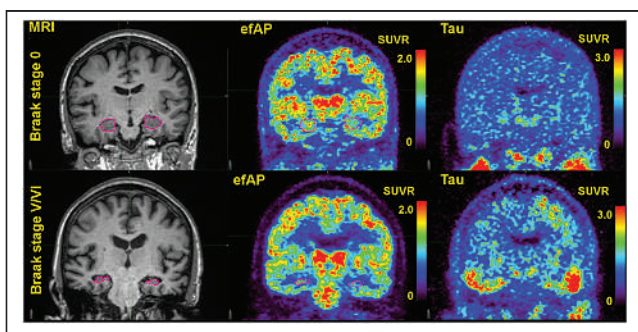


**FIGURE 3.** Example of inverse relationship between hippocampal efAP and tau PET Braak stage. Comparisons of representative subjects from tau PET Braak stage 0 and Braak stages V and VI show appearance of efAP at 2 ends of disease spectrum. First column highlights hippocampus in pink on volumetric MRI, second column shows efAP values from dynamic florbetapir PET, and third column shows tau PET. Intensity scales for PET images are shown as SUVRs.

regional correlations ( $P < 0.001$ ) were also seen in amyloid-positive participants across tau PET Braak ROIs I, II, III, IV, and V ( $r = -0.50, -0.43, -0.58, -0.66, \text{ and } -0.48$ , respectively; Supplemental Fig. 4). ROC analysis revealed that hippocampal efAP could be used to strongly predict tau positivity on tau PET in amyloid-positive participants at a global level using the tauopathy summary measure (AUC, 0.86; efAP cutoff, 1.06; sensitivity, 71%; specificity, 93%; PPV, 93%; and NPV, 72%; Fig. 5A). Regional analyses in individual Braak ROIs I, II, III, IV, and V also showed strong discrimination of tau PET positivity (AUCs of 0.75, 0.67, 0.89, 0.84, and 0.80, respectively; Supplemental Fig. 5).

**Hippocampal efAP Shows Stronger Correlation with Tau Status Than Does Hippocampal Volume**

A reduction in hippocampal volume could reduce SUVs because of partial-volume averaging. Therefore, we compared these 2 biomarkers in amyloid-positive individuals to determine whether hippocampal efAP conveyed additional information not provided by hippocampal volume measurement alone. Characterizing subjects by their tau PET Braak stage showed that both hippocampal efAP and hippocampal volume significantly decreased with increasing tau PET Braak stage (Fig. 6). Hippocampal efAP showed a stronger inverse relationship with tau PET Braak stage ( $\rho = -0.58, P < 0.0001$ ; Fig. 6A) than with hippocampal volume ( $\rho = -0.37, P = 0.0034$ ; Fig. 6B). Wilcoxon rank sum testing between individual groups showed similar results, with the differences between Braak stages I and II and Braak stages III and IV being the greatest for both hippocampal efAP ( $1.11 \pm 0.07$  vs.  $1.00 \pm 0.07$ ,

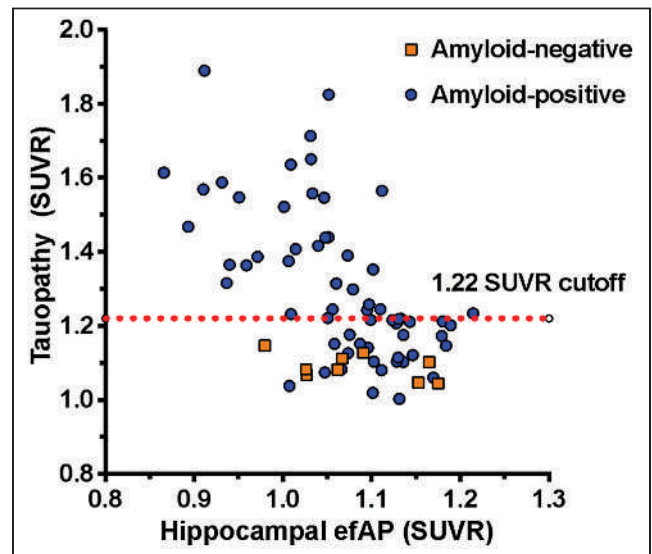


**FIGURE 4.** Comparison of hippocampal efAP and tau PET tauopathy summary measure for amyloid-positive ( $r = -0.57, P < 0.0001$ ) and amyloid-negative ( $r = 0.05, P = 0.69$ ) participants. efAP parallels and predicts tau PET pathology. Tau PET SUVr cutoff was used to stratify subjects for tau positivity.

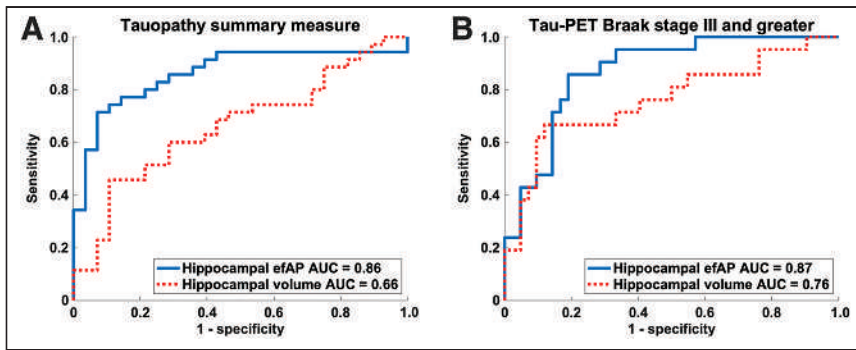


**FIGURE 5.** Predictor variables: ROC curves for efAP and normalized hippocampal volume. Outcome variables: tau PET positivity in tauopathy summary measure and Braak stage III or greater. Hippocampal efAP has stronger discriminatory ability than hippocampal volume for predicting tau PET positivity in amyloid-positive subjects. Tau positivity was defined as SUVR > 1.22. (A) AUC measured for efAP cutoff of 1.06 was 0.86, with sensitivity and specificity of 71% and 93%, respectively, and PPV and NPV of 93% and 72%, respectively; AUC measured for volume was 0.66, with sensitivity and specificity of 46% and 89%, respectively, and PPV and NPV of 84% and 57%, respectively. AUC difference was statistically significant ( $z = 3.08$ ,  $P = 0.002$ ). (B) AUC measured for efAP cutoff of 1.05 was 0.87, with sensitivity and specificity of 86% and 81%, respectively, and PPV and NPV of 69% and 92%, respectively; AUC measured for volume was 0.76, with sensitivity and specificity of 67% and 88%, respectively, and PPV and NPV of 74% and 84%, respectively. This AUC difference did not reach statistical significance ( $z = 1.54$ ,  $P = 0.12$ ).

$P = 0.0002$ ; Fig. 6A) and hippocampal volume ( $1.86 \pm 0.18$  vs.  $1.60 \pm 0.20$ ,  $P = 0.0014$ ; Fig. 6B). When looking at efAP and hippocampal volume as individual predictors of tau PET, the discriminatory ability to predict tau positivity was superior for hippocampal efAP compared with hippocampal volume across the tauopathy summary measure (AUC, 0.86 vs. 0.66;  $z = -3.08$ ;  $P = 0.002$ ) with higher sensitivity (71% vs. 46%), specificity (93% vs. 89%), PPV (93% vs. 84%), and NPV (72% vs. 57%) (Fig. 5A). Although hippocampal efAP showed a trend toward higher predictive ability than hippocampal volume for Braak stage III or greater, the results did not reach statistical significance (AUC, 0.87 vs. 0.76;  $z = 1.54$ ;  $P = 0.12$ ; Fig. 5B).

Similarly, when efAP and volume were grouped as copredictors of tau positivity, efAP showed a significant, additive benefit to simply using hippocampal volume alone to predict tau positivity when utilizing tauopathy summary ROI ( $\Delta$  standardized net

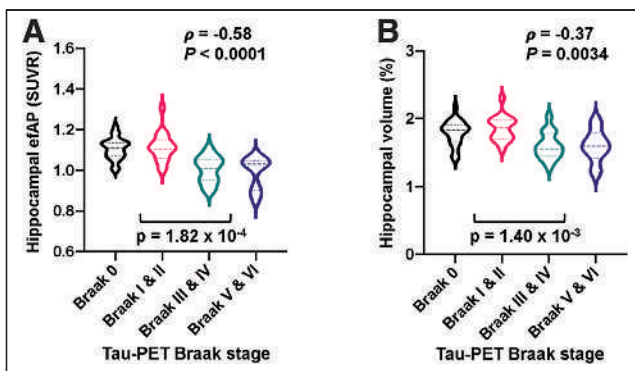


**FIGURE 6.** Amyloid-positive participants stratified by tau PET Braak stage and violin plots displayed for hippocampal efAP (A) and normalized hippocampal volume (B). Tau PET Braak stage shows stronger association with efAP than with volume within hippocampus. Spearman rank  $\rho$  was used to test for association across all groups, and Wilcoxon rank sum test was used to test for association between individual groups, with  $P < 0.05$  denoted as significant.

benefit, 0.3472;  $P = 0.0070$ ) but not when utilizing Braak stage III or greater positivity ( $\Delta$  standardized net benefit, 0.0998;  $P = 0.38$ ).

## DISCUSSION

Hippocampal efAP, a biomarker related to flow during the early frames of dynamic amyloid PET, correlates with tau PET in amyloid-positive individuals. Hippocampal efAP shows promise for predicting tau pathology measured with  $^{18}\text{F}$ -flortaucipir PET and—in predicting tau pathology—provides significant, additive utility over hippocampal volume alone. The use of efAP could add specificity to the assessment of AD with amyloid PET and allow a more comprehensive neuroimaging examination.

Our cross-sectional retrospective analysis demonstrated a strong, significant association between hippocampal efAP and tau PET Braak stage (Fig. 6A). Our results also showed that hippocampal efAP had strong discriminatory performance in

assessing tau positivity at the optimal cutoff, based on the maximum Youden index (22), whether using either a validated tauopathy measure (15) or Braak staging. For instance, hippocampal efAP had a high PPV (93%) and moderate NPV (72%) in amyloid-positive individuals, compared with the tauopathy summary measure with  $^{18}\text{F}$ -flortaucipir PET. The SUVR threshold for tau positivity (1.22) used in this study was based on the previously conducted study at the Charles F. and Joanne Knight Alzheimer Disease Research Center (15). This SUVR threshold may vary with the population and PET study parameters but likely will fall within a fairly narrow range based on studies by other groups, which reported optimal cutoffs ranging from 1.23 to 1.27 (26–28).

Among the 79 target ROIs evaluated for efAP, the hippocampus provided the strongest predictive power for tau positivity. Identification of the hippocampus as the most accurate target ROI for efAP was somewhat surprising, as the precuneus and posterior cingulate gyrus show hypometabolism (29) and hypoperfusion (30) early in the course of AD. Previous research has explored mainly direct, one-to-one regional correlations between  $^{18}\text{F}$ -FDG PET and tau PET (12,13,31) and between  $^{18}\text{F}$ -FDG PET and perfusion (9–11,32), and it is recognized that spatial differences exist between  $^{18}\text{F}$ -FDG and tau PET (31), such as in the hippocampus, where hypometabolism does not correlate well with tau pathology (12). Alternative methods for estimating perfusion from dynamic amyloid PET exist, such as pharmacokinetic modeling (11,33). In particular, Joseph-Mathurin et al. noted that pharmacokinetics-derived R1 values from  $^{11}\text{C}$ -Pittsburgh compound B spatially correlated with  $^{18}\text{F}$ -FDG PET but that early-frame intervals did not (33).

We found that the optimal early-frame time window started at 5% of peak cerebral cortex activity and ended at 180 s after injection. Importantly, efAP was found to be relatively stable up to 6 and 10 min, with small reductions in AUC. Our results were similar to another  $^{18}\text{F}$ -florbetapir study that evaluated the performance of early-frame dynamic amyloid PET imaging compared with  $^{18}\text{F}$ -FDG PET, in which the 1- to 6-min time window provided the

best surrogate for perfusion based on  $^{18}\text{F}$ -FDG PET (32). Several other studies that used  $^{11}\text{C}$ -Pittsburgh compound B instead of  $^{18}\text{F}$ -florbetapir showed similar results (6,10,11,34). One of these studies, in particular, corroborated our results by finding that a shorter interval, specifically 20–130 s after injection, best discriminated between AD patients and controls even though with  $^{18}\text{F}$ -FDG PET a longer interval correlated better (10). Our efAP method focused on quantitative analysis rather than visual interpretation, and it is possible that a longer interval would be more suitable for visual analysis by reducing image noise.

Reduction in hippocampal volume, as measured by MRI, has been robustly validated and remains one of the core biomarkers in AD because of strong evidence supporting its diagnostic and prognostic value (2,35). In our present study, decreases in both hippocampal efAP and hippocampal volume were shown to be inversely correlated with tau PET Braak staging. On the basis of the tauopathy summary measure, hippocampal efAP was a better predictor of tau positivity than was hippocampal volume measurement alone, with additive benefit. A trend toward better performance with hippocampal efAP than with hippocampal volume ( $P = 0.12$ ) was observed for Braak stage III or higher but did not reach statistical significance. The relatively small number of participants with elevated tau in Braak ROI III or higher ( $n = 21$ ) prevents a definitive conclusion regarding the additional value of hippocampal efAP versus hippocampal volume for individual Braak stages.

Our work has limitations that are important to address in future work. Our study population included a large proportion of amyloid-positive subjects who were cognitively normal or had mild cognitive impairment. Our efAP results, including the optimal brain ROI for efAP measurement, may be different in individuals with more advanced AD. For the hippocampal efAP analysis, we chose to focus on amyloid-positive subjects because  $^{18}\text{F}$ -flortaucipir is best suited for imaging the pathologic form of tau that is deposited in AD. Our evaluation of the amyloid-negative subjects was more limited because this group is potentially heterogeneous and is not expected to have many individuals positive for tau based on  $^{18}\text{F}$ -flortaucipir PET. The PET tracer injection technique was not optimized for the early-frame measurement of efAP. Although exclusion criteria did help by removing subjects if the bolus perfusion phase was inadequate based on their time to peak ( $>150$  s), the time to peak for included subjects still varied widely, from 45 to 150 s. Our findings suggest that efAP was not highly sensitive to differences in the rate of bolus delivery, but future studies would benefit from a more standardized injection technique.

## CONCLUSION

We have shown that efAP acquired concurrently with a standard amyloid PET study is a strong predictor of tau pathology in amyloid-positive individuals. Successful development of this approach has the potential to provide information on both amyloid and tau pathology in a single PET session, which may reduce imaging costs and the burden on patients and their families.

## DISCLOSURE

This work was supported by National Institutes of Health grants P20AG068024, RF1AG059009, and T32GM008361; the Medical Science Training Program, the Alzheimer Drug Discovery Foundation, and the Department of Radiology at the University of Alabama

at Birmingham. Tammie Benzinger is funded by NIH grants P50AG005681, P01AG003991, P01AG026276, UF01AG032438, R01AG05326, RF1AG053550, R01AG054567, and R01AG052550. John Morris is funded by NIH grants P50AG005681, P01AG003991, P01AG026276, and UF01AG032438. The recruitment of participants and their clinical characterization and neuroimaging were supported by NIH grants P50AG05681, P01AG03991, and P01AG026276. Avid Radiopharmaceuticals, which is a wholly owned subsidiary of Eli Lilly ( $^{18}\text{F}$ -florbetapir and  $^{18}\text{F}$ -flortaucipir imaging), provided the  $^{18}\text{F}$ -florbetapir doses and partial support for  $^{18}\text{F}$ -florbetapir scanning through an investigator-initiated research grant awarded to Washington University (John Morris and Tammie Benzinger); provided technology transfer; and provided precursor for  $^{18}\text{F}$ -florbetapir. Jonathan McConathy has declared a relationship with Eli Lilly and Avid, to which he provides consulting and from which he receives research support. No other potential conflict of interest relevant to this article was reported.

## ACKNOWLEDGMENTS

Data used in the preparation of this article were obtained from the Charles F. and Joanne Knight Alzheimer Disease Research Center at the Washington University in St. Louis and are available on request (<https://knightadrc.wustl.edu/>).  $^{18}\text{F}$ -flortaucipir was produced under a material transfer agreement between Washington University and Avid Radiopharmaceuticals.

## KEY POINTS

**QUESTION:** Do the first few frames after tracer injection on dynamic amyloid PET predict tau pathology on tau PET in amyloid-positive participants?

**PERTINENT FINDINGS:** This retrospective study showed that decreased activity in the hippocampus as measured with efAP predicts tau pathology on tau PET in amyloid-positive individuals.

**IMPLICATIONS FOR PATIENT CARE:** Our findings show that efAP may facilitate prediction of tau status from an amyloid PET study and provide a more comprehensive neuroimaging assessment of cognitive impairment, with increased specificity for AD.

## REFERENCES

1. Jack CR Jr, Bennett DA, Blennow K, et al. NIA-AA research framework: toward a biological definition of Alzheimer's disease. *Alzheimers Dement*. 2018;14:535–562.
2. Jack CR Jr, Wiste HJ, Weigand SD, et al. Age-specific and sex-specific prevalence of cerebral beta-amyloidosis, tauopathy, and neurodegeneration in cognitively unimpaired individuals aged 50–95 years: a cross-sectional study. *Lancet Neurol*. 2017;16:435–444.
3. Richards D, Sabbagh MN. Florbetaben for PET imaging of beta-amyloid plaques in the brain. *Neurol Ther*. 2014;3:79–88.
4. Wong DF, Rosenberg PB, Zhou Y, et al. In vivo imaging of amyloid deposition in Alzheimer disease using the radioligand  $^{18}\text{F}$ -AV-45 (florbetapir F 18). *J Nucl Med*. 2010;51:913–920.
5. Ossenkoppele R, Prins ND, van Berckel BN. Amyloid imaging in clinical trials. *Alzheimers Res Ther*. 2013;5:36.
6. Blomquist G, Engler H, Nordberg A, et al. Unidirectional influx and net accumulation of PIB. *Open Neuroimag J*. 2008;2:114–125.
7. Forsberg A, Engler H, Blomquist G, Langstrom B, Nordberg A. The use of PIB-PET as a dual pathological and functional biomarker in AD. *Biochim Biophys Acta*. 2012;1822:380–385.
8. Chen YJ, Rosario BL, Mowrey W, et al. Relative  $^{11}\text{C}$ -PiB delivery as a proxy of relative CBF: quantitative evaluation using single-session  $^{15}\text{O}$ -water and  $^{11}\text{C}$ -PiB PET. *J Nucl Med*. 2015;56:1199–1205.

9. Rodriguez-Vieitez E, Leuzy A, Chiotis K, Saint-Aubert L, Wall A, Nordberg A. Comparability of [<sup>18</sup>F]THK5317 and [<sup>11</sup>C]PIB blood flow proxy images with [<sup>18</sup>F]FDG positron emission tomography in Alzheimer's disease. *J Cereb Blood Flow Metab.* 2017;37:740–749.
10. Peretti DE, Vallez Garcia D, Reesink FE, et al. Relative cerebral flow from dynamic PIB scans as an alternative for FDG scans in Alzheimer's disease PET studies. *PLoS One.* 2019;14:e0211000.
11. Rodriguez-Vieitez E, Carter SF, Chiotis K, et al. Comparison of early-phase <sup>11</sup>C-deuterium-l-deprenyl and <sup>11</sup>C-Pittsburgh compound B PET for assessing brain perfusion in Alzheimer disease. *J Nucl Med.* 2016;57:1071–1077.
12. Bischof GN, Jessen F, Fließbach K, et al. Impact of tau and amyloid burden on glucose metabolism in Alzheimer's disease. *Ann Clin Transl Neurol.* 2016;3:934–939.
13. Whitwell JL, Graff-Radford J, Tosakulwong N, et al. Imaging correlations of tau, amyloid, metabolism, and atrophy in typical and atypical Alzheimer's disease. *Alzheimers Dement.* 2018;14:1005–1014.
14. Berg L, McKeel DW Jr, Miller JP, et al. Clinicopathologic studies in cognitively healthy aging and Alzheimer's disease: relation of histologic markers to dementia severity, age, sex, and apolipoprotein E genotype. *Arch Neurol.* 1998;55:326–335.
15. Mishra S, Gordon BA, Su Y, et al. AV-1451 PET imaging of tau pathology in pre-clinical Alzheimer disease: defining a summary measure. *Neuroimage.* 2017;161:171–178.
16. Su Y, Flores S, Wang G, et al. Comparison of Pittsburgh compound B and florbetapir in cross-sectional and longitudinal studies. *Alzheimers Dement (Amst).* 2019;11:180–190.
17. Fischl B, Salat DH, Busa E, et al. Whole brain segmentation: automated labeling of neuroanatomical structures in the human brain. *Neuron.* 2002;33:341–355.
18. Raman F, Grandhi S, Murchison CF, et al. Biomarker localization, analysis, visualization, extraction, and registration (BLAZER) methodology for research and clinical brain PET applications. *J Alzheimers Dis.* 2019;70:1241–1257.
19. Schöll M, Lockhart SN, Schonhaut DR, et al. PET imaging of tau deposition in the aging human brain. *Neuron.* 2016;89:971–982.
20. Risacher SL, Anderson WH, Charil A, et al. Alzheimer disease brain atrophy subtypes are associated with cognition and rate of decline. *Neurology.* 2017;89:2176–2186.
21. Obuchowski NA, Lieber ML, Wians FH Jr. ROC curves in clinical chemistry: uses, misuses, and possible solutions. *Clin Chem.* 2004;50:1118–1125.
22. Habibzadeh F, Habibzadeh P, Yadollahie M. On determining the most appropriate test cut-off value: the case of tests with continuous results. *Biochem Med (Zagreb).* 2016;26:297–307.
23. DeLong ER, DeLong DM, Clarke-Pearson DL. Comparing the areas under two or more correlated receiver operating characteristic curves: a nonparametric approach. *Biometrics.* 1988;44:837–845.
24. Vickers AJ, Elkin EB. Decision curve analysis: a novel method for evaluating prediction models. *Med Decis Making.* 2006;26:565–574.
25. Pepe MS, Fan J, Feng Z, Gerds T, Hilden J. The net reclassification index (NRI): a misleading measure of prediction improvement even with independent test data sets. *Stat Biosci.* 2015;7:282–295.
26. McSweeney M, Pichet Binette A, Meyer PF, et al. Intermediate flortaucipir uptake is associated with Aβ-PET and CSF tau in asymptomatic adults. *Neurology.* 2020;94:e1190–e1200.
27. Ossenkoppele R, Rabinovici GD, Smith R, et al. Discriminative accuracy of [<sup>18</sup>F]flortaucipir positron emission tomography for Alzheimer disease vs other neurodegenerative disorders. *JAMA.* 2018;320:1151–1162.
28. Dodich A, Mendes A, Assal F, et al. The A/T/N model applied through imaging biomarkers in a memory clinic. *Eur J Nucl Med Mol Imaging.* 2020;47:247–255.
29. Kato T, Inui Y, Nakamura A, Ito K. Brain fluorodeoxyglucose (FDG) PET in dementia. *Ageing Res Rev.* 2016;30:73–84.
30. Ishii K, Sasaki M, Yamaji S, Sakamoto S, Kitagaki H, Mori E. Demonstration of decreased posterior cingulate perfusion in mild Alzheimer's disease by means of H<sub>2</sub><sup>15</sup>O positron emission tomography. *Eur J Nucl Med.* 1997;24:670–673.
31. Ossenkoppele R, Schonhaut DR, Scholl M, et al. Tau PET patterns mirror clinical and neuroanatomical variability in Alzheimer's disease. *Brain.* 2016;139:1551–1567.
32. Hsiao IT, Huang CC, Hsieh CJ, et al. Correlation of early-phase <sup>18</sup>F-florbetapir (AV-45/Amyvid) PET images to FDG images: preliminary studies. *Eur J Nucl Med Mol Imaging.* 2012;39:613–620.
33. Joseph-Mathurin N, Su Y, Blazey TM, et al. Utility of perfusion PET measures to assess neuronal injury in Alzheimer's disease. *Alzheimers Dement (Amst).* 2018;10:669–677.
34. Gietl AF, Warnock G, Riese F, et al. Regional cerebral blood flow estimated by early PiB uptake is reduced in mild cognitive impairment and associated with age in an amyloid-dependent manner. *Neurobiol Aging.* 2015;36:1619–1628.
35. Pini L, Pievani M, Bocchetta M, et al. Brain atrophy in Alzheimer's disease and aging. *Ageing Res Rev.* 2016;30:25–48.
36. Morris JC. The Clinical Dementia Rating (CDR): current version and scoring rules. *Neurology.* 1993;43:2412–2414.
37. Folstein MF, Folstein SE, McHugh PR. "Mini-mental state": a practical method for grading the cognitive state of patients for the clinician. *J Psychiatr Res.* 1975;12:189–198.

---

---

# Relative Strengths of Three Linearizations of Receptor Availability: Saturation, Inhibition, and Occupancy Plots

Javad Khodaii<sup>1,2</sup>, Mostafa Araj-Khodaei<sup>2</sup>, Manouchehr S. Vafaei<sup>3-5</sup>, Dean F. Wong<sup>6</sup>, and Albert Gjedde<sup>3,5,7-9</sup>

<sup>1</sup>Department of Mechanical Engineering, Amirkabir University of Technology, Tehran, Iran; <sup>2</sup>Research Center for Integrative Medicine in Aging, Aging Research Institute, Tabriz University of Medical Sciences, Tabriz, Iran; <sup>3</sup>BRIDGE (Brain Research Inter-Disciplinary Guided Excellence), Department of Clinical Research, University of Southern Denmark, Odense, Denmark; <sup>4</sup>Research Unit for Psychiatry, Southern Region, University of Southern Denmark, Odense, Denmark; <sup>5</sup>Department of Nuclear Medicine, Odense University Hospital, Odense, Denmark; <sup>6</sup>Mallinckrodt Institute of Radiology, Washington University, St. Louis, Missouri; <sup>7</sup>Translational Neuropsychiatry Unit, Department of Clinical Medicine, Aarhus University, Aarhus, Denmark; <sup>8</sup>Panum Institute, Department of Neuroscience, University of Copenhagen, Copenhagen, Denmark; and <sup>9</sup>Neurosciences Research Center, Tabriz University of Medical Sciences, Tabriz, Iran

---

We derived three widely used linearizations from the definition of receptor availability in molecular imaging with positron emission tomography (PET). The purpose of the present research was to determine the convergence of the results of the 3 methods in terms of 3 parameters—occupancy ( $s$ ), distribution volume of the nondisplaceable reference binding compartment ( $V_{ND}$ ), and nondisplaceable reference binding potential ( $BP_{ND}$ ) of the radioligand—in the absence of a gold standard. We tested 104 cases culled from the literature and calculated the goodness of fit of the least-squares and Deming II methods of linear regression when applied to the determination of  $s$ ,  $V_{ND}$ , and  $BP_{ND}$  using the goodness-of-fit parameters  $R^2$ , coefficient of variation (root-mean-square error [RMSE]), and the infinity norm ( $\|X\|_{\infty}$ ) with both regression methods. We observed superior convergence among the values of  $s$ ,  $V_{ND}$ , and  $BP_{ND}$  for the inhibition and occupancy plots. The inhibition plot emerged as the plot with a slightly higher degree of convergence (based on  $R^2$ , RMSE, and  $\|X\|_{\infty}$  value). With two regression methods (the least-squares method [LSM] and the Deming II [DM] method), the estimated values of  $s$ ,  $V_{ND}$ , and  $BP_{ND}$  generally converged. The inhibition and occupancy plots yielded the best fits to the data, according to the goodness-of-fit parameters, due primarily to absence of commingling of the dependent and independent variables tested with the saturation (original Lassen) plot. In the presence of noise, the inhibition and occupancy plots yielded higher convergences.

**Key Words:** PET; Lassen plots; inhibition plot; binding potential

**J Nucl Med 2022; 63:294–301**  
DOI: 10.2967/jnumed.117.204453

---

**P**ET is a major tool of biomedical research, with clinical applications that yield images of the distribution of systemically administered positron-emitting radionuclides in tomographic sections of the bodies of human subjects and experimental animals (1,2). Positrons are positively charged anti-electrons emitted from the nuclei of short-lived isotopes typically produced in a cyclotron. Users of this technique image the high-energy (511 keV) annihilation photons that

result from the interaction of a positron with electrons in the tissue. PET images are reconstructed by means of computed tomography of the source of radioactivity, after injection of radiopharmaceuticals according to the principles of nuclear medicine (3). The imaging of neuroreceptors with radioactive ligands by PET applied to living mammalian brains makes it possible to determine receptor density and affinity by appropriate mathematic models (4).

Neuroreceptor studies of brain in vivo using PET require comparisons of so-called binding potentials of radiopharmaceutical receptor ligands at more or less inhibited receptor states to obtain estimates of receptor density and affinity (5). Naganawa et al. (6) proposed methods that reduce bias and variability, and the best use of these approaches is realized by improving the accuracy of data covariance matrices.

The quantitative determination of binding potentials uses a fundamental equation of receptor availability to obtain separate estimates of radioligand volumes of distribution of a specific radioligand (5,7–10). Application of any one of the three linearizations presented here is the first step toward determining binding potentials (or receptor availabilities), the foundation of the receptor-binding analysis. For situations in which a proper reference region with no specific binding of the ligand is not known to exist, or is known not to exist, three linearized versions of a receptor availability equation were derived to estimate the magnitude of the volume of distribution of nondisplaceable ligand ( $V_{ND}$ ) by linear regression. The three different plots emerged when the equation of receptor availability was linearized differently by Lassen et al., Gjedde and Wong, and Cunningham et al. (11–13). Here, the three different plots are referred to as the Saturation, Inhibition, and Occupancy plots, to avoid the uncertain naming of the plots associated with the presentation of the Occupancy plot solution (12), referred to by some authors as the Lassen plot rather than the plot that Lassen et al. (11) actually used and reported. The Occupancy and Saturation plots commingle the dependent and independent variables by calculating the difference between the volume estimates for baseline and inhibition states, unlike the Inhibition plot, which simply plots the apparent total volume of distribution of the radioligand ( $V_T$ , also known as the partition volume or partition coefficient of the ligand) at inhibition ( $V_{T(i)}$ , ordinate) against the values at baseline ( $V_{T(b)}$ , abscissa).

The aim of the present research was to determine the accuracy and precision of these three widely used linearizations of receptor

---

Received Dec. 15, 2020; revision accepted Apr. 23, 2021.  
For correspondence or reprints, contact Albert Gjedde (albert.gjedde@clin.au.dk).  
Published online Jun. 4, 2021.  
COPYRIGHT © 2022 by the Society of Nuclear Medicine and Molecular Imaging.

availability (Saturation, Inhibition, and Occupancy plots) from experimental data. We compared 104 cases culled from the literature, with the accuracy of each plot being evaluated by the least-squares and Deming II methods of linear regression.

## MATERIALS AND METHODS

The quantitative determination of binding potentials uses a fundamental equation of receptor availability to obtain separate estimates of radioligand volumes of distributions for a specific radioligand (5,7–10):

$$1-s = \frac{V_{T(i)} - V_{ND}}{V_{T(b)} - V_{ND}} \quad (1)$$

where Equation 1 is the formulation of the relative or fractional receptor availability in terms of the relevant volumes of distribution. Here,  $s$  represents the occupancy and  $V_{T(i)}$  is the apparent total volume of distribution of the sum of the specifically bound and the nonspecifically dissolved ligand molecules occupying the receptor, whereas  $V_{ND}$  refers to the distribution volume of the tracer in a nonbinding compartment, also known as the partition volume or partition coefficient of the ligand.  $V_{T(b)}$  refers to the apparent total volume of distribution of the radioligand in a baseline state where the receptor is not occupied by a specific inhibitor.

Application of any one of the three linearizations presented here is the first step toward determining binding potentials (or receptor availabilities), the foundation of the receptor-binding analysis. The non-displaceable reference binding potential ( $BP_{ND}$ ) enters into the particular Eadie–Hofstee version of the linearized Michaelis–Menten equation that yields both the maximum binding ( $B_{max}$ ) and the affinity constant (Michaelis half-saturation quantity or mass),  $K_D$ , of the receptors,

$$B = B_{max} - K_D BP_{ND} \quad (2)$$

where  $B$  is the quantity of bound ligand. The binding potential is defined as the ratio of the volumes of distribution of specifically bound (displaceable) and non-specifically bound (non-displaceable) ligand quantities (14,15). To determine the binding potential of a radioligand, the volumes of distribution are entered into the relationship that defines the binding potential (2,5,16):

$$BP_{ND} = \frac{V_T - V_{ND}}{V_{ND}} \quad (3)$$

which is applicable both to the receptor binding baseline and to multiple degrees of receptor blockade, provided the  $V_{ND}$  estimate is unaffected by the blockade. To calculate binding potentials, it is necessary to know the distribution of unbound ligand in a region of no binding, but a suitable reference region often does not exist or is not known to exist.

The three linearizations evaluated here served to determine a reference volume of distribution of radioligands when no reference region (i.e., a region with absence of specific binding) is known to exist in the brain. From the volumes of distribution of the radioligand in the absence of displaceable binding ( $V_{ND}$ ), we used the three different linearizations to obtain binding potentials for radioligands used in published studies.

### Saturation Plot

As a novel steady-state approach to determining the binding potentials of tracers with an unknown reference volume of distribution, in 1995, Lassen et al. (11) proposed to compare two levels of receptor occupancy, one essentially at zero for the labeled tracer itself and the other in the midrange of occupancy by addition of unlabeled ligand. The concentration of the unlabeled ligand in brain water would be zero in the tracer-alone study and would have a constant value in the inhibition studies. To obtain the volume of nonspecific binding, Lassen et al. (11) linearized Equation 1 in the form of the plot we here call the Saturation plot. The plot yields the estimate of  $V_{ND}$  by plotting the baseline volume of distribution ( $V_{T(b)}$ ) as a function of the difference between the baseline and inhibition volumes of distribution ( $\Delta V_T = V_{T(b)} - V_{T(i)}$ ) as shown in Figure 1A,

$$V_{T(b)} = \frac{1}{s} \Delta V_T + V_{ND} \quad (4)$$

where the estimate of  $V_{ND}$  is the ordinate intercept of the linear regression, and the estimate of the ratio  $1/s$  is the slope of the regression.

### Inhibition Plot

Certain receptor ligands tend altogether to lack a reference brain region of no specific binding, from which it is therefore not possible to assess nonspecific binding for the purpose of calculating the binding potential in regions of specific binding. Realizing that the uncertain choice of a reference volume of distribution for the ligand can lead to an erroneous estimation of the occupancy, in 2000, Gjedde and Wong (12) proposed to linearize Equation 1 to obtain the form of the

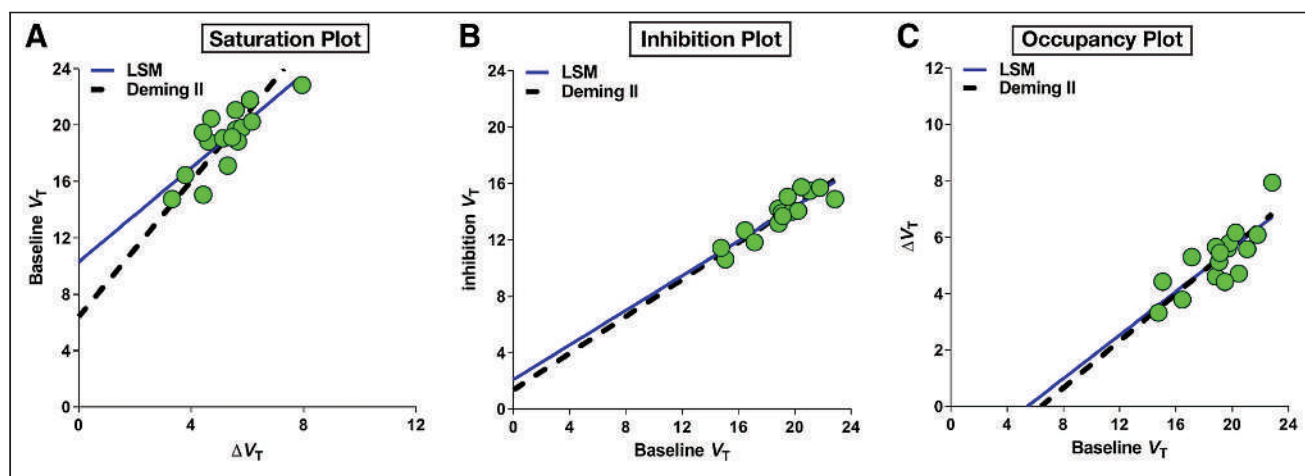


FIGURE 1. Three linearization plots ([A] Saturation, [B] Inhibition, [C] Occupancy) of data from Horti et al. (17) (inhibition dose 0.5 mg).

Inhibition plot. The plot estimates  $V_{ND}$  by relating  $V_{T(i)}$  to  $V_{T(b)}$  by linear regression, as shown in Figure 1B,

$$V_{T(i)} = (1-s)V_{T(b)} + s V_{ND} \quad (5)$$

where the estimate of  $V_{ND}$  is the intercept of the linear regression line with the line of identity.

### Occupancy Plot

In 2010, Cunningham et al. (13) inverted the axes of the Saturation plot and showed that the graphical analysis of the inverted relationship at each of the different doses of unlabeled ligand provided a means to determine drug occupancies. The inversion of the axes of the Saturation plot was presented as the *Occupancy plot*, a term we adopt here to avoid the lack of specificity of the term *Lassen plot*. The linearization known as the Occupancy plot treats the differences in the volumes of distribution between the baseline and challenge conditions,  $\Delta V_T$ , as a function of the baseline volume of distribution, as shown in Figure 1C,

$$\Delta V_T = s V_{T(b)} - s V_{ND} \quad (6)$$

where  $V_{ND}$  is the abscissa intercept. It is evident from the derivations that the Saturation and Occupancy plots have mutually inverted axes.

### Source of Published Data

To use any one of the three linearizations, at least two consecutive PET recordings with two different levels of receptor occupancy are required. For the Inhibition plot, unlike the Saturation and Occupancy plots, the dependent ( $V_{T(i)}$ ) and independent ( $V_{T(b)}$ ) variables are not commingled. The estimates of the fractional receptor availability ( $1 - s$ ) and  $V_{ND}$  are then obtained directly from the volumes of distribution. As the three linearizations are derived from the same original relative receptor availability formulation (Eq. 1), they must all meet the requirements that there are different brain regions with different receptor densities (maximum binding) that remain unchanged in the challenge condition and that the values of receptor affinity (Michaelis half-saturation concentration) and  $V_{ND}$  are the same for all relevant regions and remain the same for all challenges.

To assess the advantages and disadvantages of each of the three linearizations, the following names were searched in the PubMed and Scopus databases: "Lassen plot," "Saturation plot," "Gjedde plot," "Inhibition plot," "Cunningham plot," and "Occupancy plot." In the initial search, 60 published reports were found. The original datasets were not available for 36 of the identified studies.

### Linear Regressions of Published Data

We analyzed the 24 remaining published reports, which consisted of 104 sets of data. In 7 cases, the authors submitted data (8,17–22), and for the remaining 17 reports, we extracted the data from published graphs with GetData Graph Digitizer digitization software (11,13,23–37). The characterization of the data in terms of species, sex, age, drug, dose, and other identifiers is presented in Table 1. We used two linear regression methods, LSM and DM, to obtain parameter estimates, as implemented in MATLAB (MathWorks). Using slope and intercept estimates, we determined  $s$  and  $V_{ND}$  and evaluated the accuracy.

LSM is a standard approach in regression analysis, with its most important application being in data fitting. The best fit of LSM minimizes the sum of squared residuals, which are the differences between an observed value and the value fitted by the model. In LSM, 2 variables ( $x, y$ ) are obtained by regression of  $y$  on  $x$ , where  $x$  is assumed to represent independent-variable values obtained without error (38). DM regression is an errors-in-variables model that yields the line of best fit for a 2-dimensional dataset. It differs from LSM by the assumption of

errors in both independent and dependent variables that allow for any number of predictors and a more complicated error structure. In DM, observations are subject to additive random variations of both  $x$  and  $y$  (39,40).

To test the goodness of fit of the linear regressions, we calculated the coefficient of determination ( $R^2$ ), coefficient of variation (root-mean-square error [RMSE]), and infinity norm ( $\|X\|_\infty$ ). The  $R^2$  estimate is a commonly used indicator of the goodness of fit that is applicable only to LSM, as in other applications it may result in negative values or values greater than unity. In contrast, RMSE is applicable to all linear regressions. For  $n$  sets of ( $x_i, y_i$ ) data, the RMSE,  $R^2$ , and  $\|X\|_\infty$  measures can be expressed according to Rawlings et al. (38):

$$R^2 = 1 - \frac{SS_{res}}{SS_{tot}} \quad (7)$$

$$RMSE = \sqrt{SS_{res}/n} \quad (8)$$

where  $n$  is the number of observations, and

$$\|X\|_\infty = \max(f_i - y_i) \quad (9)$$

where  $f_i$  is the predicted value of  $y$  at  $x_i$ ,  $SS_{tot}$  is the total sum of squares or the variance of the data,

$$SS_{tot} = \sum_{i=1}^n (y_i - \bar{y})^2 \quad (10)$$

$SS_{res}$  is sum of squares of residuals,

$$SS_{res} = \sum_{i=1}^n (f_i - y_i)^2 \quad (11)$$

and  $\bar{y}$  is the mean of  $y_i$ ,

$$\bar{y} = \frac{1}{n} \sum_{i=1}^n y_i \quad (12)$$

The closer the value of  $R^2$  is to unity, the better the fit is to the linearization. The closer the RMSE and  $\|X\|_\infty$  values are to zero, the better the fit of the linearization is held to be (38,41).

### Calculation and Evaluation of Binding Potentials

We compared binding potential estimates ( $BP_{ND}$ ) for the baseline (base  $BP_{ND}$ ) and inhibition (challenge  $BP_{ND}$ ) conditions according to Equation 3. In total, we compared 104 times 12, or 1,248, sets of  $BP_{ND}$  estimates according, first, to the equation for the percentage differences in the LSM and DM results for each of the 3 linearizations, exemplified here for the inhibition plot as

$$\Delta D_{(inhib)} = 100 \frac{BP_{(LSM)} - BP_{(DM)}}{(BP_{(LSM)} + BP_{(DM)})/2} \quad (13)$$

and, second, according to the equation for the percentage differences in the three linearizations of each of the two regression methods, exemplified here for the comparison of LSM and DM results for the Inhibition and Occupancy plots,

$$\Delta D_{(LSM)} = 100 \frac{BP_{(inhib)} - BP_{(occup)}}{(BP_{(inhib)} + BP_{(occup)})/2} \quad (14)$$

and

$$\Delta D_{(DM)} = 100 \frac{BP_{(inhib)} - BP_{(occup)}}{(BP_{(inhib)} + BP_{(occup)})/2} \quad (15)$$

**TABLE 1**  
Categorization of Data

Source	Cite	Case no.	Data no.	Type	Male	Female	Age (y)	Weight (kg)	Drug or material	Doses	Duration	Tracer
Owen et al. (23)	92	10	7-15	Human	-	-	-	-	XBD173	10-90 mg	-	<sup>11</sup> C-PBR28
Naganawa et al. (24)	35	2	13	Human	-	-	25-52	-	PF-04455242	30 mg	1.5, 8 h	<sup>11</sup> C-GR103545
Cunningham et al. (13)	197	4	9	Human	-	-	-	-	5HT 1A	1.5, 10, 150 µg/kg	1 h	<sup>11</sup> C-WAY100635
Kågedal et al. (25)	31	3	10	Human	-	-	-	-	AZD2066	3.5, 6.9, 13.5 mg	-	<sup>11</sup> C-ABP688
Jucaite et al. (26)	28	2	9	Human	2	0	22-44	-	AZD5213	0.1, 0.3 mg	2 h	<sup>11</sup> C-GSK189254, <sup>11</sup> C-AZ12807110
Eimendorst et al. (27)	57	14	9-23	Human	-	-	24-68	-	Caffeine	0-9 mg/kg	36 h	<sup>18</sup> F-CP PFX
Ridler et al. (28)	24	6	12-15	<i>Papio anubis</i>	6	0	-	22.4	P943, SB-616234-S, SB-714786	25, 100 µg	-	<sup>11</sup> C-P943
Fuchigami et al. (29)	3	2	6	Rhesus monkey	-	-	-	4.90, 5.55	SSR504734	1.5 and 4.5 mg/kg	-	<sup>11</sup> C-N-methyl-SSR504734
Logan et al. (30)	4	1	7	Human	-	-	23-67	-	Letrozole	2.5 mg	2.5 h	<sup>11</sup> C-Vorozol e
Martin-Facklam et al. (31)	38	5	26-39	Human	5	-	20-51	-	Bitopertin	5, 15, 30, 60, 175 mg	-	<sup>11</sup> C-RO5013853
Lassen et al. (11)	18	1	31	Human	1	0	22-65	-	Benzodiazepines	0.6 mg	-	<sup>11</sup> C-flumazenil
Myers et al. (32)	19	12	24	Human	-	-	Avg: 43,44	-	Zolpidem, placebo	1.37-3.71 µg	1.5 h	<sup>11</sup> C-flumazenil, <sup>11</sup> C-Ro15-4513
Phan et al. (33)	1	1	9	Sprague-Dawley rats	0	1	-	0.225-0.250	Cyclosporine	1 mg/kg	1.5 h	<sup>11</sup> C-yohimbine
Etrup et al. (19)	41	5	10	Danish Landrace pigs	0	5	-	19	SSR180711 NS14492	1, 10 mg/kg	0.5, 4 h	<sup>11</sup> C-NS14492
Ramakrishnan et al. (18)	4	2	12	Wistar Hannover rat	2	0	-	-	Cutamesine	0.3, 1 mg/kg	-	<sup>11</sup> C-SA4503
Visser et al. (34)	5	1	11	Wistar rats	1	0	-	0.317	MDL 100907	1 mg/mL	-	<sup>11</sup> C-MDL 100907
Milak et al. (35)	53	6	8	<i>Papio anubis</i>	6	0	-	-	Citalopram, fenfluramine	2, 2.5, 4 mg/kg	-	<sup>11</sup> C-CUMI-101
Hillmer et al. (36)	12	3	9	<i>Macaca mulatta</i>	2	1	6-15	7-14	ASEM	0.69, 1.24 mg/kg	-	<sup>18</sup> F-DBT-10
Paul et al. (37)	11	2	14	Wistar rats	2	0	-	0.304	CPA, caffeine	0.25, 40 mg/kg	15 min	<sup>11</sup> C-IMPDX
Phan et al. (8)	11	10	6	Sprague-Dawley rats	-	-	-	0.250-0.300	Amphetamine	-	6-28 min	<sup>11</sup> C-yohimbine
Horti et al. (17)	41	2	16	Baboon	2	0	-	20.1-26.0	ASEM	0.5, 5 mg/kg	5-90 min	<sup>18</sup> F-ASEM
Narendran et al. (20)	28	6	11	Human	5	1	Avg: 24	-	Aripiprazole	15 mg	3	<sup>11</sup> C-FLB 457
Koole et al. (22)	12	3	15	Human	-	-	20-54	-	Padsevoniil	6.25 mg	2	<sup>11</sup> C-UCB-J
Wong et al. (21)	12	1	20	Human	1	0	18-52	-	DMXB-A	150 mg	40 min	<sup>18</sup> F-ASEM

Avg = average.

### Goodness of Fit

We considered sets of data ( $V_{T(b)}$ ,  $V_{T(i)}$ ) directly measured in relevant studies. Because of sources of error, which include surgery, environment, and device errors, we predicted differences to exist between the theoretic but unknown value of a parameter and the measured value (42). We expressed the theoretic value of a parameter as ( $V_{T(b)}$ ,  $V_{T(i)}$ ),

$$V_{T(i)}^* = V_{T(i)} - e_1 \quad (16)$$

and

$$V_{T(b)}^* = V_{T(b)} - e_2 \quad (17)$$

where  $e_1$  and  $e_2$  are the differences between real and measured values of  $V_{T(b)}$  and  $V_{T(i)}$ , respectively. We expressed the real value of the differences between baseline and inhibition volumes of distribution as  $\Delta V_T^*$ ,

$$\Delta V_T^* = V_{T(i)}^* - V_{T(b)}^*$$

which after substitution yielded,

$$\Delta V_T^* = (V_{T(i)} - e_1) - (V_{T(b)} - e_2)$$

or

$$\Delta V_T^* = (V_{T(i)} - V_{T(b)}) - (e_1 - e_2),$$

which yielded,

$$\Delta V_T^* = (V_{T(i)} - V_{T(b)}) - (e_3) \quad (18)$$

where  $e_3$  refers to the difference between the real and measured values of  $\Delta V_T$ .

### Source of Convergence

In this research, we defined the closeness of the fitted model to the data as convergence. For the set of ( $x_i$ ;  $y_i$ ), regardless of method, the linearization has the form,

$$y = ax + b \quad (19)$$

with the real values in the equation expressed as,

$$y = a^*x + b^* \quad (20)$$

where ( $a, b$ ) are the estimated values of slope and ordinate intercept and ( $a^*, b^*$ ) are the real values of slope and ordinate intercept. As discussed, the measurement error of ( $x_i$ ;  $y_i$ ) yields a difference between real and estimated values of slope and ordinate

**TABLE 2**

Differences Between Real and Estimated Values of  $s$  and  $V_{ND}$  of Inhibition, Occupancy, and Saturation Plots

Method	$s$	$V_{ND}$
Inhibition	$s^* + e_1$	$\frac{s^* V_{ND} - e_1}{s^* + e_1}$
Occupancy	$s^* - e_1$	$\frac{s^* V_{ND} - e_1}{s^* - e_1}$
Saturation	$\frac{s^*}{1 - s^* - e_1}$	$V_{ND}^* - e_2$

intercept as

$$a^* = a - e_1^* \quad (21)$$

and

$$b^* = b - e_2^* \quad (22)$$

where  $e_1^*$  is the error between real and estimated values of slope and ordinate intercept. By substituting Equations 20 and 21 in the 3 original equations (Eqs. 4–6), we calculated the differences between real and estimated values of  $s$  and  $V_{ND}$ . Here, occupancy and  $V_{ND}$  are the estimated values, and  $s^*$  and  $V_{ND}^*$  are the real (unknown) values. The differences between the real and estimated values of  $s$  and  $V_{ND}$  are listed in Table 2.

## RESULTS

### Digitization Accuracy

We compared the linearizations of data obtained from the authors directly or by digitization of published graphs. With the submitted data available for comparison, we showed the mean error of digitization to be less than 0.85%, confirming the accuracy of the digitization. Here, we present the results from the analysis of the digitized values of  $V_{T(b)}$  and  $\Delta V_T$  from the report of Horti et al. (17), used to obtain the  $V_{T(i)}$  values for the 0.5-mg receptor inhibitor challenge. With the Inhibition, Saturation, and Occupancy linearizations for the LSM and DM regressions, we obtained the parameter values from the linear regressions of the data presented in Figure 1, with the resulting regressions and estimates of  $s$  and  $V_{ND}$  being presented in Figure 2. For the Saturation plot, we used  $\Delta V_T$  as the independent variable ( $x$ ) and  $V_{T(b)}$  as the dependent variable ( $y$ ), whereas for the Occupancy plot, we used

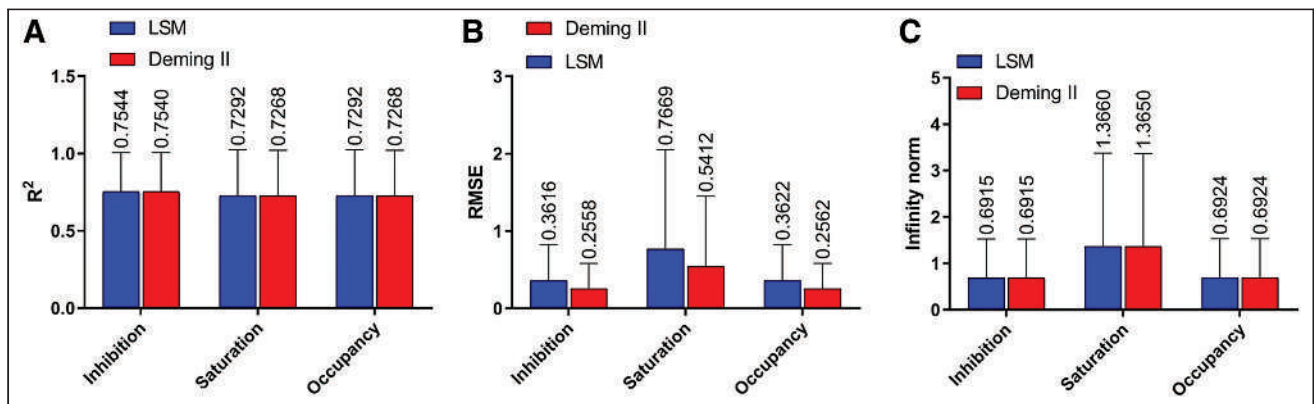


**FIGURE 2.** Average values of measures of goodness of fit of the Inhibition, Saturation, and Occupancy plots.

**TABLE 3**

Average Precision of Regressions of Inhibition, Occupancy, and Saturation Plots

Plot	Method	$R^2$	RMSE	$\ X\ _\infty$
Inhibition	LSM	$0.75 \pm 0.25$	$0.36 \pm 0.46$	$0.69 \pm 0.84$
	DM	$0.75 \pm 0.25$	$0.26 \pm 0.33$	$0.69 \pm 0.84$
Saturation	LSM	$0.73 \pm 0.29$	$0.77 \pm 1.29$	$1.40 \pm 2.01$
	DM	$0.73 \pm 0.29$	$0.55 \pm 0.91$	$1.40 \pm 2.01$
Occupancy	LSM	$0.73 \pm 0.29$	$0.36 \pm 0.46$	$0.69 \pm 0.84$
	DM	$0.73 \pm 0.29$	$0.26 \pm 0.33$	$0.69 \pm 0.84$

$\Delta V_T$  as the dependent variable ( $y$ ) and  $V_{T(b)}$  as the independent variable ( $x$ ).

**Plot Analysis**

Using the linearization goodness-of-fit parameters  $R^2$ , RMSE, and  $\|X\|_\infty$ , the comparisons yielded the results listed in Table 3 and Figure 2. The mean value of  $R^2$  (for the 104 samples) for the Inhibition plot was slightly closer to unity, identifying the Inhibition plot as the plot with slightly greater fit to the experimental data. In addition, the mean values of RMSE and  $\|X\|_\infty$  for the Inhibition plot were closest to zero, again as the most accurate of the three plots. In 87 of the 104 cases, the Inhibition plot yielded the lowest RMSE and  $\|X\|_\infty$  values, implying that the inhibition plot had superior accuracy in the 87 cases.

The effects of the regression method (LSM or DM) on the estimated values of  $s$ ,  $V_{ND}$ , and  $BP_{ND}$  are shown in Figure 3. The estimates of  $s$ ,  $V_{ND}$ , and  $BP_{ND}$  for the two regression methods (LSM and DM) generally converged. The average deviation was less than 0.1% for  $s$  and  $V_{ND}$  and was less than 3% for  $BP_{ND}$ . We also compared the effects of choice of method on the estimated values of  $s$ ,  $V_{ND}$ , and  $BP_{ND}$ . The deviations of  $s$ ,  $V_{ND}$ , and  $BP_{ND}$  for the three plots (Inhibition, Saturation, and Occupancy) are shown in Figure 3. From the figure, we conclude that the results of the Inhibition and Occupancy plots normally converged for both LSM and DM. The average difference of the inhibition and occupancy plot results was less than 2%. In contrast, we generally found considerable differences between the results of the Saturation plot and the results of the Inhibition and Occupancy plots. The average difference shown in Figure 3 is close to 40%. Bland–Altman graphs for the binding potentials determined with 0.5-mg receptor inhibitor blockade by Horti et al.

(17) are shown in Supplemental Figure 1 (supplemental materials are available at <http://jnm.snmjournals.org>).

**Analysis of Noise Simulation**

To investigate the effect of noise on the convergence of the results of different plots, two sets of theoretic data (data without noise) were created on the basis of the Horti et al. (17) data at two levels of inhibition (0.5- and 5-mg inhibitor administration). We considered five sets of data and calculated the values of  $s$  and of  $V_{ND}$  using the three plots and two different linearizations (data without noise; data with noise of  $K = 0.1$ ,  $K = 0.2$ ,  $K = 0.5$ , where  $K$  is the chosen SD). The results of the linearizations are listed in Supplemental Table 1 and Supplemental Figure 2. As shown in Supplemental Figure 3, for the data without noise, all

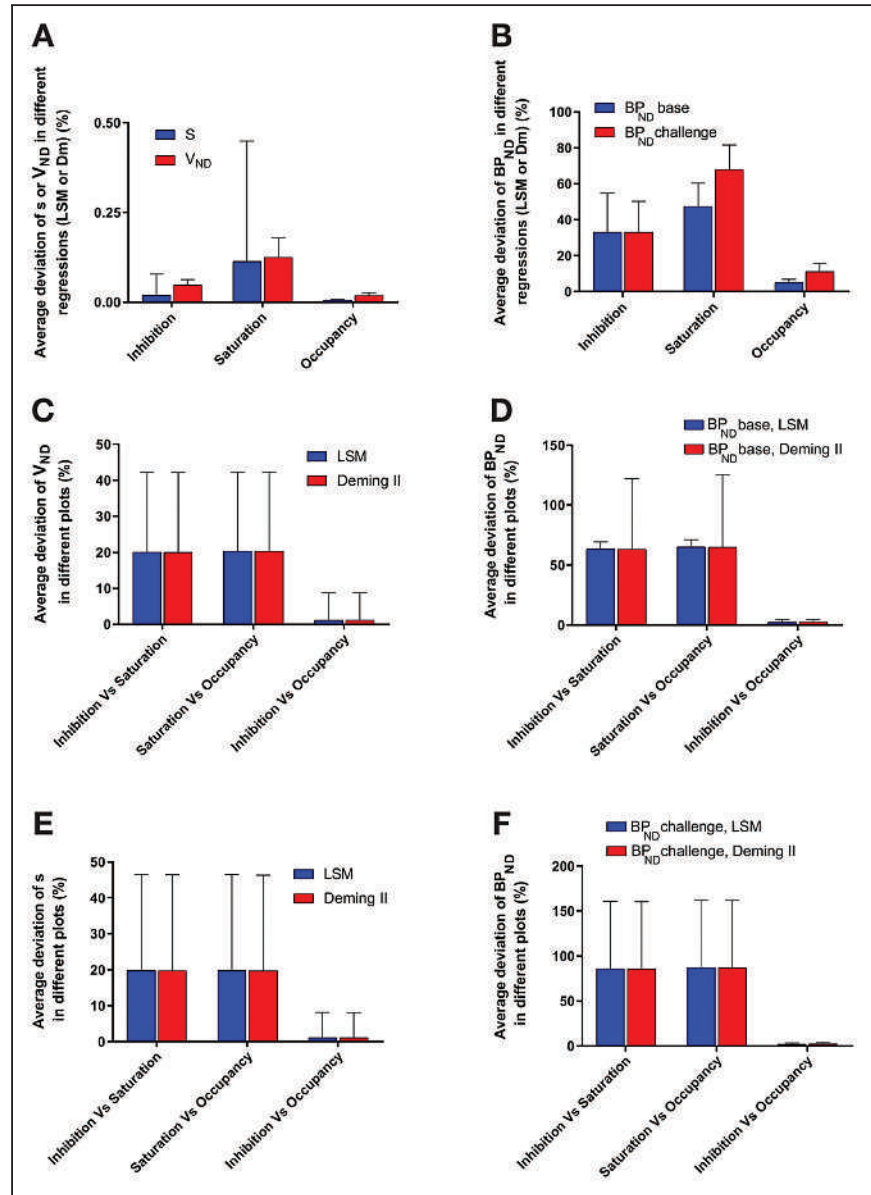


**FIGURE 3.** Differences of  $s$ ,  $V_{ND}$ , and  $BP_{ND}$  among Inhibition, Saturation, and Occupancy plots. (A)  $s$  and  $V_{ND}$  LSM vs. Deming II. (B)  $BP_{ND}$  LSM vs. Deming II. (C)  $V_{ND}$  LSM and Deming II in different plots. (D)  $BP_{ND}$  Base LSM and Deming II in different plots. (E)  $s$  LSM and Deming II in different plots. (F)  $BP_{ND}$  Challenge LSM and Deming II in different plots.

three plots and two linearizations yield identical results. For the convergence of the three plots, it is evident that the RMSE of the data without noise for all three plots is approximately zero ( $10^{-9}$ ). However, as is shown in Supplemental Figure 4, in the presence of noise, the inhibition and occupancy plots yielded a lower RMSE, consistent with greater convergence.

## DISCUSSION

In the present examination of the plots of competition, we linearized the formulation of the fractional receptor availability (Eq. 1) into three equations underlying the different regressions, which we refer to as the Saturation, Inhibition, and Occupancy plots. The purpose of all three linearizations is to estimate the reference volume of distribution,  $V_{ND}$ , required to calculate the binding potential of a radioligand. We undertook the comparisons because the extent to which the results of the three plots converge or diverge is unknown. We culled 104 cases on the basis of one or more of the plots, and we tested the results of the three plots linearized by LSM and DM regressions.

As shown in Table 3, for both  $s$  and  $V_{ND}$ , the differences between estimated and real values are of the same order of magnitude for the Inhibition and Occupancy plots but are much greater for the Saturation plot. For this reason, the average deviation of the calculated values of  $s$  and  $V_{ND}$  for the Inhibition and Occupancy plots was less than 0.1%, and the results generally converged. In contrast, there was more than a 35% difference between the results of the Saturation plots and the results of the Inhibition and Occupancy plots. In Equations 16–18,  $e_1$ ,  $e_2$ , and  $e_3$  are the error values resulting from the divergence of individual plots. The parameter  $e_3$  may be smaller than  $e_1$  and  $e_2$  but frequently is not. As  $e_1$  and  $e_2$  do not adopt exclusively positive or negative values, errors can be superimposed. For this reason, the use of  $\Delta V_T$  differences may result in higher levels of error and reductions of goodness of fit. Among the three methods, the Inhibition plot avoided the use of the commingled variable  $\Delta V_T$ . As expressed by the three indicators  $R^2$ , RMSE, and  $\|X\|_\infty$ , the Inhibition plot was shown to yield slightly greater fit for both LSM and DM. The noise analysis showed that the Inhibition and Occupancy plots yielded higher convergence in the presence of noise.

## CONCLUSION

On the basis of all three goodness-of-fit parameters ( $R^2$ , RMSE, and  $\|X\|_\infty$ ), and using both regression methods (LSM and DM), the Inhibition and Occupancy plots emerged as the plots with a superior degree of convergence. We judge this to be in part because of the absence of commingling of the original dependent and independent variables of the Saturation (original Lassen) plot. Concerning the effect of regression method (LSM and DM) on the estimated values of  $s$ ,  $V_{ND}$ , and  $BP_{ND}$ , we observed that the average differences in the results of the Inhibition and Occupancy plot linearizations were less than 0.1% and, as such, negligible. In contrast, we noted more than a 35% difference in the results of the Saturation plot comparisons—a difference that we explain by the violation of the negligible variability rule for independent variables. The noise analysis showed that the three plots resulted in the same parameter estimates in the absence of noise. However, in the presence of noise, the Inhibition and Occupancy plots yielded higher and close degrees of convergence.

## DISCLOSURE

This study was supported by Parkinsonforeningen, Lundbeck-fonden (R77-A6970), and the Danish Agency for Science and Higher Education. No other potential conflict of interest relevant to this article was reported.

## KEY POINTS

**QUESTION:** Which of the three linearizations (Inhibition, Saturation, and Occupancy) had superior convergence with the experimental results?

**PERTINENT FINDINGS:** Superior convergences among the values of  $s$ ,  $V_{ND}$ , and  $BP_{ND}$  were observed for the Inhibition and Occupancy plots. On the basis of the goodness-of-fit parameters ( $R^2$ , RMSE, and  $\|X\|_\infty$ ) and with both regression methods (LSM and DM), the Inhibition plot emerged as the plot with the slightly higher degree of convergence.

**IMPLICATIONS FOR PATIENT CARE:** The correct use of the Occupancy and Inhibition plots allows brain-imaging specialists to advise on the optimal dose of target engagement of neuroreceptor inhibitor drugs chosen to block the pathologic excess of neurotransmission.

## REFERENCES

1. Ter-Pogossian MM. Positron emission tomography. In: *Biomedical Images and Computers*. Springer; 1982:216–224.
2. Gjedde A, Wong DF, Rosa-Neto P, Cumming P. Mapping neuroreceptors at work: on the definition and interpretation of binding potentials after 20 years of progress. *Int Rev Neurobiol*. 2005;63:1–20.
3. Wahl RL. Current status of PET in breast cancer imaging, staging, and therapy. *Semin Roentgenol*. 2001;36:250–260.
4. Wong DF, Gjedde A, Wagner HN Jr. Quantification of neuroreceptors in the living human brain. I. Irreversible binding of ligands. *J Cereb Blood Flow Metab*. 1986; 6:137–146.
5. Phan J-A, Landau AM, Jakobsen S, Wong DF, Gjedde A. Radioligand binding analysis of  $\alpha 2$  adrenoceptors with [ $^{11}$ C] yohimbine in brain in vivo: extended inhibition plot correction for plasma protein binding. *Sci Rep*. 2017;7:15979.
6. Naganawa M, Gallezot J-D, Rossano S, Carson RE. Quantitative PET imaging in drug development: estimation of target occupancy. *Bull Math Biol*. 2019;81: 3508–3541.
7. Gjedde A, Wong DF, Wagner Jr HN. Transient analysis of irreversible and reversible tracer binding in human brain in vivo. In: *PET and NMR: New Perspectives in Neuroimaging and in Clinical Neurochemistry*. AR Liss; 1986:223–235.
8. Phan J-A, Landau AM, Wong DF, et al. Quantification of [ $^{11}$ C] yohimbine binding to  $\alpha 2$  adrenoceptors in rat brain in vivo. *J Cereb Blood Flow Metab*. 2015;35: 501–511.
9. Landau AM, Alstrup AK, Audrain H, et al. Elevated dopamine D1 receptor availability in striatum of Göttingen minipigs after electroconvulsive therapy. *J Cereb Blood Flow Metab*. 2018;38:881–887.
10. DeLorenzo C, Gallezot J-D, Gardus J, et al. In vivo variation in same-day estimates of metabotropic glutamate receptor subtype 5 binding using [ $^{11}$ C] ABP688 and [ $^{18}$ F] FPPE. *J Cereb Blood Flow Metab*. 2017;37:2716–2727.
11. Lassen NA, Bartenstein P, Lammertsma A, et al. Benzodiazepine receptor quantification in vivo in humans using [ $^{11}$ C] flumazenil and PET: application of the steady-state principle. *J Cereb Blood Flow Metab*. 1995;15:152–165.
12. Gjedde A, Wong D. Receptor occupancy in absence of reference region [abstract]. *Neuroimage*. 2000;11(suppl):S48.
13. Cunningham VJ, Rabiner EA, Slifstein M, Laruelle M, Gunn RN. Measuring drug occupancy in the absence of a reference region: the Lassen plot re-visited. *J Cereb Blood Flow Metab*. 2010;30:46–50.
14. Mintun MA, Raichle ME, Kilbourn MR, Wooten GF, Welch MJ. A quantitative model for the in vivo assessment of drug binding sites with positron emission tomography. *Ann Neurol*. 1984;15:217–227.
15. Karalija N, Jonasson L, Johansson J, et al. High long-term test–retest reliability for extrastriatal [ $^{11}$ C]-raclopride binding in healthy older adults. *J Cereb Blood Flow Metab*. 2020;40:1859–1868.

16. Innis RB, Cunningham VJ, Delforge J, et al. Consensus nomenclature for in vivo imaging of reversibly binding radioligands. *J Cereb Blood Flow Metab.* 2007;27:1533–1539.
17. Horti AG, Gao Y, Kuwabara H, et al. <sup>18</sup>F-ASEM, a radiolabeled antagonist for imaging the  $\alpha$ 7-nicotinic acetylcholine receptor with PET. *J Nucl Med.* 2014;55:672–677.
18. Ramakrishnan NK, Schepers M, Luurtsema G, et al. Cutamesine overcomes REM sleep deprivation-induced memory loss: relationship to sigma-1 receptor occupancy. *Mol Imaging Biol.* 2015;17:364–372.
19. Etrrup A, Mikkelsen JD, Lehel S, et al. <sup>11</sup>C-NS14492 as a novel PET radioligand for imaging cerebral  $\alpha$ 7 nicotinic acetylcholine receptors: in vivo evaluation and drug occupancy measurements. *J Nucl Med.* 2011;52:1449–1456.
20. Narendran R, Mason NS, Chen CM, et al. Evaluation of dopamine D<sub>2/3</sub> specific binding in the cerebellum for the positron emission tomography radiotracer [<sup>11</sup>C] FLB 457: implications for measuring cortical dopamine release. *Synapse.* 2011;65:991–997.
21. Wong DF, Kuwabara H, Horti AG, et al. Brain PET imaging of  $\alpha$ 7-nAChR with [<sup>18</sup>F] ASEM: reproducibility, occupancy, receptor density, and changes in schizophrenia. *Int J Neuropsychopharmacol.* 2018;21:656–667.
22. Koole M, van Aalst J, Devrome M, et al. Quantifying SV2A density and drug occupancy in the human brain using [<sup>11</sup>C] UCB-J PET imaging and subcortical white matter as reference tissue. *Eur J Nucl Med Mol Imaging.* 2019;46:396–406.
23. Owen DR, Guo Q, Kalk NJ, et al. Determination of [<sup>11</sup>C] PBR28 binding potential in vivo: a first human TSPO blocking study. *J Cereb Blood Flow Metab.* 2014;34:989–994.
24. Naganawa M, Jacobsen LK, Zheng M-Q, et al. Evaluation of the agonist PET radioligand [<sup>11</sup>C] GR103545 to image kappa opioid receptor in humans: kinetic model selection, test–retest reproducibility and receptor occupancy by the antagonist PF-04455242. *Neuroimage.* 2014;99:69–79.
25. Kágedal M, Cselényi Z, Nyberg S, et al. A positron emission tomography study in healthy volunteers to estimate mGluR5 receptor occupancy of AZD2066: estimating occupancy in the absence of a reference region. *Neuroimage.* 2013;82:160–169.
26. Jucaite A, Takano A, Boström E, et al. AZD5213: a novel histamine H3 receptor antagonist permitting high daytime and low nocturnal H3 receptor occupancy, a PET study in human subjects. *Int J Neuropsychopharmacol.* 2013;16:1231–1239.
27. Elmenhorst D, Meyer PT, Matusch A, Winz OH, Bauer A. Caffeine occupancy of human cerebral A1 adenosine receptors: in vivo quantification with <sup>18</sup>F-CPFPX and PET. *J Nucl Med.* 2012;53:1723–1729.
28. Ridler K, Plisson C, Rabiner EA, et al. Characterization of in vivo pharmacological properties and sensitivity to endogenous serotonin of [<sup>11</sup>C] P943: a positron emission tomography study in *Papio anubis*. *Synapse.* 2011;65:1119–1127.
29. Fuchigami T, Takano A, Gulyás B, et al. Synthesis and evaluation of 2-chloro N-[(S)-{(S)-1-[<sup>11</sup>C] methylpiperidin-2-yl}(phenyl) methyl] 3-trifluoromethyl-benzamide ([<sup>11</sup>C] N-methyl-SSR504734) as a PET radioligand for glycine transporter 1. *EJNMMI Res.* 2012;2:37.
30. Logan J, Kim SW, Pareto D, et al. Kinetic analysis of [<sup>11</sup>C] vorozole binding in the human brain with positron emission tomography. *Mol Imaging.* 2014;13:1–12.
31. Martin-Facklam M, Pizzagalli F, Zhou Y, et al. Glycine transporter type 1 occupancy by bitopertin: a positron emission tomography study in healthy volunteers. *Neuropsychopharmacology.* 2013;38:504–512.
32. Myers JF, Rosso L, Watson BJ, et al. Characterisation of the contribution of the GABA-benzodiazepine  $\alpha$ 1 receptor subtype to [<sup>11</sup>C] Ro15-4513 PET images. *J Cereb Blood Flow Metab.* 2012;32:731–744.
33. Phan J-A, Jakobsen S, Landau AM, Doudet D, Gjedde A. Amphetamine-induced inhibition of [C-11] yohimbine binding in rat brain. *J Cereb Blood Flow Metab.* 2012;32(suppl):S98–S99.
34. Visser AK, De Vries EF, Ramakrishnan NK, et al. Analysis of 5-HT 2A receptor binding with [<sup>11</sup>C] MDL 100907 in rats: optimization of kinetic modeling. *Mol Imaging Biol.* 2013;15:730–738.
35. Milak MS, Severance AJ, Prabhakaran J, et al. In vivo serotonin-sensitive binding of [<sup>11</sup>C] CUMI-101: a serotonin 1A receptor agonist positron emission tomography radiotracer. *J Cereb Blood Flow Metab.* 2011;31:243–249.
36. Hillmer AT, Zheng M-Q, Li S, et al. PET imaging evaluation of [<sup>18</sup>F] DBT-10, a novel radioligand specific to  $\alpha$  7 nicotinic acetylcholine receptors, in nonhuman primates. *Eur J Nucl Med Mol Imaging.* 2016;43:537–547.
37. Paul S, Khanapur S, Sijbesma JW, et al. Use of <sup>11</sup>C-MPDX and PET to study adenosine A1 receptor occupancy by nonradioactive agonists and antagonists. *J Nucl Med.* 2014;55:315–320.
38. Rawlings JO, Pantula SG, Dickey DA. *Applied Regression Analysis: A Research Tool.* Springer Science and Business Media; 2001:2–6.
39. Deming WE. *Statistical Adjustment of Data.* Dover Publications; 1943:59–127.
40. Linnet K. Estimation of the linear relationship between the measurements of two methods with proportional errors. *Stat Med.* 1990;9:1463–1473.
41. Epperson JF. *An Introduction to Numerical Methods and Analysis.* John Wiley and Sons; 2013:442–444.
42. Sydenham PH, Thorn R. *Handbook of Measuring System Design.* John Wiley and Sons; 2005:289–300.

---

---

# <sup>11</sup>C-PiB and <sup>124</sup>I-Antibody PET Provide Differing Estimates of Brain Amyloid- $\beta$ After Therapeutic Intervention

Silvio R. Meier<sup>1</sup>, Dag Sehlin<sup>1</sup>, Sahar Roshanbin<sup>1</sup>, Victoria Lim Falk<sup>1</sup>, Takashi Saito<sup>2,3</sup>, Takaomi C. Saido<sup>2</sup>, Ulf Neumann<sup>4</sup>, Johanna Rokka<sup>1</sup>, Jonas Eriksson<sup>5,6</sup>, and Stina Syvänen<sup>1</sup>

<sup>1</sup>Department of Public Health and Caring Sciences/Geriatrics, Uppsala University, Uppsala, Sweden; <sup>2</sup>Laboratory for Proteolytic Neuroscience, RIKEN Center for Brain Science, Wako, Japan; <sup>3</sup>Department of Neurocognitive Science, Institute of Brain Science, Nagoya City University Graduate School of Medical Sciences, Nagoya, Japan; <sup>4</sup>Neuroscience Research, Novartis Institutes for BioMedical Research, Basel, Switzerland; <sup>5</sup>Department of Medicinal Chemistry, Uppsala Biomedical Center, Uppsala University, Uppsala, Sweden; and <sup>6</sup>PET Centre, Uppsala University Hospital, Uppsala, Sweden

PET imaging of amyloid- $\beta$  (A $\beta$ ) has become an important component of Alzheimer disease diagnosis. <sup>11</sup>C-Pittsburgh compound B (<sup>11</sup>C-PiB) and analogs bind to fibrillar A $\beta$ . However, levels of nonfibrillar, soluble, aggregates of A $\beta$  appear more dynamic during disease progression and more affected by A $\beta$ -reducing treatments. The aim of this study was to compare an antibody-based PET ligand targeting nonfibrillar A $\beta$  with <sup>11</sup>C-PiB after  $\beta$ -secretase (BACE-1) inhibition in 2 Alzheimer disease mouse models at an advanced stage of A $\beta$  pathology. **Methods:** Transgenic ArcSwe mice (16 mo old) were treated with the BACE-1 inhibitor NB-360 for 2 mo, whereas another group was kept as controls. A third group was analyzed at the age of 16 mo as a baseline. Mice were PET-scanned with <sup>11</sup>C-PiB to measure A $\beta$  plaque load followed by a scan with the bispecific radioligand <sup>124</sup>I-RmAb158-scFv8D3 to investigate nonfibrillar aggregates of A $\beta$ . The same study design was then applied to another mouse model, *App*<sup>NL-G-F</sup>. In this case, NB-360 treatment was initiated at the age of 8 mo and animals were scanned with <sup>11</sup>C-PiB-PET and <sup>125</sup>I-RmAb158-scFv8D3 SPECT. Brain tissue was isolated after scanning, and A $\beta$  levels were assessed. **Results:** <sup>124</sup>I-RmAb158-scFv8D3 concentrations measured with PET in hippocampus and thalamus of NB-360-treated ArcSwe mice were similar to those observed in baseline animals and significantly lower than concentrations observed in same-age untreated controls. Reduced <sup>125</sup>I-RmAb158-scFv8D3 retention was also observed with SPECT in hippocampus, cortex, and cerebellum of NB-360-treated *App*<sup>NL-G-F</sup> mice. Radioligand in vivo concentrations corresponded to postmortem brain tissue analysis of soluble A $\beta$  aggregates. For both models, mice treated with NB-360 did not display a reduced <sup>11</sup>C-PiB signal compared with untreated controls, and further, both NB-360 and control mice tended, although not reaching significance, to show higher <sup>11</sup>C-PiB signal than the baseline groups. **Conclusion:** This study demonstrated the ability of an antibody-based radioligand to detect changes in brain A $\beta$  levels after anti-A $\beta$  therapy in ArcSwe and *App*<sup>NL-G-F</sup> mice with pronounced A $\beta$  pathology. In contrast, the decreased A $\beta$  levels could not be quantified with <sup>11</sup>C-PiB PET, suggesting that these ligands detect different pools of A $\beta$ .

**Key Words:** Alzheimer disease; BACE-1 inhibition; amyloid- $\beta$ ; <sup>11</sup>C-PiB; antibody-based PET

**J Nucl Med** 2022; 63:302–309

DOI: 10.2967/jnumed.121.262083

**A**lzheimer disease (AD) is a growing socioeconomic burden on society and health care in most countries that are characterized by an aging population (1). Despite intense research over the last few decades, no treatment is available that halts the underlying disease mechanisms and stops the pathologic changes in the AD brain. Accumulation of amyloid- $\beta$  (A $\beta$ ) plaques is the core feature of the histopathologic diagnosis of AD and can be visualized and quantified by molecular imaging. PET is today a valuable tool for assessment of brain amyloidosis in vivo. Amyloid imaging with PET has also become a regularly used inclusion criterion for enrollment of patients in clinical trials. New treatments, aiming to clear A $\beta$  from the brain parenchyma or to reduce A $\beta$  production and aggregation, are dependent on diagnostic tools to follow changes in brain A $\beta$  levels in vivo.

PET ligands such as <sup>11</sup>C-Pittsburgh compound B (<sup>11</sup>C-PiB) and several later-developed analogs bind to fibrillar A $\beta$ , that is, the form of A $\beta$  found in insoluble amyloid plaques. However, A $\beta$  aggregation starts years before any clinical symptoms emerge, and it appears that the PET signal with amyloid radioligands such as <sup>11</sup>C-PiB becomes saturated rather early during disease progression (2,3). In contrast, nonfibrillar A $\beta$  oligomers and protofibrils have been reported to display a more dynamic profile during the course of the clinical stages of the disease and may therefore be better biomarkers for disease severity than amyloid plaques (3,4). Treatments aimed at reducing brain A $\beta$ , such as  $\beta$ -secretase (BACE-1) inhibitors, or to facilitate A $\beta$  clearance, for example, immunotherapy, are likely to reduce nonfibrillar A $\beta$  before amyloid plaques (5,6). Furthermore, diffuse A $\beta$  plaque pathology cannot be detected by these radioligands, which bind to the ordered  $\beta$ -sheet structures of amyloid plaques (7).

A potential strategy to image nonfibrillar A $\beta$  aggregates, rather than plaques, and thus a way to circumvent the limitations of <sup>11</sup>C-PiB and other amyloid radioligands could be to use an antibody-based PET approach. Antibodies are characterized by high and specific binding to their target and can be generated to show selective affinity for a specific aggregation form of A $\beta$ , for

Received Feb. 7, 2021; revision accepted May 5, 2021.

For correspondence or reprints, contact Stina Syvänen (stina.syvanen@pubcare.uu.se).

Published online Jun. 4, 2021.

Immediate Open Access: Creative Commons Attribution 4.0 International License (CC BY) allows users to share and adapt with attribution, excluding materials credited to previous publications. License: <https://creativecommons.org/licenses/by/4.0/>. Details: <http://jnm.snmjournals.org/site/misc/permission.xhtml>.

COPYRIGHT © 2022 by the Society of Nuclear Medicine and Molecular Imaging.

example, A $\beta$  protofibrils (8). However, antibodies display very limited passage across the blood–brain barrier and are therefore not directly suitable as radioligands that require fast and efficient brain entry. We have recently introduced several bispecific radioligands based on A $\beta$ -binding antibodies functionalized with a transferrin receptor binding component to enable active transport across the blood–brain barrier (9–13).

RmAb158-scFv8D3 (14) is based on the A $\beta$  protofibril selective antibody mAb158 (8,15), the murine version of lecanemab (16) that is currently being evaluated as an anti-A $\beta$  treatment in clinical phase III trials, and 2 single-chain fragments (scFvs) of the transferrin receptor antibody 8D3 (17) to enhance brain uptake. A previous study showed that PET with  $^{124}\text{I}$  labeled RmAb158-scFv8D3 could be used to successfully follow A $\beta$  accumulation in mice 7–16 mo of age harboring the Arctic (A $\beta$  precursor protein [APP] E693G) and the Swedish (APP KM670/671NL) APP mutations (ArcSwe) (18). Further,  $^{124}\text{I}$ -RmAb158-scFv8D3 also enabled monitoring of A $\beta$  brain levels after A $\beta$ -reducing treatment with BACE-1 inhibitor NB-360 (6,19) in a cross-sectional study design in ArcSwe mice 10 mo old, that is, an age associated with limited A $\beta$  accumulation. However, in the clinical situation, it is likely that most AD cases remain undetected until clinical symptoms such as memory impairment appear. Consequently, a disease-modifying treatment will realistically be applied at a disease stage associated with advanced brain A $\beta$  accumulation. Thus, diagnostic and dynamic biomarkers reflecting pathologic changes covering also the middle to late disease stage are required.

The aim of this study was to compare the ability of the clinically established radioligand  $^{11}\text{C}$ -PiB and the novel protofibril selective radioligand  $^{124}\text{I}$ -RmAb158-scFv158 to detect and quantify effects of anti-A $\beta$  intervention using the BACE-1 inhibitor NB-360 as a model drug. The study was performed on 2 different models: the first was the ArcSwe mouse model that shows  $^{11}\text{C}$ -PiB positivity between the ages of 12 and 18 mo (9,20), and the second was the *App*<sup>NL-G-F</sup> knock-in mouse model harboring the Arctic, Swedish, and Iberian (APP I716F) mutations that is characterized by diffuse A $\beta$  pathology that is not readily detected by amyloid imaging with PET (21). By inclusion of old mice characterized by abundant brain A $\beta$  pathology, the study was designed to resemble the disease stage when patients are likely to be diagnosed and potentially enrolled into clinical trials of novel drug candidates.

## MATERIALS AND METHODS

### Animals and Treatment

All experiments were performed according to the rules and regulations of the Swedish Animal Welfare Agency, which have been in line with the European Communities Council Directive since September 22, 2010. The experiments were approved by the Uppsala University Animal Ethics board (5.8.18-13350/2017). ArcSwe mice (22) 16 mo old were administered BACE-1 inhibitor NB-360 (Novartis) (6) nutrition pellets (0.5 g of NB-360/kg of pellets) for 2 mo. *App*<sup>NL-G-F</sup> mice (23), with an earlier onset of A $\beta$  deposition, were treated between the ages of 8 and 10 mo. NB-360-treated groups were compared with age-matched groups that received only vehicle food, and further, with baseline groups reflecting pathology levels at the beginning of the treatment. In total, 44 ArcSwe mice (baseline,  $n = 15$ ; NB-360,  $n = 15$ ; control,  $n = 14$ ) and 17 *App*<sup>NL-G-F</sup> mice (baseline,  $n = 5$ ; NB-360,  $n = 6$ ; control,  $n = 6$ ) were included in the study. Two wild-type mice 8 mo old, that is, age-matched to the *App*<sup>NL-G-F</sup> baseline mice, were also included as a comparison (study design is shown in

Supplemental Fig. 1 and animal information in Supplemental Table 1; supplemental materials are available at <http://jnm.snmjournals.org>). In addition to the mice that underwent in vivo imaging, a separate group of mice, ArcSwe ( $n = 2$ ; 18 mo old) and *App*<sup>NL-G-F</sup> ( $n = 2$ ; 10 mo old) were used for ex vivo autoradiography. Mice had free access to food and water during the study.

### Radiochemistry

$^{11}\text{C}$ -PiB was synthesized using a previously described method with slight modifications related to automation using an in-house-built synthesis device (Tracer Production System) (24). The final product was reformulated using solid-phase extraction in approximately 10% ethanol in phosphate-buffered saline.  $^{11}\text{C}$ -PiB was produced with a radioactivity yield of  $2.1 \pm 1.0$  GBq (range, 0.7–4.3 GBq), a molar activity of  $33 \pm 38$  MBq/nmol, and a radiochemical purity of more than 99% at the end of the synthesis.

### Antibody Labeling

RmAb158-scFv8D3 was labeled using direct radioiodination (25) as previously described (18).  $^{124}\text{I}$  (PerkinElmer Inc.) labeling was done in 8 batches; 80  $\mu\text{g}$  of RmAb158-scFv8D3 were labeled with  $101.9 \pm 16.6$  MBq, resulting in an average yield of about  $75.7\% \pm 2.5\%$ . A similar procedure was used for  $^{125}\text{I}$  labeling of RmAb158-scFv8D3 (26); 80  $\mu\text{g}$  of RmAb158-scFv8D3 were labeled with  $38.2 \pm 4.3$  MBq of  $^{125}\text{I}$ , resulting in an average yield of  $71.7\% \pm 3.6\%$ .

### PET/SPECT Imaging

All mice underwent an  $^{11}\text{C}$ -PiB PET scan. ArcSwe mice were injected with  $13.2 \pm 3.6$  MBq of  $^{11}\text{C}$ -PiB with a molar activity of  $19.0 \pm 9.3$  MBq/nmol. *App*<sup>NL-G-F</sup> mice were injected with a  $20.1 \pm 6.6$  MBq/nmol concentration of  $^{11}\text{C}$ -PiB with a molar activity of  $6.7 \pm 1.6$  MBq/nmol. Animals were either injected at the start of the PET scan and scanned for 1 h or injected 30 min before the PET scan and kept under anesthesia until the start of a 30-min scan. For all animals,  $^{11}\text{C}$ -PiB brain retention was analyzed using data acquired 40–60 min after injection.

Within a week after their  $^{11}\text{C}$ -PiB PET scan, ArcSwe animals were PET-scanned with  $^{124}\text{I}$ -RmAb158-scFv8D3 and *App*<sup>NL-G-F</sup> mice were SPECT-scanned with  $^{125}\text{I}$ -RmAb158-scFv8D3. One day before injection with radiolabeled RmAb158-scFv8D3, mice were given drinking water containing 0.5% NaI to reduce thyroidal uptake of  $^{124}\text{I}$  and  $^{125}\text{I}$ . After injection, the concentration was decreased to 0.2% NaI until the PET or SPECT scan. ArcSwe and *App*<sup>NL-G-F</sup> mice were injected with  $11.6 \pm 2.7$  MBq of  $^{124}\text{I}$ -RmAb158-scFv8D3 and  $7.2 \pm 1.1$  MBq of  $^{125}\text{I}$ -RmAb158-scFv8D3, respectively, and scanned 4 d after injection. The molar activities were  $185.4 \pm 28.7$  MBq/nmol and  $144.5 \pm 8.8$  MBq/nmol for the  $^{124}\text{I}$ - and the  $^{125}\text{I}$ -labeled radioligands, respectively. After PET/SPECT scanning, mice underwent transcatheter perfusion with 40 mL of 0.9% NaCl for 2.5 min. The brain was then isolated and divided into right and left hemispheres, and the cerebellum was removed from the left hemisphere. Radioactivity was measured in the 3 brain samples (right hemisphere, left hemisphere without cerebellum, and cerebellum from the left hemisphere) with a Wizard 2470  $\gamma$ -counter (GE Healthcare). All samples were frozen on dry ice and stored at  $-80^\circ\text{C}$  until further processing.

PET scans were performed on either a Triumph Trimodality System (TriFoil Imaging, Inc.) or a nanoScan system PET/MRI (Mediso). All PET scans performed with the Mediso system were reconstructed with a Tera-Tomo 3-dimensional algorithm (Mediso) with 4 iterations and 6 subsets. Data obtained with the Triumph system were reconstructed using 3-dimensional ordered-subsets expectation maximization with 20 iterations. SPECT scans were performed with a nanoScan SPECT/CT system (Mediso) with 4 detectors at a frame time of 80 s. Images

were reconstructed with a Tera-Tomo 3-dimensional algorithm (Mediso) with 48 iterations and 3 subsets. Each mouse was CT-examined after the PET/SPECT scan.

All subsequent processing of the images was performed with Amide, version 1.0.4 (27). CT and PET scans were manually aligned with a T2-weighted mouse brain atlas (28) to quantify activity in regions of interest (Supplemental Fig. 2).

### Immunostaining and Autoradiography

Right brain hemispheres of PET- or SPECT-scanned animals were cryosectioned (20  $\mu$ m) for anti-A $\beta$ 1-42 chromogen staining as described previously (18) using the primary polyclonal rabbit-anti-A $\beta$ 1-42 antibody (Agrisera). Triple immunofluorescence staining of A $\beta$ , ionized calcium binding adaptor molecule 1, and glial fibrillary acidic protein and autoradiography were performed as previously described (18). Images were processed as described by Gustavsson et al. (26).

### Brain Sample Preparation

Brain tissue was sequentially extracted as previously described (29) according to Table 1, using a Precellys Evolution system (Bertin Corp.) (4  $\times$  10 s at 5,500 rpm).

### Biochemical Quantifications of Brain Tissue

Brain extraction samples (Table 1) were quantified with enzyme-linked immunosorbent assay (ELISA) as previously described (20,30). Assay details are displayed in Table 2.

### <sup>11</sup>C-PiB Nuclear Track Emulsion (NTE) and Autoradiography

A separate group of mice was injected with 18–20 MBq of <sup>11</sup>C-PiB and then underwent transcatheter perfusion at 20 or 40 min after injection. The brain was immediately removed and divided into right and left hemispheres. Brain samples were frozen on dry ice and processed into 20- $\mu$ m sagittal sections for NTE and 40- $\mu$ m sections for ex vivo autoradiography. Before NTE, sections were stained for 2 min with saturated thioflavin-S in 80% ethanol, washed 1 min in 70% ethanol,

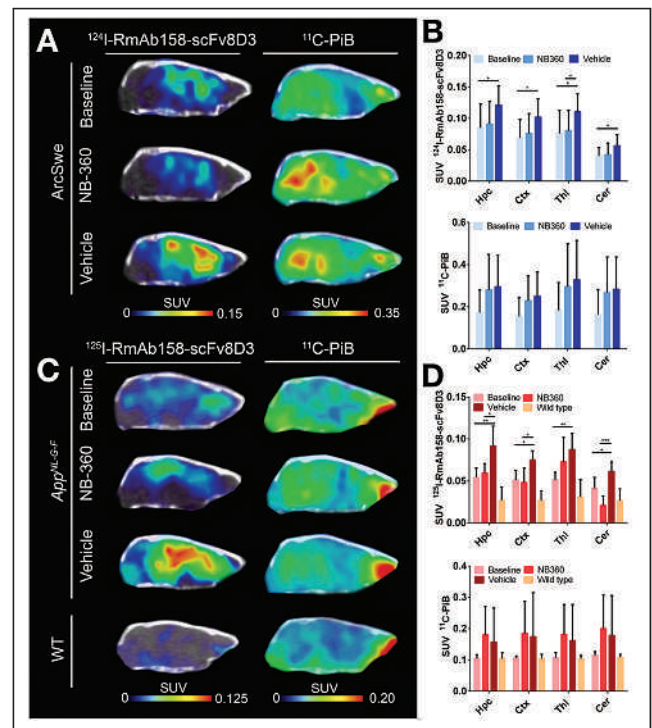


**FIGURE 1.** PET images and quantification of <sup>11</sup>C-PiB scans (40–60 min after injection) and <sup>124</sup>I-RmAb158-scFv8D3 scans (72 h after injection) expressed as SUV. (A) Comparison of representative <sup>124</sup>I-RmAb158-scFv8D3 and <sup>11</sup>C-PiB PET images in ArcSwe animals. (B) Quantification of <sup>124</sup>I-RmAb158-scFv8D3 and <sup>11</sup>C-PiB in hippocampus (Hpc), cortex (Ctx), thalamus (Thl), and cerebellum (Cer). (C) Comparison of representative SPECT and PET images of <sup>125</sup>I-RmAb158-scFv8D3 and <sup>11</sup>C-PiB in *App<sup>NL-G-F</sup>* and wild-type animals. (D) Retention of <sup>125</sup>I-RmAb158-scFv8D3 and <sup>11</sup>C-PiB in different brain regions of *App<sup>NL-G-F</sup>* and wild-type animals.

**TABLE 1**  
Extractions Performed on Brain Tissue for ELISA Analysis

Step	Material	Extraction	Medium	Centrifugation
1	Fresh-frozen brain tissue	1:5 weight:volume ratio of tissue	TBS	1 h, 16,000g
2	Pellet TBS extraction (step 1)	1:5 weight:volume ratio of tissue	70% formic acid	1 h, 16,000g
3	TBS extract (step 1)	200 $\mu$ L of TBS extract (step 1)	TBS	1 h, 100,000g

**TABLE 2**  
Antibodies and Extraction Fractions Used in ELISA Analysis

Target	Extraction sample	Primary antibody	Secondary antibody	Distributor
Nonfibrillar A $\beta$ aggregates	TBS, 16,000g	mAb3D6	mAb3D6-bio	In-house expression
Small sized, nonfibrillar A $\beta$ aggregates	TBS, 100,000g	mAb3D6	mAb3D6-bio	In-house expression
Fibrillar A $\beta$ 1-40	FA, 16,000g	Anti-A $\beta$ 40	mAb3D6-bio	Agrisera/in-house expression
Fibrillar A $\beta$ 1-42	FA, 16,000g	Anti-A $\beta$ 42	mAb3D6-bio	Invitrogen/in-house expression
sTREM2	TBS, 16,000g	AF1729	BAF1729	R&D Systems

FA = formic acid.

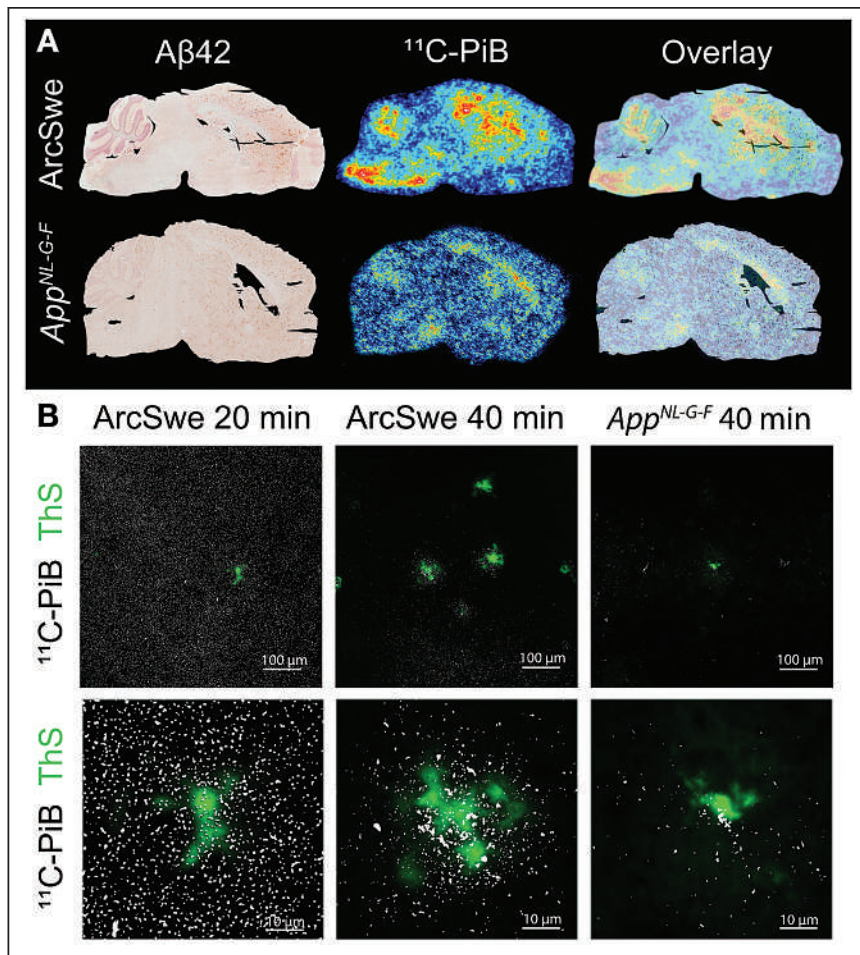


**FIGURE 2.** Ex vivo  $^{11}\text{C}$ -PiB retention in postmortem brain tissue. (A) A $\beta$ 42-stained brain sections of 18-mo-old ArcSwe mouse and 10-mo-old  $App^{NL-G-F}$  mouse and corresponding ex vivo  $^{11}\text{C}$ -PiB autoradiography images at 40 min after radioligand injection. Overlay illustrates overlap of regions with abundant A $\beta$  plaque pathology and radioligand binding. (B) Thioflavin S staining (green) and NTE (white dots) of  $^{11}\text{C}$ -PiB in ArcSwe and  $App^{NL-G-F}$  mice.

and rinsed with phosphate-buffered saline. NTE was performed as previously described (29). Exposure of the slides was started 30 min after perfusion (i.e., equal to 1.5 decay half-lives of  $^{11}\text{C}$ ). The signal was developed after 2 h. Images were acquired with an LSM700 confocal laser scanning microscope (Zeiss) and processed with Zen Zeiss software. Images were compiled with Adobe Photoshop 2020. Brain sections from the same animals were also exposed to a phosphor imaging plate (Fujifilm) within 20 min after perfusion. Plates were exposed for 80 min and read with an Amersham Typhoon imager (GE Healthcare).

#### Statistics

Data were analyzed and plotted with GraphPad Prism, version 6. Groups were compared with 1-way ANOVA using the Bonferroni post hoc test. Results are reported as mean  $\pm$  SD.

#### RESULTS

ArcSwe and  $App^{NL-G-F}$  mice, treated with BACE-1 inhibitor NB-360 or with vehicle, were PET-scanned with  $^{11}\text{C}$ -PiB followed by a  $^{124}\text{I}$ -RmAb158-scFv8D3 PET scan or a  $^{125}\text{I}$ -RmAb158-scFv8D3 SPECT scan. On the basis of visual interpretation of PET images,  $^{11}\text{C}$ -PiB retention in ArcSwe animals seemed slightly increased in the NB-360 and vehicle groups compared with the

2-mo-younger baseline group (Fig. 1A). When retention was quantified as SUV, a similar trend was observed in hippocampus, cortex, thalamus, and cerebellum, but the difference was not significant and interanimal variation was large (Fig. 1B).  $^{11}\text{C}$ -PiB retention in  $App^{NL-G-F}$  mice was alike in all 3 groups (Fig. 1C). When retention was quantified as SUV, interindividual variation was high and differences between the 3 groups and the wild-type group were not significant (Fig. 1D). In summary, neither of the mouse models showed a significant difference in  $^{11}\text{C}$ -PiB signal between the different groups, despite a trend toward an increased signal in older mice, that is, after the 2-mo treatment period (both vehicle and NB-360), compared with baseline mice. Whole-body PET images are shown in Supplemental Figure 3.

$^{124}\text{I}$ -RmAb158-scFv8D3 retention in NB-360-treated animals was clearly lower than in vehicle animals, whereas there was no notable difference from baseline animals (Fig. 1A). Radioligand concentrations were significantly lower in the thalamus ( $P = 0.049$ ) of NB-360-treated animals than in vehicle animals (Fig. 1B). The same trend was observed in cortex, hippocampus, and cerebellum but did not reach significance. Vehicle animals displayed increased levels compared with baseline (hippocampus,  $P = 0.028$ ; cortex,  $P = 0.018$ ; thalamus,  $P = 0.021$ ; cerebellum,  $P = 0.039$ ). Akin to results in ArcSwe animals, SPECT images revealed lower  $^{125}\text{I}$ -RmAb158-scFv8D3 retention in  $App^{NL-G-F}$  animals treated with NB-360

than in the vehicle group (Fig. 1C). When quantified, radioligand concentration was significantly lower in hippocampus ( $P = 0.017$ ), cortex ( $P = 0.047$ ), and cerebellum ( $P < 0.001$ ) (Fig. 1D). Vehicle animals displayed increased  $^{125}\text{I}$ -RmAb158-scFv8D3 concentrations in hippocampus ( $P = 0.008$ ) and thalamus ( $P = 0.047$ ) compared with baseline.

$^{11}\text{C}$ -PiB binding was also assessed in postmortem brain tissue with ex vivo autoradiography and compared with A $\beta$ 42 immunostaining of the adjacent brain sections (Fig. 2A). At 40 min after injection, ArcSwe animals showed  $^{11}\text{C}$ -PiB binding in regions with abundant A $\beta$  pathology such as hippocampus, cortex, and thalamus. White matter binding was observed in cerebellum, corpus callosum, pons, and medulla (Fig. 2A).  $App^{NL-G-F}$  mice displayed low  $^{11}\text{C}$ -PiB binding in hippocampus, cortex, and thalamus despite A $\beta$  pathology but, in line with observations in ArcSwe animals, also showed distinct white matter binding.  $^{11}\text{C}$ -PiB binding in the cortex was further investigated with NTE (Fig. 2B). At 20 min after  $^{11}\text{C}$ -PiB injection in ArcSwe mice, the radioligand was evenly distributed in the tissue, including the core of thioflavin S-stained A $\beta$  deposits, whereas at 40 min after injection, the radioligand was localized primarily around the dense core of thioflavin S-stained A $\beta$  plaques.  $^{11}\text{C}$ -PiB retention in  $App^{NL-G-F}$  mice

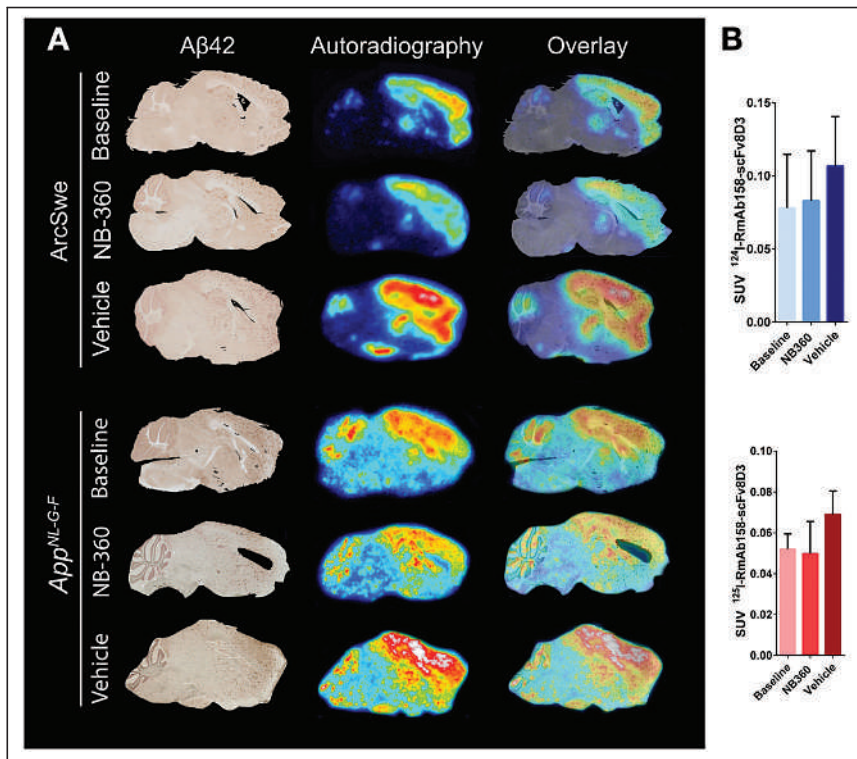


**FIGURE 3.** Aβ<sub>42</sub> immunohistochemistry and ex vivo autoradiography of <sup>124/125</sup>I-RmAb158-scFv8D3 in brain tissue. (A) Comparison of Aβ<sub>42</sub> staining and autoradiography on sagittal brain sections of 1 representative ArcSwe or *App<sup>NL-G-F</sup>* animal of each studied group. Stained brain section was merged to overlay with corresponding ex vivo autoradiography of same animal to visualize pathology and tracer binding simultaneously. (B) Postmortem ex vivo quantification of <sup>124/125</sup>I-RmAb158-scFv8D3 in complete right hemisphere in ArcSwe and *App<sup>NL-G-F</sup>* animals.

at 40 min after injection was lower than that observed in ArcSwe brain but, when present, also localized around the cores of thioflavin S-positive Aβ deposits.

Ex vivo autoradiography with radiolabeled RmAb158-scFv8D3 visualized the presence of the ligand in most parts of the brain. There was especially high retention of the radioligand in cortex, hippocampus, and thalamus already in the baseline groups in both ArcSwe and *App<sup>NL-G-F</sup>* mice (Fig. 3A). The spatial distribution of the radioligand did not change because of NB-360 or vehicle treatment, but the intensity of the radioactive signal was lower in the NB-360 and baseline ArcSwe and *App<sup>NL-G-F</sup>* mice than in vehicle-treated animals. This trend was also evident when the complete postmortem right hemispheres (from which brain sections were prepared) were measured in a γ-counter, although the difference did not reach significance because of large interindividual variation (Fig. 3B). Aβ<sub>42</sub> staining visualized Aβ-affected brain regions, and further, the overlap between pathology-rich brain regions and radiolabeled RmAb158-scFv8D3 strongly indicated a colocalization between the radioligand and Aβ-affected regions in both mouse models (Fig. 3A). NTE in combination with triple staining of glial fibrillary acidic protein, ionized calcium binding adaptor molecule 1, and Aβ is shown in the Supplemental Figure 4.

Brain homogenates of all animals that underwent PET or SPECT were biochemically assessed with ELISA. Tris-buffered saline (TBS)-soluble Aβ aggregates were quantified after centrifugation at 16,000g and 100,000g (Figs. 4A and 4D). In the 16,000g fractions, NB-360-treated ArcSwe animals showed lower levels of Aβ

aggregates than did the vehicle group ( $P = 0.0029$ ), whereas this difference was not significant in the *App<sup>NL-G-F</sup>* mice ( $P > 0.99$ ). However, this decrease was more distinctive and significant in both animal models in the 100,000g fraction ( $P < 0.0001$ ) representing smaller and more soluble aggregates. In addition, the NB-360 groups displayed lower Aβ levels in 100,000g fractions than did the baseline groups ( $P < 0.0001$ ). Aβ<sub>1-40</sub> and Aβ<sub>1-42</sub> in the formic acid fraction represent TBS-insoluble Aβ, including fibrils, and thus represent total plaque load (Figs. 4B and 4E). NB-360-treated *App<sup>NL-G-F</sup>*, but not ArcSwe, displayed lower Aβ<sub>1-40</sub> levels than vehicle-treated animals, whereas Aβ<sub>1-42</sub> levels were decreased in NB-360-treated animals compared with vehicle animals in both models. Correlations between PET/SPECT SUV and Aβ levels are included in Supplemental Tables 2–5. Microglial activation was assessed by quantification of soluble triggering receptor expressed on myeloid cells 2 (sTREM2) in the 16,000g fraction (Figs. 4C and 4F). BACE-1 inhibition decreased sTREM2 levels compared with vehicle in both models ( $P < 0.0001$ ). In the ArcSwe animals, which showed higher sTREM2 levels than the *App<sup>NL-G-F</sup>* animals at baseline, NB-360 treatment also reduced sTREM2 levels compared with baseline ( $P = 0.0143$ ).

## DISCUSSION

Amyloid imaging has become an important inclusion criterion in clinical trials of candidate drugs aimed at reducing brain Aβ. Established amyloid radioligands, such as <sup>11</sup>C-PiB, bind to Aβ fibrils deposited as insoluble plaques in the AD brain. These established radioligands may therefore be insufficient for monitoring changes in more soluble or diffuse forms of misfolded and aggregated Aβ, which are likely to be affected first by anti-Aβ drugs. In this study, we demonstrated that radiolabeled bispecific antibody RmAb158-scFv8D3, binding to soluble Aβ aggregates, was able to quantify changes in brain Aβ levels after treatment with BACE-1 inhibitor NB-360 in 2 mouse models of Aβ pathology and, further, that the readout was different from that of <sup>11</sup>C-PiB PET, which did not detect any differences between treated and untreated groups.

The NB-360 treatment was started at an age when Aβ brain pathology was already advanced and the brain tissue, at least in the ArcSwe mice, included large amounts of dense-core Aβ deposits. Thus, it may not be surprising that the <sup>11</sup>C-PiB signal did not decrease with treatment, as these deposits are likely to be difficult to dissolve. In line with this observation, formic acid-soluble Aβ<sub>1-40</sub>, the main constituent of dense-core deposits (31), displayed the smallest difference between treatment groups. However, it was somewhat surprising that despite BACE-1 inhibition, leading to a dramatic reduction of the smallest aggregates as shown by ELISA in the 100,000g TBS fraction, the <sup>11</sup>C-PiB signal tended to increase from baseline to the end of treatment. This findings implies that

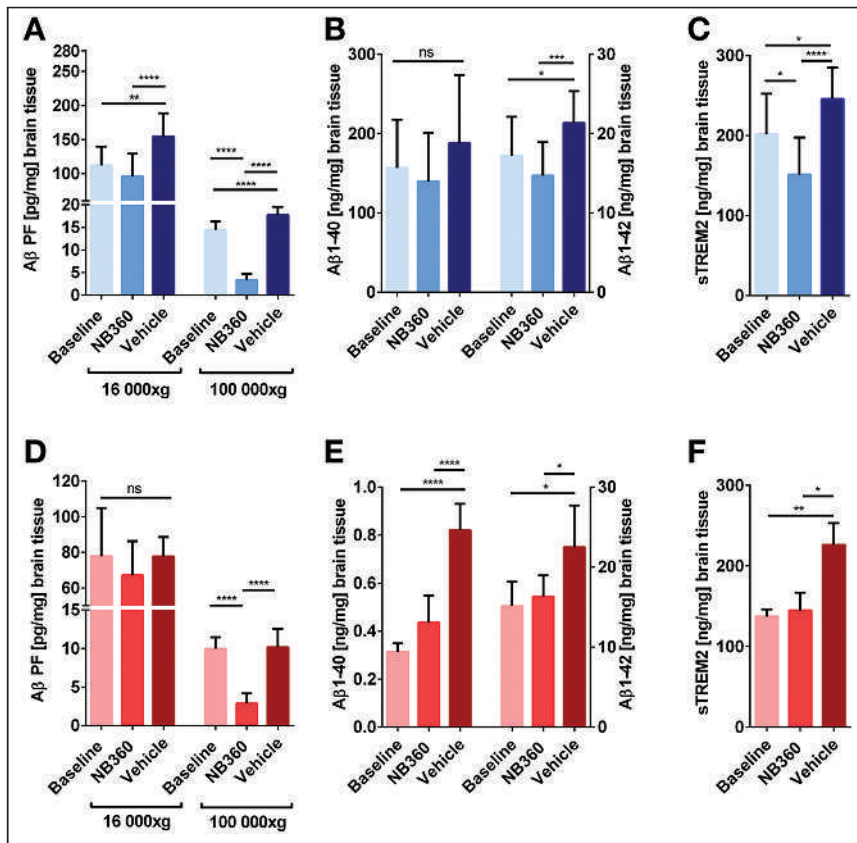


**FIGURE 4.** Quantification of A $\beta$  and sTREM2 in brain homogenates. (A) Quantification of nonfibrillar, TBS-soluble A $\beta$  aggregates separated at 16,000g and 100,000g from ArcSwe brain homogenates. (B) Insoluble A $\beta$ 1-40 and A $\beta$ 1-42 in the formic acid fraction of ArcSwe brain homogenates. (C) sTREM2 levels in the TBS fraction of ArcSwe brain homogenates. (D) Quantification of nonfibrillar, TBS-soluble A $\beta$  aggregates separated at 16,000g and 100,000g from *App*<sup>NL-G-F</sup> brain homogenates. (E) Insoluble A $\beta$ 1-40 and A $\beta$ 1-42 in the formic acid fraction of *App*<sup>NL-G-F</sup> brain homogenates. (F) sTREM2 levels in the TBS fraction of *App*<sup>NL-G-F</sup> brain homogenates.

once insoluble deposits have been formed, they may continue to increase in number and size, especially if the pool of monomers and nonfibrillar aggregates has not been completely depleted. As illustrated by the ELISA measurements, the reduction in intermediate-sized A $\beta$  aggregates, that is, the 16,000g fraction, was either smaller than that observed for the soluble aggregates in the 100,000g fraction (ArcSwe) or absent (*App*<sup>NL-G-F</sup>). A longer treatment time may be required to remove also the 16,000g aggregates. This hypothesis is supported by clinical studies of BACE-1 inhibitors that have reported decreased brain amyloid levels detected with PET after 1.5–2 y of treatment (32,33).

The spatial distribution of <sup>124</sup>I-RmAb158-scFv8D3 studied by ex vivo autoradiography in combination with A $\beta$ 42 immunohistochemistry indicated radioligand accumulation in A $\beta$ -rich brain regions in both mouse models. In contrast, ex vivo autoradiography with <sup>11</sup>C-PiB was evident in regions with abundant A $\beta$  pathology only in the ArcSwe model, not in the *App*<sup>NL-G-F</sup> model. The main reason for selecting these 2 models for the present study was their dissimilar A $\beta$  profiles, illustrated by their very different relative ratios of A $\beta$ 40 and A $\beta$ 42; A $\beta$ 40 is the major A $\beta$  species in ArcSwe mice, whereas A $\beta$ 42 dominates in *App*<sup>NL-G-F</sup> mice (Fig. 4). It has been shown that although A $\beta$ 42 is more prone to aggregate, the dense core of plaques is formed by A $\beta$ 40 (31). It

should also be noted that A $\beta$ 40 is the major A $\beta$  isoform produced in human sporadic AD (34). Thus, this fact leads to another important aspect highlighted in the present study, that is, the selection of animal models for preclinical studies of brain A $\beta$ , especially when evaluating the ability of candidate drugs to reduce pathologic changes. The application of <sup>11</sup>C-PiB, and analogs, in animal studies has indeed been debated over the last 10–15 y. First, preclinical attempts to quantify A $\beta$  deposits with <sup>11</sup>C-PiB in the PS1/APP transgenic mouse model resulted in contradictory results claiming structural differences between A $\beta$  plaque formation and cerebral pathology in mice and humans (35). Yet, more recent studies have demonstrated that A $\beta$  deposits can be assessed by <sup>11</sup>C-PiB in mouse models such as APP23 (36,37) and APP/PS1-21 (38). Further, several studies with <sup>18</sup>F-labeled analogs of <sup>11</sup>C-PiB have underlined the ability of A $\beta$  plaque assessment in different mouse models (39), especially in longitudinal studies (21,40). Several studies have reported the ability of amyloid PET to quantify disease-modifying treatments, for example, mApoE-pA-Lip in APP23 mice (41) and BACE-1 inhibition in PS2APP mice (42). Thus, the use of amyloid PET likely requires a model with dense-core A $\beta$  deposits. The present study also demonstrated that weak <sup>11</sup>C-PiB binding is not per se a sign of low brain A $\beta$  levels, as radiolabeled RmAb158-scFv8D3 was readily able to detect the abundant A $\beta$  pathology in <sup>11</sup>C-PiB-negative *App*<sup>NL-G-F</sup>

mice both in vivo and ex vivo. In line with this observation, patients with AD caused by specific mutations in the A $\beta$ PP, with confirmed diffuse pathology and absence of dense-core plaques, have also been reported as <sup>11</sup>C-PiB-negative (7). Again, this finding illustrates the need for radioligands able to quantify A $\beta$  in forms other than insoluble deposits (plaques).

We used SUV, that is, activity concentrations normalized to the injected activity per body weight, as the main readout measure from PET. This is different from most studies that have reported SUVRs—that is, activity ratios between regions of interest and a reference region. The reference region used in previous studies has in most cases been cerebellum or periaqueductal gray matter (21). However, in the present study, A $\beta$  pathology was spread in the whole brain at the start of the study, hence excluding the use of a pathology-free region as a reference. In addition, all brain regions, including cerebellum and periaqueductal gray matter, were affected by disease progression and by NB-360 treatment as shown by PET/SPECT and autoradiography and by ELISA of postmortem cerebellum homogenates (Supplemental Fig. 5). Thus, in this setting it was not possible to use reference region-based methods.

Apart from A $\beta$ , brain sTREM2 concentrations were also investigated in brain homogenates and found to be decreased in both mouse models after administration of NB-360. This finding

suggests an extenuating effect on microglia activation due to lower A $\beta$  production and aggregation.

## CONCLUSION

Antibody-based PET and SPECT imaging of soluble A $\beta$  aggregates is a sensitive tool to follow A $\beta$  pathology in the brain. This study demonstrated the ability of such ligands to quantify changes due to anti-A $\beta$  treatment at a stage of advanced A $\beta$  pathology. Thus, radioligands based on antibodies directed toward a specific form of aggregated A $\beta$  may have potential to improve and complement diagnostics in preclinical and clinical studies of AD drug candidates. We demonstrated in this study that radiolabeled RmAb158-scFv8D3 is able to quantify changes in brain A $\beta$  levels after BACE-1 inhibition in 2 AD mouse models, and further, that the readout is different from that of <sup>11</sup>C-PiB.

## DISCLOSURE

This work was supported by grants from the Swedish Research Council (2017-02413 and 2018-02715), Alzheimerfonden, Hjärnfonden, Torsten Söderbergs stiftelse, Åhlénstiftelsen, Magnus Bergwalls stiftelse, Stiftelsen för gamla tjänarinnor, and Konung Gustaf V:s och Drottning Victorias Frimurarestiftelsen. The funding bodies did not take part in design of the study; in collection, analysis, or interpretation of data; or in writing of the manuscript. The molecular imaging work in this study was performed at the SciLifeLab Pilot Facility for Preclinical PET-MRI, a Swedish nationally available imaging platform at Uppsala University, Sweden, financed by the Knut and Alice Wallenberg Foundation. Ulf Neumann is an employee and shareholder of Novartis Pharma AG, Basel, Switzerland. No other potential conflict of interest relevant to this article was reported.

## ACKNOWLEDGMENTS

We thank Dr. Derya Shimshek, Novartis, for supplying the NB-360 food pellets; Prof. Lars Nilsson for developing the ArcSwe mouse model used in this study; and BioArctic for sharing the mAb158 sequence.

## KEY POINTS

**QUESTION:** Do <sup>11</sup>C-PIB and <sup>124</sup>I-antibody PET readouts provide differing estimates of brain A $\beta$  after therapeutic intervention in ArcSwe and *App*<sup>NL-G-F</sup> mice with pronounced A $\beta$  pathology, and if they do, what is the implication for drug development for AD?

**PERTINENT FINDINGS:** The antibody-based radioligand detected changes in brain A $\beta$  levels after anti-A $\beta$  therapy in ArcSwe and *App*<sup>NL-G-F</sup> mice. In contrast, the decreased A $\beta$  levels could not be quantified with gold-standard <sup>11</sup>C-PiB PET, suggesting that these ligands detect different pools of A $\beta$ .

**IMPLICATIONS FOR PATIENT CARE:** Radioligands based on antibodies directed toward a specific form of aggregated A $\beta$  may have potential to improve and complement diagnostics in preclinical and clinical studies of AD drug candidates.

## REFERENCES

- Ziegler-Graham K, Brookmeyer R, Johnson E, Arrighi HM. Worldwide variation in the doubling time of Alzheimer's disease incidence rates. *Alzheimers Dement*. 2008;4:316–323.

- Chételat G, La Joie R, Villain N, et al. Amyloid imaging in cognitively normal individuals, at-risk populations and preclinical Alzheimer's disease. *Neuroimage Clin*. 2013;2:356–365.
- Engler H, Forsberg A, Almkvist O, et al. Two-year follow-up of amyloid deposition in patients with Alzheimer's disease. *Brain*. 2006;129:2856–2866.
- Esparza TJ, Wildburger NC, Jiang H, et al. Soluble amyloid-beta aggregates from human Alzheimer's disease brains. *Sci Rep*. 2016;6:38187.
- Keskin AD, Kekuš M, Adelsberger H, et al. BACE inhibition-dependent repair of Alzheimer's pathophysiology. *Proc Natl Acad Sci USA*. 2017;114:8631–8636.
- Neumann U, Rueeger H, Machauer R, et al. A novel BACE inhibitor NB-360 shows a superior pharmacological profile and robust reduction of amyloid- $\beta$  and neuroinflammation in APP transgenic mice. *Mol Neurodegener*. 2015;10:44.
- Schöll M, Wall A, Thordardottir S, et al. Low PiB PET retention in presence of pathologic CSF biomarkers in Arctic APP mutation carriers. *Neurology*. 2012;79:229–236.
- Englund H, Sehlin D, Johansson A-S, et al. Sensitive ELISA detection of amyloid- $\beta$  protofibrils in biological samples. *J Neurochem*. 2007;103:334–345.
- Fang XT, Hultqvist G, Meier SR, Antoni G, Sehlin D, Syvänen S. High detection sensitivity with antibody-based PET radioligand for amyloid beta in brain. *Neuroimage*. 2019;184:881–888.
- Sehlin D, Fang XT, Meier SR, Jansson M, Syvänen S. Pharmacokinetics, biodistribution and brain retention of a bispecific antibody-based PET radioligand for imaging of amyloid- $\beta$ . *Sci Rep*. 2017;7:17254.
- Sehlin D, Stocki P, Gustavsson T, et al. Brain delivery of biologics using a cross-species reactive transferrin receptor 1 VNAR shuttle. *FASEB J*. 2020;34:13272–13283.
- Syvänen S, Fang XT, Hultqvist G, Meier SR, Lannfelt L, Sehlin D. A bispecific Tribody PET radioligand for visualization of amyloid-beta protofibrils - a new concept for neuroimaging. *Neuroimage*. 2017;148:55–63.
- Sehlin D, Syvänen S. Engineered antibodies: new possibilities for brain PET? *Eur J Nucl Med Mol Imaging*. 2019;46:2848–2858.
- Hultqvist G, Syvänen S, Fang XT, Lannfelt L, Sehlin D. Bivalent brain shuttle increases antibody uptake by monovalent binding to the transferrin receptor. *Theranostics*. 2017;7:308–318.
- Lord A, Gumucio A, Englund H, et al. An amyloid-beta protofibril-selective antibody prevents amyloid formation in a mouse model of Alzheimer's disease. *Neurobiol Dis*. 2009;36:425–434.
- Logovinsky V, Satlin A, Lai R, et al. Safety and tolerability of BAN2401: a clinical study in Alzheimer's disease with a protofibril selective A $\beta$  antibody. *Alzheimers Res Ther*. 2016;8:14.
- Lee HJ, Engelhardt B, Lesley J, Bickel U, Partridge WM. Targeting rat anti-mouse transferrin receptor monoclonal antibodies through blood-brain barrier in mouse. *J Pharmacol Exp Ther*. 2000;292:1048–1052.
- Meier SR, Syvänen S, Hultqvist G, et al. Antibody-based in vivo PET imaging detects amyloid- $\beta$  reduction in Alzheimer transgenic mice after BACE-1 inhibition. *J Nucl Med*. 2018;59:1885–1891.
- Neumann U, Machauer R, Shimshek DR. The  $\beta$ -secretase (BACE) inhibitor NB-360 in preclinical models: from amyloid- $\beta$  reduction to downstream disease-relevant effects. *Br J Pharmacol*. 2019;176:3435–3446.
- Sehlin D, Fang XT, Cato L, Antoni G, Lannfelt L, Syvänen S. Antibody-based PET imaging of amyloid beta in mouse models of Alzheimer's disease. *Nat Commun*. 2016;7:10759.
- Sacher C, Blume T, Beyer L, et al. Longitudinal PET monitoring of amyloidosis and microglial activation in a second-generation amyloid- $\beta$  mouse model. *J Nucl Med*. 2019;60:1787–1793.
- Lord A, Kalimo H, Eckman C, Zhang X-Q, Lannfelt L, Nilsson LNG. The Arctic Alzheimer mutation facilitates early intraneuronal Abeta aggregation and senile plaque formation in transgenic mice. *Neurobiol Aging*. 2006;27:67–77.
- Saito T, Matsuba Y, Mihira N, et al. Single App knock-in mouse models of Alzheimer's disease. *Nat Neurosci*. 2014;17:661–663.
- Klunk WE, Engler H, Nordberg A, et al. Imaging brain amyloid in Alzheimer's disease with Pittsburgh compound-B. *Ann Neurol*. 2004;55:306–319.
- Greenwood FC, Hunter WM, Glover JS. The preparation of <sup>131</sup>I-labelled human growth hormone of high specific radioactivity. *Biochem J*. 1963;89:114–123.
- Gustavsson T, Syvänen S, O'Callaghan P, Sehlin D. SPECT imaging of distribution and retention of a brain-penetrating bispecific amyloid- $\beta$  antibody in a mouse model of Alzheimer's disease. *Transl Neurodegener*. 2020;9:37.
- Loening AM, Gambhir SS. AMIDE: a free software tool for multimodality medical image analysis. *Mol Imaging*. 2003;2:131–137.
- Ma Y, Hof PR, Grant SC, et al. A three-dimensional digital atlas database of the adult C57BL/6J mouse brain by magnetic resonance microscopy. *Neuroscience*. 2005;135:1203–1215.

29. Meier SR, Sehlin D, Hultqvist G, Syvänen S. Pinpointing brain TREM2 levels in two mouse models of Alzheimer's disease. *Mol Imaging Biol*. February 23, 2021 [Epub ahead of print].
30. Sehlin D, Englund H, Simu B, et al. Large aggregates are the major soluble A $\beta$  species in AD brain fractionated with density gradient ultracentrifugation. *PLoS One*. 2012;7:e32014.
31. Michno W, Wehrli P, Meier SR, et al. Chemical imaging of evolving amyloid plaque pathology and associated A $\beta$  peptide aggregation in a transgenic mouse model of Alzheimer's disease. *J Neurochem*. 2020;152:602–616.
32. Egan MF, Kost J, Tariot PN, et al. Randomized trial of verubecestat for mild-to-moderate Alzheimer's disease. *N Engl J Med*. 2018;378:1691–1703.
33. Phase II clinical study of elenbecestat demonstrates safety and tolerability in MCI and mild to moderate Alzheimer's disease at 18-months. Eisai Co., Ltd. website. <https://www.eisai.com/news/2018/news201844.html>. Published June 5, 2018. Accessed August 13, 2021.
34. Gregory GC, Halliday GM. What is the dominant Abeta species in human brain tissue? A review. *Neurotox Res*. 2005;7:29–41.
35. Klunk WE, Lopresti BJ, Ikonovic MD, et al. Binding of the positron emission tomography tracer Pittsburgh compound-B reflects the amount of amyloid- $\beta$  in Alzheimer's disease brain but not in transgenic mouse brain. *J Neurosci*. 2005;25:10598–10606.
36. Maeda J, Ji B, Irie T, et al. Longitudinal, quantitative assessment of amyloid, neuroinflammation, and anti-amyloid treatment in a living mouse model of Alzheimer's disease enabled by positron emission tomography. *J Neurosci*. 2007; 27:10957–10968.
37. Snellman A, López-Picón FR, Rokka J, et al. Longitudinal amyloid imaging in mouse brain with <sup>11</sup>C-PIB: comparison of APP23, Tg2576, and APPsw-PS1dE9 mouse models of Alzheimer disease. *J Nucl Med*. 2013;54:1434–1441.
38. Maier FC, Wehrli HF, Schmid AM, et al. Longitudinal PET-MRI reveals  $\beta$ -amyloid deposition and rCBF dynamics and connects vascular amyloidosis to quantitative loss of perfusion. *Nat Med*. 2014;20:1485–1492.
39. Brendel M, Jaworska A, Griebinger E, et al. Cross-sectional comparison of small animal [<sup>18</sup>F]-florbetaben amyloid-PET between transgenic AD mouse models. *PLoS One*. 2015;10:e0116678.
40. Rominger A, Brendel M, Burgold S, et al. Longitudinal assessment of cerebral  $\beta$ -amyloid deposition in mice overexpressing Swedish mutant  $\beta$ -amyloid precursor protein using <sup>18</sup>F-florbetaben PET. *J Nucl Med*. 2013;54:1127–1134.
41. Snellman A, Rokka J, López-Picón FR, et al. Applicability of [<sup>11</sup>C]PIB micro-PET imaging for in vivo follow-up of anti-amyloid treatment effects in APP23 mouse model. *Neurobiol Aging*. 2017;57:84–94.
42. Brendel M, Jaworska A, Overhoff F, et al. Efficacy of chronic BACE1 inhibition in PS2APP mice depends on the regional A $\beta$  deposition rate and plaque burden at treatment initiation. *Theranostics*. 2018;8:4957–4968.

## <sup>68</sup>Ga-NODAGA-Exendin-4 PET/CT Improves the Detection of Focal Congenital Hyperinsulinism

Marti Boss\*<sup>1</sup>, Christof Rottenburger\*<sup>2,3</sup>, Winfried Brenner<sup>3</sup>, Oliver Blankenstein<sup>4</sup>, Vikas Prasad<sup>3,5</sup>, Sonal Prasad<sup>3,6</sup>, Paolo de Coppi<sup>7</sup>, Peter Kühnen<sup>4</sup>, Mijke Buitinga<sup>1</sup>, Pirjo Nuutila<sup>8,9</sup>, Timo Otonkoski<sup>10,11</sup>, Khalid Hussain<sup>12</sup>, Maarten Brom<sup>1</sup>, Annemarie Eek<sup>1</sup>, Jamshed Bomanji<sup>2</sup>, Pratik Shah\*<sup>13,14</sup>, Martin Gotthardt<sup>1</sup>

<sup>1</sup>Department of Medical Imaging, Radboud University Medical Centre, Nijmegen, The Netherlands; <sup>2</sup>Division of Nuclear Medicine, University Hospital Basel, Basel, Switzerland; <sup>3</sup>Institute of Nuclear Medicine, University College London, London, United Kingdom; <sup>4</sup>Department of Nuclear Medicine, Charité–Universitätsmedizin, Berlin, Germany; <sup>5</sup>Institute for Experimental Pediatric Endocrinology, Charité–Universitätsmedizin, Berlin, Germany; <sup>6</sup>Department of Nuclear Medicine, University Hospital of Ulm, Ulm, Germany; <sup>7</sup>Berlin Experimental Radionuclide Imaging Center, Charité–Universitätsmedizin, Berlin, Germany; <sup>8</sup>Department of Pediatric Surgery, Great Ormond Street Hospital for Children, NHS Foundation Trust, London, United Kingdom; <sup>9</sup>Department of Endocrinology, Turku University Hospital, Turku, Finland; <sup>10</sup>Turku PET Center, University of Turku, Turku, Finland; <sup>11</sup>Stem Cells and Metabolism Research Program, Faculty of Medicine, University of Helsinki, Helsinki, Finland; <sup>12</sup>Children’s Hospital, University of Helsinki and Helsinki University Hospital, Helsinki, Finland; <sup>13</sup>Department of Pediatric Medicine, Division of Endocrinology, Sidra Medical and Research Center, Doha, Qatar; <sup>14</sup>Pediatric Endocrinology Department, Great Ormond Street Hospital for Children, NHS Foundation Trust, London, United Kingdom; and <sup>15</sup>Department of Pediatric Endocrinology, Royal London Children’s Hospital, Bart’s Health NHS Trust, London, United Kingdom

Surgery with curative intent can be offered to congenital hyperinsulinism (CHI) patients, provided that the lesion is focal. Radiolabeled exendin-4 specifically binds the glucagonlike peptide 1 receptor on pancreatic  $\beta$ -cells. In this study, we compared the performance of <sup>18</sup>F-DOPA PET/CT, the current standard imaging method for CHI, and PET/CT with the new tracer <sup>68</sup>Ga-NODAGA-exendin-4 in the preoperative detection of focal CHI. **Methods:** Nineteen CHI patients underwent both <sup>18</sup>F-DOPA PET/CT and <sup>68</sup>Ga-NODAGA-exendin-4 PET/CT before surgery. The images were evaluated in 3 settings: a standard clinical reading, a masked expert reading, and a joint reading. The target (lesion)-to-nontarget (normal pancreas) ratio was determined using SUV<sub>max</sub>. Image quality was rated by pediatric surgeons in a questionnaire. **Results:** Fourteen of 19 patients having focal lesions underwent surgery. On the basis of clinical readings, the sensitivity of <sup>68</sup>Ga-NODAGA-exendin-4 PET/CT (100%; 95% CI, 77%–100%) was higher than that of <sup>18</sup>F-DOPA PET/CT (71%; 95% CI, 42%–92%). Interobserver agreement between readings was higher for <sup>68</sup>Ga-NODAGA-exendin-4 than for <sup>18</sup>F-DOPA PET/CT (Fleiss  $\kappa = 0.91$  vs. 0.56). <sup>68</sup>Ga-NODAGA-exendin-4 PET/CT provided significantly ( $P = 0.021$ ) higher target-to-nontarget ratios ( $2.02 \pm 0.65$ ) than did <sup>18</sup>F-DOPA PET/CT ( $1.40 \pm 0.40$ ). On a 5-point scale, pediatric surgeons rated <sup>68</sup>Ga-NODAGA-exendin-4 PET/CT as superior to <sup>18</sup>F-DOPA PET/CT. **Conclusion:** For the detection of focal CHI, <sup>68</sup>Ga-NODAGA-exendin-4 PET/CT has higher clinical sensitivity and better interobserver correlation than <sup>18</sup>F-DOPA PET/CT. Better contrast and image quality make <sup>68</sup>Ga-NODAGA-exendin-4 PET/CT superior to <sup>18</sup>F-DOPA PET/CT in surgeons’ intraoperative quest for lesion localization.

**Key Words:** congenital hyperinsulinism; focal CHI; diagnostic imaging; <sup>68</sup>Ga-NODAGA-exendin-4 PET/CT; <sup>18</sup>F-DOPA PET/CT

**J Nucl Med 2022; 63:310–315**  
DOI: 10.2967/jnumed.121.262327

**C**ongenital hyperinsulinism (CHI) is the most common cause of persistent and recurrent hypoglycemia in neonates. It occurs with an incidence of 1 in 35,000–40,000 births (1). CHI often presents in neonates as poor feeding, seizures, jitteriness, hypotonia, apnea, cyanosis, hypothermia, or a hypoglycemia-induced life-threatening event (2). CHI can also manifest in infancy or childhood and, in rare cases, even in adolescents or young adults (3). To avoid brain injury, early diagnosis and proper treatment of CHI are crucial. The diagnosis of CHI is based on clinical findings and hypoglycemic events, combined with inappropriately high insulin or C-peptide levels or low insulinlike growth factor-binding protein 1 levels (4,5). In diffuse CHI, which accounts for 60%–70% of all cases, there is diffuse involvement of the pancreatic  $\beta$ -cells, with enlarged hyperfunctioning cells that have abnormally large nuclei and abundant cytoplasm (6,7). This subform is caused by recessive or dominant mutations in the *ABCC8* or *KCNJ11* genes, encoding for the  $\beta$ -cell adenosine triphosphate-sensitive potassium channels. Diffuse CHI is treated primarily with medication, such as octreotide and diazoxide. However, many patients with recessive mutations in the *ABCC8* and *KCNJ11* genes are unresponsive to this therapy, and near-total pancreatectomy may then be the only option to avoid devastating hypoglycemia. Even after such an invasive procedure, some children present with recurring hypoglycemia, requiring further treatment with medication or even reoperation (8).

Focal CHI accounts for 30%–40% of all CHI cases associated with the adenosine triphosphate-sensitive potassium channel genes. This form is characterized by focal adenomatous islet cell

Received Mar. 17, 2021; revision accepted May 5, 2021.  
For correspondence or reprints, contact Marti Boss (marti.boss@radboudumc.nl).

\*Contributed equally to this work.  
Published online Jul. 2, 2021.

Immediate Open Access: Creative Commons Attribution 4.0 International License (CC BY) allows users to share and adapt with attribution, excluding materials credited to previous publications. License: <https://creativecommons.org/licenses/by/4.0/>. Details: <http://jnm.snmjournals.org/site/misc/permission.xhtml>.

COPYRIGHT © 2022 by the Society of Nuclear Medicine and Molecular Imaging.

hyperplasia caused by the concurrence of a paternal mutation in the *ABCC8* or *KCNJ11* gene and somatic loss of heterozygosity of the maternal chromosome 11p15 region within a limited pancreatic region (9,10). Because there is involvement of only a specific pancreatic area, focal CHI can be treated successfully by partial pancreatectomy or limited lesionectomy, which can cure the disease in cases of complete removal of the lesion (7). Since focal CHI can be treated with much less invasive surgery than diffuse CHI, correct differentiation between these subforms is of great importance. Also, precise presurgical localization of the focal lesion is important for correct surgical planning and optimization of surgical outcomes. If the lesion resides in the body or tail of the pancreas, a minimally invasive, laparoscopic, procedure may be performed (11).

The current standard imaging technique for noninvasive detection of focal CHI is  $^{18}\text{F}$ -DOPA PET/CT (12). Because this technique has a sensitivity of only 85%–89% for the detection of focal CHI (13), focal lesions are still missed in some cases. In this study, we used a new radiotracer based on the peptide exendin-4, which binds with high affinity specifically to the glucagonlike peptide 1 receptor expressed on pancreatic  $\beta$ -cells (14).  $^{68}\text{Ga}$ -labeled exendin has been shown to detect insulinomas with high sensitivity (15,16). The specific tracer used in the current study,  $^{68}\text{Ga}$ -NODAGA-exendin-4, is being assessed in a large prospective trial for insulinoma imaging (NCT03189953). We have analyzed the data of patients with CHI who underwent both  $^{18}\text{F}$ -DOPA PET/CT and  $^{68}\text{Ga}$ -NODAGA-exendin-4 PET/CT to compare the effectiveness of these 2 imaging techniques for the detection and localization of focal CHI.

## MATERIALS AND METHODS

### Study Design and Patients

This prospective multicenter study (NCT03768518) included consecutive eligible patients at the Great Ormond Street Hospital in the United Kingdom (7 patients) and at the Radboud University Medical Centre in The Netherlands (1 patient). Patients were recruited directly by these centers and by referral from several tertiary centers across Europe.

Patients were enrolled with biochemically proven, endogenous CHI who were unresponsive to medical treatment and qualified for  $^{18}\text{F}$ -DOPA PET/CT on the basis of mutation analysis (no genetically proven diffuse CHI based on a homozygous or compound heterozygous *ABCC8/KCNJ11* mutation). Exclusion criteria were renal insufficiency (creatinine clearance < 40 mL/min) and evidence of malignancies other than insulin-producing lesions. The study was approved by the local institutional review board of both participating institutes. The parents of all included patients provided written informed consent in accordance with provisions of the Declaration of Helsinki.

In addition, real-world evidence data from CHI patients diagnosed and treated at the Charité University Hospital in Germany (11 patients) were analyzed in accordance with national drug regulations. Parents of these patients provided written informed consent to the use of the new radiotracer.

### Procedures

In all patients,  $^{18}\text{F}$ -DOPA PET/CT was performed according to the local guidelines for focal-CHI detection.  $^{18}\text{F}$ -DOPA (3 MBq/kg; lower limit, 40 MBq) was injected as a slow bolus over 1 min. Patients had not fasted and were not pretreated with carbidopa. A PET/CT acquisition at 1 bed position for 10 min was started 20 min after tracer injection. Depending on the assessment of the first scan, additional PET acquisitions were performed at 40 or 60 min after tracer injection.

For  $^{68}\text{Ga}$ -NODAGA-exendin-4 PET/CT, a  $1.6 \pm 0.1$  MBq/kg dose of the tracer (lower limit, 20 MBq), corresponding to a peptide dose of

maximally 0.08–0.12  $\mu\text{g}/\text{kg}$  (lower limit, 1.4  $\mu\text{g}$ ), was injected intravenously as a slow bolus over 5 min. Details on radiopharmaceutical preparation are provided in the supplemental materials. The patients had fasted for 1 h before tracer injection to reduce endogenous glucagonlike peptide 1 production. Blood glucose levels were monitored before tracer injection and at least at 5, 10, 15, 30, 60, 90, and 120 min after tracer injection. Since blood glucose levels may decrease after  $^{68}\text{Ga}$ -NODAGA-exendin-4 injection, they were closely monitored. Intravenous glucose injection with a case-specific infusion rate was given to all patients to manage glucose levels during the procedure.

PET acquisition methods varied because of differences in the institutional standard of care for CHI patients. Details on  $^{68}\text{Ga}$ -NODAGA-exendin-4 PET/CT and PET/MRI acquisition procedures for all centers and reconstruction parameters are given in Supplemental Table 1 (supplemental materials are available at <http://jnm.snmjournals.org>). At the Great Ormond Street Hospital, a protocol has been developed for  $^{18}\text{F}$ -DOPA PET/CT/CT to be performed under oral sedation with chloral hydrate in children with CHI to avoid general anesthesia (Sarah Kiff et al., unpublished data, 2021). This protocol was adopted for  $^{68}\text{Ga}$ -NODAGA-exendin-4 PET/CT acquisitions at the Great Ormond Street Hospital.

At the Radboud University Medical Centre, 1 patient was included. Scans there were performed without anesthesia with a vacuum mattress.

Real-world evidence from an institutional database of 11 CHI patients who underwent  $^{68}\text{Ga}$ -NODAGA-exendin-4 PET/CT for diagnostic purposes at the Charité University Hospital were included retrospectively. Younger children were imaged while receiving inhalation anesthesia with isoflurane under the supervision of an anesthesiologist; older children were able to undergo the procedure without sedation.

### Evaluation

Histologic evaluation and clinical outcome (normalization of blood glucose levels after surgery) were used as a reference standard.  $^{18}\text{F}$ -DOPA PET/CT and  $^{68}\text{Ga}$ -NODAGA-exendin-4 PET/CT scans were clinically read at the site of patient inclusion by nonmasked observers. The clinical reading was performed by a pediatric endocrinologist (hyperinsulinism expert) together with a nuclear medicine physician and a pediatric surgeon at the site of the PET scan. After completion of data collection, all  $^{18}\text{F}$ -DOPA and  $^{68}\text{Ga}$ -NODAGA-exendin-4 PET/CT images were reevaluated by 1 masked  $^{68}\text{Ga}$ -NODAGA-exendin-4-experienced nuclear medicine physician (expert reading). Additionally, a joint reevaluation of all images was performed by this nuclear medicine physician together with a pediatric endocrinologist highly experienced in  $^{18}\text{F}$ -DOPA PET/CT reading. All images were evaluated in terms of disease subform and, if detected, the size and location of the focal lesion. For exact localization of the focal lesion, the pancreas was divided into 6 areas based on anatomic relation to the pancreatic duct and portal vein (Supplemental Fig. 1). Images from all time points were used for interpretation.

Quantitative analysis of the  $^{18}\text{F}$ -DOPA PET/CT and  $^{68}\text{Ga}$ -NODAGA-exendin-4 PET/CT or PET/MRI scans in which focal lesions had been confirmed by histopathology was performed by a nonmasked expert. Volumes of interest (VOIs) were drawn to determine tracer uptake, expressed as  $\text{SUV}_{\text{max}}$ , in different parts of the pancreas and visible focal lesions. The  $\text{SUV}_{\text{max}}$  ratios of the focal lesion or area with the highest tracer uptake (for  $^{18}\text{F}$ -DOPA PET/CT scans in which the focal lesion was not detected) and the area with the next highest tracer uptake were determined. VOIs were drawn over the head, body, and tail of the pancreas. Within these VOIs, isocontour VOIs were created consisting of the voxels with the 30% highest intensity (examples of resulting VOIs are depicted in Supplemental Fig. 2). For quantification of the dynamic PET scans, reconstructed images of the time frames from 30 to 40 min (Charité University Hospital) and from 40 to 45 min (University College London) after injection were used.

To estimate the optimal imaging time point for  $^{68}\text{Ga}$ -NODAGA-exendin-4 PET/CT,  $\text{SUV}_{\text{max}}$  ratios in reconstructed images of 5-min intervals over the imaging period from 0 to 45 min after tracer injection were determined in 4 patients with focal disease.

To evaluate image quality and correlation of imaging results with the intraoperative findings,  $^{18}\text{F}$ -DOPA PET/CT and  $^{68}\text{Ga}$ -NODAGA-exendin-4 PET/CT images of 13 patients with a detected focal lesion were rated by the involved pediatric surgeon using a questionnaire based on the Leiden surgical rating scale (supplemental materials).

### Statistical Analysis

Imaging results confirmed by histopathology were regarded as true-positives or true-negatives. Imaging results with competing histopathology results were regarded as false-positives or false-negatives. Ninety-five percent CIs for sensitivity were calculated using the Clopper–Pearson method. Interobserver variation was calculated using the Fleiss  $\kappa$ .  $\text{SUV}_{\text{max}}$  ratios in  $^{18}\text{F}$ -DOPA PET/CT and  $^{68}\text{Ga}$ -NODAGA-exendin-4 PET/CT scans were compared using paired-sample  $t$  tests. Surgeon scores of image quality were compared using Wilcoxon signed-rank tests. Statistical analyses were performed using SPSS (version 22; IBM).

## RESULTS

### Patients

We included the data of 19 CHI patients. Baseline characteristics of the patients are given in Table 1, and clinical details are in Supplemental Table 2. All patients underwent  $^{18}\text{F}$ -DOPA PET/CT and  $^{68}\text{Ga}$ -NODAGA-exendin-4 PET/CT, with a median time of 13 d (range, 4–72 d) between the procedures. On clinical reading,  $^{18}\text{F}$ -DOPA PET/CT revealed focal areas of high tracer uptake suggestive of focal lesions in 10 patients (53%), and  $^{68}\text{Ga}$ -NODAGA-exendin-4 PET/CT revealed such areas in 14 patients (74%) (Table 2). The study profile is depicted in Supplemental Figure 3.

### Tolerability

One patient (5%) experienced vomiting after injection of  $^{68}\text{Ga}$ -NODAGA-exendin-4. In 2 patients (11%), episodes of mild hypoglycemia requiring increased glucose infusion occurred after injection of  $^{68}\text{Ga}$ -NODAGA-exendin-4. In the other patients, glucose levels were stable ( $>3.5$  mmol/L) under regular monitoring and intravenous glucose infusion. No other adverse events occurred in any of the patients.

### Surgery

The results of both imaging procedures were used for surgical planning. Suggestive lesions were detected by clinical reading of the PET images in 14 patients. These patients underwent surgery, and the presence of focal lesions was confirmed by histopathologic evaluation. All surgically treated patients with focal lesions were cured after surgery (normalization of blood glucose levels in long-term follow-up).

Of the remaining 5 patients, in whom no focal lesion was detected by clinical reading (diffuse tracer uptake on both  $^{18}\text{F}$ -DOPA and  $^{68}\text{Ga}$ -NODAGA-exendin-4 PET/CT), 1 patient underwent near-total pancreatectomy because of an insufficient response to medication. In line with the imaging results, histopathology indicated diffuse disease in this patient. The 4 patients who did not undergo surgery (aged 10, 18, 68, and 125 mo) could be sufficiently managed with diet and medication.

Since histopathology and clinical follow-up were the reference standard, patients who did not undergo surgery were excluded from analysis.

**TABLE 1**  
Patient Characteristics

Characteristic	Data
Participants	19
Age (mo)	8.3 (4.0–22.0)
Age at diagnosis (d)	7 (1.5–12)
Sex	
Female	8/19 (42%)
Male	11/19 (58%)
Genetic mutation	
Paternal ABCC8 mutation	16/19 (84%)
No or unknown mutation	3/19 (16%)
Response to medication	
Full	5/19 (26%)
Partial	14/19 (74%)

Qualitative data are number and percentage; continuous data are median and interquartile range.

### Diagnostic Performance

Imaging results are summarized in Table 2. In this patient population,  $^{68}\text{Ga}$ -NODAGA-exendin-4 PET/CT had a sensitivity of 100% (95% CI, 77%–100%) for detection of focal lesions, compared with a sensitivity of 71% (95% CI, 42%–92%) for  $^{18}\text{F}$ -DOPA PET/CT, based on clinical readings of the images. In 4 of 15 patients (27%), focal lesions were identified only using  $^{68}\text{Ga}$ -NODAGA-exendin-4 PET/CT. In these patients, the surgery planning was based solely on the results of the  $^{68}\text{Ga}$ -NODAGA-exendin-4 PET/CT.  $^{18}\text{F}$ -DOPA PET/CT and  $^{68}\text{Ga}$ -NODAGA-exendin-4 PET/CT images of these 4 patients are shown in Figure 1. On the basis of the clinical readings,  $^{68}\text{Ga}$ -NODAGA-exendin-4 PET/CT performed better for detection of focal lesions.

### Interobserver Correlation

On reevaluation of the  $^{18}\text{F}$ -DOPA PET/CT images by an expert nuclear medicine physician, 2 additional focal lesions were identified, increasing the sensitivity to 86% (range, 57%–98%). In the expert readings of the  $^{68}\text{Ga}$ -NODAGA-exendin-4 PET/CT images, 1 focal lesion was missed, decreasing the sensitivity to 93% (range, 66%–100%). Through joint reading of the images by an expert nuclear medicine physician and a pediatric endocrinologist, all focal lesions were detected on both  $^{68}\text{Ga}$ -NODAGA-exendin-4 PET/CT and  $^{18}\text{F}$ -DOPA PET/CT. Although the sensitivity of both techniques reached 100%, the interobserver agreement was higher for  $^{68}\text{Ga}$ -NODAGA-exendin-4 PET/CT than for  $^{18}\text{F}$ -DOPA PET/CT (Fleiss  $\kappa = 0.91$  vs. 0.56). For  $^{68}\text{Ga}$ -NODAGA-exendin-4 PET/CT, there was almost perfect agreement, whereas for  $^{18}\text{F}$ -DOPA PET/CT, the level of agreement between the readings was only moderate. The increased sensitivity of  $^{18}\text{F}$ -DOPA PET/CT on only reevaluation of the images, together with the higher interobserver agreement in evaluation of the  $^{68}\text{Ga}$ -NODAGA-exendin-4 PET/CT images, clearly indicates a facilitated and more reliable interpretation of the  $^{68}\text{Ga}$ -NODAGA-exendin-4 PET/CT images, resulting in less equivocal results.

### Semiquantitative Analysis

In patients with histopathologically proven focal CHI, the  $\text{SUV}_{\text{max}}$  ratios of the focal lesion to the area of the pancreas with the next

**TABLE 2**  
Sensitivity of <sup>18</sup>F-DOPA PET/CT and <sup>68</sup>Ga-NODAGA-Exendin-4 PET/CT Based on Clinical and Study Readings

Parameter	<sup>18</sup> F-DOPA PET/CT	<sup>68</sup> Ga-NODAGA-exendin-4 PET/CT
Focal lesions detected on clinical reading ( <i>n</i> )	10/14 (71%)	14/14 (100%)
True-positives	10	14
False-negatives	4	0
Sensitivity* based on ...		
Clinical reading	71% (95% CI, 42%–92%)	100% (95% CI, 77%–100%)
Expert reading	86% (95% CI, 57%–98%)	93% (95% CI, 66%–100%)
Joint reading	100% (95% CI, 77%–100%)	100% (95% CI, 77%–100%)

\*Data are value and 95% confidence interval, calculated for cases with focal lesions only.

highest tracer uptake are significantly higher in <sup>68</sup>Ga-NODAGA-exendin-4 PET/CT than in <sup>18</sup>F-DOPA PET/CT ( $2.03 \pm 0.63$  and  $1.03 \pm 0.35$ , respectively;  $P = 0.0026$ ) (Fig. 2). These quantitative data show that <sup>68</sup>Ga-NODAGA-exendin-4 PET/CT provides better contrast to discriminate between focal and diffuse disease and thus explains the difference in interobserver agreement levels.

Quantification of reconstructed images of 5-min intervals over the imaging period shows some variability between patients in the time point of the highest SUV<sub>max</sub> ratio. SUV<sub>max</sub> ratios over time are depicted in Supplemental Figure 4. For all 4 patients, the highest SUV<sub>max</sub> ratio was between 30 and 45 min after tracer injection. This therefore seems to be the best time frame for <sup>68</sup>Ga-NODAGA-exendin-4 PET/CT imaging.

#### Surgical Ease

The influence of PET image quality on surgical ease was measured by rating of the DOPA and <sup>68</sup>Ga-NODAGA-exendin-4 PET/CT images by the involved pediatric surgeons. These were all experienced surgeons who had performed more than 10 CHI surgeries during their career and more than 5 during the last 3 y. The surgeons' rating of PET image quality showed significantly higher scores for <sup>68</sup>Ga-NODAGA-exendin-4 PET/CT than for <sup>18</sup>F-DOPA PET/CT regarding the decision to perform surgery (4.5 vs. 3.8, respectively;  $P = 0.025$ ; Fig. 2B), as well as regarding correlation of the imaging results with intraoperative findings (4.4 vs. 3.7, respectively;  $P = 0.0083$ ; Fig. 2C). Of 13 cases, the surgeons reported preferring <sup>68</sup>Ga-NODAGA-exendin-4 PET/CT imaging for future CHI patients in 9 cases, versus <sup>18</sup>F-DOPA PET/CT in only 1 case and no preference in 3 cases. This finding implies a better image quality for <sup>68</sup>Ga-NODAGA-exendin-4 PET/CT than for <sup>18</sup>F-DOPA PET/CT and a possible benefit for the surgical treatment of CHI patients.

#### DISCUSSION

The results of the present study indicate that <sup>68</sup>Ga-NODAGA-exendin-4 PET/CT is a promising tool for detection and localization of focal CHI, providing a high sensitivity and diagnostic accuracy. The higher interreader agreement of <sup>68</sup>Ga-NODAGA-exendin-4 PET/CT than of <sup>18</sup>F-DOPA PET/CT indicates superior performance of <sup>68</sup>Ga-NODAGA-exendin-4 PET/CT in some patients by providing less equivocal results.

Quantitative analysis of scans of patients with histopathologically confirmed focal CHI showed significantly higher SUV<sub>max</sub> ratios on <sup>68</sup>Ga-NODAGA-exendin-4 PET/CT than on <sup>18</sup>F-DOPA PET/CT. The higher contrast between uptake in the focal lesion

and in the remainder of the pancreas on <sup>68</sup>Ga-NODAGA-exendin-4 PET/CT scans enables easier detection of focal lesions. This finding explains the increased sensitivity of <sup>68</sup>Ga-NODAGA-exendin-4 PET/CT based on the initial clinical reading, and the increased rate of agreement in readings of <sup>68</sup>Ga-NODAGA-exendin-4 PET/CT images between clinical and expert readers, in comparison to <sup>18</sup>F-DOPA PET/CT images. This increased sensitivity and agreement are of importance, especially in cases with a heterogeneous pattern of tracer uptake in the pancreas—cases that are usually difficult to diagnose (13).

The superior image quality of <sup>68</sup>Ga-NODAGA-exendin-4 PET/CT is important for both the scan reading and the surgical procedure, since successful surgery depends on precise presurgical detection of focal CHI and the subsequent discovery and complete removal of the focal lesion intraoperatively, as reflected by pediatric surgeons' image ratings. <sup>68</sup>Ga-NODAGA-exendin-4 PET/CT could benefit the surgical treatment of CHI patients by facilitating the decision to perform surgery, as well as the intraoperative localization of the focal lesion.

In our limited population of 19 CHI patients, 4 cases of focal CHI were clinically not identified using <sup>18</sup>F-DOPA PET/CT. This is a high number compared with a previous large prospective study with 50 cases and retrospective reviews of 105 and 195 cases, which reported sensitivities of 88%, 85%, and 89%, respectively, for detection of focal CHI using <sup>18</sup>F-DOPA PET/CT (13,17,18). This result is suggestive of a high complexity in the cases in this study. An overrepresentation of such difficult cases in our study population could stem from an increased incentive to refer patients with complex and equivocal <sup>18</sup>F-DOPA PET/CT imaging results for an investigative diagnostic procedure. In this population, <sup>68</sup>Ga-NODAGA-exendin-4 PET/CT outperformed <sup>18</sup>F-DOPA PET/CT in the clinical nonexpert setting, facilitating curative surgery without the need for further medicinal treatment or near-total pancreatectomy in 4 additional patients. <sup>68</sup>Ga-NODAGA-exendin-4 PET/CT therefore had a major positive impact on the clinical management of these patients.

A limitation of the current study was the inability to exclude the possibility of missed focal lesions. All focal lesions that were identified by <sup>68</sup>Ga-NODAGA-exendin-4 PET/CT were confirmed by histopathology. However, 4 patients in whom diffuse disease was indicated on both <sup>18</sup>F-DOPA PET/CT and <sup>68</sup>Ga-NODAGA-exendin-4 PET/CT did not undergo surgery but instead received continued medical treatment. In these patients, diffuse disease was not confirmed.

Another possible limitation of this study was the inclusion of patients from 3 centers with differences in the <sup>68</sup>Ga-NODAGA-

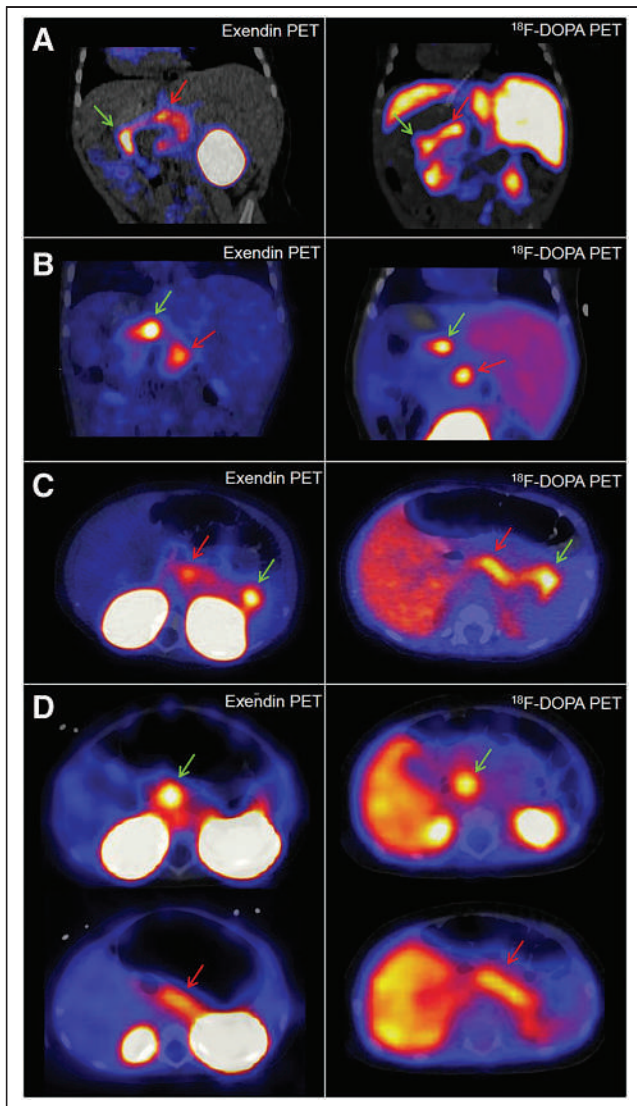


**FIGURE 1.**  $^{68}\text{Ga}$ -NODAGA-exendin-4 PET/CT and  $^{18}\text{F}$ -DOPA PET/CT images of patients 2 (A), 4 (B), 6 (C), and 9 (D), for whom  $^{68}\text{Ga}$ -NODAGA-exendin-4 PET/CT scans were reported as focal in clinical readings whereas  $^{18}\text{F}$ -DOPA PET/CT scans were reported as diffuse. Locations of focal lesions (for  $^{18}\text{F}$ -DOPA PET/CT detected during joint readings) are indicated with green arrows. In D, focal lesion in head is indicated with green arrows, and for comparison, red arrows indicate areas with the next highest tracer uptake in all images. Presence of focal lesions was confirmed by histopathology in all 4 patients.

exendin-4 PET/CT acquisition procedure (Supplemental Table 1). However, the high degree of diagnostic accuracy and interreader agreement for  $^{68}\text{Ga}$ -NODAGA-exendin-4 PET/CT in all included patients shows the robustness of this technique in clinical practice.

On the basis of the data in this study, the expected optimal time frame for  $^{68}\text{Ga}$ -NODAGA-exendin-4 PET/CT imaging is between 30 and 45 min after tracer injection. In the tail of the pancreas, focal lesions that overlap the contour of the left kidney pose a diagnostic challenge with  $^{18}\text{F}$ -DOPA PET/CT, as has been described previously (13). Because of the high renal accumulation of  $^{68}\text{Ga}$ -NODAGA-exendin-4 PET/CT, this issue also occurs with PET/CT using this tracer. In such cases, performing additional scans at later time points could be beneficial, since uptake of

$^{68}\text{Ga}$ -NODAGA-exendin-4 PET/CT in the kidneys was shown to decrease over time in adults (19).

The introduction of  $^{18}\text{F}$ -DOPA PET/CT to discriminate between focal and diffuse CHI has had a major impact on the clinical approach by obviating more invasive diagnostic procedures, such as selective arterial calcium stimulation with simultaneous venous sampling or transhepatic portal venous insulin sampling, and by optimizing surgical treatment because of increased diagnostic accuracy. This study showed that  $^{68}\text{Ga}$ -NODAGA-exendin-4 PET/CT has the potential to even further improve the treatment of patients with focal CHI by improving diagnostic accuracy and certainty. This improvement could enable curative surgery in more patients and could benefit surgical planning by providing more precise and reliable preoperative images.

In addition to the better image quality of  $^{68}\text{Ga}$ -NODAGA-exendin-4 PET/CT than of  $^{18}\text{F}$ -DOPA PET/CT, another important advantage to  $^{68}\text{Ga}$ -NODAGA-exendin-4 PET/CT is the production of  $^{68}\text{Ga}$  by a generator. Because of the short half-life of  $^{68}\text{Ga}$  (68 min), it cannot be transported between centers. However, production by a generator enables on-site production of the radiotracer even at PET centers without a cyclotron, thereby enabling broad availability. Since  $^{18}\text{F}$ -DOPA is often difficult to obtain, this capability could transform the care of focal-CHI patients at such centers. In addition, the equivocal results provided by  $^{68}\text{Ga}$ -NODAGA-exendin-4 PET/CT will also enable correct image interpretation at less experienced centers. An additional important advantage to  $^{68}\text{Ga}$ -NODAGA-exendin-4 is the

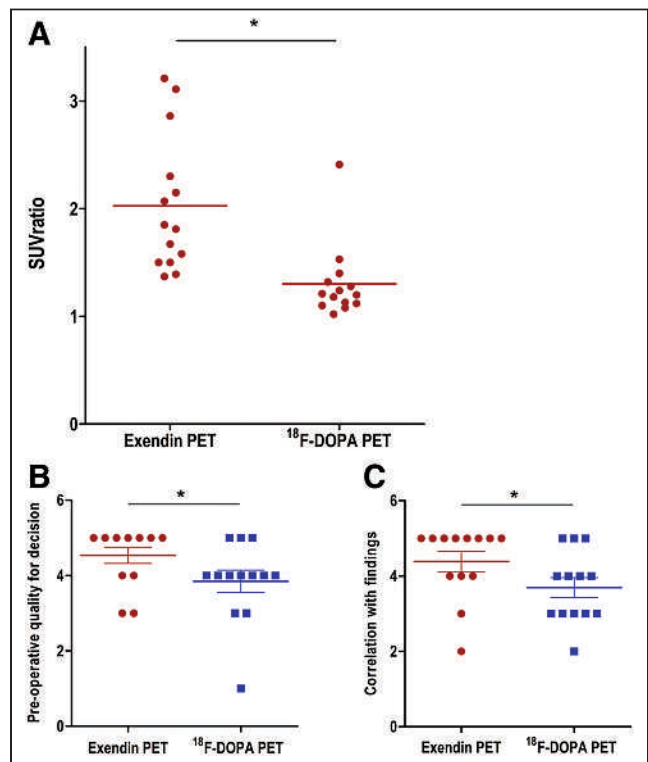


**FIGURE 2.** (A)  $\text{SUV}_{\text{max}}$  ratios between focal lesion and area with next highest tracer uptake. Data are given as mean  $\pm$  SD, as well as individual datapoints. Scans with focal lesions identified during clinical reading are depicted in red. Scans reported to show diffuse disease are depicted in blue. (B and C) Rating scores of  $^{68}\text{Ga}$ -NODAGA-exendin-4 and  $^{18}\text{F}$ -DOPA PET/CT images by pediatric surgeons. Scores are on preoperative image quality for decision to perform surgery (B) and correlation of imaging results with intraoperative findings (C). \* $P < 0.05$ .

very low PET radiation dose to the patients, which we previously calculated to be about 4-fold lower for newborn patients than the radiation dose from  $^{18}\text{F}$ -DOPA (19).

## CONCLUSION

Through this study, we provided the first (to our knowledge) clinical evidence of detection and localization of focal CHI using  $^{68}\text{Ga}$ -NODAGA-exendin-4 PET/CT. These first results show that image quality is better for  $^{68}\text{Ga}$ -NODAGA-exendin-4 PET/CT than for the standard  $^{18}\text{F}$ -DOPA PET/CT, resulting in an excellent sensitivity and diagnostic accuracy, which changed the surgical management in 4 of 19 patients. Although the performance of  $^{68}\text{Ga}$ -NODAGA-exendin-4 PET/CT needs to be further assessed in a larger patient population, we believe that it has the potential to replace  $^{18}\text{F}$ -DOPA PET/CT as the primary imaging tool for detection and localization of focal CHI.

## DISCLOSURE

This work was supported by BetaCure (FP7/2014-2018, grant 602812). PET/MRI use at Charité University Hospital was supported by Deutsche Forschungsgemeinschaft (INST 335/543-1 FUGG). Martin Gotthardt is an inventor on, and holder of, the patent “Invention Affecting GLP-1 and Exendin” (Philipps-Universität Marburg, June 17, 2009). Paolo De Coppi is supported by NIHR BRC Great Ormond Street Hospital. No other potential conflict of interest relevant to this article was reported.

## ACKNOWLEDGMENTS

We thank all patients and their parents or caretakers for participating in the study. We also thank the technical staff at the Radboud University Medical Centre, Charité University Hospital, and University College London for their support with radiochemical preparations and PET investigations.

## KEY POINTS

**QUESTION:** Is  $^{68}\text{Ga}$ -NODAGA-exendin-4 PET/CT effective for preoperative detection and localization of focal CHI?

**PERTINENT FINDINGS:**  $^{68}\text{Ga}$ -NODAGA-exendin-4 PET/CT has higher clinical sensitivity and a better interobserver correlation for the detection of focal CHI than does  $^{18}\text{F}$ -DOPA PET/CT.  $^{68}\text{Ga}$ -NODAGA-exendin-4 PET/CT provided significantly higher target-to-nontarget ratios than did  $^{18}\text{F}$ -DOPA PET/CT, and pediatric surgeons rated  $^{68}\text{Ga}$ -NODAGA-exendin-4 PET/CT superior to  $^{18}\text{F}$ -DOPA PET/CT.

**IMPLICATIONS FOR PATIENT CARE:**  $^{68}\text{Ga}$ -NODAGA-exendin-4 PET/CT has the potential to benefit the treatment of patients with focal CHI by improving diagnostic accuracy and certainty. This advantage could enable curative surgery in more patients and benefit surgical planning by providing more precise and reliable preoperative images.

## REFERENCES

1. Senniappan S, Shanti B, James C, Hussain K. Hyperinsulinaemic hypoglycaemia: genetic mechanisms, diagnosis and management. *J Inherit Metab Dis.* 2012;35:589–601.
2. Demirbilek H, Hussain K. Congenital hyperinsulinism: diagnosis and treatment update. *J Clin Res Pediatr Endocrinol.* 2017;9:69–87.
3. Gutgold A, Gross DJ, Glaser B, Szalat A. Diagnosis of ABCC8 congenital hyperinsulinism of infancy in a 20-year-old man evaluated for factitious hypoglycemia. *J Clin Endocrinol Metab.* 2017;102:345–349.
4. Galcheva S, Al-Khawaga S, Hussain K. Diagnosis and management of hyperinsulinaemic hypoglycaemia. *Best Pract Res Clin Endocrinol Metab.* 2018;32:551–573.
5. Ferrara C, Patel P, Becker S, Stanley CA, Kelly A. Biomarkers of insulin for the diagnosis of hyperinsulinemic hypoglycemia in infants and children. *J Pediatr.* 2016;168:212–219.
6. Han B, Newbould M, Batra G, et al. Enhanced islet cell nucleomegaly defines diffuse congenital hyperinsulinism in infancy but not other forms of the disease. *Am J Clin Pathol.* 2016;145:757–768.
7. Lord K, Dzata E, Snider KE, Gallagher PR, De Leon DD. Clinical presentation and management of children with diffuse and focal hyperinsulinism: a review of 223 cases. *J Clin Endocrinol Metab.* 2013;98:E1786–E1789.
8. Beltrand J, Caquard M, Arnoux JB, et al. Glucose metabolism in 105 children and adolescents after pancreatectomy for congenital hyperinsulinism. *Diabetes Care.* 2012;35:198–203.
9. Fournet JC, Mayaud C, de Lonlay P, et al. Unbalanced expression of 11p15 imprinted genes in focal forms of congenital hyperinsulinism: association with a reduction to homozygosity of a mutation in ABCC8 or KCNJ11. *Am J Pathol.* 2001;158:2177–2184.
10. Verkarre V, Fournet JC, de Lonlay P, et al. Paternal mutation of the sulfonyleurea receptor (SUR1) gene and maternal loss of 11p15 imprinted genes lead to persistent hyperinsulinism in focal adenomatous hyperplasia. *J Clin Invest.* 1998;102:1286–1291.
11. Bax KN, van der Zee DC. The laparoscopic approach toward hyperinsulinism in children. *Semin Pediatr Surg.* 2007;16:245–251.
12. Otonkoski T, Nanto-Salonen K, Seppanen M, et al. Noninvasive diagnosis of focal hyperinsulinism of infancy with [ $^{18}\text{F}$ ]-DOPA positron emission tomography. *Diabetes.* 2006;55:13–18.
13. Laje P, States LJ, Zhuang H, et al. Accuracy of PET/CT scan in the diagnosis of the focal form of congenital hyperinsulinism. *J Pediatr Surg.* 2013;48:388–393.
14. Brom M, Oyen WJ, Joosten L, Gotthardt M, Boerman OC.  $^{68}\text{Ga}$ -labelled exendin-3, a new agent for the detection of insulinomas with PET. *Eur J Nucl Med Mol Imaging.* 2010;37:1345–1355.
15. Antwi K, Fani M, Heye T, et al. Comparison of glucagon-like peptide-1 receptor (GLP-1R) PET/CT, SPECT/CT and 3T MRI for the localisation of occult insulinomas: evaluation of diagnostic accuracy in a prospective crossover imaging study. *Eur J Nucl Med Mol Imaging.* 2018;45:2318–2327.
16. Antwi K, Fani M, Nicolas G, et al. Localization of hidden insulinomas with  $^{68}\text{Ga}$ -DOTA-exendin-4 PET/CT: a pilot study. *J Nucl Med.* 2015;56:1075–1078.
17. Hardy OT, Hernandez-Pampaloni M, Saffer JR, et al. Diagnosis and localization of focal congenital hyperinsulinism by  $^{18}\text{F}$ -fluorodopa PET scan. *J Pediatr.* 2007;150:140–145.
18. Treglia G, Mirk P, Giordano A, Rufini V. Diagnostic performance of fluorine-18-dihydroxyphenylalanine positron emission tomography in diagnosing and localizing the focal form of congenital hyperinsulinism: a meta-analysis. *Pediatr Radiol.* 2012;42:1372–1379.
19. Boss M, Buitinga M, Jansen TJP, Brom M, Visser EP, Gotthardt M. PET-based human dosimetry of  $^{68}\text{Ga}$ -NODAGA-exendin-4, a tracer for beta-cell imaging. *J Nucl Med.* 2020;61:112–116.

---

---

# RADAR Guide: Standard Methods for Calculating Radiation Doses for Radiopharmaceuticals, Part 1—Collection of Data for Radiopharmaceutical Dosimetry

Michael G. Stabin<sup>1</sup>, Richard E. Wendt III<sup>2</sup>, and Glenn D. Flux<sup>3</sup>

<sup>1</sup>Radiation Dose Assessment Resource (RADAR) Task Force, Society of Nuclear Medicine and Molecular Imaging, Nashville, Tennessee; <sup>2</sup>Department of Imaging Physics, University of Texas M.D. Anderson Cancer Center, Houston, Texas; and <sup>3</sup>Department of Physics, Royal Marsden NHS Foundation Trust, Sutton, United Kingdom

---

This paper presents standardized methods for collecting data to be used in performing dose calculations for radiopharmaceuticals. Various steps in the process are outlined, with some specific examples given. This document can be used as a template for designing and executing kinetic studies for calculating radiation dose estimates, from animal or human data.

**Key Words:** image reconstruction; radiation physics; radiobiology/dosimetry; radiopharmaceuticals; clinical imaging; radiation dosimetry

**J Nucl Med 2022; 63:316–322**

DOI: 10.2967/jnumed.120.259200

---

Currently, there is renewed interest in performing radiation dosimetry for radiopharmaceuticals, particularly in therapy applications. To have any new radiopharmaceutical approved by the U.S. Food and Drug Administration (FDA), whether for diagnostic or therapeutic applications, human radiation doses must be estimated. In 1999, Siegel et al. (1) published a guide for obtaining quantitative data for use in radiopharmaceutical dosimetry. The current article, and a companion article to it (2), updates that information with practical guidance and worked examples.

## FDA REQUIREMENTS FOR RADIOPHARMACEUTICAL DOSIMETRY

The FDA expects that preclinical studies will be used to determine dosimetry in animals and that human dosimetry needs to be determined as part of phase 1, 2, and 3 studies. The FDA sets standards for the use of lasers (title 21 of *Code of Federal Regulations*) and other nonionizing radiation, food irradiation, and pharmaceuticals. Medical imaging agents are submitted for approval in investigational new drug applications, new drug applications, biologics license applications, abbreviated new drug applications, and supplements to new drug applications or biologics license applications.

The radiation safety assessment that is associated with the approval of use of medical imaging agents includes many

requirements for dose calculations to support these submissions (3). Applicants should provide a description of which organs have a significant accumulation of activity over time, what activity levels were observed at different times (with at least 2 time points obtained per phase of radionuclide uptake or clearance), an evaluation of time integrals of activity, descriptions of how they were obtained, and a description of how they were combined with dose conversion factors to obtain doses (if not done by software). Any significant radiation hazards to other patients and health-care workers should also be assessed.

FDA requirements (4) require a preclinical phase, in which studies are done on an animal species, and phase 1, 2, and 3 clinical studies, in which dosimetry data are gathered from human subjects, to establish and refine the radiation dose estimates and establish the safety and efficacy of any new drug.

First-in-humans studies can establish the safety and tolerability and preliminary efficacy of a new drug before entering into full-fledged clinical trials, but all 4 phases of study are needed to establish the radiation dosimetry of any candidate for a new drug application (5).

## PLANNING A STUDY TO OBTAIN BIOKINETIC DATA

In either animal or human studies, one must collect sufficient data to fully characterize the radiation dose (Gy) to all relevant organs and tissues in the body. Siegel et al. (1) noted that there are 5 key questions in study design: what regions are source regions, how fast the radioactivity accumulates in these source regions, how long the activity remains in the source regions, how fast the activity is excreted from the source organs, and how much activity is in the source regions as a function of time after administration.

A starting point in considering study design is the physical half-life of the radionuclide used. Gathering data over several half-lives should give a good evaluation of the complete decay of the compound in the body. A very short-lived nuclide such as <sup>11</sup>C (which has a 20-min physical half-life) does not afford a long time for gathering image data. Furthermore, one must consider the radiopharmaceutical's effective half-time (although usage varies, the term *half-life* is generally used for physical half-lives, whereas *half-time* is generally used for biologic and effective half-times):

$$T_e = \frac{T_b \times T_p}{T_b + T_p}, \quad \text{Eq. 1}$$

where  $T_e$  is the effective half-time,  $T_p$  is the radionuclide's physical half-life, and  $T_b$  is the compound's biologic half-time (the time

---

Received Oct. 27, 2020; revision accepted May 5, 2021.  
For correspondence or reprints, contact Michael G. Stabin (stabinmg17@gmail.com).

Published online Aug. 5, 2021.

COPYRIGHT © 2022 by the Society of Nuclear Medicine and Molecular Imaging.

for half the activity in a region to be cleared by biologic elimination). Physical decay and biologic clearance work in parallel to remove radioactivity more quickly overall than either one would alone. For example, because  $^{99m}\text{Tc}$  has a 6-h  $T_p$ , one might think of gathering data over 24–48 h. However, because  $^{99m}\text{Tc}$ -DTPA is cleared by the kidneys in just a few short minutes and is cleared from the body overall with about a 1.7-h biologic half-time (6), 3–10 effective half-times would be 4–13 h, and many data points would need to be gathered in a relatively short time after administration. A more slowly cleared  $^{99m}\text{Tc}$  compound could be imaged over longer times. A compound labeled with  $^{131}\text{I}$  ( $T_p = 8$  d) and whose clearance is relatively slow could possibly be sampled with a few data points on the first day and then one data point per day for several days. Study design is not an exact science, but care must be taken not to undersample the data when there may be several phases of uptake and clearance. Some radiopharmaceuticals (e.g.,  $^{131}\text{I}$  tositumomab; Bexxar [GlaxoSmithKline]) are well characterized by a single exponential decay function for the whole body, whereas others may have 2 distinct phases of clearance—an early phase that is dominated by rapid clearance of a portion of the administered activity and a later phase that is dominated by slower clearance of the remainder of the administered activity. Of course, physical decay is superimposed on these biologic clearance processes. Although it is common for most uptake in organs to be fairly rapid, some organs, tissues, and tumors may exhibit an exponential phase of uptake and one or more phases of clearance. In any case, it is important to capture the early peak uptake and rapid washout phase, covering at least 3–5 effective half-times ( $T_e$ ) of the radiopharmaceutical. Report 67 of the International Commission on Radiation Units and Measurements (7) suggests that data points typically be taken near  $1/3$ ,  $2/3$ ,  $1\frac{1}{2}$ , 3, and 5 times the  $T_e$ ; be collected from at least 2 time points during the interval in which each biologic clearance phase is dominant; account for 100% of the activity at all times; and account for all major paths of excretion (e.g., urine, feces, and exhalation).

Clinical application of these requirements can be difficult. For longer-lived radionuclides such as  $^{131}\text{I}$  and  $^{177}\text{Lu}$ , capturing the behavior of early and late clearance phases may require obtaining multiple data points on the first day, then one data point each day for several days afterward. Obtaining these at times when clinical staff are available and patients can return may present logistic challenges. Siegel et al. (1) analyzed the error that can occur if the uptake and washout phases of clearance are not adequately sampled. For example, Figure D2 of their article (Fig. 1) shows the variation of  $t_{\max}$  (the time for initial sampling) that constrains the error to a given percentage, as a function of effective washout half-time ( $T_e$ ) for 4 different values of percentage error (<10%) in estimates of an organ's area under the curve (i.e., the time-integrated activity).

Madsen et al. demonstrated that when the effective half-time of a monoexponentially clearing radiopharmaceutical is fairly consistent among patients, the time-integrated activity may be estimated by taking a single measurement at the mean lifetime (i.e., 1.443 times the effective half-time) of the radiopharmaceutical. In the case of a biexponential clearance, the effective half-time of the longer-lived component should be used. Although most of the resulting renal dose estimates in a clinical study of 47 patients who were administered  $^{90}\text{Y}$ -DOTATOC were within 10% of those based on multiple-time-point imaging, some differed by as much as 22%. The investigators suggest that the population effective half-time may be obtained from a clinical study or from

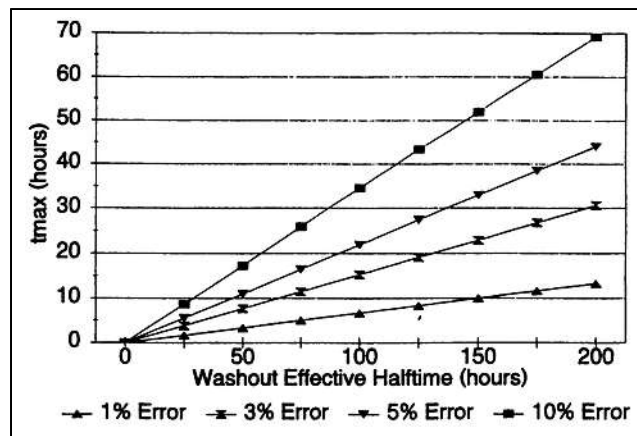


FIGURE 1. Variation in  $t_{\max}$  to constrain error on area under curve to fixed percent. (Reprinted from (1).)

pharmacokinetic modeling. This approach might not be sufficiently accurate, though, when there is a wide variation among patients or even among the source organs within individuals.

Stabin (8) provided a more comprehensive analysis of the influence of all parameter values on the overall uncertainty in internal dose estimates.

#### EXTRAPOLATING ANIMAL DATA TO HUMANS

In an animal study, the compound under study may be administered to several animals, which are then sacrificed at different times, with the activity within the organs estimated by counting (harvesting the organs and counting them in a well counter or other device), or perhaps using autoradiography techniques or imaging of the animals (e.g., with a small-animal PET or small-animal SPECT imaging system). Serial imaging with microimaging systems obviates killing of animals but may complicate the interpretation of the kinetic data that are obtained, as the animals generally need to be anesthetized, which may alter their physiologic state.

The data gathered are then used to predict uptake values in humans from the concentrations seen in animal tissues (extrapolation). Extrapolation of animal data to humans is by no means an exact science. Crawford and Richmond (9) and Wegst (10) studied some of the strengths and weaknesses of various extrapolation methods that have been proposed in the literature. One method of extrapolating animal data that has been widely applied is the % kg/g method (11). Considering %/organ or %/g in an animal to be the same as %/organ or %/g in humans is subject to certain pitfalls. In the % g/kg method, the animal organ data need to be reported as percentage injected activity per gram of tissue, and this information plus knowledge of the animal whole-body weight is used in the following extrapolation:

$$\left( \frac{\%}{\text{organ}} \right)_{\text{human}} = \left[ \left( \frac{\%}{\text{g}_{\text{organ}}} \right)_{\text{animal}} \times (\text{kg}_{\text{TB weight}})_{\text{animal}} \right] \times \left( \frac{\text{g}_{\text{organ}}}{\text{kg}_{\text{TB weight}}} \right)_{\text{human}} \quad \text{Eq. 2}$$

where % is percentage administered activity,  $\text{g}_{\text{organ}}$  is the mass of the organ in grams, and  $\text{kg}_{\text{TB weight}}$  is the mass of the whole animal in kilograms. Table 1 shows example calculations of data extrapolated from an animal species to humans using this approach (12).

**TABLE 1**

Animal Data Extrapolation Example (Mass Extrapolation)

Parameter	1 h	3 h	6 h	16 h	24 h
<b>Animal</b>					
%ID/organ	3.79	3.55	2.82	1.02	0.585
%ID/g	38.1	36.6	30.8	11.3	5.70
<b>Human (%ID/organ)</b>					
	3.26	3.12	2.63	0.962	0.486

The animal whole-body weight was 20 g (0.02 kg), and the human source organ chosen had a mass of around 300 g. The human total-body weight for the standard adult male of 70 kg was used in the calculations. For example:

$$\frac{38.1\%}{g}(\text{animal}) \times 0.020 \text{ kg} \times \frac{299 \text{ g}}{70 \text{ kg}} = \frac{3.26\%}{\text{organ}}(\text{human}). \quad \text{Eq. 3}$$

Some researchers have also suggested a transformation of the time scale, to account for the differences in metabolic rate among species of different body mass, based on the idea that faster metabolic rates will result in faster clearance of compounds from the body. One suggested scaling approach is given as follows:

$$t_h = t_a \left[ \frac{m_h}{m_a} \right]^{0.25}, \quad \text{Eq. 4}$$

where  $t_a$  is the time at which a measurement was made in an animal system,  $t_h$  is the corresponding time assumed for the human data, and  $m_a$  and  $m_h$  are the total-body masses of the animal species and of humans, respectively. Table 2 shows an example with data extrapolated from an animal species to humans using this time-scaling approach (10). In this example, the animal whole-body weight was 200 g (0.2 g), and again, the human total-body weight for the standard adult male of 70 kg was used in the calculations. For example:

$$5 \text{ min} \times \left[ \frac{70 \text{ kg}}{0.2 \text{ kg}} \right]^{0.25} = 22 \text{ min}. \quad \text{Eq. 5}$$

One problem in the area of animal data extrapolation to humans is the treatment of activity that is not accounted for in individual animal organs. Some researchers manage to successfully account for activity in the carcass, or the rest of the animal body that was not harvested for counting. If the radionuclide is particularly short-lived, this assessment may not be necessary, as one may be able to simply assume that activity unaccounted for was uniformly distributed in other tissues and eliminated only by radioactive decay. For many radiopharmaceuticals, this assumption may significantly overestimate the number of disintegrations in these remainder tissues and underestimate the number of disintegrations in excretory organs such as the urinary bladder and the intestines. An assessment of the activity in these regions, via direct counting or analysis of excreta, is usually needed. Such values are usually not extrapolated to humans on a mass basis but are assumed to apply directly (i.e., % excreted by the animal = % excreted by the human); a time extrapolation may be applied if desired. Gathering of excreta data is quite important to accounting for 100% of the administered activity. If it is known that all excretion is urinary, one can use (100% minus the total-body retention) as the excreted fraction. If both urinary and intestinal excretion are possible, the collection of both urinary and fecal data is needed.

Sparks and Aydogan (13) investigated the accuracy of animal data extrapolation to humans for several radiopharmaceuticals. They reached no solid conclusions that any particular method was superior to another. They did find, however, that extrapolated animal data tend to underestimate human organ self-doses. Figure 2, adapted from Figures 1 and 4 in their publication, show 2 examples of their results. These figures show the ratio of organ residence times (normalized number of disintegrations), which is also proportional to organ self-dose, when no extrapolation was performed (their Fig. 1) or both the time and the mass extrapolations shown above (their Fig. 4) were performed. A ratio of 1.0 represents perfect agreement, whereas ratios below 1.0 imply that the animal data underpredicted human doses, and ratios above 1.0 imply overestimation of human doses. One would like to see a normal distribution centered around 1.0. The graphs might fit a lognormal distribution, but nonetheless, in most cases, extrapolated animal data underpredicted human doses. Thus, providing dosimetry data to the FDA in preclinical studies is necessary in the drug approval process, but in most cases, reasonably accurate human doses will be derived only from the phase 1, 2, and 3 clinical studies on humans.

An important point in the elements of study design that are listed above is to account for 100% of the activity at all times. This is not always easy in preclinical studies, especially for organs that are distributed, such as the musculature and the skeleton, and for the whole body if the carcass of the animal after the removal of specific source organs is too large to be counted unless cut into numerous small pieces. The design of a preclinical study should include how this matter will be addressed, as it might well be too late to obtain this information after the performance of a study that neglects this point.

**STEPS FOR COLLECTING DATA FROM HUMAN SUBJECTS**

The external conjugate-view method, using anterior and posterior projection images from a nuclear medicine camera, is the method used most frequently used to obtain quantitative data in human studies for dosimetry. In this method, the source activity  $A_j$  is given as follows (1):

$$A_j = \sqrt{\frac{I_A I_P \bar{f}}{e^{-\mu_e t} C}} \quad \text{Eq. 6}$$

$$f_j \equiv \frac{(\mu_j t_j / 2)}{\sinh(\mu_j t_j / 2)}, \quad \text{Eq. 7}$$

where  $I_A$  and  $I_P$  are the observed counts over a given time for a given region of interest (ROI) in the anterior and posterior projections (counts/time);  $t$  is the average patient thickness over the ROI;  $\mu_e$  is the effective linear attenuation coefficient for the radionuclide, camera, and collimator;  $C$  is the system calibration factor  $C$  (counts/time per unit activity); and the  $f$  is a correction for the source region attenuation coefficient ( $\mu_j$ ) and source thickness ( $t_j$ ) (i.e., source self-attenuation correction). Figure 3 shows the geometric relationships. This expression (Eq. 6) assumes that the views are well collimated (i.e., they are oriented toward each other without offset) and also assumes a narrow-beam geometry without significant scattered radiation, septal penetration, or other interferences. Corrections for scatter are usually advisable; several proposed methods are described below.

**TABLE 2**  
Animal Data Extrapolation Example (Time Extrapolation)

Animal time scale	5 min	15 min	30 min	60 min	1.5 h
Extrapolated human time scale	22 min	1.1 h	2.2 h	4.3 h	6.5 h

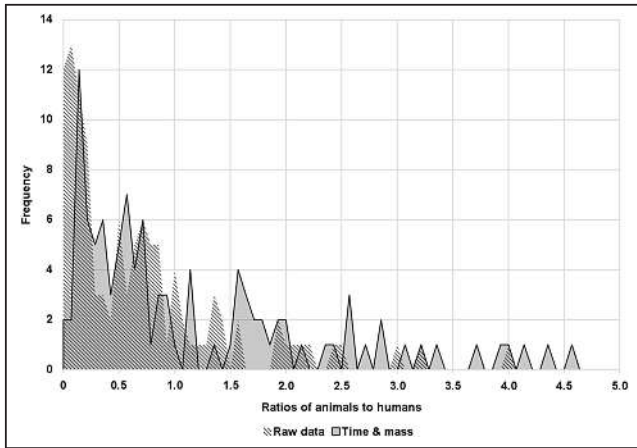


**FIGURE 2.** Frequency distribution of ratio of organ residence times using raw data or time and mass data extrapolated from animals to humans. (Adapted from (13).)

### CORRECTIONS FOR SCATTERED RADIATION

One relatively straightforward correction procedure for scatter compensation is the triple-energy-window method (14); this involves establishing counting windows on either side of the  $\gamma$ -camera photopeak window such that the area of the 2 adjacent windows is equal to that of the photopeak (or if not, the count ratios should be appropriately scaled). The corrected photopeak counts ( $C_T$ ) are given as follows:

$$C_T = C_{pp} - F_S \times (C_{LS} + C_{US}), \quad \text{Eq. 8}$$

where  $C_{pp}$  is the total count recorded within the photopeak window and  $C_{LS}$  and  $C_{US}$  are the counts within the lower and upper scatter windows, respectively. The scaling factor ( $F_S$ ) corrects for the (most common) case in which the total width of the scatter windows (in keV) is not equal to that of the photopeak window. It would be unity if they were equal. Thus, adjustment of the adjacent windows is assumed to compensate for the high-energy-photon scatter tail on which the true photopeak events ride. Even if the areas of the scatter windows are equal to the area of the photopeak window, the use of a scaling factor other than unity may provide the best correction for scatter in a given system with a particular radionuclide. This correction may be determined by studying a source of known volume submerged to a realistic depth in a water phantom whose dimensions are similar to those of a human subject (Fig. 4). An extension of the triple-energy-window approach is to use more energy windows and to apply principal-component analysis or factor analysis to the resulting data in the energy dimension.

SPECT reconstruction methods have incorporated more sophisticated methods of scatter correction such as estimating the point-spread function of the scattering and applying it during the forward projection of data in an iterative reconstruction algorithm such as maximum-likelihood expectation maximization.

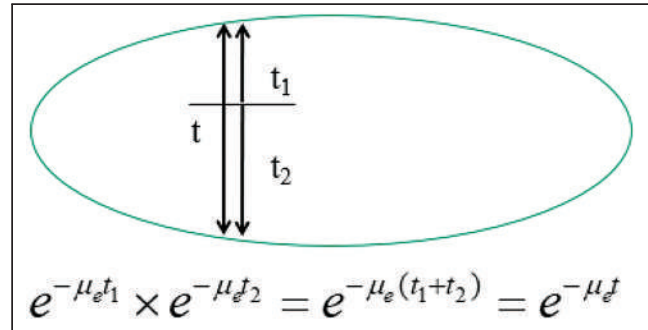


**FIGURE 3.** Geometric representation of correction for attenuation in geometric mean method.  $t$  is total thickness of subject, whereas  $t_1$  is depth of source from upper surface and  $t_2$  is depth of source from lower surface.  $t = t_1 + t_2$ . Product of upper and lower attenuation factors is dependent only on total thickness and not position of source within subject.

Commercial SPECT/CT cameras and software have recently been introduced that offer quantitative SPECT in the same manner that PET is quantitative. They include calibrations for specific radionuclides with corrections for attenuation and scatter.

### CORRECTIONS FOR BACKGROUND ACTIVITY

When an ROI is drawn over a source region on a projection image, some counts from the region will have originated from activity in the subject's body that is outside the identified source region. This includes scattered radiation from other ROIs, background radiation, and other sources. Thus, a background ROI is drawn over some region of the body that is close to the source ROI and that, in the analyst's opinion, best represents the activity of nearby tissues to the source that will provide the best estimate of a background count rate to be subtracted from the source ROI. As with the scatter correction shown above, a scaling factor may be needed to correct the number of counts in the background ROI so that the appropriate correction is made, given the number of pixels in the source and background ROI. Alternately, one may simply subtract the number of counts per pixel in the background ROI from the number of counts per pixel in the source ROI and then calculate the total number of counts in the source ROI as the corrected number of counts per pixel times the number of pixels.

One way to make a quality assurance check is to place a source of activity of the radionuclide being imaged external to the body. Then, an ROI is drawn away from the subject's body and also away from any star-pattern streaks that may accompany the source image because of septal penetration, but close enough that it captures a typical number of counts per pixel that represents background and scattered radiation within the imaging area close to the subject. The counts of this source over time should reflect the radionuclide physical half-life.

It is important to avoid drawing a background ROI over body structures that may contain a high level of activity (e.g., blood vessels and areas of the skeleton with significant uptake), as this will

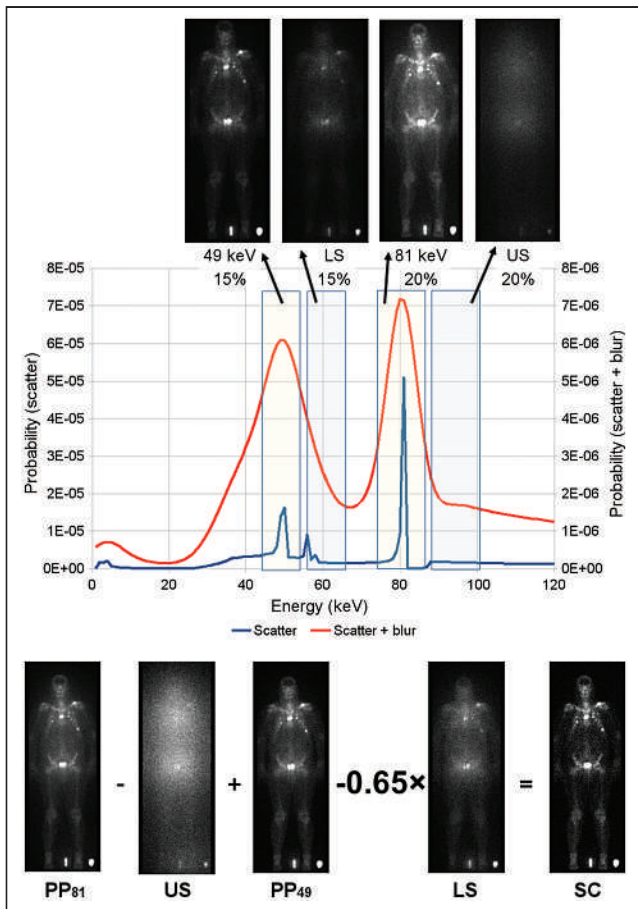


**FIGURE 4.** Example of use of multiple windows to correct for scattered radiation in  $\gamma$ -camera images. Ideal spectrum of  $^{166}\text{Ho}$  is plotted in blue, and spectrum blurred by energy resolution of  $\gamma$ -camera is plotted in orange. Upper scatter window captures down-scatter from high-energy  $\gamma$ -rays, whereas lower scatter window captures down-scatter from 81-keV  $\gamma$ -ray as well. Weighting factor of 0.65 on lower scatter window was determined empirically. LS = lower scatter window; PP = photopeak; US = upper scatter window.

remove too many counts from the source ROI. It is also important not to draw the background ROI too far away from the source region in an area of particularly low background, as this may not remove enough counts from the source ROI. The choosing of locations and sizes of background ROIs is difficult to prescribe exactly, and practices vary considerably among investigators, potentially resulting in markedly different results for the final estimates of activity assigned to a source ROI. This process should be performed with care and attention to the above points for the best and most reproducible results. The locations of the background ROIs should be documented, perhaps by graphical screen captures if necessary, to enhance the reproducibility of a dosimetric analysis.

Pereira et al. (15) showed examples of optimized background regions for regions in a water phantom representing organs of interest (Fig. 5), noting possible uncertainties in different quantification methods.

#### CORRECTION FOR OVERLAPPING ORGANS AND REGIONS

It is not uncommon for some organs or tumors to overlap other structures in projection images. The right kidney and the liver are

frequently partially superimposed in such images, as are the left kidney and spleen, in many subjects. When organ overlap occurs, the total activity within a source can be estimated by various approximate methods. For paired organs, such as the kidneys and lungs, one approach is simply to quantify the activity in one of the organs for which there is no overlap with other organs and double the number of counts in this organ to obtain the total counts in both organs. If the masses of the paired organs can be determined, perhaps using volumes that are derived from CT or MR images, and are then multiplied by the tissue density, then the scaling factor could be the combined masses of the 2 organs divided by the mass of the organ without overlap. Another approach is to draw an ROI over the region of the organ that has no overlap in scans where there is overlap, count the number of pixels, note the average count rate per pixel, use an ROI from another image in which there is no apparent overlap and the whole organ is clearly visible, count the number of pixels in a larger ROI drawn on this image, and then simply multiply the count rate per pixel from the first image by the number of pixels in the second image in order to estimate the total counts from the organ in the first image. Or, equivalently, take the total number of counts in the partial-organ ROI in the first image and multiply by the ratio of the numbers of pixels in the ROIs in the second and the first images, respectively. If no image can be found in which a significant overlap with another organ does not obscure the organ boundaries, an approximate ROI may need to be drawn just from knowledge of the typical shapes of such organs. This kind of approximation is obviously not ideal, but it may be necessary.

#### OBTAINING $\gamma$ -CAMERA SYSTEM ATTENUATION AND CALIBRATION COEFFICIENTS

##### Attenuation Coefficient

The system attenuation coefficients ( $\mu_e$ ), both for the nuclide to be imaged and for the nuclide used to establish the body thickness for the attenuation correction (typically  $^{57}\text{Co}$ ), must be measured at some time before (or possibly after) radiopharmaceutical administration in a separate experiment. The procedure involves preparation and counting of a source of activity, ideally one whose surface area is greater than that of the source region, with the same radionuclide and the same  $\gamma$ -camera settings as those that are to be used for the patient imaging study. As an example, for small regions one may fill the bottom of a Petri dish (covered and sealed to prevent possible contamination), and for large regions one may fill a flood source. A small, pointlike source can also be used, if necessary. The source should be counted for a fixed time (e.g., 5 min) in air, with no intervening attenuating material. Then, the measurement is repeated with several different thicknesses of attenuating material of approximately unit density (i.e.,  $1 \text{ g/cm}^3$ ) between the source and one of the  $\gamma$ -camera heads. One may obtain the count rates by drawing ROIs encompassing the source region (with correction for background in an adjacent ROI) and then plot the background-corrected counts in the ROIs versus the interposed attenuator thickness (another method for acquiring transmission data is to acquire a transmission scan of the stacks of attenuating material using a line or flood source). The counts may be fit by an exponential function, or the natural logarithm of the counts may be fit by a straight line. In either case, the factor  $\mu_e$  that best fits the data is the attenuation coefficient to be used in corrections in patient studies.

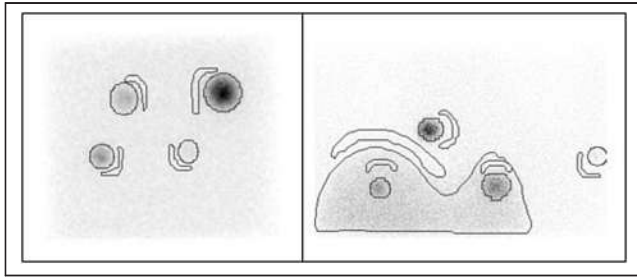


**FIGURE 5.** Background regions drawn by Pereira et al. in water phantom. Background region is positioned over area near source that has count density of object in absence of source. (Reprinted from (15).)

### System Calibration Factor

As with the attenuation coefficient, the system calibration factor,  $C$ , must be measured at some time before or after radiopharmaceutical administration in a separate experiment. For this factor, the method is to prepare a standard of known activity of the same radionuclide as that to be used for administration to subjects, usually a few tens of megabecquerels in almost any suitable container (e.g., a syringe or vial). The exact source strength is not important, as long as sufficient counts are obtained for a consistent evaluation over the course of the study and as long as not too many counts are obtained, resulting in count saturation and possibly dead time in the camera. The standard should be counted in air for a fixed time (e.g., 5 min) at a source-to-collimator distance that approximates that of the patient midline distance used for the imaging study (Fig. 6).

The count rate per unit activity (in units of, for example, cpm/Bq or cpm/ $\mu$ Ci) represents the calibration factor. The collimator count-rate response as a function of the source-to-collimator distance must be known. For parallel-hole collimators, the collimator efficiency is invariant near the center of the field of view; however, for other collimators, such as diverging, converging, and pinhole collimators, the efficiency is dependent on the source-to-collimator distance. It is also important to use the same camera settings, such as the width of the energy window, for this calibration as for the patient imaging.

In most cases the self-attenuation factor  $f$  is not significantly different from unity and is rarely important. Normally, one assumes that the variation in body thickness across individual ROIs is small, and so a single attenuation factor may be used to calculate the activity for the entire ROI. On the other hand, if the ROI is large and body thickness is thought to vary substantially within the ROI, a pixel-by-pixel calculation may be made. A pixel-by-pixel attenuation calculation can always be made, regardless of this assumption. A conjugate-view measurement is thus made at each of the time points chosen and the best ROIs for each region are superimposed on the images at each time. Because of potentially different rates of uptake and clearance in various tissues, individual organs or tumors may be best visualized at different times after administration. Some regions have most of their uptake early and clear quickly, whereas others may accumulate activity more slowly. Thus, different times may be chosen at which to draw the best ROIs for different regions. The best approach is to have a computer program that allows the ROIs to be independently defined and saved but then linked together and moved together, to allow the relative locations of all ROIs to be retained when new ROIs are defined, or when different patient images reflect slightly different patient placement on the imaging table or slightly different patient orientation toward the camera heads. Care should be taken to have the patient recline in

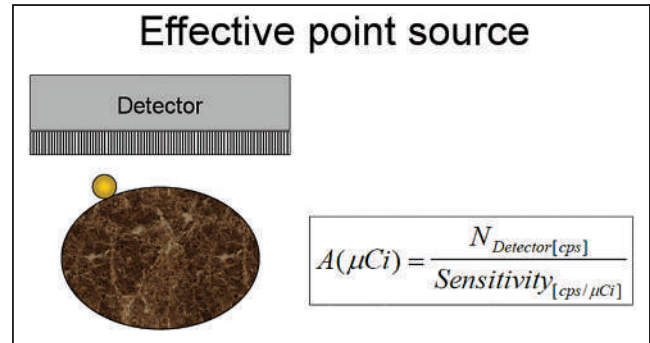


**FIGURE 6.** Use of point source to establish system calibration coefficient.

the same position in all images, as differences in patient orientation toward the camera heads may change the lateral separation between organs. One aid in achieving this consistency are the cushions that are used to stabilize the patient and produce reproducible positioning in radiation oncology.

### USE OF TOMOGRAPHIC DATA IN QUANTITATIVE IMAGING

The use of tomographic data, either SPECT or PET, for quantitative image analysis for dosimetry overcomes some of the problems inherent in anterior–posterior planar imaging. The advent of hybrid SPECT/CT cameras enable improved attenuation correction, and iterative reconstruction techniques allow correction for scattering and for depth-dependent resolution. The first quantitative SPECT/CT systems for implementing voxel-based dosimetry are appearing commercially. Scatter and attenuation corrections are inherently applied in the image reconstruction process. An important problem in planar imaging is organ overlap. For example, the right kidney is usually partially or totally obscured by the liver. Tumors may also be difficult to delineate because of other overlying structures with significant activity. In the case of PET, routine calibrations for clinical diagnoses ensure that the data provided are already quantitative and can be used directly for dose calculations. In SPECT, clinical needs normally do not necessitate an absolute activity quantification. Performing quantitative SPECT for internal dose calculations is somewhat more difficult than is planar imaging, but for the reasons noted above, may offer desirable advantages. Dewaraja et al. (16) provided an overview of methods to perform quantitative SPECT for radionuclide therapy. The steps that they outlined were as follows: acquisition, dead-time corrections, image reconstruction, compensation for image-degrading effects (attenuation, scatter, and detector response), definition of targets, determination of the camera calibration factor, completion of partial volume corrections, and integration of the time–activity curves.

As SPECT image acquisition and quantification is more difficult and time-consuming than a planar image acquisition, and each CT scan for attenuation correction imparts an additional absorbed radiation dose to the patient, one may use a hybrid method—using a series of planar images to establish the overall biokinetic behavior, with one or more SPECT images taken concurrently with a planar image—to better establish absolute accuracies (Fig. 7).

At the time that this is being written, new technology both in PET and in SPECT is promising to improve the accuracy of dosimetric workups by enabling volumetric imaging. Two recently

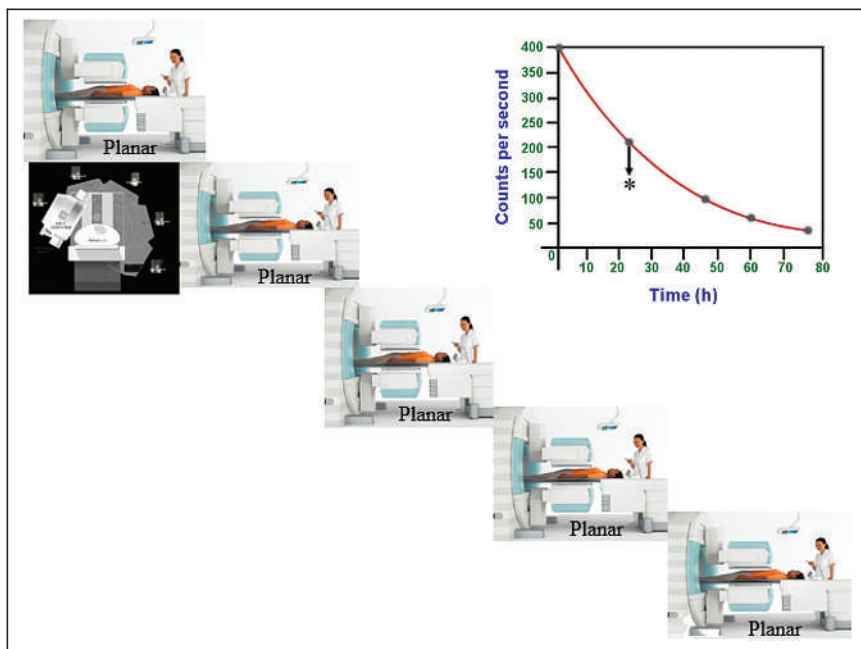


**FIGURE 7.** Combining SPECT and planar images for activity quantification. Planar images are acquired at every time point, whereas quantitative SPECT/CT images are acquired at only one time point. Volume of interest containing source in SPECT images is then used to calibrate counts from same source in planar images.

introduced commercial long-axial-extent PET systems might be characterized as whole body. One has a 2-m axial field of view, which can literally image the entire body of most patients at once. The other has a 106-cm axial field of view, which is designed to be able to image most patients from the crown of the head to the mid thigh. These systems have much higher sensitivity than more typical PET scanners and thus can acquire useful data over a longer portion of the time–activity curve, which should improve the estimation of the time-integrated activity. They also acquire the entire volume simultaneously, which again improves the time–activity curve.

Whole-body SPECT is available in preclinical instrumentation. That technology is reportedly being scaled up to accommodate adult humans. The novel SPECT technology that was originally developed for cardiac imaging acquires data from many points of view in such rapid succession that it is effectively simultaneous in 3 dimensions over the time scale of the physiologic processes of interest in internal dosimetry. That technology has been built into a full-ring SPECT camera with an axial field of view of roughly 60 cm. Although its cadmium-zinc-telluride detectors are better suited to low- and medium-energy radionuclides than to high-energy radionuclides, its higher sensitivity and better energy resolution allow SPECT scans of many radionuclides to be acquired in the time that an ordinary  $\gamma$ -camera requires for a planar whole-body scan.

## DISCLOSURE

No potential conflict of interest relevant to this article was reported.

## REFERENCES

1. Siegel JA, Thomas S, Stubbs J, et al. MIRD pamphlet no 16: techniques for quantitative radiopharmaceutical biodistribution data acquisition and analysis for use in human radiation dose estimates. *J Nucl Med.* 1999;40:37S–61S.
2. Stabin MG, Wendt RE III, Flux GD. RADAR guide: standard methods for calculating radiation doses for radiopharmaceuticals, part 2—data analysis and dosimetry. *J Nucl Med.* August 5, 2021 [Epub ahead of print].
3. Guidance for industry developing medical imaging drug and biological products, part 1: conducting safety assessments. U.S. Food and Drug Administration website. <https://www.fda.gov/media/72295/download>. Published June 2004. Accessed August 12, 2021.
4. Step 3: clinical research. U.S. Food and Drug Administration website. <https://www.fda.gov/ForPatients/Approvals/Drugs/ucm405622.htm>. Revised January 4, 2018. Accessed August 12, 2021.
5. Gieser G. Clinical pharmacology 1: phase I studies and early drug development. Food and Drug Administration (FDA) website. <https://www.fda.gov/media/84920/download>. Accessed August 30, 2021.
6. *Annals of the ICRP: ICRP Publication 53—Radiation Dose to Patients from Radiopharmaceuticals.* Pergamon Press; 1988:1–373.
7. *ICRU Report 67: Absorbed-Dose Specification in Nuclear Medicine.* International Commission on Radiation Units and Measurements, Inc.; 2002;2:7–130.
8. Stabin MG. Uncertainties in internal dose calculations for radiopharmaceuticals. *J Nucl Med.* 2008;49:853–860.
9. Crawford DJ, Richmond CR. Epistemological considerations in the extrapolation of metabolic data from non-humans to humans. In: Watson E, Schlafke-Stelson A, Coffey J, Cloutier R, eds. *Third International Radiopharmaceutical Dosimetry Symposium.* U.S. Department of Health, Education, and Welfare; 1981:191–197.
10. Wegst A. Collection and presentation of animal data relating to internally distributed radionuclides. In: Watson E, Schlafke-Stelson A, Coffey J, Cloutier R, eds. *Third International Radiopharmaceutical Dosimetry Symposium.* U.S. Department of Health, Education, and Welfare; 1981:198–203.
11. Kirschner A, Ice R, Beierwaltes W. Radiation dosimetry of  $^{131}\text{I}$ -19-iodocholesterol: the pitfalls of using tissue concentration data [reply]. *J Nucl Med.* 1975;16:248–249.
12. Stabin MG. *Fundamentals of Nuclear Medicine Dosimetry.* Springer; 2008:1–400.
13. Sparks R, Aydogan B. Comparison of the effectiveness of some common animal data scaling techniques in estimating human radiation dose. In: *Proceedings of the Sixth International Radiopharmaceutical Dosimetry Symposium.* Oak Ridge Institute for Science and Education; 1999:705–716.
14. Ogawa K, Harata Y, Ichihara T et al. A practical method for position-dependent Compton-scatter correction in single emission CT. *IEEE Trans Med Imaging.* 1991;408–412.
15. Pereira JM, Stabin MG, Lima FRA, et al. Image Quantification For Radiation Dose Calculations—Limitations And Uncertainties. *Health Phys.* 2010;99:688–701.
16. Dewaraja YK, Frey EC, Sgouros G, et al. MIRD pamphlet no. 23: quantitative SPECT for patient-specific 3-dimensional dosimetry in internal radionuclide therapy. *J Nucl Med.* 2012;53:1310–1325.

## Commercially Competitive Vendor-Agnostic Image Reconstruction Could Be a Leap Forward for PET Harmonization

**TO THE EDITOR:** I read with interest the recent publication in *The Journal of Nuclear Medicine* titled “A Guide to ComBat Harmonization of Imaging Biomarkers in Multicenter Studies” (1). The work discussed in the article presents valuable ideas and concepts to the community and continues a tradition of inspired diligence that has ushered our field toward an increasingly efficacious infrastructure for PET harmonization. Efforts to improve harmonization in PET metrology provide a significant and fundamental contribution to the field; they support our ability to work confidently with images and develop meaningful clinical assessments and innovations.

Image reconstruction is a central step in the image generation process. In recent years, significant gains have been made in PET image quality at the stage of image reconstruction, we can note that application of the technology has transitioned into the proprietary and vendor-specific domain. As we look to the future and see inevitable evolution of artificial intelligence–aided reconstruction, we can expect that in the coming years it will likely be more difficult to fully describe reconstruction algorithms because they will be partially defined by the select training datasets used to build them (2). It appears that we are on a trajectory that will usher in continued divergence of advanced reconstruction algorithms across vendors, increased layers of vendor specificity, and subsequently greater challenges to harmonize PET.

The field of data science is continually maturing, perhaps most notably in the areas of artificial intelligence and radiomics. Simultaneously we are learning to take on new roles as stewards of data (2,3). Our growth in this realm is relevant for harmonization efforts because the prospect of evolving the field toward greater access to raw data has many implications, including the potential to create reliable, cross-platform image reconstruction tools. Such a solution could present an ideal, alternative strategy for addressing the “scanner affect,” essentially through reducing the (technically unnecessary) variability of vendor-specific image reconstruction algorithms across scanners.

The importance of homogenizing PET data is fundamental to the field. A basis for the advancement of diagnostic imaging are standards established through multicenter trials. The greater the uncertainty in the trial data, the greater the possibility a study will be underpowered, and it adds an increased possibility of the trial producing incorrect conclusions (4). Uncertainty stems in part from variability in the image generation processes and can be addressed through standardization or harmonization. We can recall *standardization* refers to the process of making something conform to a standard whereas *harmonization* is the action, or process, of making something consistent or compatible. The former is preferable where possible—we cannot reasonably standardize hardware, but we could create the means to standardize processing, in support of those applications of PET that may benefit from it. A recent review of multicenter

use of PET/CT concluded that “standardization” of acquisition and processing “should precede any multicenter trial that uses PET SUVs quantitatively”; and that “This should be a high priority for future multicenter trials using quantitative imaging” (5). The priority is echoed and amplified if we consider the field’s collective responsibility to ensure that our patient’s data are being used for optimal benefit (3). It therefore becomes prudent to recognize that an infrastructure that supports optional standardized advanced image reconstruction is preferential.

We are at least several years away from having reliable third-party PET image reconstruction tools—it is possible from a technical standpoint, but we do not presently have the industrial framework to support it, and raw data formats as well as reconstruction algorithms are proprietary. But whether we are several years away from realizing this solution, or several decades, may depend on if we are willing to have the requisite discussion now. Several pathways could be considered for implementation. One method could be tuning PET systems to produce reliable, compliant raw data formats, which could enable investment in creating competitive cross-platform processing tools.

Data access across imaging is in fact a large and consequential subject. Harmonization in PET is one of many topics that are connected to this faucet on our infrastructure. Generally, opening access to raw data for third-party solution development addresses a central pivot of the PET instrumentation field and would have wide ranging implications for innovation beyond, and downstream of, improved harmonization or standardization (6). Radiomics, AI, and other avenues of imaging data science would directly reap the benefits—access to data and its quality (fidelity) is a new bottleneck for technologic advancement. Although the topic of data access is complex, cross-vendor reconstruction for supporting harmonization efforts would be a straightforward and logical solution for addressing the harmonization problem at its crux. Correspondingly, the clear and concise implication of unified reconstruction in the harmonization challenge lends support to the more general assertion that greater access to data should support a more efficacious modern imaging field.

In summary, practical solutions, such as those presented by the authors, provide real benefit to the field. But as we look to the future, it is time to add agnostic image reconstruction to the discussion of solutions for harmonization. The same advancements in computing technology that have enabled new advances in image reconstruction also make it prudent to reevaluate our infrastructure for accessing and using data at its source.

## REFERENCES

- Orlhac F, Eertink JJ, Cottreau AS, et al. A guide to ComBat harmonization of imaging biomarkers in multicenter studies. *J Nucl Med*. September 16, 2021 [Epub ahead of print].
- Reader AJ, Schramm G. Artificial intelligence for PET image reconstruction. *J Nucl Med*. 2021;62:1330–1333.
- Larson DB, Magnus DC, Lungren MP, Shah NH, Langlotz CP. Ethics of using and sharing clinical imaging data for artificial intelligence: a proposed framework. *Radiology*. 2020;295:675–682.
- Doot RK, Kurland BF, Kinahan PE, Mankoff DA. Design considerations for using PET as a response measure in single site and multicenter clinical trials. *Acad Radiol*. 2012;19:184–190.

5. Byrd D, Christopf R, Buatti J, et al. Multicenter survey of PET/CT protocol parameters that affect standardized uptake values. *J Med Imaging (Bellingham)*. 2018;5: 011012.
6. Kesner A. The cultivation of supply side data science in medical imaging: an opportunity to define the future of global health. *Eur J Nucl Med Mol Imaging*. October 23, 2021 [Epub ahead of print].

**Adam L Kesner**

*Memorial Sloan Kettering Cancer Center  
New York, New York 10065  
E-mail: kesnera@mskcc.org*

Published online Nov. 5, 2021.  
DOI: 10.2967/jnumed.121.263421

## A VISION of ALSYMPCA

**TO THE EDITOR:** I just read the 2 editorials written by Hofman (1) and by Czernin and Calais (2) commenting on the use of <sup>177</sup>Lu-PSMA-617 therapy in patients with metastatic castration-resistant prostate cancer (mCRPC), mainly on the results of the VISION trial (3). <sup>177</sup>Lu-PSMA-617 together with <sup>68</sup>Ga- or <sup>18</sup>F-labeled PSMA ligands are doubtless important theranostic technologies that provide a new perspective on mCRPC treatment, as stated in another recent editorial by Srinivas and Iagaru (4). However, I miss in the VISION trial a comparison with the results of another study performed a few years ago that analyzed the use of <sup>223</sup>Ra in the treatment of mCRPC patients, the ALSYMPCA trial (5). Although <sup>223</sup>Ra is used to treat patients with exclusive bone metastases, this group represents most patients with mCRPC. In some studies, the percentage of patients with bone metastatic disease, with or without concomitant lymph node disease but without visceral (lung and liver) disease, represents around 70% of cases (6), and in this group the presence of concomitant lymph node disease does not appear to change the overall survival (this high percentage was also confirmed in the VISION trial, in which 91% of patients had bone metastases, 50% had lymph node metastases, 9% had lung metastases, and 12% had liver metastases) (6). Therefore, <sup>223</sup>Ra could represent an adequate option to treat most patients with mCRPC. In this sense, it will be useful if the authors of the VISION study, as well as of other future studies on this issue, also present the survival results for the distinct groups of metastatic lesions or, at least, separate the results of the ones with bone metastatic disease without visceral disease from the group with visceral disease. This separation would be useful to indirectly compare the effects of <sup>177</sup>Lu-PSMA-617 with the effects of <sup>223</sup>Ra in the group without visceral metastases and also to assess the effect of <sup>177</sup>Lu-PSMA-617 in the group of patients with visceral metastases, who certainly are not candidates for <sup>223</sup>Ra therapy.

In this line of reasoning, it is interesting to note that median survival differences between groups receiving or not receiving the radionuclide therapy are similar in both trials: 4 mo (15.3 mo vs. 11.3 mo for patients receiving or not receiving the therapy, respectively) in VISION and 3.6 mo (14.9 mo vs. 11.3 mo) in ALSYMPCA. Besides, although the authors of the VISION study did not present the results of subgroups with and without visceral metastases, in the supplementary appendix of the study (3) the authors presented the survival results in subgroups with and without liver metastases and showed that there is no statistically significant difference in overall survival in the

subgroup with liver metastases. These findings, in my opinion, are worrisome and suggest that the main effect of <sup>177</sup>Lu-PSMA-617 in overall survival could be due to its action on bone metastases and not on visceral metastases.

Therefore, presentation of the survival results by subgroups will be essential to define the patients who would most benefit from <sup>177</sup>Lu-PSMA-617 therapy and to further establish the best theranostic algorithm to treat these patients (e.g., patients with exclusive bone disease would first receive <sup>223</sup>Ra, and patients with visceral disease would first receive <sup>177</sup>Lu-PSMA-617). Last, it is important to say that <sup>223</sup>Ra therapy is already a reality in several places around the world whereas <sup>177</sup>Lu-PSMA-617 is a distant vision; thus, to move from ALSYMPCA to VISION, VISION has to show where it is really effective.

## REFERENCES

1. Hofman MS. Bringing VISION to nuclear medicine: accelerating evidence and changing paradigms with theranostics. *J Nucl Med*. August 12, 2021 [Epub ahead of print].
2. Czernin J, Calais J. <sup>177</sup>Lu-PSMA617 and the VISION trial: one of the greatest success stories in the history of nuclear medicine. *J Nucl Med*. 2021;62:1025–1026.
3. Sartor O, de Bono J, Chi KN, et al. Lutetium-177-PSMA-617 for metastatic castration-resistant prostate cancer. *N Engl J Med*. 2021;385:1091–1103.
4. Srinivas S, Iagaru A. To scan or not to scan: an unnecessary dilemma for PSMA radioligand therapy. *J Nucl Med*. 2021;62:1487–1488.
5. Parker C, Nilsson S, Heinrich D, et al. Alpha emitter radium-223 and survival in metastatic prostate cancer. *N Engl J Med*. 2013;369:213–223.
6. Halabi S, Kelly WK, Ma H, et al. Meta-analysis evaluating the impact of site of metastasis on overall survival in men with castration-resistant prostate cancer. *J Clin Oncol*. 2016;34:1652–1659.

**Paulo Schiavom Duarte**

*São Paulo Cancer Institute  
São Paulo, Brazil  
E-mail: psduarte@hotmail.com*

Published online Sep. 16, 2021.  
DOI: 10.2967/jnumed.121.263160

## Reply: A VISION of ALSYMPCA

**REPLY:** Dr. Duarte urges an analysis of the VISION trial in an effort to ascertain results in subsets of men with bone and visceral disease. He then suggests an indirect comparison between <sup>177</sup>Lu-PSMA-617 and <sup>223</sup>Ra.

I agree with the first point but disagree with the second. The VISION trial (1) can be analyzed in a multiplicity of new ways. Right now, just the prespecified primary analyses have been published (1). There are many analyses that will follow that include not only the distribution of the disease (as suggested by Duarte) but also the various biomarkers that are known to be prognostic in other settings. These biomarkers might include hemoglobin, neutrophil-to-lymphocyte ratio, prostate-specific antigen, alkaline phosphatase, lactate dehydrogenase, performance status, age, time since diagnosis, pain, and others. As it turns out, the dataset from VISION is rich and there is much more to explore.

On the second point, there is disagreement. The ALSYMPCA trial with <sup>223</sup>Ra (2) was conducted in a long-ago era, before the use of novel hormones such as abiraterone and enzalutamide and before the widespread use of cabazitaxel. Further, patients enrolled in ALSYMPCA were not required to progress after docetaxel (but approximately half did). All patients enrolled in VISION had progressed after either

abiraterone or enzalutamide. Further, all patients in VISION had progressed after docetaxel and approximately 40% had progressed after cabazitaxel. Thus, the patient populations of ALSYMPCA and VISION are completely distinct. Indirect comparisons between phase III trials are always fraught with difficulty. In this case, because the populations are so distinct, comparisons would be particularly problematic.

Dr. Duarte also raises the issue that the liver metastasis patients do not have improved survival in VISION and suggests that the positive effects of  $^{177}\text{Lu}$ -PSMA-617 may be predominantly on patients with bone metastases. Although these points are well taken, the overanalysis of small data subsets can at times be erroneous. The number of patients in the VISION trial with liver metastases was far smaller than optimal for a conclusive analysis. There is much more to learn before a definitive conclusion can be drawn. Further, we would all agree that there is considerable heterogeneity for those with liver metastases and that more analyses may potentially yield interesting findings. Perhaps the patients with higher PSMA PET SUVs may be distinct from those with lower PSMA PET SUVs. Perhaps those with more than 20 liver metastases may be distinct from those having just one. Simply stated, there is much more to learn before categorical statements can be made regarding analyses of underpowered subsets.

## REFERENCES

1. Sartor O, de Bono J, Chi KN, et al. Lutetium-177-PSMA-617 for metastatic castration resistant prostate cancer. *N Engl J Med*. 2021;385:1091–1103.
2. Parker C, Nilsson S, Heinrich D, et al. Alpha emitter radium-223 and survival in metastatic prostate cancer. *N Engl J Med*. 2013;369:213–223.

Oliver Sartor

Tulane University School of Medicine

E-mail: osartor@tulane.edu

DOI: 10.2967/jnumed.121.263193

## On Semiquantitative Methods for Assessing Vascular $^{18}\text{F}$ -FDG PET Activity in Large-Vessel Vasculitis

**TO THE EDITOR:** In a series of 95 large-vessel vasculitis patients investigated with  $^{18}\text{F}$ -FDG PET imaging, Dashora et al. recently tested the performance of qualitative (PET vascular activity score [PETVAS]) and semiquantitative (SUV and tissue-to-background ratio [TBR] relative to liver and blood activity) scoring methods (1). Regarding the latter methods, 9 territories were created in each patient by segmenting the aorta and branch arteries. A territory score was calculated by averaging the  $\text{SUV}_{\text{max}}$  assessed in each axial region of interest that was manually drawn across the territory, and a global summary,  $\text{SUV}_{\text{Artery}}$ , was then calculated by averaging all territory scores. Liver TBR ( $\text{TBR}_{\text{Liver}}$ ) and blood TBR ( $\text{TBR}_{\text{Blood}}$ ) were computed by dividing  $\text{SUV}_{\text{Artery}}$  by a mean liver and blood SUV, respectively. The performance of each metric was assessed in association with reader interpretation of vascular PET activity and with physician assessment of clinical disease activity, including the area under the receiver-operating-characteristic curve. Tables 2 and 3 by

Dashora reported the metrics performance against the 2 reference standards; this performance was poor–poor for  $\text{SUV}_{\text{Artery}}$  (area under receiver-operating-characteristic curve, 0.67–0.59) and good–poor for  $\text{TBR}_{\text{Liver}}$  and PETVAS (areas under receiver-operating-characteristic curve, 0.85–0.66 and 0.87–0.65, respectively) (1).  $\text{TBR}_{\text{Blood}}$  had slightly lower performance than  $\text{TBR}_{\text{Liver}}$ .

Since  $\text{TBR}_{\text{Liver}}$  involves  $\text{SUV}_{\text{Artery}}$ , which results from  $\text{SUV}_{\text{max}}$  averaging, we suggest that instead of using  $\text{SUV}_{\text{Artery}}$ , we use an averaged  $\text{SUV}_{\text{max}}$  obtained from  $N$  hottest voxels ( $\text{SUV}_{\text{max-N}}$ ) irrespective of their location within the 9 vascular territories (2). Both  $\text{SUV}_{\text{Artery}}$  and  $\text{SUV}_{\text{max-N}}$  take into consideration the heterogeneity of the vessel-wall uptake, but  $N$  can actually be much greater than the total number of regions of interest used by Dashora et al. for calculating  $\text{SUV}_{\text{Artery}}$ . Since the greater the  $N$  number, the lower the  $\text{SUV}_{\text{max-N}}$  variability, a more reliable  $\text{TBR}_{\text{Liver}}$  can thus be provided than with  $\text{SUV}_{\text{Artery}}$  (2,3). A previous assessment of treatment response in a Takayasu arteritis patient illustrates the possible magnitude of  $N$ , with  $\text{SUV}_{\text{max-N}}$  pooling  $N = 4,100$  and 515 voxels, corresponding to a hottest volume  $V = 100$  and 12.6 mL, respectively (4).  $\text{SUV}_{\text{max-V}}$  might be preferred to  $\text{SUV}_{\text{max-N}}$ , for the voxel volume depends on the PET system at a given center. For assessing response to treatment in a large-vessel vasculitis patient, it has been previously shown that  $V$  (or  $N$ ) should be set in the scan showing the lowest total  $^{18}\text{F}$ -FDG–positive volume, which is expected to be posttreatment one (4). For assessing the severity of large-vessel vasculitis inflammation as in the study of Dashora et al., we suggest that standard  $\text{SUV}_{\text{max-V}}$ -based  $\text{TBR}_{\text{Liver}}$  metrics might be relevant, using an arbitrary value of  $V$  defined by expert consensus (e.g., of 10  $\text{cm}^3$ ). Additionally, we suggest that the hottest volume  $V$  corresponding to a standard value of  $\text{SUV}_{\text{max-V}}$ -based  $\text{TBR}_{\text{Liver}}$  could also be investigated by Dashora et al. as a further metric. This  $\text{TBR}_{\text{Liver}}$  standard value should be greater than 1, as is consistent with the qualitative territory score of 3 used in PETVAS (arterial uptake > liver uptake). The standard might be set at 1.33 according to  $\text{TBR}_{\text{Liver}}$  data reported in Table 3 by Dashora et al. for physician assessment of clinical disease activity, that is, between the clinical-active range and the clinical-remission range ( $1.33 = 1.27 + 1.96 \times 0.03 \approx 1.46 - 1.96 \times 0.06$ ) (1). A similar line of argument provides a  $\text{TBR}_{\text{Blood}}$  standard value of 2.43 (from Table 3 of Dashora et al. (1)).

To conclude, we fully agree with the authors that qualitative metrics for assessing large-vessel vasculitis inflammation severity with  $^{18}\text{F}$ -FDG PET, such as PETVAS, are attractive in clinical practice because of ease of implementation and ease of interpretation. However, we believe that  $\text{SUV}_{\text{max-V}}$ -based  $\text{TBR}_{\text{Liver}}$  (or  $\text{SUV}_{\text{max-V}}$ -based  $\text{TBR}_{\text{Blood}}$ ) could also be used daily if manufacturers are encouraged to make  $\text{SUV}_{\text{max-V}}$  (or  $\text{SUV}_{\text{max-N}}$ ) easier to assess than currently (2–4).

## REFERENCES

1. Dashora HR, Rosenblum JS, Quinn KA, et al. Comparing semi-quantitative and qualitative methods of vascular FDG-PET activity measurement in large-vessel vasculitis. *J Nucl Med*. June 4, 2021 [Epub ahead of print].
2. Laffon E, Lamare F, de Clermont H, Burger IA, Marthan R. Variability of average SUV from several hottest voxels is lower than that of  $\text{SUV}_{\text{max}}$  and  $\text{SUV}_{\text{peak}}$ . *Eur Radiol*. 2014;24:1964–1970.
3. Laffon E, Burger IA, Lamare F, de Clermont H, Marthan R.  $\text{SUV}_{\text{peak}}$  performance in lung cancer: comparison to average SUV from the 40 hottest voxels. *J Nucl Med*. 2016; 57:85–88.
4. Caubet O, Meunier V, Marthan R, Laffon E. Early assessment of treatment response in Takayasu arteritis: an  $^{18}\text{F}$ -FDG PET procedure. *Clin Nucl Med*. 2016;41:743–745.

**Eric Laffon\***  
**Roger Marthan**

\*CHU de Bordeaux, University of Bordeaux, and INSERM  
U-1045, Bordeaux, France  
E-mail: elaffon@u-bordeaux.fr

Published online Sep. 2, 2021.  
DOI: 10.2967/jnumed.121.263060

## Reply: On Semiquantitative Methods for Assessing Vascular $^{18}\text{F}$ -FDG PET Activity in Large-Vessel Vasculitis

**REPLY:** We were pleased that discussion was brought forth by Laffon and Marthan because of our recent paper on quantitative and qualitative  $^{18}\text{F}$ -FDG PET for large-vessel vasculitis (LVV) (1). Indeed, we agree it could be revealing to attempt a measurement strategy that involves the appreciation of the hottest  $N$  number of voxels ( $\text{SUV}_{\text{max-}N}$ ) as proposed by the authors. If  $N$  is greater than the number of single  $\text{SUV}_{\text{max}}$  measurements from each region of interest drawn over the entire arterial tree,  $\text{SUV}_{\text{max-}N}$  could lead to an overall more reproducible value in addition to a potentially greater contribution of abnormal activity in regions of active vasculitis than in regions without inflammation.

Although specific methodology to quantify vascular inflammation will no doubt be tested and refined, we would like to emphasize our underlying thought process for the design of our quantitative methodology, with reference to how this and other strategies for quantitative PET might be used for LVV. We will organize our discussion around 3 questions: What can be deployed clinically? What is most useful in clinical trials? What are we trying to do with vascular imaging in LVV?

For clinical deployment (question 1), even with the recent advent of greater acceptance of  $^{18}\text{F}$ -FDG PET in clinical evaluation of inflammatory disease (2), we acknowledge that large-vessel vasculitis is a rare disease that many interpreting physicians will not encounter frequently. Our experience is that extensive familiarity and care are necessary to rigorously apply a complex quantitative strategy that involves contouring of the arteries as applied in this study, which did not have the advantage of intravenous contrast medium for guidance. Regardless of how the specific voxels are aggregated mathematically, the contouring itself is likely to be beyond the abilities of the standard medical professional in routine clinical practice. Hence, our introduction of a qualitative metric such as PETVAS (3), which is similar, but not identical, to the emerging use of an ordinal scoring system in lymphoma (4). We showed that PETVAS is a reasonable clinically deployable alternative to what we felt was an inevitable question from the community, which is “why not use SUVs?” Another compelling reason to not yet favor the use of metrics such as SUV in the clinic for LVV relates to the common misapplication of quantitative metrics from the literature for sensitivity and specificity in image interpretation. The performance characteristics of a quantitative metric are appropriately applied if images can be reproduced in a uniform format, which must be standardized across vendors with identical imaging characteristics that harmonize important features such as resolution, noise, voxel size, and postreconstruction filtering. Despite recent meaningful attempts (5), such a level of uniform standardization will likely not soon be achievable in clinical practice.

For clinical trials (question 2), we see a role for complementary advanced quantitative strategies as we and others have proposed.

Clinical trials more often involve multiple imaging time points of the same subject before and after a treatment or intervention, using the same imaging characteristics. Our project highlighted that both qualitative and quantitative methods are associated with clinical measures of disease activity, and both approaches could be used to facilitate discovery in research; however, qualitative approaches potentially offer more precision and reliability.

Regarding question 3, it may sound odd to ask “what are we actually trying to do?” As investigators conducting an ongoing, large prospective observational cohort study on LVV, we would like to emphasize that interpretation of  $^{18}\text{F}$ -FDG PET findings should be considered in the context of disease activity assessment across other domains.  $^{18}\text{F}$ -FDG PET is only 1 facet of the multidisciplinary approach needed to fully realize patient-specific treatment guidance. Comprehensive clinical, laboratory, and imaging assessment is often helpful to accurately assess disease activity and inform management decisions. The cumulative burden of vascular involvement does not always correlate with clinical outcomes. A small focal inflammatory lesion in a single artery may lead to severe vascular damage with disastrous consequences, whereas profound near pan-arterial intense inflammation may occur in an otherwise asymptomatic patient. To inform the details of a better qualitative or quantitative evaluation for individualized care with advanced methods proposed by our group or others, we must continue to define the complex associations between  $^{18}\text{F}$ -FDG PET findings and clinical outcomes in LVV. Controlled environments, such as randomized clinical trials, will go further to answer questions related to the combinatory use of qualitative and quantitative PET, as well as specifics for the production of each.

### DISCLOSURE

This study was supported by the Intramural Research Programs of the National Institute of Arthritis and Musculoskeletal and Skin Diseases (NIAMS). No other potential conflict of interest relevant to this article was reported.

### REFERENCES

1. Dashora HR, Rosenblum JS, Quinn KA, et al. Comparing semi-quantitative and qualitative methods of vascular FDG-PET activity measurement in large-vessel vasculitis. *J Nucl Med*. June 4, 2021 [Epub ahead of print].
2. Wahl RL, Dilsizian V, Palestro CJ. At last,  $^{18}\text{F}$ -FDG for inflammation and infection! *J Nucl Med*. 2021;62:1048–1049.
3. Grayson PC, Alehashemi S, Bagheri AA, et al.  $^{18}\text{F}$ -fluorodeoxyglucose–positron emission tomography as an imaging biomarker in a prospective, longitudinal cohort of patients with large vessel vasculitis. *Arthritis Rheumatol*. 2018;70:439–449.
4. Cheson BD, Fisher RI, Barrington SF, et al. Recommendations for initial evaluation, staging, and response assessment of Hodgkin and non-Hodgkin lymphoma: the Lugano classification. *J Clin Oncol*. 2014;32:3059–3068.
5. Slart RHJA, writing group; reviewer group; members of EANM Cardiovascular; members of EANM Infection & Inflammation; Members of Committees, SNMMI Cardiovascular; Members of Council, PET Interest Group; Members of ASNC; EANM Committee Coordinator. FDG-PET/CT(A) imaging in large vessel vasculitis and polymyalgia rheumatica: joint procedural recommendation of the EANM, SNMMI, and the PET Interest Group (PIG), and endorsed by the ASNC. *Eur J Nucl Med Mol Imaging*. 2018;45:1250–1269.

**Mark A. Ahlman**  
**Roberto Maass-Moreno**  
**Peter C. Grayson\***

\*National Institutes of Health  
Bethesda, Maryland  
E-mail: peter.grayson@nih.gov

Published online Oct. 28, 2021.  
DOI: 10.2967/jnumed.121.263158

The most powerful words you'll ever hear.

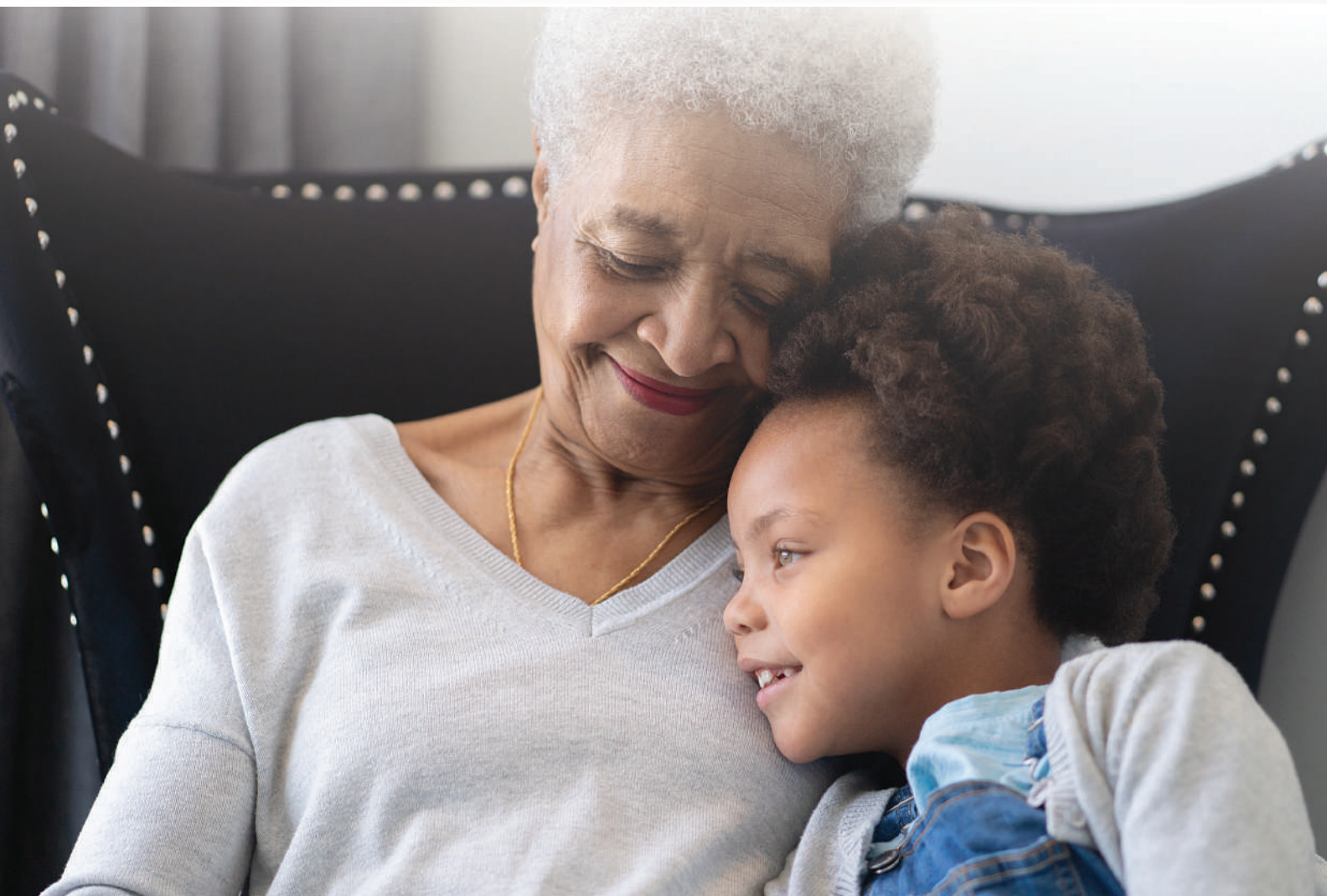
**“Thank You.”**

With your contribution, our profession can continue efforts leading to critical advances in cancer treatments and care.

The **Value Initiative Transformative Leadership Campaign** is the cornerstone for making these efforts a reality for patients of all ages.

**The world needs more “thank you’s.”**

Help improve the life of a patient. Lend your support today.



[www.snmmi.org/TransformativeLeadership](http://www.snmmi.org/TransformativeLeadership)

SNMMI is a 501 (c)(3) tax id 36-2496678. Your donation is tax deductible as per current IRS regulations. Please remember SNMMI in your estate plans.

**SNMMI** | Value Initiative  
**MI** | SOCIETY OF NUCLEAR MEDICINE & MOLECULAR IMAGING



# REACH EVEN GREATER HEIGHTS WITH CARDIAC PET IMAGING

**RUBY™** partners with you to help establish and grow your cardiac PET program today – and well into the future. Our RUBY-FILL® (Rubidium Rb 82 Generator) and RUBY Rubidium Elution System™ are supported by our comprehensive line of offerings, including financial modeling, reimbursement consultancy, education, and marketing expertise – as well as 24-hour customer assistance to ensure your growing PET practice runs smoothly and efficiently.

**Isn't it time to discover how far you can soar?**

Learn more at the **Jubilant Radiopharma booth**

#### INDICATION FOR USE:

RUBY-FILL is a closed system used to produce rubidium Rb 82 chloride injection for intravenous use. Rubidium Rb 82 chloride injection is a radioactive diagnostic agent indicated for Positron Emission Tomography (PET) imaging of the myocardium under rest or pharmacologic stress conditions to evaluate regional myocardial perfusion in adult patients with suspected or existing coronary artery disease. (1)

#### **WARNING: HIGH LEVEL RADIATION EXPOSURE WITH USE OF INCORRECT ELUENT AND FAILURE TO FOLLOW QUALITY CONTROL TESTING PROCEDURE**

Please see full prescribing information for complete boxed warning

##### **High Level Radiation Exposure with Use of Incorrect Eluent**

Using the incorrect eluent can cause high Strontium (Sr 82) and (Sr 85) breakthrough levels (5.1)

- Use only additive-free 0.9% Sodium Chloride Injection USP to elute the generator (2.5)
- Immediately stop the patient infusion and discontinue the use of the affected RUBY-FILL generator if the incorrect solution is used to elute the generator (4)
- Evaluate the patient's radiation absorbed dose and monitor for the effects of radiation to critical organs such as bone marrow (2.9)

##### **Excess Radiation Exposure with Failure to Follow the Quality Control Testing Procedure**

Excess radiation exposure occurs when the levels of Sr 82 or Sr 85 in the Rubidium Rb 82 Chloride injection exceed specified limits (5.2)

- Strictly adhere to the generator quality control testing procedure (2.6)
- Stop using the generator if it reaches any of its Expiration Limit (2.7)

The risk information provided here is not comprehensive. Please visit [RUBY-FILL.com](http://RUBY-FILL.com) for full Prescribing Information including the **BOXED WARNING**. You are encouraged to report negative side effects of prescription drugs to the FDA. Visit [www.fda.gov/Safety/MedWatch](http://www.fda.gov/Safety/MedWatch) or call 1-800-FDA-1088.

